Geological Storage of Carbon Dioxide in the UK: Opportunities and Risks

Thomas Oakley Lynch

Submitted in accordance with the requirements for the degree of Doctor of Philosophy

The University of Leeds

School of Chemical and Process Engineering

September 2014

The candidate confirms that the work submitted is his own and that appropriate credit has been given where reference has been made to the work of others.

Acknowledgements

This work was carried out as part of the Doctoral Training Centre in Low Carbon Technologies funded by the EPSRC and I would like to gratefully acknowledge this funding.

Firstly, I would like to thank my supervisors, Prof. Quentin Fisher and Dr. Doug Angus for their invaluable guidance and direction throughout my project, practical assistance with many aspects of my work, and feedback that they have provided on this thesis – much of this work wouldn't have been possible without their support.

I would also like to thank Piroska Lorinczi for assistance and guidance with fluid flow simulation problems, general guidance and advice on my project and for helping me during the installation and testing of the coupled software and Tempest.

Special thanks must also go to Rockfield Software Limited for use of their finite element codes, constitutive models and coupled software codes. Specifically I would like to thank Martin Dutko, Jose Segura, Dan Roberts, Matthew Profit, Mike Hudson, Jian Yu, Melanie Armstrong, Bruce Jones and John Cain for their advice, training and technical assistance with all aspects of Elfen software.

Thanks must also go to Roxar for use of Tempest reservoir simulation software and the technical support provided enable me run the coupled simulations. I would specifically like to thank Taha Taha for my training and always being available to answer questions on the software.

I would also like to thank all the staff and my colleagues and friends from ERI and the Low Carbon Technologies Doctoral Training Centre. I would like to thank Paul Williams, James McKay, David Haynes, Heather Strachan and Rachael Brown for their support in my day-to-day work in the department and for the many opportunities I have had throughout my studies. I would also especially like to thank all my friends on the DTC who are too numerous to mention individually, all of you have been there supporting me whether it's help with work, or just an excuse to go for pint, you have made my years at Leeds some of the most memorable and enjoyable.

Finally and most importantly, thank you to all my closest friends and my family; I could not have finished without your moral (and financial!) support. Mum, thanks for the help, especially through the last year; I would not have been able to complete it without your assistance. Lorraine thanks for all your help, love and support throughout my PhD, and of course for your superior grammatical knowledge.

Abstract

Climate change caused by greenhouse gas emissions from anthropogenic sources, primarily from fossil fuel combustion, is a major global challenge that threatens many serious adverse impacts, including sea level rise, food and water scarcity, extreme weather events and species extinction. Curbing global emissions from fossil fuels has become a major and urgent priority. Carbon Capture and Storage (CCS) has been proposed as a method to capture greenhouse gas (GHG) emissions from large point source fossil fuel combustion and store these emissions away from the atmosphere to reduce the impact on the climate. CCS involves capturing the predominant GHG produced in fossil fuel combustion, CO_2, at the point source and transporting it to a location where is can be stored for thousands of years to limit its impact on the climate. Geological storage is considered to be the most advanced and realistic option for CO_2 storage, and is the focus of this thesis.

The aim of this thesis is to assess the risks and opportunities for CO_2 storage in the UK offshore region, where the majority of UK CO_2 storage capacity is expected to exist in saline aquifers and depleted hydrocarbon reservoirs. A review of the technical considerations for geological CO_2 storage is presented and the potential storage capacities and risks to secure storage in the UK are identified., Fluid flow simulation and coupled fluid flow-geomechanical modelling are used to assess several aspects of storage, based on the assessment of the potential risks for storage in the UK. These include assessment of current capacity estimates for CO_2 injection into the largest potential source of UK storage capacity the Bunter Saline Aquifer; opportunities for brine extraction to increase capacity in saline aquifers and the potential for a reduction in capacity and risk of leakage through fracture pressure hysteresis in depleted hydrocarbon reservoirs.

Three key results are identified from the work. Firstly, significantly lower capacities are modelled for the Bunter Aquifer, compared to both static estimates and more complex models in the literature. This is due to the potential variability in parameters, such as the compressibility and fracture pressure, which control capacity. Estimates for the capacity in the Bunter from the modelling range between 3.1 and 8.7 Gt CO_2 which corresponds to between 20 and 56 years of storage capacity for the UK, this is compared to an initial estimate of 90 years of storage capacity from static estimates. Fracture pressure estimation is uncertain and fracture pressure is a significant control on capacity in the generic modelling it is shown to reduce capacity by 32 – 60% with a 20% reduction in fracture pressure. The most conservative fracture pressure assumption for the modelled capacities in the Bunter Aquifer would indicate a reduced capacity as low as 2.5 Gt CO_2 . Potential variability in the fracture pressure is the second major finding of this work and is intrinsically related to variability in capacity. Coupled fluid flow geomechanical modelling indicates that the fracture pressure in depleted hydrocarbon reservoirs with similar stress conditions and material parameters to those found in the UK North Sea could be up to 19% lower during injection compared to the depletion fracture pressures. This is without including the effect of thermally induced tensile stresses developed due to the injection of cold CO_2 which may reduce fracture pressures further. Finally, capacity modelling in the Bunter Aquifer has also identified a potential legacy risk for CO_2 storage in a large aquifer such as the Bunter. The peak fracture pressure risk is not observed in the model until 6 – 136 years after injection has stopped, and occurs great distances from the injection point. This poses questions as to the methodology for monitoring this risk, the potential remediation options and the impact on other activities within the aquifer.

The research highlights several areas where further investigation are essential for constraining CO_2 storage capacity and leakage risks, with the primary uncertainty relating to the quantification of fracture pressure in both saline aquifers and depleted hydrocarbon reservoirs.

Table of Contents

Acknowledgements ..... **iv**

Abstract ..... **v**

Table of Contents ..... **vi**

Table of Figures ..... **x**

1 Introduction **2**

1.1 Climate Change 2

1.2 Fossil Fuels and Climate Change 2

1.3 Carbon Capture and Storage 2

1.4 Thesis Outline 5

2 CO_2 Storage, Risks and Uncertainty **6**

2.1 Geological Storage - Principles 6

2.2 Geological Storage Options I 7

2.3 Subsurface Flow Properties and Trapping Mechanisms 9

2.3.1 Reservoir and Fluid Properties 9

2.3.2 Reservoir Compressibility 9

2.3.3 Multiphase flow in porous media 12

2.3.4 Trapping Mechanisms 14

2.3.5 Structural Trapping and Cap Rocks 16

2.3.6 Residual Trapping 18

2.3.7 Geological Variability 18

2.3.8 Summary 20

2.4 Subsurface Storage Conditions 20

2.4.1 Subsurface Temperature and Pressure 20

2.4.2 Deformation and Stress 22

2.4.3 Deformation Mechanisms 26

2.4.4 Deformation in Geological Materials 34

2.4.5 Faults and Fluid Flow 38

2.5 Reservoir Geomechanics 43

2.5.1 Stress Path Parameters 44

2.5.2 Geomechanical Modelling 46

2.6 Storage Options II 50

2.6.1 Hydrocarbon reservoirs 50

2.6.2 Saline Aquifers 52

2.7 Monitoring and Seismic Data 54
2.7.1 Seismic Parameters 57
2.8 Risk and Uncertainty 60
2.9 Risk Identification and Research Opportunities 64
2.9.1 Storage Capacity and Injectivity – UK Offshore 64
2.9.2 Fracture Pressure and Stress Path Hysteresis – Leakage Potential and Capacity Reduction 74
2.9.3 Capabilities and Resources 79
2.9.4 Primary Goals 80
2.9.5 Secondary Goals 81
2.10 Conclusions 82

3 UK Storage Potential – Bunter Saline Aquifer 85
3.1 Brine Extraction – Generic Model 86
3.1.1 Model Set-up 86
3.1.2 Geological Model 87
3.1.3 Fluid Properties and Modelling Parameters 88
3.1.4 Results 89
3.2 Bunter Large Scale Model 94
3.2.1 Model Setup 94
3.2.2 Geological Model 95
3.2.3 Fluid Properties and Modelling Parameters 97
3.2.4 Results 99
3.3 Discussion 144
3.3.1 Pressure Cell Model and Brine Extraction 144
3.3.2 Large Scale Bunter Model 152
3.3.3 Capacity Modelling Approaches in the Bunter Aquifer 163
3.3.4 Fracture Pressure Uncertainty and Evolution 169
3.4 Conclusions 170
3.4.1 Pressure Cell Model and Brine Extraction 170
3.4.2 Large Scale Bunter Model 172
3.4.3 Capacity Modelling Approaches in the Bunter Aquifer 176
3.4.4 Fracture Pressure Uncertainty and Evolution 177

4 Modelling Stress Path and Fracture Pressure Hysteresis 178
4.1 Introduction 178
4.2 Model Set-up 179
4.2.1 Model Geometry 179
4.2.2 Constitutive Model 180

4.2.3 Geological Model and Material Properties 180
4.2.4 Modelling Parameters 188
4.3 Results 190
4.3.1 High Stiffness Case 190
4.3.2 Low Stiffness Case 215
4.3.3 Initial Stress Ratio Cases 225
4.3.4 Maximised Stiffness 240
4.3.5 Reservoir Poisson's Ratio 241
4.3.6 Other Material Parameters 244
4.3.7 Geometric Effects 245
4.3.8 Overburden Parameters and Stress State 252
4.3.9 Fault Movement and Failure Potential 257
4.3.10 Coupled and Non-Coupled Flow Simulation 273
4.3.11 Seismic Data 279
4.4 Discussion 289
4.4.1 Stress Arching and Stress Changes in the Model 289
4.4.2 Fracture Pressure Hysteresis 305
4.4.3 Fault Behaviour 310
4.4.4 Fluid Flow Simulation 312
4.4.5 Seismic Data 314
4.5 Conclusions 316
4.5.1 Stress Changes and Stress Arching 316
4.5.2 Fracture Pressure Hysteresis 321
4.5.3 Fault Behaviour 322
4.5.4 Fluid Flow Simulation 323
4.5.5 Seismic Data 324

5 Conclusions and Further Work 325
5.1 Conclusions 325
5.1.1 CO_2 Storage, Risks, and Uncertainty 325
5.1.2 UK Storage Potential – Bunter Saline Aquifer 326
5.1.3 Modelling Stress Path and Fracture Pressure Hysteresis 328
5.2 Further Work 330
5.2.1 UK Storage Potential – Bunter Saline Aquifer 330
5.2.2 Modelling Stress Path and Fracture Pressure Hysteresis 331
5.3 Summary of Findings 332

References 334

A. Appendix 347

B. Appendix 353

Table of Figures

Figure 1.1 – From (Haszeldine 2009), idealised image of the full chain of carbon capture transport and storage technologies. In this case, the CO_2 is captured at a power plant, transported by pipeline and stored in geological formations. 4
Figure 2.1 – The density of CO_2 with depth below ground level in geological storage (from Holloway 2008). 7
Figure 2.2 – Schematic diagram of the main locations proposed for geological storage of CO_2, blue represents CO_2, red represents hydrocarbons, black represent coal beds (from CO_2CRC 2011). 8
Figure 2.3 – Formation compressibility for a range of sandstones collated from the literature (from Yale et al. 1993). 11
Figure 2.4 – Compiled database of converted formation compressibility values at initial reservoir stress conditions (IRSC) from Crawford et al. (2011). Colours represent geographical location of values, red – Nigeria, blue – Gulf of Mexico, green – Angola, pink – North Sea, purple – Alaska, orange – Chad, yellow – Australia, South America and Germany. The figure is overlaid with type curves of compressibilities corrected from hydrostatic tests from Newman (1973), where ν is Poisson's ratio and k_o is coefficient of earth pressure at rest. 12
Figure 2.5 – Relative permeability curves for a CO_2-brine system (Tueckmantel 2010)..... 14
Figure 2.6 – Trapping mechanisms in geological storage. The plot compares the contribution to CO_2 trapping of each mechanism against time (IPCC 2005). 15
Figure 2.7 - Examples of structural and stratigraphic traps for oil and gas reservoirs (from ACEP 2009), the figures shows different examples of the formation of traps, in these examples an enclosed volume is formed in three dimensions, although shallow dipping beds that provide slow migration times may also be used to trap CO_2. 16
Figure 2.8 – Diagram illustrating the concept of contact angle θ, if the phase is non-wetting on the substrate the angle θ will be low, and if it is wetting the angle, θ will be high. Theoretically, a fully non-wetting phase angle θ can be zero, and a fully wetting angle θ 180°. 17
Figure 2.9 – Diagram of residual trapping in the pore spaces of a reservoir rock, the flow of CO_2 moves through the rock, and the trailing edge is trapped by the ingress of displaced water back in to the pore spaces (CO_2CRC 2010). 18
Figure 2.10 – Plot demonstrating the concept of pore pressure deviation with depth. Hydrostatic represents the pressure corresponding to a column of water with depth, lithostatic the pressure of the overburden with depth, and the regions of over and underpressure related to the hydrostatic pressure (Swarbrick and Osborne 1998). 21
Figure 2.11 – The effect of pore pressure on failure mode of rocks from (from Fossen 2010), P_f represents the pore fluid pressure, σ_1 and σ_3 are the maximum and minimum principal stress, the red line is the failure envelope. (a) illustrates shear failure, where the Mohr circle touches the failure envelope and the minimum principle stress is positive. (b) illustrates

tensile fracture formation when the Mohr circle touches the failure envelope and the minimum principal stress is negative. 22
Figure 2.12 – General stress strain graph for an elastic-plastic material, showing elastic strain 1-3, plastic strain hardening 3-4 and possible further stress-strain paths. 23
Figure 2.13 – Mohr circle representation of the Mohr-Coulomb yield surface in normal-shear stress space. 27
Figure 2.14 – Generic description of a yield surface in p-q space showing shear, compaction and tensile failure/yield regions based on (Fjær et al. 2008) 28
Figure 2.15 – Compression plane or v-p' plot of specific volume with p', describing permanent plastic deformation during compaction/consolidation and the elastic unloading-reloading response based on (Wood 1990). 29
Figure 2.16 – Graphical representation of the response of soils to shearing under the critical state theory. Peak strength of the dense material is reached when maximum interlocking resistance is mobilised, and then strength reduces as interlocking is overcome, this peak strength is represented by the steepest gradient on the volumetric/shear strain graph. The loose material gradually mobilises peak strength as volume is reduced and the material approaches critical state. 30
Figure 2.17 – Slope of the critical state line at the apex of a series of yield surfaces adapted from Wood (1990). 31
Figure 2.18 – v-log(p') plot of isotropic normal consolidation line, critical state line and unloading-reloading line (Wood 1990) 32
Figure 2.19 – Hvorslev and Roscoe surfaces and the critical state and isotropic consolidation line in p'-q-v space (left) and the projection of the surface at a particular p_c on the p'-q plane (right) (Fjær et al. 2008) 33
Figure 2.20 – Cam Clay associated plastic potential surface and yield surface showing plastic strain increment vectors for different stress states. Adapted from Wood (1990). 34
Figure 2.21 – Failure modes of rock cylinders under axi-symmetric loading, a) tension fracture, b) extension fracture, c) dilational/hybrid extension shear fracture, d) shear fracture, e) multi-shear cataclasis (from Mandl 2005). In this case σ'_c is confining stress. 35
Figure 2.22 – Transition from brittle to ductile behaviour in triaxial compression and extension tests, stress-strain curves show variability in behaviour (ruled sections) and transition between cases 3, 4 and 5, this represents the brittle-ductile transition zone, characterised by multiple deformation bands. (Diagram from Griggs and Handin 1960). 36
Figure 2.23 – Plot of porosity (black line) and p/p* (grey line), for an arenite with initial 30% porosity for (a) fine grained, (b) medium grained, (c) coarse grained (Fisher et al. 2007). 38
Figure 2.24 – Schematic representation of fault seal mechanisms from (from Yielding et al. 2010). Juxtaposition seal shows juxtaposition of a permeable sand layer against impermeable shale, forming a seal that is effectively as good as a caprock at the side of the reservoir. Fault-rock seal illustrates that the properties of the rocks in the faults are inhibiting movement of fluids across the fault between two sand horizons. Fault reactivation shows

fluid movement due to reactivation of a fault, which causes the fault to become a permeable conduit. 39
Figure 2.25 – Example of a juxtaposition diagram, the colour contours show the depth and fault throw (displacement) at which various lithology interactions occur, this can be used to identify leakage points (from Knipe 1997). 40
Figure 2.26 – Fault rock clay content and permeabilities of fault rocks found in the North Sea (from Fisher and Knipe 2001). 42
Figure 2.27 – Normal effective stress vs. shear stress plot of the effect of stress path parameters on the Mohr circle plot from (from Segura et al. 2011). 45
Figure 2.28 – Flow chart for an explicit coupling method from Minkoff et al. (2004), the chart shows the exchange of pore pressure to the geomechanics simulator, and porosity and permeability to the flow simulator for each time step. 48
Figure 2.29 – Water drive in an oil reservoir, if the water forces out the oil it means that it is connected to a larger body of water and could be displaced for CO_2 storage (Schlumberger 2010b). 52
Figure 2.30 – Saline aquifer system showing open, closed and semi-closed systems, (from Zhou et al. 2008). 53
Figure 2.31 – Map of UK sedimentary basins and the distribution of oil, gas and condensate fields. The Bristol and St Georges Channel Basins are not included, but these do not have significant storage capacity (from Holloway et al. 2006a). 66
Figure 2.32 – Illustration of pressure cell concept and no flow boundary between adjacent injecting wells. Only the area represented by the red square is actually modelled and represents 1 quarter of the injection well capacity. The results of the model can then be scaled up using multiplication. 68
Figure 2.33 – Storage capacity of the Bunter aquifer against well spacing (left) and number of wells (right) for pressure cell modelling. The well spacing is inversely proportional to the number of wells (from Lynch 2010). 69
Figure 2.34 – Map of the Bunter Sandstone distribution and model boundary of Noy et al. (2012) the extent of the model is approximately centred around latitude 54°10'01"N and 1°49'28"E. 72
Figure 2.35 – CO_2 pressure relief operation, brine extracted from the aquifer for pressure relief is treated to produce a potable water and waste brine (Neal et al. 2011). 72
Figure 2.36 – Pore pressure –stress coupling principle from Hillis (2001) figure (a) shows the 'classic' case where pore-pressure is decoupled from total stress, (b) shows pore pressure coupling with depletion γ_h = 0.7, and (c) for overpressure (proxy for re-pressurisation) where γ_h = 0.7 also. 76
Figure 2.37 – Schematic diagram of the behaviour observed in a North Sea oil field undergoing secondary recovery from Santarelli et al. (1998). The diagram shows a hysteretic stress path and lower fracture pressures during re-pressurisation than may be predicted assuming the pore pressure-stress coupling assumption. 77

Figure 2.38 – Stress transfer in the reservoir-cap rock system, a reduction in the minimum horizontal stress in the caprock resulting from a corresponding increase in the reservoir. Potential for fracturing is increased in the caprock, which could lead to leakage pathways (from IEAGHG 2011b). 78
Figure 3.1 – Pressure cell model with producing well and injecting well at opposite corners (vertical scale exaggerated). 86
Figure 3.2 – Diagram of the theoretical layout of the pressure cell model with brine producers implemented into the model. 87
Figure 3.3 – Cumulative storage capacity of base case models without brine production for different sizes of model at different fracture pressures over the full injection period. The flattened sections indicate where injection has been reduced or stopped due the pressure control on the well. 90
Figure 3.4 – Pressure distribution (bar) at the end of injection for the smallest and largest cell sizes. 91
Figure 3.5 – Storage capacity including brine production at 500 m^3/day and 4000 m^3/day, compared against cases with no brine production for a fracture pressure limit of 212 bar. ..92
Figure 3.6 - Storage capacity including brine production at 500 m^3/day and 4000 m^3/day, compared against cases with no brine production for a fracture pressure limit of 264 bar. ..93
Figure 3.7 – Plan view comparison of vertically non-refined (left) and vertically refined (right) grids for the analysis of plume spreading. The figure shows that the grid refined vertically (in the plane of the section) shows much wider plume spreading than the unrefined model. 94
Figure 3.8 – Tempest simulation model for the Bunter aquifer derived from the structural data provided in Noy et al. (2012), depths are in metres. The boundary of the model corresponds to that shown in Figure 2.34. 95
Figure 3.9 – Simulation model aquifer locations in the Tempest flow model to allow non-sealing marginal boundaries to be added to the model. 97
Figure 3.10 – CO_2 injection rates and totals for the base case model and two additional scenarios including a pressure control on the injection well (BHPT), and an increased flow rate to the maximum permissible through the well with a BHPT (BHPT max. flow). 100
Figure 3.11 – Water outflow rate and total volume from the seabed outcrop for the base case and the maximum injection rate cases. 101
Figure 3.12 – Map of the difference between the lithostatic pressure and pore fluid pressure in the top layer of the aquifer model after 53 years of the model run. 102
Figure 3.13 – CO_2 injection rate and injection capacity for the model with a reduced global permeability of 20 mD. 103
Figure 3.14 – Water outflow rates from the seabed outcrop for scenarios with the base-case flow rate and K_v/K_h ratios between 1 and 0.001. 104
Figure 3.15 - Water outflow rates from the seabed outcrop for scenarios with the maximised flow rate and K_v/K_h ratios between 1 and 0.001. 105
Figure 3.16 – CO_2 injection rate and CO_2 injection capacity for the single well scenario with maximised injection rate with K_v/K_h ratio. 106

Figure 3.17 – Extent of CO_2 saturation plume in cases with different K_v/K_h ratio, ratio decreases from 0.1 top left, to 0.01 top right, to 0.001 bottom right. 107
Figure 3.18 – Vertically exaggerated cross section through CO_2 saturation plume showing K_v/K_h ratio of 0.001 case at the top and K_v/K_h ratio 0.1 case at the bottom. Restriction in vertical permeability means that plume is more distributed throughout reservoir thickness in 0.001 case. 108
Figure 3.19 – Comparison of water outflow from the seabed outcrop for different compressibility cases using the base case flow rate and single well. 109
Figure 3.20 – Injection rates for the compressibility scenarios with maximised injection rates for the single well case. 110
Figure 3.21 – Peak injection rates and total injected CO_2 volume with formation compressibility for the single well maximised injection case. 110
Figure 3.22 – Water outflow rates from the seabed outcrop for the compressibility scenarios with maximised injection rates with a single injection well. 111
Figure 3.23 - Well locations for the 12 well model, with a depth contour map of the model, the scale is in meters. 112
Figure 3.24 – Graphs of CO_2 injection rate and cumulative CO_2 injection total for the base case and maximised injection case for the model with 12 injection wells. 114
Figure 3.25 – Graph of water outflow from the seabed outcrop for base case and maximised injection rate case for the model with 12 injection wells. 115
Figure 3.26 – Plots of the CO_2 saturation plumes for the base case and maximised flow cases for the model with 12 injection wells showing plume spreading after injection is stopped (2050). 116
Figure 3.27 – Plot of the 75% lithostatic pressure limit minus the current pore pressure at 50 years for the 12 well model with maximised injection. The plot represents how close regions of the model are to breaching the pressure limit. 117
Figure 3.28 – Injection rate for all 12 well scenarios (excluding base case) with no modification to boundary conditions. 118
Figure 3.29 – Total CO_2 injection for all 12 well scenarios with no modification to boundary conditions. 119
Figure 3.30 – Brine outflow rate at the seabed outcrop for all 12 well scenarios (excluding base case) with no modification to boundary conditions. 121
Figure 3.31 - Brine outflow rate at the seabed outcrop for all 12 well scenarios (excluding base case) with no modification to boundary conditions. 121
Figure 3.32 – Pressure changes in the reservoir 20 years after the start of injection for the k_v/k_h = 0.001 (top) and 20 mD (bottom) case for the 12 well scenario. 122
Figure 3.33 – Total CO_2 injection for all 12 well scenarios with no seabed outcrop compared against the same cases with the seabed outcrop. 124
Figure 3.34 – Total CO_2 injection for 12 well scenarios with different boundary condition scenarios. 126

Figure 3.35 – Brine outflow rates for the 12 well scenario with fully open boundaries in the western and north-western boundary and the seabed outcrop open. 127
Figure 3.36 – Total brine outflow for the 12 well model with the scenarios with and without marginal aquifers implemented. 128
Figure 3.37 – Pressure increase in bars in the model with all marginal aquifers and seabed outcrop implemented. The red arrow indicates the SE-NW structural highs that are connected up-dip to the marginal NW aquifer. 129
Figure 3.38 – Well locations for the 24 well model, with a depth contour map of the model, the scale is in meters. 131
Figure 3.39 - Total CO_2 injection for 24 well scenarios with varying boundary conditions and pore volume and flow properties. 132
Figure 3.40 - Brine outflow rates for the 24 well scenario with for different scenarios. 133
Figure 3.41 – Total CO_2 injection capacity for all modelled cases with varying well deployment density. 134
Figure 3.42 – Total brine output at 100 years for all modelled cases with varying well deployment density. 136
Figure 3.43 – Storage efficiencies for all modelled cases with varying well deployment density. 137
Figure 3.44 – Curve fitting for the standard model, based on the 1, 12 and 24 well runs, showing the modelled capacity using up to 200 wells. 138
Figure 3.45 – Graph of total CO_2 injection capacity against the number of wells required to achieve capacity using extrapolated data from the models for all scenarios. 139
Figure 3.46 – Comparison of 20 mD and standard case with 24 wells, the red circle indicates a zone of pressure build-up interference between 3 of the wells in the northern area of the model, reducing the efficiency of the injection. 140
Figure 3.47 – Graph of modelled CO_2 storage cost with total CO_2 storage capacity for the standard model case, with data extrapolated to 200 wells. 140
Figure 3.48 - Graph of modelled CO_2 storage cost with total CO_2 storage capacity for all cases, with data extrapolated to 24 wells for well costs of £100 million per well. 141
Figure 3.49 - Graph of modelled CO_2 storage cost with total CO_2 storage capacity for all cases, with data extrapolated to 200 wells for well costs of £100 million per well. 142
Figure 3.50 – Cost of CO_2 storage per tonne with varying compressibility extrapolated for different well penetrations. 143
Figure 3.51 – Total storage capacity with varying compressibility extrapolated for different well penetrations. 143
Figure 3.52 – Graph of storage capacity with brine production rate for the low fracture pressure case, dotted line shows maximum capacity of each cell size. 147
Figure 3.53 - Graph of storage capacity with brine production rate for the high fracture pressure case, dotted line shows maximum capacity of each cell size. 148

Figure 3.54 – Graph of storage capacity with number wells required for the low fracture pressure case. Dotted line represents intersection of the curves for 4000 m^3/day brine production and no production cases, intersection at 93 wells, 4.95 Gt CO_2 150
Figure 3.55 - Graph of storage capacity with number wells required for the high fracture pressure case. Dotted line represents intersection of the curves for 4000 m^3/day brine production and no production cases, intersection at 103 wells, 10.8 Gt CO_2 151
Figure 3.56 – Cross section of structure adjacent to seabed outcrop in the Bunter aquifer from Dingwall et al. (2013) showing hypothesised existence of halite made ground and cement dissolution due to influx of low salinity brines. 161
Figure 3.57 – a) Techno-economic resource capacity pyramid and b) data resolution and assessment scale graph from Bachu et al. (2007). 169
Figure 4.1 – Geometry of generic faulted model, a) shows the full model with the outer finite element mesh discretised with rectangular grids representing the overburden, and the central reservoir grid showing a pressure contour, b) shows three sections through the model with dimensions, and c) shows the geometry of the 2 faults. 179
Figure 4.2 – State boundary surface and critical state line for the shale overburden and sandstone reservoir at a pre-consolidation pressure of 1 MPa. The dashed line represents the critical state line. 182
Figure 4.3 – Young's modulus as a function of porosity using empirical relationship in Elfen for the shale and sandstone. 183
Figure 4.4 – Porosity depth curve for the shale and sandstone, data provided by Rockfield Software Ltd. 184
Figure 4.5 – Young's modulus curve with depth for the shale and sandstone. 184
Figure 4.6 – Variation of pre-consolidation pressure (pc) and tensile strength (pt) with plastic volumetric strain for the shale and sandstone 185
Figure 4.7 – Distribution of initial plastic volumetric strain with depth for the shale and sandstone. 186
Figure 4.8 – Initial pre consolidation pressure (p_c) and tensile strength (p_t) intercepts for the shale and sandstone. 186
Figure 4.9 - Plot of SR3 empirical correlations and theoretical models from the literature for Young's modulus and porosity. 187
Figure 4.10 – Pore pressure at the well for the base case model for high and low friction cases for both non-sealing (high TM) and sealing (low TM) cases. 192
Figure 4.11 – Section through high transmissibility (non-sealing fault) case showing pressure equilibration in the model after shut-in. This leads to a pressure increase at the well, observed on the pore pressure profile. 193
Figure 4.12 – p'-q plot for non-sealing fault (high TM) cases for the base case model at the well, arrows demonstrate direction of stress path going from the start of depletion to the end of injection. The chart shows the elastic stage of depletion from point 1 to 3, transitional plastic stage from point 2 to 3, continued plastic depletion from point 3 to 4, and final elastic

injection from point 4 to 5. Both lines plot together on the figure and so are indistinguishable. 194
Figure 4.13 – Schematic diagram showing the stress differences between the yield surface and the stress path required to calculate the fracture pressure hysteresis parameters. 195
Figure 4.14 – Mohr circle diagram for the non-sealing low friction faults case with yield surface transformed into s'-t parameters and s'-t stress path plot. 196
Figure 4.15 – Contour plot of σ_1' in the non-sealing low fault friction case, showing initial stage, end of depletion and end of injection. Figure shows X plane section through centre of the model at the location of the well, with well injection compartment, fault and part of the central compartment shown. Compressive stresses are negative in Elfen. 198
Figure 4.16 - Contour plot of σ_3' in the non-sealing low fault friction case showing initial stage, end of depletion and end of injection. Figure shows X plane section through centre of the model at the location of the well, with well injection compartment, fault and part of the central compartment shown. Compressive stresses are negative in Elfen. 199
Figure 4.17 – Contour plot of the change in σ_1 during depletion and injection for the X plane section through the reservoir at the well. 200
Figure 4.18 - Contour plot of the change in σ_3 during depletion and injection for the X plane section through the reservoir at the well. 201
Figure 4.19 – Contour plot of displacement in the vertical direction for the central X plane section through the injection compartment and centre of model. The change in displacement during depletion and injection is shown, with a refined scale plot for the injection stage (bottom). Positive displacement represents movement upwards. 202
Figure 4.20 - Contour plot of displacement in the horizontal direction for central X plane section through the injection compartment and centre of model. Horizontal displacement is in the plane of the section with positive displacement left to right. 203
Figure 4.21 – Contour plot of strain in the X-direction (horizontal in plane of section) during the elastic and plastic depletion phase for the central X plane section through the model. 205
Figure 4.22 - Contour plot of strain in the X-direction (horizontal in plane of section) during the injection phase for the central X plane section through the model. 205
Figure 4.23 - Contour plot of strain in the Z-direction (vertical in plane of section) during the elastic and plastic depletion phase. The reservoir is excluded to emphasise strain in the overburden for the central X plane section through the model. 206
Figure 4.24 - Contour plot of strain in the Z-direction (vertical in plane of section) during the depletion phase for the central X plane section through the model. The reservoir is included to show the significant changes in the reservoir compared to the overburden. 207
Figure 4.25 - Contour plot of strain in the Z-direction (vertical in plane of section) during the elastic injection phase for the central X plane section through the model. 207
Figure 4.26 – Comparison of p'-q plots for sealing fault 'low TM' cases and non-sealing fault 'high TM' cases. The arrows on the Low TM High Friction case indicate the direction of all the stress paths from start of depletion to end of injection. The High TM and Low TM high and low friction cases follow identical stress paths to each other. 209

Figure 4.27 - Mohr circle diagram for the sealing low friction faults case with yield surface transformed into s'-t parameters and s'-t stress path plot. 210
Figure 4.28 – Contour plots of effective stress in the sealing low fault friction case for the high stiffness base case at the end of the injection period for the central X plane section through the model. 211
Figure 4.29 – Contour plot of the change in σ_1 in the overburden for the non-sealing case during the depletion and injection stages for the central X plane section through the model. 212
Figure 4.30 - Contour plot of the change in σ_1 in the overburden for the non-sealing case during the depletion and injection stages for the central X plane section through the model. 213
Figure 4.31 – Contour plot of Z displacement in the sealing low fault friction case for the high stiffness base case at the end of injection for the central X plane section through the model. Positive Z displacement represents upwards movement. 214
Figure 4.32 - Contour plot of X displacement in the sealing low fault friction case for the high stiffness base case at the end of injection for the central X plane section through the model. Positive X displacement represents movement left to right. 215
Figure 4.33 – Plot of p'-q stress paths for low stiffness cases with high stiffness non-sealing low friction case for comparison. 216
Figure 4.34 – Mohr circle and s'-t plot for non-sealing low friction fault low stiffness case. 217
Figure 4.35 – Contour plot of effective stress in the reservoir and overburden for the low stiffness case with non-sealing low friction fault for the central X plane section through the model. 218
Figure 4.36 – Contour plot of a section through the reservoir at the well showing change in σ_1 during depletion and injection for the low stiffness case for the central X plane section through the model. 219
Figure 4.37 – Contour plot of a section through the reservoir at the well showing change in σ_3 during depletion and injection for the low stiffness case for the central X plane section through the model. 220
Figure 4.38 – High resolution contour plot of a section through the reservoir at the well showing change in σ_3 during injection for the low stiffness case for the central X plane section through the model. 221
Figure 4.39 – Contour plot of displacement in the vertical direction for a section through the injection compartment for the low stiffness case for the central X plane section through the model. Positive displacement represents movement upwards. 222
Figure 4.40 - Contour plot of displacement in the horizontal direction for a section through the injection compartment for the low stiffness case for the central X plane section through the model. Horizontal displacement is in the plane of the section with positive displacement left to right. 223

Figure 4.41 – Contour plot of strain in the X-direction (horizontal in plane of section) during the elastic and plastic depletion phase for the low stiffness reservoir for the central X plane section through the model. 224
Figure 4.42 - Contour plot of strain in the X-direction (horizontal in plane of section) during the elastic injection phase for the low stiffness reservoir for the central X plane section through the model. 225
Figure 4.43 – p'-q plot for the high stiffness cases with an initial stress ratio K = 0.9, the path for the non-sealing low friction fault case with K = 0.7 is shown for comparison. Arrows demonstrate direction of stress path is reversed compared to lower initial stress ratio. 226
Figure 4.44 – Mohr circle plot for the high stiffness case with an initial stress ratio K = 0.9. Arrows show that the stress path is reversed compared to the lower initial stress ratio cases, green arrow shows start of depletion path direction, and red arrow shows end of injection stress path direction. 227
Figure 4.45 - Contour plot of the change in total vertical stress during depletion and injection for high stiffness case with non-sealing low friction faults and K = 0.9 for the central X plane section through the model. 228
Figure 4.46 - Contour plot of the change in total horizontal stress during depletion and injection for high stiffness case with non-sealing low friction faults and K = 0.9 for the central X plane section through the model. 229
Figure 4.47 - Contour plot of displacement in the vertical direction for a section through the injection compartment for the K = 0.9 case for the central X plane section through the model. Vertical displacement is in the plane of the section with positive displacement upwards. 230
Figure 4.48 - Contour plot of displacement in the horizontal direction for a section through the injection compartment for the K = 0.9 case for the central X plane section through the model. Horizontal displacement is in the plane of the section with positive displacement left to right. 231
Figure 4.49 - Contour plot of strain in the X-direction (horizontal in plane of section) during the injection phase in the K=0.9 initial stress ratio case for the central X plane section through the model. 232
Figure 4.50 – p'-q plot for the high stiffness cases with an initial stress ratio K = 0.5, the path for the non-sealing low friction fault case with K = 0.7 is shown for comparison. Arrows show direction of stress path from initial depletion to final injection. 233
Figure 4.51 – Mohr circle plot for the high stiffness case with an initial stress ratio K = 0.5. 234
Figure 4.52 - Contour plot of the change in total stress during depletion for high stiffness case with non-sealing low friction faults and K = 0.5 for the central X plane section through the model. 235
Figure 4.53 - Contour plot of displacement in the vertical direction for a section through the injection compartment for the K = 0.5 case for the central X plane section through the

model. Vertical displacement is in the plane of the section with positive displacement upwards. 236
Figure 4.54 - Contour plot of displacement in the horizontal direction for a section through the injection compartment for the K = 0.5 case for the central X plane section through the model. Horizontal displacement is in the plane of the section with positive displacement left to right. 237
Figure 4.55 – Comparison of cases with 13.8 GPa non-sealing low friction faults for all values of K. The opposite direction of the stress path for the high initial stress ratio should be noted. 238
Figure 4.56 – Relationship of calculated fracture pressure hysteresis factor with initial stress ratio for the high stiffness cases. 239
Figure 4.57 – p'-q plot for the low stiffness cases with an initial stress ratio K = 0.5, the path for the non-sealing low friction fault case for the high stiffness case with K = 0.7 is shown for comparison. 239
Figure 4.58 – p'-q plot for the very high stiffness cases with non-sealing low friction faults and initial stress ratios between K = 0.5 and K = 0.9. The path for the non-sealing low friction fault case for the high stiffness case with K = 0.7 and K = 0.5 is shown for comparison. 240
Figure 4.59 – p'-q plot for the non-sealing case with low friction faults showing stress paths for different Poisson's ratios in the reservoir. 241
Figure 4.60 – Graph of fracture pressure hysteresis factor (f_{ph}) with Poisson's ratio (ν) for the non-sealing low friction fault case. 242
Figure 4.61 - Contour plot of the change in σ_1 during depletion for high stiffness case with non-sealing low friction faults and ν = 0.35 for the central X plane section through the model. 243
Figure 4.62 - Contour plot of the change in σ_3 during depletion for high stiffness case with non-sealing low friction faults and ν = 0.35 for the central X plane section through the model. 244
Figure 4.63 – p-q plot of simulation runs with variable constitutive model parameters compared against the base case model with high friction faults. 245
Figure 4.64 – Diagram of cell locations for analysis of the impact of model geometry on reservoir stress path. 246
Figure 4.65 – p'-q plot of non-sealing low friction fault cases where K = 0.7 for various locations within the reservoir. 247
Figure 4.66 – p'-q plot of sealing low friction fault cases where K = 0.7 for various locations within the reservoir. 248
Figure 4.67 – Mohr circle diagram for the cell in the outer corner of the K = 0.9 initial stress ratio case. 249
Figure 4.68 – p'-q plot of non-sealing low friction fault cases for a range of initial stress ratios comparing the cell at the well and the cell in the outer corner of the reservoir. 250

Figure 4.69 – Graph of fracture pressure hysteresis factor against initial stress ratio for the cell and the well and outer edge of the reservoir. 251
Figure 4.70 – p'-q plot of non-sealing low friction fault cases with low stiffness for a range of initial stress ratios comparing the cell at the well and the cell in the outer corner of the reservoir. 252
Figure 4.71 - p'-q plot of cases with low stiffness overburden compared against base case overburden stiffness, with comparison of cells at the well and the outer corner of the reservoir. 253
Figure 4.72 – Contour plot of the change in σ_1 for high stiffness case with non-sealing low friction faults and the overburden stiffness reduced to 2.35 GPa reference stiffness for the central X plane section through the model. 254
Figure 4.73 - Contour plot of the change in σ_3 for high stiffness case with non-sealing low friction faults and the overburden stiffness reduced to 2.35 GPa reference stiffness for the central X plane section through the model. 255
Figure 4.74 - p'-q plot base case overburden Poisson's, compared to a case with a reduced Poisson's ratio of $\nu = 0.3$. 256
Figure 4.75 – Mohr circle plot of stress in the overburden directly above the reservoir for the non-sealing low friction case. 257
Figure 4.76 – Contour of vertical sliding along the fault contact for the non-sealing low friction base case model. 258
Figure 4.77 - Contour of horizontal sliding along the fault contact for the non-sealing low friction base case model. 259
Figure 4.78 - Contour of vertical sliding along the fault contact for the non-sealing high friction base case model. 260
Figure 4.79 - Contour of horizontal sliding along the fault contact for the non-sealing high friction base case model. 260
Figure 4.80 - Contour of vertical sliding along the fault contact for the sealing low friction base case model. 261
Figure 4.81 - Contour of horizontal sliding along the fault contact for the sealing low friction base case model. 262
Figure 4.82 - Contour of vertical sliding along the fault contact for the sealing high friction base case model. 262
Figure 4.83 - Contour of horizontal sliding along the fault contact for the sealing high friction base case model. 263
Figure 4.84 - Mohr circle plot for the stress state in the sealing low friction base case model for cells adjacent to either side of the fault within the reservoir. The failure criterion for the fault is shown for comparison with the stress state. 264
Figure 4.85 - Mohr circle plot for the stress state in the sealing low friction base case model for cells adjacent to either side of the fault within the overburden. The failure criterion for the fault is shown for comparison with the stress state. 265

Figure 4.86 – Mohr circle plot for the stress state in the non-sealing low friction base case model for cells adjacent to either side of the fault with the failure criterion for the movement along the fault. 265
Figure 4.87 - Mohr circle plot for the stress state in the non-sealing low friction low stiffness model for cells adjacent to either side of the fault with the failure criterion for the movement along the fault. 266
Figure 4.88 – Contour of horizontal contact displacement along the fault contact for the sealing low friction K = 0.5 model during depletion. 267
Figure 4.89 – Contour of vertical contact displacement along the fault contact for the sealing low friction K = 0.5 model during depletion. 267
Figure 4.90 - Contour of horizontal contact displacement along the fault contact for the sealing low friction K = 0.5 model during injection. 268
Figure 4.91 - Contour of vertical contact displacement along the fault contact for the sealing low friction K = 0.5 model during injection. 268
Figure 4.92 – Contact displacement vectors for nodes along the fault plane in the K = 0.5 case with sealing low friction faults. 269
Figure 4.93 – Exaggerated representation of the deformed grid after depletion compared to the original grid for the sealing K = 0.5 case. 270
Figure 4.94 – Mohr circle plot for the stress state in the sealing low friction K = 0.5 model for cells adjacent to either side of the fault in the reservoir during depletion. 271
Figure 4.95 – Mohr circle plot for the stress state in the sealing low friction K = 0.5 model for cells adjacent to either side of the fault in the reservoir at the end of injection 271
Figure 4.96 – Mohr circle plot for the stress state in the sealing low friction K = 0.5 model for cells adjacent to either side of the fault in the overburden at the start of injection. 272
Figure 4.97 – Mohr circle plot for the stress state in the non-sealing low friction K = 0.5 model for cells adjacent to either side of the fault in the reservoir during depletion. 272
Figure 4.98 – Mohr circle plot for the stress state in the sealing low friction K = 0.5 model for cells adjacent to either side of the fault in the reservoir at the start of injection. 273
Figure 4.99 – Mohr circle plot for the stress state in the sealing low friction K = 0.5 model for cells adjacent to either side of the fault in the overburden at the end of injection. 273
Figure 4.100 – Production and injection rate for the coupled model compared against the same model without coupling. 274
Figure 4.101 – Production and injection volumes for the coupled model compared against the same model without coupling. 275
Figure 4.102 – Pressure at the well location for the coupled and non-coupled model during production and injection. 275
Figure 4.103 – Modified porosity in the coupled model at the end of depletion with non-sealing faults. 276
Figure 4.104 – Modified porosity in the coupled model at the end of depletion for the model with sealing faults. 276

Figure 4.105 – Porosity multipliers for compaction in the non-coupled model derived from the coupled model results. 277
Figure 4.106 – Comparison of production and injection rates for the coupled and non-coupled model including pressure dependent pore volume multipliers to model compaction for the non-sealing low friction fault case. 278
Figure 4.107 - Comparison of production and injection volumes for the coupled and non-coupled model including pressure dependent pore volume multipliers to model compaction for the non-sealing low friction fault case. 278
Figure 4.108 – Comparison of production and injection pressures for the coupled and non-coupled model including pressure dependent pore volume multipliers to model compaction for the non-sealing low friction fault case. 279
Figure 4.109 – Comparison of production and injection pressures for the coupled and non-coupled model including pressure dependent pore volume multipliers to model compaction for the sealing low friction fault case. 279
Figure 4.110 – Comparison of Gassman's P-wave velocities for the non-sealing low friction base case model at the end of injection. 280
Figure 4.111 – Comparison of Gassman's P-wave velocities for the sealing low friction base case model at the end of injection. 281
Figure 4.112 – Comparison of Gassman's P-wave velocities for the non-sealing low friction base case model at the end of injection. 282
Figure 4.113 – Difference in P-wave velocity during depletion and injection in the coupled model when the porosity multiplier is included in the P-wave calculation. 282
Figure 4.114 – Plot of difference in P-wave velocity in the overburden for the depletion stage in the high stiffness non-sealing low friction base case model. The approximate position of the reservoir is indicated by the blue line. 283
Figure 4.115 - Plot of difference in P-wave velocity in the overburden for the injection stage in the high stiffness non-sealing low friction fault base case model. The approximate position of the reservoir is indicated by the blue line. 284
Figure 4.116 – Plot of difference in P-wave velocity in the overburden for the depletion stage in the high stiffness sealing low friction fault base case model. The approximate position of the reservoir is indicated by the blue line. 285
Figure 4.117 – Plot of difference in P-wave velocity in the overburden for the injection stage in the high stiffness sealing low friction fault base case model. The approximate position of the reservoir is indicated by the blue line. 286
Figure 4.118 – Plot of difference in P-wave velocity in the overburden for the depletion stage in the low stiffness non-sealing low friction fault base case model. The approximate position of the reservoir is indicated by the blue line. 287
Figure 4.119 – Plot of difference in P-wave velocity in the overburden for the injection stage in the low stiffness non-sealing low friction fault base case model. The approximate position of the reservoir is indicated by the blue line. 288

Figure 4.120 - Plot of difference in P-wave velocity in the overburden for the injection stage in the low stiffness non-sealing low friction fault base case model. The plot scale has been range is reduced to highlight the positive P-wave change around the reservoir. The approximate position of the reservoir is indicated by the blue line. 289
Figure 4.121 - Effective horizontal and vertical stress for the centre of the reservoir with time for each of the initial stress ratio cases. 294
Figure 4.122 - Total horizontal and vertical stresses for the centre of the reservoir with time for each of the initial stress ratio cases. 297
Figure 4.123 – Total horizontal stress for the centre and edge of the reservoir with time for each of the initial stress ratio cases. 298
Figure 4.124 – Summary of stress path responses with change in Poisson's ratio, overburden and reservoir stiffness and position within the reservoir. Flattening of the injection stress path such as in the 0.35 Poisson's ratio case shows indicates reduce fracture pressure during injection. This is due to reduced horizontal stress, the base case 13.8 GPa stress path which has a steeper injection stress path, would have a higher horizontal stress and fracture pressure. 300
Figure 4.125 – Mohr circle and s'-t stress path plot for a cell at the well for the K = 0.9 initial stress ratio case with a projection of a case with $\gamma_h = 0$ stress path as observed by Santarelli et al. (1998). 306
Figure 4.126 – Mohr circle and s'-t stress path plot for a cell at the well for the K = 0.9 initial stress ratio case with a projection of a case with $\gamma_h = 0$ stress path as observed by Santarelli et al. (1998). 307
Figure 4.127 – Plot of thermally induced stress around the injection well using data from the material model and typical values from Luo and Bryant (2011). 309
Figure 4.128 – Re-plotted PVM table comparing the compartmentalised and non-compartmentalised fluid flow simulation compressibility gradients. 314

1 Introduction

1.1 Climate Change

Anthropogenic climate change has been identified as one of the largest, most complex and destructive problems ever faced by humanity (Stern 2007), although the very existence of the phenomenon is still called into question by some (Cook et al. 2013). The cause of this climate change is the strengthening of the greenhouse effect via the increase in atmospheric greenhouse gas concentration due to the addition of various greenhouse gases into the atmosphere from anthropogenic sources. The adverse consequences of anthropogenically generated climate change are predicted to include such effects as sea level rise, droughts, crop failure, species extinction, epidemics, and extreme weather events, along with other more subtle effects.

Aside from the more popular debate over atmospheric and global climate impacts of CO_2 emissions, a lesser known but potentially equally serious impact of CO_2 emissions is the acidification of ocean waters. Termed by some workers (Henderson 2006, Doney et al. 2009) as "the other CO_2 problem", referring to the under-researched and under-acknowledged nature of the problem; ocean acidification has the potential to have serious impacts on life forms that utilise carbonate ions to form shells and reef systems.

1.2 Fossil Fuels and Climate Change

The dominant source of greenhouse gases (GHGs) contributing to anthropogenic climate change is the use of fossil fuels for electricity and heat generation, transport, and chemical and consumer goods manufacturing. Thus, fossil fuels are an obvious target for the development of mitigation technologies and strategies. Humans continue to consume fossil fuels on a significant scale. For example, the International Energy Agency (IEA) predicts that world demand for coal will rise in the future from its current level of 3000Mtoe to over 4000Mtoe by 2030 (IEA 2009a). This means that technologies that can reduce emissions from fossil fuel use such as coal combustion will be very useful tools for the mitigation of climate change in the near to medium term before wide-scale rollout of other forms of low carbon energy can be achieved. Carbon Capture and Storage (CCS) is one such potential technology and allows the capture of GHG emissions from combustion, and storage of these emissions away from the atmosphere. The component technologies of CCS are discussed in the following section.

1.3 Carbon Capture and Storage

Carbon Capture and Storage is a phrase used to describe a suite of technologies designed to capture CO_2 emissions from the combustion of carbon based fuels as well as industrial and fuel refining processes and then transport them to site where they are safely stored for a sufficient length of time that they will not impact the climate.

Geological storage sites are considered to be the most advanced and realistic storage option (Holloway 2008). Ocean storage has also been suggested but this is less developed than geological storage and there is still uncertainty as to the possible environmental impacts, and permanence of storing large volumes of CO_2 in the ocean. The reader is referred to Kita et al. (2005), Adams and Caldeira (2008) and Israelsson et al. (2009) for some discussion on the impacts of ocean storage.

According to the IPCC (2005), the storage time for CO_2 from CCS schemes should be long enough to store a significant volume of the captured CO_2 well beyond the fossil fuel era. The storage duration is generally determined as a set proportion of CO_2 remaining in storage for a specific timescale. The Special Report on Carbon Capture and Storage by the IPPC (IPCC 2005) reports details of work from several authors and suggests that the storage time is normally accepted to be on the scale of 100s to 1000s of years, and the proportion of CO_2 remaining in storage between 60% and 99% to make CCS a viable climate change mitigation tool (IPCC 2005). This is based on the premise that some release from storage will occur over time, and this release should not significantly increase the atmospheric concentrations of CO_2.

Carbon capture and storage is generally accepted to be applicable only to large point sources of CO_2 such as coal fired power stations and refineries, and not small mobile sources such as cars. Emissions capture from vehicles and small sources could be achieved by using energy carriers such as hydrogen produced by fossil fuels but emissions controlled using CCS; in this case capture is effectively occurring upstream of the source (IPCC 2005).

The most commonly proposed applications and technologies involved in each step of the process are:

- **Capture** – Amine based capture from coal and gas fired power plant flue gas, steel production and refinery operations such as acid gas treatment (CO_2 is removed). Advanced combustion processes such as oxyfuel combustion have also been proposed, which directly increase the flue gas concentration of CO_2 for capture (IPCC 2005).
- **Transport** – Compression of the captured CO_2 stream and transport via road/rail based tanker, ship or through onshore and offshore pipelines (IPCC 2005).
- **Storage** – Storage of compressed CO_2 in depleted oil and gas reservoirs, saline aquifers, un-mineable coal seams (and controversially the ocean water column). Storage by conversion to minerals, algae, chemicals and fuels has also been proposed (IPCC 2005).

Figure 1.1 shows an idealised carbon capture and storage scheme where the CO_2 is captured in a power plant using gas or coal as a fuel source. The CO_2 is then transported

via onshore and offshore pipelines to geological storage in un-mineable coal seams, saline aquifers and depleted hydrocarbon reservoirs.

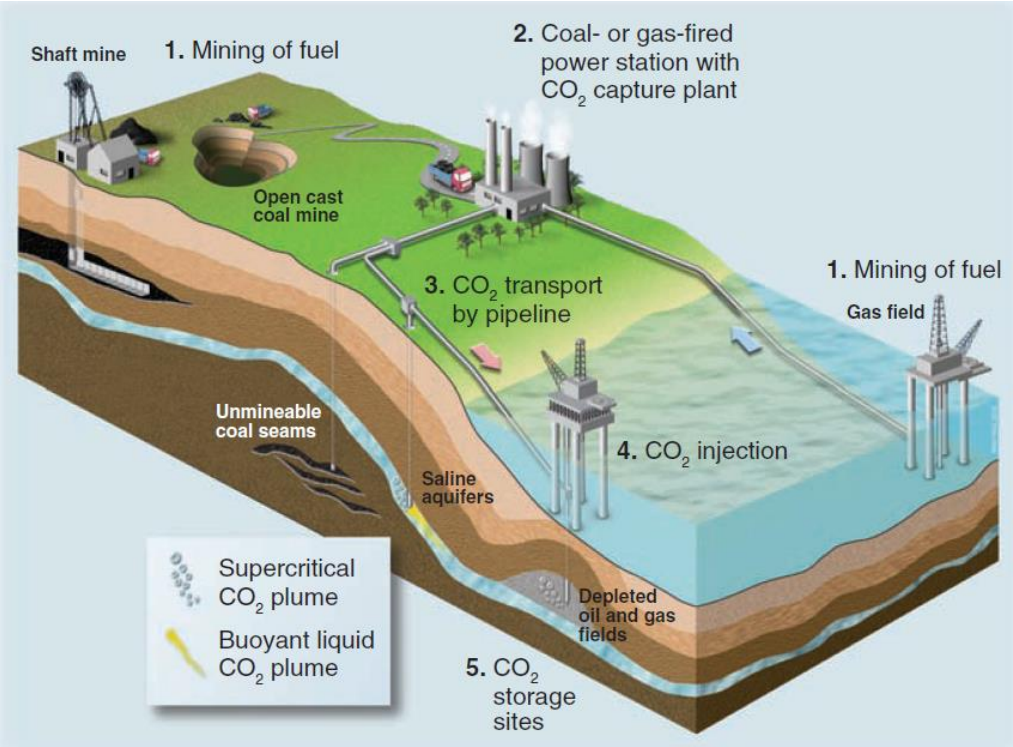

Figure 1.1 – From (Haszeldine 2009), idealised image of the full chain of carbon capture transport and storage technologies. In this case, the CO_2 is captured at a power plant, transported by pipeline and stored in geological formations.

At the time of writing CCS does not operate anywhere in the world in a manner that could be described as a commercial CCS operation, however many of the components do operate separately on large scales, and there are many significant demonstration projects operating, which can provide information relating to CO_2 storage.

The preceding components of CCS prior to storage, the capture and transport phases, have the potential to impact the storage component through their influence on the CO_2 stream including the physical properties of the CO_2 such as temperature and pressure, and the chemical properties such as acidity. These may affect the storage solution, for example through chemical impacts on the storage reservoir. Whilst these aspects are not discussed explicitly in terms of a separate review, they are included implicitly in the analysis of the likely properties of CO_2 that will enter storage. The main focus of this study is the opportunities for storage of CO_2 in the UK, and the associated risks of storing CO_2 in geological structures, the background to storage of CO_2 is discussed in detail in the following chapter, and no further reference is made to the other components of CCS unless they are pertinent to storage operations.

1.4 Thesis Outline

This thesis aims to assess the risks and opportunities for geological storage of CO_2 for CCS projects in the UK offshore region. **Chapter 2** provides an overview of the scientific and technical background to geological storage and identifies storage capacities in the UK and risks to secure storage. **Chapter 3** investigates brine extraction and potential storage capacity in the offshore Bunter Sandstone aquifer based on fluid flow simulations conducted using industry-standard production simulation models. The Bunter aquifer has the largest single storage potential in the UK, and this chapter aims to assess current capacity estimates and the effectiveness of brine extraction on increasing capacity. **Chapter 4** investigates the phenomenon of fracture pressure hysteresis, observed in field data from a North Sea oil reservoir. Fracture pressure hysteresis has the potential to reduce the storage pressure for CO_2 injection and therefore presents a risk to capacity estimates and secure storage. This is investigated using a coupled fluid flow-geomechanical model, which also has the capacity to generate synthetic seismic data. Seismic surveys in the field can provide a monitoring tool and can provide information on stress changes and fluid saturation changes during depletion and re-pressurisation operations, accurately modelling such data can improve understanding of field observations. **Chapter 5** provides a summary of the thesis and discusses areas for further research.

2 CO_2 Storage, Risks and Uncertainty

CO_2 storage is the final element in the CCS system. The efficiency of the storage solution directly affects the ability of CCS to mitigate climate change by isolating CO_2 that would otherwise exist in the atmosphere over long timescales. The storage component is the longest-lived component of the CCS system and must operate over inter-generational timescales, and for this reason it is subject to some of the largest uncertainties. The critical considerations for any storage scheme are:

- What volume of CO_2 can be stored? – **Storage capacity**;
- At what rate can CO_2 be placed into storage? – **Storage Injectivity;**
- Will the CO_2 remain within the desired storage location? – **Storage security and leakage;**
- Is the CO_2 in storage behaving as expected? – **Storage Monitoring;**
- Will the CO_2 remain in storage in the long term, without damage to the environment, and is the storage option economically viable and sustainable? – **Storage economics and regulation.**

The following sections present a brief background to geological storage and a review of the state-of-the-art in the context of the critical considerations for CO_2 storage as discussed above.

2.1 Geological Storage - Principles

There are several proposed options for storage of CO_2, including mineral carbonation and ocean storage, however geological storage represents the option that is closest to market, has the most industrially-related experience and is the most practical in terms of immediate environmental and logistical concerns.

The general principle behind geological storage is to inject CO_2 into deep geological formations that have significant storage space in the pore spaces in the rock. The design of the storage solution is such that there is at least one mechanism of long-term immobilisation of the CO_2. Generally, the depth, and therefore pressures and temperature, of the storage formation is chosen to maximise the storage space available by maintaining the dense phase or supercritical state of the CO_2. A dense phase represents a fourth phase for a compound that is not liquid, gaseous or solid. The dense phase occurs above the critical point for a compound, which is unique to each compound. Above the critical point, the compound has the density of a liquid, but the viscosity of gas (IPCC 2005). The critical point for CO_2 is 31.1 °C and 7.39 MPa. Figure 2.1 illustrates that the temperature and pressure gradients generally observed at depth dictate that the ideal conditions for storage would exist below 800m-900m (Holloway 2008).

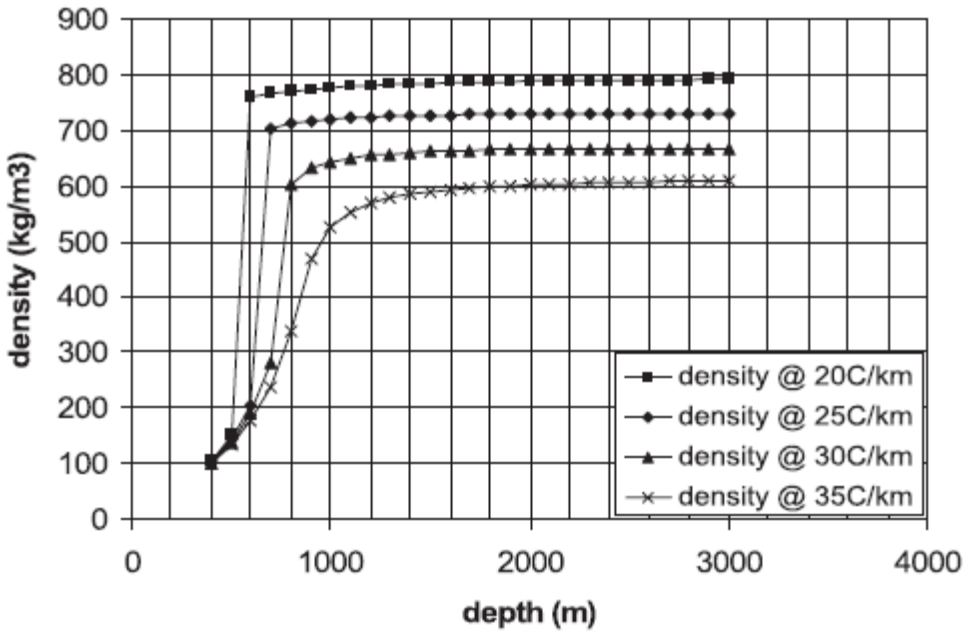

Figure 2.1 – The density of CO_2 with depth below ground level in geological storage (from Holloway 2008).

The geological storage solution utilises natural formations, but the requirement to satisfy capacity, injectivity and storage security constraints dictates the choice of storage location and the techniques for injection and long-term storage management. The final engineered storage solution will include:

- **Trapping mechanism/s** – e.g. impermeable cap rock seal or engineered residual trapping (IPCC 2005, Qi et al. 2009);
- **Significant capacity** – high porosity provides storage volume and high permeability allows significant, industrial-scale volumes to be injected. High permeability can be natural or artificially engineered, although the later involves increased expense (IPCC 2005, Holloway 2008);
- **Long-term storage security** – ongoing storage operations and natural phenomena will not compromise storage security and produce leakage (IPCC 2005, Holloway 2008).

2.2 Geological Storage Options I

The options for geological storage location generally fall into four categories:

- storage in depleted hydrocarbon reservoirs:
  - oil reservoirs;
  - gas reservoirs;
- storage in deep un-mineable coal seams; and
- storage in saline aquifers.

Figure 2.2 illustrates the proposed storage locations for CO_2. For all cases, except storage in saline aquifers, the combination of storage operations with the recovery of fossil fuels is also possible. A hydrocarbon reservoir is unlikely to be used for storage unless it has been fully depleted of hydrocarbons, and in fact a concept often attached to considerations of CCS storage is the ability to employ enhanced oil recovery (EOR) and enhanced gas recovery (EGR), where the CO_2 injection improves the recovery of hydrocarbons, whilst also storing CO_2. Storage in un-mineable coals seams allows a similar recovery of coal bed methane (CBM), based on the preferential adsorption of CO_2 onto the carbonaceous macerals of coal, thus displacing the methane gas (Holloway 2008).

Some authors dispute the effectiveness of both EOR (Economides and Ehlig-Economides 2009) and CBM (Holloway 2008) storage combinations, and consider the volumes of CO_2 that will be stored in these situations as minimal. EOR is particularly optimised for minimal CO_2 input to reduce costs and some researchers suggest a comparison with a storage scheme is ill advised (Economides and Ehlig-Economides 2009). However other opinions suggest it is merely a case of optimisation and that EOR can be successfully combined with CO_2 storage (Orr 2004).

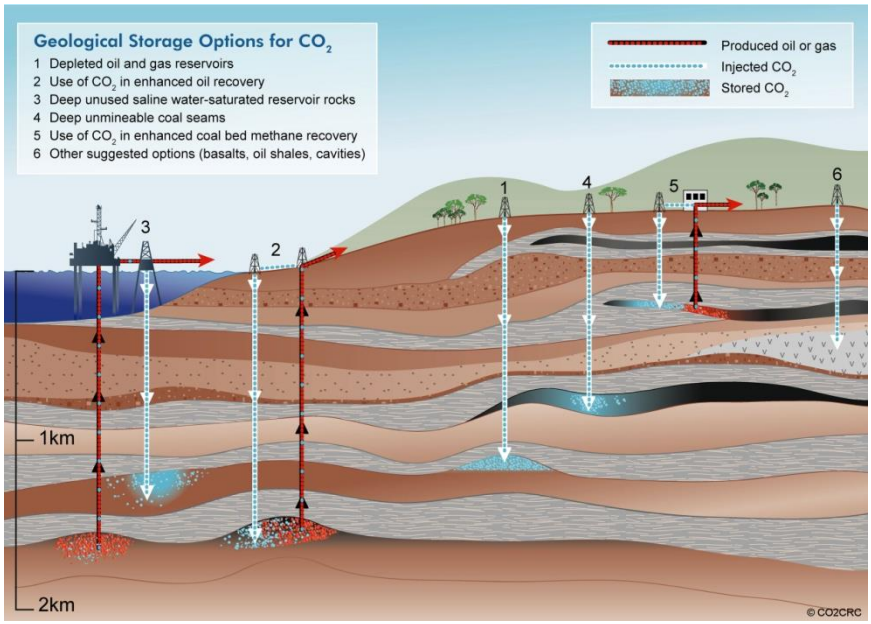

Figure 2.2 – Schematic diagram of the main locations proposed for geological storage of CO_2, blue represents CO_2, red represents hydrocarbons, black represent coal beds (from CO_2CRC 2011).

Much of the literature is focussed on the development of geological storage within depleted oil and gas reservoirs, and saline aquifers. In the UK, CBM recovery even without CO_2 storage has so far proven unsuccessful and is not considered further in this study (Holloway 2008).

2.3 Subsurface Flow Properties and Trapping Mechanisms

2.3.1 Reservoir and Fluid Properties

The space between the grains of the rock, the pore space, provides the storage space in a geological storage reservoir, and is a measure of void space as a percentage of total rock volume. The pore space will be filled with some form of pore fluid; generally, this will brine, and potentially oil and/or gas. Freshwater may also be present, but this would usually only be only at shallow depths. For CCS shallow aquifers with potable water would not be considered for storage as it would be a resource for human consumption. Typical values of porosity for storage reservoirs are around 15-20% for example In-Salah (Rutqvist et al. 2010), but can be as high as 30-40% for example Sleipner (Chadwick et al. 2005). Assuming that the reservoir is at a sufficient depth to maintain the appropriate temperature and pressure conditions, the CO_2 will be stored in the pore spaces in the dense phase. Most storage reservoirs should also be highly permeable to allow the rapid injection of large volumes of CO_2. This is a common feature of many gas and oil reservoirs, as high permeabilities allow efficient production of hydrocarbons. Typical permeabilities for CO_2 demonstration projects range from a very high permeability of up to 5000 mD for the Sleipner project in Norway (Bickle et al. 2007), down to a low permeability of 5 to 10 mD for the In-Salah project in Algeria (Ringrose et al. 2013).

CO_2 is not miscible in water/brine, and so will form a separate phase in the reservoir. CO_2 is, however, miscible with oil and gas and so will readily mix with these phases. The dynamics of fluid/gas interactions must be taken into account as it will determine how easily fluids can be injected into a reservoir, and how the fluid/gas will behave after they have been injected.

As shown by Figure 2.1, CO_2 in its densest phase is less dense than water (water density >900kg/m^3), and therefore CO_2 will be buoyant in the water filled pore space of the storage reservoir and subsurface (Holloway 2008). CO_2 will therefore tend to migrate upwards to the surface. To prevent upward movement of the CO_2 some form of trapping mechanism is required to isolate the CO_2 and prevent migration of CO_2 to the surface, and subsequent escape to the atmosphere.

2.3.2 Reservoir Compressibility

The mechanical properties of reservoirs play a critical role in their ability to act as CO_2 storage sites. In particular, deformation of the reservoir leads to a change in the bulk or pore volume with pressure or stress and a measure of this change is defined as the compressibility. Changes in pore volume (pore compressibility) are required for reservoir modelling problems whereas changes in bulk volume (bulk compressibility) are of most interest for subsidence problems, and so in this context are not discussed further. Changes in rock volume and expansion of grains lead to a change in the volume of the pore space (Ahmed 2010). Zimmerman (1990) defines the pore compressibilities as:

$$c_{pc} = \frac{-1}{v_p}\left[\frac{\Delta v_p}{\Delta \sigma_c}\right], \qquad \textbf{Equation 2.1}$$

and

$$c_{pp} = \frac{-1}{v_p}\left[\frac{\Delta v_p}{\Delta P_p}\right], \qquad \textbf{Equation 2.2}$$

where c_{pc} is the formation compaction coefficient and represents change in pore volume v_p with confining stress σ_c, and c_{pp} is the effective pore compressibility and is the pore volume change with pore pressure P_p. The units of compressibility are psi^{-1} or bar^{-1}, data in the literature are generally of the order of 10^{-6} psi^{-1}.Convention in the literature is to refer to the effective pore compressibility as the formation compressibility and the formation compaction coefficient as the pore compressibility (Fatt 1958, Yale et al. 1993, Crawford et al. 2011). Additionally pore compressibility is often used to refer to both pore and formation compressibility without distinction. All rock compressibilities discussed in the remainder of this thesis relate to the formation compressibility c_f.

The pore compressibility can be measured in the laboratory using hydrostatic stress tests or uniaxial strain tests. To correct from laboratory measurements of pore compressibility in sandstones to formation compressibility Geertsma (1957) suggests a factor of 0.5 should be applied to hydrostatic measurements. The factor of 0.5 is derived from the relationships presented by Geertsma (1957) for the different stress distributions observed in the laboratory and the reservoir, where the boundary stress in the reservoir is uniaxial (vertical loading from the overburden) as opposed to uniform in the laboratory. Yale et al. (1993) suggest several factors based on rock type to convert from pore compressibility to formation compressibility; 0.45 for consolidated sandstones, 0.60 for friable sandstones, 0.75 for unconsolidated sands and 0.55 for carbonates. They also present a set of type curves, based on the effective mean stress (equivalent lab stress) for a compilation of data from unconsolidated, friable and consolidated sandstones, which are shown in Figure 2.3.

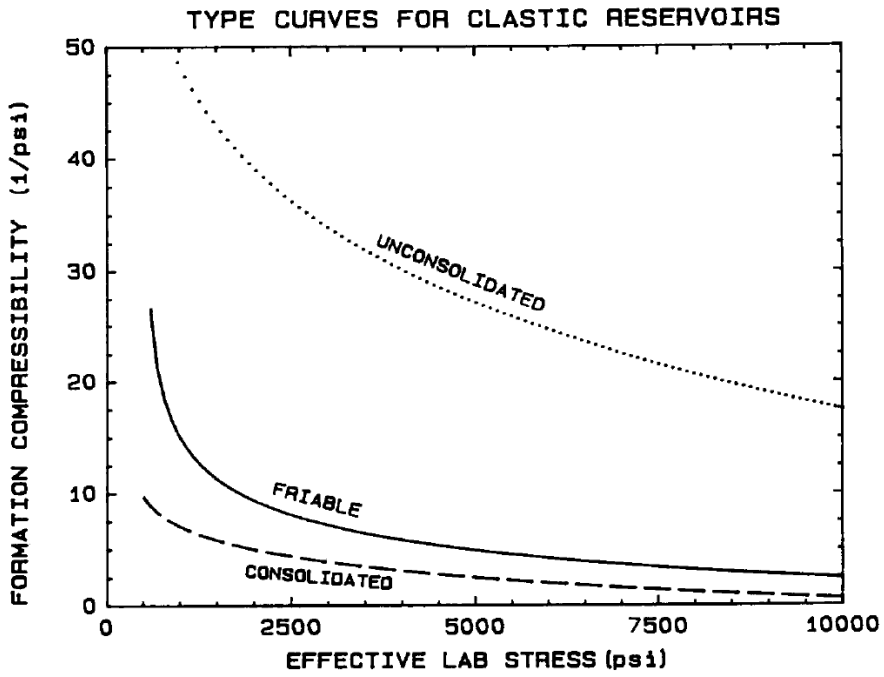

Figure 2.3 – Formation compressibility for a range of sandstones collated from the literature (from Yale et al. 1993).

Crawford et al. (2011) have compiled a database of pore compressibility measurements for offshore and onshore siliciclastic reservoirs worldwide. The data have been converted to represent formation compressibility based on the approach of Yale et al. (1993) and a strain correction factor. The database is presented in Figure 2.4 with the c_f values at initial reservoir stress conditions (IRSC) plotted against porosity for each of the samples, the plot includes converted values of pore compressibility values for cemented, friable and unconsolidated sandstones from Newman (1973). Statistical analysis of the data shows a minimum value of c_f of 0.8 x 10^{-6} psi^{-1}, a mean of 12.9 x 10^{-6} psi^{-1} and a maximum of 75.1 x 10^{-6} psi^{-1} (Crawford et al. 2011). Figure 2.4 shows the highest values are for unconsolidated sands, and a reasonable range for cemented to friable sandstone is between 0.8 x 10^{-6} psi^{-1} and 10 x 10^{-6} psi^{-1} or 1.2 x 10^{-5} bar^{-1} to 14.5 x 10^{-5} bar^{-1} dependent on porosity. Corrected data from Fatt (1958) also falls within the range of formation compressibilities for cemented to friable sandstones.

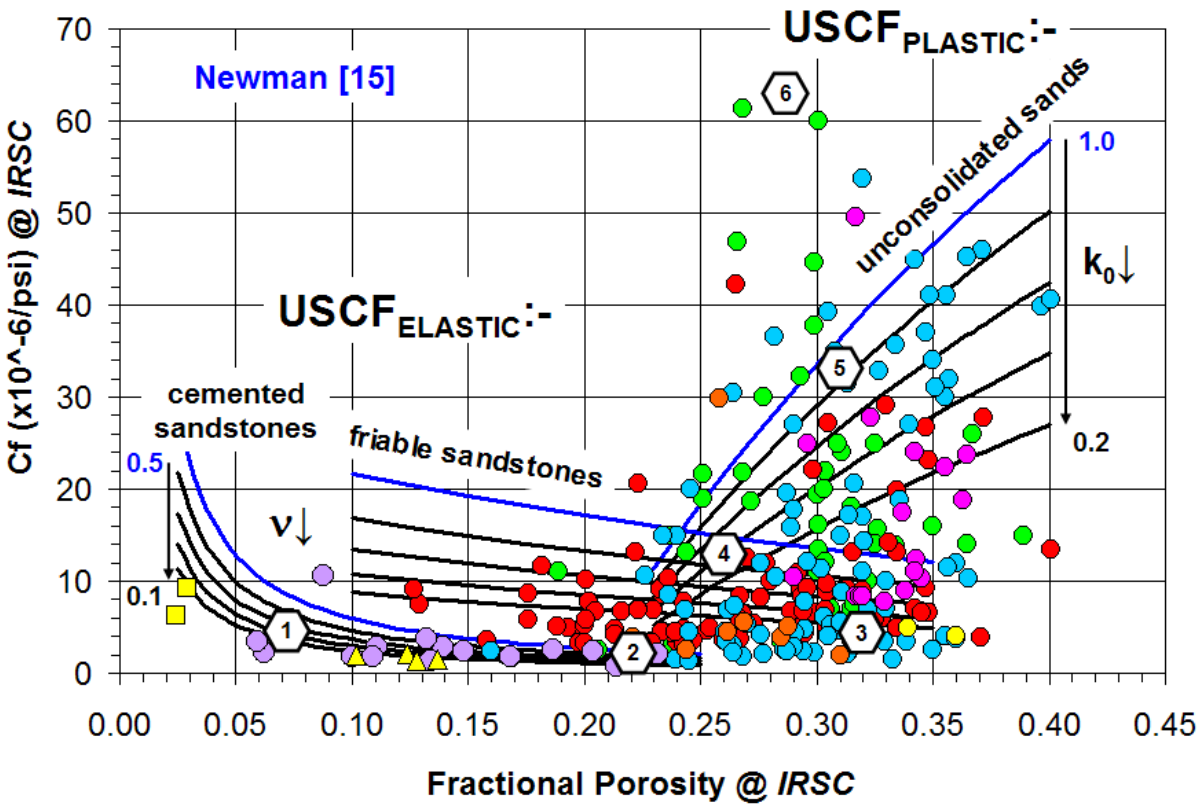

Figure 2.4 – Compiled database of converted formation compressibility values at initial reservoir stress conditions (IRSC) from Crawford et al. (2011). Colours represent geographical location of values, red – Nigeria, blue – Gulf of Mexico, green – Angola, pink – North Sea, purple – Alaska, orange – Chad, yellow – Australia, South America and Germany. The figure is overlaid with type curves of compressibilities corrected from hydrostatic tests from Newman (1973), where ν is Poisson's ratio and k_o is coefficient of earth pressure at rest.

The equation for formation compressibility in a reservoir in terms of porosity is given by Ahmed (2010) as:

$$c_f = \frac{1}{\phi}\frac{\partial \phi}{\partial p} \qquad \textbf{Equation 2.3}$$

where c_f is the formation compressibility in psi^{-1} or bar^{-1}, ϕ is porosity and p is pore pressure in psi or bar. Ahmed (2010) shows that c_f can be used to determine porosity using the initial porosity ϕ_0 and the change in pore pressure:

$$\phi = \phi_0[1 + c_f(p - p_0)] \qquad \textbf{Equation 2.4}$$

this is used in some reservoir simulation programs to calculate porosity change with change in pore pressure. As will be discussed in later sections of this thesis, the compressibility parameter is not always an adequate description of the behaviour of the overburden and reservoir system, and a more complex analysis technique is required.

2.3.3 Multiphase flow in porous media

The fundamental law for single-phase flow in porous media, Darcy's Law, describes the flow of a single-phase, homogeneous fluid through a porous media:

$$\frac{q}{A} = -\frac{k}{\mu}\frac{dp}{dx}. \qquad \textbf{Equation 2.5}$$

Where q is the volumetric flow rate ($cm^3.s^{-1}$), A is total cross sectional area of flow (including interstitial porous media and pore spaces) (cm^2), k is the permeability of the porous media in Darcy units (D), μ is the viscosity of the fluid in centipoise (cP), and the pressure gradient dp/dx is in atmospheres per centimetre ($atm.cm^{-1}$). The relationship is only valid for single-phase flow. In CO_2 storage, and reservoir modelling in general, where more than one phase will typically be present, the relative permeability of the phases must also be taken into account to allow Darcy's law to be applied. The relative permeability accounts for the interference of the different phases of a system on the flux of each phase. The relative permeability for different phases are defined as:

$$\boldsymbol{k_o = k_{ro}k}, \qquad \textbf{Equation 2.6}$$

$$\boldsymbol{k_g = k_{rg}k}, \qquad \textbf{Equation 2.7}$$

and

$$\boldsymbol{k_w = k_{rw}k} \qquad \textbf{Equation 2.8}$$

where k_o, k_g, k_w are the effective permeabilities of oil, gas and water phases, k_{ro}, k_{rg}, and k_{rw} are the relative permeabilities to oil water and gas, and k is the absolute permeability of the porous media. The relative permeability is dimensionless, and so the units of effective permeability are the same as absolute (Darcy or m^2) (Ahmed 2010).The effective permeability can then be incorporated into formulations of Darcy's law to calculate the flow of the different phases.

Values of k_r range between 0 and 1, and in general are assumed to be non-hysteretic and are derived empirically from laboratory tests. A relative permeability plot for CO_2-brine is shown in Figure 2.5 (Tueckmantel 2010). The graph is plotted in terms of gas saturation, for water and gas, where the endpoint of the graph is defined by the residual saturation of brine in the pore space (~ 0.2).

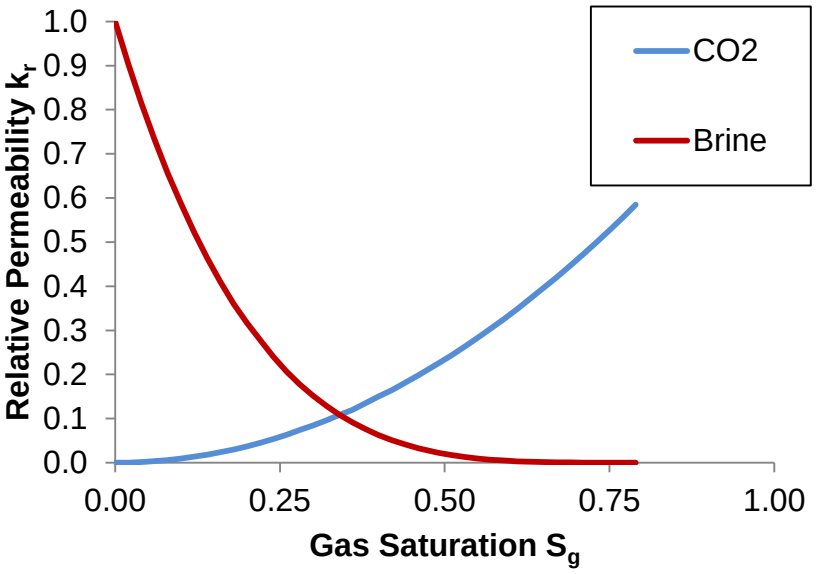

Figure 2.5 – Relative permeability curves for a CO_2-brine system (Tueckmantel 2010).

The graph shown in Figure 2.5 only represents relative permeabilities for a two-phase system and only two-phase behaviour is considered in the modelling in this thesis. Correlations such as Stone's Model II are used to represent a three phase system based on two phase data but this is not considered further, the reader is referred to Ahmed (2010) for further detail. Relative permeabilities can also be hysteretic depending on whether the CO_2 is the displacing (drainage) or displaced (imbibition) phase. Work by several authors suggests that relative permeability hysteresis is an important factor in residual CO_2 trapping (Flett et al. 2004, Juanes et al. 2006, Bennion and Bachu 2008, Hesse et al. 2008, Qi et al. 2009), which is discussed in Section 2.3.6.

2.3.4 Trapping Mechanisms

Four types of trapping mechanism can be identified. The predicted contribution to the quantity of CO_2 trapped by each mechanism and the timescales each of the trapping mechanisms are predicted to operate over are illustrated in Figure 2.6.

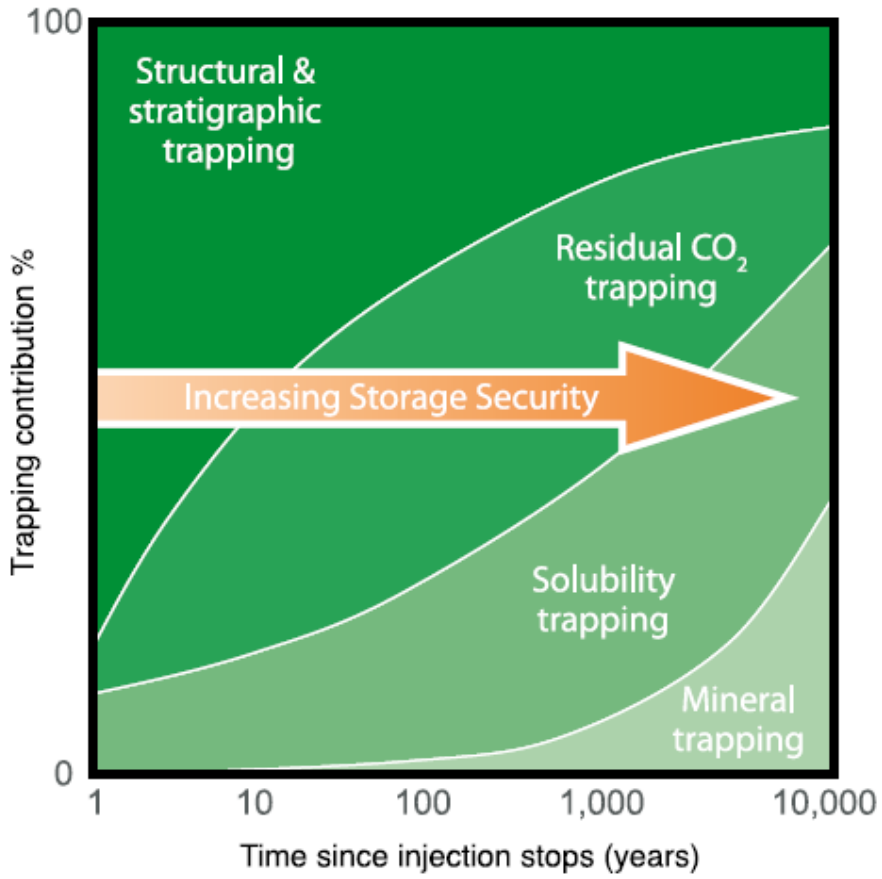

Figure 2.6 – Trapping mechanisms in geological storage. The plot compares the contribution to CO_2 trapping of each mechanism against time (IPCC 2005).

The four types of trapping mechanism are (IPCC 2005, Holloway 2008):

- **Structural and stratigraphic trapping** – the isolation of free buoyant CO_2 beneath a sealing layer of rock, often referred to as the cap rock. The seal can be compromised by faults and fractures, unsatisfactory rock properties, and geological variability. Structural trapping and sealing is discussed further in Section 2.3.5.
- **Residual trapping** – the isolation of CO_2 'pockets' in pore spaces surrounded by water that renders the CO_2 immobile. The concept is discussed further in Section 2.3.6.
- **Solubility trapping** – CO_2 will dissolve in water over time. The resulting brine-CO_2 solution is denser than the surrounding brine and will immobilise CO_2 via sinking brine plumes. Solubility trapping is likely to take 1000s of years to make a significant contribution, but is likely to be secure unless released by mobilisation of the CO_2 rich brine through aquifer flows (Holloway 2008).
- **Mineral trapping** – this involves the conversion of CO_2 into minerals. The timescales are long (~ 10000yrs), and perhaps only contribute 30% towards the trapped volume after thousands of years, and less than 1% in the short term (IPCC 2005, Holloway 2008). As the critical period for storage is likely to be in the order of

1000s of years and the contribution is small (see Section 1.3), this is the least important trapping mechanism.

Since solubility and mineral trapping mechanism are both long-term trapping mechanisms, it is critical to ensure some form of effective short term trapping mechanism. This implies that an adequate seal must be present, at least in the short term, to ensure immobilisation of CO_2. Residual trapping may also be able to contribute a significant proportion of trapped CO_2 in the short term.

2.3.5 Structural Trapping and Cap Rocks

A structural trap relies upon a sealing cap rock, and some form of structural trap to contain the CO_2. The structure can be an enclosed volume that contains the CO_2 and does not allow the CO_2 plume to migrate such as those shown in Figure 2.7. Alternatively, it can consist of a structure that allows the CO_2 to migrate, but restricts the movement, so that over very long timescales residual trapping and solubility/mineral trapping will immobilise the CO_2 plume. For example, Thibeau and Dutin (2011) show generic modelling work for an aquifer with dip of 1% where migration of the plume after 400 years is less than 50km, according to Figure 2.6 around 80% could be immobilised by this time.

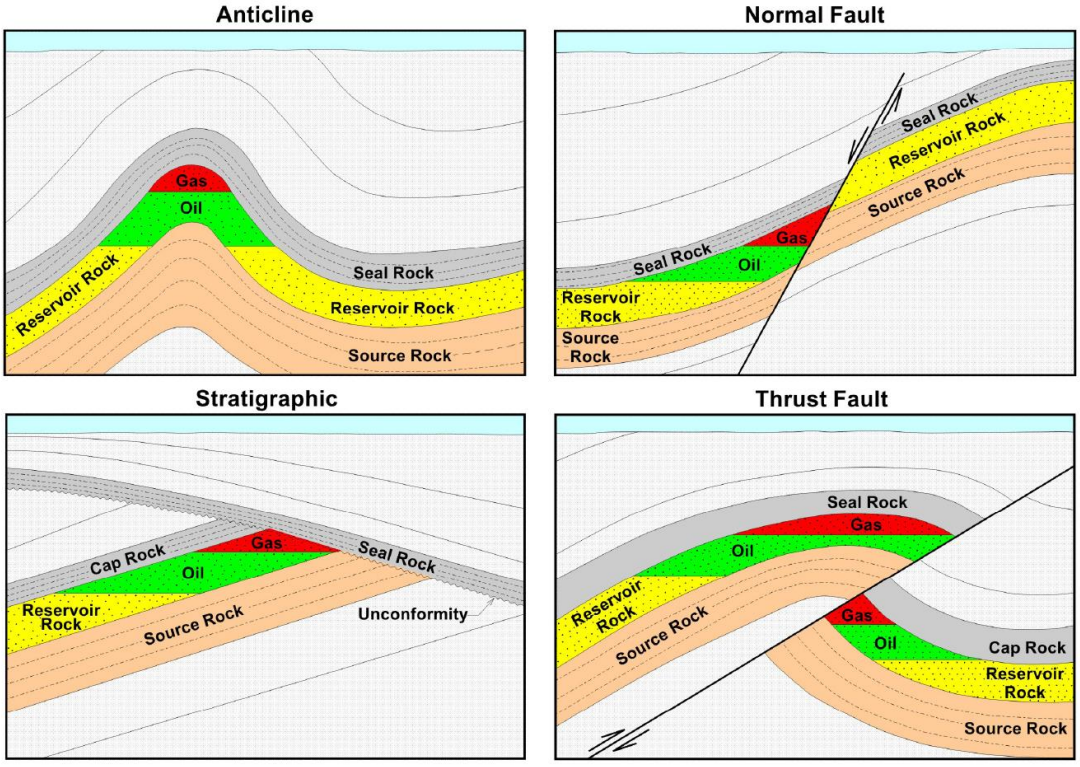

Figure 2.7 - Examples of structural and stratigraphic traps for oil and gas reservoirs (from ACEP 2009), the figures shows different examples of the formation of traps, in these examples an enclosed volume is formed in three dimensions, although shallow dipping beds that provide slow migration times may also be used to trap CO_2.

The sealing cap rock needs to have a good sealing capacity to minimise fluid flow and maximise storage volumes. In a pore fluid system with only one phase Darcy flow will

control the flow rate of the liquid throughout the system and hence the sealing capacity. Very low permeabilities would be required to seriously inhibit flow over a long time scale, typically in the range of 0.001 to 0.000001mD (10^{-18} to $10^{-21}m^2$) (Fleury et al. 2011). However, when two or more immiscible phases are present in the system, the capillary entry pressure (P_c) of a non-wetting phase into pore spaces occupied by the wetting phase is controlled by Washburn's equation:

$$P_c = \frac{2\sigma \cos\theta}{r}. \qquad \textbf{Equation 2.9}$$

P_c (in dynes/cm^2) is the entry pressure for a fluid into the pore space, σ is the interfacial tension (in dynes/cm), θ is the contact angle and r is the pore throat radius in μm. The equation is a modified version of Washburn's (1921) equation (Berg 1975, Schowalter 1979, IEAGHG 2011b). Wetting and non-wetting behaviour refers to the fluid behaviour in contact with the rock surface. The diagram in Figure 2.8 illustrates the concept. The wetting behaviour is measured in degrees using the contact angle concept; 0° contact angle refers to a completely non-wetting phase and 180° refers to a fully wetting phase. CO_2 is assumed to be the non-wetting phase and so the Washburn principle can be applied (IEAGHG 2011b).

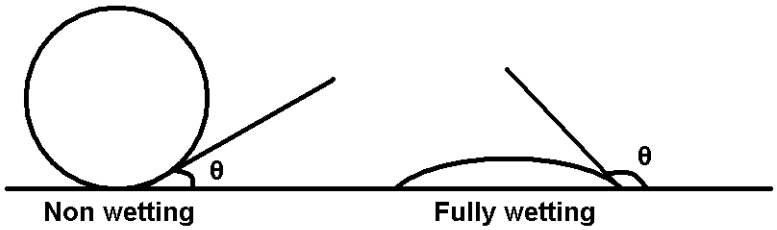

Figure 2.8 – Diagram illustrating the concept of contact angle θ, if the phase is non-wetting on the substrate the angle θ will be low, and if it is wetting the angle, θ will be high. Theoretically, a fully non-wetting phase angle θ can be zero, and a fully wetting angle θ 180°.

If the CO_2 is a non-wetting phase, the capillary entry pressure (P_c) will resist the buoyancy force of the buoyant CO_2 plume, and therefore provides a barrier to the vertical movement of CO_2. The buoyancy pressure of the CO_2 must overcome the capillary entry pressure for the CO_2 to breach the capillary seal and enter the cap rock. If the capillary entry pressure is exceeded the permeability (relative permeability if multi-phase flow) controls flow through the seal (Cartwright et al. 2007). The rock will only act as a capillary seal if the contact angle with the CO_2 is close to 0°, if the contact angle with CO_2 is close to 180° then the CO_2 is the wetting phase and no capillary seal will exist. The capillary entry pressures will then give an indication of the column height of CO_2 that can be supported by a potential seal (IEAGHG 2011b). Most systems are generally assumed to be water wet, and so have a contact angle close to zero, providing the best conditions for a capillary seal to CO_2. However, recent investigations have indicated that the contact angle of CO_2/brine/rock systems can be as high as 130° in limestone, and 60° on quartz/clay substrates in high pressure high salinity systems with supercritical CO_2 (IEAGHG 2011b). In this case, CO_2 would become the

wetting phase and this could compromise the effectiveness of the capillary seal, leading to lower column heights.

2.3.6 **Residual Trapping**

The behaviour of CO_2 capillary entry into pore spaces also has implications for trapping within the reservoir itself, and the potential for artificially improving the residual trapping in a storage location. When a non-wetting phase (i.e. CO_2) enters a pore space and displaces a wetting phase (i.e. brine), this is termed drainage, and when a wetting phase displaces a non-wetting phase, this is termed imbibition. When a plume of CO_2 moves through the reservoir, both drainage and imbibition will occur, and the relative permeabilities of the CO_2–brine system has been determined to be hysteretic between drainage and imbibition conditions (Flett et al. 2004, Bennion and Bachu 2005, Juanes et al. 2006, Bennion and Bachu 2008, Hesse et al. 2008). The hysteresis behaviour leads to trapping of residual pockets of CO_2, Figure 2.9 illustrates the concept. The leading edge of the CO_2 plume displaces the brine (drainage), the trailing edge of the plume then experiences imbibition of brine back into the pore space with different relative permeabilities; this causes residual pockets of CO_2 to be trapped in the pore space.

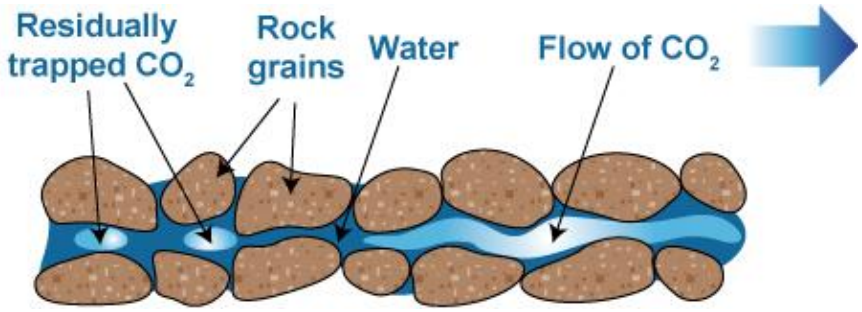

Figure 2.9 – Diagram of residual trapping in the pore spaces of a reservoir rock, the flow of CO_2 moves through the rock, and the trailing edge is trapped by the ingress of displaced water back in to the pore spaces (CO_2CRC 2010).

Qi, LaForce et al. (2009) present work on optimisation of residual trapping. The optimised system is based upon combined injection of CO_2 and brine allowing a uniform spread of the CO_2. The injection is followed by a brine only injection, to trap the CO_2. Trapping efficiency of this method is suggested to be up to 90% of injected CO_2 (Qi et al. 2009).

2.3.7 **Geological Variability**

Geological CO_2 storage represents an interface between an engineered CO_2 transport system and a natural storage system. Whilst the properties of the transport system are comparatively well known, one of the main considerations of a storage system is the geological variability. Rock units used for geological storage will have varying thickness, continuity, physical make-up and physical and chemical properties, these all affect their suitability for CO_2 storage. The variability within the rock unit may be overlooked in the engineering description. Some of the properties that must be taken into account include:

- **Pore properties** – pore volume, connectivity, shape and size are all influenced by the formation history of a rock. The pore volume controls the storage space and is influenced by the grain structure of a rock and the level of compaction and diagenesis a rock has experienced. For example, sandstone with a high clay content, may have a much lower pore volume than a 'clean' sand, with a low clay content, due to clay minerals infilling the porosity. Permeability is a measure of flow in rocks, but the connectivity of pore spaces is also an important issue; high permeabilities may be measured in a rock, but there may be natural barriers to fluid flow that may not be picked up in core examination of a rock. For example, cementation along fractures may compartmentalise an otherwise highly permeable reservoir. High permeability zones within a cap rock layer would also reduce compromise the seal.
- **Pore structure/rock fabric** – Pre-existing structures and fabric in the rock affect the grain packing and pore structure, and this can affect flow within the rock, leading to preferential flow directions and flow baffles. On the field scale, this is manifested as anisotropic permeability and can seriously affect flow behaviour in a storage reservoir. Permeability anisotropy in reservoir rocks generally results from cross bedding and the presence of shale beds (Lake 1988). Truss (2004) reports baffles to vertical flow in unsaturated zone of the Sherwood Sandstone resulting from deltaic river flood deposits. The Sherwood Sandstone is a major sandstone unit that is found offshore as the Bunter Sandstone; it is a major potential storage unit for $CO_2$and will be discussed further in later sections. The most common parameter used to describe permeability anisotropy is the k_v/k_h ratio. This is the ratio of vertical to horizontal permeability. Morton, Thomas et al. (2002) discuss methods for up-scaling measurement of the k_v/k_h ratio in the Sherwood Sandstone from field and core measurements to reservoir simulation models. They show that values can range from 0.0001 up to ~1, and that significant errors can occur in up-scaling to field models. Begg et al. (1989) also show similar work for the Sherwood Sandstone in the Wytch Farm field, history matched simulations show that the up-scaled values of the k_v/k_h ratio are as low as 0.001, whilst non-scaled values are around 0.4 to 0.6.
- **Continuity** – As rock units are not laid down uniformly and consistently they may vary in thickness and be discontinuous in nature. Varying thickness if not quantified correctly may alter storage volume estimates and discontinuities in a rock layer can inhibit connectivity or compromise seals. For example, a reservoir layer can 'pinch out' diminishing volume estimates. Examples of discontinuities include river channels in deltaic sediments and sand lenses in mudstones.
- **Physical and chemical properties** – Measurements of physical and chemical properties of a rock, for example the compressibility, are often only undertaken on very small samples of the rock. Due to the variable nature of rocks, this may give a very inaccurate understanding of the real behaviour of the rock when extrapolating from lab scale to field scale. For example in the case of compressibility, this could

lead to unexpected differential compaction or expansion of the reservoir, which would alter storage capacity and injectivity into the reservoir.

2.3.8 **Summary**

The processes and conditions required for trapping and the flow properties that must be considered for CO_2 storage have been discussed specifically in relation to reservoirs. To ensure secure storage and understand the behaviour of CO_2 in storage, the entire storage system must be considered, this includes the rocks above and surrounding the reservoir. The remaining properties of the storage system are discussed in the following section, including a discussion of specific types of storage reservoirs that will be considered.

2.4 **Subsurface Storage Conditions**

Geological storage sites will exist deep underground to ensure suitable properties for efficient and secure storage, as previously discussed. As a result of the subsurface conditions the storage reservoirs will be subject to large pressures exerted by the rocks above the storage reservoir, the overburden, and confining pressures from the rocks surrounding the reservoir the side and underburden. Temperature also increases with depth in the subsurface. The deformation of the reservoir, the overburden, and the stress state in and around the reservoir are a significant concern for secure storage. Changes in the stress state can lead to deformation, re-activation of faults, and the formation of fractures; these can all lead to loss of secure storage and compromise the storage capacity, and injectivity of formations. The important principles relating to stress state, deformation, faults and geomechanics are outlined below.

2.4.1 **Subsurface Temperature and Pressure**

The temperature of the reservoir is dependent on the geothermal gradient in the region. Figure 2.1 shows typical gradients of between 20-35°C/km (Holloway 2008). The geothermal gradient can vary markedly across a region. For example, in the North Sea (UK, Dutch and Norwegian sectors) the gradient varies from 18°C/km south of Norway to >40˚C/km in the Central Graben, with an average of 29°C/km (Harper 1971, Evans 1974, Angus et al. 2009). North Sea reservoir depths range from 1100m to over 5000m, with many around 2000-3000m suggesting typical reservoir temperatures of around 60-100°C (Glennie 1998). The temperature in the reservoir will affect the density and volume of the CO_2 in storage, which must be reflected when modelling the CO_2 in storage. If CO_2 is transported through surface pipelines at ambient conditions, the temperature difference between the CO_2 and reservoir fluids could be significant. This has implications for stress conditions in and around the reservoir and this will be discussed in the discussion of specific risks in Section 2.8.

All rocks at reservoir depths will contain fluid in the pore spaces of the rock. The pressure of this fluid, the pore pressure, can vary due to many different factors. The pore pressure is said to be hydrostatic if it is the same as the pressure at depth that would be exerted by an

equivalent column of water (head pressure). Hydrostatic pressures suggest that the pore spaces are interconnected in some form from the surface to depth (Zoback 2007, Holloway 2008). Typical pore pressure-depth gradients for the hydrostatic condition are 9.71MPa/km for freshwater and 11.44MPa/km for a saturated brine (Swarbrick and Osborne 1998). The pore pressure can deviate above and in rare cases below the hydrostatic pressure and this is termed overpressure or underpressure respectively. Figure 2.10 shows the concept and relationship of underpressure, overpressure, hydrostatic and lithostatic pressures in a plot of pressure against depth. Fluids with different densities, such as oil, gas and CO_2, will alter the gradient of the pore pressure plot, pressure measurements are often used as indicators of subsurface hydrocarbons.

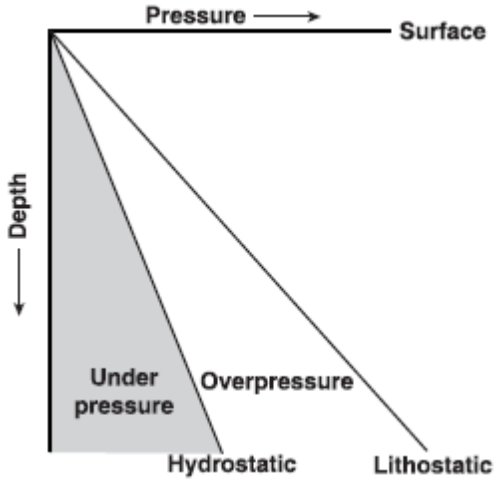

Figure 2.10 – Plot demonstrating the concept of pore pressure deviation with depth. Hydrostatic represents the pressure corresponding to a column of water with depth, lithostatic the pressure of the overburden with depth, and the regions of over and underpressure related to the hydrostatic pressure (Swarbrick and Osborne 1998).

Overpressures are sustained in a confined pore volume when pressure cannot equilibrate to the hydrostatic. Theoretically, the overpressure can reach the level of the overburden pressure, and is termed lithostatic pressure at this point. However, due to the low tensile strength of rock, the pore pressure will always be less than the least principal stress due to tensile fracturing (Zoback 2007). Several mechanisms have been suggested for the generation of overpressures. According to Swarbrick and Osborne (1998) the most likely mechanisms are disequilibrium compaction due to rapid loading of fine grained sediments and volume expansion associated with gas generation. Disequilibrium compaction occurs in young Tertiary delta basins including the Mississippi and Nile, and young intra-cratonic basins including the North Sea (Swarbrick and Osborne 1998). Gas generation may occur from gas-prone source rocks and oil-to-gas cracking in deep North Sea basins, the Gulf of Mexico, and the Anadarko Basin (Swarbrick and Osborne 1998). Underpressures occur when reservoirs are depleted of hydrocarbons, and less commonly due to natural phenomena relating to rock uplift, dilation and cooling (Swarbrick and Osborne 1998).

Consideration of the pressurisation state of the reservoir is critical, as the injection of fluids will increase the reservoir pressure. Figure 2.11 shows the effect of increasing the pore pressure P_f. If pore pressure increase is large enough, failure will occur in the reservoir leading to tensile or shear fracturing, which could lead to potential leakage, or reduce capacity of the reservoir due to a lowering of the safe injection pressure. The safe injection pressure of a reservoir below which fracturing will not occur is termed the fracture pressure, and any injection into a reservoir must be below this pressure. Usually a safety factor margin is incorporated into the fracture pressure estimation to safeguard against exceeding the fracture pressure due to error (e.g. 80% of fracture pressure is a typical limit). Deformation, stress and failure in the reservoir and overburden are discussed in the following sections.

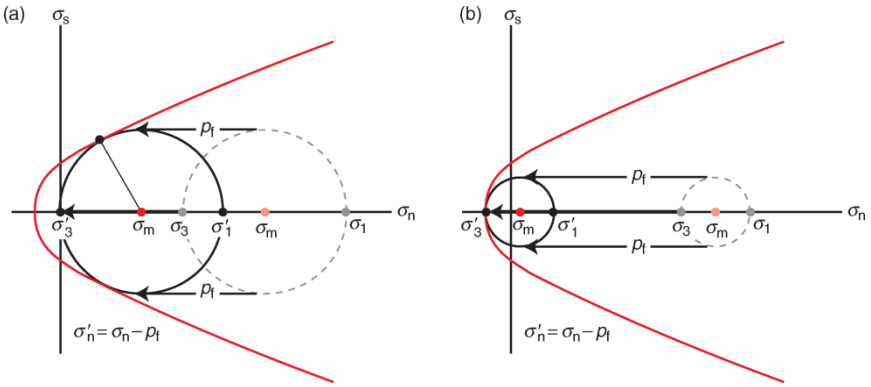

Figure 2.11 – The effect of pore pressure on failure mode of rocks from (from Fossen 2010), P_f represents the pore fluid pressure, σ_1 and σ_3 are the maximum and minimum principal stress, the red line is the failure envelope. (a) illustrates shear failure, where the Mohr circle touches the failure envelope and the minimum principle stress is positive. (b) illustrates tensile fracture formation when the Mohr circle touches the failure envelope and the minimum principal stress is negative.

2.4.2 Deformation and Stress

The rocks that make up the overburden and reservoir will deform when they are subjected to a change in stress. This deformation is either recoverable (where the strains are recovered) elastic deformation or it is non-recoverable plastic deformation.

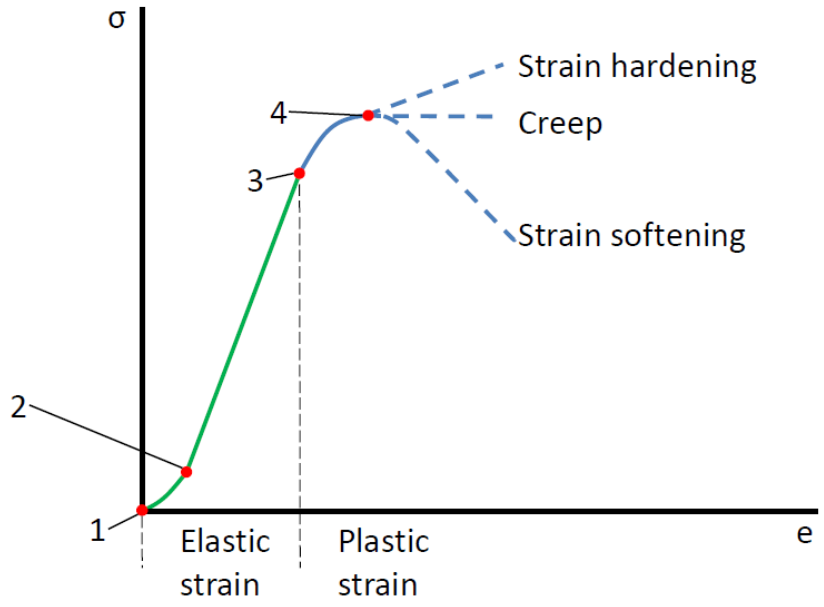

Figure 2.12 – General stress strain graph for an elastic-plastic material, showing elastic strain 1-3, plastic strain hardening 3-4 and possible further stress-strain paths.

Figure 2.12 shows a general stress strain graph for the response of an elastic-plastic material. The elastic strain region shows a non-linear elastic response (1 – 2) and a linear elastic response (2 -3). The non-linear response is associated with the closure of microcracks. This strain is entirely recoverable, and is common in geological materials. Point 3 on the graph represents the yield point beyond which plastic strain are also developed in addition to elastic strains. At this point, the material exhibits elasto-plastic behaviour. The yield point represents the onset of material dependent micro-scale deformation processes. In terms of geological materials, these can range from unconsolidated sediments to competent rock, and the processes can include grain boundary sliding or grain rearrangement in loose sediments, to atomic dislocations in more competent material, such as crystalline rocks. Point 4 represents the peak strength of the material. Between points 3 and 4 the material exhibits strain hardening, where an increase in applied stress is required to generate additional strain in the material. Beyond this point, possible stress-strain trajectories are illustrated. Continued strain hardening increases the peak strength of the material, the mechanisms for strain hardening are related to the micro-scale deformation processes previously mentioned. These processes occur on various scales, from an accumulation of atomic dislocations to increased grain contact resulting from grain rearrangement and filling of pores with grain fragments from breakage (Schutjens et al. 2001, Fossen 2010, Al-Zadjali 2011). Creep involves continued strain with no increase in stress and strain softening is a reduction in the stress required to develop strain in the model. Strain softening arises from failure within the material by the formation of fractures or fractures zones, and once again the type of material will affect the processes by which this occurs (Schutjens et al. 2001). The deformation and failure mechanisms are discussed in more detail in the following section.

The stress state in the subsurface is controlled by the material properties of the rock and gravity, and is also affected by the pore pressure in situations where the rock contains fluid. When pore pressures are present both the total, and effective stresses must be considered. The total stress is the sum of pore pressure and the effective stress, which is the stress carried by the framework of the rock or:

$$\sigma' = \sigma - P_0 \qquad \textbf{Equation 2.10}$$

where σ' is effective stress, σ is total stress and P_0 is pore pressure. The vertical stress is the simplest stress to define and is the product of gravity, density and thickness of the rock overlying the point in the subsurface in question:

$$\sigma_v = \rho g z. \qquad \textbf{Equation 2.11}$$

σ_v is the total vertical stress, ρ is the density of the material overlying the point, g is gravitational acceleration and z is the thickness of material overlying the point. Under the assumption of uniaxial strain, where the free surface of the earth permits vertical strain but horizontal strain is constrained, the principal stresses are considered in terms of the vertical stress, and horizontal stresses (σ_H and σ_h). The horizontal stresses are the confining stresses in the subsurface. In sedimentary basins the vertical stress is often the first principal stress σ_1 and the horizontal stresses are the second and third principal stresses, σ_2 and σ_3. In this case $\sigma_v > \sigma_H > \sigma_h$, and is termed an extensional regime. The models presented in this thesis are only considered for an extensional initial stress regime and so all discussion of horizontal, vertical and principal stresses is in this context.

Under the uniaxial strain assumption the vertical shortening of compaction of rock leads to horizontal stresses due to the Poisson's effect, the stresses arise as the rock is not able to expand horizontally. Thus, the vertical stress is related to the horizontal stress by Poisson's ratio:

$$\sigma_H = \sigma_h = \frac{\upsilon}{1-\upsilon}\sigma_v \qquad \textbf{Equation 2.12}$$

where ν is the Poisson's ratio (Fossen 2010). Equation 2.12 is only valid under monotonic loading and assuming isotropic elasticity. The Poisson's ratio term is often replaced with the coefficient K or assuming a uniaxial static condition K_0. Additionally, the stresses should be expressed in terms of effective stresses to account for pore pressures, as at very high pore pressures (overpressured formation) the relationship between horizontal and vertical stresses could be 1:1 (Bjørlykke and Høeg 1997). The relationships between horizontal and vertical (effective) stress then become:

$$\boldsymbol{\sigma'_v = K\sigma'_h} \qquad \textbf{Equation 2.13}$$

or

$$\sigma'_v = K_0 \sigma'_h \qquad \textbf{Equation 2.14}$$

where K is lateral stress coefficient and K_0 the lateral stress coefficient (or coefficient of earth pressure) at rest (Bjørlykke and Høeg 1997). The lateral stress coefficient at rest becomes important for initialising geomechanical models, where the initial stage represents the sedimentation and burial loading of the model termed geostatic initialisation. This initial stage will determine the ratio of horizontal to vertical stress. The lateral stress coefficient can be determined from laboratory tests, and the value for normally consolidated (existing at historically maximal vertical stress) sediments and soft sedimentary rocks ranges between 0.2 and 0.6 (Bjørlykke and Høeg 1997).

As discussed in section 2.4.1, the temperature also increases with depth, but may also be reduced by artificial processes in the reservoir (e.g. the injection of cold CO_2). As with other materials, rocks are subject to expansion and contraction during heating and cooling, and this can generate additional stresses in the subsurface. The equation relating temperature change with changes in stress is:

$$\Delta\sigma^T = \frac{E\alpha_T(\Delta T)}{1-\upsilon} \qquad \textbf{Equation 2.15}$$

where $\Delta\sigma^T$ is temperature induced changes in stress, E is Young's modulus, α_T is the coefficient of linear thermal expansion, and ΔT is temperature change. In the case of cooling, a reduction in the stress may be observed and in certain scenarios, this could promote tensile fracturing or contribute to shear fracturing. This may be particularly significant in the case of horizontal stresses, as this is likely to be the lowest principal stress and therefore more prone to failure in shear or tensile failure, as described in Figure 2.11.

The Mohr circle of stress is used to describe a 2D representation of the stress state in terms of the horizontal and vertical stress. The equations for a Mohr circle defined by the maximum and minimum stresses for a plane dipping at an angle θ_s to the maximum stress direction in of the shear τ and normal σ' stresses are:

$$\boldsymbol{\sigma' = \frac{\sigma'_v+\sigma'_h}{2} + \frac{\sigma'_v-\sigma'_h}{2} cos2\theta_s} \qquad \textbf{Equation 2.16}$$

and

$$\tau = \frac{\sigma'_v-\sigma'_h}{2} sin2\theta_s. \qquad \textbf{Equation 2.17}$$

It is possible to simplify the Mohr circle to a point designation using composite stress parameters that allow stresses to be plotted as a line and provide a description of the stress path. The Massachusetts Institute of Technology (MIT) parameters are:

$$\boldsymbol{s' = \frac{\sigma'_v+\sigma'_h}{2}} \qquad \textbf{Equation 2.18}$$

and

$$t = \frac{\sigma'_v-\sigma'_h}{2} \qquad \textbf{Equation 2.19}$$

where *s'* represents the centre of the Mohr circle and *t* represents the radius of the Mohr circle. *t* represents the deviator stress and s' represents the mean (effective) stress. Further composite stress parameters that are often used are the Cambridge parameters:

$$\boldsymbol{q = \frac{1}{\sqrt{2}}\sqrt{(\sigma'_1 - \sigma'_2)^2 + (\sigma'_2 - \sigma'_3)^2(\sigma'_1 - \sigma'_3)^2}} \qquad \textbf{Equation 2.20}$$

and

$$p' = \frac{1}{3}(\sigma'_1 + \sigma'_2 + \sigma'_3). \qquad \textbf{Equation 2.21}$$

The Cambridge *p'* and *q* terms define the deviator stress invariant q and mean stress invariant *p'*, and where $\sigma_2 = \sigma_3$ the simplified relationships are given by:

$$\boldsymbol{q = \sigma'_1 - \sigma'_3} \qquad \textbf{Equation 2.22}$$

and

$$p' = \frac{1}{3}(\sigma'_1 + 2\sigma'_3). \qquad \textbf{Equation 2.23}$$

If $\sigma_2 = \sigma_3$ it is possible to manipulate both equations into the relationships:

$$\boldsymbol{t = \frac{q}{2}} \qquad \textbf{Equation 2.24}$$

and

$$s' = p' + \frac{q}{6}. \qquad \textbf{Equation 2.25}$$

2.4.3 **Deformation Mechanisms**

There are a spectrum of responses observed in geological materials in relation to the way they deform and this is related to the nature of formation processes and the materials current state. Rocks are formed through diagenetic processes cementing, compacting and solidifying sediments. Sediments that have not been diagenetically altered are termed engineering soils. As such, there is a transition from a soil to a rock, and the two end members of this transition are covered by soil and rock mechanics. Many of the sediments in the UK North Sea, which will be the focus of this thesis, are poorly lithified and weakly cemented sediments (Bjørlykke and Høeg 1997, Fisher et al. 2007) and thus present many of the deformational characteristics of a soil. Consequently, the remaining focus of this thesis considers the mechanics of these sediments in particular and the aspects of soil and rock mechanics that are relevant.

Regardless of the differing phenomenological responses of materials to deformation, the numerical treatment of deformation is common among many materials. Several constitutive models have been developed to quantify this behaviour numerically. The Mohr-Coulomb model is the most well-known model in the region of rock and soil mechanics, and is one of the simplest to implement. The Mohr-Coulomb model is a frictional failure/yield surface that describes the onset of shear failure in a material at yield, the equation for the surface is:

$$\tau = S_0 + \mu\sigma' \qquad \textbf{Equation 2.26}$$

where S_0 is cohesion, which represents the inherent shear strength, and μ is the coefficient of internal friction. The Mohr-Coulomb model is commonly used in rock mechanics as it describes shear failure well for a range of engineering applications. Stress states in $-\sigma'$ space represent tensile failure. Figure 2.13 shows a representation of the yield surface in normal-shear stress space and shows that failure will occur at the point of intersect of the line at an angle 2β from σ_1, which is the orientation of the plane of shear failure.

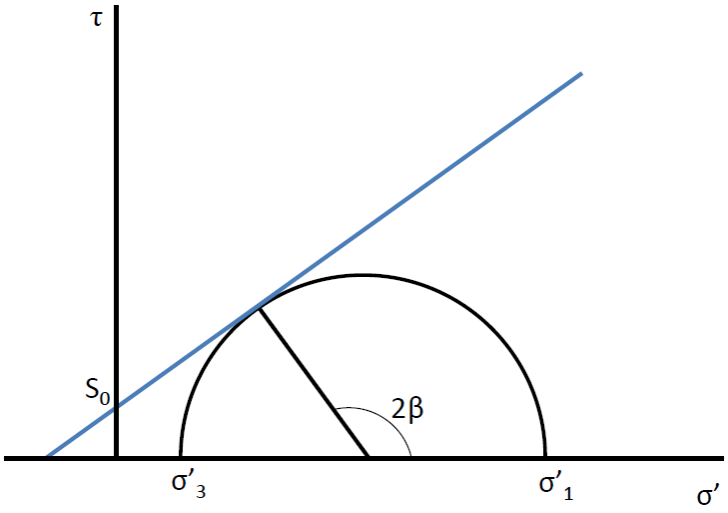

Figure 2.13 – Mohr circle representation of the Mohr-Coulomb yield surface in normal-shear stress space.

Simple models such as the Mohr-Coulomb model are only capable of modelling certain aspects of soil behaviour. However, soil behaviour involves many other aspects that are important for a range of applications including reservoir geomechanics, such as compaction and shear softening/hardening. This has led to the development of more complicated constitutive models for soils, which are also useful in computational modelling of soil behaviour. Critical state soil mechanics was formalised as a concept in the late 1950s and describes how soil behaviour tends towards an ultimate condition during continued plastic shearing where no changes in volume or effective stress are observed. This holds true regardless of the type of engineering soil under consideration (Roscoe et al. 1958, Wood 1990). A simple model that incorporates the critical state concept along with treatment of compaction failure is the Modified Cam-Clay model developed in the late 1960s. This model forms the basis for many more complex models that have since been developed (Wood 1990). The elements required for a constitutive model sufficient for numerical modelling are now described, along with further discussion of soil deformation behaviour.

From Equation 2.17 and Equation 2.19, it is evident that the deviator stress invariant q relates to shear stress development in a material, and traversing along the q axis in a p'-q (also known as effective stress plane) plot at a constant mean stress will lead to shear failure. Equally, traversing along the p' (mean stress) axis will lead to isotropic compression

of the material, which leads to compaction. These two deformation modes then define how the material behaves, and a yield surface which describes both of these behaviours is required. Additionally, with negative (tensile stresses) a yield surface that describes failure in tension is required. Figure 2.14 shows a generic yield surface in p'-q space. A material may follow any stress path within the yield surface and will only yield once a stress state on the yield surface is reached. States outside the yield surface are not possible and represent non-recoverable plastic damage that has occurred to the material. For stress states within the yield surface deformation is elastic.

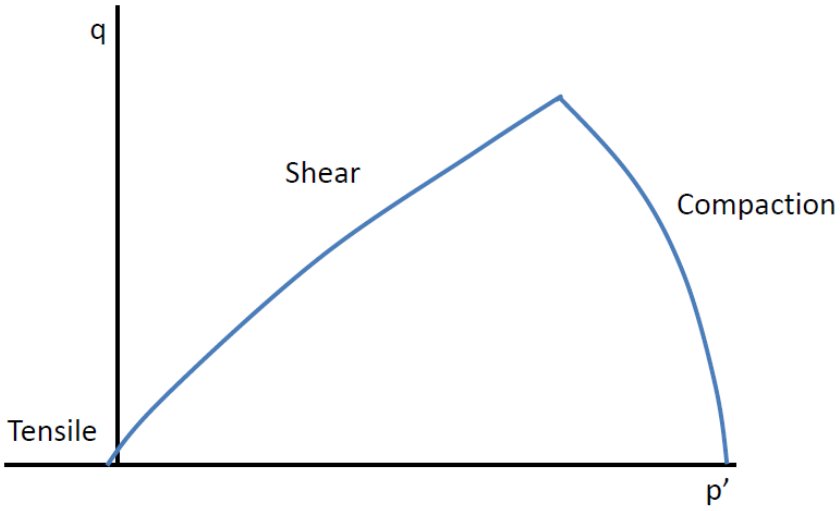

Figure 2.14 – Generic description of a yield surface in p-q space showing shear, compaction and tensile failure/yield regions based on (Fjær et al. 2008)

In addition to the stress state of the material, consideration of volume change is also necessary. The volume will change during deformation, for instance during isotropic compression, and is a limiting condition of the critical state i.e. zero volume change during plastic shearing. Compaction or consolidation of the material leads to strength increase and yield surface expansion representing plastic deformation. Volume change is generally represented by the v-p' (or compression plane) plot:

$$v = 1 + e = 1 + \frac{n}{1-n} \qquad \textbf{Equation 2.27}$$

where v is the specific volume, and e and n are the void ratio and porosity. A v-p' plot is shown in Figure 2.15, the normal consolidation line represents volume decrease during consolidation (increase in p'). The volume change during consolidation has a plastic component, represented by expansion of the yield surface during compaction. When unloading and reloading occurs the elastic volumetric strains are recovered along the unloading-reloading line.

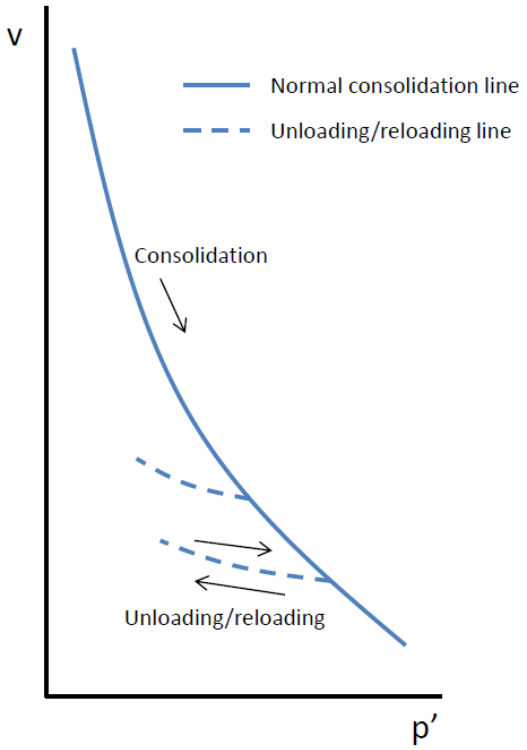

Figure 2.15 – Compression plane or v-p' plot of specific volume with p', describing permanent plastic deformation during compaction/consolidation and the elastic unloading-reloading response based on (Wood 1990).

The soil will reach an ultimate condition during continued plastic shearing, where no volume change or change in effective stress is observed. The physical basis for this ultimate state involves the behaviour of the soil particles during shearing and depends on the initial state of the soil prior to shearing. So-called dense sands or overconsolidated clays will dilate when sheared, whereas loose sands or normally consolidated clays will contract when sheared. This differing behaviour is due to the packing of particles in the material. Loose or normally consolidated refers to a loose packing of particles that will easily collapse into pores spaces and increase in strength when sheared. Dense or overconsolidated refers to a particle arrangements that must overcome the interlocking of particles to shear, and is accompanied by a reduction in shear strength after all interlocking is overcome. The state of consolidation refers to the historical maximum consolidation stress that the soil has been subjected to. Normally consolidated soils are currently at the maximum consolidation stress, whereas overconsolidated soils have experienced a higher consolidation stress than the current state in their past. The maximum consolidation stress invariant of a soil is p_c. The behaviour of normally and overconsolidated soils is illustrated by typical shear stress vs. shear strain plots as shown in Figure 2.16.

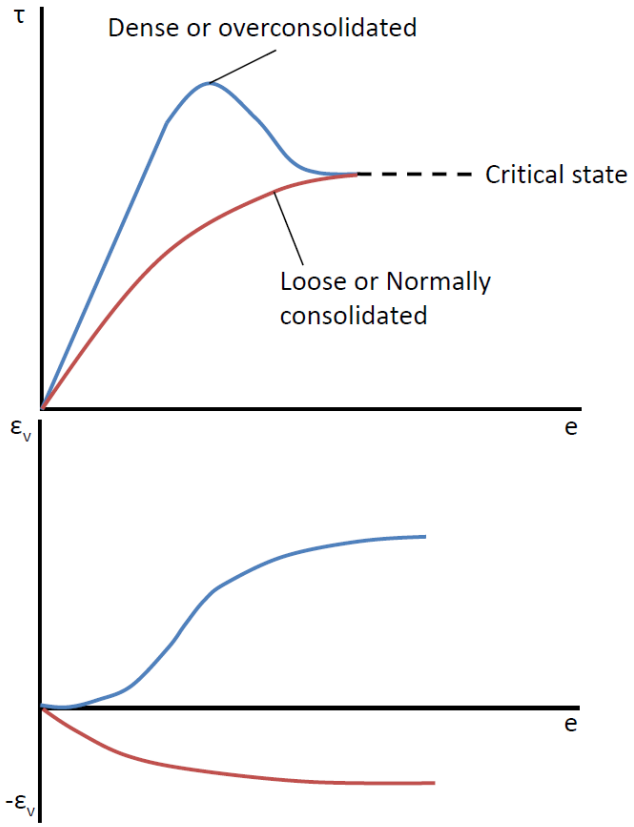

Figure 2.16 – Graphical representation of the response of soils to shearing under the critical state theory. Peak strength of the dense material is reached when maximum interlocking resistance is mobilised, and then strength reduces as interlocking is overcome, this peak strength is represented by the steepest gradient on the volumetric/shear strain graph. The loose material gradually mobilises peak strength as volume is reduced and the material approaches critical state.

The critical state based model must therefore take account of hardening/strengthening and weakening/softening, the observed volume change during deformation as well as describing the critical state condition. The Cam Clay model is the simplest of this class of model, and the elliptical yield surface of this model is used to describe critical state theory below.

It is found that the critical state condition is reached for a specific effective stress ratio that is:

$$\frac{q_{cs}}{p'_{cs}} = \eta_{cs} = M \qquad \textbf{Equation 2.28}$$

where η_{cs} is the effective stress ratio at critical state and M gives the slope of the critical state line in p'-q space. The critical state line (CSL) in p'-q represents ratios of effective stress where the critical state can be reached, and represents the apex of a series of yield surfaces as illustrated in Figure 2.17. The Cam Clay yield surface is elliptical and is described by:

$$\frac{q^2}{p'^2} + M\left(1 - \frac{p'_c}{p'}\right) = 0 \qquad \textbf{Equation 2.29}$$

where p_c is the intercept of the yield surface with the p' axis.

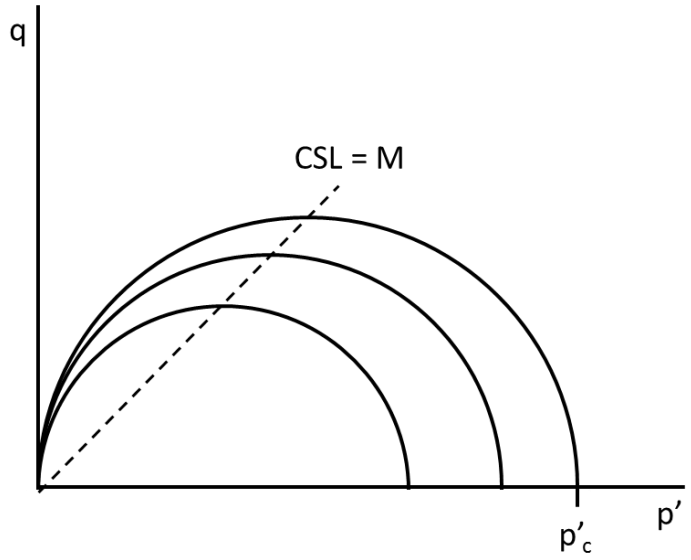

Figure 2.17 – Slope of the critical state line at the apex of a series of yield surfaces adapted from Wood (1990).

The yield surface will expand if stress paths intersect the yield surface to the right of the critical state line in Figure 2.17 until the stress path reaches the apex of the yield surface, and thus critical state. This corresponds to the behaviour of lightly overconsolidated or normally consolidated materials and is associated with volume decrease and represents hardening behaviour. If the stress path intersects the yield surface to the left of the critical state line the yield surface will contract until the critical state is reached. This corresponds to the behaviour of heavily overconsolidated material, and is associated with volume increase and represents softening behaviour. If the stress path is purely isotropic the critical state cannot be reached as the stress path will travel along the p' axis, and the yield surface will simply expand. The maximum intersect of the yield surface with the p' axis p_c (sometimes called p_o) represents the initial pre-consolidation stress and represents the maximum degree of consolidation the soil has been subjected to.

Examining the model in v-p' space, or v-log(p') space as in Figure 2.18, shows that the right hand intersect of the yield surface forms the isotropic normal consolidation line, on a v-log(p') plot this becomes a straight line. The CSL can also be plotted and is a straight line parallel to the isotropic normal consolidation line. In this plot normally to lightly overconsolidated materials lie to the right of the CSL and heavily overconsolidated materials to the left of the CSL. Figure 2.18 can then be used to define the specific volume (*v*) at critical state as:

$$\boldsymbol{v_{cs} = \Gamma - \lambda \ln p'_{cs}} \qquad \textbf{Equation 2.30}$$

where

$$\Gamma = N - (\lambda - \kappa)\ln 2 \qquad \textbf{Equation 2.31}$$

λ is the slope of normal consolidation line, κ is the slope of the unloading-reloading line and N is the value of v on the normal compression line at p' = 1kPa (unit dependent).

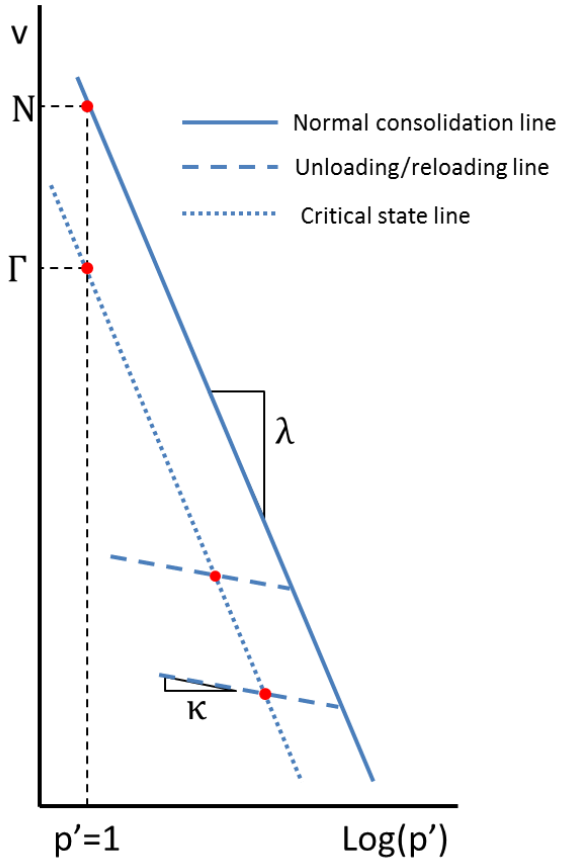

Figure 2.18 – v-log(p') plot of isotropic normal consolidation line, critical state line and unloading-reloading line (Wood 1990).

A triaxial plot of p'-q-v allows the form of the yield surface to be appreciated, Figure 2.19 shows the components of the yield surface in p'-q-v space, along with the positions of the critical state line and the isotropic consolidation line. As can be seen from the diagram on the left, based on previous discussion of the p'-q surface, the yield surface expands with increasing consolidation (decreasing v). It can be demonstrated that a state boundary surface exists, based on the critical state theory, that defines the attainable stress and volume states of soils, this consists of the Hvorslev surface and Roscoe surface (Wood 1990). Stress states exceeding the yield surface must generate plastic strains. In the case of stress states, exceeding the Hvorslev surface the plastic strains will be positive (dilative) and strain softening will occur with associated contraction of the yield surface towards critical state. In the case of states exceeding the Roscoe surface, the strains will be negative (contractive) and will expand the yield surface.

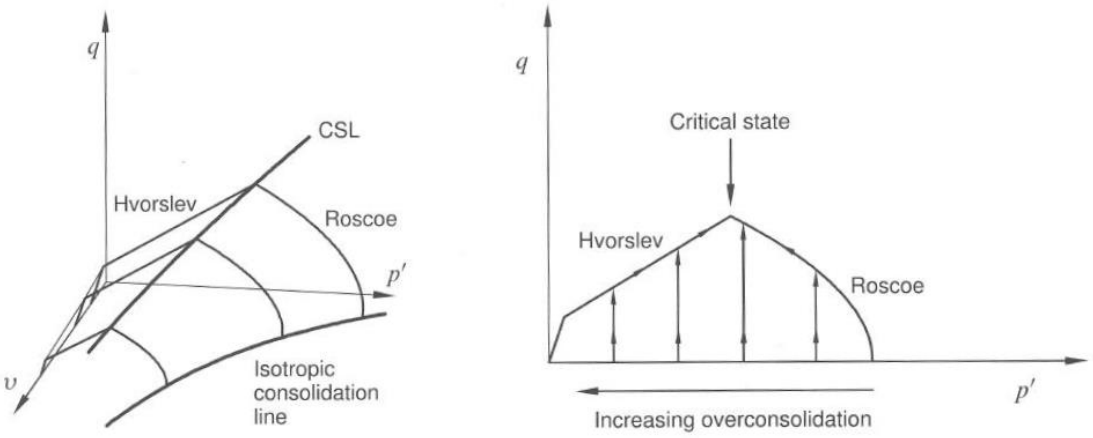

Figure 2.19 – Hvorslev and Roscoe surfaces and the critical state and isotropic consolidation line in p'-q-v space (left) and the projection of the surface at a particular p_c on the p'-q plane (right) (Fjær et al. 2008)

Any constitutive model must also be formulated to describe the plastic volumetric behaviour, which is defined by the plastic flow rule, this can be plotted as the plastic potential surface. Thus far, the flow rule has been implicitly described as identical to the yield surface, as in the case of the Cam Clay model shown in Figure 2.20. Models with plastic potential surfaces that are identical to the yield surface are termed associated flow rules. For the Cam Clay model the plastic volumetric strain increment is given by:

$$\delta\varepsilon_p^p = \frac{\lambda-\kappa}{1+e}\left(\frac{\delta p\prime}{p\prime} + \frac{2\eta\delta\eta}{M^2+\eta^2}\right) \qquad \textbf{Equation 2.32}$$

the plastic shear strain increment by:

$$\delta\varepsilon_p^q = \frac{\lambda-\kappa}{1+e}\left(\frac{\delta p\prime}{p\prime} + \frac{2\eta\delta\eta}{M^2+\eta^2}\right)\frac{2\eta}{M^2-\eta^2} \qquad \textbf{Equation 2.33}$$

and the ratio of strain increments is given by:

$$\boldsymbol{\delta\varepsilon_p^q = \delta\varepsilon_p^p \frac{2\eta}{M^2-\eta^2}} \qquad \textbf{Equation 2.34}$$

where

$$\frac{\delta\varepsilon_p^q}{\delta\varepsilon_p^p} = \frac{2\eta}{M^2-\eta^2} \qquad \textbf{Equation 2.35}$$

Non-associated plastic flow rules are also possible, and simply describe a separate plastic flow rule surface to the yield surface. Non-associated flow rules are important for materials such as sand where associated flow rules may often overestimate the dilation (Wood 1990).

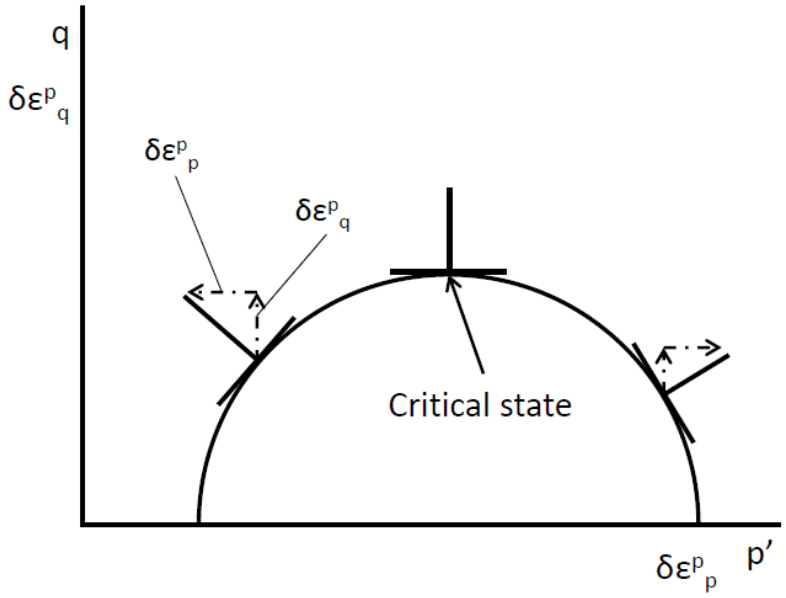

Figure 2.20 – Cam Clay associated plastic potential surface and yield surface showing plastic strain increment vectors for different stress states. Adapted from Wood (1990).

The plastic potential surface determines the plastic strain increment vector, this is dependent upon the stress state at yielding and not the stress path leading to yield. The vector shown in Figure 2.20 describes the two components of plastic strain, plastic volumetric strain $\delta\varepsilon^p_p$ and plastic shear strain $\delta\varepsilon^p_q$. The figure shows that on the overconsolidated side of critical state (left of figure) volumetric strain is negative (dilation), and on the normally consolidated side (right) volumetric strain is positive (contraction), as is consistent with the previous discussion of material behaviour. The volumetric strain at critical state is 0 and only shear strain is observed, as is consistent with the critical state description.

This section had presented the key elements of critical state constitutive models that are relevant to rocks and sediments. More complex models exist and these can include modified yield surface shapes to improve numerical analysis, rate dependence, creep and orthotropic properties. An in depth discussion of advanced constituent models is beyond the scope of this thesis.

2.4.4 **Deformation in Geological Materials**

The general background to the mechanics of material deformation has been presented in the previous section. Issues specific to geological materials, including modes of deformation and the differences between geological materials and pure engineering soils are discussed here.

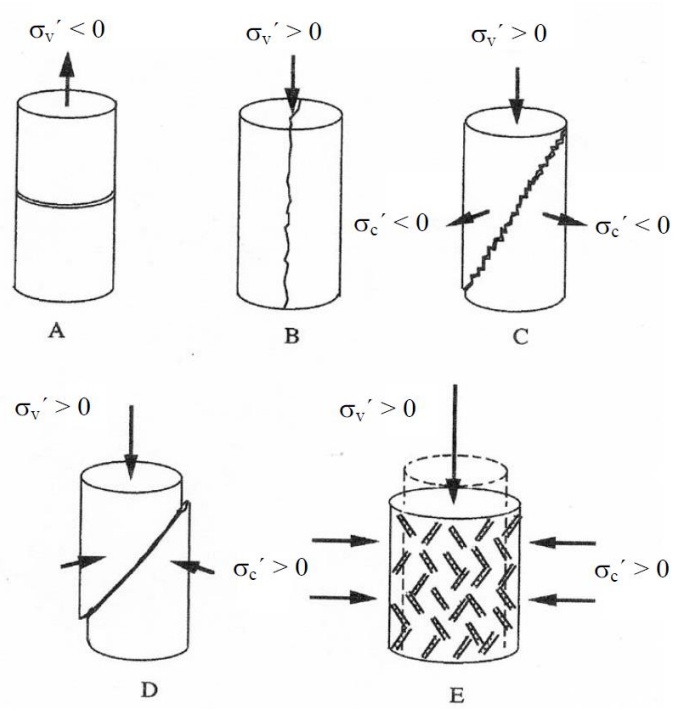

Figure 2.21 – Failure modes of rock cylinders under axi-symmetric loading, a) tension fracture, b) extension fracture, c) dilational/hybrid extension shear fracture, d) shear fracture, e) multi-shear cataclasis (from Mandl 2005). In this case σ'$_c$ is confining stress.

Figure 2.21 shows how the failure modes of the rock cylinders in triaxial tests are related to the stress acting upon the rock. Some of the stress combinations shown in the figure can arise due to fluid pressure changes (stresses in diagram are effective stress). For example, increased fluid pressure can lead to tensile or shear fracturing, as is the case in hydraulic fracturing operations (Solberg et al. 1977). The failure modes shown in Figure 2.21 are manifestations of different types of material behaviour. In Figure 2.21 a) to d) the material is behaving in a brittle manner, only d) would exhibit strain softening as the others in this triaxial test would fail catastrophically and fall apart. All samples exhibit a peak stress followed by a post peak reduction in strength characteristic of brittle failure. Brittle failure would produce a stress-strain curve similar to the dense/overconsolidated material in Figure 2.16. Figure 2.21 e) would exhibit strain hardening and would produce a stress-strain curve similar to the loose/normally consolidated material in Figure 2.16. This type of curve describes a ductile response. The application of this term ductile is not consistent in the literature. Mandl (2005) points out that in the case of Figure 2.21 e) the curve would be phenomenologically ductile, yet rheologically the strain would occur as a multi-shear brittle process or grain scale brittle deformation. Mandl (2005) reserves the use of the term ductile for rate sensitive processes including creep and stress relaxation, and so behaviour similar to Figure 2.21 e) is termed semi-brittle. In this study, most attention is paid to materials that are transitional between engineering soils and rocks, and so the use of term ductile (especially in reviewed literature) applies to phenomenologically ductile materials and is interchangeable with the semi-brittle definition used by Mandl (2005).

The typical failure modes illustrated in Figure 2.21 only describe the orientation and basic types of failure planes in tri-axial stress conditions. The actual discontinuities developed due to failure in both in the lab and in nature may be more complex and more diffuse. For example discrete failure planes may be less visible, and may depend upon extent of cementation, confining pressures and grain size, which can all be related to burial depth (Byerlee 1968, Scott and Nielsen 1991, Wong et al. 1997, Fisher et al. 2003, Fisher et al. 2007). Figure 2.22 shows the range of failure behaviour between brittle and ductile end members by Griggs and Handin (1960) for triaxial compression and extension tests, with the associated stress-strain curves. Cases 3, 4 and 5 in Figure 2.22 show a transitional regime between brittle behaviour with strain softening, and ductile behaviour with strain hardening. In the brittle regime, the failure is restricted to a discrete plane, and in the ductile regime, deformation is distributed without an obvious failure plane. The transitional regime shows multiple failure 'bands', referred to as multiple deformation bands, and characterise the brittle-ductile transition (Scott and Nielsen 1991, Fisher et al. 2003).

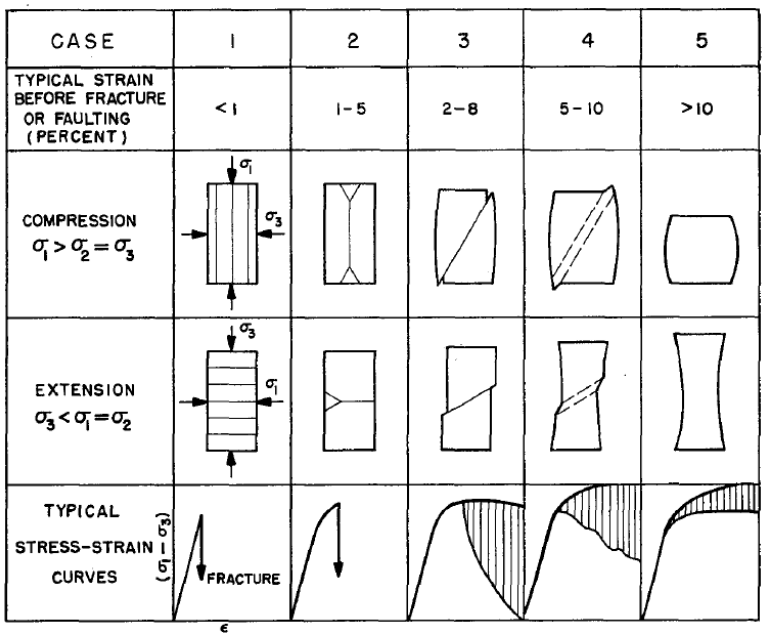

Figure 2.22 – Transition from brittle to ductile behaviour in triaxial compression and extension tests, stress-strain curves show variability in behaviour (ruled sections) and transition between cases 3, 4 and 5, this represents the brittle-ductile transition zone, characterised by multiple deformation bands. (Diagram from Griggs and Handin 1960).

Fisher, Harris et al. (2007) and Fisher, Casey et al. (2003) present a framework for defining the behaviour of arenites (defined as poorly-lithified sands to well-lithified sandstones) undergoing deformation, drawing on the work of Zhu and Wong (1997) and Walderhaug (1996). They link the mode of deformation (brittle to ductile) to the stress state based on the influence of grain size (influences area available for cementation), porosity (influenced by level of compaction and quartz cementation), burial rate and geothermal gradient (affects diagenetic processes such as quartz cementation). The model presented by Fisher, Harris et al. (2007) and Fisher, Casey et al. (2003) is able to predict the volumetric behaviour of the arenites during deformation and so can provide information on the potential for

permeability increase or decrease in a fault zone, and thus the potential for a fault to act as a fluid flow conduit. The key parameter, *p**, used to determine deformational behaviour is defined by:

$$\log p* = 3.9 - 1.1 \log(r\varphi) \qquad \textbf{Equation 2.36}$$

where *p** represents critical effective pressure for onset of grain crushing, *r* is grain size radius and ϕ is porosity. This work is relevant to CO_2 storage as it provides a link between purely mechanical models and further considerations necessary in natural geological materials and the way in which leakage pathways or flow baffles may be created in deforming reservoir materials. For example, Figure 2.23 illustrates the results of the model for a 30% porosity arenite for different grain sizes, where the deformational behaviour at different depths and the permeability changes in the fault are predicted (Fisher et al. 2003, Fisher et al. 2007). In some cases e.g. 3-5km depth in Figure 2.23 a) the fault permeability is increased, this could promote leakage along a fault, in other cases e.g. 2-4km in Figure 2.23 b) permeability is reduced along the fault forming a flow baffle. A full review of the method of Fisher, Harris et al. (2007) and Fisher, Casey et al. (2003) is beyond the scope of this work, yet the important points to note from the work are that:

- a constitutive model alone is not enough to predict mechanical behaviour in diagenetically altered sediments;
- changes in deformation behaviour in the subsurface are non-linear, and will impact the fluid flow properties of the deformed sediment;
- several assumptions are included and so the model should only provide a semi-quantitative description of the deformation behaviour.

The most pertinent aspect of Figure 2.23 for this study is the way in which the permeability of faults may be influenced by the deformation behaviour and is dependent on depth. Not only may the faults become more permeable to fluids at certain depths but also there is potential for flow baffles to be formed, potentially adversely affecting injectivity through compartmentalisation. The model of Fisher, Harris et al. (2007) and Fisher, Casey et al. (2003) is restricted to arentitic sediments and carries many assumptions. However, the main point to consider is that faults may be both sealing and non-sealing to fluid in the subsurface and this will be an important consideration in CO_2 storage, this is discussed further in the next section.

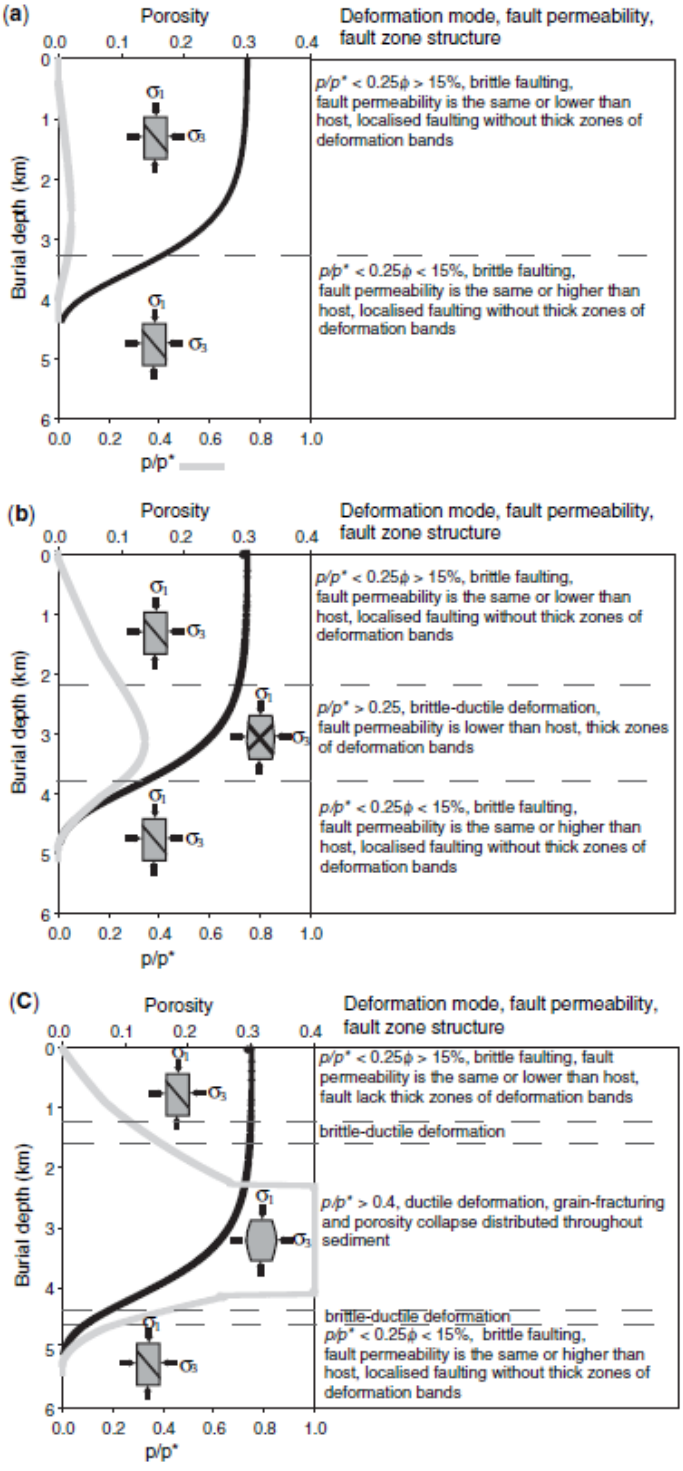

Figure 2.23 – Plot of porosity (black line) and p/p* (grey line), for an arenite with initial 30% porosity for (a) fine grained, (b) medium grained, (c) coarse grained (Fisher et al. 2007).

2.4.5 **Faults and Fluid Flow**

Non-sealing faults and the reactivation and formation of faults and fractures can provide a leakage pathway for CO_2. Sealing faults may also act as flow barriers and compartmentalise a reservoir. Both of these factors can affect the overall storage capacity of a formation. The presence of a fault may affect the flow of fluids by three different mechanisms (Jones and Hillis 2003, Manzocchi et al. 2010):

- Fluid flow normal to a fault can be controlled by the juxtaposition of materials with different flow properties. For example a low permeability sealing unit can be juxtaposed next to a reservoir horizon, or different stratigraphies (geological layers) can be juxtaposed so fluids could flow from one reservoir unit to another;
- Fault normal fluid flow can also be controlled by the properties of the fault itself. Fault rock within the fault zone can have different petrophysical properties to the host rock; and
- In some circumstances, fault parallel fluid flow can occur along the fault due to mechanisms such as fault reactivation (movement) which may increase fault permeability through dilation. This may lead to flow out of a storage location e.g. through the cap rock. However, even where dilation does occur on a fault, the permeability can also decrease (Fisher and Knipe 1998).

Figure 2.24 illustrates the concepts (Yielding et al. 2010).

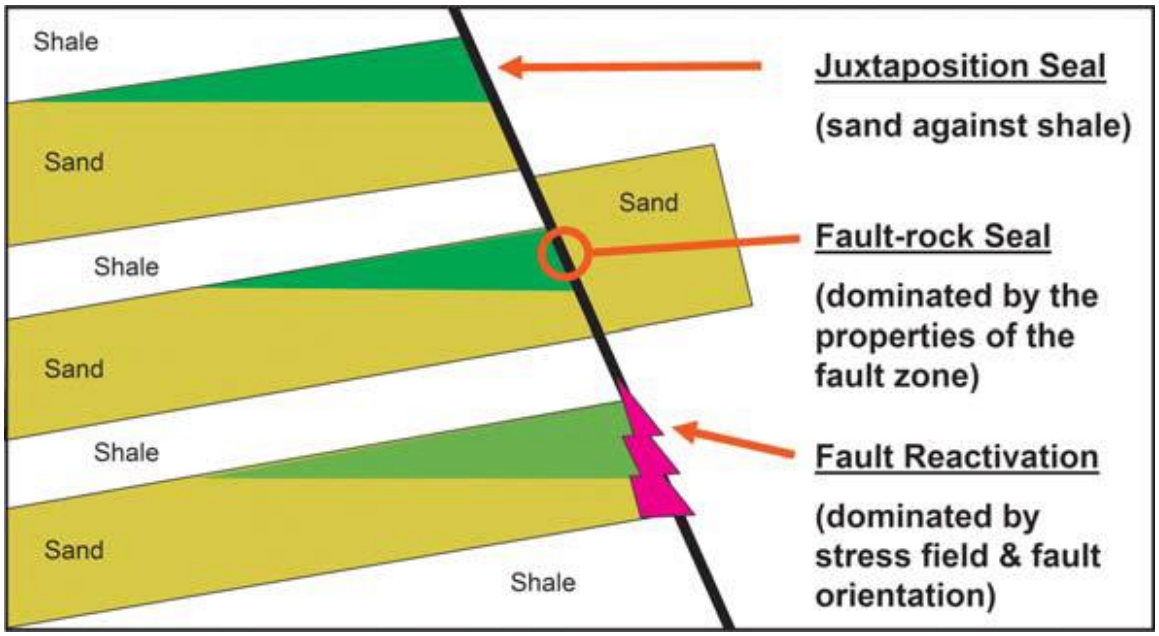

Figure 2.24 – Schematic representation of fault seal mechanisms from (from Yielding et al. 2010). Juxtaposition seal shows juxtaposition of a permeable sand layer against impermeable shale, forming a seal that is effectively as good as a caprock at the side of the reservoir. Fault-rock seal illustrates that the properties of the rocks in the faults are inhibiting movement of fluids across the fault between two sand horizons. Fault reactivation shows fluid movement due to reactivation of a fault, which causes the fault to become a permeable conduit.

An accurate understanding of faults and the way in which they can be incorporated into a fluid flow and geomechanical simulation is necessary to provide realistic models of a CO_2 storage scenario. Modelling correct fluid flow in injection scenarios is also important in understand the impact on the use of monitoring techniques in the subsurface. Juxtaposition can provide a very good seal to a reservoir via the physical imposition of a rock unit with very good sealing capacities (e.g. shale), thus providing a seal that can be similar in capacity to a cap rock (Yielding et al. 2010). Juxtaposition along a fault plane can be

analysed by various, the classic examples of which are the Allen diagram (Allan 1989) and the juxtaposition diagram (Knipe 1997). Figure 2.25 shows an example.

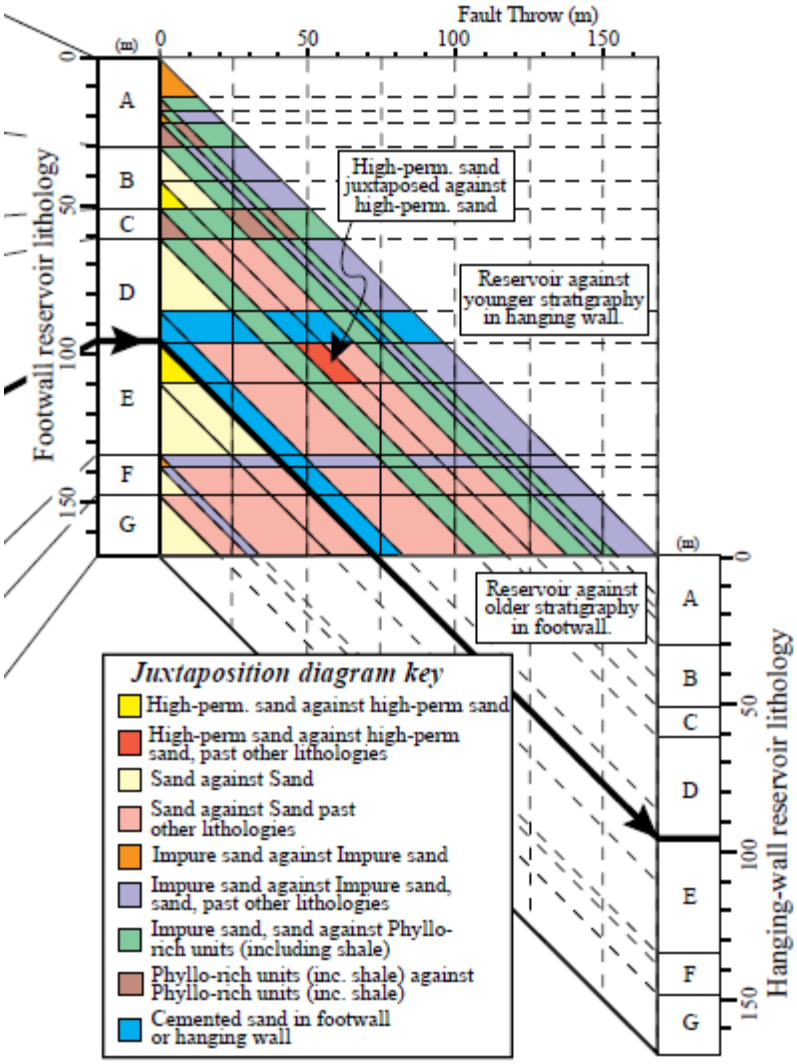

Figure 2.25 – Example of a juxtaposition diagram, the colour contours show the depth and fault throw (displacement) at which various lithology interactions occur, this can be used to identify leakage points (from Knipe 1997).

Juxtaposition analysis provides information on where leakage points may be in a system and describes the basic 'plumbing' of the system. Consideration of this is important as if information is lost during modelling simplifications it can seriously affect the accuracy and reality of the model (Jolley et al. 2007).

The second mechanism of fault seal is the capacity of the fault rock itself to form a seal. This is related to the flow properties of the rock, which are controlled by several factors including, the relative and absolute permeability of the fault rock, the thickness of the fault, and the capillary pressures/capillary sealing properties (Manzocchi et al. 1999, Fisher and Knipe 2001, Al-Hinai et al. 2008, Tueckmantel et al. 2012). The thickness of a fault is particularly important for production/injection timescales as the thickness controls the length

of the pathway the fluid must travel across. Thickness combined with permeability is included in the determination of transmissibility multipliers used to simplify the modelling of the impact of fault zones in simulation models. One relationship used to define transmissibility multipliers in a simulation model is (Manzocchi et al. 1999, Fisher and Jolley 2007):

$$TM = \frac{\frac{2}{\frac{L_i - t_f}{k_i} + \frac{2t_f}{k_f} + \frac{L_j - t_f}{k_j}}}{\frac{2}{\frac{L_i}{k_i} + \frac{L_j}{K_j}}}. \qquad \textbf{Equation 2.37}$$

The relationship defines transmissibility between two blocks in a reservoir simulation separated by a fault. The fault is not explicitly modelled and the transmissibility is used to describe the effect of the fault on the fluid flow. *L* is the width of the simulation block on either side of the fault, t_f is the thickness of the fault, k_i, k_j, and k_f are the single phase permeabilities of the blocks and faults respectively The permeability and capillary properties are controlled by the rock structure and mineralogy of the fault rock. The mineralogy of fault rock relates to the type of rock the faults formed in, and this influences porosity, clay content and grain size, and the deformation history of the rock. An example of this has already been discussed in the previous section for arenites, where the permeability in faults was controlled by grain size, porosity and quartz cementation (Fisher and Knipe 2001, Fisher et al. 2003, Fisher et al. 2007). For the North Sea the relationship between permeability and clay content is described well by the diagram in Figure 2.26 from Fisher and Knipe (2001), which describes the porosity distribution of types of fault rocks. The least permeable rocks have experienced the most burial, and are cataclasites and clay smears.

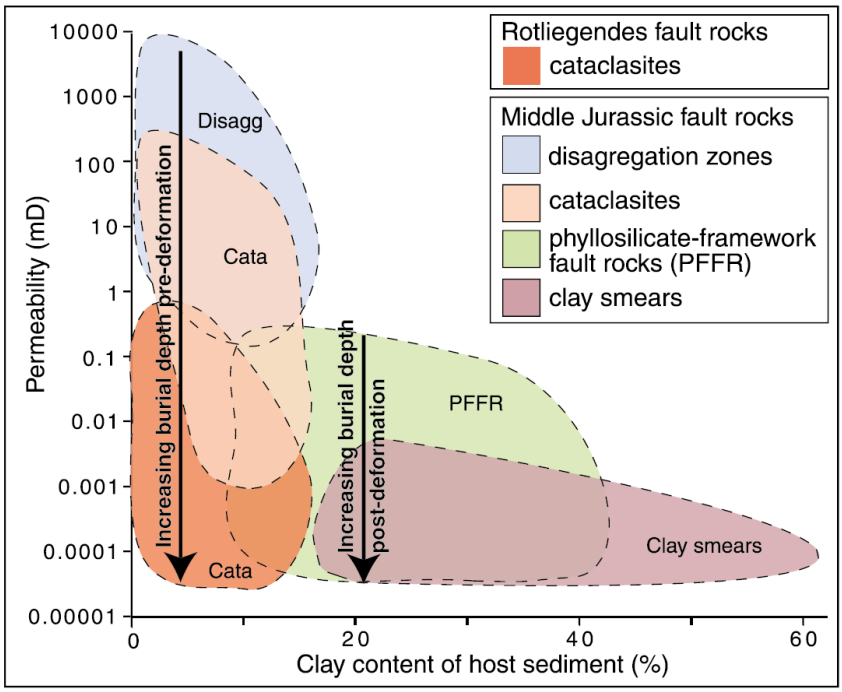

Figure 2.26 – Fault rock clay content and permeabilities of fault rocks found in the North Sea (from Fisher and Knipe 2001).

Clay smears (and clay rich faults rocks) have been shown to have high capillary entry pressures and good seal potential for two phase flow, well in excess of 13MPa and up to 60MPa (Fisher and Knipe 1998). Algorithms have been developed to describe the likely presence of clay rich rocks along faults in order to determine potential seals provided by these fault rocks. The classic example is the Shale Gouge Ratio (SGR) proposed by Yielding Freeman et al. (1997). This information can then be incorporated into flow models for faults by incorporating the SGR into an estimation of a modified average fault permeability (e.g. Manzocchi et al. (1999)).

Most flow models do not use relative permeabilities for faults and only consider single-phase flow, and this is because little information has been gathered on the relative permeabilities in faults rocks. However, Al-Hinai et al. (2008) discuss the effect of considering relative permeabilities using measurements made in the laboratory, and they suggest that without relative permeability consideration transmissibilities could be seriously over estimated in faults.

The final impact of faults on fluid flow is the potential for conduit flow along the fault. The concept behind conduit flow along faults is that many brittle deformation features such as fractures are dilatant. Dilatancy increases the porosity and permeability of the fault zone, and may be preserved by cementation or favourable normal stresses holding the fault open (Wilkins and Naruk 2007). The concept of critically stressed faults, or active faults, is related to this dilatancy principal. The concept of critically stressed faults relates to observations that some faults on the verge of movement are associated with fluid flow along the faults (Barton et al. 1995, Wiprut and Zoback 2000). These observations are, however, particularly

associated with non-sedimentary rocks (less likely to be used for CO_2 storage). Some researchers call into question the applicability of these observations for CO_2 storage as they are made in brittle crystalline rocks (Wilkins and Naruk 2007). Observations by Fisher Casey et al. (2003) and Fisher Harris et al. (2007) also suggest that at certain burial depths and for certain timings of cement formation in the rock, there is no increase in permeability in the rock during brittle faulting. Another observation is that some hydrocarbon fields are sealed by active faults, suggesting that faults are not always conductive to fluids (Wilkins and Naruk 2007). It is clear that the state of knowledge surrounding fault leakage is far from certain and so care should be taken with faults in CO_2 storage projects.

The parameters for the controls of fault rock sealing have been briefly outlined above and, based on these parameters and the structure of a fault, fluid flow can be affected in two different ways. Static sealing faults will prevent fluids flowing across the fault over geological (and storage) timescales and this represents completely sealed faults. Dynamic sealing faults act as membrane baffles that inhibit the flow of fluids due to very low permeabilities and this will prevent significant fluid flow in the short term (i.e. injection scale), but allow equilibration across the fault over geological time (Freeman et al. 2010, Jolley et al. 2010). The transmissibilities can be set in modelling programs to account for this range between sealing and non-sealing behaviour. The main issue to consider in the context of CO_2 storage is that it is unlikely that a storage scheme would rely on anything other than a fully sealing static seal, such as a juxtaposition seal, for storage security. Dynamic sealing across fault seals would most likely complicate the injection of CO_2, by reducing injectivity, and represent an economic risk. The range of behaviour of dynamic seals can be modelled using transmissibility multipliers described in the literature and this should be adequate for modelling injection scenarios.

2.5 **Reservoir Geomechanics**

In the other sections of this thesis various aspects of reservoirs, overburden properties, seismic methods, fluid and rock mechanics have been discussed in isolation. Reservoir geomechanics involves the consideration of the interrelation between fluid and pressure changes in the reservoir and the mechanical properties of the reservoir and surrounding material. Simplified approaches include derivation of parameters such as compressibility (mentioned earlier) to account for the total geomechanical response of reservoir and overburden. However, inevitably in complex situations, where high confidence is needed in analysis techniques and mechanisms other than production rates are of interest, more complex physical assessments are required. For example, standard fluid flow modelling of CO_2 injection is unlikely to be able to account for the onset of shear fractures in a cap rock as the model does not consider the overburden or include analysis of the stress state in the reservoir. Reservoir simulation is purely fluid flow based and associated changes in the stress state are based only on empirical or analytical techniques. Reservoir geomechanical modelling allows information to be provided about future development of a storage formation in terms of the stress state, for example the maximum stress to avoid fracturing of

the formation. A distinction is made here between reservoir geomechanics, which seeks to assess the general impact of reservoir fluids on the geomechanical state in the subsurface, and reservoir hydro-geomechanical modelling or coupled fluid-flow geomechanical modelling, which are specific forms of assessment where fluid flow and geomechanical models are integrated. Some common parameters that are of interest in reservoir geomechanics and commonly discussed in the literature are presented, along with a brief discussion of some approaches to geomechanical modelling for reservoirs.

2.5.1 **Stress Path Parameters**

One of the main considerations of reservoir geomechanics is the change in stress state in the reservoir and associated pore pressure changes. Simplistic analysis of reservoirs has often assumed that total stress in a reservoir does not change, and that pore pressure is the dominant control on effective stresses. However, work by Teufel et al. (1991), Addis (1997), Santarelli et al. (1998), Segura et al. (2011), Hillis (2001) and Schutjens et al. (2001) amongst others indicate that generally the total stress distribution in a reservoir will change with pore pressure. The change in total stress distribution in depleting reservoirs has been termed pore-pressure stress coupling or stress path and it is common to derive several parameters to describe the stress path of the reservoir in relation to the pore fluid pressure (Hillis 2001). Nomenclature varies in the literature for these stress path parameters. Those defined by Segura et al. (2011) are used in this study, but similar parameters are also defined by Schutjens et al. (2001), Khan et al. (2000), and Santarelli et al. (1998) and others. The stress path parameters from Segura et al. (2011) are:

$$\boldsymbol{\gamma_v = \frac{\Delta\sigma_v}{\Delta p}} \qquad \textbf{Equation 2.38}$$

$$\boldsymbol{\gamma_h = \frac{\Delta\sigma_h}{\Delta p}} \qquad \textbf{Equation 2.39}$$

$$\boldsymbol{K_{sp} = \frac{\Delta\sigma'_h}{\Delta\sigma'_v} = \frac{\gamma_h - \alpha}{\gamma_v - \alpha}}. \qquad \textbf{Equation 2.40}$$

Where:

- γ_v is the ‘stress arching’ parameter and indicates how vertical total stress is changing with pore pressure;
- γ_h is the horizontal stress path parameter and determines how total horizontal stress is changing with pore pressure;
- K_{sp} is the stress anisotropy or deviatoric stress path parameter and is the ratio of the change of vertical and horizontal effective stresses.

The stress arching parameter indicates whether increased effective stresses occur in the reservoir during depletion due to the weight of the overburden, stress is transfer to the sideburden, or unloading in the overburden. This stress transfer to the side and overburden is known as stress arching (Segura et al. 2011). The stress path parameter is perhaps not intuitive but can be best understood when considering total stress as the sum of effective

stress and pore pressure. If stress arching occurs, effective stress increase in the reservoir will be reduced and the sum of effective stress and pore pressure will be lower (increased $\Delta\sigma_v$) than if stress arching had not occurred. This will lead to a higher value of γ_v, or $\gamma_v \rightarrow \alpha$ for stress arching. The stress anisotropy ratio, K_{sp}, is the ratio of effective stresses in the reservoir; K_{sp} = 1 indicates no change in the relationship of the horizontal and vertical effective stresses whereas K_{sp} = 0 indicates that horizontal effective stress change is at a minimum compared to vertical. This is termed the deviatoric stress parameter. As $K_{sp} \rightarrow 0$ a change in the deviator or shear stress will be observed. The horizontal stress path parameter changes in a similar manner to the stress arching parameter, and will be related to the geomechanical behaviour of the reservoir in the overburden. The effect of these parameters can more easily be described by representation on a Mohr circle plot and this is shown in Figure 2.27.

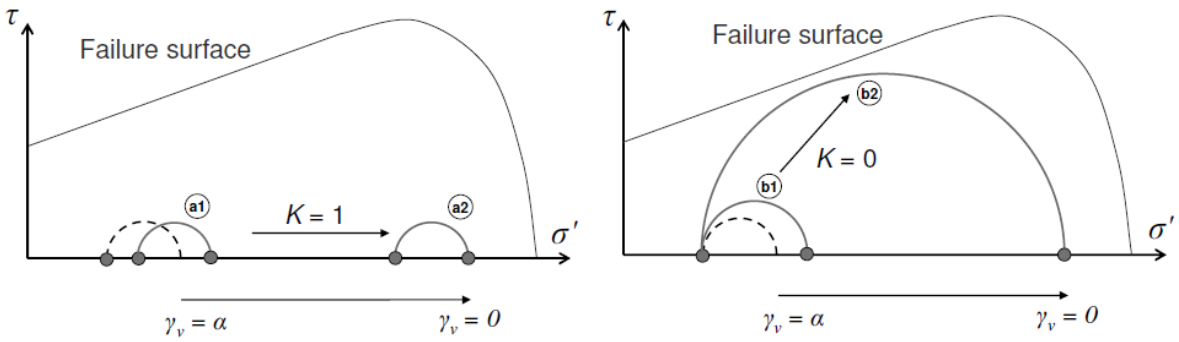

Figure 2.27 – Normal effective stress vs. shear stress plot of the effect of stress path parameters on the Mohr circle plot from (from Segura et al. 2011).

In the diagram on the left in Figure 2.27, the Mohr circle translates as K_{sp} = 1. The ratio of effective vertical and horizontal stress remains the same, and so shear stresses do not develop, and the Mohr circle stays the same size. Stress arching occurs in a1 so the increase in normal effective stress is reduced and the right hand Mohr circle intercept does not move much, whereas in a2 there is no stress arching and the increase in normal effective stress is related to the weight of the overburden. This is intuitive as in case a1 the full weight of the overburden is not transferred to the reservoir so the vertical stress does not increase as much. In the diagram on the right in Figure 2.27, K_{sp} = 0 and the increase in shear stress can be seen to be a maximum with the expansion of the Mohr circle (radius increase, and centroid translates). Once again, the effect of stress arching can be seen on the right hand intercept of the Mohr circle, in case b1 the intercept does not move as much as b2 as the full weight of the overburden is not transferred to the reservoir. As can be seen from inspection of Equation 2.38 to 2.40 only two of the parameters K_{sp}, γ_v or γ_h are required to completely define the Mohr circle, they are related by equation c). It is important to remember that during injection the Mohr circle will translate in the opposite direction, and the stress path parameters only describe the change in geometry and relative position of the Mohr circle.

The minimum horizontal stress can be measured in the field using leak off or extended leak off tests, or fracture tests. The minimum fluid pressure required to keep a fracture open against the minimum far field stress can be obtained from various plots of pressures and thus yields the minimum horizontal stress (Lee and Haimson 1989, White et al. 2002). The vertical stress can be estimated using the weight of the overburden. However, as indicated by the discussion of the stress path parameter and pore pressure stress coupling, it is evident that the change in these parameters throughout depletion and reinjection cannot be predicted without modelling the geomechanical response of the reservoir and overburden. Geomechanical modelling is used to determine the likely stress response and deformation in the reservoir. In terms of CO_2 storage, geomechanical modelling will provide information on the fracture pressure of the reservoir and overburden, and the capacity and injectivity of the reservoir.

2.5.2 **Geomechanical Modelling**

The finite element method (FEM) has been a standard computational modelling tool for problems in mechanics since the 1960s when the concept was formalized. The method has been applied to many classes of problems, including the elastic and plastic deformation of soil and rocks (Zienkiewicz and Cheung 1964, Zienkiewicz and Taylor 1977). The FEM involves the discretisation of a problem into a continuous mesh formed of elements (joined together at nodes) of sufficiently small size to accurately calculate the solution of complex global equations using simpler local element equations. Free element edges require the formulation of a boundary condition (e.g. for a simple foundation slab no lateral movement may be specified) and any holes or gaps in the mesh require a boundary condition or special element type (e.g. contact element) or must be filled in, in order for the finite element solution to be valid. Faults are a specific area where natural discontinuities exist and these must be incorporated into the finite element mesh. One approach is to use special contact elements which have frictional properties and are able to move relative to each other.

Another approach used in analysis of soil/rock mechanics problems is the discrete element method (DEM), where the problem is discretised using discrete elements, usually spheres. The DEM is naturally discontinuous and has advantages over the FEM for modelling fractures and problems where discontinuities are formed (Oñate and Rojek 2004, Rousseau et al. 2010). The main drawback with the DEM is the level of computational effort required to formulate a problem with huge numbers of discrete elements. So some workers have developed methods to incorporate the DEM into FEM formulations to represent localised features such as fractures, where the main bulk of the model is defined using the less computationally expensive FEM (Oñate and Rojek 2004, Rousseau et al. 2010).

For reservoir geomechanical problems, the problem is not limited to mechanical deformation. The main consideration is of deformation associated with fluid flow within the reservoir. Thus solutions are sought to couple mechanical models with fluid flow models or derive a formulation to analyse fluid flow (pore pressures and saturations) and mechanical

deformation in a fully coupled solution. Dean et al. (2003) and Settari and Walters (2001) discuss approaches to coupled geomechanical-fluid flow simulation, and have identified four methods:

- **Decoupled**, where the simulations of fluid flow (may only include flow simulation with consideration of compressibility) and geomechanics are carried out independently in existing standard simulators. Any coupling, for example loading of the mechanical model caused by pore pressure changes, is applied manually. In this case, there is no feedback between pressure changes, resulting deformation, and subsequent deformation induced pore pressure changes, and so this method can also be termed one-way coupling (Settari and Walters 2001);
- **Explicitly (incrementally) coupled and iteratively coupled**, where separate existing simulators for flow and geomechanics are used. Although separate simulators are used information is passed between the flow and geomechanical simulators, using some form of coupling code module to handle the interface between the programs. Iterative coupling involves numerous iterations in each of the simulators, and comparison of the solutions until the coupled solution has converged for each time step, Explicit coupling is a special case of iterative coupling, where only one iteration is carried out in each program for each time step (Dean et al. 2003). The information exchange between the simulators involves updates of pressures from the reservoir simulator to the geomechanics simulator to provide loading to the mechanical model. Updates of pore volume and permeability from the results of mechanical deformation from geomechanics simulator are then passed back to the flow simulator. This is illustrated in Figure 2.28 for an explicit scheme;
- **Fully coupled solution**, where the flow solution, and stress and displacement (mechanical) calculations are performed together in one formulation. This is the most stable approach and preserves second order convergence for nonlinear iterations. However it is not possible to implement in existing fluid flow and geomechanical solvers, and it can be slower for some problems (Dean et al. 2003).

The performance of the different methods of coupling can be problem dependent, and the choice is also often dictated by program availability or code development. The iterative techniques have the advantage that they can utilise pre-existing software (Dean et al. 2003), although work is still required to couple the programs together.

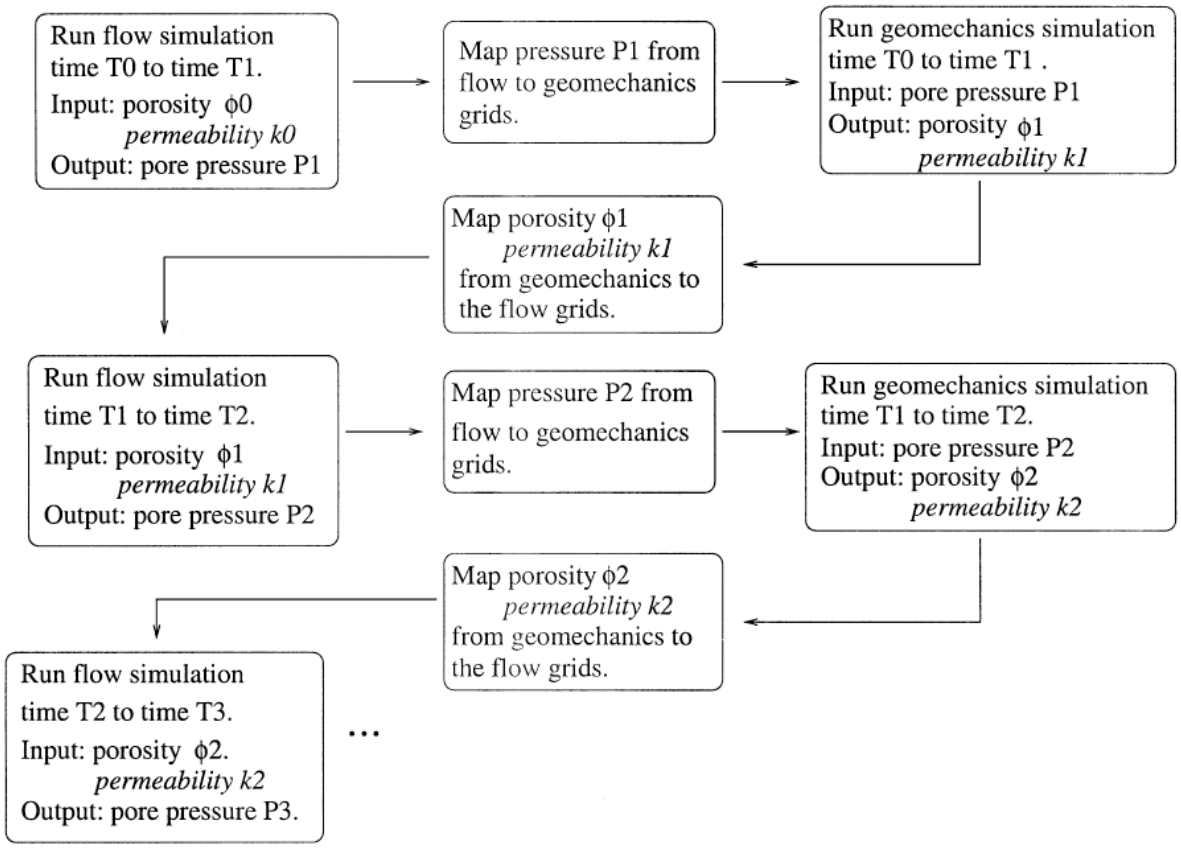

Figure 2.28 – Flow chart for an explicit coupling method from Minkoff et al. (2004), the chart shows the exchange of pore pressure to the geomechanics simulator, and porosity and permeability to the flow simulator for each time step.

A full review of coupled modelling approaches is beyond the scope of this work, but some applications relevant to CO_2 storage are outlined:

- Minkoff et al. (2004) use a loosely coupled (explicit) technique to model the Belridge diatomite reservoir. Specifically, they model the change in Gassman's fluid substitution solution between coupled and non–coupled techniques. In this case, identification of a change in the saturated rock density in the weakest layer in the coupled solution indicated compaction within the reservoir and this was not apparent in the non-coupled model.
- Herwanger and Horne (2009) use a coupled model to demonstrate the influence of stress changes in a producing reservoir on seismic velocity. They show that changes in the triaxial stress state led to seismic anisotropy, which can be used as a geomechanical monitoring tool through observable times-lapse seismic attribute changes.
- Angus et al. (2010) use failure predicted by an iterative coupled technique to simulate microseismic events in a reservoir. In this case, the microseismic events are useful in identifying compartment boundaries of a faulted reservoir.
- Verdon et al. (2011) present microseismic monitoring data from the Weyburn demonstration project and show how it can be used to ground truth a

geomechanical model so that it conforms to observed deformation in the field obtained from analysis of microseismic data. The model stiffness was reduced to account for the observed microseismic response.

- Segura et al. (2011) use an explicitly coupled analysis to examine the influence of reservoir geometry and material properties on stress path in the reservoir. Amongst their findings they show that stiff reservoirs (compared to overburden) with high aspect ratios experience less stress arching and that, in laterally extensive reservoirs, the horizontal stress evolution is controlled by Poisson's ratio. One of the outcomes of the work is the implementation of the stress arching findings into pore volume multiplier tables, which improve pore pressure estimates when stress arching is taking place. This is an example of generic coupled modelling being used to improve de-coupled solutions.
- Bissell et al. (2011) present the development of a coupled-geomechanical (apparently elastic) model using the STARS simulator for the In-Salah storage project. Thermal considerations were also introduced and the model includes fractures. They found that the cool CO_2 initially reduced injection volumes, and matched the surface uplift response through elastic deformation and fracturing. The model is an example of matching a coupled approach with real world observations. Ringrose et al. (2013) discuss the importance of fractures at In-Salah, the importance of developing monitoring techniques, such as microseismic monitoring, capable of determining the onset of fracturing.
- Goodarzi et al. (2012) and Goodarzi et al. (2013) present two studies in Ohio and Alberta (based on the a similar approach) of the thermal effects of CO_2 injection using an iterative coupled geomechanical-fluid flow model with consideration of fracture propagation and temperature. The models are linear elastic and examine the effects of temperature on fracture propagation during cold CO_2 injection (30°C) into a warmer formation (60°C). The study concludes that there is significant potential for the reduction of fracture pressure through injection of cold CO_2, but that that extent of propagation, specifically propagation into the caprock, is highly sensitive to caprock stress state and mechanical properties. The study also suggests that fracture propagation can be beneficial to injectivity (increased permeability), but that careful modelling would be required to ensure these fractures did not propagate to the caprock. Emphasis is placed on the importance of coupled modelling to satisfy regulatory demands, and operational effectiveness of storage schemes. The studies show that it is not sufficient to base injection pressure limits on empirical rules (e.g. minimum in-situ stress) and that careful modelling is required due to the sensitivity of the problem to the stress state and mechanical properties.

This section has summarized the principles of reservoir geomechanics and presented a brief outline of the state-of-the-art in terms techniques for modelling (and monitoring) of the

injection of CO_2 into storage reservoirs. The importance of coupled geomechanical-fluid flow modelling has been highlighted, in addition to the benefits of such modelling for monitoring activities and the benefits of feedback into models from seismic monitoring activities (e.g. Herwanger and Horne 2009).

2.6 **Storage Options II**

In light of the general discussion on storage conditions, specific considerations for hydrocarbon reservoirs and saline aquifers are covered in the following sections.

2.6.1 **Hydrocarbon reservoirs**

Due to the investigation of oil and gas reservoirs by the oil industry, and subsequent production from many of the reservoirs, much is known about their capacity to store CO_2. The presence of a good quality cap rock is also implied by the fact that the hydrocarbon reservoir has stored an accumulation of hydrocarbons suitable for economic extraction. Hydrocarbon reservoirs used in CO_2 storage projects would need to be depleted to the maximum economic extent of any hydrocarbons they previously contained, as injection of CO_2 may complicate future recovery of remaining reserves. In some cases, the reservoirs would consist of discrete units of pores space, or they may be connected regionally. The main considerations for the injection of CO_2 into depleted reservoirs should be:

- **Seal capacity**, both capillary seal, and rock fracture pressure limits, and other mechanisms to compromise storage security (e.g. faults and wellbore stability). Knowledge of the development history of the field (e.g. pressure history, water, gas or steam injection etc.) is also crucial;
- **Storage capacity**, calculated from the volume of hydrocarbons removed, and consideration of reservoir conditions. This also includes a consideration of the fracture pressure limits as fracturing would reduce allowable injection pressures; and
- **Reservoir fluids**, the presence of any residual or encroaching fluids, such as aquifer water or residual oil;

The first and final points are discussed in previous sections and in later sections on risk. The second and third points, relating to volumetric capacity and reservoir fluids, are considered here in the context of existing reservoir conditions.

The main impact of the prevailing reservoir conditions will be on injectivity and capacity. Bachu, Bonijoly et al. (2007) and Holloway, Vincent et al. (2006a) discuss methodologies for estimating storage capacity in hydrocarbon reservoirs based upon the production history and reservoir properties. Storage capacity estimates from Bachu et al. (2007) for gas, oil, and gas and oil reservoirs under reservoir conditions are respectively:

$$\boldsymbol{M_{CO_2 t} = \rho_{CO_2 r} R_f (1 - F_{IG}) OGIP \left[\frac{(P_s Z_r T_r)}{(P_r Z_s T_s)}\right]} \qquad \textbf{Equation 2.41}$$

$$M_{CO_2 t} = \rho_{CO_2 r}\left[\frac{R_f OOIP}{B_f} - V_{iw} + V_{pw}\right] \quad \textbf{Equation 2.42}$$

$$M_{CO_2 t} = \rho_{CO_2 r}\left[R_f Ah\phi(1 - S_w) - V_{iw} + V_{pw}\right] \quad \textbf{Equation 2.43}$$

The equations are based on:

- the recovery factor R_f (ratio of recoverable hydrocarbon to hydrocarbons in place);
- F_{IG} fraction of injected gas (used in gas production);
- P pressure, T temperature and Z gas compressibility factor at the surface (s) or in the reservoir (r);
- the formation volume factor B_f that adjusts the oil volume from standard conditions to reservoir conditions;
- V_{iw} and V_{pw} the volumes of injected and produced water;
- ρCO_{2r} the density of CO_2 at reservoir conditions.
- A, h, ϕ and S_w are the area and thickness of the reservoir, and the porosity and water saturation in the reservoir; and
- any gas and miscible solvents that are injected should also be accounted for.

The framework for capacity estimation presented by Bachu et al. (2007) includes the main factors that need to be taken into account when assessing storage in hydrocarbon reservoirs. This includes the production and reservoir engineering history of the storage site, any fluids that have been removed, injected or that remain in the reservoir, and the intrinsic properties of the reservoir. Oilfields with significant residual oil (given by recovery factor) may be candidates for EOR operations.

Another factor that is acknowledged by Bachu et al. (2007) is the connectivity of aquifers to the hydrocarbon reservoir. Many hydrocarbon reservoirs experience pressure support from a connected aquifer, which assists with the production of oil or gas (see Figure 2.29). In the case of CO_2 storage, the aquifer water may have encroached into the proposed storage zone, and so this encroaching water may not be displaced easily by CO_2 injection due to relative permeability hysteresis, without dangerously (in terms of storage security/leakage) exceeding the original reservoir pressure (Bachu et al. 2007).

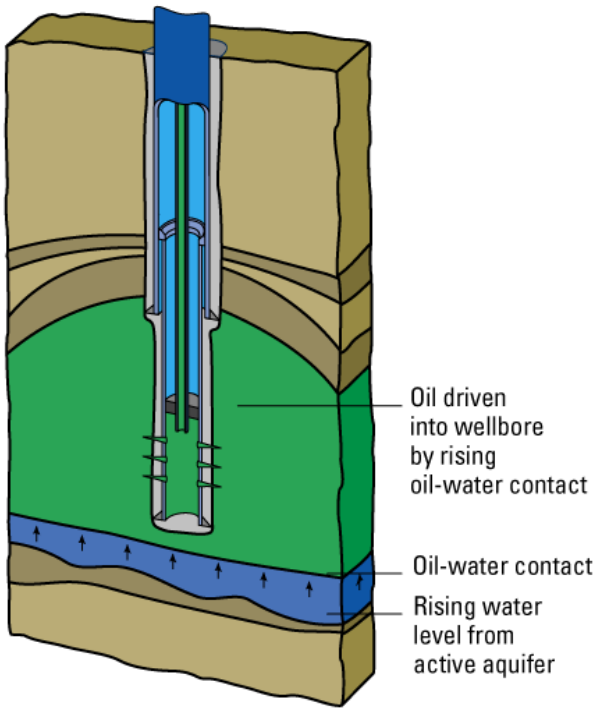

Figure 2.29 – Water drive in an oil reservoir, if the water forces out the oil it means that it is connected to a larger body of water and could be displaced for CO_2 storage (Schlumberger 2010b).

2.6.2 Saline Aquifers

Unlike hydrocarbon reservoirs, saline aquifers have no current economic value. Thus, the available data relating to saline aquifers is sparse because little investigatory work has been carried out beyond the identification of individual aquifers. To date there is only one active investigation of a UK offshore saline aquifer in the Bunter Sandstone with one test well drilled, however, the data are not in the public domain (Dingwall et al. 2013, Furnival, personal communication, 2013).

Saline aquifers are simply porous, permeable rock strata (aquifer) filled with highly saline brine. Generally, the brine has no economic value as it cannot be used for drinking water and industrial purposes, and so is considered suitable for storing waste CO_2. Saline aquifers have not been depleted for resource extraction and therefore contain water at hydrostatic pressure as a minimum. Consequently any injected CO_2 would have to displace the brine or, if the aquifer is confined, would have to compress the water and/or expand the pore spaces (Zhou et al. 2008).

Figure 2.30 shows the concept of open, closed and semi-closed saline aquifers. The pressure can dissipate in the open system, whereas in the closed system the pressure cannot dissipate. The semi-closed system would allow pressure dissipation through brine migration, but this would not be instantaneous and would be due to slow migration of brine through low permeability cap rocks (Zhou et al. 2008).

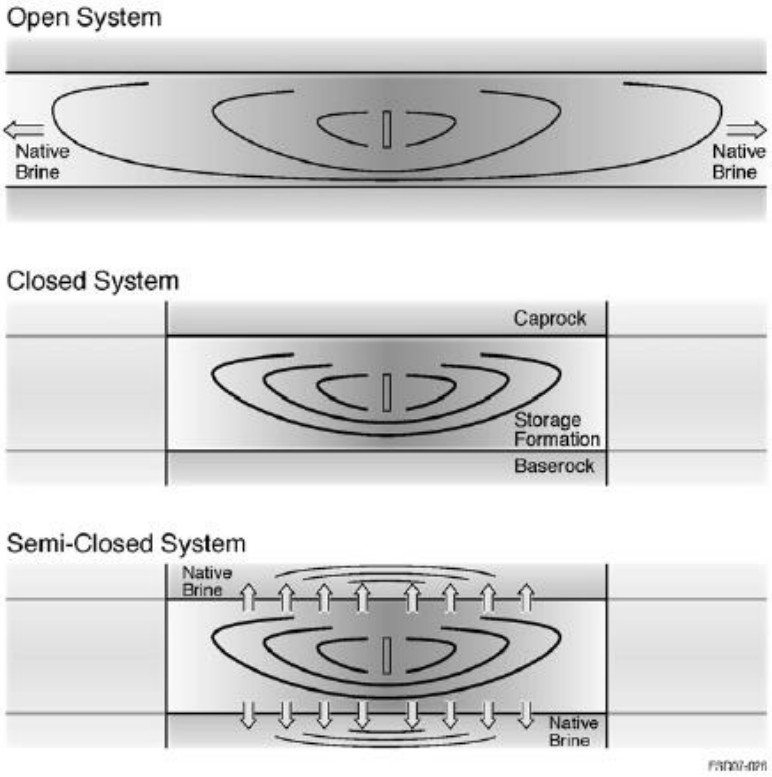

Figure 2.30 – Saline aquifer system showing open, closed and semi-closed systems, (from Zhou et al. 2008).

Given that very few studies have been carried out in saline aquifers, there is currently debate surrounding how natural saline aquifers are likely to behave when CO_2 is injected into them. The debate centres on whether they would act as open or closed systems, and if this could severely limit the storage capacity of the aquifers for CO_2 storage (Brook et al. 2003, Zhou et al. 2008, Economides and Ehlig-Economides 2009, Cavanagh et al. 2010). Storage of several millions tonnes of CO_2 in the Sleipner saline aquifer has been carried out successfully, however the permeabilities are exceptionally high in this case, between 1000 and 5000 mD and so this does not represent a 'standard' saline aquifer storage case (Bickle et al. 2007, Chadwick et al. 2010).

There are various methodologies for assessing the storage capacity of saline aquifers, and these are mainly based on estimates of reservoir parameters (e.g. pore volume, capillary pressure and pore compressibility) along with various assumptions. As there is sparse data on these aquifers, storage estimations are open to large errors. Bachu et al. (2007) propose several equations to estimate structural, residual, hydrodynamic and mineral trapping in saline aquifers. Holloway et al. (2006a) use a simplified formula to arrive at an estimate of 14Gt CO_2 storage in the Bunter Sandstone Aquifer in the UK Southern North Sea. Both methods require specific reservoir data, or assumptions and estimations to be made to quantify the complex nature of saline aquifers.

The top seal for saline aquifers is another additional uncertainty. Generally, all hydrocarbon accumulations possess a highly impermeable sealing layer by virtue of the resource. Saline

aquifers however do not implicitly possess any form of seal. Therefore, any storage scheme in a saline aquifer will have to prove that a seal sufficient to store CO_2 for a significant period exists.

2.7 **Monitoring and Seismic Data**

The previous sections have discussed the physical conditions of storage reservoirs, in terms of factors that are relevant to the injection and containment of CO_2. An additional key factor in terms of ensuring containment and managing a storage project is monitoring of the emplaced CO_2. Many monitoring schemes from environmental, petroleum and related disciplines have been proposed. A complete review will not be provided here, but a summary of a 'typical' monitoring programme from the In-Salah demonstration project is provided in Table 2.1. Table 2.1 illustrates the range of testing and monitoring activities that can be used for a storage project. The types of activity can be split into monitoring activities required to determine ongoing behaviour of the CO_2, leakage detection activities and general data collection, and some activities fulfil several or all of these functions.

Seismic monitoring is one of the most ubiquitous monitoring methods in the current CO_2 storage demonstration projects. It is a standard data set collected in all oil and gas developments, and is essential in the storage design (geological model construction). Time-lapse seismic surveys are also frequently proposed for monitoring the injected CO_2 plume. The seismic method involves the generation of elastic waves in the subsurface to determine structure from the reflected waves. The data provide information on the elastic wave velocities and structure. Time-lapse surveys involve multiple surveys of the same area over time to detect changes in velocity caused by CO_2 plume movement. The main issue with this monitoring technique is the cost. At In-Salah, the first time lapse survey (excluding the initial baseline) was not taken until 5 years after the first injection (Ringrose et al. 2013). However surface seismic and vertical seismic profile (VSP) time-lapse surveys have demonstrated the capability of temporally and spatially tracking the storage of CO_2 within the subsurface geological formation in most of the demonstration projects so far (e.g., Daley et al. (2008) at Frio, Chadwick et al. (2010) at Sleipner; White (2011) at Weyburn).

Microseismic monitoring is a passive seismic technique that monitors seismic energy generated by small earthquakes in the subsurface, (for example shear failures on pre-existing zones of weakness – faults and fractures). The microseismic events are very small magnitude events compared to tectonic related earthquakes. The microseismic method has been used to monitor the injection of CO_2, and specifically monitor the integrity of the cap rock and the level of geomechanical deformation occurring in several demonstration projects (e.g., Urbancic et al. (2009) at Ostego, Verdon et al. (2010) at Weyburn, Ringrose et al. (2013) at In-Salah).

Satellite monitoring using InSAR has also been used at In-Salah. This involves monitoring ground uplift resulting from injection of CO_2 into a reservoir at depth. The surface uplift can

be used to infer the behaviour of the CO_2 at depth using geomechanical modelling techniques (e.g. Onuma and Ohkawa (2009); Mathieson et al. (2009)). An important point to note, especially for UK projects, is that InSAR is ineffective for offshore reservoirs as it relies up on measuring ground uplift, which is not possible under water.

The remaining monitoring techniques shown in Table 2.1 are routine for oil and gas developments, with the exception of surface, soil and groundwater monitoring and gas tracers. In the context of offshore settings dominant in UK CO_2 storage, the use of seabed and groundwater monitoring are likely be either complex or irrelevant and so are not considered further. Since the storage of CO_2 is still a novel process, the monitoring activities discussed are only some of the types of monitoring that have been proposed. An example of a more novel technique that is being developed and maybe applicable in an offshore setting is the using of cosmic rays through muon tomography. The aim of these types of novel techniques is to provide more cost effective and flexible monitoring options in the future. Discussion of these are beyond the scope of this study (Kudryavtsev et al. 2012).

Table 2.1 – Table of monitoring (monitoring, modelling and verification (MMV)) technologies used by the In-Salah Joint Industry Project (from Ringrose et al. 2013).

Monitoring, Modelling and Verification Technology	As implemented at In Salah	Lessons Learned for implementation elsewhere
3D seismic baseline survey	Acquired in 1997. Essential to the CO_2 storage design and well placement plan.	Improved quality 3D seismic baseline survey with imaging of overburden is desirable.
4D seismic monitoring	First land time-lapse survey for CO_2 monitoring acquired in 2009 (5 years after injection start).	Significant benefits for overburden imaging and time-lapse responses with improved acquisition plan (but this is expensive).
Microseismic monitoring	Only one pilot well with a vertical array of geophones over one injector has been deployed.	Microseismic data has been very useful for monitoring geomechanical response to injection. Consider deploying a full array with relatively cheap shallow wells.
Satellite InSAR monitoring	Both C-Band and X-band InSAR data acquired routinely during injection period (from 2007 and onwards).	Extremely valuable and cost effective monitoring data for onshore CO_2 injection sites. Needs calibration (e.g. Digital GPS) and careful processing of atmospheric and surface artefacts.

Monitoring, Modelling and Verification Technology	As implemented at In Salah	Lessons Learned for implementation elsewhere
Tracers in CO_2 injection wells	PerFlouroCarbon gas soluble tracers (PMCH, PDMCH, n-PPCH) used in each injection well.	Valuable and cost effective method for checking the origin of CO_2 observations at wells and in the storage complex.
Core analysis (storage unit)	Routine core plugs and SCAL data collected for reservoir intervals.	Good petrophysical data is essential. Rock mechanical properties are especially critical.
Core analysis (caprock unit)	Some caprock samples were acquired close to the injection interval.	Core sampling throughout most of the caprock interval is desirable for long-term storage integrity assessment.
Well log data	Routine petrophysical logs throughout; Image logs and array sonic on selected wells; LWD in horizontal well sections.	An advanced array of well logging tools is highly valuable; resistivity image logs and array sonic especially useful for storage integrity issues.
Soil and surface gas sampling	Surface gas (open path laser system); soil gas probes (flux and penetrative tubes); Barasol and passive gas (charcoal) devices deployed in several campaigns. Natural low-level CO_2 variations observed.	Need for more reference data on natural CO_2 variations in different environments and associated seasonal fluctuations.
Groundwater monitoring wells	Surface gas (open path laser system); soil gas probes (flux and penetrative tubes); Barasol and passive gas (charcoal) devices deployed in several campaigns. Natural low-level CO_2 variations observed.	Establishing local and regional hydraulic gradients and natural variations in water chemistry is essential for establishing a useful baseline for groundwater hydrology.

2.7.1 **Seismic Parameters**

Whilst there is some seismic field data now available from operational storage demonstration projects, modelling the seismic response due to CO_2 injection and comparison with real field data is an important research area. An accurate understanding of the seismic response of storage reservoirs will be a key asset, particularly for the North Sea, where it is likely to be one of the few monitoring tools available.

Although seismic data are sensitive to fluids, one of the key problems in linking seismic data to reservoir modelling results is the prediction of seismic velocities in fluid saturated rocks. Fluid substitution is the conventional approach used. The classic fluid substitution relationships are provided by Gassmann (1951). When the shear modulus of the saturated rock, μ_s, is equal to the dry shear modulus of the rock, μ_d, the relationship for the bulk modulus of the saturated rock K_s is:

$$\frac{K_s}{K_m - K_s} = \frac{K_d}{K_m - K_d} + \frac{K_f}{\phi(K_m - K_f)}. \qquad \textbf{Equation 2.44}$$

Where K_m is the bulk modulus of the mineral grains, K_d is the bulk modulus of the dry rock, K_f is the bulk modulus of the fluids in the pore spaces, and ϕ is the porosity of the rock. K_s can then be found when:

$$\Pi = \frac{K_d}{K_m - K_d} + \frac{K_f}{\phi(K_m - K_f)} \qquad \textbf{Equation 2.45}$$

thus:

$$\frac{\boldsymbol{K_s}}{\boldsymbol{K_m - K_s}} = \boldsymbol{\Pi} \qquad \textbf{Equation 2.46}$$

and:

$$K_s = \frac{\Pi K_m}{(1+\Pi)} \qquad \textbf{Equation 2.47}$$

Mineral and dry rock bulk moduli can be found from laboratory experiments. The fluid bulk modulus, K_f, can be found from laboratory experiments for a single fluid. For multiphase fluids the fluid bulk modulus must be derived from the fluid mixture present, and is sensitive to the mixing of the fluid. The Reuss and Voigt bounds are used to estimate the multiphase fluid bulk modulus based on full mixing (Reuss):

$$\frac{\boldsymbol{1}}{\boldsymbol{K_f}} = \sum \frac{\boldsymbol{S_i}}{\boldsymbol{K_i}} \qquad \textbf{Equation 2.48}$$

and patchy fluid mixing (Voigt):

$$K_f = \sum S_i K_i \qquad \textbf{Equation 2.49}$$

where K_i and S_i are the bulk modulus and saturation of each phase (Mavko et al. 2009). The seismic velocities can then be calculated, the P-wave (primary compressional wave) velocity is:

$$\boldsymbol{V_p = \sqrt{\frac{K_s + 4/3 \times \mu}{\rho_s}}} \qquad \textbf{Equation 2.50}$$

and S-wave (secondary shear waves) velocity is:

$$V_s = \sqrt{\frac{\mu}{\rho_s}} \qquad \textbf{Equation 2.51}$$

where K_s is the bulk modulus of the saturated rock, μ is the shear modulus of the rock, and ρ_s is the bulk density of the saturated rock (Mavko et al. 2009). The saturated bulk density ρ_s can be obtained from:

$$\boldsymbol{\rho_s = \rho_f \phi + \rho_r (1 - \phi)} \qquad \textbf{Equation 2.52}$$

if:

$$\rho_f = \rho_g S_g + \rho_w (1 - S_g) \qquad \textbf{Equation 2.53}$$

where ρ_r is the density of the dry rock, ρ_f is the density of the fluid in the pore space, ρ_g is the density of the gas, ρ_w is the density of the water and S_g is the gas saturation (two-phase system).

An increase in seismic velocity represents an increase in compressive stress, and so can provide a general indication of sub-surface stress changes. Additionally, the velocity of seismic waves in the subsurface can also be anisotropic (i.e. directional dependence of velocity). This seismic anisotropy has several significant sources, including:

- the microstructure of some rocks(e.g. shales, sandstones, siltstones) can cause seismic anisotropy through mechanisms such as lattice preferred orientation and grain morphology (e.g. Newman 1973, Johnston and Christensen 1995, Sayers 2005, Kendall et al. 2007);
- fractured rock can affect the propagation of seismic waves via scattering and induce anisotropy. Fractures reduce the effective elastic moduli of rocks and so preferential fracture sets will induce anisotropy (e.g. Schoenberg and Sayers 1995, Smith and McGarrity 2001). With slower velocities normal to fracture surface and faster velocities parallel to the fracture surface;
- the stress state in the rock can induce seismic anisotropy through opening and closing of preferentially orientated cracks or the stiffening of grain contacts (Mavko et al. 2009). Several studies have linked changes in stress in reservoirs and

overburden to seismic anisotropy (e.g. Felício Fuck et al. 2008, Herwanger and Horne 2009);

- Fine scale microstructure (e.g. laminations as in Bandyopadhyay 2009);

Knowledge of the impacts of the subsurface conditions on seismic anisotropy is important for accurate interpretation of seismic data, but also provides an opportunity to use seismic anisotropy as a tool for understanding subsurface processes. Clearly, perturbations in the seismic signal caused by fractures and stress changes are of great interest in the context of CO_2 storage as they have the potential to provide information of changes to fracture networks and the stress state, especially from time-lapse surveys. The use of seismic anisotropy as a geomechanical monitoring tool is put forward by Herwanger and Horne (2009) and Sayers (2006) who link triaxial stress changes to changes in seismic anisotropy attributes in time lapse surveys.

Seismic anisotropy relating to stress and fracturing is a growing focus of research in both CO_2 storage as well as conventional and unconventional (shale gas, tight gas etc.) oil and gas production. Other studies that consider modelling anisotropy, including significant consideration of microseismic sources include those of Angus et al. (2011) and Verdon and Kendall (2011). Angus et al. (2011) describe how microseismicity and 4D seismic data from integrated reservoir modelling can be used to detect reservoir compartmentalization and determine top seal integrity. They use Thomsen parameters to describe seismic anisotropy. Verdon et al. (2011) discuss progress in linking measured microseismic data from the Weyburn CO_2 storage project with predictions of microseismicity from coupled fluid flow-geomechanical models of the reservoir. In this study, anisotropy changes are not modelled for the seismic data that are generated and only the changes is seismic velocities are analysed. Mavko et al. (2009) provide a more detailed discussion of the background to anisotropy and the applications for CO_2 storage have been briefly discussed.

Another parameter that is commonly used in seismic analysis is the impedance, this is the product of the velocity and density. The impedance is related to changes in reflectivity at seismic interfaces (at an interface an incident wave will be both transmitted and reflected producing a one reflected and one transmitted wave). Seismic impedance can be used to model synthetic seismic data and infer CO_2 plumes from seismic data. For example, Arts et al. (2004) discuss reduction of P-wave impedance with CO_2 saturation in the Utsira formation of the Sleipner storage project. Small-scale mudstone layers (1-2 m), which affect the plume distribution are resolvable with this technique. The impedance changes create more complex seismic attributes such as AVO (amplitude variation with offset) and AVOA (amplitude variation with offset and azimuth) which analyse the change in reflection amplitudes with source-receiver position; these techniques are beyond the scope of the review.

This section has presented a brief summary of monitoring techniques with specific regard to the use of seismic data and associated parameters in CO_2 storage. Seismic data provide

useful information for geomechanical modelling, and geomechanical modelling can also provide useful insight into seismic properties, which has potential uses in monitoring technologies. Seismic data can be considered an integral consideration of reservoir geomechanical modelling.

2.8 **Risk and Uncertainty**

As has been alluded to so far, the process of CO_2 storage is complex, uncertain, and carries many risks. Table 2.2 represents a generic risk register and is an attempt to catalogue the potential risks associated with a CO_2 storage project specifically those risks associated with the geological and subsurface aspects of CO_2 storage. The table identifies technical risk from three broad categories; capacity and injectivity, leakage, and monitoring. The table incorporates implicit economic impacts of storage, for example identifying the risk of extra costs due to the requirement for increased well drilling on a project, but does not discuss wider economic issues related to CO_2 storage. The aim of the risk register is to identify possible areas of research in CO_2 storage and provide a structure and rationale for the specific areas of focus of this thesis.

Table 2.2 highlights the broad range of research topics within the area of CO_2 storage, a full review of each topic is beyond the scope of this report. The items highlighted in red have been identified as high priority for research with good opportunities for novel and valuable research with the resources available. The items highlighted in light red are those items that will be contributed to by research into a specific technique, or which could easily be investigated using the methodology developed for the priority areas of research. The priority research areas will form individual work packages, and these are discussed in the following sections.

The priority research areas highlighted are:

- items 1F, 1G capacity estimation including pressure relief through brine extraction, items 1B to 1E are implicitly related to this;
- item 2H potential for exceeding the fracture pressure of the reservoir and caprock.

Hazard/Issue	Hazard ID		Specific Hazard	Potential Consequences	Research Opportunities and Comments
Capacity and Injectivity	1A	Injection	Reservoir compartmentalisation.	Increased injection costs – multiple wells needed to maximise capacity and pore volume usage. Brine displacement limited – capacity reduced.	Site specific modelling - compartmentalisation will arise from sealing faults – generally will be well understood in a developed reservoir – lack of data for saline aquifers.
	1B		**Closed boundaries at reservoir margins.**	**Increased injection costs –**	**Site specific modelling - generally will be well understood in a developed**

Hazard/Issue	Hazard ID		Specific Hazard	Potential Consequences	Research Opportunities and Comments
				multiple wells/complex wells needed to maximise capacity and pore volume usage. Brine displacement limited – capacity reduced.	reservoir – lack of specific data for saline aquifers – can be generically modelled for a saline aquifer target – sensitivity cases.
	1C		Lower permeability in reservoir formation.	Injection rates reduced – multiple wells/complex wells needed to maximise capacity and pore volume usage e.g. horizontal wells.	Site specific modelling – well characterised/tested in hydrocarbon reservoir – lack of data for saline aquifers and so likely to be a greater risk – data may be sparse in saline aquifer – risk of lack of understanding of distribution - can be generically modelled for a saline aquifer target – sensitivity cases.
	1D		Low coefficient of compressibility of reservoir – geomechanical behaviour of overburden	Low compressibility and stiff overburden reduces expansion related capacity in reservoir.	Site specific modelling using coupled flow-geomechanical models – lack of data for saline aquifers – generic sensitivity cases possible for saline aquifer target.
	1E		Low porosity in reservoir formation esp. If heterogeneous.	Capacity reduced. Implications for injectivity if associated with low permeability e.g. cementation	Site specific modelling – well characterised in hydrocarbon reservoir – lack of data for saline aquifers - generic sensitivity cases possible for saline aquifer target.
	1F		Curtailment of injection activites due to fracture pressure constraints. If fracture pressure estimates are poor this may lead to premature cessation of injection. Items 1B to 1E may reduce volume of CO_2 that can be injected within pressure limits. This limit represents the controlling factor on the 'ultimate capacity' of storage	Capacity reduced. Maximum reservoir pressure reached - CCS projected is jeopardised. Extra costs incurred – new/additional storage site may be sought. Brine extraction may be required (item 1G). Additional wells required.	Detailed site-specific geomechanical and coupled models will reduce uncertainty – large uncertainty with saline aquifers due to constraints on data collection. Stress path hysteresis maybe important for –re-pressurisation of existing reservoirs if fracture pressure is lower than expected.

Hazard/Issue	Hazard ID		Specific Hazard	Potential Consequences	Research Opportunities and Comments
			project.		
	1G		**Brine displacement issues require brine extraction.**	**Additional costs and regulatory and environmental impacts from brine disposal.**	**Simple models can be analysed for representative benefit in saline aquifers – full field hydrocarbon models can be analysed for information on operating such a scheme in complex field.**
	1H		Saline aquifer closures not constrained.	Capacity targets are uncertain. CO_2 leaks from closures (see item 2E).	More field data is required e.g. seismic surveys field models, seal analysis for closures.
Leakage	2A	Static Processes	Poorly constrained sealing unit.	Vertical and lateral CO_2 migration – escape from storage.	Sealing unit highly constrained for hydrocarbon fields. More data public in domain data required for saline aquifers, regional mapping could provide potential storage locations.
	2B		Sealing capacity of cap rock exceeded.	Vertical and lateral CO_2 migration – escape from storage.	Site-specific data available for hydrocarbon reservoirs related to capillary entry pressures etc. Risking exercise using data on sealed and non-sealed hydrocarbon analogues may provide further information for both saline aquifers and hydrocarbon reservoirs.
	2C		Containment compromised at well bore – poor construction or corrosion - – mechanical failure and wellbore stability	Small-scale leakage. Large-scale blowout.	Corrosion and chemical testing for wellbore materials. Analysis of historical databases for abandoned wellbores. Wellbore mechanical modelling and wellbore stability assessment. Most likely in depleted hydrocarbon reservoirs, site specific considerations and wellbore scale geomechanical modelling required.
	2D		Dissolution of CO_2 in brine – mobility through aquifer flow.	CO_2 pollutes groundwater, leaching of heavy metals/toxins into groundwater.	Reactive transport modelling and research on potential impacts on groundwater sources – storage offshore may reduce importance.
	2E		Saline aquifer closures not constrained.	CO_2 escapes closure and migrates to leakage points.	More field data is required e.g. seismic surveys.
	2F		**Permeable fault zone in reservoir.**	**CO_2 leaks along fault zone.**	**Flow along faults is a complex area in literature – examples of both sealing and conductive faults in literature – site-specific considerations are likely to be critical – material properties of reservoir/overburden critical.**
	2G	Dynamic Processes	**Permeable fault zone in reservoir resulting from fault reactivation.**	**CO_2 leaks along fault zone.**	
	2H		**Fracture pressure of reservoir/overburden exceeded by CO_2**	**Fractures in overburden allow CO_2 to**	**Coupled fluid flow-geomechanical modelling of process that can lower fracture pressure – stress path**

Hazard/Issue	Hazard ID		Specific Hazard	Potential Consequences	Research Opportunities and Comments
			injection. Would result from poor characterisation of fracture pressure.	**escape from storage. Risk of fracturing seal high. Capacity reduced See item 1F.**	**hysteresis may be important in re-pressurisation of reservoirs.**
	2I		**Themo-poroelastic response of reservoir to cold CO_2 reduces fracture pressure.**	**Fractures may form allowing CO_2 escape. Risk of fracturing seal high. Capacity reduced see item 1F.**	**Coupled fluid flow-geomechanical-thermal modelling can incorporate considerations of stresses caused by temperature.**
	2J		Residual trapping of CO_2 is not stable.	Residual CO_2 does not behave as expected, migrates to leakage points.	Analysis of work from other disciplines e.g. volcanology – degassing. Depends upon security measures relied upon e.g. seal, closure – if residual trapping is main trapping mechanism could be high risk – unlikely to be permitted by regulation.
Monitoring	3A	Regulation, Tacking and Accountability.	**Quantification of stored CO_2 volume.**	**Proof of stored volumes maybe required for regulation and carbon credit payments.**	**Key research areas are likely to be in the refinement of the ability of seismic surveys** • **to determine concentrations of CO_2 in the subsurface,** • **development of modelling techniques (e.g. geomechanical models) to compliment and predict monitoring responses,** • **refinement/development of seismic surveys to be able to provide quantitative information on the CO_2 concentrations in the subsurface,** • **refinement/development of seismic surveys to be able to provide information on stress changes in the subsurface including failure** • **Development of modelling techniques for analysing ground deformation responses to subsurface deformation (for satellite technologies).** **Coupled flow-geomechanical modelling can provide several opportunities in this research area.**
	3B		**CO_2 plume tracking within reservoir – leakage potential.**	**Tracking plume will assist in preventing leakage through migration, may also detect damage to caprock.**	
	3C		**CO_2 plume tracking within reservoir – predictive model calibration.**	**Plume tracking assists with calibration of predictive models – aids reservoir engineering and safety/regulatory assessments.**	
	3D		**Detection of stress changes and potential failure in subsurface.**	**Detection techniques through monitoring are likely to be one of few ways to determine response of the subsurface and potential leakage (see above items).**	

Hazard/Issue	Hazard ID		Specific Hazard	Potential Consequences	Research Opportunities and Comments
	3E		Shallow surface leakage detection – sub-marine and sub-aerial.	Unidentified surface leakage can cause agricultural/plant and marine damage and poses human health risk.	Research programmes on soil gas detection and sub-marine CO_2 leak detection, examine natural analogues for CO_2 release and indications of release e.g. vegetation change.
	3F		Long term monitoring program.	Long term monitoring required to ensure storage does not deviate from modelled behaviour, likely to be a regulatory requirement – long-term time lapse surveying for example will be expensive.	Research into capabilities and economics of long term monitoring options, this will also involve consideration of regulatory requirements.

Table 2.2 – The table presents specific hazards associated with CO_2 storage, the potential consequences of each hazard, and potential research opportunities in each area. Items highlighted in deep red are areas identified as priorities for research in the UK which provide good opportunities for research progress, while items in light red are associated research areas that may benefit from the highlighted research opportunities.

2.9 Risk Identification and Research Opportunities

Based on the discussion of factors that affect CO_2 storage and the identification of generic risks for CO_2 storage it is possible to identify areas for further research to further quantify risks.

2.9.1 Storage Capacity and Injectivity – UK Offshore

In the UK, the main targets for CO_2 storage are the offshore geological structures, as storage onshore is considered unlikely due to public perception concerns. The ultimate storage capacity and the contributing factors that have the potential to reduce storage capacity are identified as a storage risk in Table 2.2, in items 1B to 1F. Item 2H is also relevant to the storage capacity in that initial characterisation of the fracture pressure provides the control on the ultimate capacity of a storage reservoir, and defines the pressure at which injection must be terminated. The implementation of brine extraction may be necessary if capacity is found to be low, and this would increase the cost of a project, this is identified as a risk in item 1G in the table. This section assesses the capacity estimates that have been made for the UK and identifies a research opportunity to further refine capacity estimates and assess potential methods to increase capacity using brine extraction.

2.9.1.1 *Storage Capacity Estimates and Storage Potential in UK*

The potential storage capacity in the UK exists predominantly offshore. Some onshore capacity does exist although it is considered highly speculative due to lack of information and exploration, public perception concerns, relative magnitude of capacity, and conflict with other uses of the subsurface such as mining, oil and gas, gas storage and water extraction (Holloway et al. 2006a, Senior 2010). The provisions of infrastructure and exploration activities are much higher in the offshore UK basins, and so storage activities are likely to be focussed here first as this will be the easiest option for the development of storage capacities.

The storage capacities for the UK have been analysed by Holloway et al. (2006a) for the Department of Trade and Industry (DTI) Carbon Abatement Programme. For the oil and gas reservoirs, the estimations were based on similar equations to those discussed in Section 2.6.1 using evaluation of production data from the oil and gas reservoirs. The calculation of aquifer capacity was based on the simplified relationship:

$$\boldsymbol{M_{CO_2 t} = V_{\phi} \rho_{CO_2 r} S_{CO_2}} \qquad \textbf{Equation 2.54}$$

where MCO_{2t} is the storage capacity of the reservoir in tonnes (t), V_{ϕ} is the pore volume of the formation, ρCO_{2r} is the density of CO_2 at reservoir conditions, and SCO_2 is the saturation of CO_2 assumed for the formation. For the Bunter Sandstone Aquifer storage was assumed to be in the structural closures that were identified. It was further assumed that CO_2 would fully fill the structural closures with a saturation (SCO_2) of 40%. Relevant information is not available to make volumetric calculations for all potential saline aquifer storage locations, as pore volume estimates are not available. Figure 2.31 is a map of the sedimentary basins in the UK, and the associated oil, gas and condensate ('wet' gas) fields, and Table 2.3 shows the estimates of CO_2 storage capacity in each of these areas (Holloway et al. 2006a).

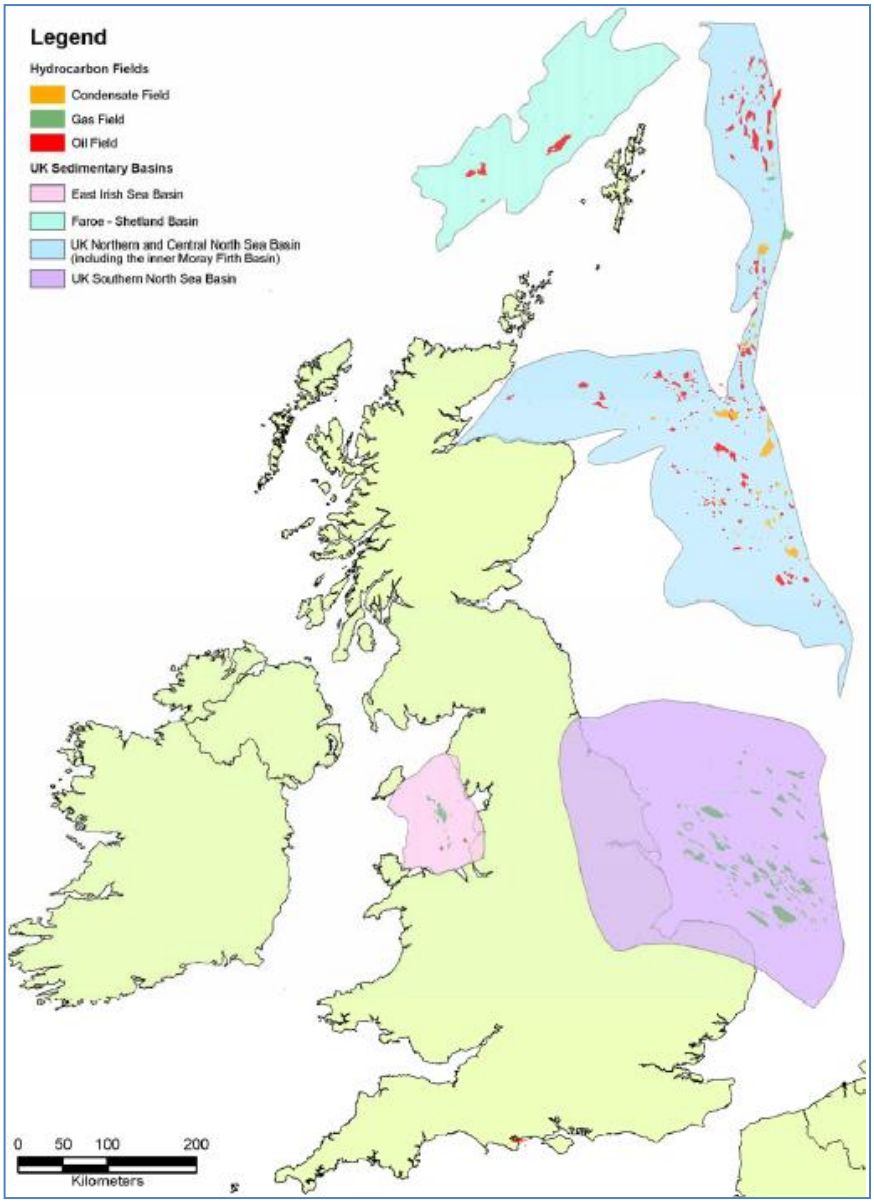

Figure 2.31 – Map of UK sedimentary basins and the distribution of oil, gas and condensate fields. The Bristol and St Georges Channel Basins are not included, but these do not have significant storage capacity (from Holloway et al. 2006a).

Storage Type	Location	Capacity (Gt CO_2)
Gas offshore	Southern North Sea	3.9
	East Irish Sea	1.0
	Northern and Central North Sea (Frigg)	0.02
Oil offshore	All fields – non-optimized EOR	1.2
	All fields – optimized EOR	1.8 - 3.5
Saline Aquifer	Bunter Sandstone – Southern North Sea	14.3
	Palaeocene and Eocene Sandstone – Northern and Central North Sea	3.0
	Sherwood Sandstone – East Irish Sea	0.6
Total		**25.8 – 27.5**

Table 2.3 – Summary of capacity estimates excluding onshore capacity (from Holloway et al. 2006a).

The estimates of storage in gas reservoirs are considered to be low risk and likely to be accurate. The main complication results from the behaviour of brine encroaching into the reservoir in water-drive reservoirs (Holloway 2008). Similarly, the estimates for storage in oil reservoirs are fairly straightforward and low risk. The main issue is that EOR operations are likely to be used in conjunction with storage, and this complicates estimates, as the optimization and level of implementation are uncertain. Storage in saline aquifers however is considered to be high risk and uncertain. There are many issues that complicate capacity estimation, not least the lack of information on the subsurface structure and aquifer properties (Holloway et al. 2006a, Bachu et al. 2007, Holloway 2008). Datasets for oil and gas reservoirs and information relating to remaining lifetime of producing assets is confidential, and so research in oil and gas field storage potentially is difficult without an industry partner. Clearly, the priority for capacity estimation is therefore research into saline aquifer storage due to the potential high capacity. To refine estimates of saline aquifer storage, it is necessary to obtain information on reservoir properties, structure, regional hydraulic properties and trapping mechanisms. Generally the estimate will rely on a local site specific analysis (as is the case with gas and oil reservoirs) using numerical simulation (Holloway 2008). Such site-specific information at the required level of detail is not currently available, at least not in the public domain, and so the only option for refinement of capacity estimates in saline aquifers is using assumptions and estimates from regional studies to refine the upper limit of storage capacity.

2.9.1.2 *Injectivity in the Bunter Sandstone*

One control on the capacity of a saline aquifer is the rate at which CO_2 can be injected into the aquifer, or the injectivity. Injectivity is limited by brine displacement, fracture pressure, and the properties of the reservoir rocks (e.g. compressibility and overburden deformation). Currently at Sleipner, In-Salah and Weyburn, large volumes (~1Mt CO_2) of CO_2 are injected into large storage volumes, but only in a small number of wells. This means that the total

injected volume is low compared to the levels that would be required for an industrial scale regional injection project, for example, the emissions from all UK power stations in 2012 was 156.1Mt CO_2 (DECC 2013a). One approach to assessing the impacts of such large-scale injection is to model the injection using a simplified model, with parameters reflecting the likely reservoir properties, injection rates and fractures pressures. Modelling of the Bunter sandstone aquifer using a pressure cell simplification was carried out by Lynch (2010). This approach considers the interference of multiple closely spaced injection wells and the constraints on injection pressure due to fracture pressure. The model consists of one injection well injecting into a confined area of varying sizes, and hence models the no flow boundary of adjacent virtual wells. The results are then scaled up to reflect the areal extent of the aquifer and the number of wells multiplied accordingly. Figure 2.32 illustrates the concept.

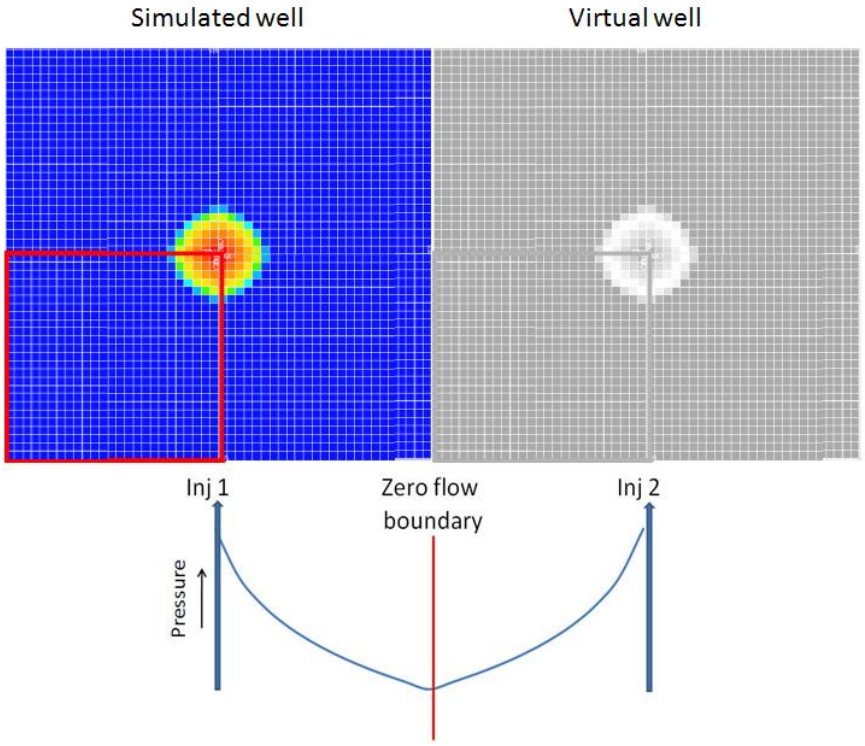

Figure 2.32 – Illustration of pressure cell concept and no flow boundary between adjacent injecting wells. Only the area represented by the red square is actually modelled and represents 1 quarter of the injection well capacity. The results of the model can then be scaled up using multiplication.

In pressure cell simulations (Lynch 2010), the CO_2 injection pressure was limited to the maximum fracture pressure based on a fracture pressure gradient of 0.8 psi/ft (18.1 MPa/km). The porosity was 20%, permeability 10mD vertically and 100mD horizontally, and pore compressibility was 3.6 x 10^{-6} psi^{-1} (5.22 x 10^{-5} bar^{-1}). The CO_2 was injected into a 40000km^2 aquifer based on the area of the aquifer estimated from Gough and Shackley (2005). The total injection capacities against the well spacing and number of wells estimated from this approach are shown in Figure 2.33. The graph shows that there is a trade-off between the capacity and well spacing/number of wells. A reduction in well spacing can give

a dramatic increase in capacity, but with a resultant impact on the number of wells that must be drilled. A capacity of 8Gt CO_2 can be achieved, but this requires nearly 700 wells at spacing of 8.6 km. Considering that a single well can cost tens of millions of pounds, this may not be economical (Lynch 2010). A more realistic capacity of 4.5Gt CO_2 was modelled using 170 wells at a spacing of 13.13 km.

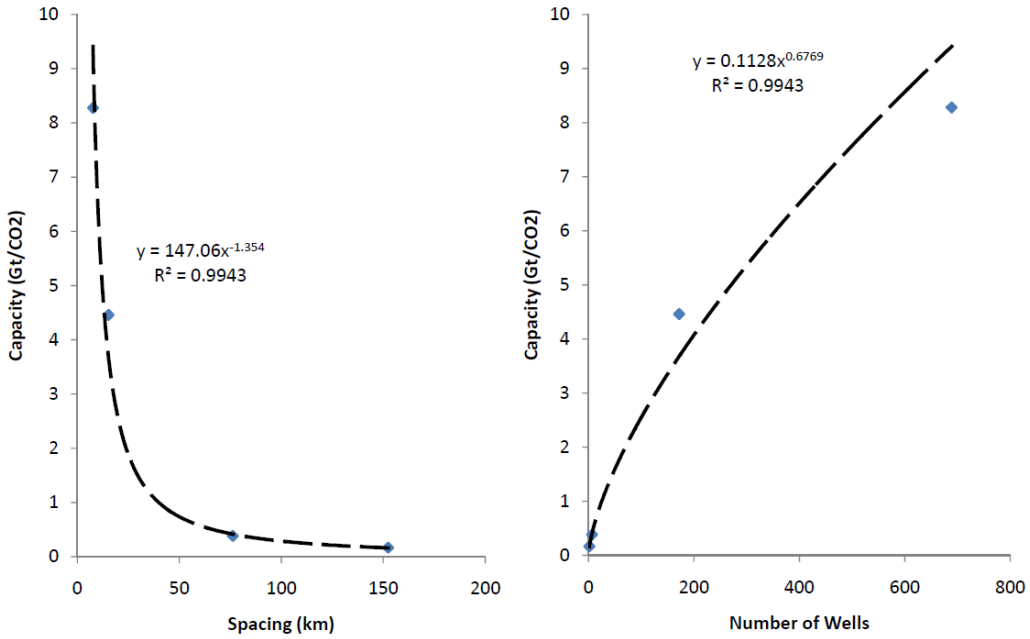

Figure 2.33 – Storage capacity of the Bunter aquifer against well spacing (left) and number of wells (right) for pressure cell modelling. The well spacing is inversely proportional to the number of wells (from Lynch 2010).

Heinemann et al. (2010), in a similar pressure cell study, determined that a capacity of 7.8Gt of CO_2 was possible. They assumed that the wells were at a 14.8 km spacing, and that 259 wells would fit within the area of the Bunter Sandstone, which was estimated to be 56660 km^2. In a subsequent study, they refined the estimate to between 3.8-7.8Gt CO_2, with storage efficiencies between 0.3 and 0.6%, depending on well spacing (Heinemann et al. 2012). They use a fracture pressure gradient of 15 MPa/km in the optimistic case and 12 MPa/km for the conservative case. The injection rate was 1 Mt injection per year for 30 years, and the aquifer was assumed to have 250mD horizontal permeability.

The different estimates from the two pressure cell studies are likely to be due to different estimates of areal extent of the reservoir. The larger area used by Heinemann et al. (2012) is likely to be more accurate as it is taken from a published estimate, the area used by Lynch (2010) was a coarse map based approximation. The different assumptions relating to the permeability may also be important, Heinemann et al. (2012) used a permeability of 250 mD throughout the model, and Lynch (2010) used 100mD. Additionally no compressibility values were published by Heinemann et al. (2012). However, both of the pressure cell studies highlight the additional constraints on capacity in saline aquifers, and shows that the

estimate of 14Gt CO_2 by (Holloway et al. 2006a) is almost certain to be a significant overestimation. The pressure cell approach assumes that the pressure developed by injecting CO_2 would be build-up within the pore water of the aquifer, and models a closed boundary aquifer. The closed boundary assumption means that the CO_2 injection can only be accommodated through expansion in pore space, which is controlled by the compressibility. As pointed out by Brook et al. (2003) this is unlikely to be realistic. In reality, pressure dissipation would also occur through migration of brine from the reservoir through leak off points. Although the boundaries are unlikely to be fully open and the aquifer behaviour is likely be a combination of both expansion and brine migration (Brook et al. 2003).

More recent studies have advanced the data available for the Bunter Sandstone. Noy et al. (2012) present simulation results for a model that represents a section of the Bunter aquifer to the east of the Dowsing Fault zone, (illustrated in Figure 2.34). The areal extent of the model is approximately 13600km^2, which is 25% of the area modelled by Heinemann et al. (2012). The model was generated using sparse 2D seismic sections and well logs and, although the model resolution is not high, it does provide a broad indication of the structure in the aquifer, which is a significant change from generic block pressure models (Noy et al. 2012). Noy et al. (2012) and Dingwall et al. (2013) both report the presence of an outcrop at the seabed of the Bunter sandstone within the modelled area, and so brine expulsion from this outcrop to the seabed is also present in the model. Total storage capacities of between 0.7Gt CO_2 and 1.1Gt CO_2 are calculated for formation permeabilities of 20-100mD respectively and 12 injection wells leading to a maximum 1% storage efficiency (fraction of pore space filled with CO_2). Crudely speaking, the model of Noy et al. (2012) approximates 25% of the volume of the pressure cell model by Heinemann et al. (2012) and, scaled up, represents 2.8Gt CO_2 to 4.4Gt CO_2 total storage, which is a lower range than the pressure cell model. However the pressure cell model of Heinemann et al. (2012) has no outcrop or open boundaries and includes many more wells. Thus, it is reasonable to expect a greater capacity with the more realistic model of Noy et al. (2012) if more injector wells were used. There are also other uncertainties and assumptions that differ between the two models (and that of Lynch 2010). For example, a homogeneous permeability of 100mD was used in the more realistic model, whereas a homogeneous permeability of 250mD was assumed in the pressure cell model. In a more detailed modelling of specific structures within the Bunter aquifer, Williams et al. (2013) reveal almost a 50% reduction in the expected storage efficiency of the structure when factors such as heterogeneous permeability and low permeability layers are taken into account. Storage efficiencies of between 4% and 33% were calculated in the study by Williams et al. (2013) for several domes modelled with connection to a larger aquifer, representing the Bunter Sandstone. The efficiencies are much higher than either the pressure cell or more realistic Bunter model as the efficiency calculation is only based upon the storage structure and not the entire area affected by the pressure increase (Heinemann et al. 2012). The model is approximately 1200 km^2 in areal extent, and capacities of between 0.07 and 1.0 Gt CO_2 were modelled (Williams et al. 2013).

All of the capacity models use fixed parameters for the permeability, compressibility, boundary conditions and other flow properties and do not explore the potential variation in parameters. The discussion of modelling parameters earlier in this chapter has shown that permeability is difficult to quantify accurately and may vary anisotropically. The capacity models discussed above also derive the values of compressibility from estimates in the literature that are not based on laboratory measurements or rigorous assessment of potential values. The discussion on compressibility earlier in this chapter has also shown that compressibility may vary in materials, and is often a poorly constrained parameter that may be overlooked in parameter derivation. The boundary conditions for the more realistic model are also not backed up by any empirical data due to the lack of any detailed investigation in the Bunter aquifer. The estimates of boundary condition behaviour are only based on estimates of the performance of the boundary, and so are subject to variation. The potential variation in the capacity estimates due to parameter variation therefore provides an opportunity to further evaluate and refine the capacity estimates.

The models of Smith et al. (2011), Noy et al. (2012), Heinemann et al. (2012) and Lynch (2010) all incorporate closed lateral boundaries as a conservative assumption. In most of the studies it is stated that brine extraction would increase the storage capacity due to the pressure relief afforded by removal of pore water. The concept of brine extraction as a capacity increasing technique is discussed in the following section.

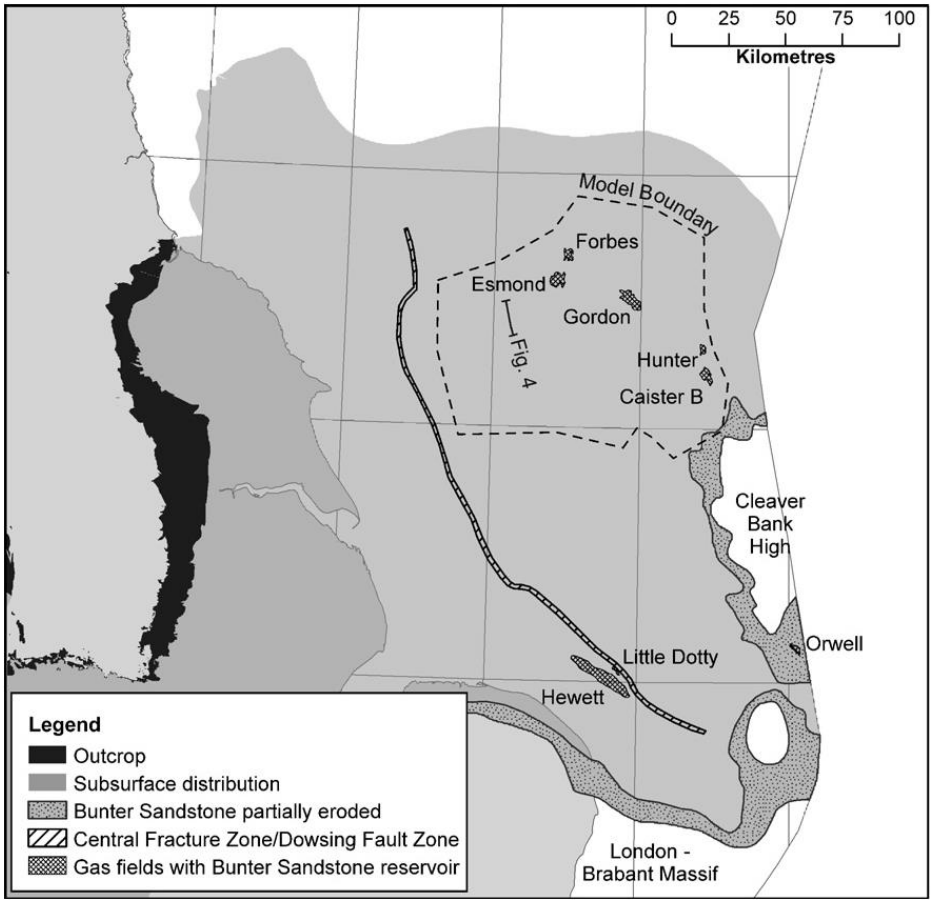

Figure 2.34 – Map of the Bunter Sandstone distribution and model boundary of Noy et al. (2012) the extent of the model is approximately centred around latitude 54°10'01"N and 1°49'28"E.

2.9.1.3 *Brine Extraction and Pressure Relief*

Pressure can build up during injection if brine is not displaced by the injected CO_2. This pressure build-up can be relieved by the removal of brine from the reservoir using production wells. Pressure relief has been considered by several workers, such as Michael et al. (2011) and Neal et al. (2011) for projects in Australia and in a report by the Scottish Centre for Carbon Capture and storage (SCCS) (2011b) for a project in Scotland. In the Australian context, the production of brine from reservoirs can theoretically be coupled with production of potable water using desalination. This is practical and economically viable due to the scarcity of water in some parts of Australia, Figure 2.35 illustrates the concept (Neal et al. 2011).

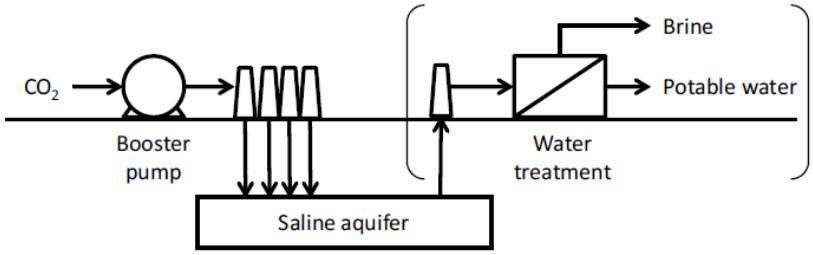

Figure 2.35 – CO_2 pressure relief operation, brine extracted from the aquifer for pressure relief is treated to produce a potable water and waste brine (Neal et al. 2011).

The production of potable water from waste brine extracted for pressure relief has the potential to improve the economics of CO_2 storage in Australia. In the UK, however, offshore production of potable water is unlikely to be economic and there is unlikely to be demand for treated water over rainfall capture. Nevertheless, pressure relief may still be a useful technique for enhancing storage capacity and there may be other opportunities for economic benefit, such as recovery of mineral salts, or hot produced water, although as study of the economic practicality of these aspects is beyond the scope of this study. In the study by Neal et al. (2011), CO_2 was injected into a 1000m^2 aquifer with high and low permeability cases and thicknesses between 3 and 30m, and analysed with and without pressure relief. The modelling showed that the pressure relief was most beneficial at high injection rates for the high permeability thick aquifer, with injection rates increased by up to seven times. The pressure relief was less effective in the thin low permeability aquifer. In the low permeability case, remaining below the fracture pressure at the well flow would require low injection rates. Pressure relief would not improve this situation and the low permeability would exert a greater influence over the volume of CO_2 that can be injected compared to the restriction on injection due to pressure build up. The pressure relief technique would also be less effective at removing brine in a low permeability case. Water extraction rates of between 2000m^3/yr and 44x10^6 m^3/yr were modelled, with the highest extraction corresponding to injection rates of 45Mt CO_2/yr. 25 producer wells were used, which would give a maximum extraction rate of over 3350m^3/day per well, the ratio of producers to injectors varied between 4:1 and 1.4:1.

Pressure relief has also been analysed in a report by Scottish Carbon Capture and Storage (SCCS). The report contains a case study of the Captain Sandstone in the Forth Approaches Basin, in which the aquifer covers an area of approximately 3000km^2. The injection simulation involved 12 wells each injecting 2.5Mt CO_2/yr over 100 years (SCCS 2011b). Various cases were assessed with different boundaries in the model opened or closed. In the simulations with some open boundaries, all wells experienced a decrease in injectivity after 10 years, and only one well was injecting after 50 years. With the aquifer boundaries closed, injection ceased after 30 years, whereas with the boundaries open, injection capacity remained after 100 years. For this reason pressure relief was also modelled in the simulations (SCCS 2011b). The results of the pressure relief modelling for the closed boundary case show capacity was increased 4.65 times, using 15-20 pressure relief wells with 4000m^3/day of water extraction per day. This amounted to a ratio of producers to injectors of approximately 1.7:1. The report does not mention whether the water production rate is per well or total, but based on comparison with Neal et al. (2011) this would be per well. The comparison indicates water extraction of between 21.9x$10^6$$m^3$/yr and 29.2x$10^6$$m^3$/yr. Using pressure relief, the same capacity of CO_2 storage was achieved for the closed case as that modelled with the open boundary case, suggesting pressure relief may be a useful mitigation tool if brine migration becomes an issue.

The analysis of the Bunter Saline Aquifer by Lynch (2010) assumed closed boundaries for the analysis as a conservative estimate. The model could not incorporate open boundaries due to the scaling up assumption used to model well interference. The logical extension of this work involves assessing pressure relief in the aquifer to determine the potential for pressure relief and to assess the likely capacity if the boundaries were open.

2.9.1.4 *Summary*

This section has highlighted the potential offshore storage capacity in the UK. The Bunter Sandstone represents the major source of storage potential for the UK, with anywhere between 52-55% of the total potential storage capacity of the offshore UK (Holloway et al. 2006a). As such, it is likely to be the dominant location for storage of CO_2 in the UK. It has been shown that the initial estimate of storage potential in the Bunter could be at least twice the value that is achievable once pressure constraints are taken into account, which would represent a reduction in estimated storage potential for the UK. Such a large difference in storage estimate has significant implications for proposals for storage schemes within the Bunter aquifer and so research to refine this estimate will be an important contribution to the body of knowledge relating to potential storage capacities. Techniques to increase capacity or mitigate risks of proposed storage projects are also important and, in terms of capacity, brine extraction or pressure relief may be one of the key mechanisms. The contribution of pressure relief to storage capacity is then also an important avenue of research.

2.9.2 **Fracture Pressure and Stress Path Hysteresis – Leakage Potential and Capacity Reduction**

Fracture pressure, as discussed previously, is the pressure at which fractures will be induced or reactivated in the rock due to injection fluid pressures exceeding the shear or tensile strength of the injection formation. Fracture pressure is measured based on the pressure required to open a fracture against the minimum principal stress. The fracture pressure is a key parameter in the design of any storage project as it determines the ultimate capacity of any storage formation. The pressure of the formation cannot exceed this pressure otherwise leakage may occur and CO_2 may escape along fractures. However, these fractures will close once the pressure drops below the critical level and, as such, the risk is greater in terms of capacity estimation as opposed to large-scale leakage from the reservoir. Although the risk of leakage of a storage reservoir via fractures is secondary to the risk of capacity estimation errors, leakage will cause public concern and will indicate to regulators that there is not a full understanding of the storage system. Poor characterisation of fracture pressures or unexpected behaviour of the fracture pressure has been identified as a risk in item 2H of Table 2.2 and implicitly controls the ultimate capacity as identified by item 1F. This section assesses the understanding of the fracture pressure in reservoirs, and the possible evolution of the fracture pressure with pore pressure changes. It is mainly relevant to storage in oil and gas reservoirs that are reused for CO_2 storage.

To understand the fracture pressure in a reservoir, it is important to understand the likely stress path of the reservoir as this will make it possible to predict the point at which failure in the reservoir will occur, (i.e. on a Mohr circle representation the point at which the circle would intercept the failure envelope). The complexity of determining the stress path has already been discussed in Section 2.5.1. There is little field data for stress paths of reservoirs that have been depleted and then re-pressurised, which will be important for oil and gas reservoirs that are re-used for CO_2 storage. Most of the work in the literature is focussed on depletion stress paths as this is associated with common problems such as borehole failure, sand production, faulting and fracturing, seismic activity, pore collapse and hydro-fracturing operations (Segura et al. 2011). There is very little evidence in the literature of the predicted stress paths for re-pressurised reservoirs. For example, would the re-pressurisation stress path will be identical to the depletion stress path, or, as may be more intuitive from the material behaviour characteristics (e.g. plastic deformation) and reservoir complexities previously mentioned, would there be hysteresis in the depletion-re-pressurisation stress paths. Stress path hysteresis would lead to a situation where the fracture pressure upon re-pressurisation would be different from that predicted from a non-hysteretic stress path and this would have obvious implications for planning a CO_2 storage project. The paper by Hillis (2001) summarises the most common assumptions relating to stress path and associated fracture pressure in reservoirs. The key diagram from this paper is shown in Figure 2.36. Figure 2.36 (a) shows the case where total stress is not coupled to pore pressure and there is no change in total stress. As Hillis (2001) suggests, case (a) is a common assumption and in this case the fracture pressure will be determined by the increment of pore pressure increase required to translate the Mohr circle to the point of failure. Where $\sigma_3 - P_0 = \sigma'_3$, and total stress does not change, σ'_3 will be directly related to the pore pressure change. As Hillis (2001) demonstrates from field evidence there is actually some level of coupling between pore pressure and minimum total horizontal stress, termed pore-pressure stress coupling. Figure 2.36 (b) illustrates the behaviour of the Mohr circle when effective horizontal stress does not increase at the same rate as vertical effective stress with decreasing pore pressure. Case (b) is based on observations of the stress path from a case study of the Ekofisk field, which is also discussed by Teufel et al. (1991). Case (b) leads to a lower total horizontal stress increase compared to total vertical stress, as $\sigma_3 = \sigma'_3 + P_0$. In this case (without stress arching), using the stress path parameters defined in 2.5.1, the stress path parameter K_{sp} would be <<1, and the horizontal stress path parameter γ_h would be close to 1 (approximately 0.7) and depletion related shear failure is observed. In fact Hillis (2001) shows that in the absence of stress arching the horizontal stress path parameter $\gamma_h = 1 - K_{sp}$, so in Figure 2.36 (b) $K_{sp} = 0.3$. Figure 2.36 (c) illustrates an extension of the theory of pore pressure-stress coupling by Hillis (2001) for increasing pore pressures, determined from overpressure studies of sedimentary basins rather than reservoir field data. This suggests that the same relationship for increasing pore pressure is valid (i.e. $\gamma_h = 0.7$). For CO_2 storage (and injection in general), case (c) would imply a non-hysteretic stress path and suggests that fracture pressures would be higher than case (a) would predict with

injection. It would also imply that in general fracture pressure would increase with increasing field pressure. Clearly, it is then important to find field evidence from reservoirs that supports the theory of fracture pressure decrease during depletion and subsequent increase during injection. However, as pointed out by Santarelli et al. (2008), there is little field evidence to support the assumption that the stress path will be the same during depletion and re-pressurisation. They present data, along with a previous paper by Santarelli et al. (1998) that indicates hysteresis in a Central North Sea reservoir that has undergone secondary recovery using water flooding.

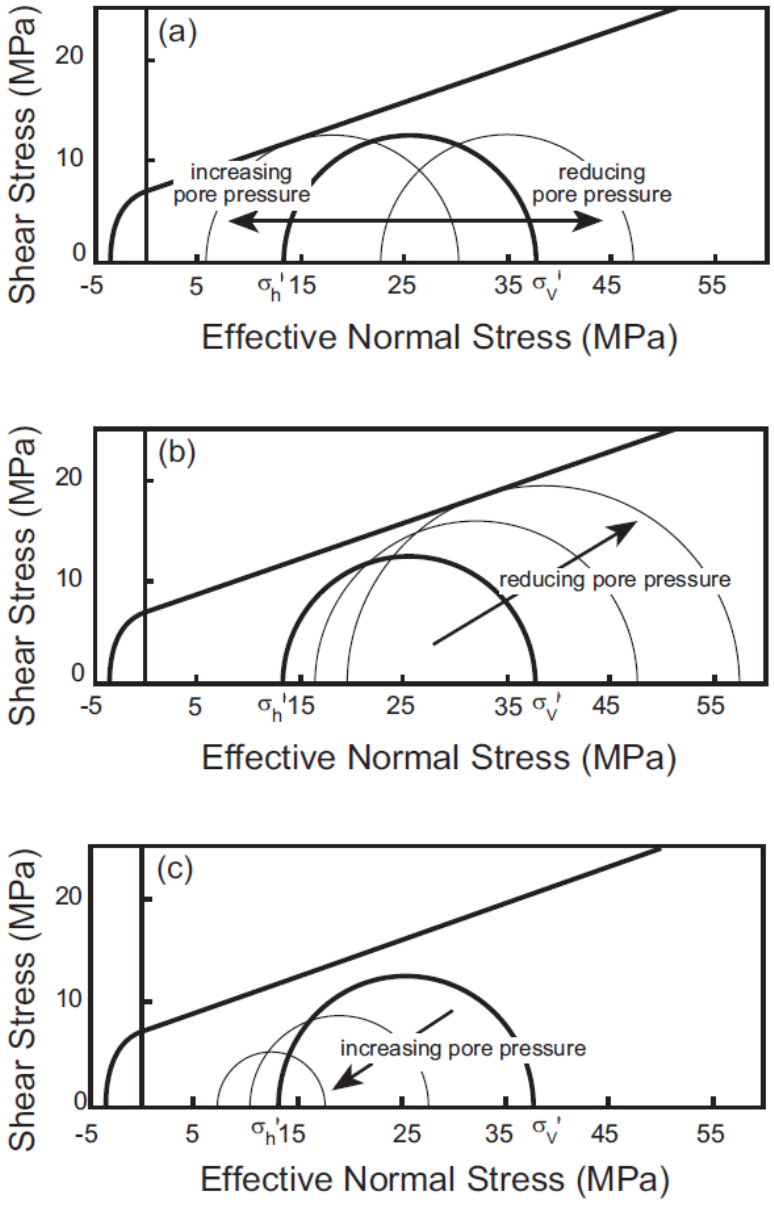

Figure 2.36 – Pore pressure –stress coupling principle from Hillis (2001) figure (a) shows the 'classic' case where pore-pressure is decoupled from total stress, (b) shows pore pressure coupling with depletion $\gamma_h = 0.7$, and (c) for overpressure (proxy for re-pressurisation) where $\gamma_h = 0.7$ also.

The data presented by Santarelli et al. (1998) and Santarelli et al. (2008) relates to the measurement of fracture pressure (using mini-frac and step rate tests) during depletion and

re-pressurisation. They report the stress path using the horizontal stress path parameter (called stress path in their study). During depletion they observed pore pressure-stress coupling as predicted by Hillis (2001) and report values of γ_h = 0.7005 for the Northern part of the field and γ_h = 0.4244 for the Southern part of the field. Assuming no stress arching is taking place, this equates to K_{sp} = 0.30 to 0.58. The theory laid out by Hillis (2001) would predict the same stress path for re-pressurisation. However the value of γ_h for re-pressurisation in the study by Santarelli et al. (1998) was found to be effectively 0 (i.e. K_{sp} = 1 without stress arching), indicating no pore pressure-stress coupling during re-pressurisation of the field. This hysteretic behaviour of the horizontal stress path is more easily visualised in Mohr circle space, as shown in Figure 2.37. Figure 2.37 shows a schematic version of the behaviour observed by Santarelli et al. (1998):

- during depletion/production the stress path K_{sp} is approximately 0.3 to 0.4, this leads to expansion of the Mohr circle radius and translation of the centre. The horizontal effective stress does not increase as much as the vertical effective stress and an increase in the differential stress is observed;
- during re-pressurisation/re-injection the stress path K_{sp} is 1 and the circle translates without a reduction in differential stress. This leads to fracture at lower pressures than may be predicted assuming pore-pressure stress coupling.

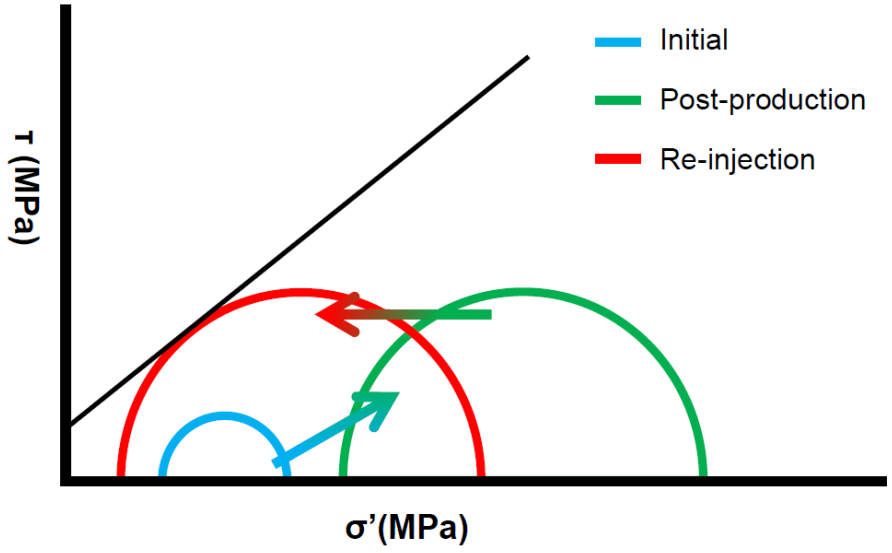

Figure 2.37 – Schematic diagram of the behaviour observed in a North Sea oil field undergoing secondary recovery from Santarelli et al. (1998). The diagram shows a hysteretic stress path and lower fracture pressures during re-pressurisation than may be predicted assuming the pore pressure-stress coupling assumption.

Santarelli et al. (1998) do not conclude on a mechanism for the observed stress-path hysteresis, but speculate it may result from plastic behaviour of the rock on a reservoir scale, not observed from core scale measurements. The reservoir material is a poorly lithified normally consolidated sand. In a later paper, Santarelli et al. (2008) observe that there seems to be no published literature available that provides evidence of non-hysteretic

behaviour in other fields. However, it is difficult to determine whether this lack of evidence is due to lack of investigation in this area or lack of non-hysteretic behaviour in other reservoirs. Santarelli et al. (2008) also link temperature changes to the observed behaviour with much lower fracture pressures being observed with cold water injection in the weak sediments discussed.

Much of the discussion relating to stress path has assumed a stress arching parameter of 0, (i.e. constant vertical total stress). However there is no reason suggest this needs to be constant and so this will add further complexity to the stress path analysis (Sayers and Schutjens 2007, Segura et al. 2011). The implications of stress arching and stress path are further discussed in a report by the IEAGHG 'Caprock Systems for CO_2 Geological Storage', where particular reference is made to the effect on the cap rock. It is suggested that stress arching could lead to fracture formation and fault reactivation in the cap rock during re-pressurisation, particularly when the largest principal stress is vertical. This would be critical in terms of leakage pathways (IEAGHG 2011b). Stress arching is suggested as the mechanism for the uplift and fracturing observed by Rutqvist et al. (2010) at In-Salah (IEAGHG 2011b). Another risk discussed in the IEAGHG report is stress transfer. A stiff overburden (associated with stress arching) can lead to stress transfer in the reservoir-cap rock system, which could lead to potential fracturing in the overburden. This is illustrated in Figure 2.38. The minimum horizontal stress will reduce in the cap rock above, which could increase the likelihood of tensile fracturing and fault reactivation in the cap rock above (IEAGHG 2011b). Similar stress transfer is also discussed in the work of Segura et al. (2011), where stress changes in the overburden are associated with a stiff caprock during production.

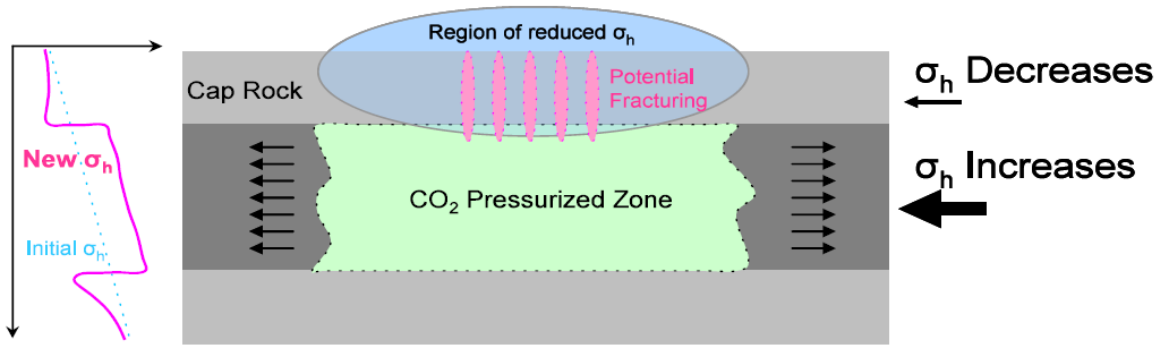

Figure 2.38 – Stress transfer in the reservoir-cap rock system, a reduction in the minimum horizontal stress in the caprock resulting from a corresponding increase in the reservoir. Potential for fracturing is increased in the caprock, which could lead to leakage pathways (from IEAGHG 2011b).

There is clearly uncertainty surrounding the stress path behaviour of depleted reservoirs during depletion and injection. The associated potential for stress path hysteresis and stress arching during CO_2 injection operations has been highlighted from field evidence. The risk of overestimating the fracture pressure in abandoned fields could be significant if stress paths

hysteresis is not taken into account during injection of CO_2 and this presents a risk both to capacity estimates and to storage security in terms of leakage.

2.9.3 **Capabilities and Resources**

The capabilities available for this project are focused in the area of reservoir fluid flow and geomechanical simulation and synthetic seismic modelling. Petrophysical laboratory data is used to compliment the simulations by providing physical measurements of some simulation inputs.

Reservoir simulation capabilities are provided by the Tempest simulation suite from Roxar Software. This is an industry standard finite difference reservoir simulator capable of simulating 3 phase, and pseudo-4 phase (additional phase is solvent option) black oil and compositional problems. The software includes standard treatment of faults, including options for fault transmissibility multipliers and specification of aquifer boundary conditions.

A coupled geomechanical-fluid flow model has been developed at the University of Leeds as part of the IPEGG (Integrated Petroleum Engineering, Geophysics and Geomechanics) JIP undertaken by the University of Leeds, the University of Bristol and Rockfield Software Limited (sponsored by BG group, BP, Eni and StatoilHydro). The coupling workflow is an iteratively coupled (including explicit/incremental capability) model using a two-way algorithm to pass information between the fluid flow simulator and the Elfen Geomechanical Software Suite (Rockfield Software Ltd.). The fluid flow simulator can be one of several industry standard simulators (e.g. Eclipse) in this case Tempest from Roxar has been used. The coupling process is controlled by the ElfenRS module developed by Rockfield, which handles the exchange of information between the two programs using message passing interface (MPI) protocols to update the information in the reservoir simulator. As part of the IPEGG JIP, a rock physics and seismic modelling code was integrated into the coupled geomechanical-fluid flow workflow. The principle behind the code is described in various studies including Angus et al. (2008), Verdon et al. (2008) and Angus et al. (2011). The seismic model allows evaluation of stress and fluid dependent seismic velocities, which can be used to assess seismic attributes within the geomechanical model. The seismic modelling codes incorporate a rock physics model that is used to derive a seismic stiffness matrix (i.e. elasticity tensor) from fluid saturation, pore pressure and effective stress. The rock physics model is based on building an aggregate elasticity based on micro to macro scale features (Angus et al. 2011). The seismic workflow incorporates fluid substitution effects using Gassman's equation, microstructural rock properties, stress-dependent velocities and empirical scaling of static (geomechanical) stiffness with dynamic (seismic) stiffness (Angus et al. 2011). The stress dependent velocities are incorporated using the empirical microstructural model presented by Verdon et al. (2008), this model assumes that a fraction of the total porosity of the rock is comprised of compliant microcracks. The microcracks dominate the nonlinear stiffness response, at low stresses the microcracks are open and the seismic velocity is reduced, however, with increasing stress the cracks close

which increases seismic velocity and reduces stress sensitivity (Angus et al. 2011). The microcrack density and aspect ratios which were calibrated in the model by Verdon et al. (2008) and Angus et al. (2009). A full description of the seismic model is beyond the scope of this review, however this workflow has been used in multiple studies and the reader is referred to the literature for further information and other more complex implementations of the workflow than used here. The seismic modelling provides valuable information relating to seismic characteristics, for example changes in seismic velocity, and stress sensitivity of seismic velocities, during CO_2 injection, with the long-term aim being to compare this with real field data. Comparison with field data will allow further ground-truthing of the geomechanical model, and as such is an iterative process.

Laboratory data for relative permeability measurements of brine and CO_2 mixtures in fault and (sandstone) host rocks carried out at Leeds are available, as presented in the thesis of Tueckmantel (2010). The relative permeability for host rocks is implemented in all the reservoir simulation models used to represent two-phase flow, the fault rock data is not used as flow within faults is not modelled explicitly in the simulations carried out.

2.9.4 **Primary Goals**

Industrial scale carbon capture and storage is only feasible if sufficient economically viable capacity is available. Without reliable estimates of available storage capacity, it is difficult to plan storage projects or have confidence in the future availability of storage capacity; this will make investment in CO_2 storage highly uncertain. Improving capacity estimates and techniques for capacity increase is therefore an important research area. Therefore, Chapter 3 investigates brine extraction and potential storage capacity (items 1B and 1G from Table 2.2) in the offshore Bunter Sandstone aquifer, which has the largest single storage potential in the UK, to assess current capacity estimates and the effectiveness of brine extraction on increasing capacity. The brine extraction modelling is carried out using Tempest reservoir simulation software to model brine extraction in a generic pressure cell capacity model of the Bunter Aquifer developed by Lynch (2010). The investigation of the storage capacity is based on a large scale regional model of the Bunter Aquifer derived from the model presented by Noy et al. (2012). The capacity modelling extends the work carried out by Noy, Holloway et al. (2012) to investigate the impact of uncertainties in the model such as compressibility, permeability variations and boundary conditions (items 1B to 1D in Table 2.2). The work aims to constrain the feasible range of capacities modelled in the aquifer based on the possible range of uncertainties. The model also allows comparison between a regional flow model derived from seismic data with a simplified generic pressure cell model such as those presented by Lynch (2010) and Heinemann et al. (2012).

Chapter 4 uses a coupled geomechanical-fluid flow model to investigate stress path hysteresis in a normally consolidated poorly lithified reservoir similar to the reservoir in case study reported by Santarelli et al. (1998). The reservoir used in Chapter 4 is a simplified reservoir, with faulted compartments and the capability to vary movement and sealing

characteristics on the faults. The aim of the chapter is determine if stress path hysteresis and associated fracture pressure hysteresis can be modelled with realistic parameters, and provide information on the likely controls on stress path hysteresis, temperature effects will also be considered. Chapters 5 aims to provide a deeper understanding of the risks highlighted by items 2H Table 2.2 which relates to the risk of a poorly quantified fracture pressure, the control of the fracture pressure on the capacity means that this is also relevant to item 1F, which is the ultimate capacity of the storage reservoir.

2.9.5 **Secondary Goals**

The coupled geomechanical-fluid flow code allows seismic data to be generated with minimal computational effort for both of the models analysed, therefore seismic data will be output for both of the coupled geomechanical models that are analysed in Chapters 4. The seismic data will provide information on stress changes during different stress paths in reservoirs, and data relating to changes in fluid saturations during depletion and re-pressurisation operations. Analysis of the seismic data contributes knowledge to items 3A to 3D in Table 2.2, and could prove useful in the application of seismic monitoring techniques to CO_2 storage.

2.10 **Conclusions**

This chapter has discussed the many factors that must be taken into consideration when planning a project to safely store CO_2 in saline aquifers and hydrocarbon reservoirs. The key findings of the chapter are:

- The five critical considerations for CO_2 storage project are, the storage capacity, injectivity of the storage reservoir, storage security and leakage pathways, storage monitoring capabilities, and storage economics and regulation. To some extent these aspects are interrelated, for example, leakage pathways may control the capacity in a reservoir.
- The ideal storage reservoir is located at the depths greater than 1000 m to maximise the compression of CO_2 due to pressure and temperature, has a robust trapping mechanism, generally involving an impermeable cap rock, and has high porosity and permeability to allow high volumes to be injected into the reservoir. The long-term security of storage must also be assured.
- The most promising prospects for storage in the UK are offshore oil and gas reservoirs and offshore saline aquifers, most focus is placed on storage in the North Sea region as this contains the most promising prospects and significant oil and gas exploration.
- Injection into storage will be controlled by the same flow properties that are used to model oil and gas reservoirs, including porosity and permeability, compressibility, and relative permeabilities and this forms the basis for modelling CO_2 storage using flow simulators.
- An additional consideration for CO_2 storage is the trapping mechanism that will secure CO_2 in storage, this can be a physical barrier such as a cap rock, which is most important in the short term, or a flow barrier such as residual trapping. This is one of the significant differences from oil and gas reservoirs as the aim is to trap rather than liberate the fluid phase.
- Geological variability will be particularly important for CO_2 storage and more critical when compared to oil and gas extraction, as the geology must be predicted accurately to ensure secure storage. Variability can affect the flow properties such as permeability and compressibility, or the sealing capacity of rocks and can seriously affect predicted storage capabilities.
- CO_2 reservoirs will exist at depth with elevated temperatures and pressures, Injecting CO_2 into storage reservoirs, which may often be depleted hydrocarbon reservoirs, will elevate pressures in the reservoir and alter the stress state. Changing stresses in the reservoir can lead to deformation and failure in the reservoir, and at leakage pathways such as faults and fractures. Storage security requirements therefore mean that analysis of stress and deformation in storage projects will be important.

- Reservoir geomechanics is the discipline that unifies the analysis of fluid flow (pore pressure changes) and stress changes in reservoirs. The stress path is one of the main considerations in the case of CO_2 storage and describes the change in stress in the reservoir and the overburden with pore pressure.
- Analysis of reservoir geomechanical problems increasingly involves the use of simulators that are more complex than industry standard fluid flow simulators. This is driven by the novel nature of some of the problems presented by CO_2 injection. This involves some form of coupled fluid flow-geomechanical simulator, which combines a fluid flow model, a geomechanical model, and some form of information transfer between the two models.
- The final aspect of CO_2 storage is the monitoring and verification that must be carried out, both to satisfy regulatory demands to prove that CO_2 is not leaking, and to verify the storage project is operating as expected. In the UK offshore setting seismic monitoring is most likely to be the key option for monitoring due to the accessibility of the reservoirs under the sea.
- Seismic data can provide information on both fluid movement and saturation in storage, and the change in stress in and around the reservoir. As a result, consideration of seismic parameters can also be incorporated into coupled modelling, through both synthetic seismic data generation and application of seismic field data in improving model accuracy.
- CO_2 storage is complex, uncertain and carries many risks. Assessment of potential risks and potential opportunities for researching and refining these risks shows that without detailed specific field scale data the best opportunity for research are capacity estimate refinement in the UK offshore setting, specifically in the data sparse saline aquifers, and analysis of potential novel risks relating to the limiting fracture pressure in abandoned hydrocarbon reservoirs.
- Estimates of capacity for the Bunter saline aquifer suggest it may comprise the most significant portion of potential storage capacity for the UK, possibly up to 55% or 14 Gt CO_2. However, generic and more specific fluid flow assessments of the Bunter suggest that the actual practical capacity may be much smaller. Potential geological variability in the aquifer is not incorporated into any of the assessments of capacity, and this has the potential to affect the capacity. Therefore, capacity assessment in the Bunter aquifer has been identified as a research goal for Chapter 3 of this thesis.
- Brine extraction is suggested as a technique for improving capacity in many studies on CO_2 storage capacity in the Bunter aquifer and has been assessed for other CO_2 storage projects in Australia and Scotland. Therefore, brine extraction is also incorporated into the capacity modelling for the Bunter aquifer to assess the potential for improving capacity with brine extraction.
- With the exception of the site specific volumetric capacity of a storage structure the fracture pressure in a reservoir presents perhaps the critical factor in determining

the amount of CO_2 that can be stored in a reservoir. The fracture pressure controls the injection rate and final pressure of a storage reservoir as leakage from the reservoir through fractures must be avoided. The fracture pressure is generally assumed to be predictable based a non-hysteretic variation with reservoir depletion and re-pressurisation. However, field evidence suggests that in some instances the fracture pressure could be lower during re-pressurisation than it is during depletion, presenting a clear risk in re-pressurising depleted hydrocarbon reservoirs. Chapter 4 investigates the potential for this fracture pressure hysteresis using coupled fluid flow-geomechanical modelling.

3 UK Storage Potential – Bunter Saline Aquifer

The Bunter Sandstone Formation has been identified as one of the key resources for offshore CO_2 storage in the UK. The capacity has been assessed as being up to 14 Gt CO_2 (Holloway et al. 2006a) and this is equivalent to 90 years of total CO_2 emissions from the UK power stations based on 2012 levels (DECC 2013a). The Bunter Aquifer therefore makes up roughly 55% of the estimated UK storage potential. However, as acknowledged by Holloway et al. (2006a) and Holloway (2008), this is only a theoretical estimate, and there are numerous factors that can diminish the estimate of capacity. An accurate estimate depends on extensive knowledge of the storage site, and lower estimates have the potential to dramatically reduce UK CO_2 storage potential. Due to the significance of the storage resource in the Bunter Sandstone Formation, there is particular interest in refining the capacity estimate. One of the projects that remains in the current UK CCS competition for commercialisation, the White Rose Project (DECC 2013b), proposes injection of 40Mt CO_2 per year into the Bunter aquifer (Dingwall et al. 2013).

The main constraints on the ultimate capacity of a storage site is the maximum allowable pressure of the field and the maximum CO_2 saturation of pore space achieved during injection operations up to the limiting fracture pressure. These constraints arise due to a combination of factors that have been discussed in the previous chapter. The maximum allowable pressure of the field is dominated by the pressure at which fracturing of the formation and potential leakage will occur, and this is in turn affected by the method of injection into the field. For example, closely spaced injectors increase the likelihood of exceeding the fracture pressure at a specific location. The extent of saturation of pore space by CO_2, termed the storage efficiency, will be affected by the fluid flow properties of the reservoir such as porosity and permeability, and controls the volume of the CO_2 that can be injected prior to reaching the maximum allowable pressure of the field. There have been several investigations of the capacity of the Bunter sandstone using fluid flow modelling. One approach is the generic pressure dependent capacity analysis or 'pressure cell' approach (e.g. Heinemann et al. 2010, Lynch 2010, Heinemann et al. 2012). Another approach is to study pressure development for a specific injection scenario, but using a realistic model of a large portion of the Bunter aquifer (e.g. Smith et al. 2011, Noy et al. 2012). The generic pressure dependent capacity analysis assumes that the aquifer has closed boundaries, and in this case, it is logical to investigate the impact of brine extraction on the storage capacity. Brine extraction is often cited as a technique to increase capacity, particularly in problematic storage reservoirs, or to improve the economics of CO_2 storage, although specific analysis if often not included. Therefore, the potential performance of such an activity in the UK is an interesting research area. The realistic model approach in the literature only explores one injection scenario with fixed parameters, and so the ultimate capacity of the aquifer is not fully explored. Further refinement of the capacity with a more realistic model and a range of modelling parameters will provide new insight on the potential storage capacity in the Bunter. This chapter presents the results of two models that have

been developed to assess brine extraction and ultimate capacity in the Bunter. The first model will assess the effectiveness and feasibility of brine extraction for the Bunter aquifer, and the second model will aim to refine the realistic capacity of the Bunter Aquifer using a range of realistic modelling parameters which have not been explored fully in the literature in similar capacity assessments of the Bunter Aquifer. The first model discussed is a pressure cell model that was created for the Bunter, the second model is a reconstructed version of the model presented by Noy et al. (2012).

3.1 Brine Extraction – Generic Model

3.1.1 Model Set-up

The model was set up in a similar manner to that illustrated in Figure 2.32, with a 'central' injector well and a 'peripheral' brine producer well (Figure 3.1). The model represents one quarter of a full pressure cell and so the well flow rates represent one quarter of the true injection/production rate of the well. The pressure cell dimensions in the lateral x and y direction are equal. Simulation is carried out for one pressure cell and the results of the modelling can be scaled up to represent the full size of the Bunter aquifer.

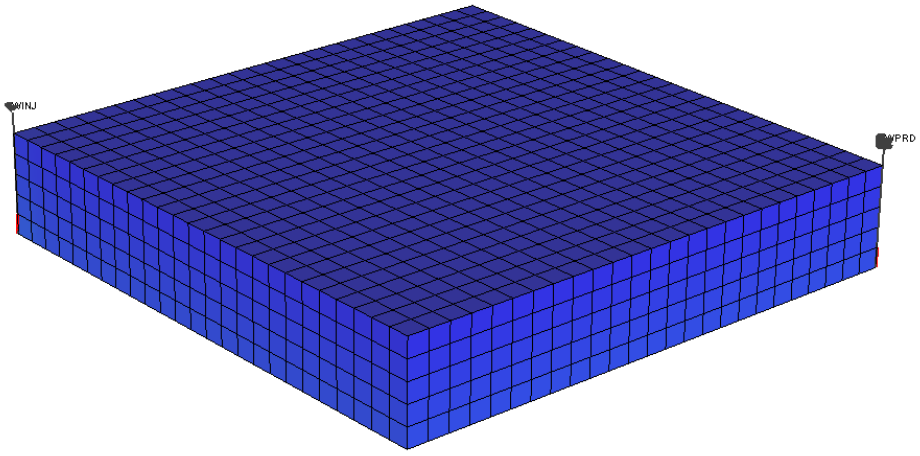

Figure 3.1 – Pressure cell model with producing well and injecting well at opposite corners (vertical scale exaggerated).

The cell represents a central injector well with four peripheral producing wells, or equivalently a central producing well with four peripheral injecting wells. The pattern is therefore a 1:1 ratio of producer to injector. Different ratios could be achieved by adding half wells along the peripheral boundary. Figure 3.2 illustrates the concept more clearly, showing the arrangement of pseudo-cells and pseudo-wells surrounding the modelled quarter cell. The areal extent of the pressure cell is varied to represent a different spacing of wells. The lateral length of the simulation model represents half of the lateral length of the actual pressure cell, and dictates spacing of the wells. In this study, simulation model lateral dimensions of 7.62 km, 15.24 km, and 26.5 km were used, representing pressure cell

lengths of 15.24 km, 30.48 km and 53 km. The total area of the Bunter aquifer reported by Holloway et al. (2006b) was adopted as the area of the sandstone aquifer to scale the results of the simulation to, as this is more accurate than the initial estimate by Lynch (2010). This yields 244, 61 and 20 injector wells, with an equal number of producing wells with the lateral dimension spacings used in this study and based on an area of 56660 km^2 for the Bunter aquifer.

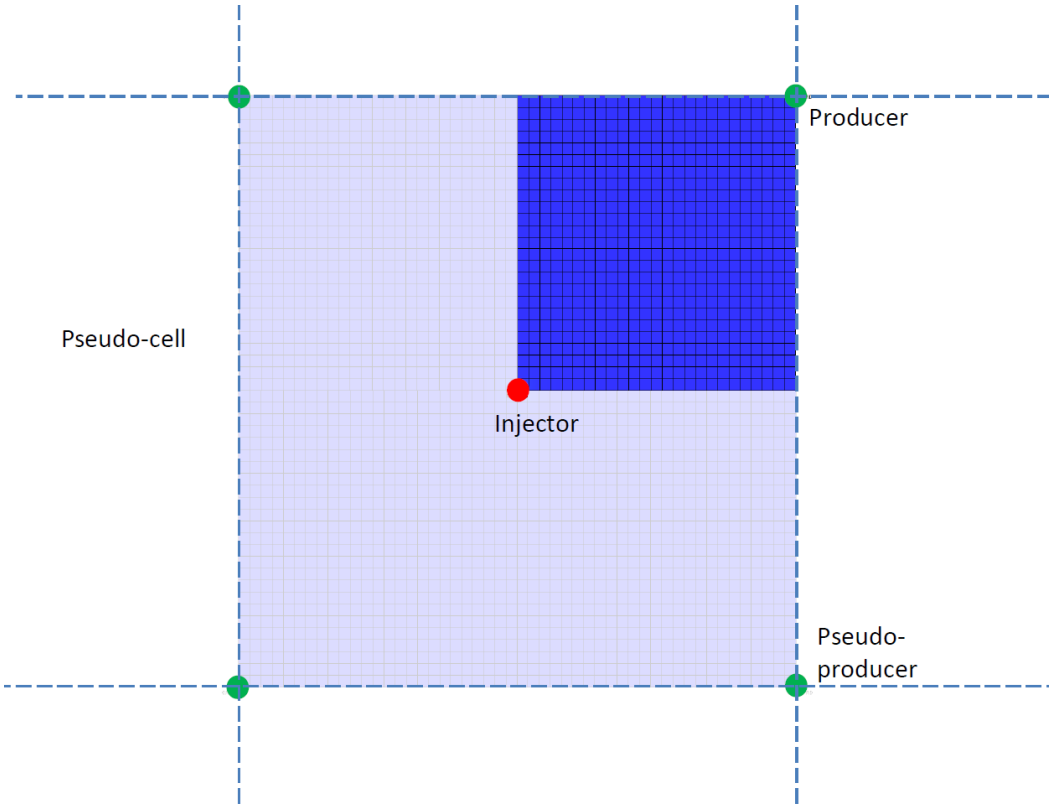

Figure 3.2 – Diagram of the theoretical layout of the pressure cell model with brine producers implemented into the model.

The model represents a horizontal reservoir with uniform thickness, which in the case of the Bunter is a highly simplified case and is merely aimed at understanding model capacity with dynamic pressure dependence and brine withdrawal.

3.1.2 Geological Model

Generic parameters were estimated from data available from gas fields in the Bunter Sandstone as well as other sources of literature due to a lack of specific data on the Bunter Sandstone. The Bunter sandstone has a thickness that varies between < 50 m up to 350 m with an average thickness of 140 m (Cameron et al. 1992, Holloway et al. 2006b). Thus in the generic model the thickness was set at 140 m, and the rock properties were assumed to be homogenous. The depth was set at 1500 m based on estimated depths of the Bunter Sandstone from well logs provided in the literature (an average depth of 1481.5 m was calculated from Johnson et al. 1994). The porosity in the Bunter generally ranges between 18-22% a value of 20% was selected as a representative value (Ketter 1991, Cooke-

Yarborough and Smith 2003, Bentham 2006). The permeability was assumed to be 100 mD horizontally, which represents the most conservative cases presented in Cameron et al. (1992) and Bentham (2006). Cameron et al. (1992) describe the Bunter Sandstone as having discontinuous layers of mudstone around 2 m thick. Whilst not extensive, the mud layers do suggest there may be a risk of vertical flow baffles. The vertical permeability was therefore set at 10 mD, based on an assumption of a k_v/k_h ratio of 0.1, due to the potential presence of vertical flow baffles. The k_v/k_h ratio is a particularly uncertain parameter. A likely range of permeability ratio is from 1 to <0.001 (Begg et al. 1989, Ayan et al. 1994, Morton et al. 2002), the ratio of 0.1 was adopted as a slightly conservative estimate based on values discussed earlier in this thesis for the Sherwood Sandstone (onshore nomenclature for Bunter Sandstone Formation) reported by Begg et al. (1989) and Morton et al. (2002).

The fracture pressure is an important consideration in this type of model. With no structural closures or leak points, the fracture pressure is the limiting factor on injection. It is common to select the fracture pressure based on either estimating the minimum horizontal stress as a percentage of the vertical stress, which is derived from the lithostatic gradient (i.e. weight of overburden), or from leak off test (LOT)/minifrac data. Edwards et al. (1998) present LOT data for the North Sea and present ratios of σ_h/σ_v, for the central, northern and southern North Sea, based on calculations of the vertical stress. The LOTs for the Central North Sea give a much lower fracture pressure for the model; based on a depth of 1500 m the fracture pressure would be 212 bar (bar units are used by the Tempest simulator). Edwards et al. (1998) estimate a σ_h/σ_v ratio of ~ 0.88 for the Southern North Sea, for a lithostatic gradient of 22 MPa (Ramm 1992, Fisher et al. 1999) this yields a fracture pressure of 290 bar. Thus a conservative assumption of σ_h/σ_v = 0.8 would give a fracture pressure of 264 bar. Simulation results are presented for both the conservative leak off test fracture pressure of 212 bar and the conservative ratio based estimate of 264 bar. At a depth of 1500 m, the lithostatic pressure would be 330 bar at the top of the reservoir, such that a fracture pressure of 264 bar would correspond to 80% of the lithostatic and a fracture pressure of 212 bar would correspond to 64%.

The formation compressibility was derived from the literature, as it was not possible to find specific data for the Bunter sandstone. The value of 4.5×10^{5} bar^{-1} presented by Zhou et al. (2008), for a study on closed and semi-closed saline aquifers, was used in the analysis. Subsequent analysis of data in the literature shows that the value of 4.5×10^{-5} bar^{-1} falls in the range of cemented sandstones for a porosity of 20%, as discussed in section 2.3.2, and so represents a reasonable estimation.

3.1.3 **Fluid Properties and Modelling Parameters**

The model was assumed to be a two-phase system containing an initial brine phase with injection of pure CO_2. The system was idealised as a black oil system without dissolution of the CO_2 in the brine. The brine properties were based on a brine used by Tueckmantel (2010) in a numerical and experimental study on CO_2 and brines in host and fault rocks. The

brine salinity was 12 wt%, brine compressibility was 3.75 x 10^{-5} bar^{-1} and the viscosity was 0.555 cp. The reservoir temperature was 55 °C and the initial pressure at the top of the reservoir model was 159 bar (15.9 MPa). The CO_2 properties are those for a pure CO_2 stream.

The two phase relative permeabilities were taken from an experimental study on two phase flow of brine and CO_2 in cores of host (sandstone) and fault rocks by Tueckmantel (2010). The host rock relative permeabilities as shown in Figure 2.5 were used.

The model boundaries were assumed to be fully closed, with a seal assumed above and below the model. The rock unit overlying the Bunter Sandstone is the Rotliegend Halite Unit and so in theory should provide a secure seal to the aquifer (Cameron et al. 1992). Although the seal will be a critical feature in any storage project, it is beyond the scope and availability of data to assess the integrity of the seal for the Bunter aquifer in this study and so this is not discussed further.

The CO_2 is injected over a period of 30 years, where injection is limited to the maximum sustainable flow without causing fracture at the wellbore. The fracture pressure is therefore used as pressure control on the well specification. Brine production is carried out at a constant rate of 100, 250, 500, 1000, 2000 and 4000 m^3/day per production well and all wells are perforated throughout the entirety of the formation. An example of the flow model input for the smallest cell size and 100 m^3/day brine production is presented in Appendix A.

3.1.4 **Results**

3.1.4.1 *Base Case Models*

Figure 3.3 shows the capacity in Gt CO_2 for the base case models with no brine production. The graph shows the results for the two fracture pressure cases of 80% and 64% of lithostatic pressure, or 264 and 212 bar respectively. For the 264 bar fracture pressure cases, the graph shows a maximum capacity of 11.3 Gt CO_2 for the closest well spacing with cell sizes of 15.24 km, 10.7 Gt CO_2 for the 30.48 km cell size and 5.9 Gt CO_2 for the largest cell size of 53 km. The well requirements for the three cases are 244, 61 and 20 wells respectively. The capacity of the medium and largest cell sizes are 5.3% and 47.8% lower than the closest well spacing with the smallest cell size after 30 years. The closest spacing of wells in the 15.24 km cells achieves maximum capacity at around 10 years, whilst the spacing in the 30.48 km cells achieve a similar capacity, but only after 30 years of injection. For the 212 bar case the pattern is similar, but with lower overall capacities, due to the restriction of the lower fracture pressure. The capacities achieved are 5.4 Gt CO_2, 4.9 Gt CO_2, and 2.4 Gt CO_2, these capacities have a similar relationship to those in the higher fracture pressure case. The medium and large size cell cases have capacities that are 7% and 55% less than the smallest cell size. The 15.24 km cell size at 212 bar fracture pressure has a capacity that is 48% of the 264 bar case, the 30.48 km cell size at 212 bar has a capacity that is 46% of the 264 bar case, and the 53 km cell size has a capacity that

is 41% of the high fracture pressure case. The comparison of results shows that a 20% reduction in the fracture pressure will lead to a 40 - 48 % reduction in the capacity of the reservoir for a wide range of cell sizes and well numbers.

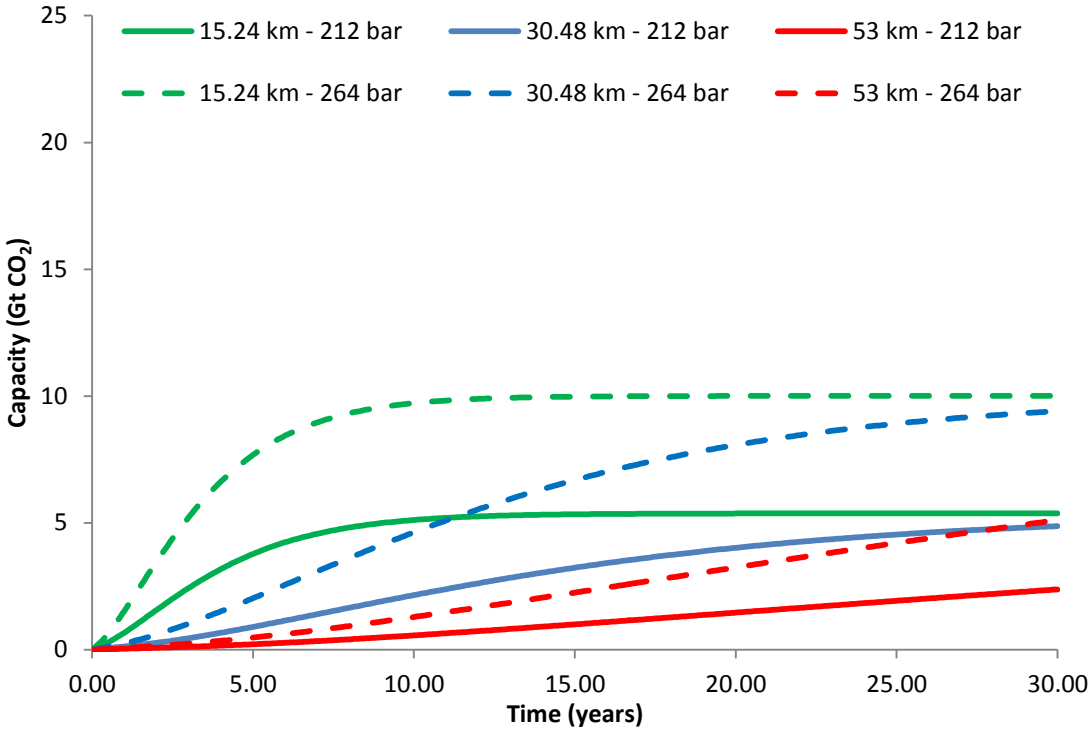

Figure 3.3 – Cumulative storage capacity of base case models without brine production for different sizes of model at different fracture pressures over the full injection period. The flattened sections indicate where injection has been reduced or stopped due the pressure control on the well.

The profiles of the injection curves in Figure 3.3 show that only the closest well spacing case has reached capacity within the 30-year time limit, where maximum capacity is reached at around 10 years when the curve levels off in both fracture pressure cases. The 30.48 km cell appears to have almost reached capacity by the end of the 30-year injection period, as the curve is beginning to level off. The total mass of CO_2 that is injected into the largest cell size (53 km) is still increasing linearly at the end of the 30-year period. The profiles of the curves can be explained by the pressure build up and relative sizes of the injection cells. Figure 3.4 shows the pressure distribution at the end of injection for the smallest and largest cell sizes. The figure shows that the smallest cell size has reached maximum pressurisation at the end of injection, whereas only a small portion of the largest cell has been pressurised to capacity. This is due to the restriction on the injection pressure limiting flow into the large cell.

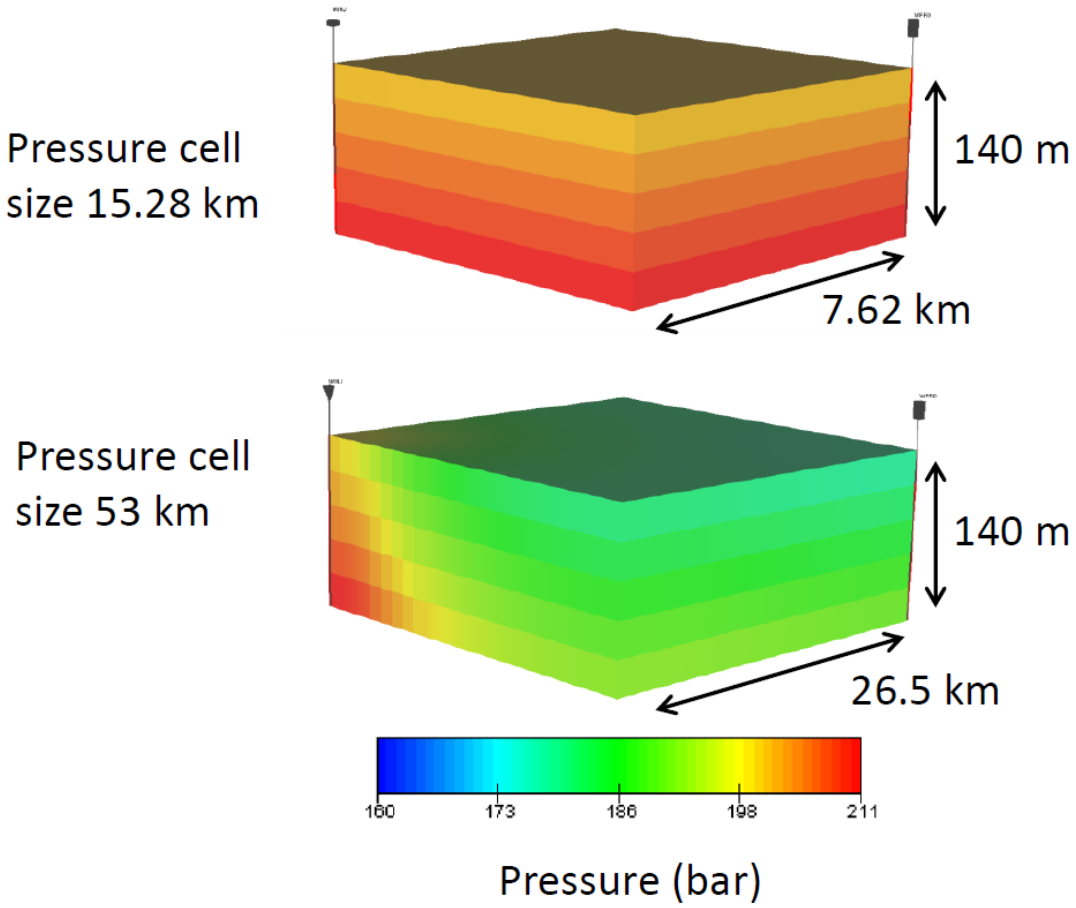

Figure 3.4 – Pressure distribution (bar) at the end of injection for the smallest and largest cell sizes.

3.1.4.2 *Brine Extraction*

Figure 3.5 compares capacities for different rates of brine production against the base case with no brine production for the low fracture pressure case (212 bar). The maximum capacity achieved was 13.4 Gt CO_2 for the closest well spacing in the smallest cell size (15.24 km), this was achieved using 4000 m^3/day of brine extraction per well. With 500 m^3/day of brine production in the smallest cell size, 6.4 Gt CO_2 of capacity can be achieved. The results show that there is a linear correlation, and that each 500 m^3/day increment of brine removal per well will increase storage capacity by 1 Gt CO_2 in the smallest cell size. For the 30.48 km cell size the maximum capacity achieved was 6.3 Gt CO_2 with 4000 m^3/day of extraction, 5.1 Gt CO_2 was stored using 500 m^3/day of brine extraction, in this case each 500 m^3/day increment of brine extraction per well is associated with a 0.18 Gt CO_2 increase in capacity. The maximum capacity for the 53 km cell size is only 0.17 Gt CO_2 greater than the base case, which is equivalent to 0.02 Gt CO_2 of extra capacity per increment of 500 m^3/day of brine extraction for each well. The profiles of the injection curves generally show a similar pattern to the base case curves with the water extraction increasing the slope of the curve. The most marked impact of water extraction is observed for the highest flow rate (4000 m^3/day) in the smallest cell size. An increase in capacity of 248% is observed from the base case to the highest flow rate. The increase of capacity with

brine extraction rates is not linear between different cell sizes, the medium size cell only shows an increase of 128% at the maximum flow rate, and the largest cell size only shows a 107% increase.

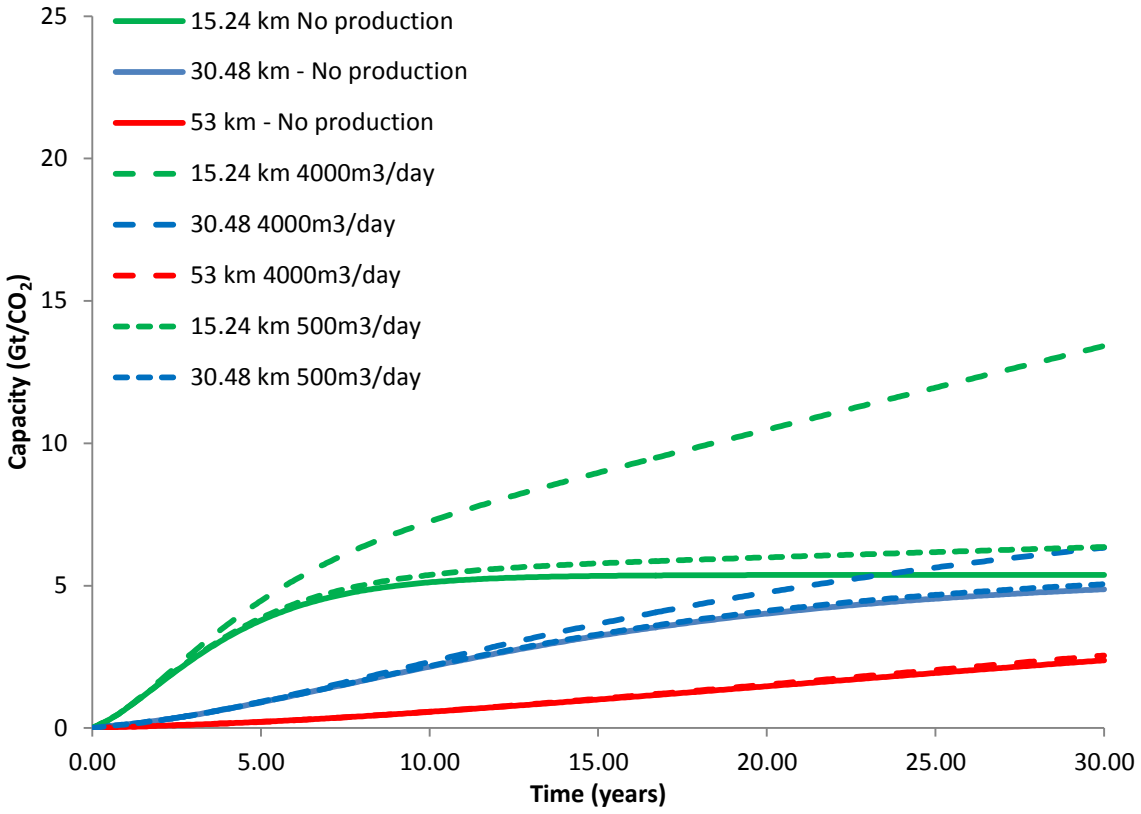

Figure 3.5 – Storage capacity including brine production at 500 m^3/day and 4000 m^3/day, compared against cases with no brine production for a fracture pressure limit of 212 bar.

Figure 3.6 compares capacities for different rates of brine production against the base case with no brine production for the high fracture pressure case (264 bar). The maximum capacity achieved in this case is 19.7 Gt CO_2 with the closest well spacing in the smallest cell size (15.24 km) with 4000 m^3/day of brine extraction per well. A 12.3 Gt CO_2 capacity can be achieved with 500 m^3/day of brine production in the smallest cell size. As before, there is a linear correlation, each 500 m^3/day increment of brine removal per well will increase storage capacity by 1.05 Gt CO_2 . The maximum capacity achieved was 12.3 Gt CO_2 with 4000 m^3/day of extraction for the 30.48 km cell size while 10.9 Gt CO_2 was stored using 500 m^3/day of brine extraction. In this case each 500 m^3/day increment of brine extraction per well is associated with a 0.2 Gt CO_2 increase in capacity. The maximum capacity for the 53 km cell size is only 0.21 Gt CO_2 greater than the base case, which is equivalent to 0.03 Gt CO_2 of extra capacity per increment of 500 m^3/day of brine extraction for each well. The relative increase in capacity for each cell size with brine extraction is almost identical to the low fracture pressure case. The profiles of the injection curves also show a similar pattern to the low fracture pressure case. Comparison between the cell sizes shows an increase of 174% is observed from the base case to the highest flow rate with the smallest cell size, the medium size cell only shows an increase of 115% at the maximum

flow rate, and the largest cell size only shows a 104% increase. The brine extraction is more effective in the lower fracture pressure case.

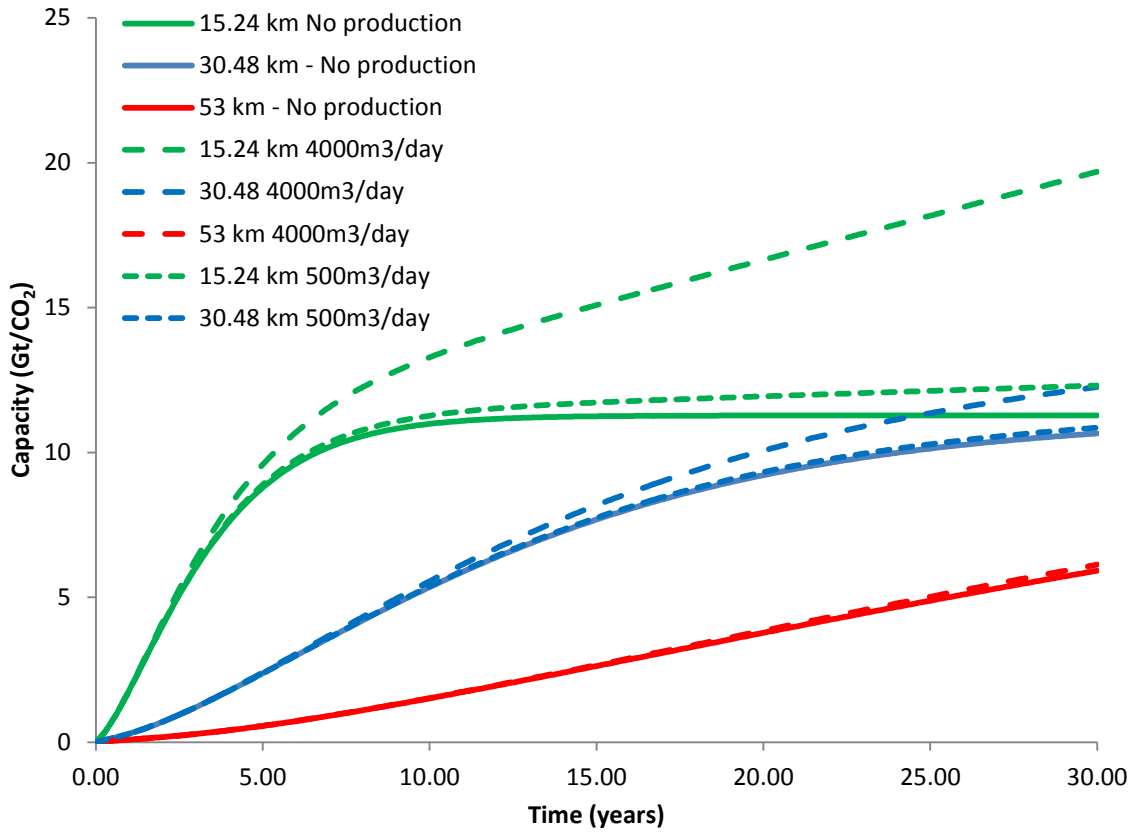

Figure 3.6 - Storage capacity including brine production at 500 m^3/day and 4000 m^3/day, compared against cases with no brine production for a fracture pressure limit of 264 bar.

Comparison of the difference between the two fracture pressure cases with brine extraction shows a similar reduction in capacity with fracture pressure to the case without brine extraction for the largest two well spacings (30.48 km and 53 km). The capacity in the low fracture pressure case with brine extraction for the largest two well spacings varies between 40 and 50 % of the higher fracture pressure case, for a 20% reduction in fracture pressure. The smallest well spacing case (15.24 km) shows a smaller reduction in capacity in the lower fracture pressure case, and the capacity varies between 49 and 68% of the high fracture pressure case. This implies that the brine extraction is more effective in the smaller well spacing case, and negates the fracture pressure restriction to a greater extent than the wider well spacing cases.

3.1.4.3 *Brine Plume Spreading*

An interesting observation from the work, which has been mentioned by other authors (e.g. Neal et al. 2011), relates to the accuracy of the model representation of the CO_2 plume. The CO_2 is buoyant and forms a plume that spreads out predominantly in the top layer of the model. To accurately model the extent of the plume spreading it is necessary to vertically refine the upper layer of the model to a very fine scale. High levels of refinement indicate a much wider plume spread, although the modelled volume of injected CO_2 is unaffected.

Figure 3.7 shows the comparison of a plan view of vertically non-refined (left) and vertically refined (right) grid on the extent of plume migration. The non-refined plume represents approximately half the area of the refined plume model. The plume spreading problem only becomes important when the production and injection wells are closely spaced, and the plume is likely to interact with the production well. Production of CO_2 at a brine extraction well would lead to curtailment of brine production, as the effectiveness of CO_2 storage would be compromised. If the field pressure was close to the fracture pressure, halting brine production may also prevent further CO_2 injection.

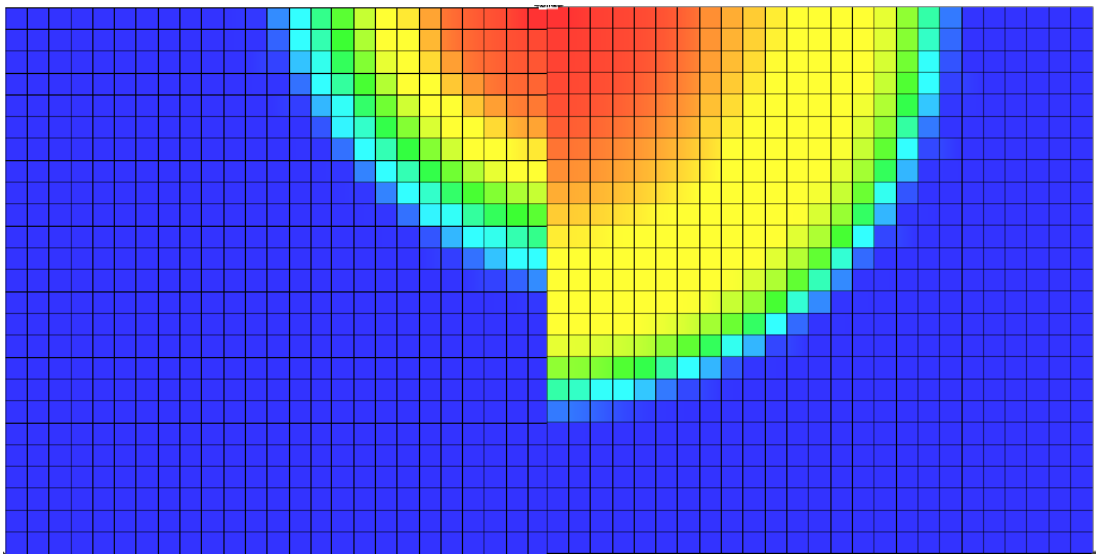

Figure 3.7 – Plan view comparison of vertically non-refined (left) and vertically refined (right) grids for the analysis of plume spreading. The figure shows that the grid refined vertically (in the plane of the section) shows much wider plume spreading than the unrefined model.

3.2 Bunter Large Scale Model

3.2.1 Model Setup

The large scale model represents a significant section of the offshore Bunter aquifer (13600 km^2) and was constructed using the thickness map and contour map for the top of the Bunter sandstone presented in Noy et al. (2012). To the knowledge of the author, this study is the only publicly available source of structural data for the Bunter aquifer. The model boundary and location of the model has already been presented in Figure 2.34. The model that was generated from the structural data is presented in Figure 3.8. The model has aquifers connected on the western and north-western margins to enable modelling of open and closed boundaries. These margins lie in the Dowsing Fault Zone (west) and another unidentified fault zone (north-west), and were conservatively considered to be closed in the study by Noy et al. (2012). The north-north-eastern, southern and eastern margins were modelled as closed boundaries as in the original model (Noy et al. 2012). The northern-north-eastern, southern and eastern margins are likely to impede flow due to stratigraphic limits of the Bunter Sandstone (north and east) and salt walls (south and east) (Noy et al. 2012). The model also includes a sea bed outcrop; the area of this outcrop is 7.68 km^2 in

the original study and the sea bed outcrop is assumed to be open (Noy et al. 2012). In the reconstructed model presented here, the outcrop has been deactivated in some scenarios in order to assess the capacity in the case of cementation, or closure of the outcrop to brine flow.

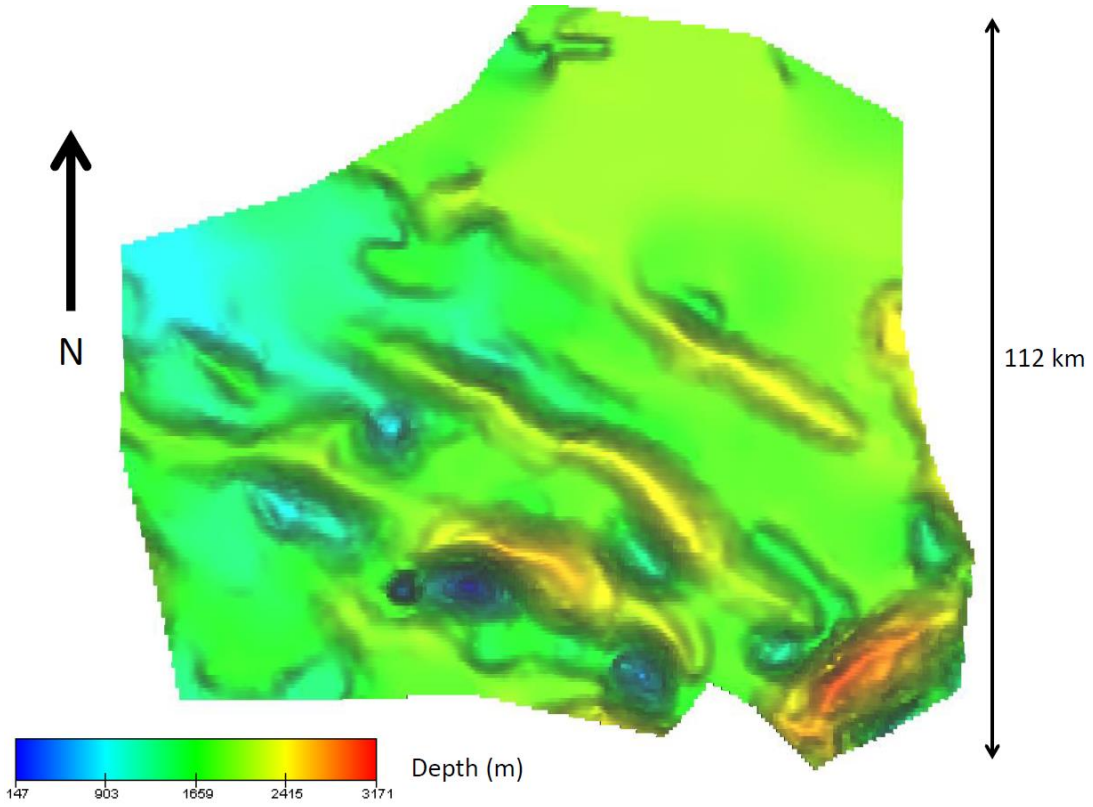

Figure 3.8 – Tempest simulation model for the Bunter aquifer derived from the structural data provided in Noy et al. (2012), depths are in metres. The boundary of the model corresponds to that shown in Figure 2.34.

The model includes up to 24 wells depending upon the modelled scenario. The wells were located so that the injected CO_2 would not migrate to potential leak points such as aquifer boundaries or the seabed outcrop. Generally, the wells are located at structural closures in order to minimise the migration of the CO_2. The wells are also separated from each other as far as possible to minimise interference between the pressurised zones surrounding the wells. The previous generic model in Section 3.1 included a much greater number of wells. The run times are much longer because the model is a full size model rather than a symmetrical model that is scaled up. Time constraints therefore dictated the number of scenarios that could be run and limited the maximum number of wells that were analysed in the scenarios.

3.2.2 **Geological Model**

The geological model was matched to that used in the original model of Noy et al. (2012) for the base case scenario, the parameters that were used for the base case scenario are listed in Table 3.1. The temperature and brine pressure gradients and salinity are used to derive the density of brine at reservoir depth and Tempest's internal algorithms are used to derive

brine properties for the simulation, the brine properties are summarised in Table 3.2 in Section 3.2.3.

Table 3.1 – Parameters for the large scale Bunter model from summarized and adapted for Tempest from Noy et al. (2012)

Horizontal permeability (mD)	100
Vertical permeability (mD)	100
Porosity (%)	20
Compressibility (bar^{-1})	4.5×10^{-5}
Lithostatic pressure gradient (MPa/km)	22.5
Pore pressure gradient (MPa/km)	10.67
Temperature gradient (°C/km)	35
Fracture pressure - % of lithostatic pressure	75

The reservoir has two simulation model aquifers attached to the western and north-western margins to allow alterations to the boundary conditions in scenarios other than the base case. The locations of the aquifer connections are illustrated in Figure 3.9, the properties of the aquifer match those of the reservoir, and the aquifers are very large, so that they represent a fully open boundary.

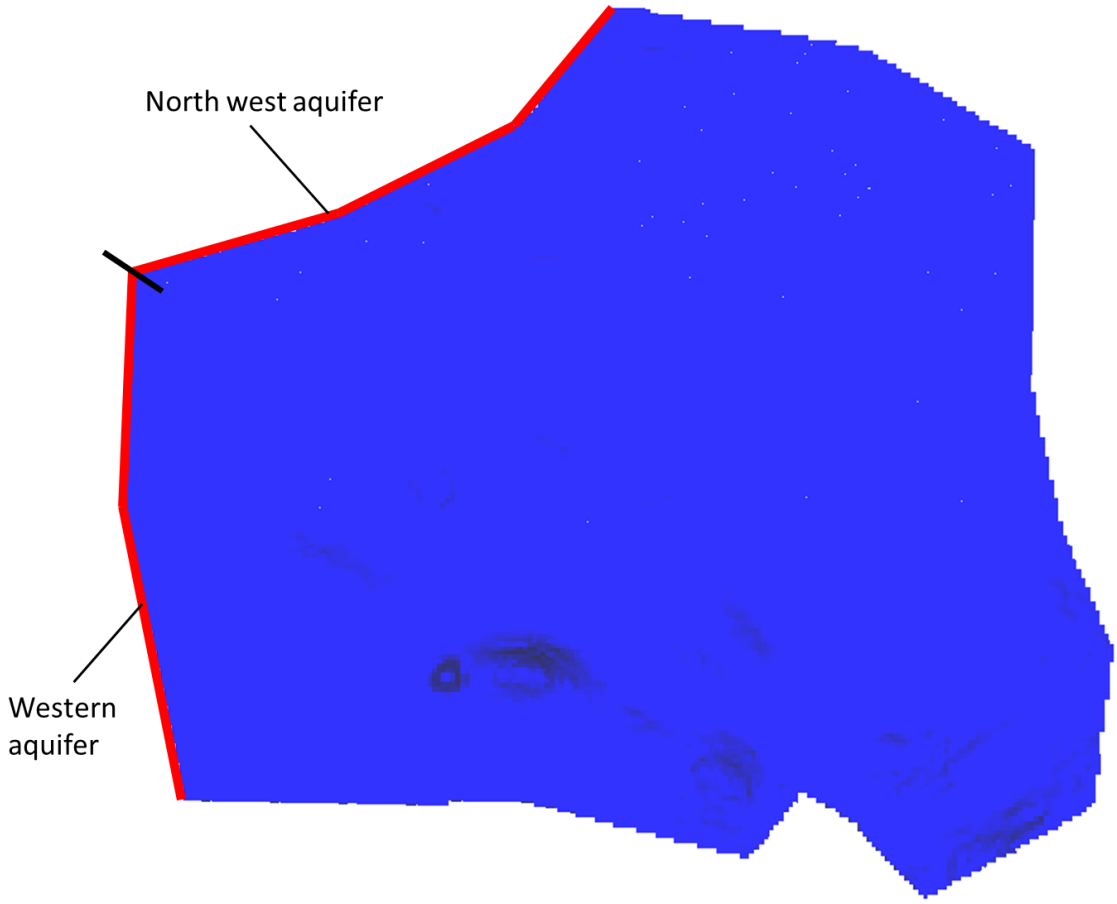

Figure 3.9 – Simulation model aquifer locations in the Tempest flow model to allow non-sealing marginal boundaries to be added to the model.

3.2.3 Fluid Properties and Modelling Parameters

The model is a two phase model, and the brine properties are derived using internal algorithms in Tempest based on the brine salinity from Noy et al. (2012) using the approach of (McCain 1990). The derived brine properties are shown in Table 3.2. The fluid properties for the CO_2 are based on a pure CO_2 stream using the same approach as in the generic model as described in Section 3.1.3.

Table 3.2 – Brine properties derived using Tempest algorithms from McCain (1990) based on the brine salinity from (Noy et al. 2012)

Brine salinity (ppm)	130000
Brine compressibility (bar^{-1})	3.2×10^{-5}
Brine viscosity (cP)	0.673

As in the previous section the two phase relative permeabilities were taken from an experimental study on two phase flow of brine and CO_2 in cores of host (sandstone) and fault rocks by Tueckmantel (2010). The host rock relative permeabilities shown in Figure 2.5 were used.

Noy et al. (2012) use a formation compressibility of 4.5 x 10^{-5} bar-1 in their model of the Bunter aquifer, this is based on the value assumed by Zhou et al. (2008) in their study on saline aquifers. The formation compressibility used by Zhou et al. (2008) does not relate to any specific aquifer case study and is probably based on a judgement of a reasonable value for sandstone. As discussed previously, reservoir sandstone data from the literature would suggest that the estimate of 4.5 x 10^{-5} bar^{-1} is probably a sound median estimate for the sandstone (Fatt 1958, Yale et al. 1993, Crawford et al. 2011). In the derived model in this study, the formation compressibility is one of the parameters that were altered to assess the impact on injection into the large-scale model. The formation compressibility was therefore varied from the base case of 4.5 x 10^{-5} bar^{-1} to the extreme values of 1 x 10^{-5} and 10 x 10^{-5} bar^{-1} in the model. The range of formation compressibilities represents one order of magnitude. In terms of capacity, the lower compressibility limit is a pessimistic estimation and represents the lowest possible compressibility estimated from the data (Fatt 1958, Yale et al. 1993, Crawford et al. 2011). The upper limit represents a cemented to friable sandstone of 18% porosity and represents an optimistic estimate of the compressibility as the Bunter sandstone (Fatt 1958, Yale et al. 1993, Crawford et al. 2011). The consolidation/cementation state of Bunter sandstone is not easily discernible from the literature, but it is found to be weak and un-lithified where weathered onshore e.g. Yates (1992) but also heavily cemented in other areas offshore e.g. Dingwall et al. (2013). The variability of the formation compressibility assessed is therefore a reasonable range for this investigation. In the remainder of the chapter all compressibilities referred to relate to the formation compressibility unless explicitly stated.

The k_v/k_h ratio is particularly uncertain parameter than can only be determined from detailed investigation. As mentioned in Section 3.1 a likely range for the k_v/k_h ratio is between 1 and <0.001. The base-case model from Noy et al. (2012) has a k_v/k_h ratio of 1, so the k_v/k_h ratio was varied from 1 to 0.1, 0.01 and 0.001 in various scenarios in this model to investigate the uncertainty in k_v/k_h ratio. The range of values chosen were consistent with values reported by Begg et al. (1989) and Morton et al. (2002) for the shale baffles in the Sherwood Sandstone (as discussed in the previous generic modelling section) and the presence of discontinuous layers of mudstone throughout the Bunter Sandstone. The global permeability, where $k_v=k_h$, was also changed from the base-case 100 mD to 20 mD as analysed in the original paper of Noy et al. (2012).

The remaining parameters to be changed from the original base case were the boundary conditions at the north-western and western margins, and the seabed outcrop. The scenarios were set up to model a completely closed model, with all boundaries closed (more conservative than original model), and then all permutations of the marginal boundaries and sea bed outcrop closed and open in combination (e.g. north-western boundary closed, with western and seabed outcrop open). The boundary conditions were changed to assess the impact on capacity of uncertainty in the flow characteristics of the model boundaries. For example, investigations of the seabed outcrop in Dingwall et al.

(2013) show extensive cementation in the proximity of the outcrop. Cementation could potentially inhibit flow of brine out of the outcrop and in the most pessimistic case completely seal the outcrop to brine flow.

Scenarios were analysed with 1, 12 and 24 wells perforated in the aquifer. The wells were generally located in the structural highs where possible, as this is the likely injection scenario that would be pursued. The scenarios were run for 50 years, and the flow rates in the reservoir were set so that at the end of the 50-year period the fracture pressure criteria of 75% lithostatic was not exceeded within the model. The following section describes the scenarios, and the results obtained from the analysis of each scenario.

3.2.4 **Results**

3.2.4.1 *Base Case*

An initial base case model was run to check the agreement between the reconstructed model and the original model presented by Noy et al. (2012). In the base-case model the single well placement was approximate compared to the original model. The gas injection rate and total injected CO_2 are shown in Figure 3.10 and the water outflow from the seabed outcrop is shown in Figure 3.11. The injection rate was constant and set to the same value used in the original model at 5 x 10^6 t/CO_2/yr. Figure 3.10 shows that the same amount of CO_2 was injected as the original model. The injection rate corresponds to approximately 13700 t/CO_2/day, which over the 50-year period equates to 250 Mt CO_2.

Comparison of the water outflow from the seabed outcrop indicates how well the reconstructed model matches the original model. The outflow rate in the original model peaked at 6500 tonnes/day and Figure 3.11 shows the peak rate in the reconstructed model was of a similar magnitude peaking at 7000 tonnes/day shortly after the end of injection. In the reconstructed model the total water outflow from the aquifer over 100 years was 169 Mt, in the original model 360 Mt was ejected, but over hundreds of years. Due to time constraints, the reconstructed models in this study were not generally run beyond 100 years. Comparison of the total outflow from the original model at 100 years shows approximately the same volume as the reconstructed model however (Noy et al. 2012). The discrepancy in the response of water output is probably due to the inaccuracy of the reproduction of the model, the different assumptions made regarding modelling the fluid properties using algorithms built into the modelling software and the differing relative permeabilities. However, the reconstructed model represents a reasonable reconstruction of the original model, which is itself acknowledged to be a coarse representation derived from sparse data.

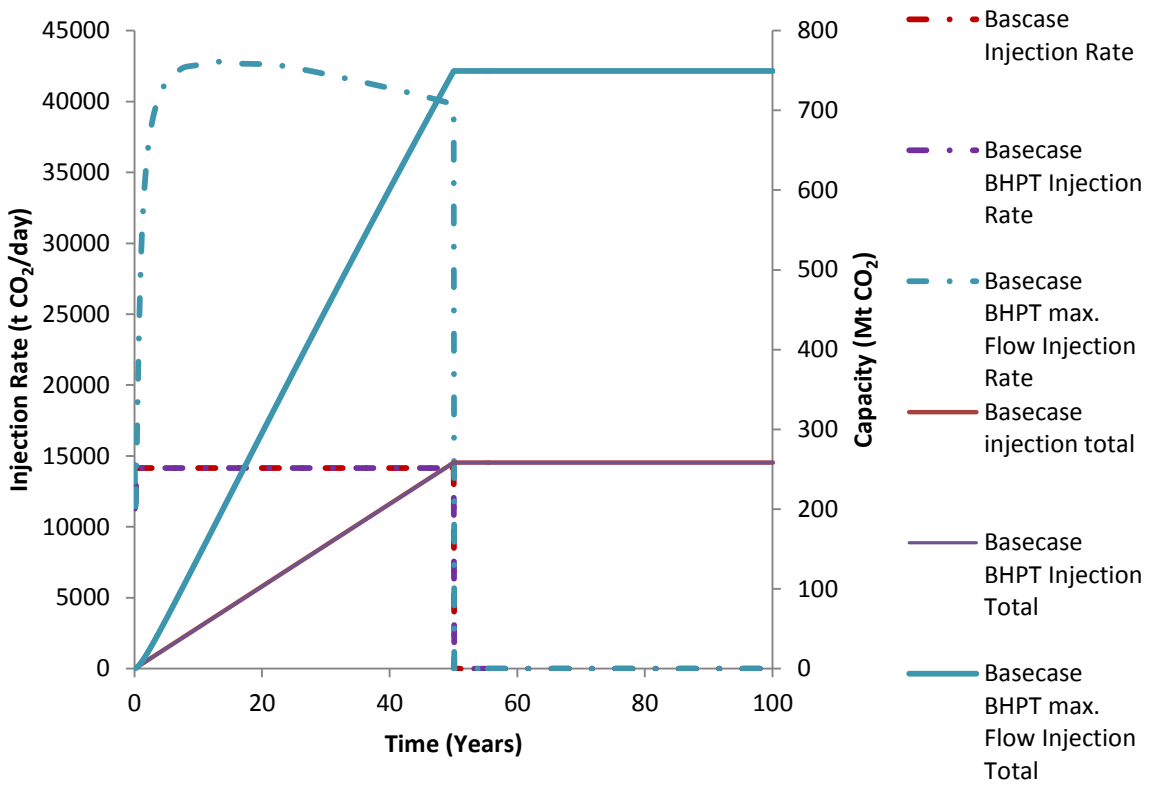

Figure 3.10 – CO_2 injection rates and totals for the base case model and two additional scenarios including a pressure control on the injection well (BHPT), and an increased flow rate to the maximum permissible through the well with a BHPT (BHPT max. flow).

In the base case model the injection well was implemented without a pressure control to match the case in the original model of Noy et al. (2012). The lack of pressure control leads to the same high pressure transient that is reported for the original model by Noy et al. (2012). Noy et al. (2012) suggest that a staged injection strategy would be required to minimise the high-pressure transient at the start of injection. To analyse a staged injection strategy a scenario was analysed where the bottom hole well pressure target (BHPT) was set to the 75% lithostatic pressure. The BHPT scenario is shown on Figure 3.10 and the impact of the pressure restriction on final capacity is shown to be minimal. The decrease in capacity from the base case to the scenario with pressure control is only 0.22 Mt.

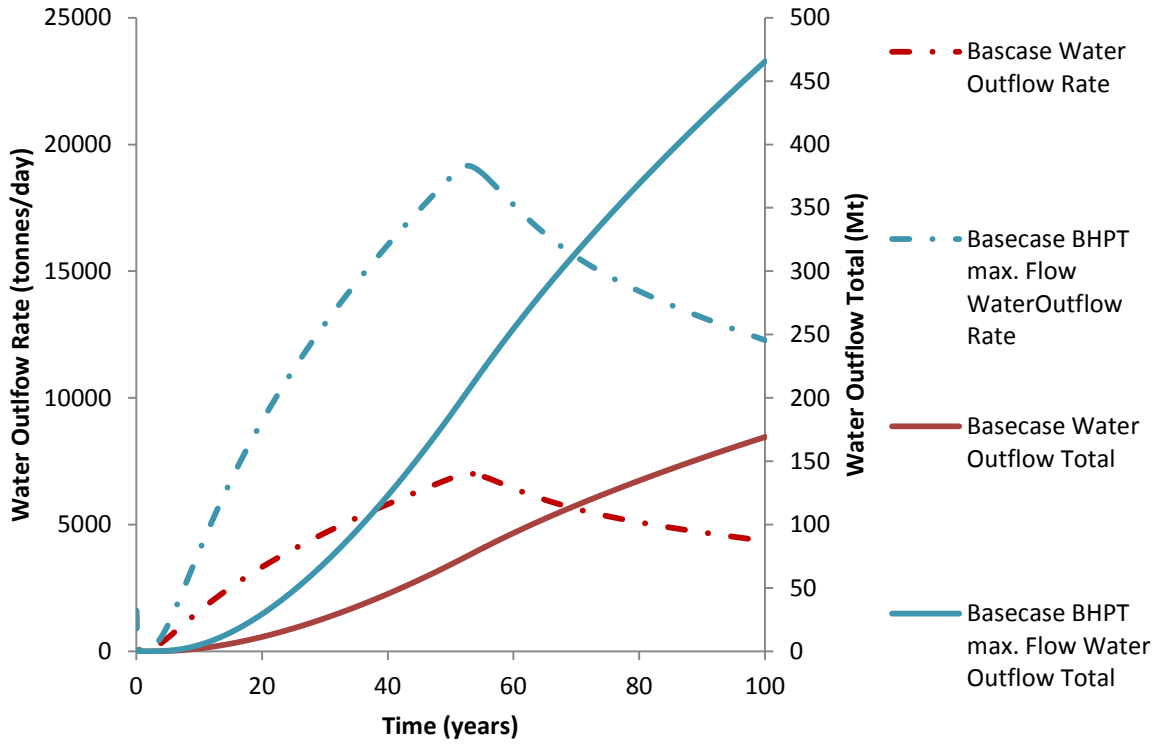

Figure 3.11 – Water outflow rate and total volume from the seabed outcrop for the base case and the maximum injection rate cases.

Analysis of the pressure build-up for the base case shows that apart from the localised pressure transient during the start of injection, the pressure does not reach the fracture pressure limit during injection. A scenario was therefore developed to analyse the maximum rate of CO_2 that could be injected into the base case scenario and determine the ultimate capacity using one well. The scenario used a very high injection rate, with a BHP control to prevent the well injecting above the fracture pressure. The maximum injection scenario is shown in Figure 3.10 and Figure 3.11. The scenario shows that a peak rate injection of 42800 t/CO_2/day or 15.6 Mt CO_2/yr was possible, the amount of CO_2 injected over the 50 years was 750 Mt CO_2. The water outflow from the seabed outcrop was 465 Mt tonnes, and the outflow rate peaked at 19160 tonnes/day. The injection scenario was checked to ensure that the pressure in the aquifer did not exceed the 75% fracture pressure limit. A plot of the difference between the pore fluid pressure and the calculated lithostatic pressure is shown in Figure 3.12. The plot of the pressure difference shows that the fracture pressure is not exceeded anywhere in the model. However, several areas do come within 10 bar of the fracture pressure. These highly pressured areas include the area surrounding the injection well, and several structural highs that are separated from the injection area by structural low points, including the region of the seabed outcrop. There is also a broad region, up-dip from the injection well to the north-west, where the pressure increases significantly, and comes within 50 bar of the fracture pressure. The model pore fluid pressure comes closest to the fracture pressure three years after injection into the aquifer has ceased, showing a lag effect in the pressure response.

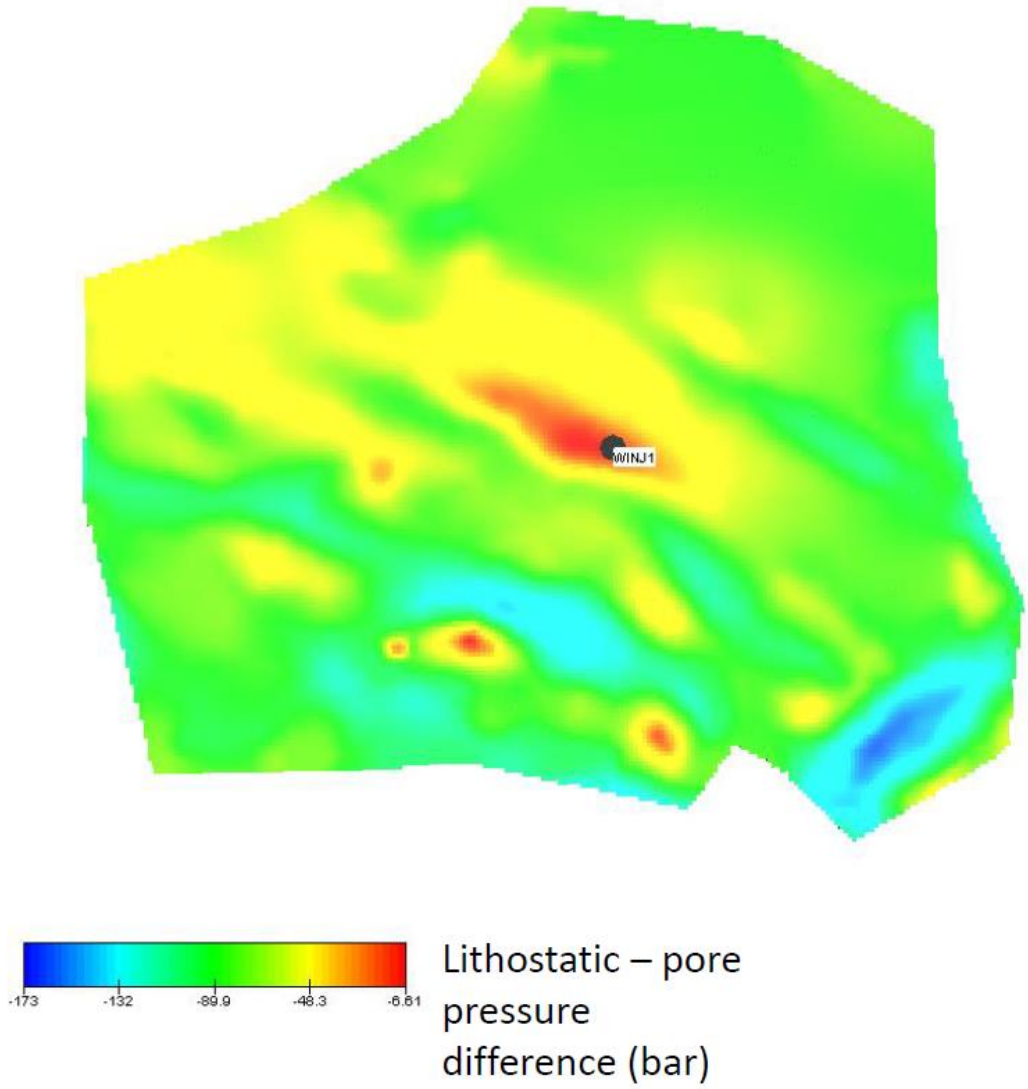

Figure 3.12 – Map of the difference between the lithostatic pressure and pore fluid pressure in the top layer of the aquifer model after 53 years of the model run.

The storage efficiency achieved in each of the scenarios is very small, ranging between 0.09% for the base case and 0.18% for the maximum injection case. Low efficiencies would be expected as there is only a single well injector injecting into a large reservoir. The mass ratio of gas injection to water outflow after fifty years in the base case was 1.48, and in the maximum injection case, the ratio was 1.6.

3.2.4.2 *Base Case Sensitivity Scenarios*

As discussed in the introduction to the model, there are several areas of uncertainty in the parameters of the model and this section discusses the results of some sensitivity runs where the compressibility and permeability are varied for the base case model.

A scenario was analysed where the global permeability was reduced to 20 mD to match one of the cases presented for the original model. In the original model Noy et al. (2012) observe that the injection rate of 5 x 10^6 t/CO_2/yr was too high when the permeability is reduced to 20 mD. In the reconstructed model, the pressure exceeded the fracture pressure

by 25 – 40 bar in the area immediately surrounding the cell for the entire injection period. However, the remainder of the field was not over pressurised. The injection rate was therefore reduced by applying a BHP control to a second scenario to analyse the injection capacity under a reduced global permeability. Figure 3.13 shows the results of the rate limited scenarios with a BHPT applied to the well, the maximum capacity attained is 140 Mt CO_2 injected at a peak rate of 8521 t/CO_2/day or 3.1 Mt CO_2/yr. The rate of water outflow from the seabed outcrop was 1091 tonnes/day and 23 Mt had flowed from the outcrop after 100 years. The storage efficiency of the run was 0.09% and the ratio of injected CO_2 to water outflow was 6.1 at the end of the fifty-year period. The pressure did not exceed the fracture pressure limit anywhere within the model. The pressure came closest to the fracture pressure limit in the area immediately surrounding the well, and was within 21 bar of the limit, the pressure at the well was the most critical region in this model.

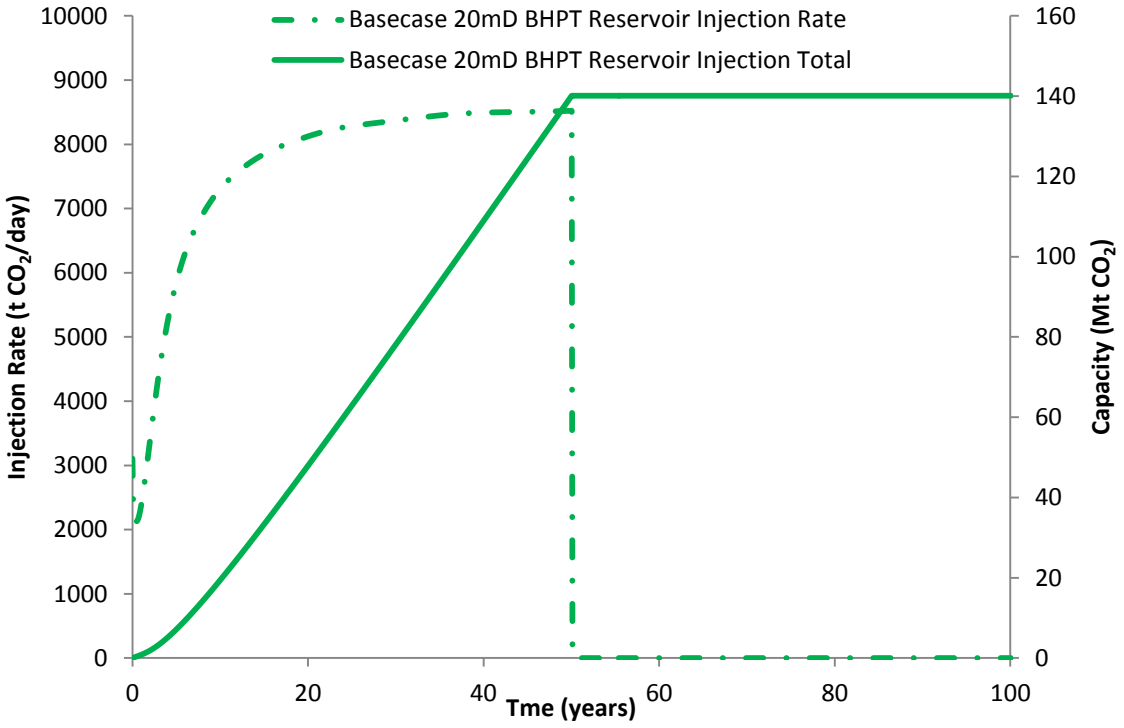

Figure 3.13 – CO_2 injection rate and injection capacity for the model with a reduced global permeability of 20 mD.

Variation in the k_v/k_h ratio is likely to occur and so three different cases were analysed with different k_v/k_h ratios. The horizontal permeability remained at 100 mD, and the vertical permeability was varied from 10 to 0.1 mD, giving K_v/K_h ratios of 0.1 to 0.001. The models were run with the base case flow rate with no bottom hole pressure control on the well, with base case flow rate with a pressure control on the well (BHPT), and at the maximum sustainable pressure with a pressure control on the well (BHPT), producing nine different scenarios.

There is a negligible difference between the base case injection rate scenarios with and without the pressure control. The same capacity (due to the same injection rate) was

modelled in each case, and almost exactly the same water outflow rates from the outcrop were observed. The major difference is in the amount of water that emerged from the seabed outcrop with different K_v/K_h ratios. The rate of water outflow from the outcrop for the cases with the base case injection rate is illustrated in Figure 3.14. The peak rate for a K_v/K_h ratio of 0.001 was almost exactly half the peak rate of the base case of 7017 tonnes/day at 3505 tonnes/day, for K_v/K_h = 0.01 the peak flow was 5702 tonnes/day, and at K_v/K_h = 0.1 the peak flow was 6770 tonnes/day. The total water outflow for each case (K_v/K_h 0.001 to 0.1) was 88,139 and 163 Mt, again this is regardless of whether a pressure control was applied. The shapes of the rate response for water outflow in Figure 3.14 show that the K_v/K_h = 0.001 case has a slower decline in water outflow rate after injection ceases than the other cases. The slower outflow of water in the low K_v/K_h case can be explained by the fact that vertical permeability is lower in this case and water is slower to migrate upwards out of the outcrop. If the model was run for a sufficiently long time, the final total of water expulsion in each case would probably be of a comparable magnitude.

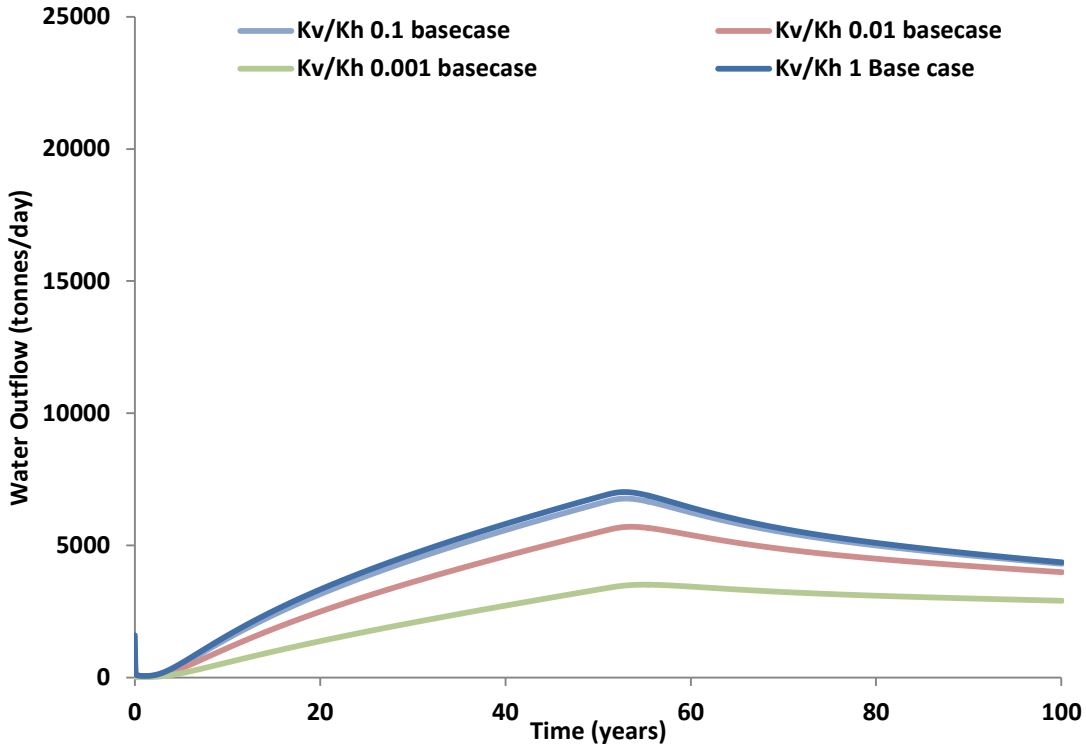

Figure 3.14 – Water outflow rates from the seabed outcrop for scenarios with the base-case flow rate and K_v/K_h ratios between 1 and 0.001.

The final three scenarios have a maximised injection rate using a well pressure control and high injection rate. These models produced higher brine outflow rates, and have higher CO_2 injection rates and total CO_2 capacities. The models are compared to the maximum injection rate base-case scenario. The water outflow rates from the seabed are shown in Figure 3.15. The brine outflow rates are higher than with the base case injection rate and show a similar pattern to the results with the lower injection rate. The peak brine outflow flow rates for K_v/K_h

ratios 0.1 to 0.001 are 16861, 12592 and 7462 tonnes/day, compared to 7017 tonnes/day for the $K_v/K_h = 1$ case.

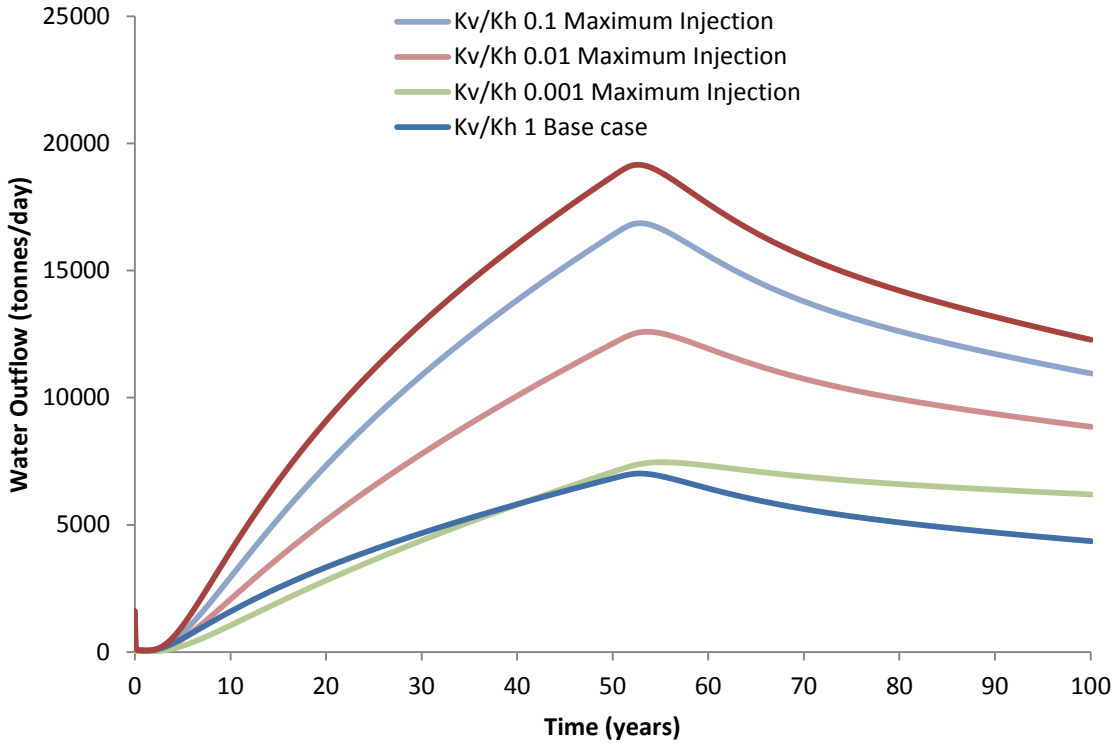

Figure 3.15 - Water outflow rates from the seabed outcrop for scenarios with the maximised flow rate and K_v/K_h ratios between 1 and 0.001.

The change in CO_2 injection rate and CO_2 injection capacity with K_v/K_h is shown in Figure 3.16. The biggest decrease in capacity occurs between 1 and 0.01 K_v/K_h with capacity decreasing from 749 Mt CO_2 to 589 Mt CO_2, the capacity then only decreases by 22 Mt CO_2 from 0.01 to 0.001 with the lowest capacity achieved being 567 Mt CO_2. The peak injection rate shows a similar pattern, with the peak injection rate decreasing to 32290 t/CO_2/day at 0.001 K_v/K_h from 42807 t/CO_2/day at 1 K_v/K_h.

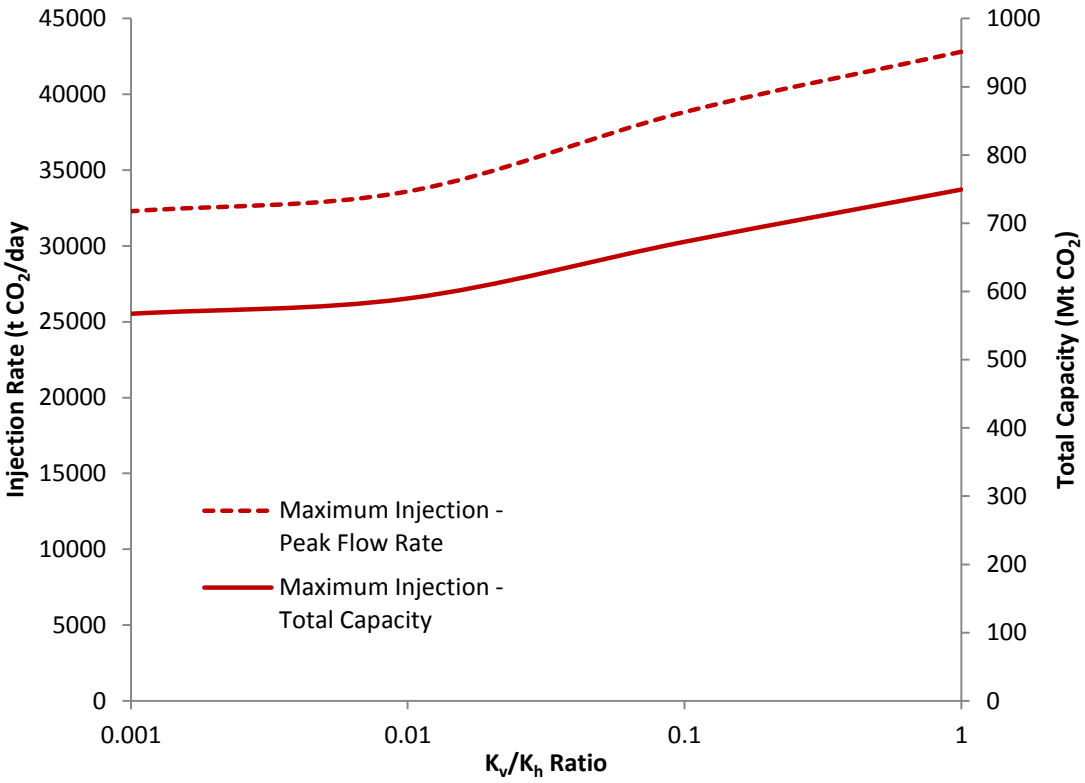

Figure 3.16 – CO_2 injection rate and CO_2 injection capacity for the single well scenario with maximised injection rate with K_v/K_h ratio.

A reduction in K_v/K_h ratio significantly reduces the capacity for CO_2 injection in the Bunter model. The mechanism for this reduction in capacity can be related to the reduction in the outflow of water from the seabed outcrop due to the reduction in vertical permeability. With a reduction in brine outflow, pressure relief in the aquifer is diminished and less CO_2 can be injected before the fracture pressure is reached. Analysis of the injection plume of the CO_2 also shows the effect of the reduced vertical permeability on the spread of the CO_2 within the aquifer, the plume spread is greatly reduced with a low K_v/K_h ratio. The reduced spread with low K_v/K_h ratio is caused by the CO_2 migrating horizontally preferentially throughout the entire thickness of the aquifer due to the restriction on vertical flow. With a high K_v/K_h ratio the CO_2 rises to the top quickly and then spreads out horizontally in one layer at a higher saturation. The lateral plume spread with different K_v/K_h ratios is illustrated by Figure 3.17. Figure 3.18 shows a cross section through the plume, and it can be seen more that the plume saturation is more homogeneous throughout the depth of the aquifer with low K_v/K_h ratio. The high K_v/K_h ratio shows a more typical plume response. A lower K_v/K_h ratio will reduce the volume of CO_2 that can be injected (in this case by around 24% when the ratio is reduced from 1 to 0.001) however this reduction in ratio will also restrict the lateral migration of the plume. After 100 years the high K_v/K_h ratio plume has spread much further than for the low K_v/K_h ratio. A reduction in the spread of the plume aerially will allow more time for dissolution of the CO_2 and minimise possible spillage of the CO_2 outside of a specific storage structure, which may reduce access to leak points.

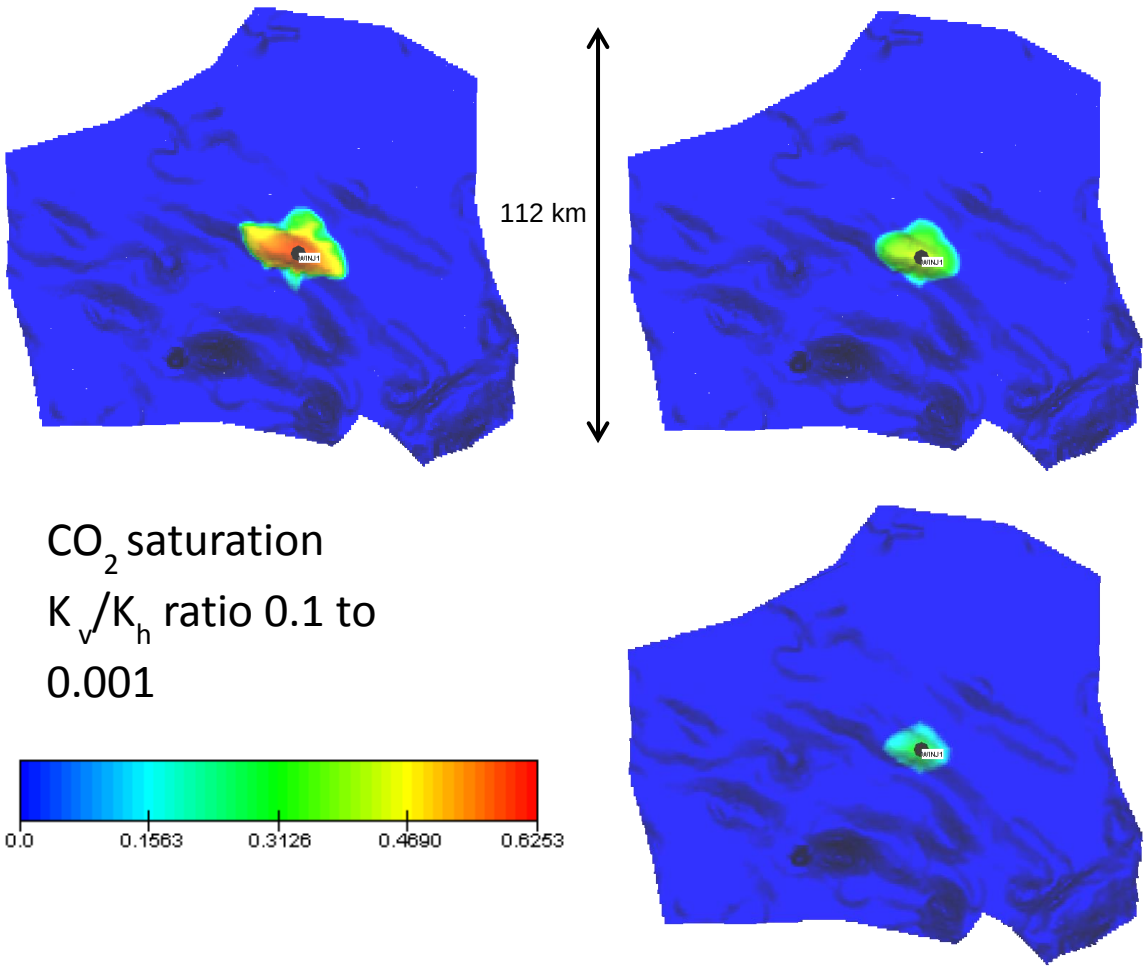

Figure 3.17 – Extent of CO_2 saturation plume in cases with different K_v/K_h ratio, ratio decreases from 0.1 top left, to 0.01 top right, to 0.001 bottom right.

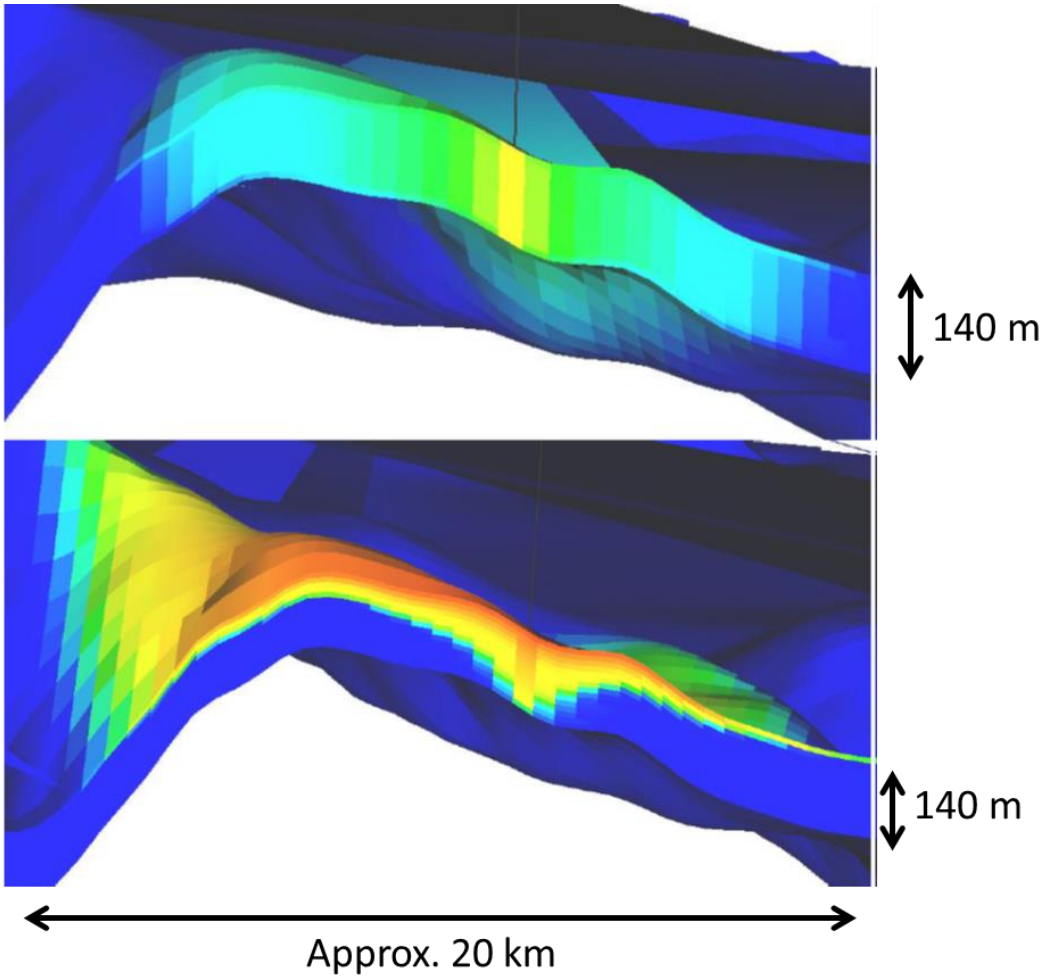

Figure 3.18 – Vertically exaggerated cross section through CO_2 saturation plume showing K_v/K_h ratio of 0.001 case at the top and K_v/K_h ratio 0.1 case at the bottom. Restriction in vertical permeability means that plume is more distributed throughout reservoir thickness in 0.001 case.

The formation compressibility was varied between 1 x 10^{-5} and 10 x 10^{-5} bar^{-1} in the same set of scenarios analysed for the K_v/K_h ratio. Once again, in the cases with the constant base case injection rate (5 x 10^6 $t/CO_2/yr$), the ultimate capacity and injection rate are evidently the same as the base case and none of the scenarios exceeded the fracture pressure. The water outflow from the seabed outcrop for the base-case injection rate cases is shown in Figure 3.19. The peak brine outflow for the lower compressibility of 1 x 10^{-5} bar^{-1} is 3448 tonnes/day higher than the base case (7017 tonnes/day) at 10465 tonnes/day. The peak flow of the higher compressibility case of 1 x 10^{-5} bar^{-1} is 2263 tonnes/day less than the base case at 4754 tonnes/day. The total water ejected from the low compressibility case after 100 years was 243 Mt and the total water ejected in the high compressibility was 114 Mt. For comparison, the water ejected from the outcrop in the base case was 169 Mt. For the same flow rate the low compressibility case emits more water from the seabed outcrop than the high compressibility case. The difference in brine outflow rates is because the higher compressibility permits a greater expansion in pore volume with pressure, so less water needs to be forced out of the outcrop to accommodate the pressure change. The CO_2

saturation plume only differs in this case due to the volume of CO_2 that is injected, with the higher compressibility case the plume extends slightly further than the low compressibility case, but the effect is minimal.

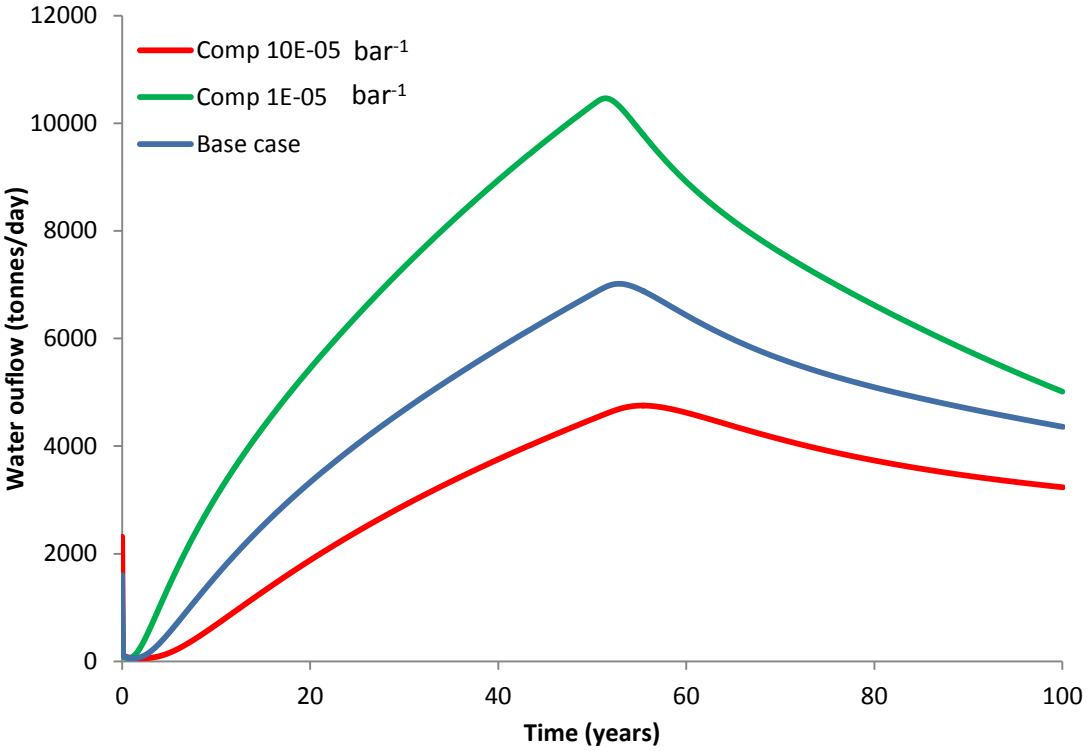

Figure 3.19 – Comparison of water outflow from the seabed outcrop for different compressibility cases using the base case flow rate and single well.

Figure 3.20 shows the injection rates for the cases where the injection rate was maximised for the two different compressibility cases, with the bases cases for comparison. The graph shows that the highest injection rates were achieved for the high compressibility case, and injection rates for the low compressibility case were below the base case maximised injection case. The graph shows that the rate for the high compressibility case peaks at 49093 t/CO_2/day, and the low compressibility case peaks at 37376 t/CO_2/day, compared to 42807 t/CO_2/day for the maximum injection base case. The peak injection rates and the total injection volumes for the maximised injection cases, including the maximised base case, are summarised in Figure 3.21. The total injection for the high compressibility case was 867 Mt CO_2 and for the low case the total volume injected was 637 Mt CO_2 this is compared to 749 Mt CO_2 for the maximised base case.

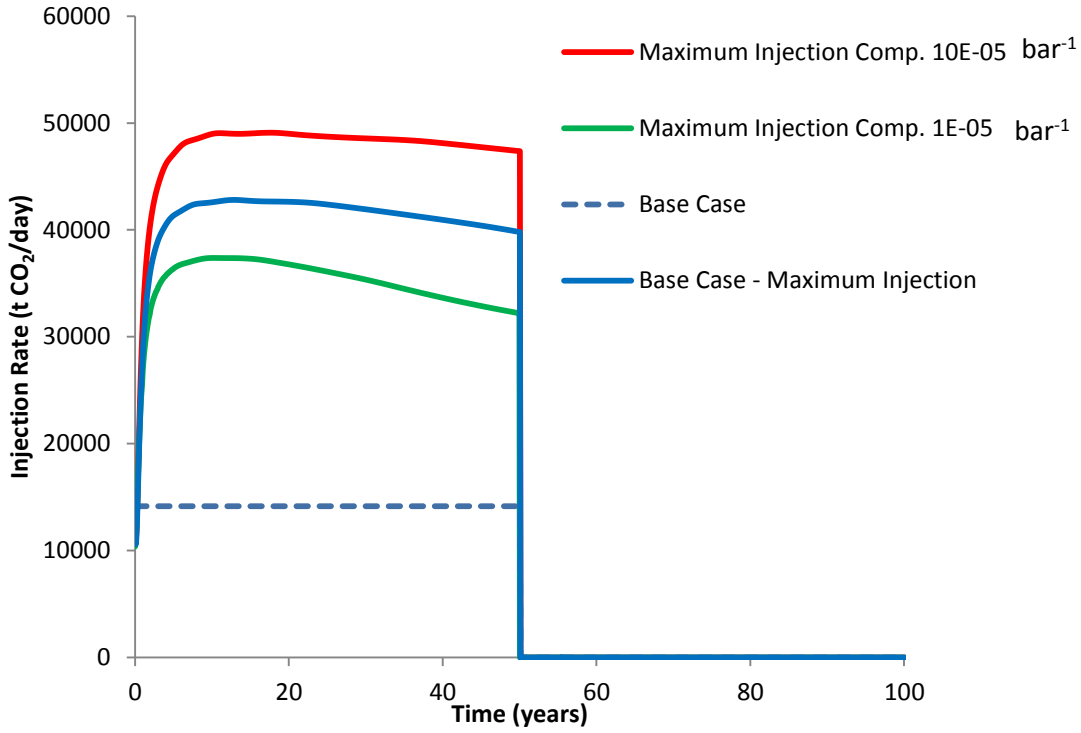

Figure 3.20 – Injection rates for the compressibility scenarios with maximised injection rates for the single well case.

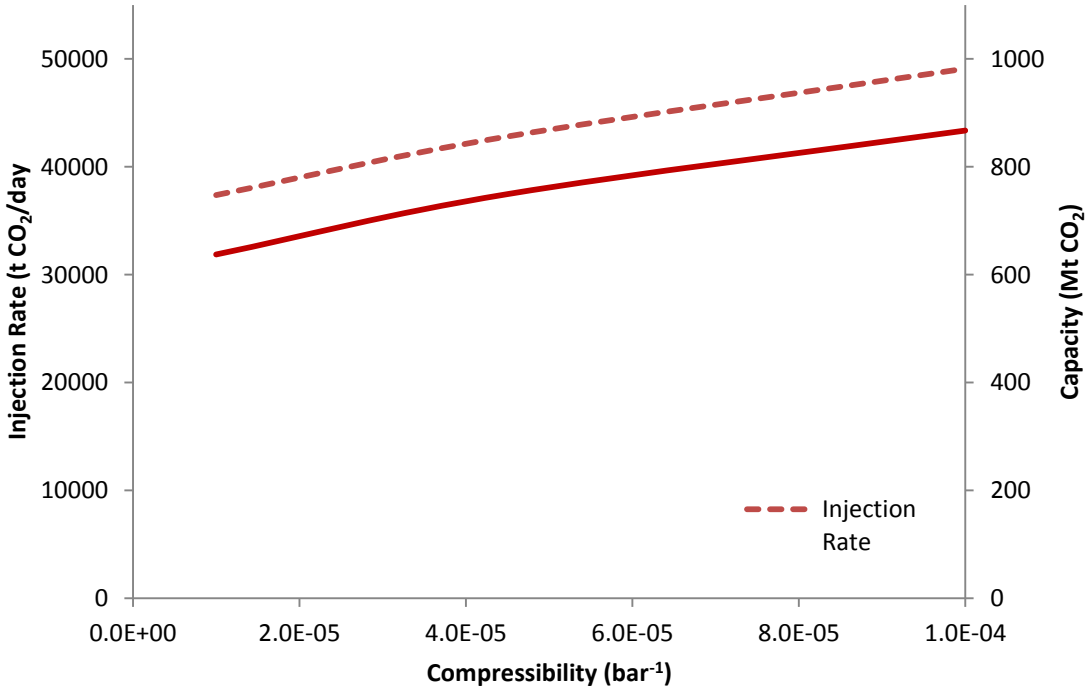

Figure 3.21 – Peak injection rates and total injected CO_2 volume with formation compressibility for the single well maximised injection case.

Figure 3.22 shows the water outflow rates for the compressibility scenarios with maximised injection rates. The water outflow rates show the same pattern as for the compressibility scenarios with base-case injection rates. The lowest compressibility case shows the largest

brine outflow from the seabed outcrop. The peak outflow rate for the low compressibility case is 24465 tonnes/day, and for the high compressibility case is 14829 tonnes/day, with the maximum injection base case peak outflow rate at 19159 tonnes/day for comparison. The most interesting observation from Figure 3.22 is the profile of the graphs, which reveals the water outflow response in each case. The decline of the low compressibility curve is much steeper than the base case after injection has stopped, whereas the high compressibility case shows a similar profile to the base case. The profile of the low compressibility case is probably due to the effective rigidity of the aquifer when the compressibility is low. The low compressibility restricts the pore volume expansion under pressure and so more water is forced from the outcrop. The compression of the pore volume is also reduced when the pressure reduces, and so there is less force pushing water from the outcrop and the flow drops off quickly. The water outflow rate for the low compressibility case actually drops below that of the base case after 95 years. The total volume of brine ejected from the outcrop after 100 years is 580.0 Mt in the low compressibility case, 357.8 Mt in the high compressibility case, and 465.7 Mt in the maximised injection base case compressibility.

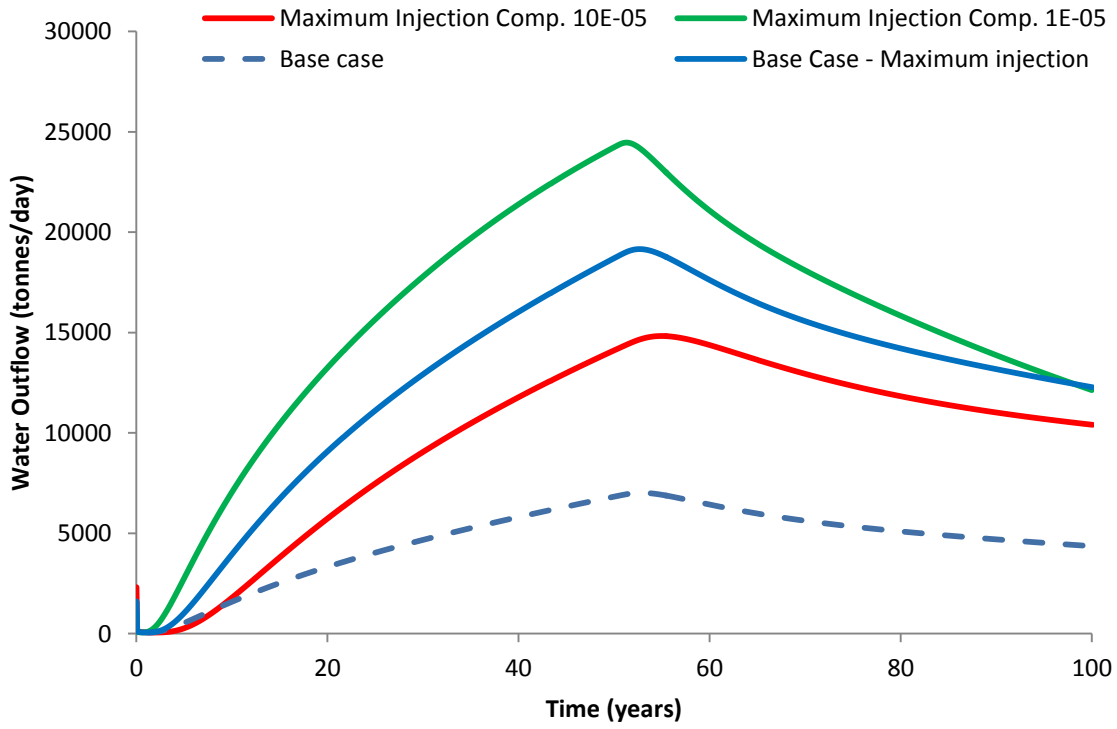

Figure 3.22 – Water outflow rates from the seabed outcrop for the compressibility scenarios with maximised injection rates with a single injection well.

3.2.4.3 *Multiple Injection Wells – 12 Injection Wells*

The single well scenarios indicate the influence of various parameters on the injection characteristics into the Bunter, the multiple well injection scenarios build on this to assess the capacity of the aquifer under more realistic large-scale injection. Once again a base case comparison is also available for comparison from the paper by Noy et al. (2012). The

well locations used in this study are not the same as the original model, and only two scenarios are presented in the paper, a base case model, and a case with maximised injection rates with base case parameters. The intention of this section is to explore the capacity of the model with multiple wells using the original model from Noy et al. (2012) as a comparison, and then to extend the analysis to consider the impact on the capacity of parameters such as the compressibility. The well locations chosen for the 12 well model are shown in Figure 3.23.

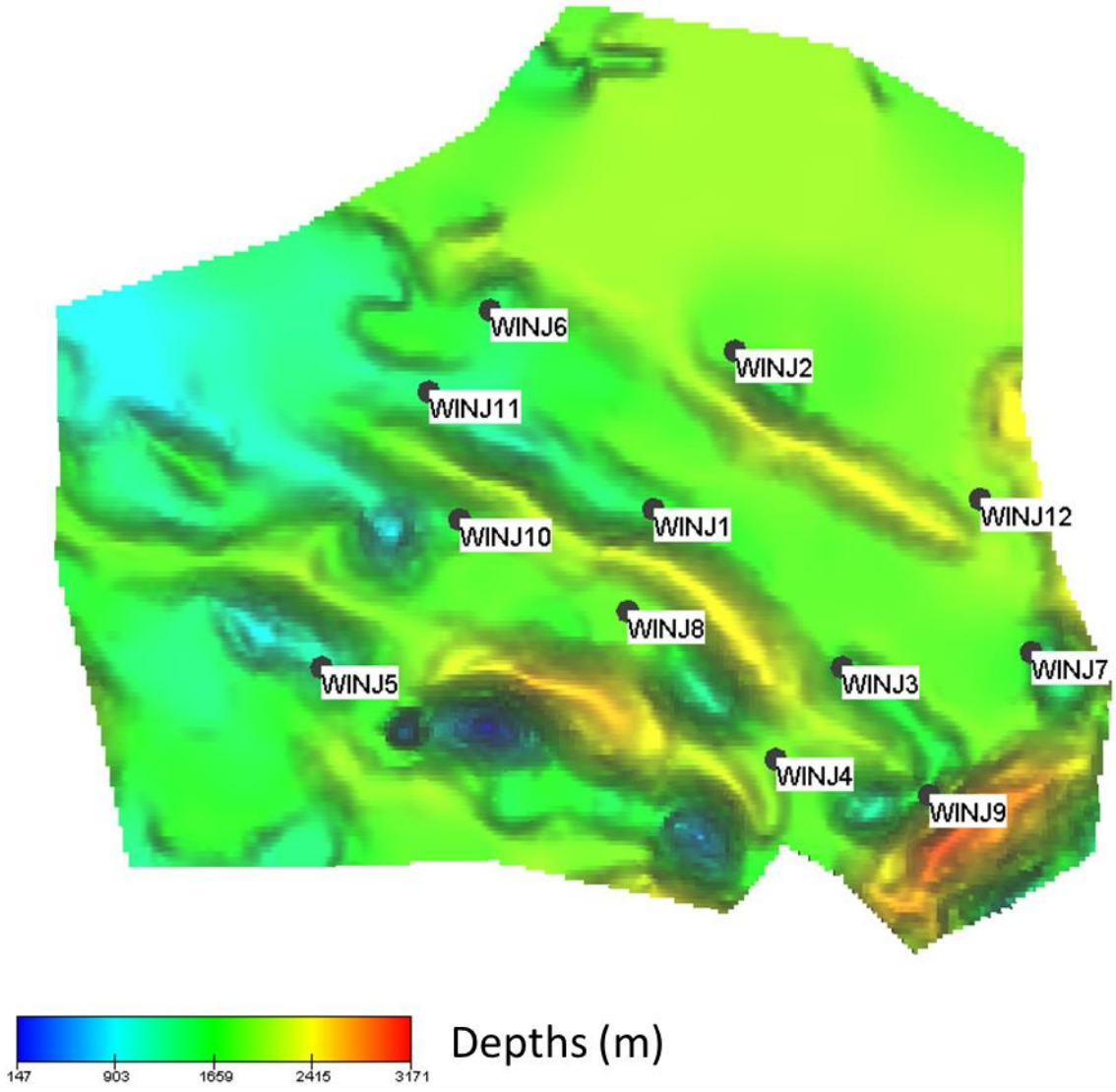

Figure 3.23 - Well locations for the 12 well model, with a depth contour map of the model, the scale is in meters.

Six scenarios were analysed with the same boundary conditions as the base case model, they used parameters similar to those analysed in the single well section and include:

- Base case scenario, with injection rate matched to the Noy et al. (2012) model;

- Maximised injection rate model, with injection increased to the maximum level, whilst remaining beneath fracture pressure;
- Global permeability reduced to 20mD with maximised injection rate;
- High Formation Compressibility (10 x 10^{-5} bar^{-1}) with maximised injection rate;
- Low Formation Compressibility (1 x 10^{-5} bar^{-1}) with maximised injection rate;
- K_v/k_h ratio set to 0.001 with maximised injection rate.

A further eight scenarios were analysed where the boundary conditions were altered to consider cases where connectivity and flow boundaries within the aquifer may be worse or better than predicted. The first four scenarios consider a case where the seabed outcrop does not provide a route for brine migration, and the outcrop is deactivated in the model, this could perhaps represent cementation in the outcrop. The scenarios analysed in the 'no outcrop' case were:

- Maximised injection rate model with no outcrop;
- High Formation Compressibility (10 x 10^{-5} bar^{-1}) with maximised injection rate and no outcrop;
- Low Formation Compressibility (1 x 10^{-5} bar^{-1}) with maximised injection rate and no outcrop;
- K_v/k_h ratio set to 0.001 with maximised injection rate and no outcrop.
- 20 mD case with maximised injection rate and no outcrop

There is some uncertainty in the boundary conditions, and it is likely that some of the boundaries may be at least partially permeable to the outflow of brine. Therefore, the two boundaries where most uncertainty existed (NW and W) were remodelled as large aquifers to model the effect of open boundaries. Three scenarios were considered:

- Maximised injection rate with both the western and north-western aquifers activated;
- Maximised injection rate with the western aquifer activated;
- Maximised injection rate with the north-western aquifer activated.

The results for each scenario are discussed in the following sections.

3.2.4.4 *Multiple Injection Wells – 12 Injection Wells – Standard Boundary Conditions*

The base case multiple well scenario had an injection rate of 1 Mt CO_2/yr, meaning 600 Mt CO_2 were injected by the end of the 50 year period. The injection rate is a cumulative rate split equally between each of the wells. The base case injection rate matches the rate used by Noy et al. (2012) although the well locations were not identical. A maximised injection rate scenario was also developed, to compare with a similar case from Noy et al. (2012). Unlike the single well scenarios, the maximised injection rate could not be set to an unrealistically high level and the injection controlled by the well pressure control, as this caused the fracture pressure to be exceeded in many structural high points. Instead, the injection rate had to be determined through an iterative trial and error process. A final

injection rate of 21.7 Mt CO_2/yr (59296 t/CO_2/day) was determined for this study, this compares well with the rate of 21.9 Mt CO_2/yr found by Noy et al. (2012). The maximised injection resulted in injection of 1083 Mt CO_2 into the model during the 50-year period. The injection rates were constant at each well throughout the simulation, and set at a level that would prevent the fracture pressure being exceeded in the structural high points in the model. The injection rates were too low to be constrained by pressure build up around the well. Therefore, the injection rate and cumulative injection graphs shown in Figure 3.24 are linear. The flow rate at each well in the maximised case was the same except for well 4. The structural closure next to well 4 was particularly susceptible to failure from a high flow rate in well 4. It was found that reducing the injection rate in well 4 increased the allowable injection rates in other wells, and thus increased overall capacity slightly. The rate in well 4 was therefore set at 36% of the flow rate in the other wells.

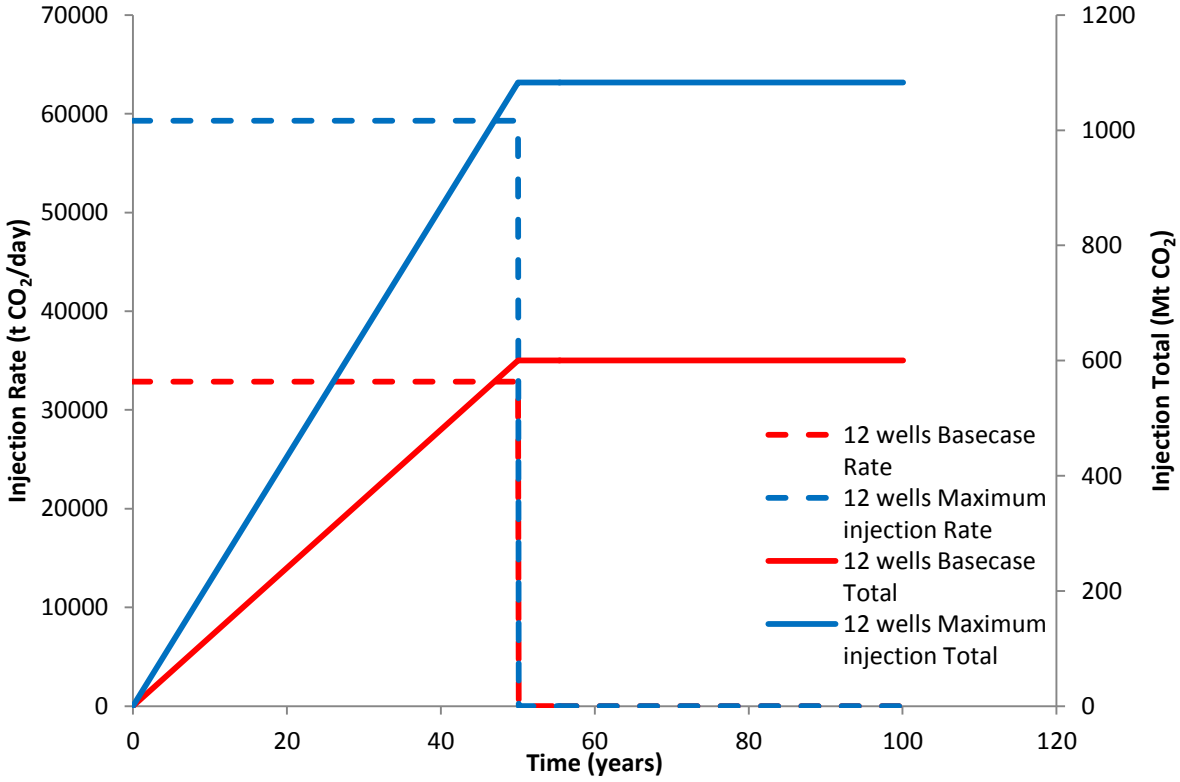

Figure 3.24 – Graphs of CO_2 injection rate and cumulative CO_2 injection total for the base case and maximised injection case for the model with 12 injection wells.

The comparison of performance between the models is best achieved using the brine outflow from the model as the injection rate is linear and matched between the two models. the. The brine outflows from the seabed outcrop for the 12 well base case and maximised injection rate models are shown in Figure 3.25. The peak outflow rate for the base case model was 15058 tonnes/day or 174 kg s^{-1}. The peak outflow for the maximised injection rate model was 26409 tonnes/day or 306 kg s^{-1}. The peak outflows occur at 51.7 years after the start of injection in both models. The water outflow rates are a reasonable match with the model presented by Noy et al. (2012) with peak outflow rate of 170 kg s^{-1} reported for the base case, and 291 kg s^{-1} for the maximised injection rate case. The base case model

was run for a maximum of 100 years and the total output of brine at this point is 377 Mt. Noy et al. (2012) only report total outflow at 1500 years and this is 840 Mt. However, the rates correlate well between the two models and the graph presented in the paper shows a similar total outflow after 100 years for the base case model (Noy et al. 2012). The maximised injection case was only run to 150 years by Noy et al. (2012) due to a convergence error in their model. The total outflow in the maximised injection case was 952 Mt after 150 years, compared to 833 Mt from the model by Noy et al. (2012). Based on the good agreement between the models for the base case run, the maximised injection case was run for 1000 years to approximate the total volume of water outflow that would have been calculated by Noy et al. (2012). The total outflow calculated in this model at 1000 years was 1637 Mt. Clearly, there is some difference between the two estimates at the 150 year point, with the estimate of Noy et al. (2012) 0.875 times the value predicted by the model in this study. Applying the factor of 0.875 to the estimate at 1000 years would yield a predicted total outflow of 1432 Mt for the model of Noy et al. (2012).

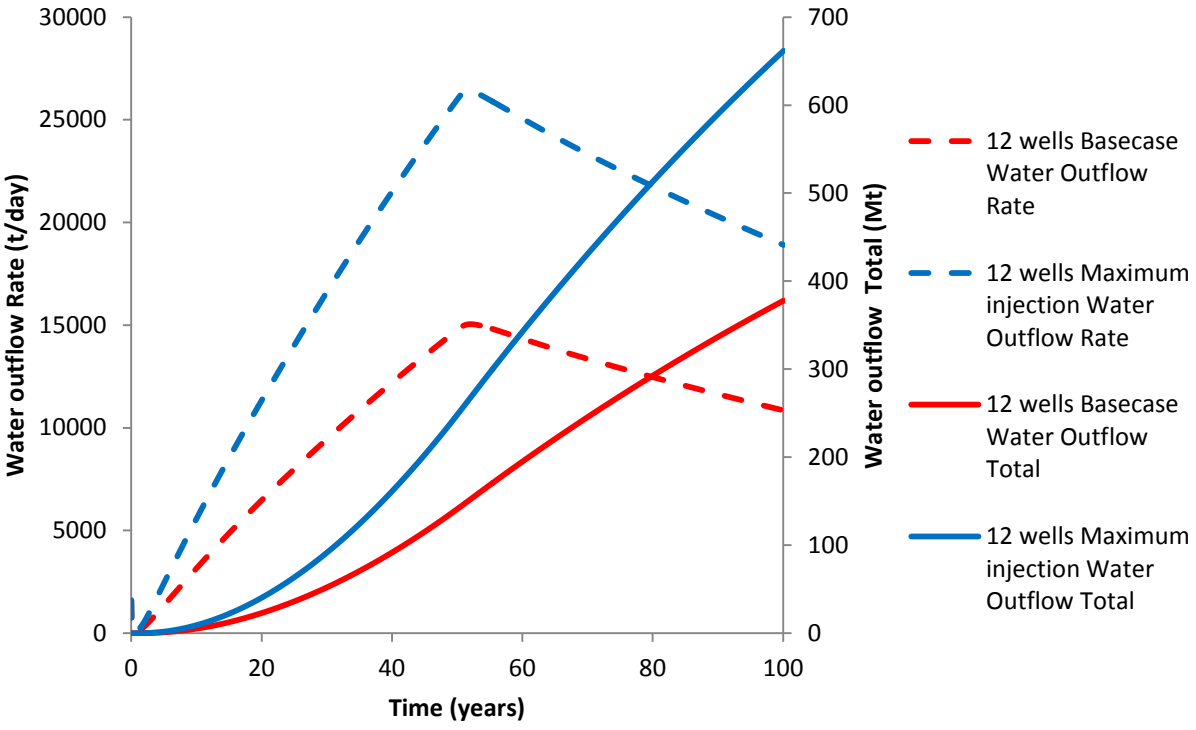

Figure 3.25 – Graph of water outflow from the seabed outcrop for base case and maximised injection rate case for the model with 12 injection wells.

Figure 3.26 shows a comparison of the CO_2 saturation in the model for the base case and maximised injection rate case at 50 (end of injection) and 100 years after the start of injection. The plumes are initially laterally more widespread in the maximised injection rate case and this is due to increased injection rates. After 100 years the models show that the plume extents diminish in both cases as the CO_2 migrates into the structural highs that were targeted by the injection wells. The overall storage efficiency for the base case model was 0.22% and for the maximised flow case was 0.39%.

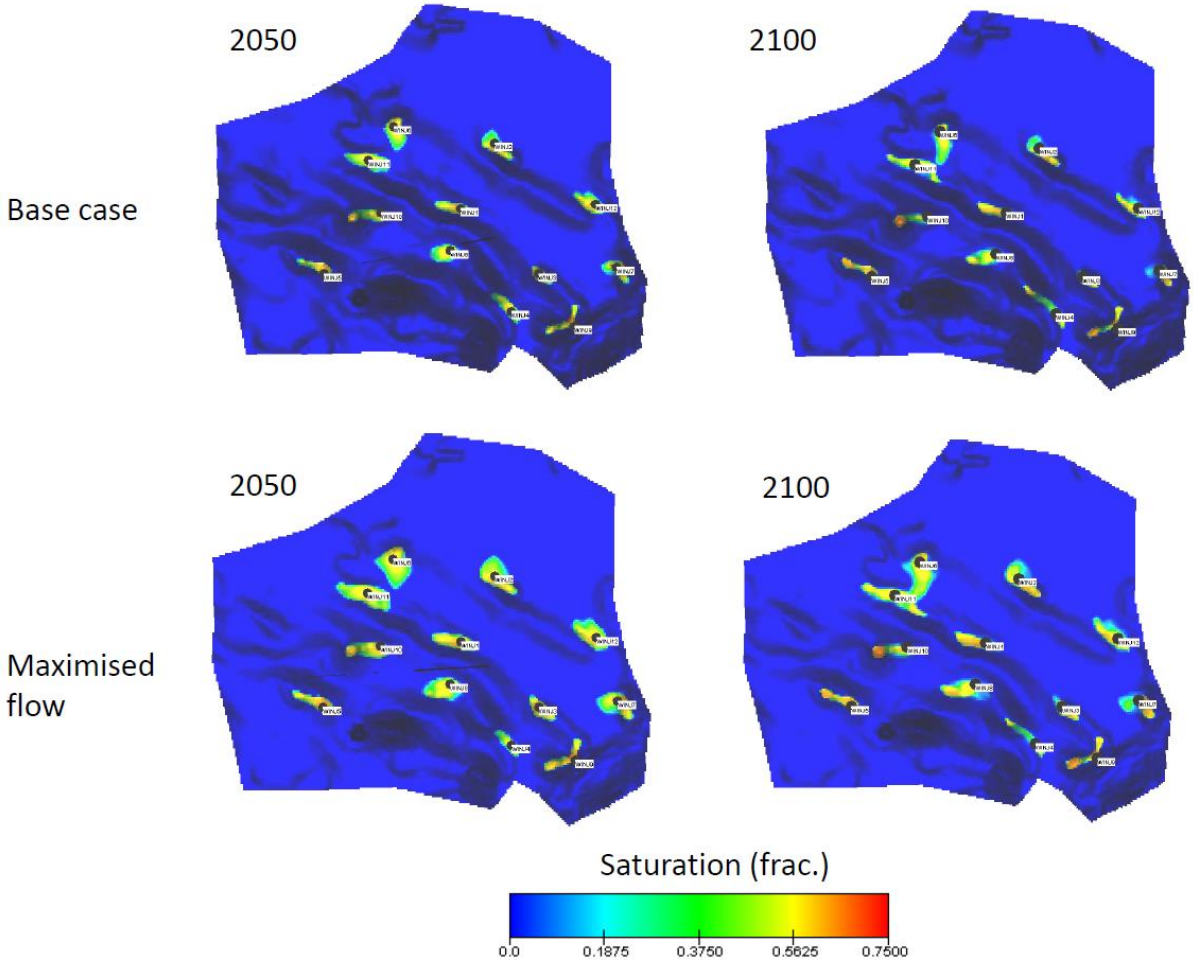

Figure 3.26 – Plots of the CO_2 saturation plumes for the base case and maximised flow cases for the model with 12 injection wells showing plume spreading after injection is stopped (2050).

Figure 3.27 shows a plot of the difference between 75% lithostatic pressure limit and pore pressure (bar) throughout the model at 50 years after the start of injection. The plot indicates the areas in which the pressure is closest to exceeding the lithostatic pressure limit. The plot shows that the areas most at risk of exceeding the pressure limit are:

- the structural highs near wells 10, 9 and 7;
- the central region between wells 11, 6 and 1;
- and the structural high to the south west of well 4.

The critical point in the model is the region to the south west of well 4, the risk of exceeding the lithostatic pressure limit is greatest in this region. Pressure in the region near well 4 comes within 0.06 bar of the 75% lithostatic pressure limit 56 years after the start of injection, this is 6 years after injection into the aquifer has halted. Pressure in the rest of the model has already begun to stabilise during this time. The results show that there is a lag time during which the pressure continues to increase in regions of the model even after injection has halted. After this lag time, the stabilising effect of aquifer brine leaving the seabed outcrop allows the pressure to decrease in all areas of the model. The peak

pressure in the model is observed approximately 4.3 years after peak brine outflow from the seabed outcrop.

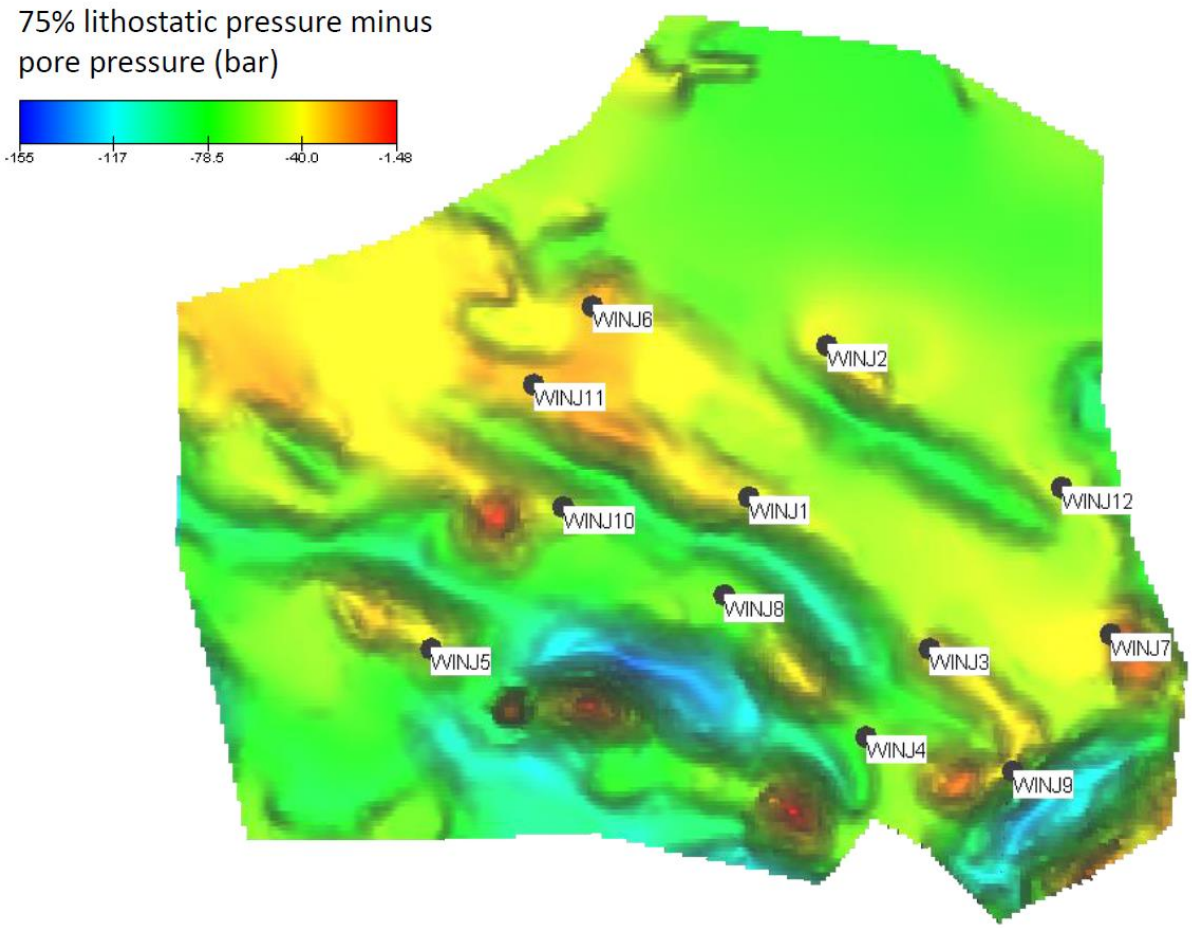

Figure 3.27 – Plot of the 75% lithostatic pressure limit minus the current pore pressure at 50 years for the 12 well model with maximised injection. The plot represents how close regions of the model are to breaching the pressure limit.

Four other scenarios were analysed with the same boundary conditions and a maximised injection rate, in these scenarios, the permeability and compressibility were varied. The global permeability was modified to 20 mD (as in another model from Noy et al. 2012) in one scenario, the compressibility was set at 1 x 10^{-5} bar^{-1} and 10 x 10^{-5} bar^{-1} in two different scenarios, and the k_v/k_h ratio of permeability was set to 0.001 in the final scenario. The total volume injected in each of these scenarios (including the previous multiple well scenarios) are summarised in Figure 3.29, and the injection rate profiles are shown in Figure 3.28.

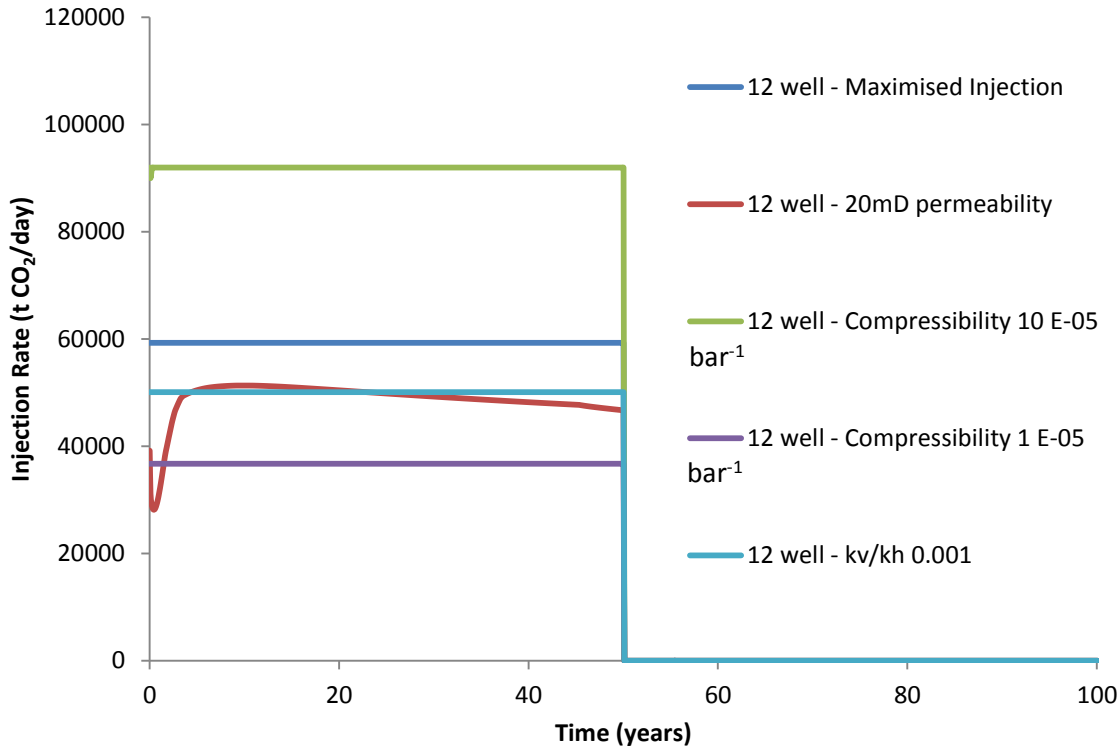

Figure 3.28 – Injection rate for all 12 well scenarios (excluding base case) with no modification to boundary conditions.

Figure 3.28 shows that the only scenario where the injection rate is seriously affected by pressure build-up around the well is the 20 mD permeability case. In the 20 mD, case the injection rate is variable throughout the 50 year injection period due to the well pressure control limiting the injection rate. The peak injection rates were 59295 tonnes/day for the standard maximised flow case, 91981 tonnes/day for the high compressibility (10×10^{-5} bar^{-1}) case, 36746 tonnes/day for the low compressibility (10×10^{-5} bar^{-1}) case and 50098 tonnes/day for the $k_v/k_h = 0.001$ case. The injection rate for the 20 mD case varies between a minimum of 28163 tonnes/day at 0.5 years rising rapidly to a maximum of 51330 tonnes/day at 10 years after injection is started. The injection rate only remains at the peak rate for approximately 0.3 years, after which it slowly declines to a rate of 46707 tonnes/day at the end of the 50-year period.

In all of the cases the flow rate was the same for each well, except for wells 4, 7 and 10 in some of the cases. Wells 4, 7 and 10 are close to the points previously identified as susceptible to fracture pressure failure in the model. Through the iterative process of maximising the flow rates in the wells it was found that reducing the injection rate in some of these wells increased capacity slightly in some cases. The process of reducing the well flow rates in these particular wells was carried out semi-systematically, although the rate at each particular well is likely to be non-unique. In the high compressibility case well 4 was set at 70.5% of the injection rate of the other wells, and 7 and 10 were set at 77%. In the low compressibility case, well 4 was set at 46%, and in the k_v/k_h 0.001 case well 4 was set to 42%. For the 20 mD case wells 4, 7 and 10 were set to 72% of the main injection rate. Well

4 seemed to have the greatest impact and it is likely that in the cases where 3 wells were adjusted that reducing only well 4 to a lower level would have a similar effect on the overall pressurisation of the susceptible sections of the model. Once again, in all of the cases, a significant lag time was observed between the end of injection and the peak pressure increase in the area of the model most susceptible to fracture pressure failure. The largest lag time was 51 years and was observed was in the 20 mD case. The time lag in other cases was close to the 6-year period observed in the standard case.

The total injected CO_2 mass for each scenario is shown in Figure 3.29. The high compressibility case is the highest at 1680 Mt CO_2, over 1.5 times the mass injected in the standard maximised injection case. The low compressibility case has the lowest injected mass of 671 Mt CO_2, 0.62 times the mass injected in the standard maximised case. The mass injected in the 20 mD case was 891 Mt which is 82% of the standard maximised injection capacity and in the k_v/k_h case 915 Mt CO_2 were injected which is 84% of the standard maximised capacity. Interestingly, the total CO_2 injected mass and injection rates for the 20 mD and the k_v/k_h case were similar.

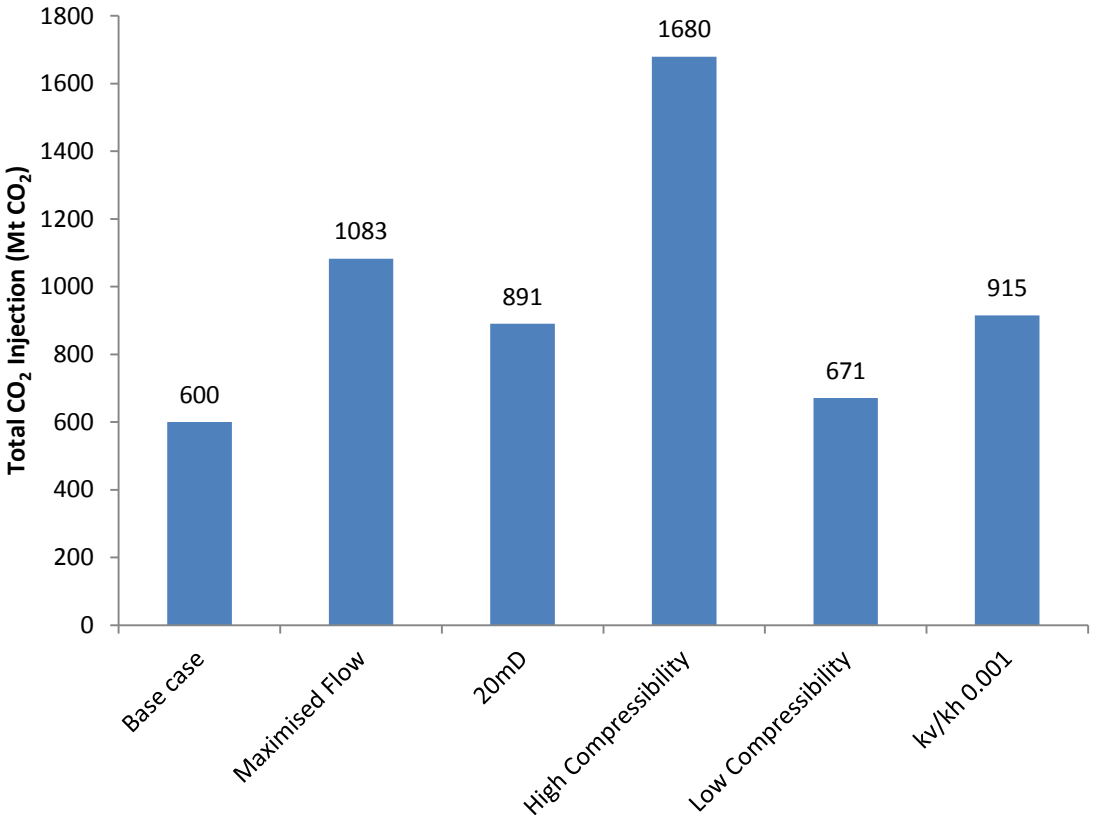

Figure 3.29 – Total CO_2 injection for all 12 well scenarios with no modification to boundary conditions.

The seabed outcrop brine outflow rates for all cases with the maximised injection rate are shown in Figure 3.30, and the totals for the mass of brine outflow from the seabed outcrop

are shown in Figure 3.31. The two compressibility cases show very similar brine outflow rates to the maximised base case up until 50 years, peaking at 26409 tonnes/day for the maximised base case, 26036 tonnes/day for the high compressibility case, and 26032 tonnes/day for the low compressibility case. The total brine outflow after 100 years is 662 Mt for the maximised base case, 665 Mt for the high compressibility case, and 618 Mt for the low compressibility case. Unlike the single well cases, the brine outflow rate in the two compressibility cases is very similar to that of the standard maximised case up to 50 years. After 50 years, the brine outflow rates diverge, with the outflow rate in the low compressibility case dropping off the fastest and the outflow rate for the high compressibility case staying above that of the standard case. The initially similar response of the compressibility and standard cases results from the fact that the limiting factor in the multiple well models is pressure build-up in the structural highs and the pressure relief available from the outcrop, rather than injection well constraints. The injection in the multiple well cases is constrained by setting a satisfactory injection rate to meet a target pressure in the most at risk structural high. Only a certain volume of water can flow from the outcrop over the injection time and this dictates the pressure relief available in the model. The model injection rate is essentially tuned to the response of the aquifer brine outflow capacity, which does not change with compressibility, the compressibility only acts to afford more of less capacity due to pore volume changes. The divergent response of the brine outflow rates after 50 years relates to the relative stiffness of the response of the model based on the compressibility. With the removal of injection pressure after 50 years the model will begin to compact forcing out more water and dissipating pressure build up. Less compaction occurs in the low compressibility model, and so less water ejected and pressure dissipation is faster i.e. the outflow rate drops off faster.

The CO_2 injection rates and total injection capacity for the 20 mD case and the k_v/k_h case are very similar, however, the brine outflow rates are quite different. Both the peak rate of outflow and total outflow for the 20 mD are roughly half that of the k_v/k_h case. The difference in brine outflow is related to the mechanism by which injection is limited in each of the cases. In the 20 mD case injection volume, and thus brine displacement, is limited by the pressure build-up around the well due to low permeability. In the k_v/k_h case the injection rate is limited by the restriction on brine outflow pressure relief at the outcrop due to the low vertical permeability. The differing pressure response of the 20 mD case and the k_v/k_h case is illustrated by Figure 3.32. The figure illustrates localised pressure build up around wells in the 20 mD case and widespread pressure changes in the laterally highly permeable k_v/k_h case at 20 years after injection. The peak pressure at the critical outcrop was at 60 years in the k_v/k_h case, and 100 years in the 20 mD case.

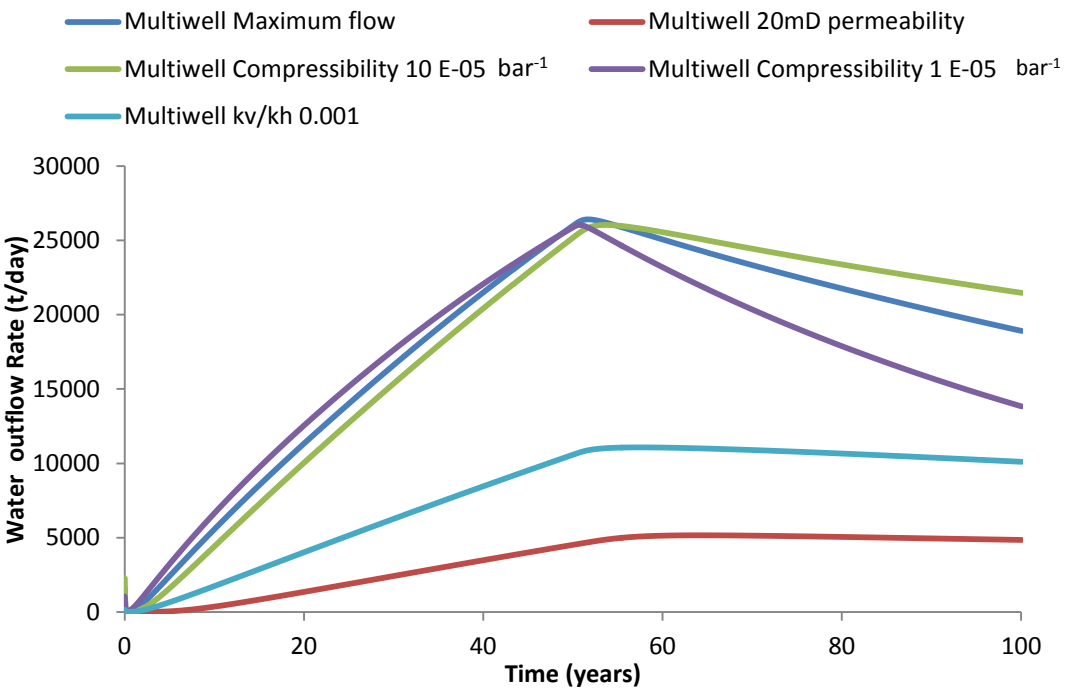

Figure 3.30 – Brine outflow rate at the seabed outcrop for all 12 well scenarios (excluding base case) with no modification to boundary conditions.

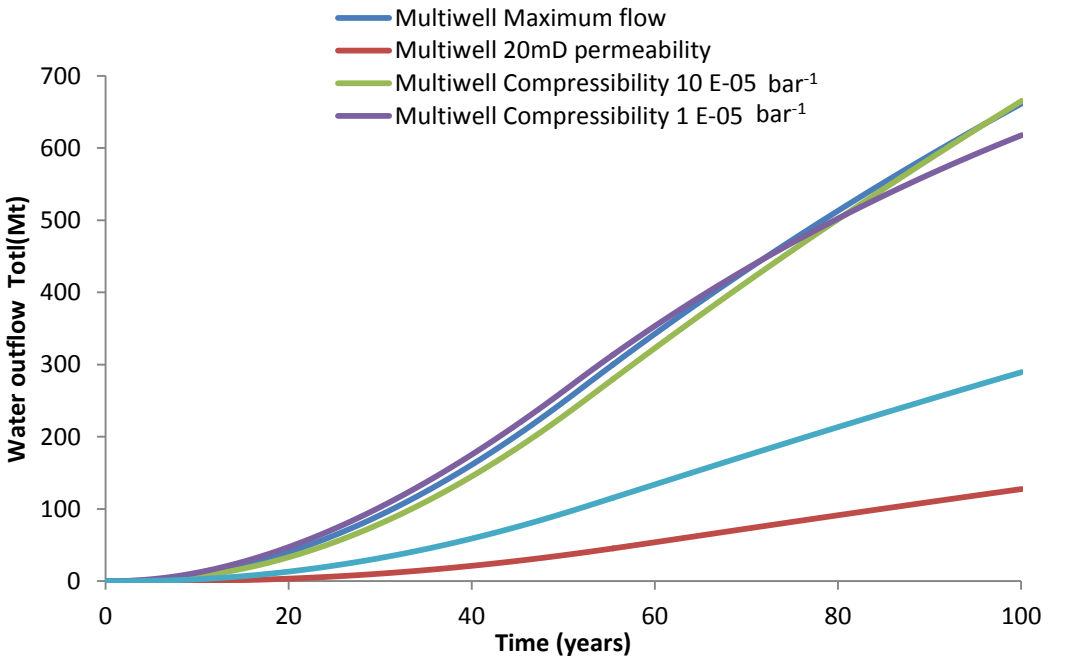

Figure 3.31 - Brine outflow rate at the seabed outcrop for all 12 well scenarios (excluding base case) with no modification to boundary conditions.

Storage efficiencies for each of the cases were between 0.25% and 0.60%, with the highest efficiency resulting from the high compressibility case, and the lowest efficiency resulting from the low compressibility case. The efficiencies for the two permeability scenarios were also similar at 0.31% for the 20 mD case and 0.32% for the k_v/k_h case.

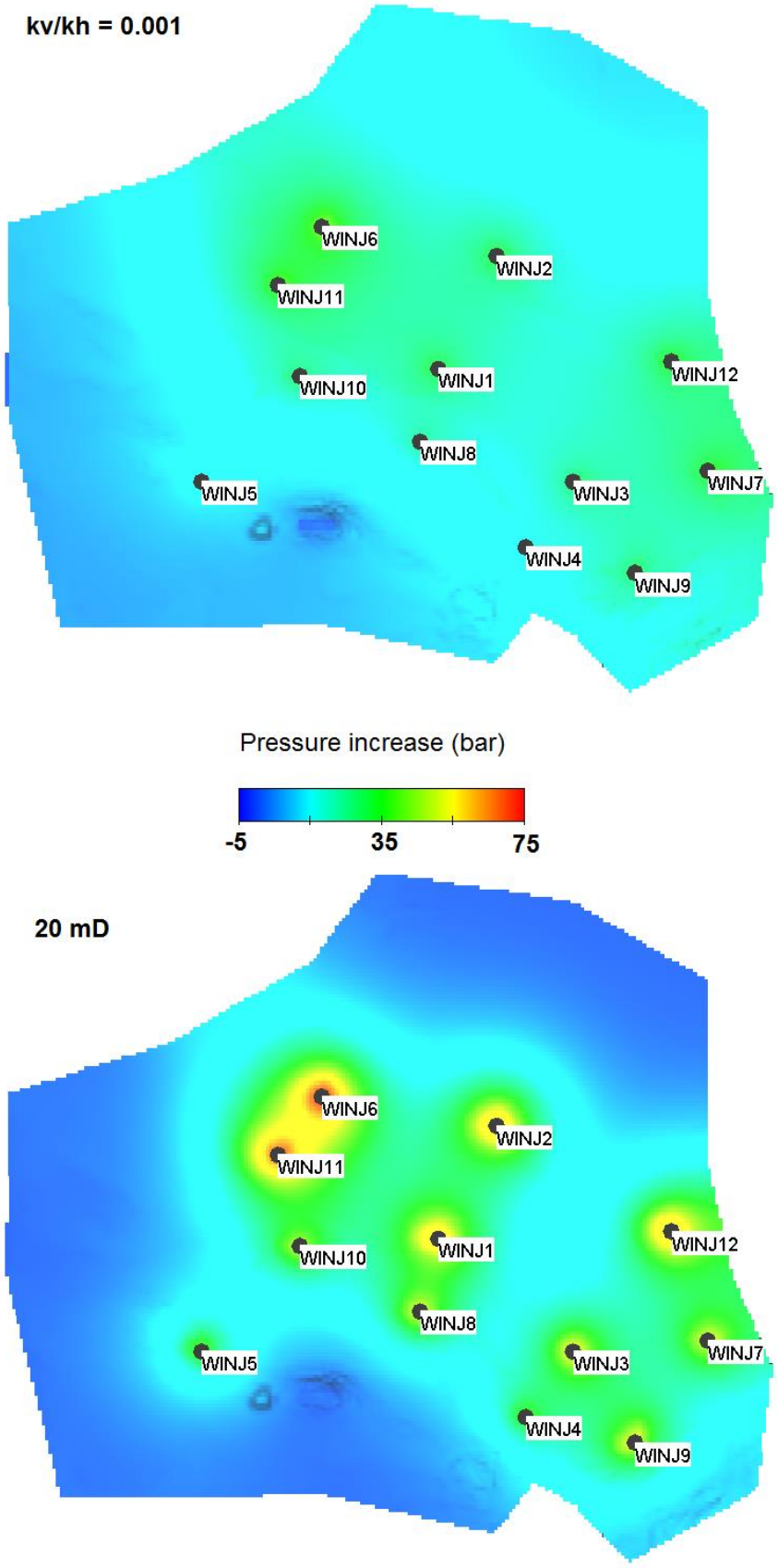

Figure 3.32 – Pressure changes in the reservoir 20 years after the start of injection for the k_v/k_h = 0.001 (top) and 20 mD (bottom) case for the 12 well scenario.

3.2.4.5 *Multiple Injection Wells – 12 Wells – Fully Closed Boundary Conditions*

The seabed outcrop was removed from the model in the second set of scenarios with 12 wells in order to determine the effect of brine flow from the outcrop being inhibited. Removal of the outcrop and closed conditions at the margins prevents any pressure relief from the model. This set of scenarios examines the ultimate capacity of the structure alone.

The total injected mass for each scenario with the closed seabed outcrop is shown in Figure 3.33. Figure 3.33 compares each case with the closed outcrop against the equivalent case with the seabed outcrop open. The injection rates for each case were constant except for the 20 mD injection case which was inhibited by the well pressure control. The injection rate was 71690 t/CO_2/day for the high compressibility case injection rate, 22655 t/CO_2/day for the low compressibility case, 41587 t/CO_2/day for the standard case, and 42033 t/CO_2/day for the k_v/k_h case. The minimum injection rate for the 20 mD case 27973 t/CO_2/day at 0.43 years, rising to a maximum of 41791 t/CO_2/day at 4.2 years, the final rate at 50 years was 39942 t/CO_2/day. Again, the injection rates were constant in all wells except for well 4. The reduction of injection rate in well 4 varied between 76% and 100% for these cases. The lowest rate was in the high compressibility case, which also had the highest flow rates in the wells, the other cases were between 90 and 100%. The time lag between the end of injection and the peak pressure increase in the area of the model most susceptible to fracture pressure failure is even more significant in the models with no flow at the outcrop. The largest lag time is observed in the 20 mD case with a time lag of 117 years, followed by the high compressibility case with a lag time of 35 years. The other lag times are also significant, for example they are 17 years for the case with no flow at the outcrop and the k_v/k_h = 0.001 case. Interestingly, the shortest lag time was 8 years with the low compressibility case.

Comparison between the closed outcrop models shows the same general trend as observed in the open outcrop models for varying compressibility. The high compressibility case yielded the highest total injected mass of 1309 Mt CO_2, the low compressibility case yielded the lowest at 414 Mt CO_2, with the standard case giving an intermediate value of 760 Mt CO_2. Comparison of the cases with varying permeability shows a different trend to the open outcrop cases however. The standard case and the k_v/k_h = 0.001 case gave very similar results without the outcrop. In fact, the k_v/k_h case actually allowed slightly more CO_2 to be stored in the model (8 Mt CO_2). The similarity between the standard case and the k_v/k_h case is possibly because the model no longer receives pressure relief from the outcrop, and so the k_v/k_h ratio is not acting as a limiting factor to vertical flow out of the outcrop. The capacity of the k_v/k_h case is larger as the CO_2 plume and pressure perturbation is distributed throughout the model rather than at the top of the model where the greatest pressure impact in the structural highs occurs. The 20 mD case also gave a very similar capacity to the standard and k_v/k_h cases but is slightly lower than both the standard (11 Mt lower) and the k_v/k_h cases (19 Mt lower). The reduced capacity in the 20 mD case is due to the initial restrictions on the well from pressure build-up near the injection point. The injection rates for

all of the permeability cases are generally similar apart from the initially low rate in the 20 mD case. The 20 mD, k_v/k_h = 0.001 and standard case are similar in the scenarios with no outcrop as the each model has essentially the same mass balance (same pore volume).

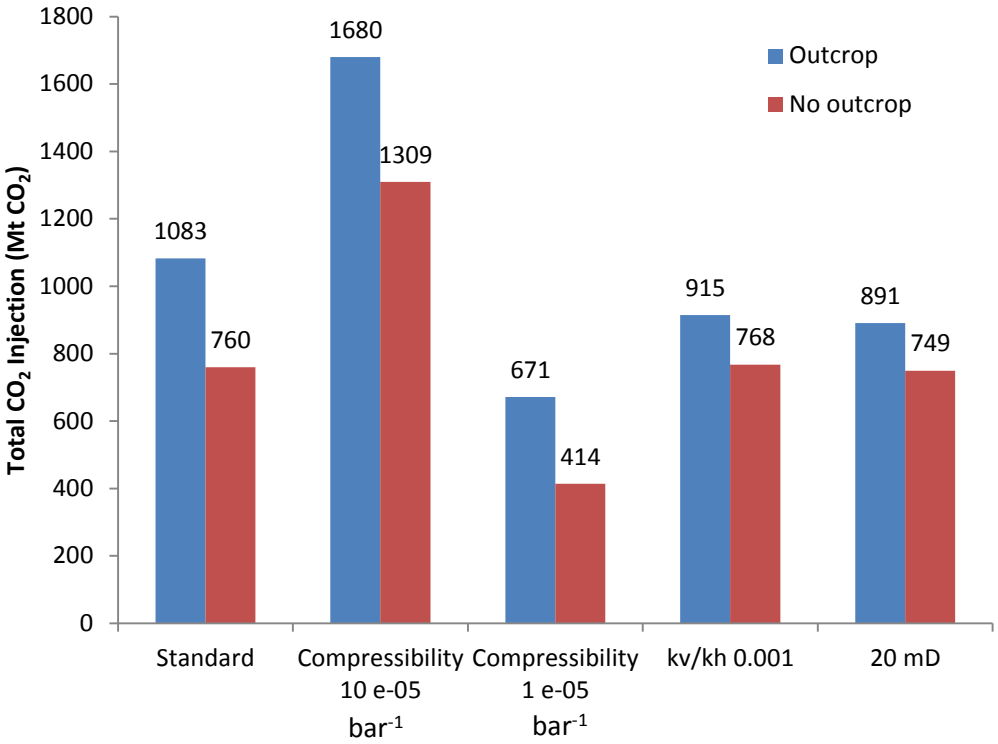

Figure 3.33 – Total CO_2 injection for all 12 well scenarios with no seabed outcrop compared against the same cases with the seabed outcrop.

Figure 3.33 allows comparison of individual cases with and without the outcrop and shows a reduction in storage capacity of between 16% and 38% from the case with the outcrop to the case without the outcrop. The largest reduction (38%) was in the low compressibility case, the reduction in this model is probably due to the stiffer response of the model to pressure increase meaning the model is more sensitive to the removal of pressure relief created by removing the outcrop. The high compressibility case shows a reduction of 22% and the standard compressibility case shows an intermediate reduction in between the high and low compressibility cases (30%). The k_v/k_h case shows the smallest reduction in capacity between the case with and without the outcrop at 16%. The k_v/k_h case is essentially the same as the standard case when no outcrop is considered. The reason for the similarity in capacity between the k_v/k_h outcrop and no outcrop case is that the vertical permeability inhibits vertical brine flow and thus pressure relief when the outcrop is implemented. The 20 mD case shows the same 16% reduction between the outcrop and no outcrop cases as the k_v/k_h case, once again the pressure relief is inhibited in the outcrop open case and so the reduction due to closing the outcrop is relatively small.

The storage efficiencies for the cases without the outcrop varied between 0.15% and 0.46%. The highest value was for the high compressibility case, and the lowest value for the

low compressibility case. The standard case and k_v/k_h case were intermediate at 0.27%, with the 20 mD slightly lower at 0.26% due to the slightly lower storage capacity.

3.2.4.6 *Multiple Injection Wells – 12 Wells – Open Boundaries at North-Western and Western Boundary*

In the final set of 12 well injection scenarios, the effect of adding open boundaries at some of the margins was analysed. As discussed in the section on the model setup the open boundaries were added at the western and north-western margins, where it was considered most likely that an open, or semi-open boundary could exist.

The total calculated capacity for the cases with fully closed (no outcrop, no open margins), seabed outcrop only, western aquifer (plus seabed outcrop), north-western aquifer (plus seabed outcrop), marginal aquifers only (no seabed outcrop), and fully open (all outcrops and aquifers implemented) are shown in Figure 3.34. Figure 3.34 shows that fully open marginal boundaries will only provide a relatively small increase in the storage capacity of the model. With only the seabed outcrop open the capacity is 1083 Mt CO_2, adding two marginal aquifers increases this capacity to 1202 Mt CO_2, which is an 11% increase. The total capacity figures and the graph show that the largest component of capacity increase is provided by the implementation of the north-western aquifer. The north-western aquifer provides a 9% increase on the case with the outcrop and no marginal aquifers. The western aquifer contributes 2% to the increased capacity. Figure 3.34 also shows the modelled capacity when the marginal aquifers are considered without the seabed outcrop. The capacity with only the marginal aquifers implemented is 911 Mt CO_2, which is 15.9% less than the model with only the seabed outcrop implemented (1083 Mt CO_2). The seabed outcrop alone (1083 Mt CO_2) provides an increase of 42.5% from the model with completely closed boundaries (760 Mt CO_2), whereas the marginal aquifers alone (911 Mt CO_2) only provide a 19.9% increase from the closed boundary model.

In all of the marginal aquifer cases the flow rate in all of the wells was constant except in well 4. The reduction flow rate in well 4 fairly consistent and varied between 33% and 43% of the flow rate of the other wells.

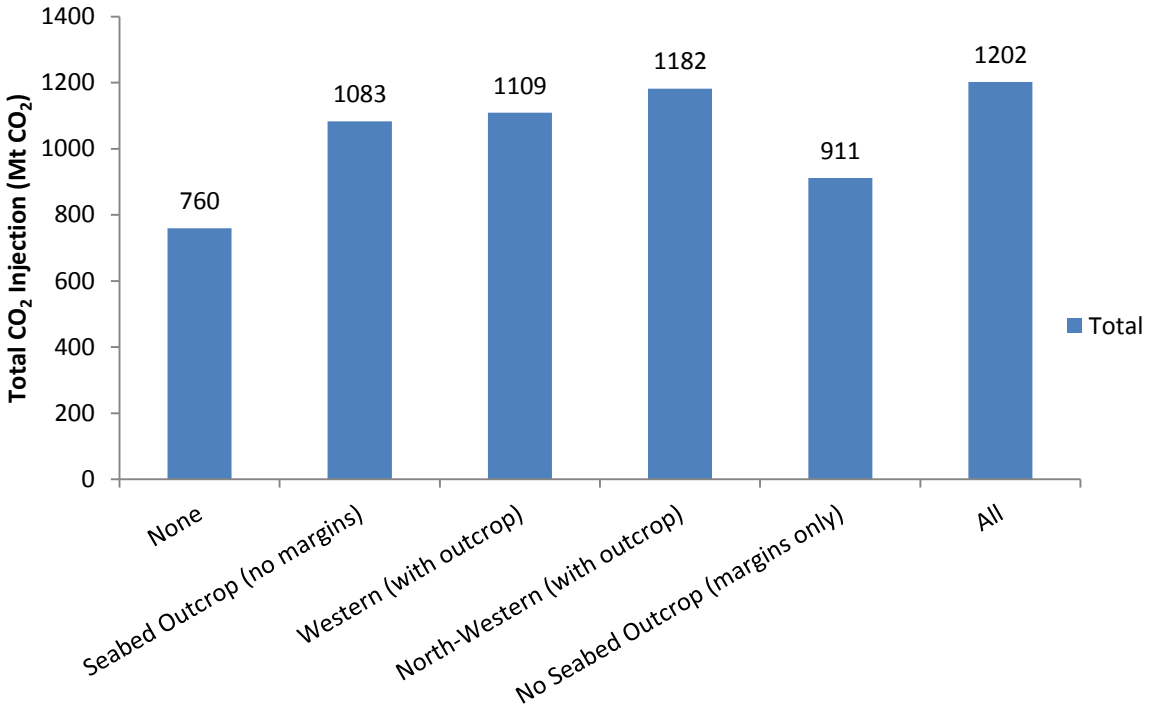

Figure 3.34 – Total CO_2 injection for 12 well scenarios with different boundary condition scenarios.

The graph of water outflow for the model with all aquifers and the outcrop open is shown in Figure 3.35. The graph in Figure 3.35 shows that the highest rates of brine outflow from the model occurs through the north-western aquifer followed by the seabed outcrop, with the western aquifer contributing a much smaller rate of brine outflow and thus less pressure relief in the model. The north-western aquifer is also more sensitive to the injection activity, with the outflow peaking rapidly with the onset of CO_2 injection, and dropping off rapidly at 50 years once injection has stopped.

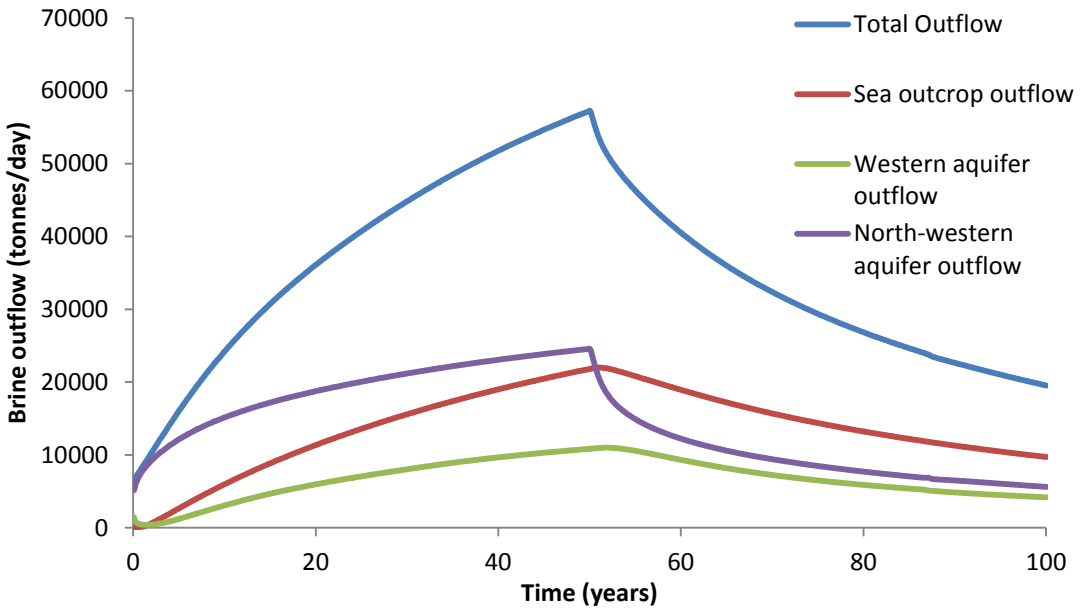

Figure 3.35 – Brine outflow rates for the 12 well scenario with fully open boundaries in the western and north-western boundary and the seabed outcrop open.

The total brine outflow for each case is shown in Figure 3.36. In the case where all boundaries are open 1270 Mt of brine have flowed out of the model after 100 years. In the case with the only north-western marginal aquifer and the outcrop active, the total outflow is 1140 Mt, the western and outcrop only case is 906 Mt, and the seabed outcrop only is 661 Mt. The brine outflow volumes and storage capacities show that the seabed outcrop is the most effective boundary for increase in capacity despite the fact that a greater volume of brine can flow out of the north-western margin of the model. This suggests that brine outflow pressure relief is more important if it occurs at the top rather than the margins of the model.

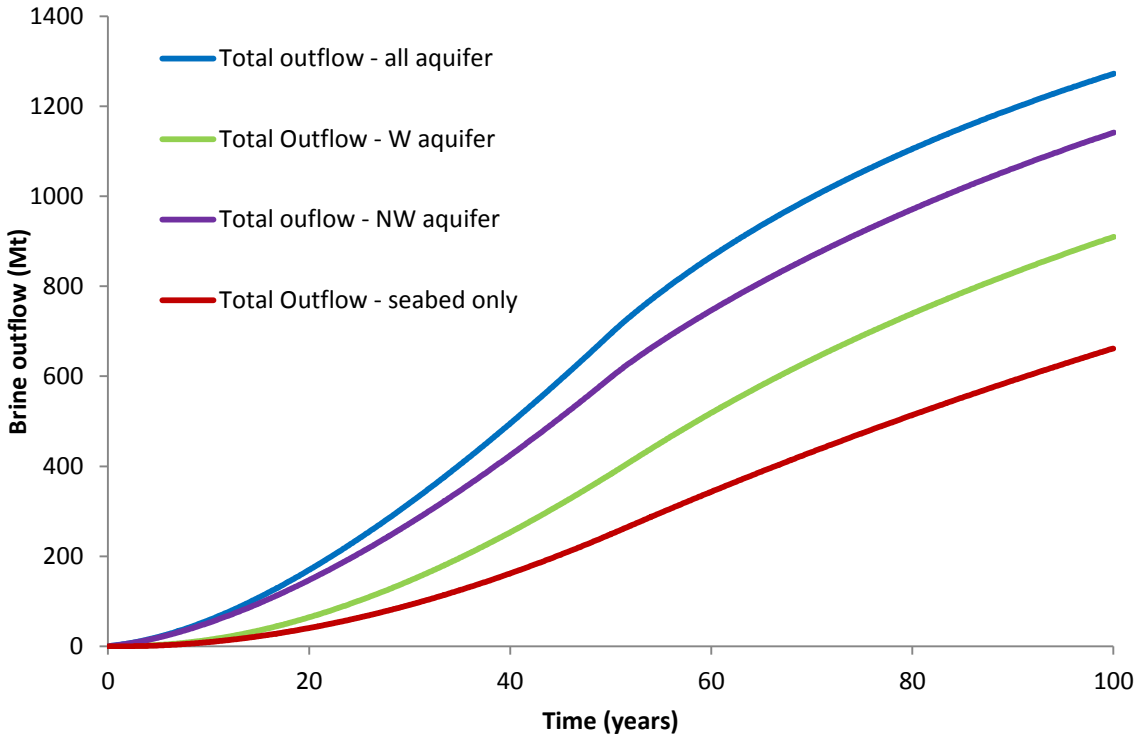

Figure 3.36 – Total brine outflow for the 12 well model with the scenarios with and without marginal aquifers implemented.

The north western aquifer provides a significantly greater capacity increase compared to the western aquifer, however the connected area of the north western aquifer is much smaller (3.36×10^6 km^2) than the connected area of the western aquifer (12.15×10^6 km^2). The north-western aquifer has a much smaller connected area because the reservoir is very thin along the north-western margin. The reason that the north-western aquifer provides more capacity from pressure relief and brine outflow appears to be related to the structure of the aquifer and the injection method. Figure 3.37 shows the pressure increase in the aquifer in the case where all aquifers and the outcrop are implemented. Figure 3.37 shows that significant pressure increase mainly occurs in the flat northern section of the model, and in the SE-NW running structural highs, that are connected up-dip to the NW margin. It appears that the pressure increase close to the NW aquifer, and connection of the structural highs to the northwest margin causes brine to flow preferentially from the north western aquifer.

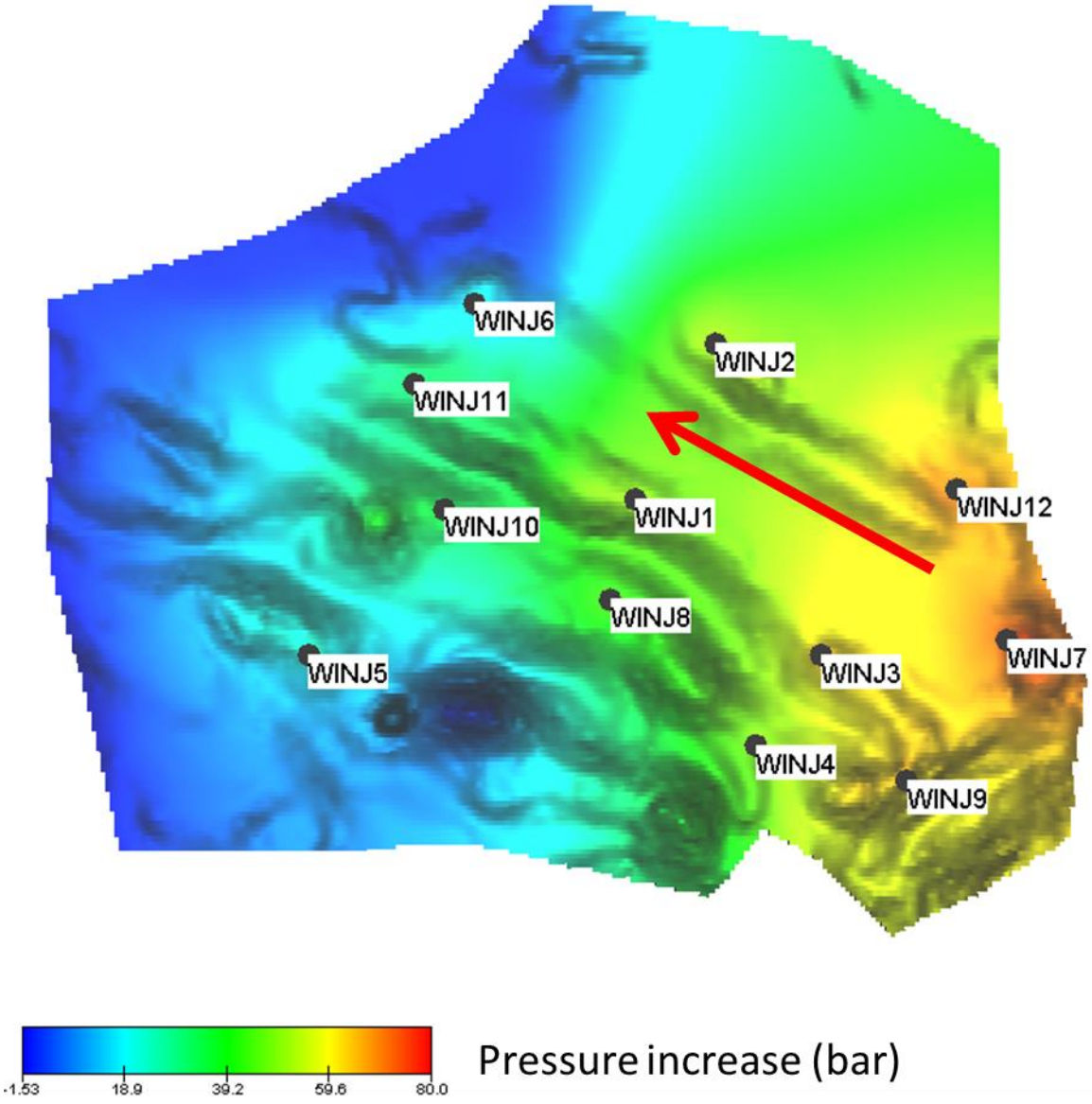

Figure 3.37 – Pressure increase in bars in the model with all marginal aquifers and seabed outcrop implemented. The red arrow indicates the SE-NW structural highs that are connected up-dip to the marginal NW aquifer.

The storage efficiencies for the model with the seabed outcrop, and the marginal aquifers was 0.44%, the model with the seabed outcrop and only the western aquifer had an efficiency of 0.41%, whilst with only the north-western aquifer and seabed outcrop implemented the storage efficiency was 0.43%.

3.2.4.7 *Multiple Injection Wells – 24 Wells*

The final set of scenarios that were assessed were a set of multiple well scenarios with an additional 12 wells. The aim was to assess the potential capacity increase from a higher density of well penetration in the model. The scenarios that were run were based on the

previous scenarios that had been analysed for the single and multiple well models to allow comparison across the range of well numbers. The scenarios are:

- Maximised injection rate model;
- No seabed outcrop or marginal aquifer implemented in the model with maximised injection rate;
- Marginal aquifers attached to the western and north-western margin of the model with maximised injection rate;
- Global permeability reduced to 20mD with maximised injection rate;
- High Compressibility (10×10^{-5} bar^{-1}) with maximised injection rate;
- Low Compressibility (1×10^{-5} bar^{-1}) with maximised injection rate;
- K_v/k_h ratio set to 0.001 with maximised injection rate.

The well locations were chosen using the same rationale as the initial 12 wells, and the distribution is shown in Figure 3.38.

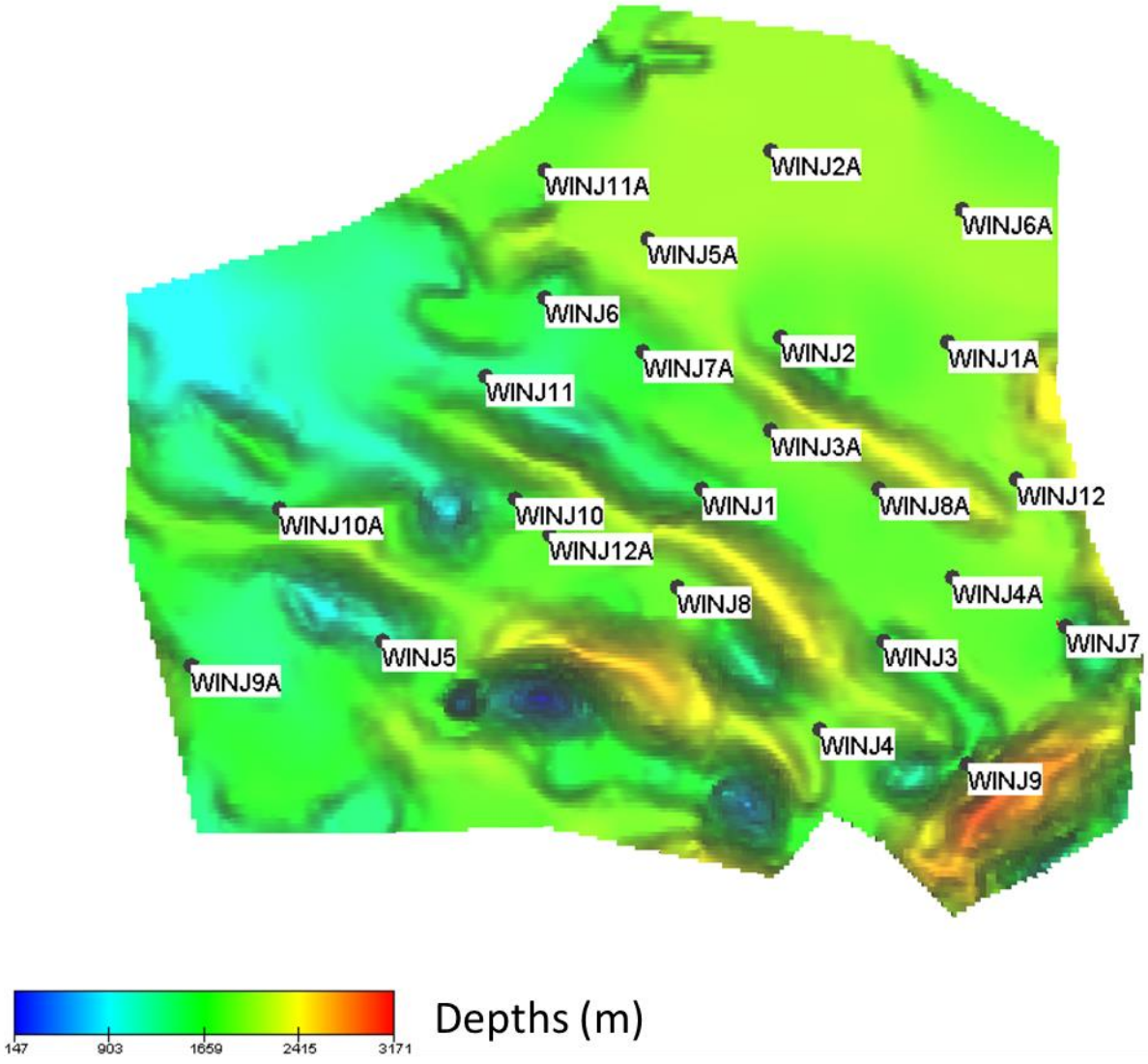

Figure 3.38 – Well locations for the 24 well model, with a depth contour map of the model, the scale is in meters.

The total CO_2 injected in each scenario for the 24 well model is shown in Figure 3.39, where the total injected mass is compared against that achieved in the 12 well model for the equivalent scenarios. The injection rates in each case were constant. The highest flow rate was in the high compressibility case at 113723 t/CO_2/day, the next highest was the marginal aquifer case at 80944 t/CO_2/day. The flow rate achieved in the standard case was 68680 t/CO_2/day. Very similar rates were observed in the k_v/k_h = 0.001 case and 20 mD which were 56504 t/CO_2/day and 58199 t/CO_2/day respectively. However once again the rate in the 20 mD case was variable. The lowest injection rates was in the low compressibility case which was 41252 t/CO_2/day. Unlike the 12 well case, the injection rate was kept the same in all wells, this was mainly due to time constraints and the complexity of varying flow rates in the extra wells that had been added to the model. The lag time between the end of injection and the point at which the model is most at risk of fracture pressure failure is similar to the standard 12 well case for most scenarios. The notable exceptions are for the k_v/k_h = 0.001

case which had a lag time of 20 years and the case where no outcrop was implemented which had a lag time of 136 years, the largest of all the lag times observed.

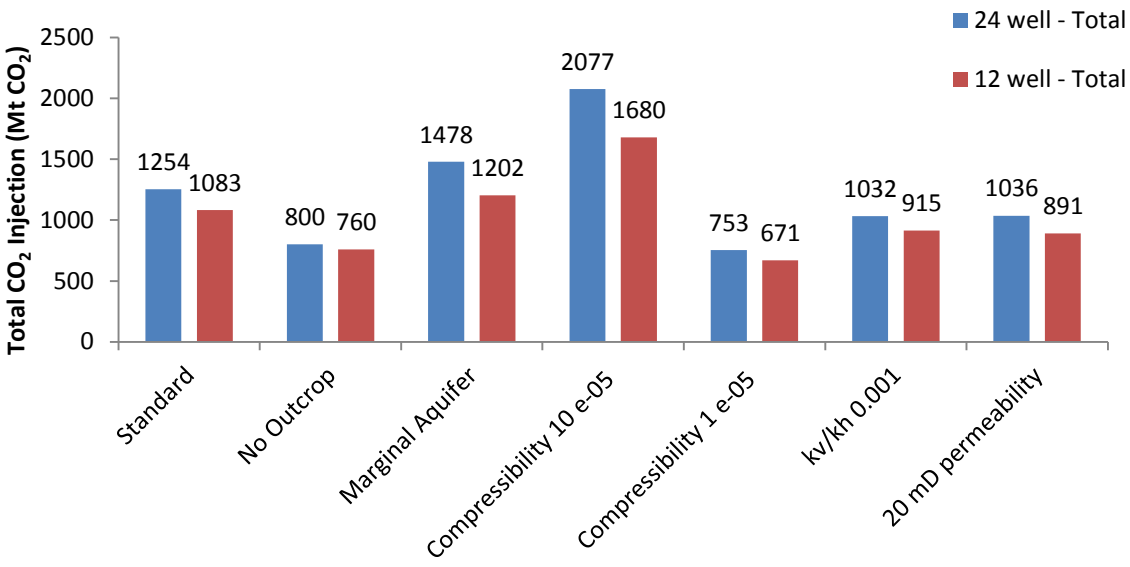

Figure 3.39 - Total CO_2 injection for 24 well scenarios with varying boundary conditions and pore volume and flow properties.

The maximum increase in capacity is observed in the high compressibility case, with a 23.6% increase in modelled storage capacity from the 12 well case to the 24 well case. Over 2 Gt CO_2 are stored in the high compressibility model in the 50 year period. The case with the two marginal aquifers implemented shows a similar capacity increase to the high compressibility case, with a 23% increase in capacity to nearly 1.5 Gt CO_2 . The increase in capacity in the standard case is 15.8% to 1.3 Gt CO_2 , and the low compressibility case is 12.3% to 753 Mt CO_2. The lowest increase in capacity is in the case with no outcrop, with only a 5% increase in capacity in the 24 well case from 760 Mt CO_2 to 800 Mt CO_2. The similarity in injection rate between the 20 mD case and the $k_v/k_h = 1000$ case is reflected in the injection totals of the 24 well scenarios, the increase in injection capacity from the 12 well case in each case is 13.6% and 11.3% respectively.

The graphs of brine outflow for the different scenarios in the model in Figure 3.40 reveal the differing mechanisms of capacity accommodation within the model. There is a large and significant outflow of brine in the marginal aquifer case, the rate rises quickly from the start of injection, and peaks at the 50-year injection termination. The capacity in the marginal aquifer case is controlled by the brine outflow. In contrast, the brine outflow for the compressibility cases and the standard case is similar, and shows a broadly linear trend during injection. The brine response is illustrating the pore volume control on the injection capacity in the compressibility cases rather than the brine outflow control in the marginal aquifer case. Compressibility related pore volume increase controls the injection capacity.

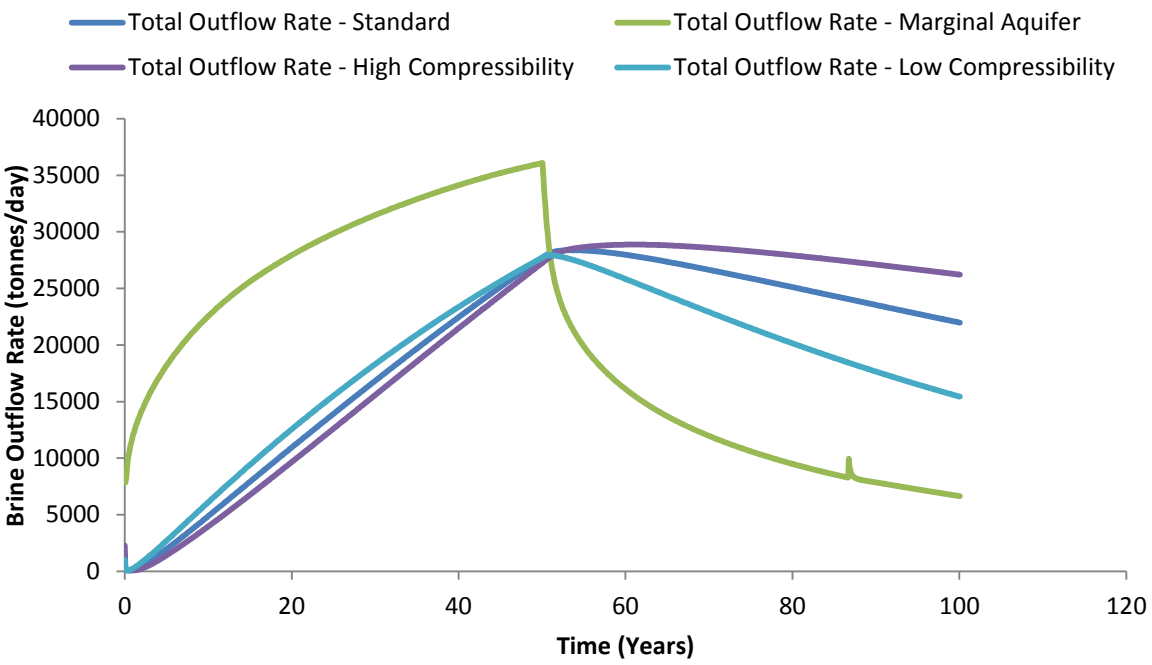

Figure 3.40 - Brine outflow rates for the 24 well scenario with for different scenarios.

3.2.4.8 *Comparison of All Well Scenarios*

The analysis of multiple and single well cases allows the capacity to be compared for various different scenarios, with a range of well densities. The graph in Figure 3.41 shows the modelled capacities for all scenarios that have data available for each different well density (1, 12 and 24). The values are also shown in Table 3.3. The graphs show that all cases show an increase in capacity with an increase in the number of wells. However, capacity increase in the low compressibility and no outcrop cases is marginal, increasing from 637 Mt CO_2 to 753 Mt CO_2 and 728 Mt CO_2 to 800 Mt CO_2, respectively. With the exclusion of the low compressibility and no outcrop cases, the largest increase in capacity comes between the 1 and 12 well scenarios, with a reduced capacity increase observed between the 12 and 24 well scenarios. This suggests that in some cases, particularly the 20 mD scenario, the restriction of pressure around the wellbore is a key factor when only 1 well is considered, but that when more wells are drilled the overall pressure increase in the field is the key consideration. The wellbore pressure restriction versus field pressure limits explains the marked increase between the single well 20 mD case and the 12 well 20 mD case. The actual rates of capacity increase with well density are discussed in more detail later in the following section.

The total capacity estimates shown in Figure 3.41 show that with the exception of the high compressibility case the range of storage capacity that could be expected within the model is between 500 and 1500 Mt CO_2 depending upon the number of wells deployed and the conditions encountered within the aquifer. The two compressibility cases show the variability that can occur in the estimate of CO_2 injection capacity, the two extreme compressibility case estimates encompass almost the entire range of capacities estimated in the modelling.

In the 24 well scenario, the difference between the two compressibility case estimates is over 1300 Mt CO_2, which is more than the maximum total capacity estimate observed for the standard base case model with 24 wells. Another interesting observation is the similarity between the k_v/k_h = 0.001 and the 20 mD case with 12 and 24 wells where the capacity estimates are almost identical. This indicates that poor characterisation of the vertical permeability could lead to a five-fold reduction in the global permeability of the model. The final observation to be made is the significant restriction on capacity if the scenario has no open boundaries. The impact of fully closed boundaries is particularly marked in the 24 well scenario with a 450 Mt CO_2 difference between the standard and no outcrop case.

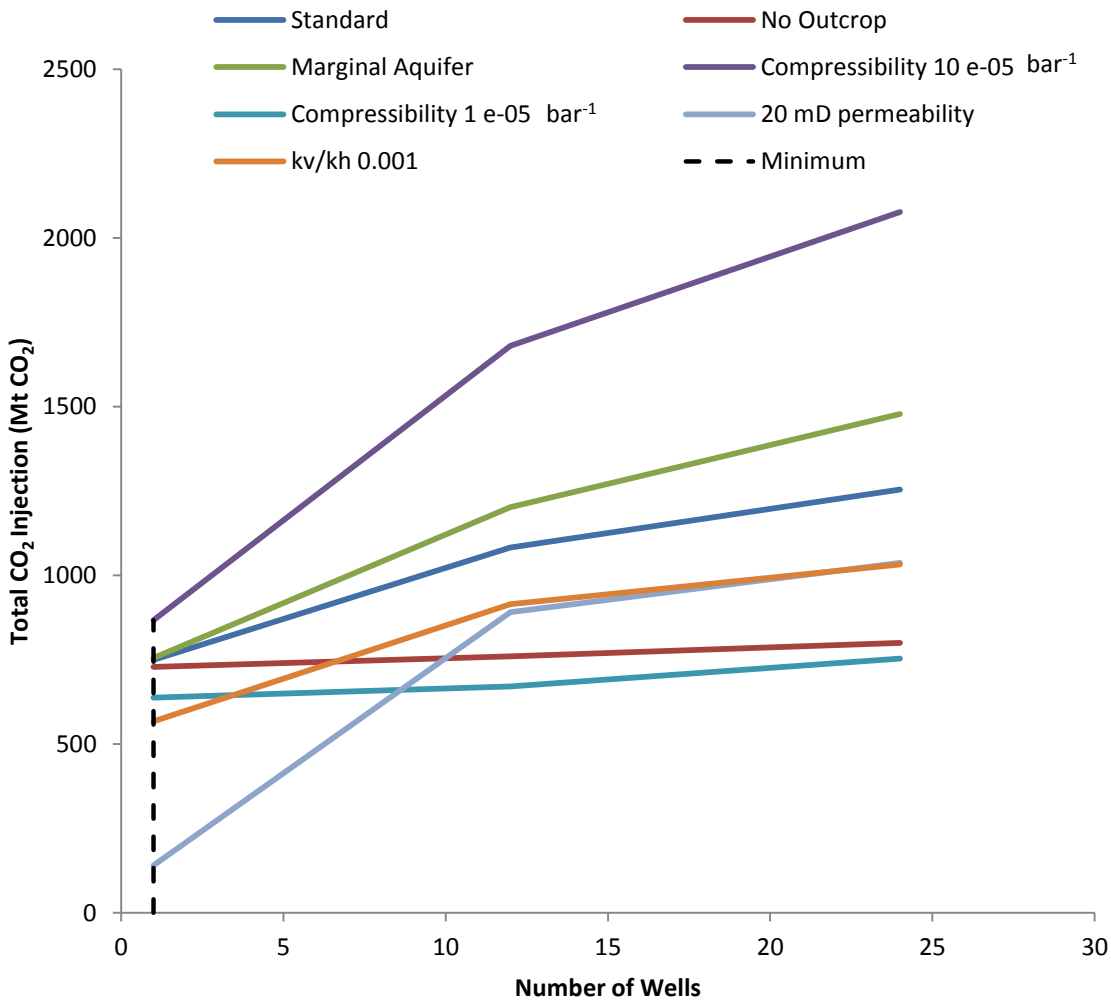

Figure 3.41 – Total CO_2 injection capacity for all modelled cases with varying well deployment density.

Table 3.3 – Table of modelled capacities for all scenarios and well numbers.

Scenario	**Wells**	**Total Capacity (Mt CO_2)**
Standard	1	749.3

Scenario	Wells	Total Capacity (Mt CO_2)
	12	1082.9
	24	1254.3
No Outcrop	1	728.3
	12	759.5
	24	800.2
Marginal Aquifer	1	755.2
	12	1202.4
	24	1478.3
Compressibility 10 x 10^{-5} bar^{-1}	1	867.2
	12	1679.8
	24	2076.5
Compressibility 1 x 10^{-5} bar^{-1}	1	637.5
	12	671.1
	24	753.4
kv/kh 0.001	1	567.3
	12	914.9
	24	1031.9
20 mD permeability	1	140.1
	12	890.6
	24	1036.5

Figure 3.42 shows the total water output from the seabed outcrop and marginal aquifers (if present) for each of the modelled scenarios for different well densities at 100 years. The graph shows three clear groups:

- the high volume output in the case with marginal aquifers which relates to the additional open boundaries available in the model, the 24 well case has a maximum total output of 1590 Mt of brine;
- the standard and compressibility cases output a similar amount, between 350 and 750 Mt of brine depending upon the well deployment and particular case;
- The lowest output is observed in the low permeability cases with the volumes being between 180 and 300 Mt for the kv/kh = 0.001 case and between 20 and 120 Mt for the 20 mD case.

As discussed in previous sections, the brine output at 100 years is only a fraction of the final volume of brine that will be expelled. In most cases, the total at 100 years simply reflects the response time of the aquifer, i.e. it may take many 100s of years for brine to stop flowing from the outcrop in the 20 mD case.

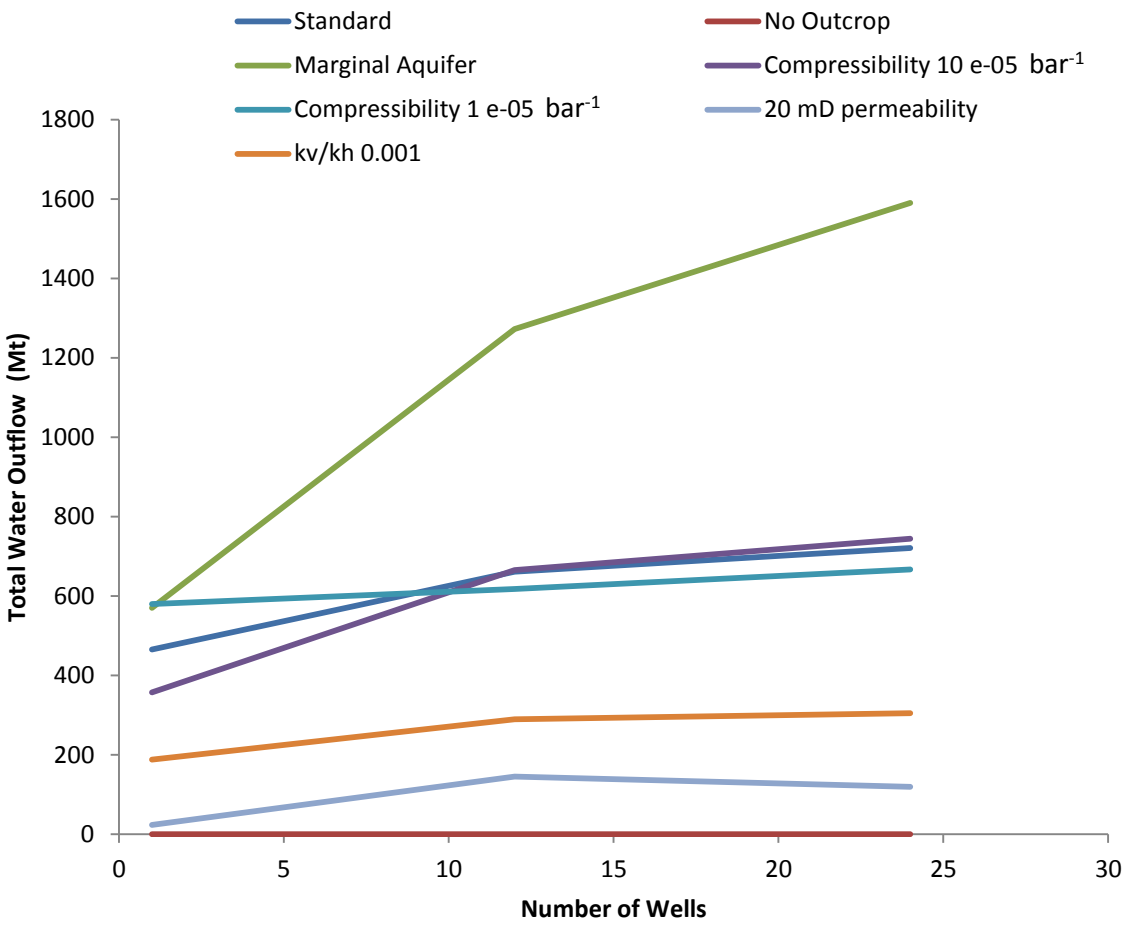

Figure 3.42 – Total brine output at 100 years for all modelled cases with varying well deployment density.

The storage efficiencies have been calculated for each of the cases for the different well density scenarios and are shown in Figure 3.43. The storage efficiencies general follow the same pattern as the storage capacities as they are essentially a non-dimensional measure of injected volume. Excluding the single well capacities the storage efficiencies range between 0.25 and 0.72% once again, the range is encompassed by the compressibility cases.

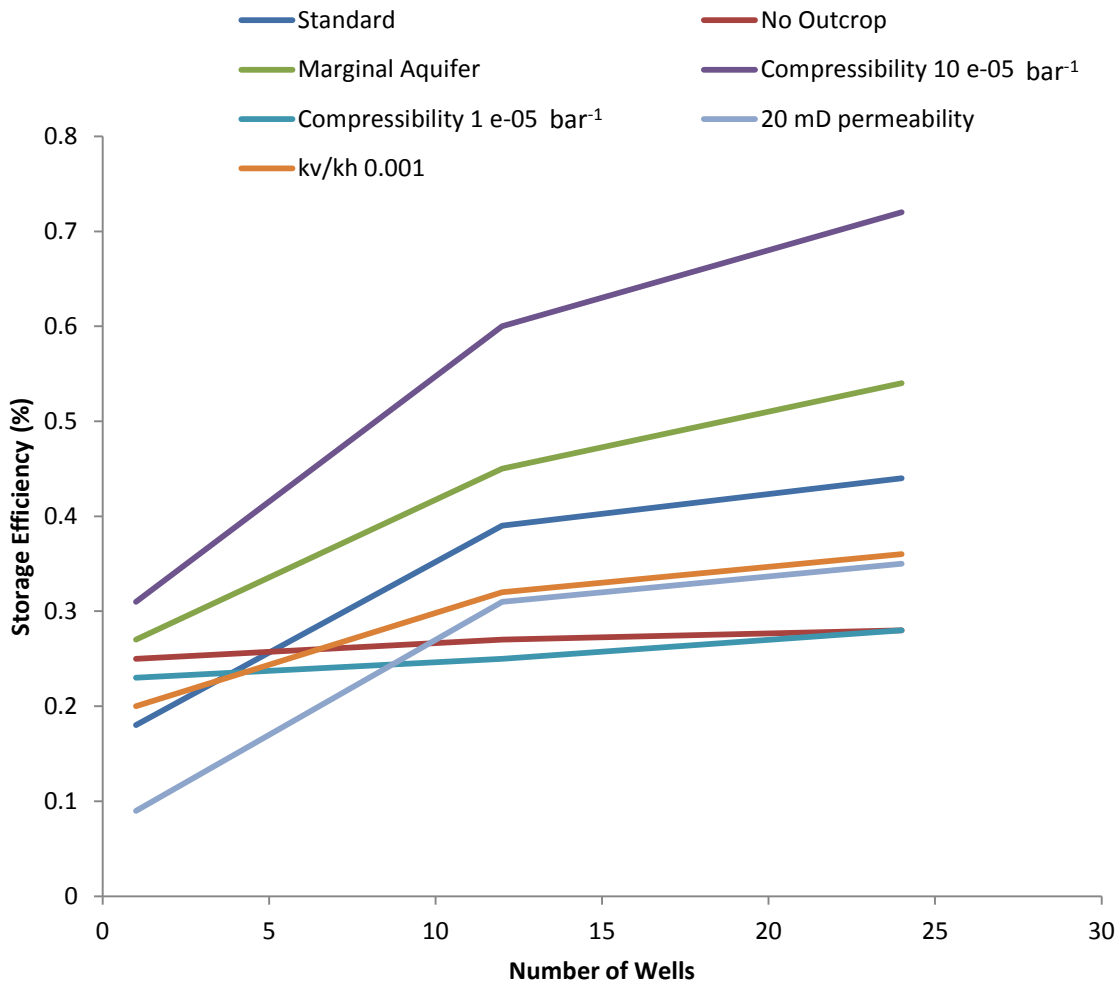

Figure 3.43 – Storage efficiencies for all modelled cases with varying well deployment density.

3.2.4.9 *Modelling Capacity Ranges and Project Cost*

Based on the well densities modelled in this study it is possible to extrapolate the potential capacity of the different scenarios by fitting curves to the response of the model. A series of curves were fitted against to data from the modelling studies. With the exception of the 20 mD model the best fit is achieved using a power law curve. The relationship for the standard base case for all wells is shown in Figure 3.44. The data was extrapolated to model a maximum of 200 wells. This is an unrealistically high well density, but is used to illustrate the trend in the modelling. In the model, 200 wells would represent wells at approximately 4 km equal spacing.

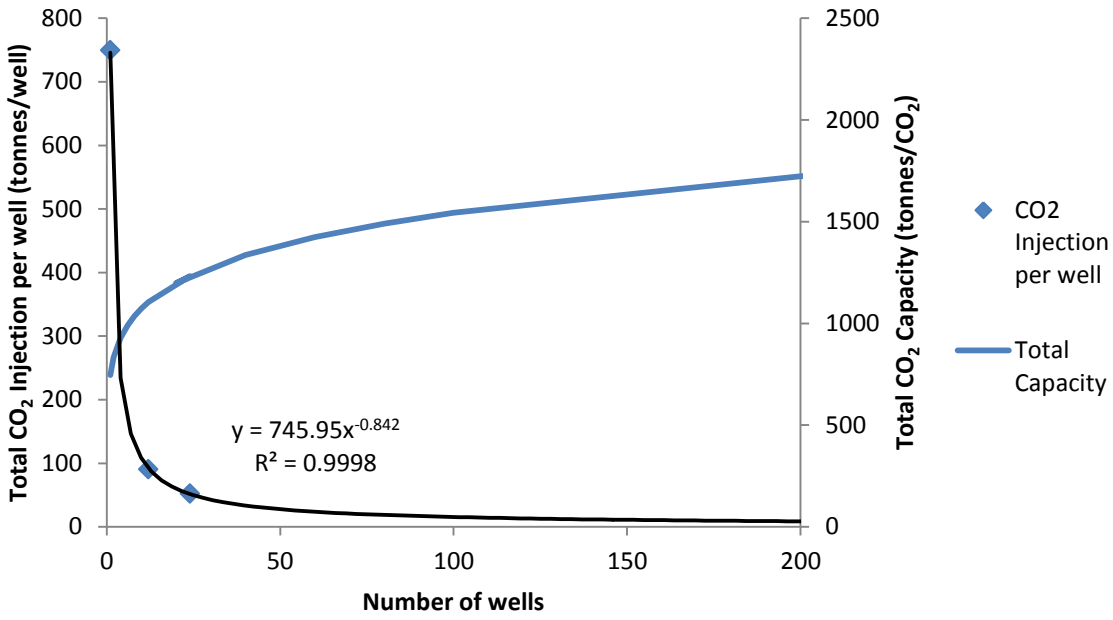

Figure 3.44 – Curve fitting for the standard model, based on the 1, 12 and 24 well runs, showing the modelled capacity using up to 200 wells.

The extrapolated capacities give a clearer illustration of the range of capacities arising from variations in the different parameters, and the effect and efficiency of increasing the well density in the model in each case. The capacities are compared for each case in Figure 3.45 extrapolated to 125 wells, which is equivalent to an equal well spacing of 5.2 km. The extrapolation shows that there is only a marginal gain in most scenarios resulting from increasing well density above 24 wells. In the standard case doubling the number of wells from 24 to 48 will only yield an extra 143 Mt CO_2 storage (in the extrapolated model). The cases where the outcrop is ineffective or where compressibility is much lower than expected will barely yield any extra capacity even with a large number of extra wells. Increasing the number of wells from 24 to 125 yields 71 Mt CO_2 extra capacity in the low compressibility case. Increasing well density is most effective in the high compressibility case where doubling the number of wells from 24 to 48 will yield 426 Mt CO_2 extra capacity.

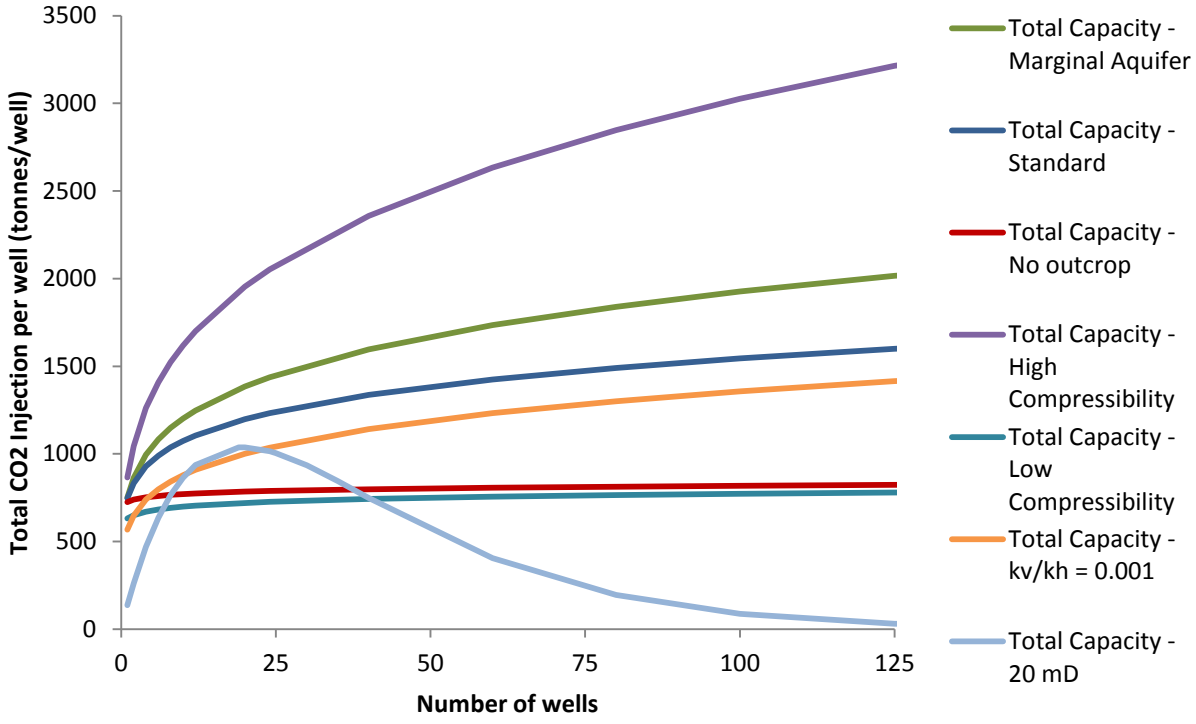

Figure 3.45 – Graph of total CO_2 injection capacity against the number of wells required to achieve capacity using extrapolated data from the models for all scenarios.

The best-fit curve for the 20 mD case was an exponential decay curve and so beyond a certain well density less capacity is predicted. The peak capacity of 1037 Mt CO_2 is reached with 19 wells. Comparison of the pressure increase plots for the 20 mD case and standard case with 24 wells in Figure 3.46 shows that pressure build-up around the wells in 20 mD case is significant. Zones of significant pressure increase around certain wells begin to coalesce (red circle in the Figure 3.46), which represents pressure interference between wells. This pressure interference is the likely to be the cause of declining capacity with increasing well density. Beyond a critical well spacing closely spaced wells make injection more inefficient. It is probable that the other cases would also exhibit the same pressure interference if high enough well densities were modelled. Therefore, the power law curves applied to the other models are likely to be a simplification of the actual behaviour of the models, but the constraints of the project do not allow a more in depth investigation.

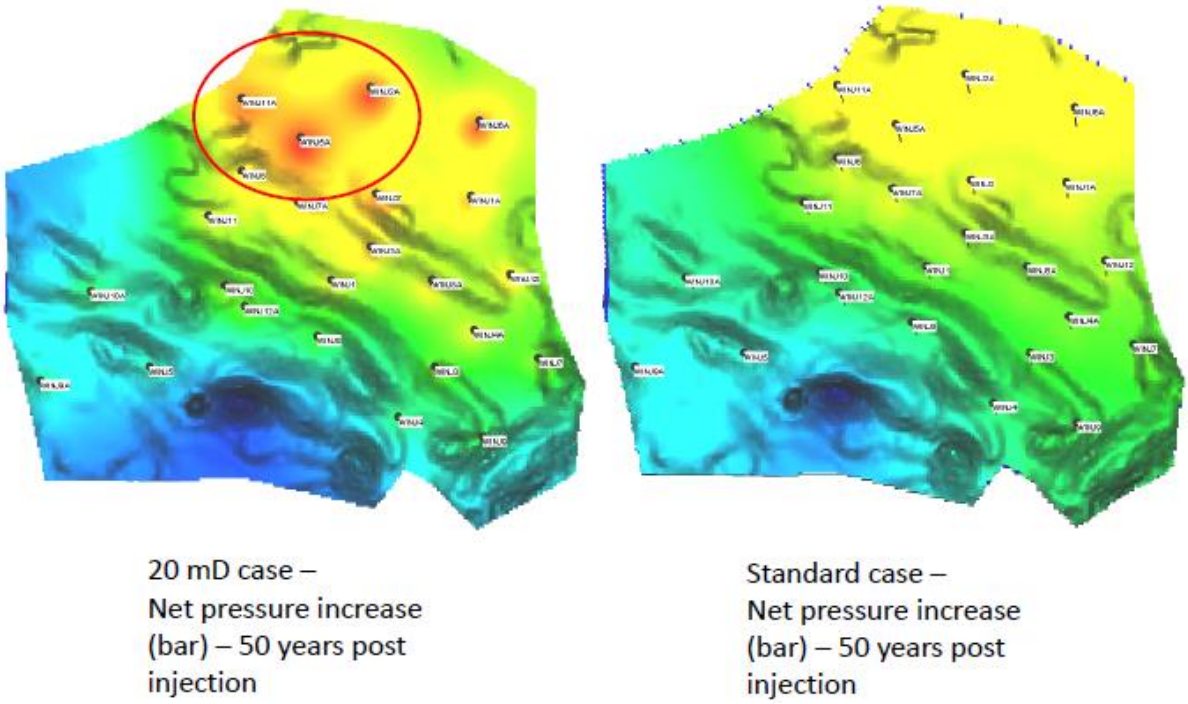

Figure 3.46 – Comparison of 20 mD and standard case with 24 wells, the red circle indicates a zone of pressure build-up interference between 3 of the wells in the northern area of the model, reducing the efficiency of the injection.

To put the capacity modelling data into context in terms of economic feasibility and efficiency for various scenarios it is possible to apply a simple costing analysis to the data by applying a well cost to simulate the likely magnitude of storage project costs. A well cost of £100 million was assumed based on the proposed (now shelved) Baird gas storage project where 14-16 wells were proposed at a cost of £1.5 billion for the entire project (RPS Energy 2009, IMechE 2013). Figure 3.47 shows a plot of CO_2 storage costs per tonne, against potential storage capacity of the standard scenario using this cost analysis, the data in the figure is extrapolated for 200 wells.

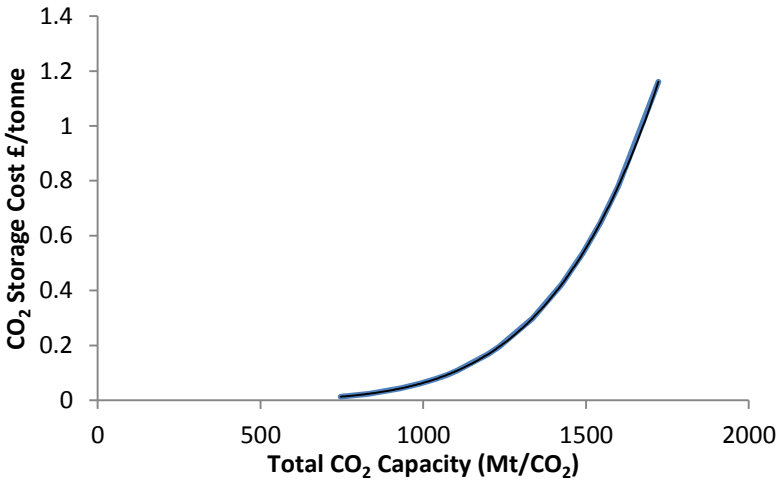

Figure 3.47 – Graph of modelled CO_2 storage cost with total CO_2 storage capacity for the standard model case, with data extrapolated to 200 wells.

Figure 3.48 shows the cost/capacity plot for all the cases analysed across the different well densities for a cost of £100 million per well. The figure highlight the feasibility of different capacity ranges for each of the scenarios, and the cost and capacity range that may be encountered with varying reservoir parameters.

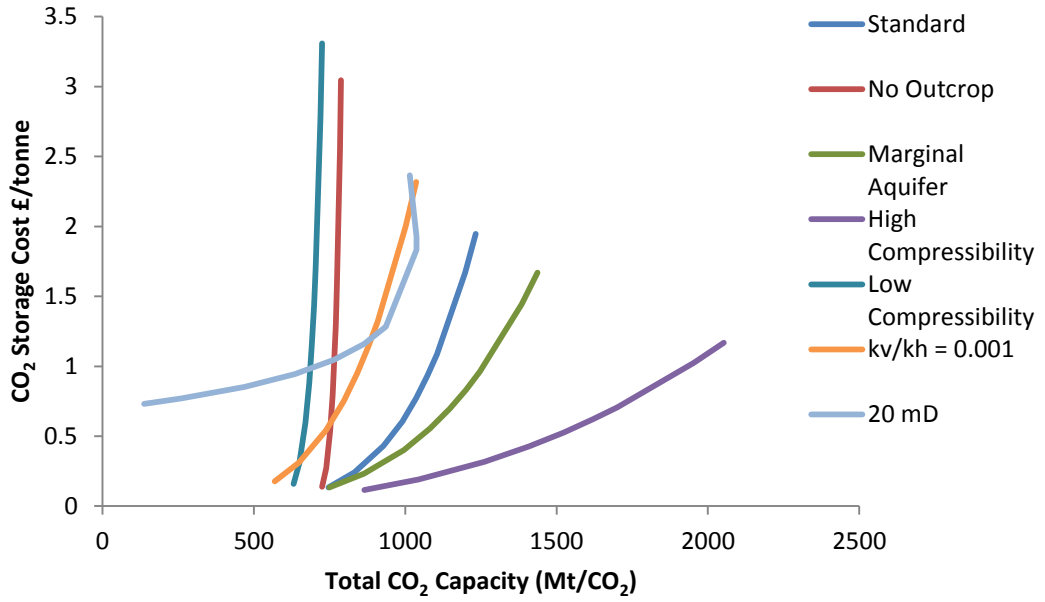

Figure 3.48 - Graph of modelled CO_2 storage cost with total CO_2 storage capacity for all cases, with data extrapolated to 24 wells for well costs of £100 million per well.

The figure of capacity and cost shown above highlights the impact of variable parameters in the reservoir on the viability of a project. The case with low compressibility has very limited capacity and adding additional wells at great expense contributes negligible additional capacity. For the low compressibility case the cost of storing 630 Mt CO_2 with one well is 0.15 £/tonne with 1 well rising to 3.30 £/tonne for 725 Mt CO_2 using 24 wells. The no outcrop case costs 0.13 £/tonne for a single well to 3.04 £/tonne for 24 wells increasing capacity from 725 Mt CO_2 to 787 Mt CO_2. For the 20 mD case the benefit of installing additional wells up to a certain level is clear. With one well, the cost for storing 136 Mt CO_2 with one well is 0.73 £/tonne, yet capacity can be increased almost 8 times to 1036 Mt CO_2 for a cost of 1.83 £/tonne using 19 wells, for 2.5 times the cost. The profile of the 20 mD case also shows that a well penetration above 19 wells is inefficient and capacity actually declines with more well penetration. The remaining cases do show significant increase in capacity, but for a significant increase in cost. For the kv/kh = 0.001 case, capacity can be increased by 1.8 times from the single well to the 24 well density, but the cost increase to achieve this is roughly 13 times as much as for the single well from 0.18 to 2.31 £/tonne. For the standard case the capacity increase is 1.65 times the single well case, for a cost increase factor of 10, rising from 0.13 £/tonne for the single well to 1.94 £/tonne for 24 wells. The marginal aquifer case capacity increase factor is 1.9 and the cost increase factor is 13 (0.13 to 1.70 £/tonne). The best performing case is the high compressibility case with an

increase in capacity 2.4 times, with a cost increase factor of 10, with storage costs of 0.12 to 1.17 £/tonne.

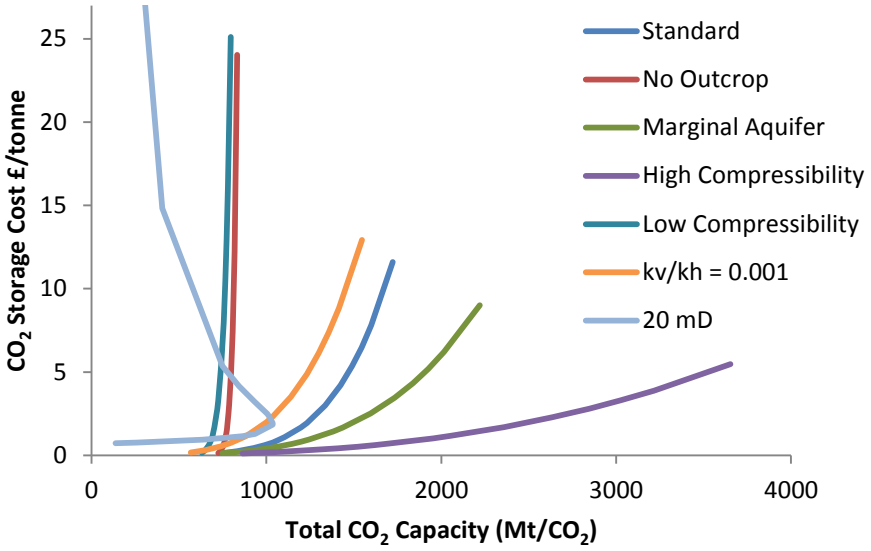

Figure 3.49 - Graph of modelled CO_2 storage cost with total CO_2 storage capacity for all cases, with data extrapolated to 200 wells for well costs of £100 million per well.

Figure 3.49 shows the cost data extrapolated to 200 wells to illustrate the range in costs and capacities modelled. An important caveat is that these data do not necessarily reflect the behaviour of the model with increasing well density, and at some point it is likely that a critical well density will be reached which will reduce injection efficiency as in the 20 mD case. The graphs of cost against capacity such as Figure 3.49 also show the significant impact on capacity and cost of the compressibility of the model, with higher compressibility leading to much lower storage costs, and low compressibility making storage impractical. Figure 3.50 and Figure 3.51 are plots of compressibility with storage cost (£/tonne) and storage capacity, for the extrapolated data up to 200 wells. The figures illustrate the impact of compressibility on both cost and capacity. With a decrease in compressibility in the model the increase in cost is exponential, and is accompanied by a similarly non-linear exponential decrease in storage capacity. The trend of capacity versus compressibility is however linear using 24 wells or less, only the 100 and 200 well cases show exponential increase in capacity with compressibility. The trend is more pronounced in models with greater well penetration due to the inherent cost in additional wells.

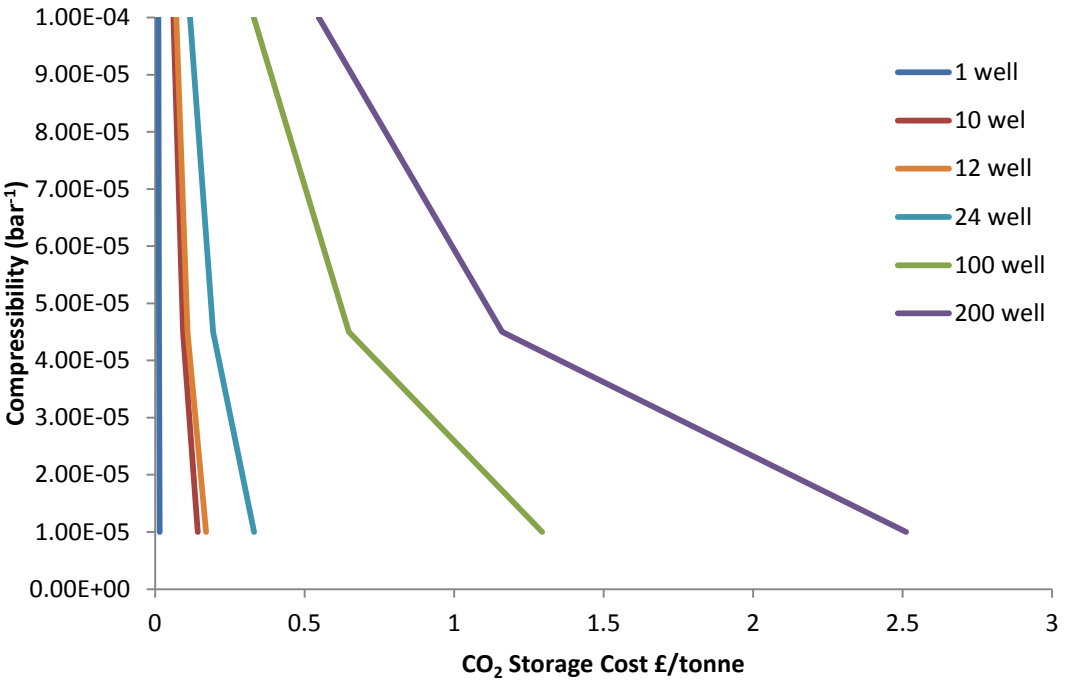

Figure 3.50 – Cost of CO_2 storage per tonne with varying compressibility extrapolated for different well penetrations.

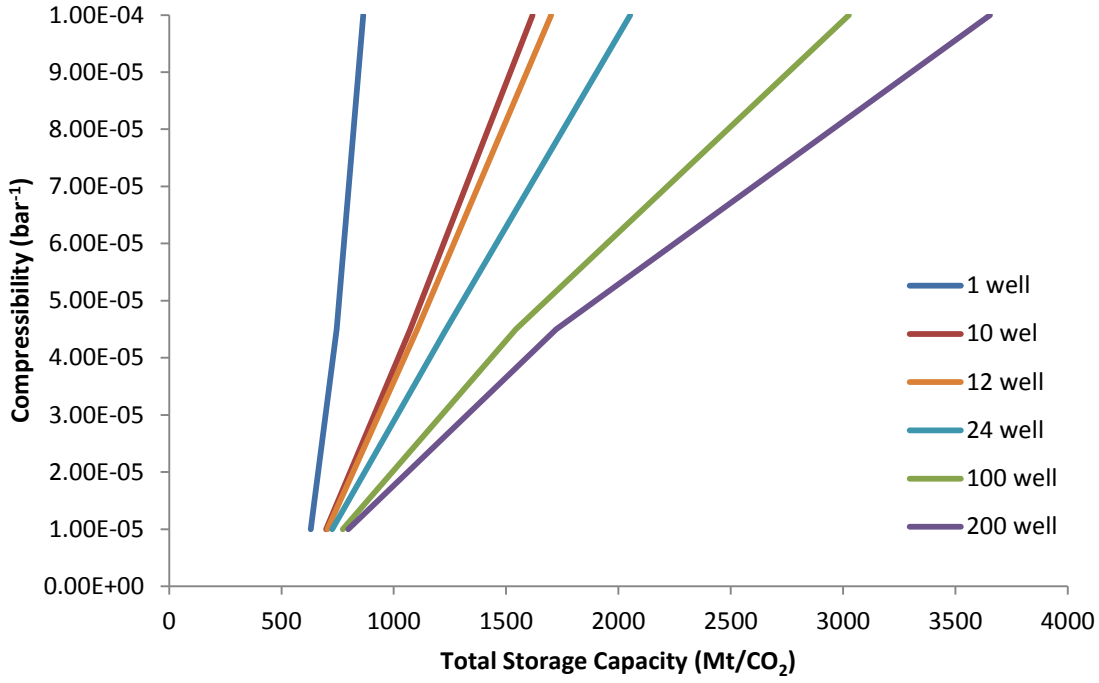

Figure 3.51 – Total storage capacity with varying compressibility extrapolated for different well penetrations.

3.3 **Discussion**

3.3.1 **Pressure Cell Model and Brine Extraction**

The results sections illustrate the impact of brine removal on potential storage capacities within the generic pressure cell model. The base case model also provides estimates of capacity with no brine production. Discussion of the effectiveness and practicality of the brine extraction is required to place the capacity estimates in context. For example, very low rates of brine extraction may be inefficient due to the high numbers of wells required. Table 3.4 shows a comparison of the different cell sizes, the total number of wells, flow rate, capacity and storage efficiency for all of the cases analysed. The base cases are highlighted in blue. Due to the 1:1 injector to producer ratio the base case models have half the number of wells than the cases with brine production (highlighted in red). First, the base case results are compared with similar studies from the literature.

3.3.1.1 *Capacity Estimates*

The summary in Table 3.4 shows that the modelled capacity for the base cases range from 2.38 – 5.38 Gt CO_2 for the low fracture pressure case, to 5.92 – 11.27 Gt CO_2 for the high fracture pressure case. Storage efficiencies for the two cases range between 0.19 – 0.85% for the base cases. With brine extraction the modelled capacities are between 2.39 Gt CO_2 and 13.42 Gt CO_2 for the low fracture pressure case and 5.92 Gt CO_2 and 19.69 Gt CO_2 for the high fracture pressure case. The highest capacities are for cases with 488 injection and production wells, where the highest storage efficiency was 1.48%. The upper estimates with brine extraction are very high, and exceed the 14 Gt CO_2 capacity predicted for a static assessment in Holloway et al. (2006a) of storage within structural closures.

The results can be compared with the pressure cell model of Heinemann et al. (2012). Heinemann, Wilkinson et al. (2012) use a slightly higher fracture pressure (225 bar) than the lower fracture pressure case presented, and a higher permeability (250 mD) and unknown compressibility. Heinemann et al. (2012) calculate a capacity of 7.8 Gt CO_2 using 259 wells at a spacing of 14.8 km. In this study the most similar case for comparison is the smallest model cell size of 15.24 km with 244 wells and fracture pressure limit of 212 bar (64% lithostatic), this model yields a lower capacity of 5.38 Gt CO_2 . The combination of higher permeability, higher fracture pressure and consideration of CO_2 dissolution may explain the higher capacity in the study by Heinemann et al. (2012). Heinemann et al. (2012) do not report the compressibility used in their model, if this is higher than the compressibility used in this study this would also lead to a higher capacity. Purely based on modelled capacity the most similar case to the study by Heinemann et al. (2012) is the cell sized at 15.24 km with 1000 m^3/day of brine withdrawal. In this case the storage efficiency of 0.58% matches that modelled in their study.

Table 3.4 – Summary table for modelled capacities and storage efficiencies of Bunter generic model.

Cell size (km)	Number of Wells	Brine Flow Rate (m^3/day)	Capacity (Gt CO_2) at 212 bar	Capacity (Gt CO_2) at 264 bar	Storage Efficiency (%) fracture pressure 212 bar	Storage Efficiency (%) fracture pressure 264 bar
15.24	244	0	5.38	11.27	0.42	0.85
15.24	488	100	5.57	11.48	0.44	0.86
15.24	488	250	5.87	11.79	0.46	0.88
15.24	488	500	6.36	12.31	0.50	0.92
15.24	488	1000	7.35	13.35	0.58	1.00
15.24	488	2000	9.35	15.46	0.74	1.16
15.24	488	4000	13.42	19.69	1.06	1.48
30.48	61	0	4.87	10.65	0.38	0.80
30.48	122	100	4.91	10.69	0.39	0.80
30.48	122	250	4.96	10.75	0.39	0.81
30.48	122	500	5.05	10.85	0.40	0.82
30.48	122	1000	5.23	11.05	0.41	0.83
30.48	122	2000	5.60	11.45	0.44	0.86
30.48	122	4000	6.33	12.26	0.50	0.92
53	20	0	2.38	5.92	0.19	0.45
53	40	100	2.39	5.92	0.19	0.45
53	40	250	2.39	5.93	0.19	0.45
53	40	500	2.40	5.94	0.19	0.46
53	40	1000	2.42	5.97	0.19	0.46
53	40	2000	2.47	6.02	0.20	0.46
53	40	4000	2.55	6.13	0.20	0.46

The results from the Bunter model used by Noy et al. (2012), incorporating structural closures, can also be compared to the results of this study. The results from this more realistic model must be scaled up, as it only represents a small section (13600 km^2) of the full area of the Bunter aquifer (56660 km^2). Noy et al. (2012) report an injection capacity of 0.022 Gt CO_2 /yr for a permeability of 100 mD (comparable to this study) using 12 wells with a fracture pressure limit of 75% lithostatic (261 bar at the depth analysed in this study). Over 50 years, injection at 0.022 Gt CO_2 /yr would result in 1.1 Gt CO_2 being stored. Scaling up the 1.1 Gt CO_2 capacity from Noy et al. (2012) yields a capacity of 4.3 Gt CO_2 , using 48 wells, that can be compared to the generic model results in this study. The most appropriate fracture pressure case to compare from this study is the 80% lithostatic fracture pressure case (264 bar). The cases used in this study do not match the well spacing used by Noy, Holloway et al. (2012), but the 53km and 30.48km cell sizes using 20 and 61 wells provide

an upper and lower bound. Interpolating between the upper and lower bound in the base case to find the equivalent capacity for 48 wells yields a capacity of 9.1 Gt CO_2 , which is 2.1 times greater than the capacity derived from the model from Noy et al. (2012). The base case has closed boundaries, whereas the model from Noy, Holloway et al. (2012) has an open boundary at a seabed outcrop. Therefore it seems appropriate to compare a model with brine extraction, as this can mimic the impact of open boundaries in a model. In the Noy, Holloway et al. (2012) model the brine expulsion at the outcrop is equivalent to 3500 m^3/day of brine per well in this study. Using another interpolation the capacity modelled for this level of brine extraction is 10.3 Gt CO_2 , which is almost 2.4 times greater than the adjusted capacity derived from the model of Noy et al. (2012). The model in this study uses similar parameters to the model presented by Noy et al. (2012). The large difference between capacity estimates suggests that pressure build up is not the main control in the structurally more realistic model from Noy et al. (2012). Noy et al. (2012) and Williams et al. (2013) suggest that pressure build up at the crest of structures is likely to be critical in a storage model. Any pressure increase in the aquifer will lead to failure in the crest first due to the dependence of fracture pressure on depth. The generic model lacks the capability to model pressure build up in structural highs and this is the likely explanation in the divergence of capacity estimations for the generic and structurally realistic model. The model from Noy et al. (2012) has therefore been used to model further capacity estimation scenarios in Section 3.2.

The final observation in this section relates to the comparison of the storage efficiencies with the study of Williams et al. (2013). They model storage efficiencies of between 4% and 33% and storage capacities up to 1.2 Gt CO_2 for a small section (1200 km^2) of the Bunter aquifer. The efficiencies are much higher than the efficiencies calculated in this study (all less than 1%). They focus on optimising storage in several domes using multiple wells, using around 10 wells in each of the three domes. The efficiencies and capacities modelled by Williams, Jin et al. (2013) use simulation model generic aquifers to model the remainder of the Bunter aquifer, so it is difficult to determine the increase in pressure in the rest of the aquifer. It is therefore not possible to scale up their results, as the area affected by pressure increase is much larger than just the dome models they present. As a result the storage efficiency for the total aquifer may be much lower than presented for the domes. Brine extraction may be beneficial in this case if pressure buildup in the generic aquifers attached to the simulation model is significant. They model a maximum capacity of 1.1 Gt CO_2 in the best case, which would evidently suggest a very large capacity for the Bunter, considering their model is approximately 2% of the area of the offshore Bunter. However, due to potential pressure build up outside of their model, the scaling up of this capacity is very unlikely to be linear.

The following section assesses effectiveness of brine extraction on the generic model presented in this study.

3.3.1.2 *Brine Extraction Effectiveness*

The modelled capacities for the cases with brine extraction shown in Table 3.4 can be plotted against the rate of brine production. The low-pressure case is shown in Figure 3.52 and the high-pressure case in Figure 3.53. The graphs show the range of achievable capacity for the different cell sizes and rates of brine production. The graphs show the decreasing effectiveness of brine production as well spacing (cell size) increases. The benefit of brine production over the base case in the largest cell size is small, between 0.17 and 0.20 Gt CO_2 , and requires the deployment of twice the number of wells to achieve this capacity. The range of modelled capacities for the smaller cell sizes, 30.48 km and 15.24 km, overlap. Additionally, although it is not clear from Figure 3.52 and Figure 3.53 the base case capacities with no brine production also overlap the range of capacities modelled with brine production. For example, higher rates of brine production 30.48 km cell size can achieve the same capacity as the lower brine production rates in the 15.24 km cell size when the larger cell size is filled to less than optimum capacity. Clearly, there is a case for optimisation in the solutions, as it may be beneficial to use either a higher brine extraction rate, or a greater number of wells. Figure 3.52 and Figure 3.53 can be reconstructed to determine a Pareto efficiency type plot showing the optimum capacity with different numbers of well and different flow rates. The Pareto efficiency plots are presented for both fracture pressure cases in Figure 3.54 and Figure 3.55.

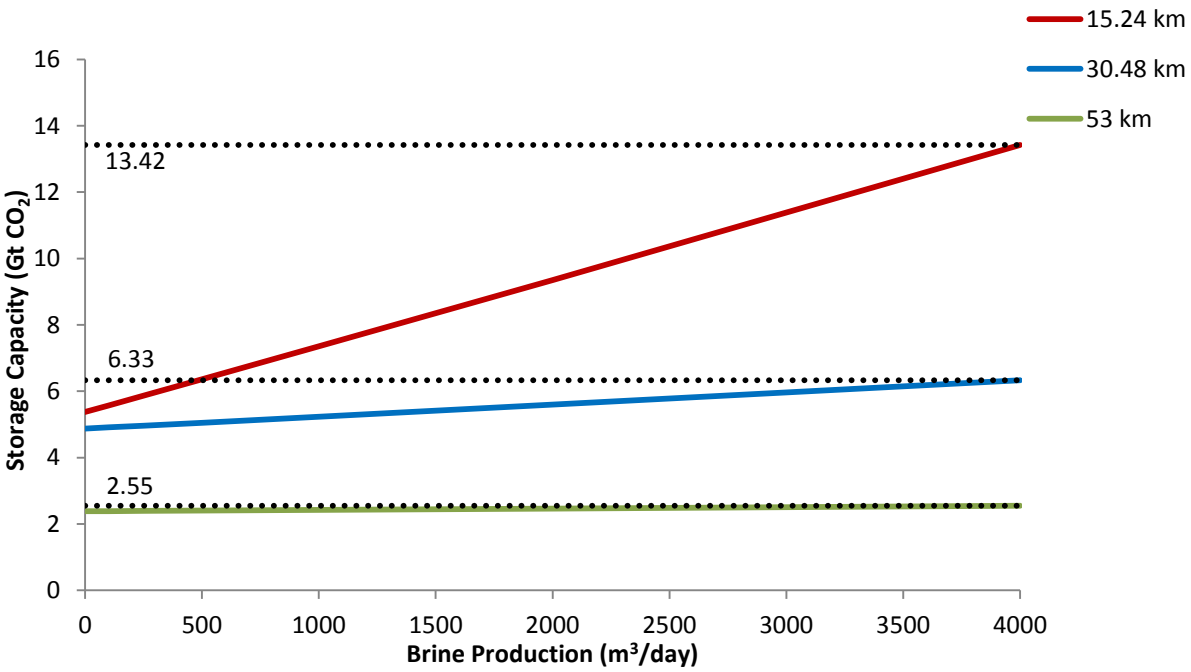

Figure 3.52 – Graph of storage capacity with brine production rate for the low fracture pressure case, dotted line shows maximum capacity of each cell size.

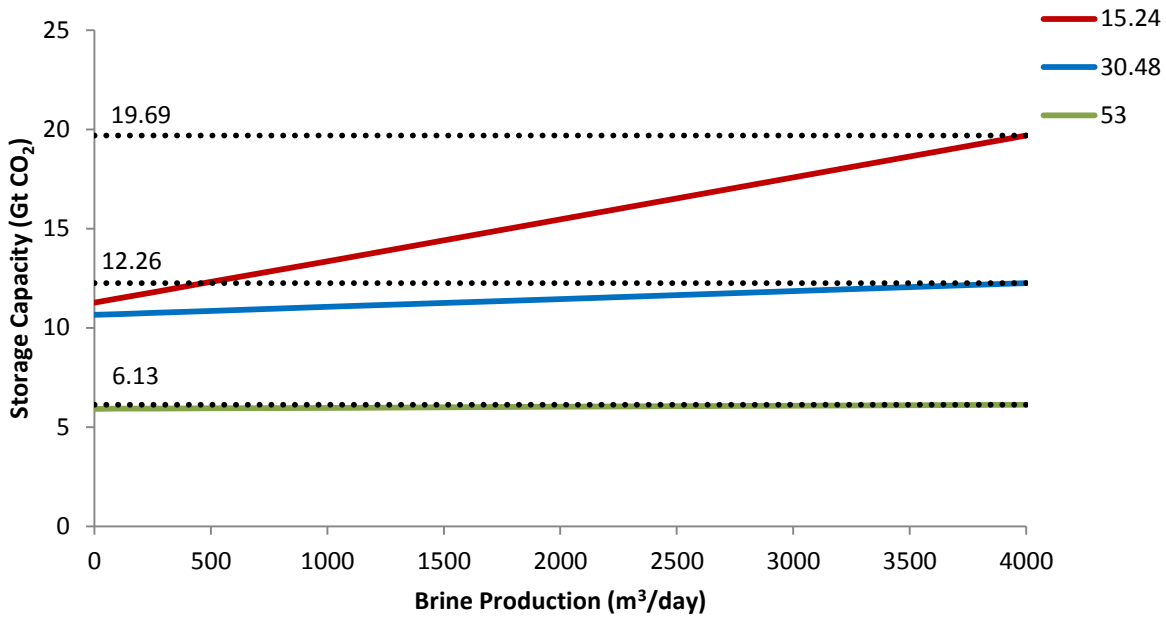

Figure 3.53 - Graph of storage capacity with brine production rate for the high fracture pressure case, dotted line shows maximum capacity of each cell size.

Figure 3.54 (low fracture pressure case) and Figure 3.55 (high fracture pressure case) show a set of curves of capacity versus number of wells for different brine extraction rates. The curves considered as a set of Pareto efficiency curves that are dependent on flow rate. All cases that lie above and to the left of the set of curves are not feasible, and those cases that lie below and to the right of a specific curve are below the maximum efficiency of that specific curve. The curve for no production (red in each figure) represents the cut off limit for the implementation of brine extraction, any cases that fall below this, are inefficient and will take more wells to achieve a desired capacity than the no production case. For both the high and low fracture pressure cases the 100 m^3/day and 250 m^3/day cases are shown to be inefficient and there would be no reason to implement brine production at the flow rates as they fall entirely beneath the no production curve. The remaining curves for both fracture pressure cases fall at least partially below the no production curve and the intersection point dictates the point at which it becomes more efficient to employ brine extraction at a specific flow rate to achieve the desired capacity. For example, the black dotted line on each graph illustrates the intersection point for the 4000 m^3/day curve and the no production curve. The no production line also indicates the capacity limits of the case with no brine production, and desired capacities above this limit will require brine extraction.

Clearly, the optimal case of brine extraction is the highest flow rate that can be achieved, this has been assumed to be 4000 m^3/day based on previous studies in the literature. The 8000 m^3/day case is shown in the low fracture pressure case, along with the maximum achievable capacity with brine extraction (on both graphs), which was attained with 60000 m^3/day of brine extraction. Optimisation of the flow rate is beyond the scope of this work, and will depend on operational parameters, for example, the stability of the well bore under high extraction rates that will dictate if the flow rate is achievable. The graphs show that the

minimum number of wells required before brine extraction should be considered is the intersection point with the maximum brine extraction line (60000 m^3/day). This corresponds to 53 wells at 4.35 Gt CO_2 capacity in the low fracture pressure case and 63 wells at 10.65 Gt CO_2 capacity in the high fracture pressure case. The more realistic case representing the maximum capacity and number of wells that should be considered without brine extraction is the intersection with the 4000 m^3/day case. For the low fracture pressure case, this corresponds to 93 wells at 4.95 Gt CO_2 capacity, and the high fracture pressure case 103 wells at 10.8 Gt CO_2 capacity. The 500 m^3/day flow rate becomes more effective than the no production case at between 122 – 123 wells and 5.04 – 10.85 Gt CO_2 capacity although as can be seen from the graph the increase in capacity is marginal. To put the capacities into perspective 4.95 Gt CO_2 is equivalent to 3.2 years of CO_2 emissions from all UK power stations and 10.8 Gt CO_2 is equivalent to 6.9 years of emissions.

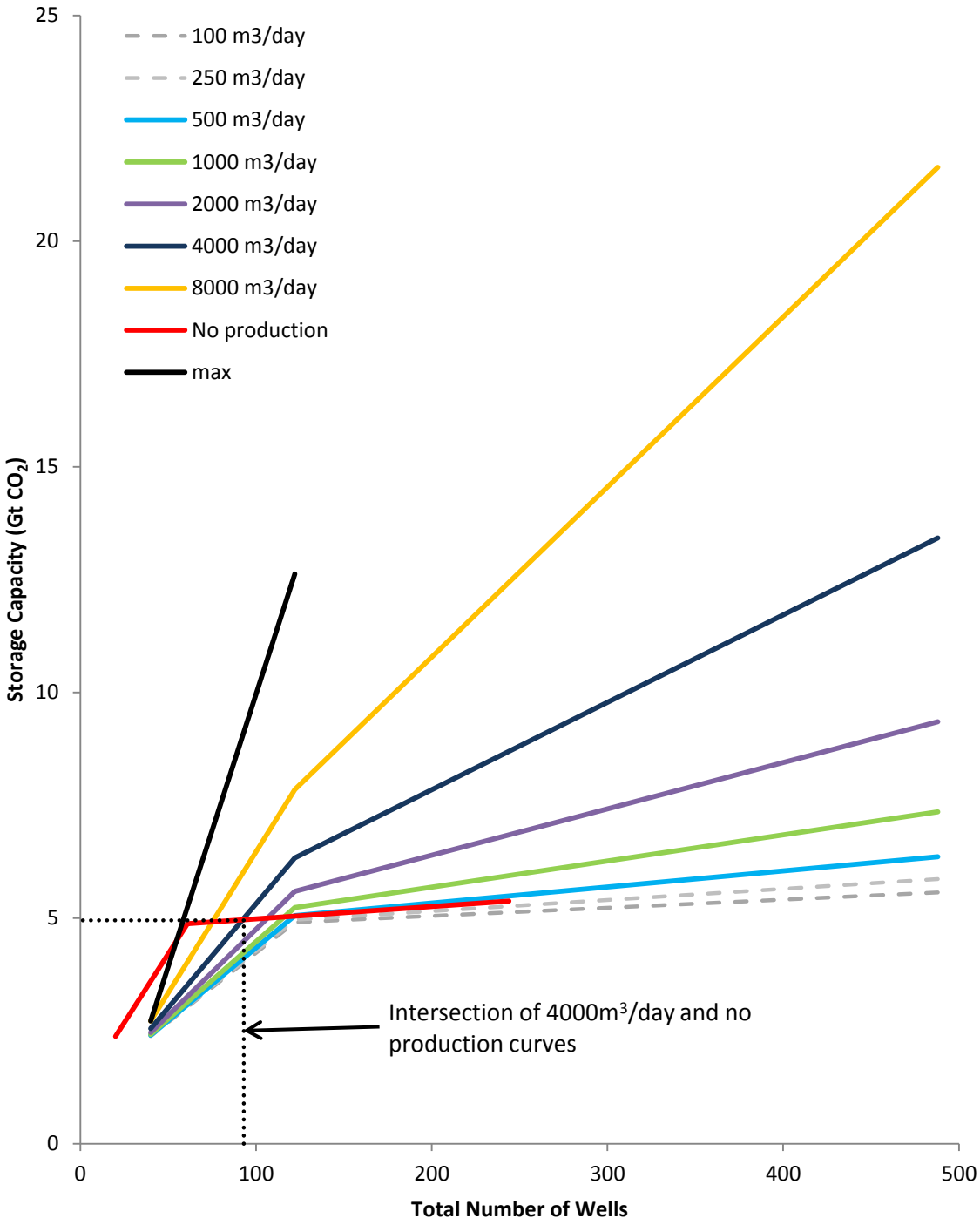

Figure 3.54 – Graph of storage capacity with number wells required for the low fracture pressure case. Dotted line represents intersection of the curves for 4000 m^3/day brine production and no production cases, intersection at 93 wells, 4.95 Gt CO_2 .

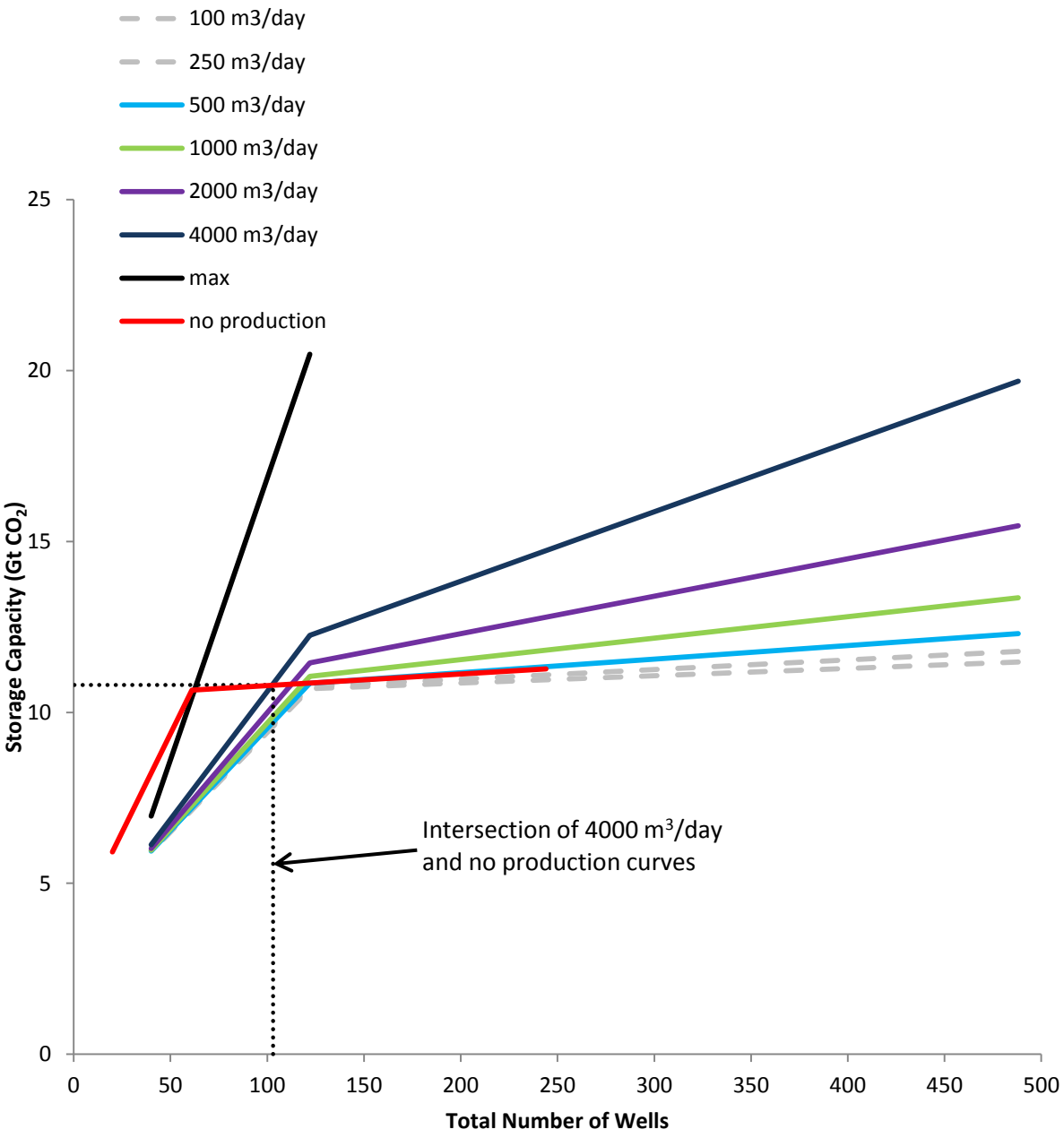

Figure 3.55 - Graph of storage capacity with number wells required for the high fracture pressure case. Dotted line represents intersection of the curves for 4000 m^3/day brine production and no production cases, intersection at 103 wells, 10.8 Gt CO_2 .

The results show that maximisation of the brine extraction rate can significantly reduce the numbers of wells required for a specific capacity for the brine extraction cases. Considering offshore wells cost millions to tens of millions of pounds per well this could be a critical consideration. The results also show that the minimum number of wells for implementation of brine production to be considered is somewhere in the region of 50 – 60 wells, which corresponds to a spacing of injector wells between 30 – 33 km. For a more feasible brine production flow rate (4000 m^3/day) the minimum number of wells for implementation of brine production would be between 90 – 100, with a spacing of between 23 – 25 km. In the study by Noy et al. (2012) they suggest that capacity may be increased by brine extraction.

However, they use 12 wells, which roughly corresponds to a spacing of 34 km in the generic model, which is greater than the threshold determined in this study for the efficient implementation of brine production. The generic model presented here also assumes closed boundaries, which is the most conservative case. The model of Noy et al. (2012) includes a likely brine outlet through the seabed outcrop, which would make brine production less critical. As previously discussed, pressurisation of structural crests is also likely to be more important than total pressure build-up.

3.3.2 **Large Scale Bunter Model**

3.3.2.1 *Overview*

The second half of this chapter has analysed the storage capacity and injection response of a more realistic model of the Bunter aquifer, which incorporates the likely structure of the field, and examines some of the potential impacts of the variability in reservoir parameters such as compressibility and permeability.

The model is derived from the published model of Noy et al. (2012) and benchmarked against the original model. Results of the benchmarking show that the derived model represents a reasonable approximation of the original model; with the same injection rate, a similar (slightly greater) volume of water is ejected from the outcrop in the derived model and total outflow magnitudes are similar. The peak brine outflow rate of the derived model is 107% of the peak outflow rate from the original model. The difference in the model could arise from several factors:

- The model is derived from the structural contours and thickness maps presented in the paper, and so is likely to include errors in the digitisation of the model which may lead to geometrical errors in the model;
- A regular grid with equal size cells is used in this study, whereas in the original model the grid size was optimised within the model;
- The well locations are not the same, and only approximately recreate the well placement in the original model;
- The CO_2 fluid formulation is not the same; different relative permeabilities are used, and different internal algorithms are used to calculate CO_2 properties;
- Simulator differences can often lead to discrepancies between modelling results from different algorithms. For instance, by default Tempest will use linear compressibility terms in calculations (e.g. pore volume) unless specified otherwise, whereas Eclipse uses quadratic terms by default, and thus there may be some unspecified algorithmic differences in the TOUGH2 simulator used for the original model and the Tempest model presented here.

Noy et al. (2012) acknowledge that their original model was a first approximation built on many assumptions, and so the discrepancies between the original model and that presented here are less important. The purpose of the modelling was to assess the capacity

and controls on capacity in the aquifer using a more sophisticated model than the initial generic pressure cell model. A series of reservoir parameters were explored for various different scenarios, including differing boundary conditions, different well densities, two different injection rates and the application of a well pressure control.

The modelled capacities varied widely within and between different scenarios. The capacities were modelled for a single well up to 24 wells. For the standard scenarios with the outcrop acting as an open barrier the modelled capacity is between 750 Mt CO_2 for a single well and 1254 Mt CO_2 for 24 wells. The capacity is between 728 Mt CO_2 and 800 Mt CO_2 with the outcrop acting as a barrier to flow in the model. The modelled capacity in case with the lower bound compressibility of 1 x 10^{-5} bar^{-1} is between 637 Mt CO_2 and 753 Mt CO_2. For the upper bound compressibility of 10 x 10^{-5} bar^{-1} the modelled capacity is between 867 Mt CO_2 and 2076 Mt CO_2. For the case with low vertical permeability and a k_v/k_h ratio of 0.001, the capacity ranges between 567 Mt CO_2 and 1031 Mt CO_2, and with a low global permeability of 20 mD, the capacity ranges between 140 Mt CO_2 and 1036 Mt CO_2.

A simple costing was applied to the storage capacities by using estimates of cost for a similar sized gas storage project. Costs of storage ranged between £1.17 and £3.30 £/tonne for the models with 24 wells, based on a 2008 estimate of well costs. The highest costs are associated with the low compressibility and cases with a no flow boundary at the outcrop, and the lowest cost is associated with the high compressibility case and the case with marginal aquifers. Estimated costs of storage of between £7.90 and £8.70 £/tonne (2008 prices adjusted for historic exchange rate) are given by Company (2008), these are significantly higher than those derived from this analysis. It is difficult to compare the costs, as the estimate from the literature is not accompanied by a full methodology. However, the estimate from the literature does incorporate monitoring (including a period equal to the operating lifetime of the project after project closure) and operating expenditure (OPEX) costs, whereas this analysis is based only on capital expenditure (CAPEX) costs. The monitoring and OPEX costs appear to add roughly 40% to the cost in the literature analysis. Adjusting that values in this analysis based on monitoring and OPEX gives vales between 1.90 and 5.33 £/tonne. Additionally, it is not clear what capacity is assumed for each well in the literature, as this will have a significant impact on the cost per tonne. The large size of the Bunter model and the significant capacity would mean that costs should be low and this is mentioned as an important factor in Company (2008) in reducing the cost of storage. They also assume only one storage project per emitter, which is clearly more costly than assuming storage in the entire Bunter Aquifer using only one project (lower CAPEX., this would also impact the assumed storage capacity per well. The costing exercise is speculative as it cannot be based on real world example, and is most useful in illustrating the economic impact of factors such as low compressibility and lack of pressure relief on a project, rather than to provide definitive values of cost for storage in the Bunter.

Overall, the results show that with single well injection, the capacity is dominated by well pressure constraint on the well flow rate, whereas the multiple well scenarios are controlled by the fracture pressure limit on pressure build-up in structural highs throughout the model. The fracture pressure is difficult to predict, as accurate assessments can only be made from leak-off and mini-frac tests in wells, this is especially difficult and costly (and unlikely to be carried out) over such a large area, and means that this presents a significant risk for implementation of multiple wells. This behaviour means that in the single well scenario the injection well is able to operate at maximum capacity, whereas in the multiple well scenarios the wells are only able to operate at reduced capacity to prevent exceeding the fracture pressure. This observation explains the pattern of diminishing returns on capacity increase with increasing well densities in the model. Extrapolation of the capacity trend with number of wells shows the diminishing effectiveness of adding extra wells into the model beyond the number of wells analysed in this study. The trend of capacity with well density appears to obey a power law for most of the scenarios analysed. However, the cases where the global permeability was set to 20 mD appear to obey an exponential decay curve, with capacity in the model diminishing when more than 19 wells are implemented. The exponential decay in capacity results from wells being so closely spaced that they interfere with each other due to the well pressure control limit reducing injection in each well to remain below the fracture pressure limit. Further data would be needed to determine if this pattern is applicable to all of the scenarios rather than just the 20 mD scenarios, but it seems logical that this would be the case. The results show that brine extraction wells would only be effective if targeted to reduce pressures in the structural high points that dominate the point of failure in the model or for very high well densities. Elsewhere in the model, the risk of exceeding the fracture pressure is low as the injection rates are by necessity kept low to prevent excessive pressures in the structural high points.

In most of the scenarios analysed a well pressure control was applied to prevent injection exceeding the fracture pressure at the well. The cases without well pressure control were mainly used to compare the reconstructed model with the original, as it was not apparent that this control was applied in the original model. The base-case comparisons were run with and without a well pressure control, to compare the difference, in all other runs a well pressure control was applied. The difference in capacity between the unrestricted base case run and the same run with a pressure control was only 0.22 Mt $CO_{2,}$ which is a 0.1% reduction on the unrestricted case. The well pressure control only affects the injection rate when it is too high and the pressure cannot be dissipated quickly enough in the area around the wellbore. In the base-case scenarios, the injection rates used were generally too low to cause the wellbore pressure to exceed the fracture pressure. However, the application of a well pressure control is essential to prevent exceeding the fracture pressure with elevated injection rates and adverse reservoir properties and so was applied in all other cases. The application of the pressure control allowed multiple cases to be run without the need to consider risk of fracturing occurring at the well bore and staged injection strategies. The well pressure control was only significant in cases where the injection rate was maximised based

on the pressure limit, which was only important for the single well cases and for the case with the global permeability set to 20 mD. The well scenarios do not take account of the flow capacity of each well, for example, whether the flow rates modelled could be sustained by the pipeline infrastructure and well platforms. However, multiple wells in a single location could achieve a similar effect to a single well if infrastructure issues were a problem.

The well flow rates in each of the scenarios were generally kept constant. However, it was found that the optimal solution to maximise capacity in some cases was to lower the well flow rate in the well closest to the failure point in the model (generally well 4). Reduction of specific well flow rates allowed flow rates in the other wells to be increased without breaching the fracture pressure and thus increased capacity. Due to time constraints, a systematic investigation of this capacity increase was not undertaken. The capacity increase from specific well flow rate reduction is however limited, as the pressure increase from other wells inevitably affects the fracture pressure limit at the failure point. This observation suggests that well flow rate optimisation would be an interesting area for further research and shows how technical factors of increasingly complexity affect the capacity estimation as the detail of the model increases.

3.3.2.2 *Monitoring*

To confirm that the fracture pressure was not exceeded in each scenario the model had to be checked for peaks in pore pressure that were close to the fracture pressure limit. In all models it was found that there was a significant time lag between cessation of injection operations and the peak pore pressure that came closest to the fracture pressure limit. The peak pressures in terms of fracture pressure failure occurred in structural highs, generally the location to the south of well 4. Lag times of 6 to 9 years were common in the models with at least one open flow boundary and good flow properties. With low permeability and closed flow boundaries lag times of between 17 and 136 years were observed. This is a significant observation as it highlights the importance of forward modelling for CO_2 injection projects to ensure containment of CO_2. The failure point of the storage project is likely to be at least 5 years after injection has finished and so monitoring programs need to account for this. The results imply that a significant monitoring component in the project will be necessary just to reach the point in time at which the peak risk from injection pressures is reached. The modelled lag times suggest this post-injection monitoring period for the pressures alone will be at least 12% of the injection period, and up to 272% in the very worst scenario. The results also highlight the spatial challenge of monitoring a CO_2 storage project. The modelling shows several areas that are vulnerable to fracture pressure failure and these are spread over a 13600 km^2 model. A storage project injecting significant volumes, even if confined to a smaller portion of the aquifer, would potentially still have to account for pressure changes a great distance away from the site. This point is even more relevant when considering the model presented for this section represents only one quarter of the Bunter sandstone aquifer.

Pore pressure lag time and potential failure in the model presents several key challenges. Firstly, the monitoring technique is difficult to determine, the only method to measure the pressure is downhole monitoring, so this implies that wells at the crests of vulnerable structures would be required. However, as discussed in section 3.3.4, fracture pressure can only be measured using downhole tests, and can change with pore pressure, and the critical pressure in vulnerable structures is only likely to be approached after injection is finished at the storage location. This means that fracture pressure monitoring would be required in many different locations, this is likely to be highly costly, and unlikely to provide full coverage of risk prone areas. Secondly, the monitoring would only allow a reactive response to the pressure fluctuation and potential fracture pressure failure, as it would be occurring after injection has stopped, this would mean that rather than reducing the injection rate a remedial strategy would need to be derived. This may take the form of pressure relief wells in vulnerable structures, although uncertainty in the fracture pressures across the aquifer may necessitate multiple monitoring and remediation wells. Additionally, the remediation may not occur in the modelled locations, due to the inherent uncertainty and would result in fracture initiation, with no immediate method to mitigate the fracturing. Although this may only lead to the leakage of brine and not CO_2, this may have implications for other developments in the aquifer, e.g. pre-existing gas fields, other storage schemes. This kind of failure is also likely to compromise regulatory restrictions and demonstrate failure of the storage strategy, this also has implications for public confidence in the storage scheme.

3.3.2.3 *Permeability Variation*

The permeability is often a significant area of uncertainty in a reservoir due to heterogeneity, anisotropy and data sparsity. The lack of permeability data for the Bunter aquifer is particularly significant. In this study, the effect of variable permeability was explored using both global and anisotropic permeability variation. The effect of reducing the global permeability to 20 mD inhibits both brine and CO_2 flow in all directions. The global reduction of permeability limits flow of brine from the seabed outcrop and the marginal aquifers if they are active flow boundaries. The reduction also inhibits flow of CO_2 away from the wellbore and promotes pressure build up around the well. The capacity modelling of the 20 mD scenarios produces fairly low capacity estimates compared to the base case and cases with open boundaries, with a maximum modelled capacity of 1036 Mt CO_2 (using 24 wells). However, the likelihood of the global permeability being equivalent to 20 mD is also very low, based on observations of the permeability in the Bunter sandstone. Measured permeabilities in the Bunter range from 100-700 mD, and the Hewitt Gasfield (reservoir in the Bunter sandstone) reservoir has an average permeability of 1310 mD (Cameron et al. 1992, Brook et al. 2003). Although some areas exhibit significant halite cementation, 100 mD would seem to be a conservative estimate and 20 mD an unrealistic estimate for the average global permeability across the aquifer. To examine other possible variations in the permeability, anisotropic variation was explored using ratios of vertical to horizontal permeability. Ratios of vertical to horizontal permeability of less than 1 (i.e. lower vertical

permeability) were used as is the most likely case in layered sedimentary reservoirs. The impact of lowering the permeability anisotropy ratio was explored for different flow rates and different well penetrations, and can be studied in terms of the impact on brine flow as well as the effect on CO_2 injection flow rates and capacity. Lowering the vertical permeability inhibits vertical flow of fluids in the reservoir. This reduces vertical flow of the CO_2 once it is injected and leads to a plume that is dissipated throughout the thickness of the aquifer rather than concentrated in the upper layer. Reduced vertical permeability also inhibits the vertical flow of brine, which restricts the rate that brine can flow from the seabed outcrop and thus reduces brine outflow pressure relief. Brine outflow pressure relief is a particularly important consideration for this model, as a significant proportion of the modelled capacity is dependent on pressure relief from the seabed outcrop. For example, a capacity difference of 454 Mt CO_2 is observed between the base case and the model with no outcrop (using 24 wells). In the single well scenario the restriction on capacity of a low k_v/k_h ratio is not as significant as reducing the global permeability 20 mD. Storage capacity in the single well low k_v/k_h ratio case is 182 Mt CO_2 less than the base case compared to 609 Mt CO_2 less for the 20 mD case. However, at higher well densities, the low k_v/k_h and 20 mD capacities converge and almost identical capacities are observed. The capacities of the two cases are over 200 Mt CO_2 less than the base case for the 24 well scenario, which is >16% reduction in capacity compared to the base case. The restriction on brine outflow from the outcrop due to a low k_v/k_h leads to a significant decrease in the capacity, around 45% of the reduction observed with no outcrop in the model. For 24 wells, the reduction in capacity in a 0.1 reduction in the k_v/k_h ratio is 22 Mt CO_2 roughly one year's worth of emissions from the Drax power station. The modelling of the permeability variation reveals strikingly similar behaviour between both anisotropic and global permeability cases. Whilst not implying a correlation between the two values chosen, the modelling does show that global and anisotropic permeability can have a negative impact of a similar magnitude on capacity. The results of the modelling are important because permeability anisotropy may be more easily overlooked than low global permeability, particularly in initial modelling estimates. Due to the scale and resolution of features that can impact vertical permeability (for example shale lenses and discontinuous shale beds) vertical permeability can only be estimated accurately from core scale measurements and well logs (Begg et al. 1989, Morton et al. 2002). Begg et al. (1989) present an example of the impact of small-scale features affecting effective vertical permeability for a reservoir model in the Sherwood Sandstone. The clean sand in the study has good apparent vertical and horizontal permeability around 100 mD, however in an up-scaled model of the reservoir, when the other muddy silt, muddy sand and shale lenses are taken into account the effective horizontal permeability has to be reduced to 30-50 mD, and the k_v/k_h ratio to 0.001-0.007 to match production data. Whilst the Sherwood Sandstone reservoir case presented by Begg et al. (1989) does not provide a direct analogue to the Bunter Sandstone it does indicate the type of risk that could be encountered in the aquifer when more site specific data is available. Modelled capacities presented for a

low permeability anisotropy ratio show the impact this may have on capacity estimates in the Bunter.

3.3.2.4 *Compressibility Variation*

The compressibility of the Bunter aquifer is also a difficult parameter to determine, requiring specific field data and laboratory tests to assess accurately. This specific data is not currently available for the Bunter sandstone and so assumed values have been used in all capacity assessments of the aquifer to date. Most assessments that have included consideration of the compressibility have used a value of 4.5×10^{-5} bar^{-1}, as used for the base case in this model and the preceding generic model. There is no evidence to suggest whether this is a reasonable estimate for the Bunter aquifer, and so a feasible range of compressibility values from the literature was selected to assess the impact of variability in compressibility on the capacity of the aquifer. The compressibility was varied between 1×10^{-5} bar^{-1} and 10×10^{-5} bar^{-1} and the capacity for 1-24 wells assessed for this range. Except for the single well case, where the lowest capacity is observed in the 20 mD case, the compressibility scenarios produced the highest and lowest estimates of capacity observed in all of the modelling scenarios. Using 24 wells the high compressibility scenario produces over 0.8 Gt CO_2 more capacity than the base-case, the low compressibility produces 0.5 Gt CO_2 less than the base case. Using 24 wells in the low compressibility case only improves upon the single well capacity for the same case by 116 Mt CO_2. The compressibility controls the expansion of pore volume in the model with pore pressure, in high compressibility cases, the pore volume will expand more with increased pressure, and with low compressibility, less expansion occurs. Extrapolating the modelled data for 24 wells shows that a 1×10^{-5} bar^{-1} compressibility increment either side of the base case value alters the capacity by almost 150 Mt CO_2, which is roughly 11% of the base case capacity or 1 year of CO_2 emissions from UK power stations. Using 100 – 200 wells shows a non-linear relationship between compressibility and capacity with high compressibilities yielding higher capacities than would be expected with a linear trend. The extrapolated figures above 24 wells should however be treated with caution, due to the limit of well density discussed previously. The results also show that increasing the well density when the compressibility is low produces a marginal capacity increase, but is very significant when the compressibility is higher. Pressure builds up more rapidly in the more 'rigid' low compressibility case, leading to minimal impact of increased well numbers, whereas pore volume in the high compressibility is able to expand significantly with increased pressure from multiple wells. The addition of injection wells is therefore more effective in high compressibility cases. In terms of the Bunter aquifer the compressibility is an important factor to be considered. A lower compressibility than expected combined with unfavourable flow properties could seriously reduce the capacity of the aquifer for storage. Equally, higher formation compressibility could significantly increase the expected capacity for storage in the Bunter aquifer. The range of formation compressibilities considered is within the range reported in the literature for cemented to the cemented-friable sandstones. It is reasonable to expect that the compressibility could vary significantly from the base case assumption

without specific field data. Variability in the compressibility can have a serious impact on the capacity estimate, in the best case a 66% increase is observed with high compressibility, and in the worst case a 40% decrease is observed with low compressibility. This analysis and the previous analysis in the literature have also assumed that compressibility is constant throughout the aquifer. In reality, over such a large area, the compressibility is likely to be variable, further complicating the capacity estimate. For example, areas with significant cementation may be linked with lower compressibility values (Fatt 1958, Yale et al. 1993, Crawford et al. 2011). Additionally, the single value of compressibility does not take into account interaction of the reservoir and overburden system. For example, overburden stress arching can reduce the rate of increase of vertical effective stress during depletion, which could affect the compressibility of the reservoir system. The single value of compressibility used in most standard reservoir simulators is not able to model the interaction of the reservoir and overburden. The effects of stress arching could only be incorporated into a standard simulation by changing the compressibility for the whole system, but this would only be possible through history matching based on the response of the reservoir system. A coupled model fluid flow-geomechanical model could more accurately model the deformation in and above the reservoir, which could provide a more accurate characterisation of pore volume change. Segura et al. (2011) discuss a hybrid method that uses pore volume multiplier tables derived from coupled modelling studies to improve the modelling of pore volume changes in reservoirs with different stress paths (e.g. stress arching), without the need for full coupled modelling.

3.3.2.5 *Boundary Conditions*

The final aspect that was studied in the Bunter aquifer was the boundary conditions of the model, including the flow properties of the bounding margins and the seabed outcrop (i.e. open or sealing). In the most optimistic case, with both aquifers and the outcrop open, the capacity was more than doubled by using 24 wells, from 755 Mt CO_2 (1 well) to 1478 Mt CO_2 (24 wells). The case with no outcrop and sealed margins only achieves 728 Mt CO_2 capacity with 1 well with a slight increase to 800 Mt CO_2 with 24 wells. For 24 wells, the case with additional aquifers provides an 18% increase on the base case capacity while a 36% reduction in capacity is observed in the case with no outcrop compared to the base case. In both boundary condition scenarios the addition of more wells in the models leads to a greater divergence of the capacity estimate from the base case capacity. The boundary conditions of the model are uncertain and there is little evidence to suggest that the marginal boundaries would be either sealing, or non-sealing. In the base case model the sealed margins assumption is conservative it is reasonable to expect some brine flow through the marginal boundaries, which would improve capacities. A maximum of 0.23 Gt CO_2 of additional capacity could be expected from the open margins scenario compared to the base case scenario. The seabed outcrop has more information relating to its structure and potential flow properties. The investigation of a dome structure close to the north-west of the outcrop presented in Dingwall et al. (2013) shows that halite cement is found in the flanks of the structure but not in the crest. This is illustrated in Figure 3.56 (Dingwall et al.

2013). It is suggested that the halite cement in the crest of the structure was removed by influx of low salinity surface waters from the seabed outcrop. Whilst the brine influx dissolution theory supports the suggestion that brine flow properties in the outcrop may be good and that brine could flow from the seabed outcrop, it also indicates that the connectivity of the seabed outcrop to the Bunter aquifer as a whole could be compromised. The connectivity of the seabed outcrop may not be totally sealed, but there could be a constriction on the brine outflow from the outcrop due to halite cementation. The capacity in the models of the Bunter is significantly reliant upon pressure relief from the seabed outcrop halite and therefore cementation around the outcrop could be a significant factor in the storage capacity estimates in the Bunter. Conversely, there is also the possibility that brine outflow may occur through the marginal boundaries to a greater extent than assumed, even if the seabed outcrop was not connected effectively to the rest of the aquifer. Pressure relief from the marginal boundaries is however less significant. A test case run with only marginal aquifers and no outcrop using 12 wells, resulted in a capacity that was almost 150 Mt CO_2 larger than the no-outcrop case, but 171 Mt CO_2 smaller (a 15% reduction) than the base case (with the outcrop) and 291 Mt CO_2 smaller than the marginal aquifer case (with the outcrop). The boundary condition scenarios show that the capacity in this Bunter model is significantly reliant upon the efficiency of brine outflow pressure relief through the seabed outcrop. Pressure relief from brine outflow through the margins of the model would not fully compensate for problems with brine flow through the outcrop, but could provide up to an additional 18% capacity in the model if fully open boundaries existed.

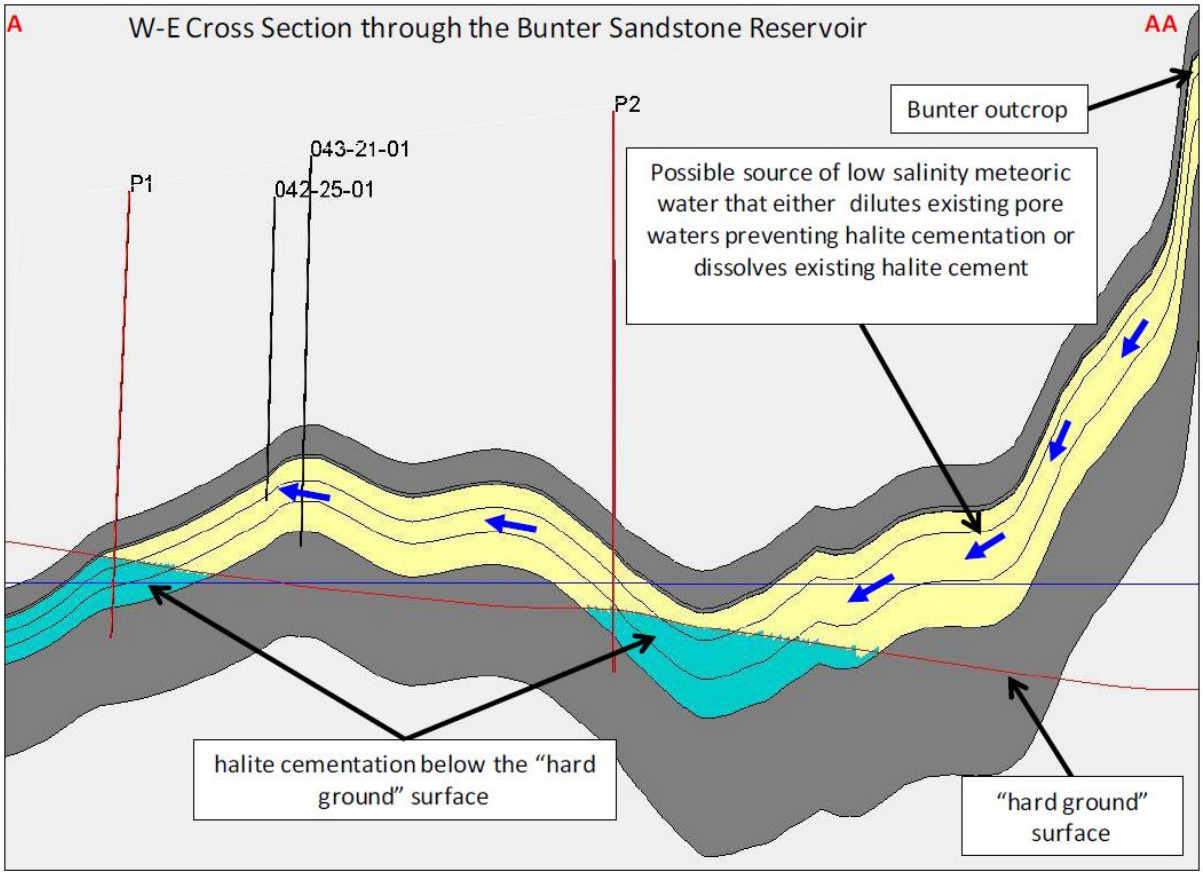

Figure 3.56 – Cross section of structure adjacent to seabed outcrop in the Bunter aquifer from Dingwall et al. (2013) showing hypothesised existence of halite made ground and cement dissolution due to influx of low salinity brines.

3.3.2.6 *Bunter Capacity Estimates*

It is possible to extrapolate the results from the sensitivity cases in the model to represent a model the size of the full area of the Bunter aquifer. This is achieved by multiplying the estimated capacities by the ratio of the area of the Bunter aquifer to the area of the large-scale model, which is 4.17. The extrapolated estimates of capacity are shown in Table 3.5 for 1 to 24 wells. The capacities for models using 24 wells range between 3.1 and 8.7 Gt CO_2 and for 12 well models range between 2.8 and 7.0 Gt CO_2 . The standard case extrapolated capacity is between 4.5 Gt CO_2 for 12 wells and 5.2 Gt CO_2 for 24 wells. The extrapolation is subject to significant errors and probably only represents an upper limit on each of the cases. Sections of the Bunter aquifer outside of the large-scale model are likely to have adverse storage properties compared to the large-scale model. For example, the area immediately to the south has numerous salt intrusions, which may compartmentalise the aquifer, provide leakage pathways and generally complicate CO_2 injection (Noy et al. 2012). Initially the range of capacities estimated appear to be similar to the capacity estimates by Heinemann et al. (2012) mentioned previously. However the fracture pressure used in the large scale model is higher (264 bar at the well) than that used by Heinemann et al. (2012) (225 bar at the well). If a lower fracture pressure was used in the large-scale model the estimated extrapolated capacities would be much lower.

Further improvements could be made to the realistic model with more resources. For example, a more complex version of the model could be developed which incorporated a stochastic analysis of the input parameters, multiple realisations of the stochastic simulation could provide more information of the sensitivity of the model to the parameters inputs. Additionally an investigation programme to gather data from a wider are in the Bunter Aquifer would also provide more accurate modelling inputs, although public availability of this type of data is unlikely to be forthcoming in the near future.

Table 3.5 – Table of extrapolated capacity estimates for the sensitivity cases in the large-scale structure based Bunter model.

Scenario	Wells	Capacity extrapolated to full Bunter area
Standard	1	3.1
	12	4.5
	24	5.2
No Outcrop	1	3.0
	12	3.2
	24	3.3
Marginal Aquifer	1	3.1
	12	5.0
	24	6.2
Compressibility 10 x 10^{-5} bar^{-1}	1	3.6
	12	7.0
	24	8.7
Compressibility 1 x 10^{-5} bar^{-1}	1	2.7
	12	2.8
	24	3.1
kv/kh 0.001	1	2.4

Scenario	Wells	Capacity extrapolated to full Bunter area
	12	3.8
	24	4.3
20 mD permeability	1	0.6
	12	3.7
	24	4.3

This section has discussed a modelled study for the potential CO_2 storage capacity in the Bunter aquifer using a more realistic structurally based model, the following section compares the results of this modelling to the generic pressure cell assessment presented in the early part of this chapter.

3.3.3 Capacity Modelling Approaches in the Bunter Aquifer

Two models for capacity estimation in the Bunter Aquifer have been examined. One model is a generic assessment without consideration of the structure of the aquifer, and based on the pressure constraint on capacity. The other model is an assessment using a model of the structure of a large section of the aquifer. The two models provide an opportunity to examine the difference between the modelling approaches and the resultant capacity estimates and reveal the likely evolution of capacity estimates with increasing data availability.

Table 3.6 shows a comparison between the generic pressure cell model presented in the first part of this chapter, and the more sophisticated full field model presented in the second half of this chapter. The models are compared based on:

- the modelled scenario;
- number of wells used in the model, including brine production wells where used;
- the total modelled capacity of the scenario;
- the area of the model per CO_2 injection well (excludes brine production wells);
- the total brine outflow from the model during injection operations;
- the ratio of brine output to the total injected CO_2 mass;
- the storage capacity per unit area of the model;
- the storage efficiency in each scenario;

- the capacity of the model normalised to the area of the Bunter Aquifer, in the small full field model the capacities are scaled up to represent the capacity for the total area of the Bunter;
- the storage cost per tonne based on a well cost of £100 million.

Table 3.6 – Comparison of performance of generic and full field Bunter models.

Pressure Cell Model – Total Area 56660 km^2									
Modelled Scenario	Number of Wells	Capacity (Gt)	Area per well (km^2/well)	Brine Outflow (Gt)	Brine output ratio (Gt/Gt CO_2)	Storage Capacity per unit area (kt/km^2)	Storage Efficiency (%)	Capacity Adjusted for Bunter Area (Gt)	Storage Cost (£/t)
No brine production	244	11.27	232.3	0	0	199.0	0.85	11.27	2.20
4000 m^3/day production	488	19.69	232.3	11.58	0.59	347.5	1.48	19.69	2.50
No brine production	**61**	**10.65**	**929.0**	**0**	**0**	**188.0**	**0.80**	**10.65**	**0.60**
4000 m^3/day production	**122**	**12.26**	**929.0**	**2.89**	**0.24**	**216.4**	**0.92**	**12.26**	**1.00**
No brine production	20	5.92	2809	0	0	104.4	0.45	5.92	0.30
4000 m^3/day production	40	6.13	2809	0.95	0.15	108.1	0.46	6.13	0.70
Full Field Model – Total Area 13600 km^2									
Modelled Scenario	Number of Wells	Capacity (Gt)	Area per well (km^2/well)	Brine Outflow (Gt)	Brine output ratio (Gt/Gt CO_2)	Storage Capacity per unit area (kt/km^2)	Storage Efficiency (%)	Capacity Adjusted for Bunter Area (Gt)	Storage Cost (£/t)
No outcrop case	**12**	**0.76**	**1133.3**	**0**	**0**	**55.8**	**0.27**	**3.16**	**1.60**
Standard	**12**	**1.08**	**1133.3**	**0.66**	**0.61**	**79.6**	**0.39**	**4.51**	**1.10**
Marginal Aquifers	**12**	**1.20**	**1133.3**	**1.27**	**1.06**	**88.4**	**0.45**	**5.01**	**1.00**
No outcrop case	24	0.80	566.7	0	0	58.8	0.28	3.33	3.00
Standard	24	1.25	566.7	0.72	0.58	92.2	0.44	5.22	1.90
Marginal Aquifers	24	1.48	566.7	1.59	1.07	108.7	0.54	6.16	1.70

In Table 3.6, two cases from the generic model and three cases from the full field model are presented. The no brine production case from the generic model is comparable to the no outcrop case in the full field model. The generic model case with 4000 m^3/day of brine production is comparable to the standard case and case with marginal aquifers in the full field model. In order to compare the two different models it is also necessary to compare models with similar well spacings, and these are highlighted in bold in the table. The comparison of model area per well shows that the 61 well case in the generic model (or 122 well with production wells) and the 12 well case in the full field model are the most comparable. The 61 well generic model has an area to well ratio of 929 km^2/well and the 12 well full field model 1133.3 km^2/well. It is immediately apparent from the table that the capacities modelled for the generic model are much greater than the equivalent normalised capacities estimated by the full field model across all comparable cases. The range of storage capacity per unit area illustrates the relative performance of the models. The generic model values of capacity per unit area range between 104.4-347.5 kt/km^2 and the full-field model value range between 55.8-108.7 kt/km^2. The generic model storage capacity per unit area exceeds almost all of the modelled values for the full field model, even the densest well spacing of 566.7 km^2/well for the full field model only yields 108.7 kt/km^2 compared to 104.4 kt/km^2 for the sparsest well spacing in the generic model of 2809 km^2/well. The storage efficiencies, a similar metric to the storage per unit area, are also consistently higher in the generic model, ranging between 0.45 - 1.48%, whereas the full field model storage efficiencies range between 0.28-0.58%. The generic model also requires less brine extraction to achieve higher capacities, with brine output to capacity ratios ranging between 0.15-0.59 Gt/Gt CO_2 and values in the full field model ranging between 0.58-1.07 Gt/Gt CO_2. The brine outflow values are not directly comparable between the two models as the generic model requires brine extraction, and the wells are shut in at the end of the injection whereas the brine flow in the full field model is due to natural pressure build up and dissipation.

It is evident that the generic model predicts much higher storage capacities than the full field model, however the differing well densities mean that the models are not directly comparable. To give a more meaningful comparison the data from the generic model was extrapolated to match the well density of the 12 well full field scenario. Table 3.7 shows the extrapolated data with the normalised capacities from the full field model, and the generic model capacities extrapolated to a well density of 1133.3 km^2/well, this equates to 50 injection wells in the generic model. The most straightforward comparison can be made between the two closed boundary scenarios, with no brine extraction in the generic model, and no outcrop specified in the full field model. The full field model adjusted capacity with closed boundaries is 3.16 Gt CO_2 and for the generic model is 9.38 Gt CO_2 . The generic model predicts a capacity that is almost 3 times greater than the full field model. The cases with brine extraction and open boundaries also show much higher estimated capacities in the generic model. Based on the volume of brine outflow/extraction, the standard full field case is most comparable to the 4000 m^3/day generic brine extraction case. The modelled

capacity for the generic brine extraction case is 10.61 Gt CO_2 which is 2.4 times larger than the 4.51 Gt CO_2 capacity modelled for the full field standard case. The brine output is however slightly larger for the full field model. The capacity of the generic brine extraction case is 2.1 times greater than the full field marginal aquifer case, but the brine outflow from the full field model is more than 2 times that of the generic model.

Table 3.7 – Comparison of generic and full field models with values adjusted to account for well spacing and area of model.

Modelled Scenario	Well Density (km^2/well)	Brine Outflow (Gt)	Up-scaled Capacity (Gt)
Generic Bunter – no brine extraction	1133.3	N/A	9.38
Generic Bunter – 4000 m^3/day brine extraction	1133.3	2.37	10.61
Full field model – No outcrop	1133.3	N/A	3.16
Full field model - standard	1133.3	2.75	4.51
Full field model – marginal aquifers	1133.3	5.29	5.01

The full field model capacities have been normalised to represent an equivalent capacity estimation for a model the same size as the full Bunter Aquifer. The normalisation does not imply that these would be achievable throughout the whole aquifer, and is merely used as a comparative tool. The remainder of the Bunter aquifer (around 43000 km^2) not included in the more realistic full field model may have attributes that reduce the capacity estimate or it is possible that this area has better storage properties, thus improving estimates. The comparison is made merely to point out the large disparity in the estimates of the models and to highlight the mechanisms leading to the differences in the capacity estimate. The two models have similar properties, for example similar permeabilities, fracture pressure magnitudes and compressibility, however the mechanism that dictates when failure occurs and capacity is curtailed is very different. In the generic model injection is efficient and continues until a critical pressure state is reached in the model. Apart from improvements that could be achieved with horizontal wells or more efficient CO_2 distribution the generic model has the maximum amount of CO_2 injected. In the full field model where the reservoir top is undulating and the fracture pressure varies with depth, the failure point is variable, and structures at shallower depths are more vulnerable to failure. The point at which failure occurs in the full field model depends upon the rate and duration of injection, and the point

at which the fracture pressure is reached in specific structures. Even if failure occurs at a specific point in the full field model, it could also be considered safe to continue injection if it was unlikely that CO_2 could reach the leak point or that it would cause a problem with regulation of the project. Failure was ignored at the top of the outcrop in the full field model, as this is unlikely to cause a problem, injection was limited to a rate the would prevent failure in any structure that could feasibly be a leak point. It is possible that a production well in the crest of the most vulnerable structure in the full field model could relieve pressure and improve capacity in the model, or that a more complex injection strategy would reduce pressure increase in vulnerable structures but these scenarios were not modelled in this study due to time constraints.

Although not directly comparable, the area adjusted capacity estimates from the full field modelling are much more similar to the low fracture pressure (212 bar) case in the generic pressure cell model. The generic pressure model case with no brine production has a capacity of 4.2 Gt CO_2 and the case with brine production has a capacity of 5.3 Gt CO_2 . This shows that the impact of considering aquifer structure is similar to reducing the fracture pressure in a pressure cell model by an additional 16% of lithostatic pressure.

Consideration of all the results presented here and other capacity estimates in the literature shows that pressure cell modelling predicts capacities for the Bunter Aquifer between 3.8 Gt CO_2 and 11.3 Gt CO_2 without brine production (Heinemann et al. 2012). The highest capacities required significant numbers of wells, in excess of 200 are required for the highest cases. Brine production adds significant capacity in the pressure cell models with very high well densities capacities of over 14 Gt CO_2 are possible, but require over 400 wells. Estimates from this study and the literature with comparable well densities, fracture pressure and other properties show that the pressure cell estimates are significantly higher than a more realistic model incorporating the structure of the aquifer. The pressure cell estimates are 3 times larger than the model incorporating structure where no brine production or open boundaries are considered and 2.1 to 2.4 larger where brine production is considered as a proxy for natural open boundaries. All of the reasonable estimates using dynamic modelling (pressure cell and realistic structure model) are significantly lower than the 14 Gt CO_2 estimate from a static assessment of pore space from Holloway et al. (2006a). Only pressure cell models with very high rates of brine extraction could achieve capacities of 14 Gt CO_2 or above. Generally, comparable pressure cell capacity estimates are around 1.4 to 1.8 smaller than the static capacity estimates, and more realistic models considering the structure predict capacities around 2 to 3 times smaller than the pressure cell estimates. The Bunter Aquifer represents 55% of offshore storage capacity in the UK by some estimates (Holloway et al. 2006a), capacity modelling shows that a reduction in this capacity of a factor of 4 is feasible. This represents a significant reduction in UK storage potential, with the further possibility that additional data collection will reduce the estimate further. Assuming the remaining UK storage potential was undiminished the modelling would indicate that the Bunter Aquifers contribution to UK storage potential could be lower

by up to 40%. This is excluding further issues with storage that may be uncovered with further exploration.

Pressure cell models are based on a fundamentally different assumption of how fracture pressure failure occurs in the model than the more realistic model, and this dictates when injection capacity is reached. The flat surface of the pressure cell means that the depth or relative depth in the model does not effect when the fracture pressure is exceeded. Whereas, in the more realistic structure based model, the fracture pressure is exceeded in structural highs first, and these areas of the model control when injection must stop. The observations of decreasing capacity with improved model quality and resolution are supported by the concept of the techno-economic resource pyramid and data and assessments scale used by Bradshaw et al. (2007), Bachu et al. (2007) and Holloway (2008) when assessing capacity estimation. The pyramid and data scale are shown in Figure 3.57 a) and b). The pyramid shows the decreasing volume of capacity that is observed when technical, legal, regulatory, economic, and infrastructure factors are taken into account. Theoretical capacity is based purely on the physical limit of a storage system, this would correspond to the static estimate of the Bunter aquifer from Holloway et al. (2006a). The effective capacity requires only technical factors to be taken into account, such as the viability of accessing particular parts of the storage system, for example storage would not occur in the outcrop sector of the Bunter model. The practical capacity includes consideration of all factors other than just technical factors, and the matched capacity requires matching of the storage locations to sources of CO_2 emissions, and would correspond to an actual storage project attached to a capture and transport project. The pressure cell and more realistic model presented here and by others represent models that advance the storage capacity estimate from a theoretical level to an effective capacity estimation. The pressure cell estimation would represent an estimate at the base of the effective capacity section, and with more information the more realistic model represents a more robust estimate further up the effective capacity section. On the graph of data and assessment scale the Bunter aquifer would lie in the regional scale, but the addition of a structure model means that the data resolution is higher, and pushes the assessment using this information more towards a local scale investigation.

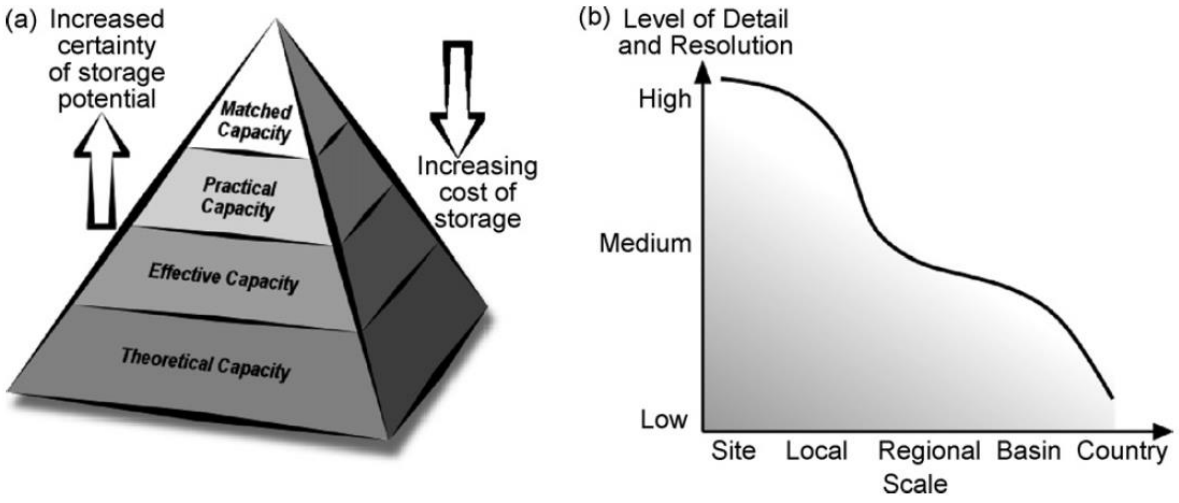

Figure 3.57 – a) Techno-economic resource capacity pyramid and b) data resolution and assessment scale graph from Bachu et al. (2007).

3.3.4 Fracture Pressure Uncertainty and Evolution

As demonstrated by both of the models the fracture pressure forms the dominant control on the capacity of CO_2 storage in the model. The generic model shows that a 20% reduction in the fracture pressure can lead to a reduction in storage capacity of up to 60%, although high levels of brine extraction with a dense concentration of wells can reduce this to as low as 32%. Recent assessments in the literature suggest that the fracture pressure could be as low as 13.4 MPa/km in the Bunter in some areas, which assuming a lithostatic gradient of 22 MPa/km, would indicate a fracture pressure of 60% of lithostatic pressure (Williams et al. 2014). This is lower than the low fracture pressure case in the generic model. The equivalent low fracture pressure case generic model capacity estimate for the structure based model is approximately 5 Gt CO_2 ; as observed in the modelling, this is roughly twice as large as the structure model estimate in general. This would suggest that a low fracture pressure, similar to that in the generic model of 64% lithostatic, could reduce the capacity estimate to 2.5 Gt CO_2 in the structure based model, roughly 50% of the capacity estimate from the higher fracture pressure used in the structure based model. This low estimate for the structure based model is also still based on a fracture pressure that is 4% of lithostatic higher (64%) than that indicated in the literature (60%), suggesting an even lower capacity estimate is likely. Applying the correlation of reduction in fracture pressure and capacity form the generic model, would suggest a further 11% reduction in capacity from the 2.5 Gt CO_2 structure based estimate. With the difference in mechanisms in the model it is difficult to justify this further 11% capacity estimate reduction without further modelling of fracture pressure variation in the structure based model.

The fracture pressure is equivalent to the minimum total horizontal stress (assuming no tensile rock strength), this is difficult to measure accurately without well testing (leak-off and mini-frac) and is generally predicted from an assessment of the likely stress ratio of horizontal to vertical stress. As already highlighted in the discussion of the large-scale

model, this means that quantifying the fracture pressure accurately even for a small area is difficult, and highlights the significant uncertainty that will be associated with the fracture pressure assessments. Fracture pressure estimation is further complicated by the fact that the horizontal stress and pore pressure can exhibit coupling, whereby the total horizontal stress changes with pore pressure. This is discussed earlier in Section 2.9.2 and in the next chapter for depletion and reinjection. This pore pressure coupling is also important for injection without an initial depletion stage, as overpressure measurements in the North Sea show that total horizontal stress can increase with increasing pore pressure (Hillis 2001). This means that fracture pressure can increase with increasing pore pressure to a certain extent.

The significant uncertainty in the fracture pressure and the associated impact on capacity is a significant risk for CO_2 storage. The uncertainty in the fracture pressure is also important for the lag effect observed in the pore pressure throughout the model discussed in 3.3.2.2. The pressure effect of the CO_2 injection will not be experienced in some parts of the model for several years after injection has stopped, the usual method of preventing a leak through hydraulic fracture is to reduce the injection pressure below the fracture pressure which allows the fractures to close. However, clearly, there will be no possibility of controlling fracturing in this way if the fracture pressure is overestimated, and as discussed in 3.3.2.2 an alternative remedial strategy must be sought, the most likely option would be targeted pressure relief wells.

The uncertainty in the fracture pressure, the observed impact on storage capacity of changes in the fracture pressure and the challenges in remediating or mitigating fracture pressure failure in large aquifer scale storage projects present a complex problem. Modelling is likely to be one of the most important methods for predicting all of these aspects, both through mechanical modelling of fracture pressure and flow modelling of storage, and this highlights the importance of the development of accurate modelling for CO_2 storage projects.

3.4 **Conclusions**

This chapter has presented capacity estimations for the Bunter aquifer for two different simulation models, including consideration of brine extraction in the first model. The key findings from each of the models are presented below.

3.4.1 **Pressure Cell Model and Brine Extraction**

3.4.1.1 *Capacity Estimates*

- The capacity estimates for the Bunter Aquifer from the pressure cell model without brine extraction pressure relief range from 2.38 Gt CO_2 to 5.38 Gt CO_2 for the low fracture pressure case, to between 5.92 to 11.27 Gt CO_2 for the high fracture pressure case, with varying well penetration densities.

- The capacities estimated with brine extraction varied widely based upon the brine extraction rate. With brine extraction, the low fracture pressure case estimated capacities were between 2.39 Gt CO_2 and 13.4 Gt CO_2 and the high fracture pressure case estimates were between 5.92 Gt CO_2 and 19.69 Gt CO_2 with varying well penetration densities.
- The highest estimated capacities with brine extraction were close to or in excess of the static estimate of 14 Gt CO_2 capacity from Holloway et al. (2006a).
- A comparable case from the literature predicts a significantly larger capacity of 7.8 Gt CO_2 compared to the equivalent estimate 5.4 Gt CO_2 from this study (Heinemann et al. 2012).
- The discrepancy between the model and estimates from the literature results from the higher fracture pressure, permeability and undefined (but probably larger) compressibility used in the study in the literature. The comparison highlights the very significant variability and uncertainty in estimates of capacity with the limited data available.
- Comparison of capacity estimates is also made with a structurally more realistic model from a smaller section of the Bunter Aquifer presented by (Noy et al. 2012) using interpolation of the results. The literature model includes brine expulsion through a seabed outcrop, and so an equivalent level of brine extraction is modelled to enable a comparison.
- The interpolated modelled capacities vary between 9.1 Gt CO_2 with no brine extraction and 10.3 Gt CO_2 with brine extraction for the pressure cell model, compared to 4.3 Gt CO_2 from the model in the literature that incorporates the aquifer structure, including structural closures. The pressure cell model estimates capacities that are between 2.1 and 2.4 times larger.

3.4.1.2 *Brine Extraction*

- Brine extraction in the pressure cell model is most effective at higher well penetration densities due to increased cumulative brine extraction volume with a higher number of wells, and to the increased effectiveness of brine extraction when wells are closely spaced and pressure signatures of each well interfere.
- Optimisation of brine extraction in the pressure cell model shows that the maximum optimal spacing for a 1:1 injector/producer ratio with a brine extraction rate of 4000 m^3/day is 23-25 km, corresponding to 90 – 100 injector and producer wells for the aquifer. Wider spacing is inefficient compared to a case without brine extraction.
- Noy et al. (2012) suggest that capacity in their model could be increased through brine production. However, optimisation of the brine extraction modelling shows that their well spacing would fall outside the optimal spacing modelled using the pressure cell study, suggesting brine production would not be necessary.
- The main mechanism of capacity restriction in the model of Noy et al. (2012) is pressure build-up in structural closures throughout the model, rather than over-

pressurisation around densely spaced wells. Therefore, brine production, as modelled by the pressure cell modelled, may be less effective.

- Analysis of a greater well density in the realistic model may give more insight into the effectiveness of brine extraction pressure relief and pressure relief in the structural closures most prone to over-pressurisation may also increase modelled injection capacities.

3.4.2 **Large Scale Bunter Model**

3.4.2.1 *Overview*

- The model presented by Noy et al. (2012) was reconstructed to further analyse uncertainty in capacity estimations using different modelling parameters and boundary conditions.
- The reconstructed model was benchmarked against the existing model using the brine outflow rates with constant CO_2 injection rates an acceptable match was achieved with reconstructed model achieving 107% of the peak outflow rates for the existing model.
- The discrepancies between the models are likely to result from different gridding techniques, well locations, simulation model properties (e.g. relative permeabilities), errors in the digitisation of structural information in the literature, and algorithmic differences between simulation software packages.
- The model represents a section of the Bunter approximately one quarter of the area of the aquifer, modelled capacities varied widely within and between different scenarios. The capacities were modelled for a single well, up to 24 wells. The capacity ranges for different scenarios from 1 to 24 wells are:
    - Standard scenario with outcrop open - 750 Mt CO_2 to 1254 Mt CO_2;
    - No outcrop in the model - 728 Mt CO_2 to 800 Mt CO_2;
    - Lower bound compressibility (1 x 10^{-5} bar^{-1}) - 637 Mt CO_2 to 753 Mt CO_2;
    - Upper bound compressibility (10 x 10^{-5} bar^{-1}) - 867 Mt CO_2 to 2076 Mt CO_2;
    - Low vertical permeability (k_v/k_h ratio of 0.001) - 567 Mt CO_2 to 1031 Mt CO_2;
    - Global permeability 20 mD - 140 Mt CO_2 to 1036 Mt CO_2.

- The wells in the single well scenarios were operating at maximum efficiency as they did not adversely impact the pressures throughout the model due to a small pressure footprint. The control on capacity in the multiple well scenarios was the fracture pressure in structural highs throughout the model. The injection rates in the multiple well scenarios had to be adjusted to prevent the fracture pressure being exceeded in the crests of certain structures within the model, and injection rates at the well were not critical.

- The injection rates in multiple well scenarios were far lower than rates that could cause the wellbore fracture pressure to be exceeded. The wells in the multiple well scenarios were therefore operating at sub-optimal injection rates.
- The rate of capacity increase with additional wells is a negative correlation, and obeys a power law relationship, with diminishing returns on additional well penetration.
- A critical point is reached with increasing well density after which additional wells inhibit injection and make scenarios with high well densities less effective. The critical point (19 wells) is modelled for the 20 mD scenario, but too few wells were added to prove this relationship for other scenarios.
- Closely spaced wells inhibit injection due to interaction of the pressure signature of each injection well causing over-pressurisation around the wells. Over-pressurisation activates the bottom hole pressure controls on the wells and lowers the injection rate in the wells.
- Brine extraction pressure relief is unlikely to improve capacities in the model unless it is targeted in the structural high points in the model, which are the locations of failure of the fracture pressure criterion.

3.4.2.2 *Monitoring*

- There is a significant lag time between the end of injection and the point at which the model is closest to failure. The lag time was at least 6 years, and varied up to 136 years, which is equivalent to anywhere between 12% and 272% of the injection period. The modelling also shows that the areas susceptible to failure may be a large distance away from the injection point.
- The modelling highlights the scale of the monitoring project required both in terms of the duration and in terms of the area that must be covered. The nature of the pore pressure change, with a significant time lag, and the uncertainty in the fracture pressure mean that monitoring will be difficult, involving downhole measurements of fracture pressure and pore pressure, this is likely to be costly, and may not achieve full coverage of risk prone areas.
- A remedial strategy is likely to be necessary as the fracture pressure changes will occur in some areas of the model after injection has stopped, meaning there is no method for preventing the fracture pressure from being exceeded in some areas of the model by switching off injection. Remediation may involve targeted pressure relief wells, although the effectiveness of the strategy would need assessment and the remediation project would potentially be a very large scale undertaking. Remediation would be especially important if areas were affected that were used by other storage projects or hydrocarbon extraction projects.

3.4.2.3 *Permeability Variation*

- Permeability was varied to reflect a global reduction in the permeability to 20 mD (presented in the original model in the literature) and a reduction in the vertical permeability to produce a k_v/k_h ratio = 0.001.
- The capacity for the 20 mD case is very low with a single well (140 Mt CO_2), flow rate is critical and the permeability restricts the maximum CO_2 injection rate. With more wells he injection rate in in the well is no longer the limiting factor as the injection rate is decreased from the maximum sustainable rate to prevent failure elsewhere in the model. With increased well densities (12-24) the 20 mD case capacities are around 200 Mt CO_2 less than the standard case.
- The capacity for the k_v/k_h ratio = 0.001 case with a single well is much higher (567 Mt CO_2) than the 20 mD case. Injection into the well is not as restricted as brine can be displaced easily in the high permeability horizontal direction, although the capacity is still 180 Mt CO_2 less than the standard case. With increasing well density (12-24 wells) the capacity estimates for the 20 mD and k_v/k_h ratio = 0.001 cases converge and are around 170 to 200 Mt CO_2 less than the standard case.
- For 24 wells, the reduction in capacity in a 0.1 reduction in the k_v/k_h ratio is 22 Mt CO_2 roughly one year's worth of emissions from the Drax power station.
- The impact of low vertical permeability on brine flow from the outcrop can be as significant as a global reduction in the permeability throughout the model. A reduced k_v/k_h ratio is considered to be the more likely scenario, as there is less information relating to effective horizontal and vertical permeabilities in the Bunter aquifer.
- A low k_v/k_h ratio could arise from thin mud lenses within the sandstone which may be below the resolution of coarse seismic data. Nevertheless, a k_v/k_h ratio = 0.001 is probably a conservative estimate as it lies at the lower end of the likely range of k_v/k_h ratios (Ayan et al. 1994).

3.4.2.4 *Compressibility Variation*

- Varying the compressibility in the model gave the largest range of estimated capacities, the high and low compressibility scenarios provide the upper and lower bound to the capacity estimates.
- The base case compressibility was 4.5 x 10^{-5} bar^{-1} with an estimated capacity of 1.25 Gt CO_2 .
- The estimated capacity for the high compressibility case, with a compressibility of 10 x 10^{-5} bar^{-1}, was 2.1 Gt CO_2 which is 0.8 Gt CO_2 or 66% larger than the base case.
- The estimated capacity for the low compressibility case, with a compressibility of 1 x 10^{-5} bar^{-1} was 753 Gt CO_2 which is 0.5 Gt CO_2 or 40% smaller than the base case.
- The increase in capacity with compressibility is approximately linear for 1 - 24 wells. In the 24 well case a 1 x 10^{-5} bar^{-1} change in compressibility is accompanied by a

150 Mt CO_2 change in capacity, this is approximately 11% of the base case capacity, or 1 years' worth of emissions from UK power stations.

- The cases analysed show that with a low formation compressibility the effect of adding additional injection wells is limited. An additional 23 wells only increases the single well capacity by 18% for the low compressibility case, compared to 139% for the high compressibility case.
- The analysis of different compressibility scenarios shows the large variability in capacity estimates with compressibility and suggests capacity estimates could be seriously impacted by variability in compressibility.
- The study has only taken account of a single global value of compressibility for the model, this is unlikely to be realistic for such a large model, variable compressibility across the model will further complicate capacity analysis.
- The compressive response of the aquifer to injection is implicitly related to the interaction of the reservoir and overburden and this may also vary spatially, for example through stress arching in the overburden.
- Interaction of the overburden and reservoir deformation could only be analysed by more sophisticated analysis techniques such as coupled fluid flow geomechanical modelling.

3.4.2.5 *Boundary Conditions*

- The boundary conditions of the model are poorly constrained, capacity analysis shows that adding two open boundaries in the west and north-west margins (marginal boundaries with the greatest uncertainty) of the model increases the base case capacity by a maximum of 18% (using 24 wells).
- There is no evidence to determine flow properties of the north-western and western margins so this represents a significant uncertainty in the capacity estimate.
- Removing the outcrop from the model and having fully closed boundaries reduces the base case capacity by a maximum of 36% (24 wells), almost to the same level as the lowest compressibility case.
- There is evidence to suggest that brine influx has occurred into the seabed outcrop (Dingwall et al. 2013), however there is no evidence to suggest that the outcrop would act as an effective brine outflow pressure relief conduit for the entire model.
- Performance of the seabed outcrop brine flow represents a very significant uncertainty for the capacity estimate. In the absence of a seabed outcrop but with marginal boundaries open the capacity would be reduced by 15% from the base case value (with 12 wells), the marginal boundaries are less effective at relieving pressure in the model than the seabed outcrop.

3.4.2.6 *Bunter Capacity Estimate*

- Extrapolating the results of all the cases analysed to scale to the area of the Bunter aquifer allows estimates for the capacity of the Bunter aquifer to be derived. The capacity estimates range between 3.1 and 8.7 Gt CO_2 for the highest well density.
- The estimates are likely to be the upper limit for each case due to the potentially adverse storage conditions elsewhere in the Bunter aquifer, for example the presence of salt domes and walls and other problems such as thinning of the formation reducing pore volume.
- Stochastic modelling using multiple realisations and analysis of statistical variation of parameters such as permeability could provide a further refinement to the model, however this would involve significant computation and model development time.

3.4.3 **Capacity Modelling Approaches in the Bunter Aquifer**

- The capacity estimates for the pressure cell model ranged between 2.1 and 3 times larger than the comparable capacity estimates from the realistic model.
- Comparison of the static estimate of storage capacity in the Bunter also shows that the comparable pressure cell estimates from this thesis and the literature are 1.4 to 1.8 times smaller than the static capacity estimate of 14 Gt CO_2 (Holloway et al. 2006a, Heinemann et al. 2012).
- The incremental reductions in capacity estimate with increasing model sophistication show that even with moderately conservative parameters the contribution of the Bunter Aquifer to estimated UK storage potential could be reduced by 40%.
- The difference between the capacity estimates results from the way in which pressure builds up in the model, and the assessment of fracture pressure failure. In the pressure cell model the top surface of the model is flat, and so the fracture pressure is reached at the same time across the whole model area. In the structure-based model the areas that fail the fracture pressure criterion first are the shallower regions of the model, where the depth base fracture pressure limit is lower.
- This fundamental difference between the models explains the larger capacity estimations in the pressure cell model, and also conforms to the predictions techno-economic resource pyramid proposed by Bradshaw et al. (2007), where increased knowledge of the technical (and other) factors leads to a reduction in the volume of estimated capacity.
- Recent work in the literature suggests there may be sufficient evidence to reduce the fracture pressure to a lower value around 60% of the lithostatic gradient. This would have significant impacts on the estimated capacity of the Bunter.
- Further refinements to the model would potentially further reduce the capacity estimates, for example regulators may apply more stringent fracture pressure limits and further field investigation may reveal compartmentalisation or adverse flow properties.

3.4.4 **Fracture Pressure Uncertainty and Evolution**

- Reductions in fracture pressure can have a significant impact on the capacity in the generic model, a 20% reduction in fracture pressure can reduce capacity by up 60%, although this can be reduced to as little as 32% intensive brine extraction.
- Lower fracture pressure gradients from modelling in the literature suggest that the capacity predicted by the realistic structure model may be as much as 50% lower than modelled.
- The fracture pressure has a significant impact on capacity and is a significant control of CO_2 injection, however it is difficult to measure accurately without well tests and can also change with changes in pore pressure; over a large region such as the Bunter aquifer this uncertainty is shown to be a significant risk.
- The uncertainty in fracture pressure, and the fact that the most likely time for the fracture pressure to be exceeded is after injection has stopped means that modelling of the fracture pressure within the area of interest is likely to be very important. Failure to accurately constrain the fracture pressure may result in having to implement a major remediation strategy, which may be both costly and difficult to implement, or the use of highly conservative fracture pressures on storage models which would severely limit capacity estimates.

4 Modelling Stress Path and Fracture Pressure Hysteresis

4.1 Introduction

The fracture pressure is one of the key parameters that will govern the storage capacity of a storage project. Injection cannot continue at pressures above the fracture pressure, due to the potential for leakage from the reservoir, and so accurate characterisation of the fracture pressure is essential to determine the capacity limits of the project. The fracture pressure is dependent on the stress path in the reservoir. The prediction of fracture pressure and the field evidence for potential hysteresis in the fracture pressure during depletion and re-injection has been discussed in Chapter 2. The aim of this chapter is to present a coupled geomechanical fluid flow simulation model for a depletion-reinjection scenario in a generic reservoir, in order to investigate the potential for stress path hysteresis and the consequent effect on fracture pressure. The modelling approach will also incorporate the generation of synthetic seismic time-lapse attributes to analyse the change in seismic properties during depletion and reinjection in the reservoir.

The modelling in this chapter aims to investigate some of the observations from field data reported by Santarelli et al. (1998) and Santarelli et al. (2008) for normally consolidated weakly cemented sands in a large oil field in the Norwegian North Sea, where the stress path and prediction of fracture pressure were shown to be hysteretic during depletion and re-pressurisation. The geological formation and location of the field are not revealed, although similar observations are found in the literature for the Ekofisk field in the Central North Sea, e.g. Teufel et al. (1991).

The model is constructed using the coupled geomechanical-fluid flow workflow developed as part of the IPEGG project discussed in Section 2.9. The workflow uses Rockfield Software's ELFEN finite element modelling software coupled to Roxar's Tempest Reservoir Simulation software using the ELFEN RS module. The geomechanical model uses Rockfield's SR3 (soft rock 3) constitutive model to represent the reservoir and non-reservoir material properties. The SR3 model is an elasto-plastic model that extends the critical state theory to unify the shearing and consolidation properties of soils. The model is therefore applicable to soft rocks that have behaviour characteristics similar to engineering soils (Crook et al. 2006).

Several scenarios are used involving depletion of the reservoir and subsequent re-injection of CO_2 into the depleted reservoir. The scenarios represent the conditions that may be encountered when using abandoned fields for CO_2 storage that may react in a similar way to the cases presented by Santarelli et al. (1998). The stress path and the fracture pressure are then analysed for each case, and seismic attributes for several of the cases are also derived. The main reasons for the unpredictable behaviour of the stress path in a reservoir

are summarised by Santarelli et al. (1998) and they are in-elastic behaviour of the reservoir materials, stress arching, effects of faulting and differences of material properties between small (core scale) and large scale analysis.

4.2 Model Set-up

4.2.1 Model Geometry

The model used is a generic faulted reservoir that was originally constructed for a previous study and was presented by Angus et al. (2010). The geometry of the model is illustrated in Figure 4.1. The reservoir in the model is a sandstone graben structure with two faults offsetting the central compartment. The reservoir is 6.7 km long, 3.35 km wide, and 76 m thick, and the fault offset is 38 m. The reservoir is surrounded by a shale in the side, under and overburden and lies at 3.05 km depth. The faults extend into the overburden as shown in Figure 4.1 c). The discretisation of the reservoir in the flow modelling program and the finite element program are identical.

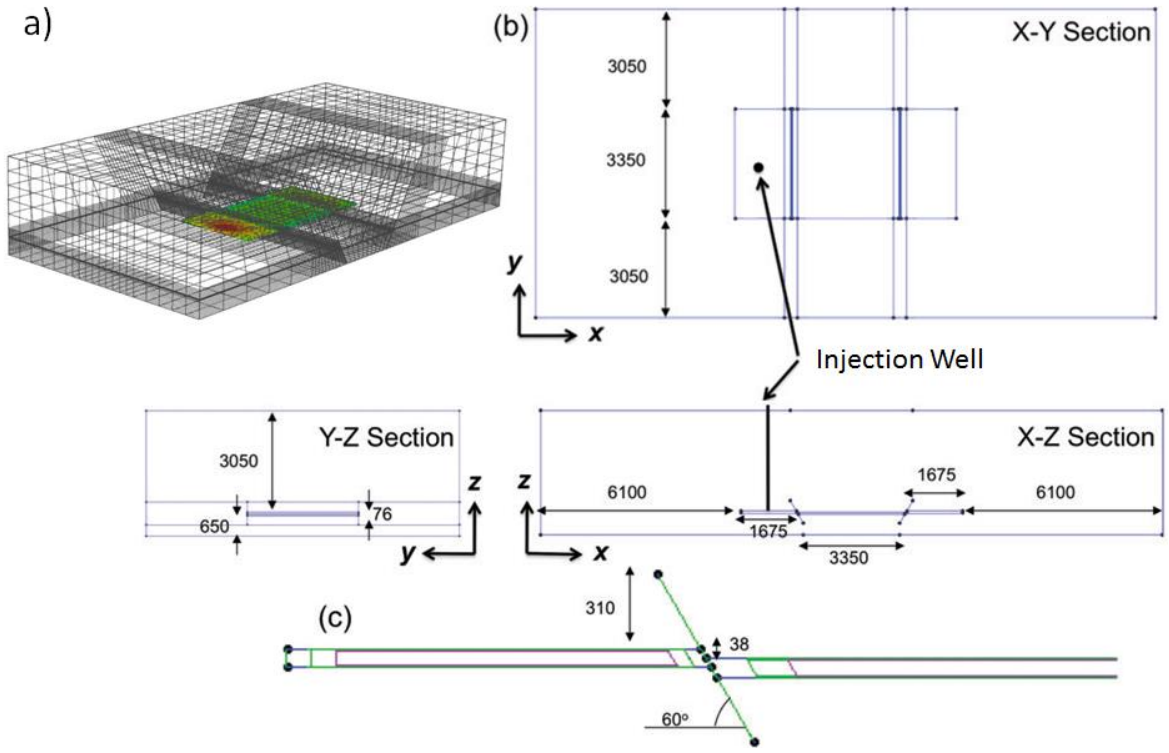

Figure 4.1 – Geometry of generic faulted model, a) shows the full model with the outer finite element mesh discretised with rectangular grids representing the overburden, and the central reservoir grid showing a pressure contour, b) shows three sections through the model with dimensions, and c) shows the geometry of the 2 faults.

In the finite element mesh, the faults are represented by contact elements that have a frictional constraint placed at the contact between the elements along the fault, and they are able to move in parallel to each other if sufficient force is applied to overcome friction. The fault properties can be altered to restrict or promote fault movement. In the remaining standard elements, lateral movement is restricted at the sides of the mesh, vertical

movement is restricted at the base of the mesh, but the top of the mesh (representing the surface) is a free surface and vertical movement is not restricted.

4.2.2 **Constitutive Model**

The SR3 constitutive model is used to represent the material properties in the geomechanical model, and can include various levels of sophistication including anisotropy and rate dependence (Crook et al. 2006). However, in this case the model is rate independent and isotropic. The definition of the constitutive model is presented in Crook et al. (2006) and relevant elements are presented in B to define the material parameters that must be set in the model.

The material properties for the sandstone and shale (including properties required for the SR3 model, poro-elastic properties and the properties that are required in the flow model) are described in the following section for the sandstone and shale.

4.2.3 **Geological Model and Material Properties**

In this model only two materials are specified: the overburden, sideburden and underburden are set as a generic shale material; and the reservoir is a generic sandstone. Only the permeability needs to be specified in the flow model, and the flow model only relates to the sandstone reservoir (as the shale is assumed to be impermeable). The porosity is controlled by the geomechanical simulator, which updates and modifies the pore volume in the flow model rather than using the compressibility in the flow model. Therefore, the majority of the material property set-up is carried out in the geomechanical model. It is necessary to specify the empirically-derived poro-elastic relationships of stiffness with porosity and porosity with depth, the parameters for the SR3 model and hardening relationships, and the initial geostatic geomechanical conditions in the model.

Both sets of geomechanical properties are derived from a compilation of test data presented in the 'ELFEN GeoDB Generic Materials' database from Rockfield Software Limited (2012) and workflows developed by Rockfield Software. The Elfen material database contains a set of generic material properties for shale and sandstone derived from data in the literature. The shale data in the database is obtained from Nygård et al. (2004) and Nygård et al. (2006) for the Kimmeridge Westbury Clay, Kimmeridge Bay Clay, Drammen Clay, London Clay, Lillebelt Clay and North Sea Shale. The sandstone data in the database is obtained from Wong et al. (1997), Zhang et al. (2000) and Coop and Willson (2003) for the Castlegate, Louisiana, Kayenta, Rothbach 2, Darley Dale, Boise II, Berea, Adamswiller, Saltwash, Wyoming Sandstones and a sand sample from Coop and Willson (2003) known as 'Sand C'. The generic materials are based on cases that are representative of the material data in the literature. The porosity is linked to the compaction and the plastic deformation of the material, and so two cases of high and low porosity provide two different cases for the elastic and plastic loading/unloading curves. The friction parameter β is used to define three strength cases of the shape of the state boundary surface: weak medium

and strong. Finally, three cases of cementation are specified; low, medium and high cementation; which determine the intercept of the state boundary surface (sometimes known as cohesion) with the q axis, by setting the initial value of P_t.

4.2.3.1 *SR3 Model*

The SR3 parameters for the state boundary surface and hardening response for the shale and sand are set out in Table 4.1. The parameters chosen for the shale correspond to a high porosity shale, with medium strength and a medium degree of cementation. For the sand they correspond to a low porosity sandstone, with medium strength and a medium to low degree of cementation according to the derivations presented in the EFLEN materials database.

Table 4.1 – SR3 state boundary and hardening material parameters for shale and sand.

Rock Type	Shale	Sand
Initial Pre-consolidation Pressure P_c (Pa)	1×10^6	1×10^6
Friction parameter β (degrees)	60	61
Tensile intercept P_t (Pa)	-0.05×10^6	-0.015×10^6
Exponent n	1.3	1.7
Dilation Parameter Ψ (degrees)	51	51
Deviatoric plane correction N^{π}	0.25	0.25
Deviatoric plane correction β^{π}_0	0.6	0.6
Deviatoric plane correction β^{π}_1 (Pa^{-1})	4.25×10^{-7}	7.25×10^{-7}
Elastic URL parameter κ	0.012	0.012
Plastic NCL parameter λ	0.103	0.091
Initial porosity ϕ	38%	41.8%

Figure 4.2 shows the state boundary surfaces and critical state lines (dashed line) for the shale and sandstone in p'-q space, the intercept with the p' axis at 1.0 MPa represents P_c and the intercept in the negative p' axis is P_t, the surface shown is prior to geostatic initialisation, i.e. surface conditions.

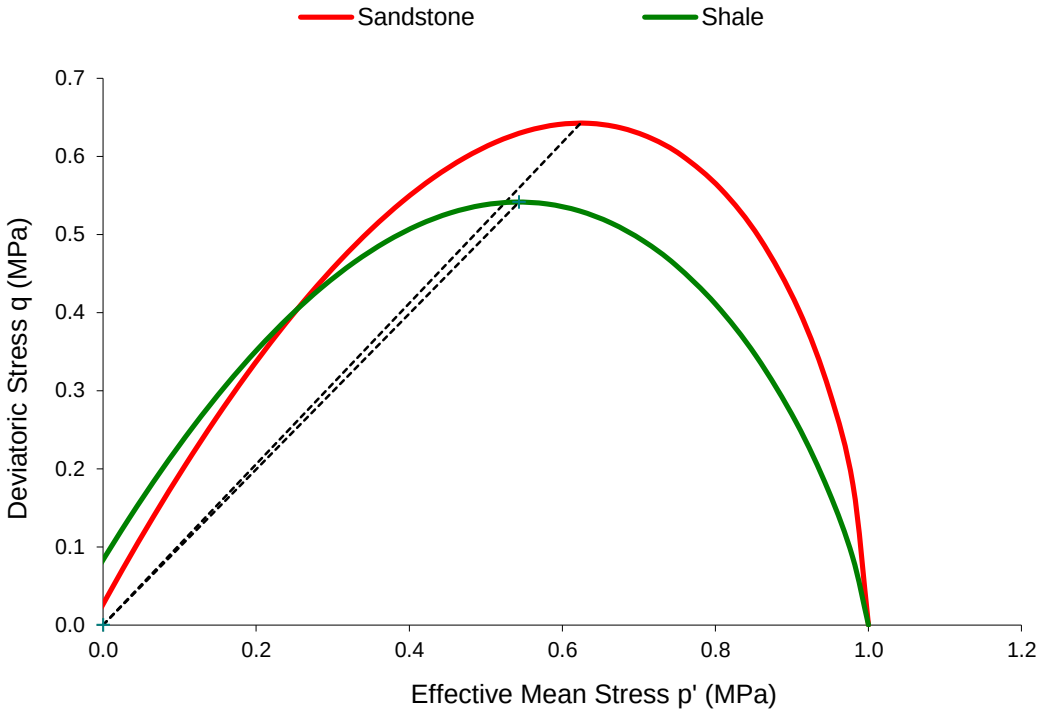

Figure 4.2 – State boundary surface and critical state line for the shale overburden and sandstone reservoir at a pre-consolidation pressure of 1 MPa. The dashed line represents the critical state line.

4.2.3.2 *Porosity, Stiffness and Initial Geostatic Data*

To initialise the elastic stiffness (Young's modulus) with depth in the model, data from a compilation of measurements of Young's modulus with porosity was used to calibrate one of the empirical poroelasticity models built into the Elfen material description. The empirical relationship between porosity, reference Young's modulus and the Young's modulus in the model is:

$$E = E_{ref}\left[\frac{p'+A}{B}\right]^{n}\phi^{c} \qquad \textbf{Equation 4.1}$$

where *A* and *B* constants used to prevent problems at low p' values, and *n* and *c* are material constants. In the base case for the shale the reference stiffness was set at 5.35 GPa, *n* was 0 and *c* was -0.372. The variation of Young's modulus with porosity assumed for the shale and sandstone are plotted in Figure 4.3.

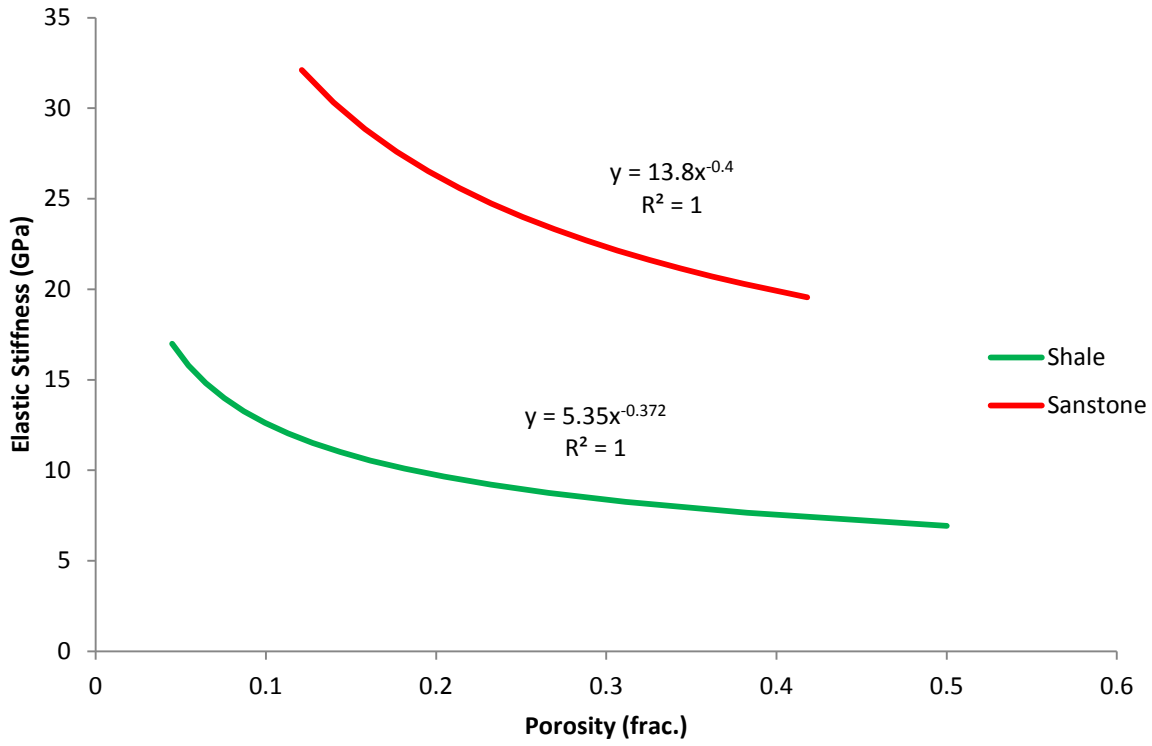

Figure 4.3 – Young's modulus as a function of porosity using empirical relationship in Elfen for the shale and sandstone.

To initialise the elastic stiffness a porosity depth curve and the relationships in Figure 4.3 are required. The assumed porosity depth curves for this study are shown in Figure 4.4, from data provided by Rockfield Software Ltd. The variation of Young's modulus with depth can then be derived for the model, and is shown in Figure 4.5.

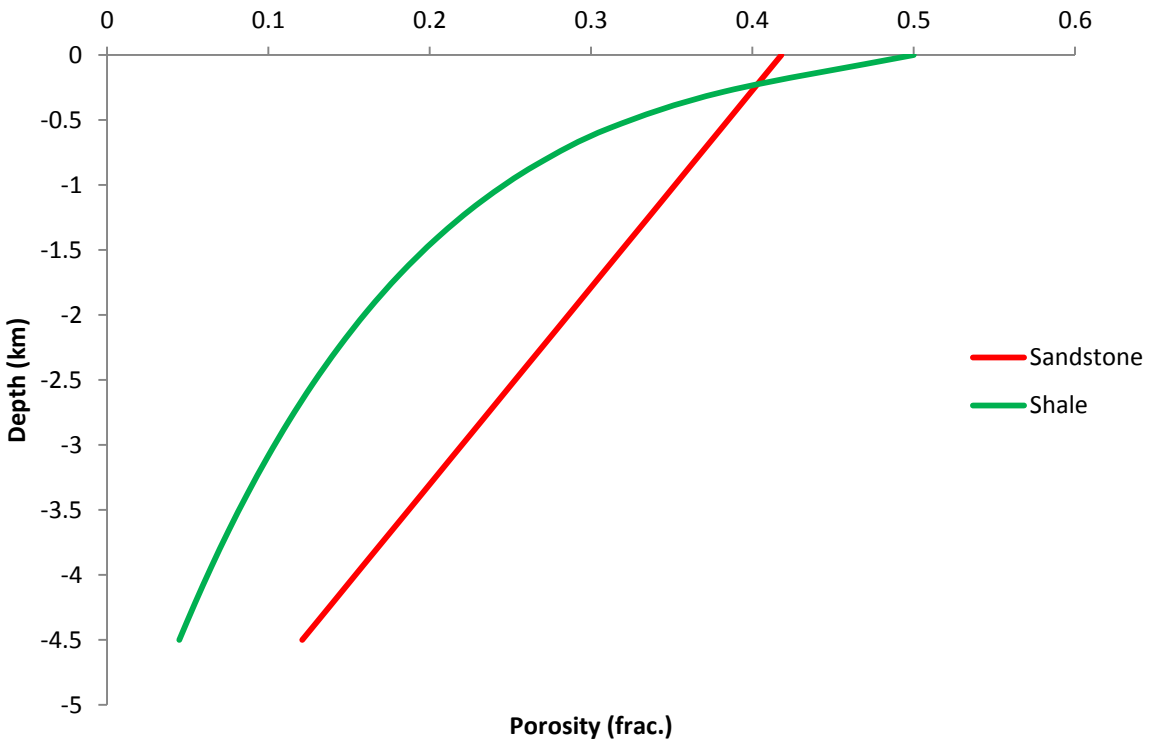

Figure 4.4 – Porosity depth curve for the shale and sandstone, data provided by Rockfield Software Ltd.

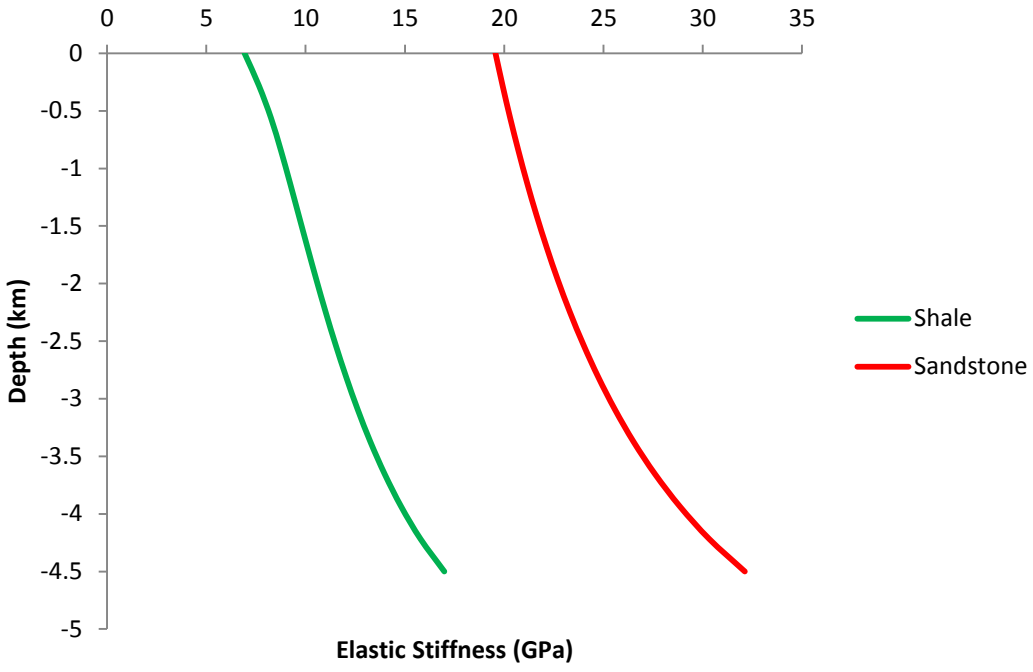

Figure 4.5 – Young's modulus curve with depth for the shale and sandstone.

The hardening functions that define p_c and p_t as a function of plastic volumetric strain are shown in Equation B.2 and can be plotted for a range of volumetric strains as in Figure 4.6. This is a required input for the Elfen program. The hardening functions are used to initialise

the initial p_c and p_t throughout the model based on the porosity depth curve. The relationship for plastic volumetric strain with porosity is:

$$\varepsilon_{vol} = \varepsilon_{vol0} + \ln\left(\frac{1-\phi_0}{1-\phi}\right) \qquad \textbf{Equation 4.2}$$

(from Thomas et al. 2003), where ε_{vol} is plastic volumetric strain and ϕ_0 is initial porosity.

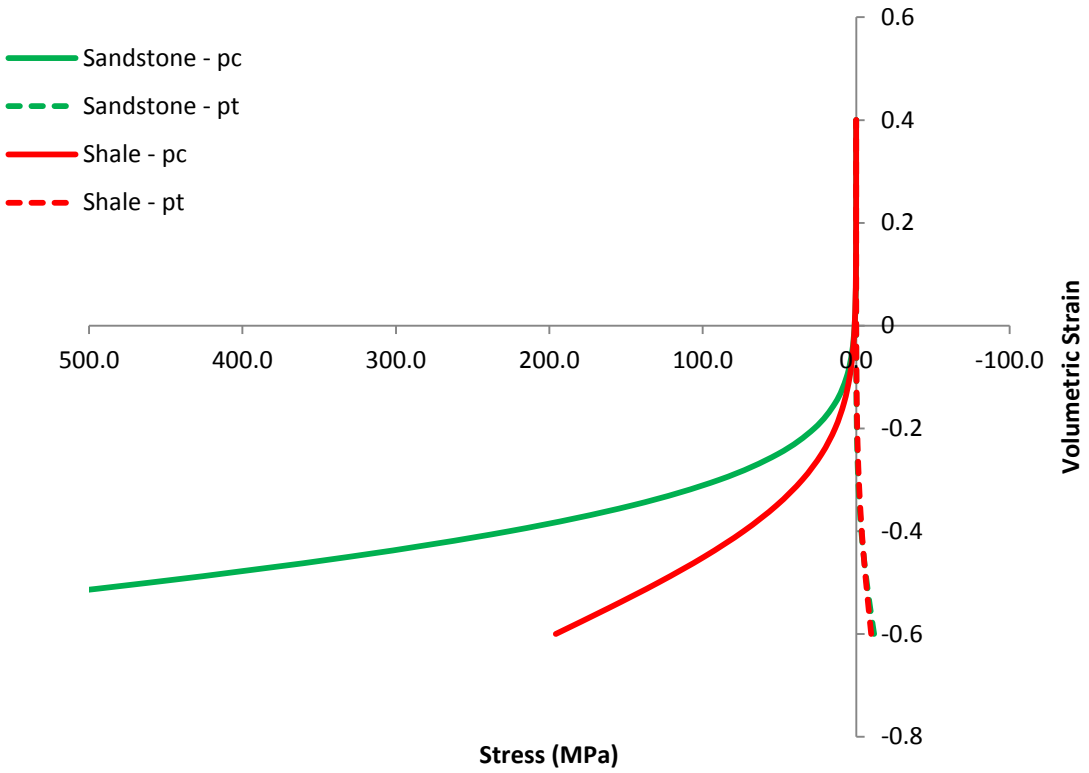

Figure 4.6 – Variation of pre-consolidation pressure (pc) and tensile strength (pt) with plastic volumetric strain for the shale and sandstone

The initial distribution of volumetric strain with depth is shown in Figure 4.7, and based on this the initial p_c and p_t with depth is shown in Figure 4.8.

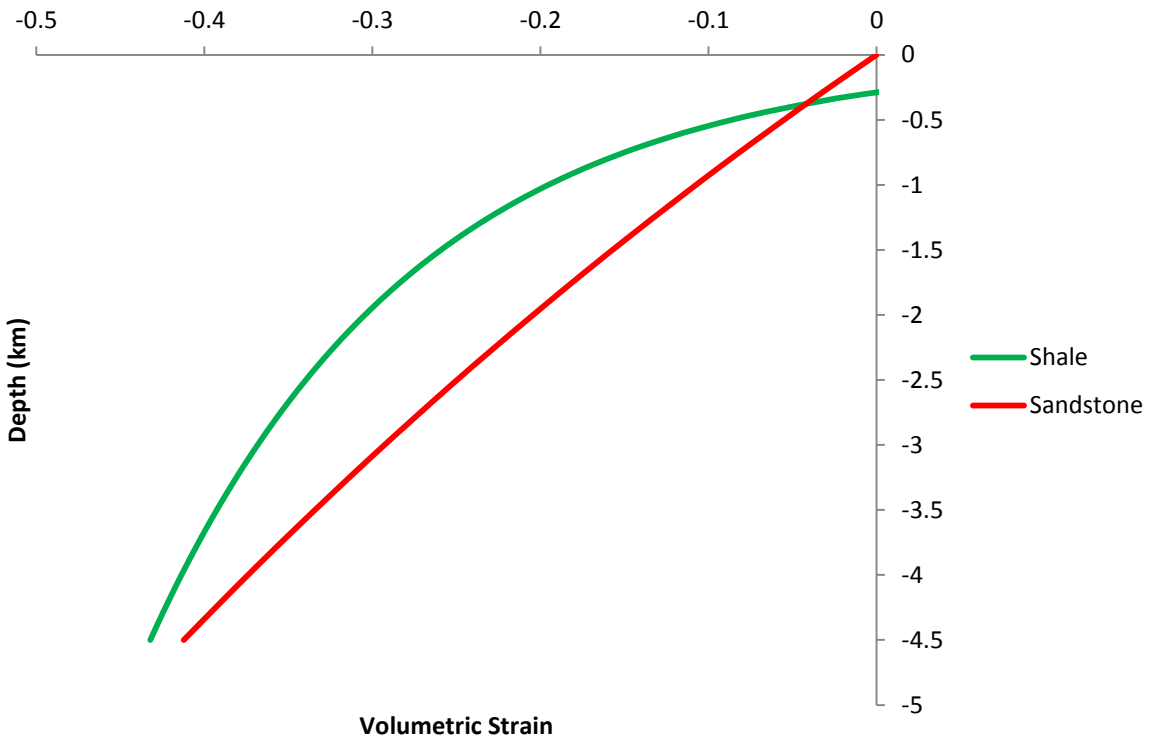

Figure 4.7 – Distribution of initial plastic volumetric strain with depth for the shale and sandstone.

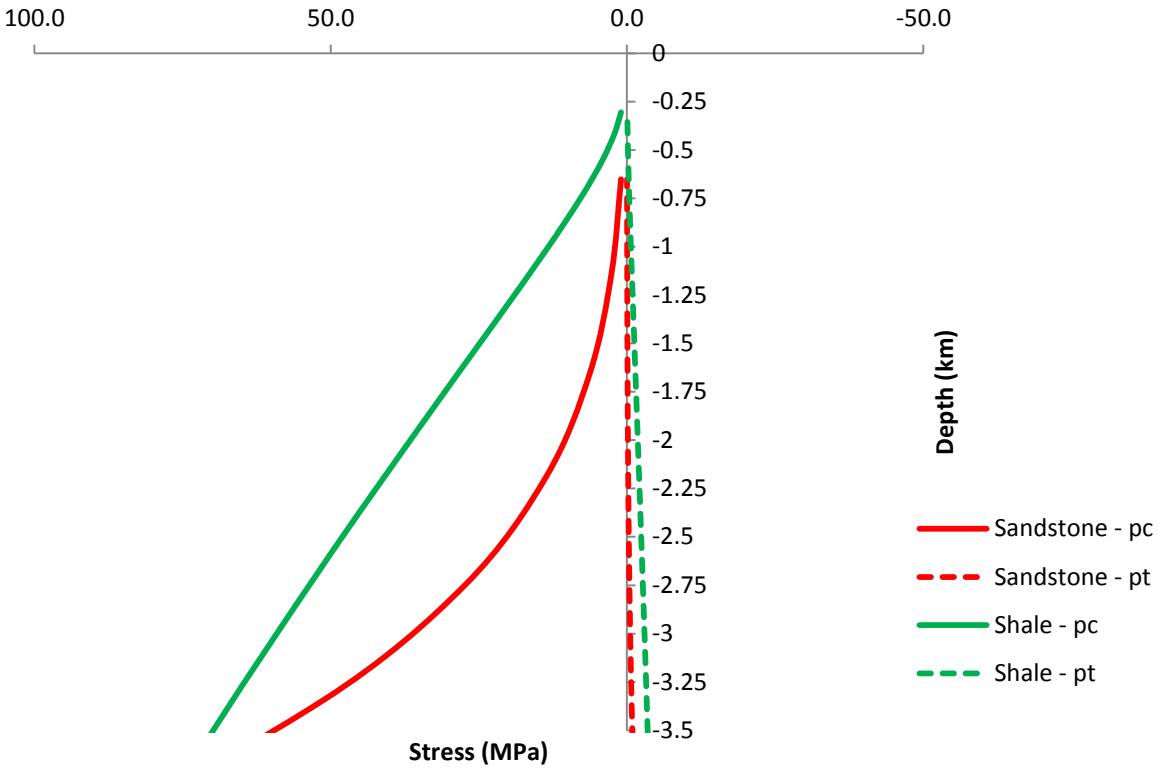

Figure 4.8 – Initial pre consolidation pressure (p_c) and tensile strength (p_t) intercepts for the shale and sandstone.

4.2.3.3 *Elastic Stiffness Correlation*

The stiffness values selected for the sandstone can be compared against theoretically and empirically derived correlations from the literature, which are based on the elastic modulus of solid quartz. There are various relationships, but the general form is a power law relationship in some form. One such model is proposed by Ji et al. (2006):

$$E = E_0 \left(1 - \frac{\phi}{\phi_c}\right)^{1/J} \qquad \textbf{Equation 4.3}$$

where E is the Young's modulus, E_0 is the Young's modulus of the solid material (i.e. porosity of 0), ϕ is the porosity, ϕ_c is the porosity at which the effective Young's modulus is 0 (taken as maximum theoretical porosity), and J is an exponent based on pore geometry. Equation 4.3 is essentially the same relationship as proposed by Kováčik (1999) where the exponent $1/J$ is replaced by f. Values of J vary between 0.5 (f = 2) for spherical porosity e.g. glass to 0.25 (f = 4) for polycrystalline pore e.g. basalt. Based on a Young's modulus of solid quartz of 73 GPa the estimated Young's modulus for a porous pure quartz sandstone can then be estimated, and is plotted in Figure 4.9 against the empirical estimates from the SR3 model. At very low porosities when pores become isolated, and very high porosities where the framework breaks down, the theoretical equation is not applicable, however the area of most interest is the reservoir depth where porosities are intermediate at 20 – 22%.

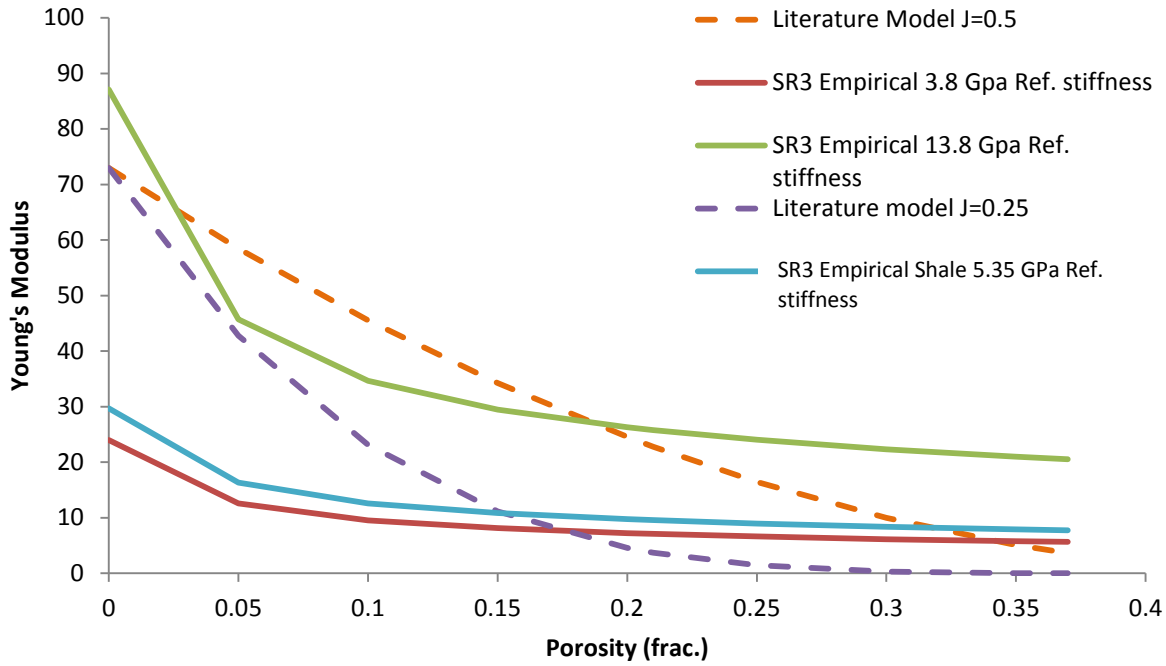

Figure 4.9 - Plot of SR3 empirical correlations and theoretical models from the literature for Young's modulus and porosity.

At the depth of the reservoir in the model the porosity is around 21%. There is good agreement with the upper bound of the theoretical model for the 13.8 GPa reservoir case at reservoir depth, although the SR3 model predicts a higher stiffness, the 13.8GPa stiffness

therefore forms the high stiffness base case. The lower bound of theoretical model is close to the SR3 model with a reference Young's modulus of 3.8 GPa and so this is chosen as a softer comparison case. The shale stiffness is set to form a low stiffness case that falls in between the two reservoir stiffnesses so that cases with a stiffer and softer reservoir than the overburden can be assessed.

4.2.3.4 *Poisson's Ratio*

The Poisson's ratio of a material is the ratio of transverse strain to axial strain under uniaxial strain, where the material is behaving elastically (Gercek 2007). The Poisson's ratio is a required input for the geomechanical model to determine the deformational behaviour with applied stress. The Poisson's ratio of rocks can vary widely, and is not necessarily isotropic. The theoretical range for isotropic materials is 0.5 to -1, however for rocks the typical upper and lower bounds are 0.05 to 0.45, the Poisson's ratio is also higher in saturated rocks compared to dry rocks (Hudson 1993, Gercek 2007).

As discussed by Gercek (2007), there is less information in the literature relating to the Poisson's ratio of rocks compared to other elastic constants and specific data are difficult to obtain. Hamilton (1979) presents a compilation of Poisson's ratio data for silty clays and mudstones derived from in-situ seismic velocity measurements for unconsolidated and consolidated clays. The Poisson's ratio ranges from 0.5 for the unconsolidated clays to 0.41 for the consolidated material. Dvorkin and Nur (1996) present data from seismic velocity measurements for high porosity sandstones from the Osberg and Troll fields in the North Sea. For sandstones with a porosity of 20 – 25% and at confining pressures equivalent to reservoir depth, the Poisson's ratio ranges from 0.2 to 0.3. In the model the shale overburden was therefore set at an isotropic Poisson's ratio of 0.45 and the sandstone reservoir was assigned a Poisson's ratio of 0.25 for the base case.

4.2.3.5 *Initial Stress State*

The lateral stresses in the model can be initialised using a lateral stress coefficient (K) to set the horizontal stress as a fraction of the vertical stress. Values of K in the Northern and Central North Sea range from 0.75 to 0.95, and generally increase with depth, they are generally more consistent in the Southern North Sea at around 0.9 (Edwards et al. 1998). In the models used in this study, three different values of K were considered, 0.5, 0.7 and 1. These were set in order to encompass the range of expected values, whilst also investigating maximum and minimum potential values.

4.2.4 **Modelling Parameters**

The main material parameters for the model have been described above, further relevant modelling parameters for both the geomechanical and flow models are discussed in the following sections.

4.2.4.1 *Geomechanical*

The geomechanical model boundary conditions are specified so that no vertical displacement is permitted at the base of the model, and no horizontal displacement is permitted at the sides. The top of the model is a free surface and lateral displacement in the base and vertical displacement in the sides are permitted. The model is large enough to allow negligible change in the far field stress at the fixed boundaries of the model.

Two faults are specified in the model using contact elements. The contact elements have a frictional contact with the friction controlled by a Mohr Coulomb failure criterion. To specify the strength of the fault, only the friction angle (as coefficient of friction μ) of the material needs to be specified. Two fault strength cases were modelled, a high strength fault with a friction angle (θ) of 36.9°, where $\mu = \tan\theta = 0.75$, and low strength fault where $\theta = 20.6°$ and $\mu = 0.375$.

4.2.4.2 *Fluid Flow*

The fluid properties and relative permeabilities were set up in an identical manner to those used in the studies in the previous chapter. The model was run as a two-phase model with only brine and CO_2 specified. To assess the depletion–re-injection scenario it was necessary to deplete an initial gas in place, and re-inject CO_2. Initially it was proposed that the model should be run with a reservoir gas with typical natural gas properties initially in place and re-inject CO_2 using the solvent option within the flow model. However, the model would not converge under this set up, and so CO_2 was specified as the only reservoir gas. This assumption is slightly unrealistic as it results in a CO_2 filled reservoir that is depleted and refilled. For this initial assessment, however, the main interest is in the pressure and stress path of the reservoir, and so this CO_2 depletion re-injection scenario is sufficient.

The permeability of the reservoir was set as 100 mD in the horizontal direction and 10 mD in the vertical direction giving a k_v/k_h ratio of 0.1. Unlike the porosity, which is updated by the geomechanical program, the permeability of the reservoir does not change during the simulation. For this assessment permeability updates are considered to be an unnecessary complexity as the relationships between deformation and permeability are more complex and less certain.

The fault flow properties were set to provide two fault sealing cases, a sealing case and a non-sealing case, with the transmissibility multiplier parameter for each fault set at 0.0001 and 0.98 for the sealing and non-sealing cases, respectively. According to the transmissibility multiplier calculation of Manzocchi et al. (1999) and Fisher and Jolley (2007) and the fault rock properties of Fisher and Knipe (2001) a low multiplier of the order of 0.0001 would represent a fault rock such as a cataclasite or clay smear, with fault thicknesses of 10m and permeability of 0.001. A higher multiplier of 0.98 could represent a disaggregation zone of the same thickness with a permeability around 100 mD. The flow and geomechanical fault properties allow for the investigation of cases where faults may be active and conductive, or inactive and sealing, but also cases where the fault maybe

inactive but conductive, or active but still sealing. The sealing properties mean that in the sealed case the injection is compartmentalised with only the compartment containing the well being depleted or injected with CO_2. The sealed and non-sealed faults change the size of compartments and geometric characteristics of the model. For example in the sealed case the pressure is only changing in a small section of the reservoir on one side of the fault, whereas in the non-sealed case the pressure changes across a much larger section of the reservoir encompassing both the faults.

The base case production-injection scenario that is considered involves production from the reservoir for 15 years, 1 year of well shut in and 15 years re-injection to the initial pore pressure. In both the sealing and non-sealing fault scenarios the reservoir was depleted to around 100 bar, it was not possible to achieve greater depletion in the non-sealing case due to using only 1 well for the production. In the sealing scenario only one compartment containing the well was affected by the depletion, whereas the whole model was affected in the non-sealing fault case. To make the cases comparable the model was depleted to the same pressure in both the sealing and non-sealing cases, and the depletion and injection rates were the same. The flow rate in the sealing case was 375 ksm^3/day and in the non-sealing case 1200 ksm^3/day.

4.3 **Results**

The constituent parameters in the model have been discussed in the preceding section, and a suite of model runs were developed to analyse the impact of varying pertinent parameters for assessing a depletion re-injection cycle. An initial base-case was developed and is used to discuss the initial results of the model followed a by a comparison of the other cases that were analysed. To summarise, the main parameters that were altered in the runs are:

- the stiffness of the reservoir;
- initial stress ratio;
- SR3 model parameters;
- and the sealing and frictional properties of the fault.

4.3.1 **High Stiffness Case**

The initial higher stiffness base-case with a reference stiffness of 13.8 GPa uses the material properties as described in the previous section, the initial stress ratio was set at 0.7 and all four cases were analysed for the sealing and frictional properties of the fault. Seismic data was also generated for all of the base case models.

The coupled model allows stresses, strains, pore pressure profiles, seismic data, yield data and numerous other data to be interrogated for the model, with high-resolution data at specified history points, and broader contours for the whole model. The most useful plots to assess the stress path are: p-q plots which show the stress path, high resolution stress and pore pressure data, which can be used to calculate stress path parameters, and stress

contour sections through the model which show the stress in the reservoir and overburden. Initially results are presented from the cell corresponding to the well location at the top of the model, as this is where the greatest pressure changes occur.

Figure 4.10 shows the pore pressure profiles for each fault sealing and fault friction case for the base case model for depletion well shut in and reinjection. The initial 4 years of the graph represents the geostatic initialisation period, where the two models are not connected and the geomechanical initialises. After the geostatic initialisation period the models are connected and the depletion begins. The graph shows two different trends for the depletion section with the high fault transmissibility (fault non-sealing) and low fault transmissibility (fault sealing) following separate paths. The fault sealing cases are depleted faster than the non-sealing cases initially however both cases converge to a similar pressure by the end of the depletion stage. The depletion stage is controlled by the depletion rates that were set and a minimum pressure of 0 bar on the well, the differences in the initial depletion profiles are probably due to the size of the compartment being depleted. The depletion rates were set with the aim of producing a similar total pressure depletion. Post-depletion three different trends emerge in the pore pressure profiles. In the non-sealing cases, the pressure increases as soon as the well is shut in, before injection commences, and the high and low friction non-sealing cases follow the same path. In the sealing cases pressure increase is delayed but still occurs before injection starts. There is a slight difference between the sealing cases with the low friction case pressure increasing earlier than the high friction case, but following the same trend. The pressure increase after well shut-in but prior to injection is the same response observed in pressure build-up well testing. The pressure build-up occurs through pressure equilibration throughout the model. The larger pore volume of the model with the non-sealed faults equilibrates faster than the smaller compartment of the model with sealed faults. The faster equilibration is likely to be due to higher pressures elsewhere in the large compartment supporting re-pressurisation, whereas the compartmentalised model is pressure depleted throughout and re-pressurisation is slower. The pressure equilibration that occurs in the non-sealing fault case is illustrated in Figure 4.11, pressure at the well is low prior to shut in, but then equilibrates to the model average after shut-in raising pressure at the well by 28 bar. In the compartmentalised model, the average compartment pressure is only 2-3 bar higher than at the well, so re-pressurisation does not occur. The slight difference in pressure profiles between the high and low friction cases in the sealed fault cases may be due to geomechanical effects of movement along the fault in the low friction case. The low friction case may re-pressurise faster due to compaction aided by fault movement. Fault movement may be less important in the non-sealed case for pressure build-up as the model is at a higher pressure on average after depletion at the well. The pressure difference between the initial pressure and maximum depletion is 17.6 MPa in the non-sealing fault cases and 18.1 MPa in the sealed fault cases. The pressures are restored to the initial value at the end of the injection period.

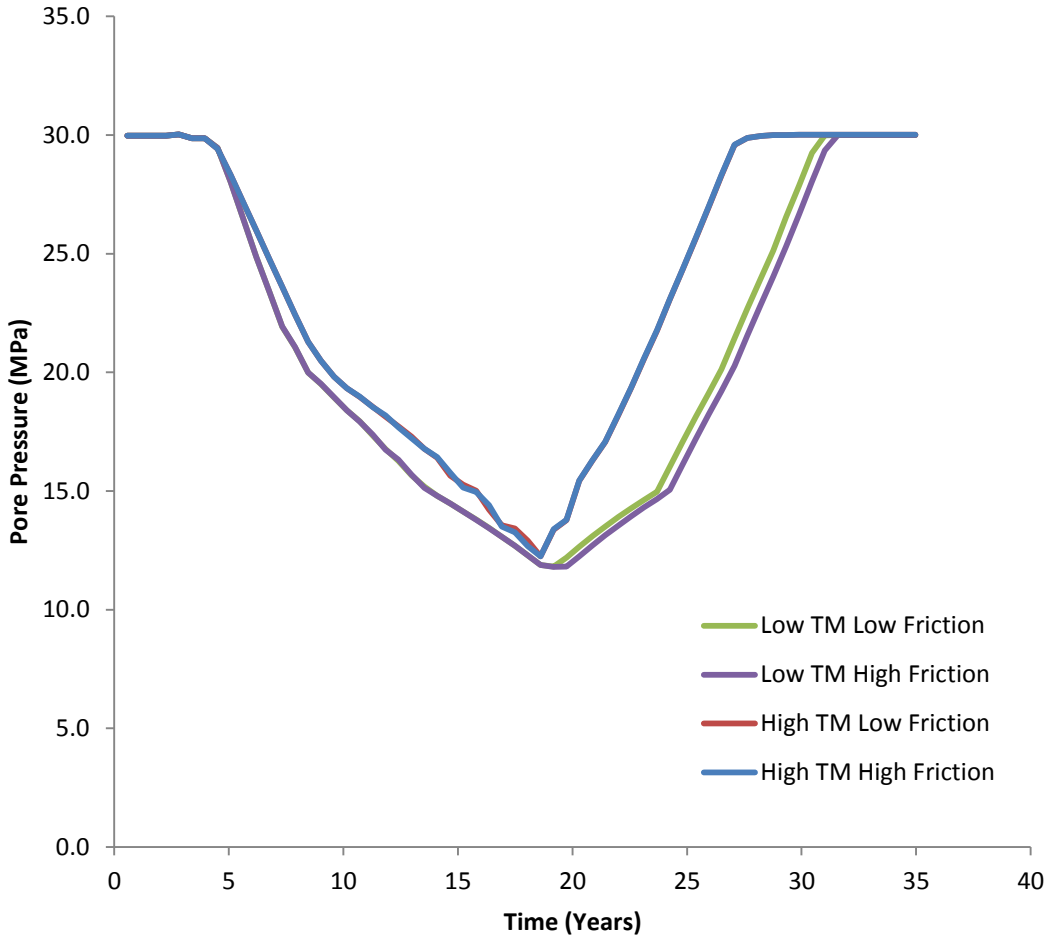

Figure 4.10 – Pore pressure at the well for the base case model for high and low friction cases for both non-sealing (high TM) and sealing (low TM) cases.

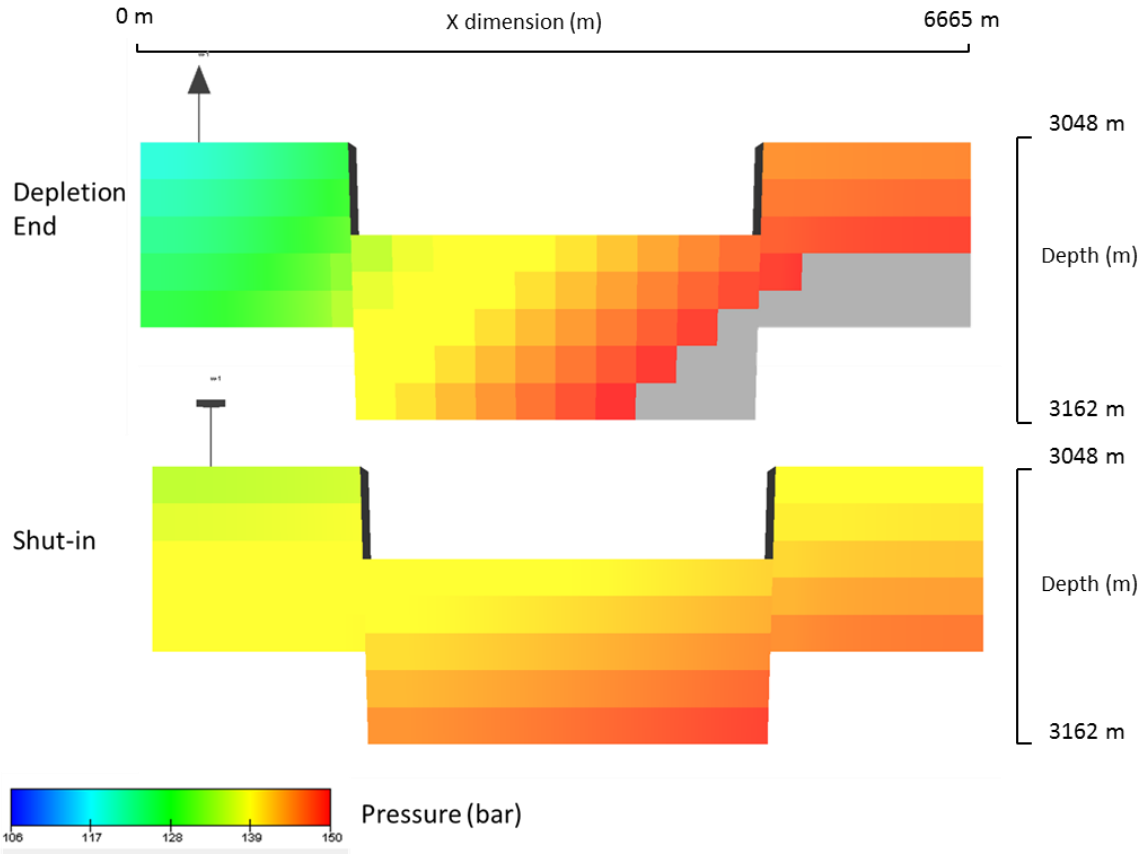

Figure 4.11 – Section through high transmissibility (non-sealing fault) case showing pressure equilibration in the model after shut-in. This leads to a pressure increase at the well, observed on the pore pressure profile.

4.3.1.1 *Non-sealing fault case*

Figure 4.12 is a p'-q plot of the stress path for the high transmissibility non-sealing fault cases for the base case model. The initial yield surface after geostatic initialization and the final yield surface after plastic deformation is shown on the graph. The general trend of both p'-q plots is similar and is described first for the low fault friction case. Upon initialization the p-q stress state is at p' = 29.3 MPa and q = 13.1 MPa. As depletion commences both p and q stresses increase linearly towards the initial yield envelope. During the initial linear period deformation is elastic (points 1 to 2 on figure) as the stress state falls within the initial yield envelope. The stress path intersects the initial yield envelope at p' = 34.5 MPa q = 19.0 MPa, this occurs after approximately 4 years of production. At the next time-step the material at this location is deforming plastically, p' has continued to increase, but q has dropped significantly. At the first point of plastic deformation p' = 38.6 MPa and q = 13.7 MPa. The reduction in q is related to the increase in horizontal stresses in the reservoir. Whilst σ_1' has increased by 0.5 MPa in the time-step from elastic to plastic deformation σ_3' has increased by 5.8 MPa whereas the changes in stress during each elastic deformation time step were of the order of 1.2 MPa for σ_1' and 0.5 MPa for σ_1'. With continued depletion the reservoir continues to deform plastically (points 2 to 3 to 4 on the figure) and the yield surface continues to expand. p' continues to increase during plastic deformation and q also increases but at a lower rate than in the elastic deformation. At maximum depletion p' = 42.9

MPa and q = 15.1 MPa. After depletion the well is shut in, however, as described pressure begins to rise immediately due to pressure equilibration re-pressurisation at the well. The stress path then follows an elastic unloading path (points 4 to 5) as p and q reduce during injection. The elastic unloading injection stress path is parallel to the elastic path during depletion. At the end of injection when the pressure in the reservoir has returned to the initial pressure p' = 31.2 MPa and q = 3.7 MPa, comparison with the initial stress state shows that q is much lower at the end of injection, whereas p' is similar but slightly higher. σ_1' is 33.7 MPa at the end of injection compared to 38.0 MPa initially and σ_3' is 30.0 MPa at the end of injection compared to 24.7 MPa initially.

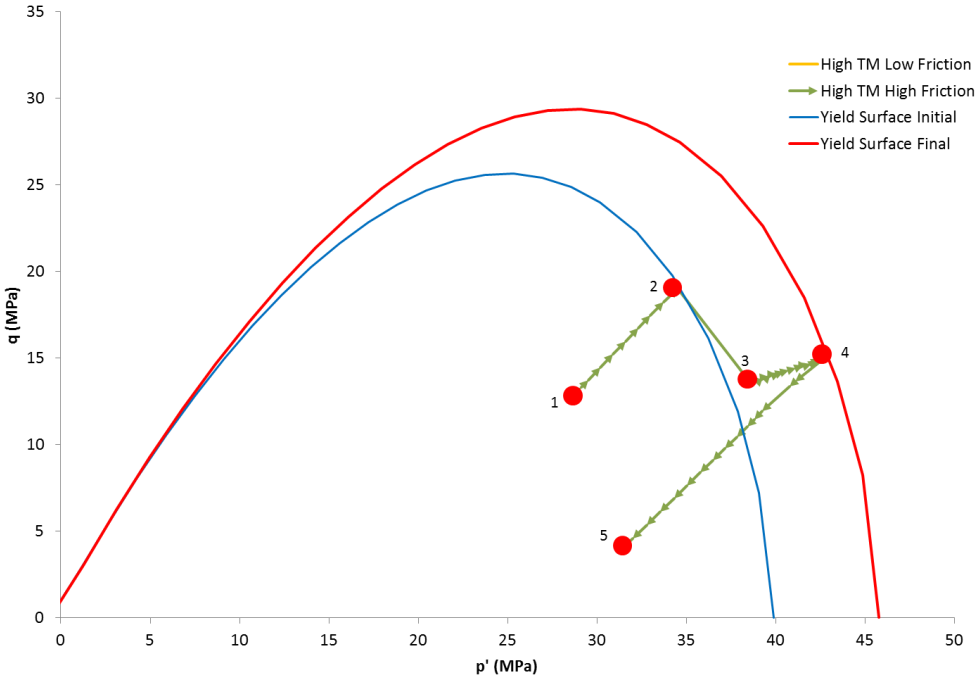

Figure 4.12 – p'-q plot for non-sealing fault (high TM) cases for the base case model at the well, arrows demonstrate direction of stress path going from the start of depletion to the end of injection. The chart shows the elastic stage of depletion from point 1 to 3, transitional plastic stage from point 2 to 3, continued plastic depletion from point 3 to 4, and final elastic injection from point 4 to 5. Both lines plot together on the figure and so are indistinguishable.

From the plot of the stress path in Figure 4.12 it is evident that there is significant hysteresis in the stress path. However, it is clear that the hysteresis in this case does not lead to lower fracture pressure at the end of injection. The *p'* stress at the end of injection the stress state is further from failure than the initial stress state indicating a higher fracture pressure and deviator stress is also reduced (lower q). A further parameter, the fracture pressure hysteresis factor f_{ph} can be derived to describe the change in fracture pressure from the initial case to the case after depletion and reinjection:

$$f_{ph} = \frac{\Delta p_{ff}}{\Delta p_{fi}} \qquad \textbf{Equation 4.4}$$

Where Δp_{ff} is the difference in *p* stress between the final stress state and the failure envelope and Δp_{fi} is the difference in *p* stress between the initial stress state and the failure

envelope. The concept and stress differences required are illustrated in Figure 4.13. For f_{ph} >1 the fracture pressure is higher at the end of injection than at the start of depletion and thus there is less risk of fracture pressure failure. For f_{ph} <1 the fracture pressure is lower at the end of injection than at the start of depletion and there is greater risk of failure. f_{ph} = 0 indicates failure at the end of injection, assuming that the fracture pressure was not 0 prior to depletion. The f_{ph} factor measures the distance to failure, and implicitly takes into account pore pressre and stress coupling in the stress path. However, the increment of pore pressure representing the distance to failure does not represent the actual pore pressure change that would lead to failure, as total stress would also change with a change in pore pressure. The factor is therefore only a non-dimensional index to compare fracture pressure change across different scenarios.

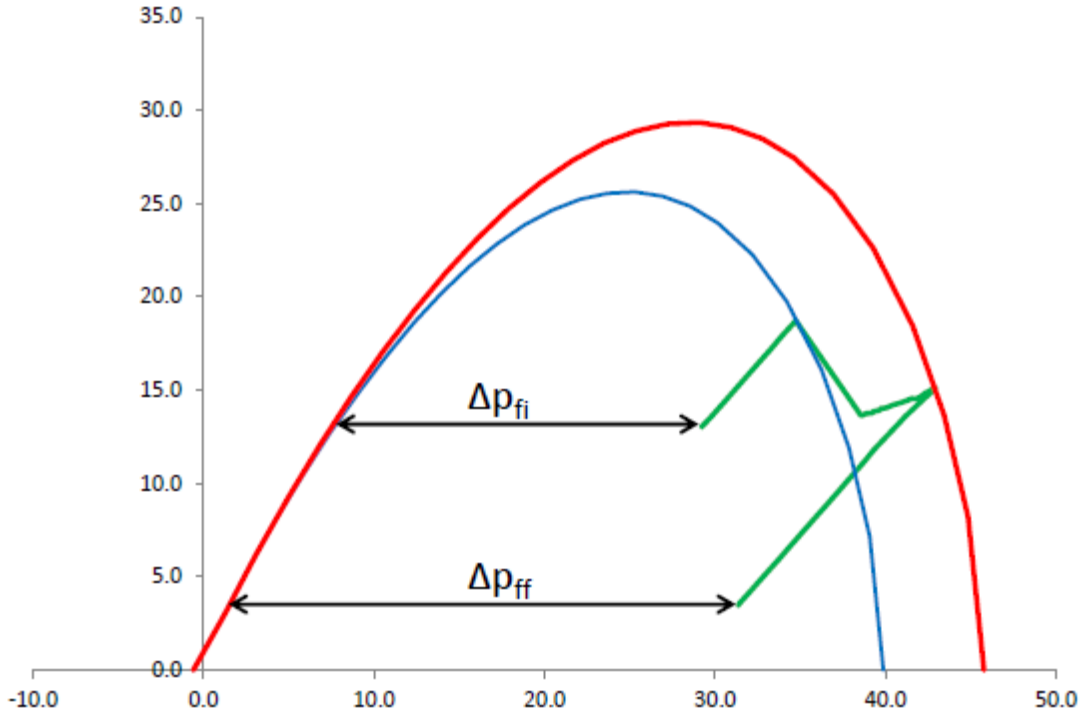

Figure 4.13 – Schematic diagram showing the stress differences between the yield surface and the stress path required to calculate the fracture pressure hysteresis parameters.

For the non-sealing cases discussed previously the f_{ph} is 1.4 indicating that there is less risk of failure after depletion and reinjection in this case.

The stress path parameters discussed earlier in this chapter can be calculated for the stress paths. For the non-sealing fault cases shown in Figure 4.12, the stress path parameters are essentially the same. For the depletion stage (at maximum depletion) γ_v = 0.24, γ_h = 0.33 and K_{sp} = 0.88. The stress path parameters from maximum depletion to the end of the injection are γ_v = 0.02, γ_h = 0.60 and K_{sp} = 0.41. Comparison of these parameters with a plot of Mohr circles for normal and shear stress for the non-sealing low fault friction case illustrates the evolution of the stress path parameters. The Mohr circle plot is shown in

Figure 4.14, the yield surface has been re-plotted in terms of s' and t and the s' and t values corresponding to the p'-q plot are also shown. The s'-t plot defines the top centre of each Mohr circle. During depletion K_{sp} is close to 1, and γ_v and γ_h are of a similar magnitude to each other and >0. Therefore, there is a minimal growth in the radius of the Mohr circle, the movement of the Mohr circle is mainly translational, and some minimal stress arching and horizontal stress arching occurs which restricts the increase of σ_1' and σ_3'. The behaviour of the Mohr circle indicates a minimal change in shear stress and uniform increase in vertical and horizontal stresses. Interestingly there seems to be minimal indication of pore-pressure stress coupling during depletion. After maximum depletion the pressure increase due pressure equilibration at well shut in is indicated by the offset of the 'depletion end' and 'injection start' Mohr circles. During the injection stage γ_v is much lower than during depletion and so the σ_1' intercept of the Mohr circle moves back down the axis beyond the initial position. γ_h is higher on the injection stage and so the σ_3' intercept of the Mohr circle does not move as far down the axis and does not reach the initial position. The relative change in σ_1' and σ_3' during injection suggests that the stress arching during depletion in the horizontal and vertical direction is not recovered uniformly during injection. Vertical stress decreases by a greater proportion with pore pressure than horizontal stress suggesting horizontal confinement may be more important during injection in this case. K_{sp} is much lower during injection due to the change in γ_v and γ_h and this is manifested in the significant shrinkage of the Mohr circle. The final value of p' or s' stress is similar to the initial value as the increase in σ_3' compensates for the decrease in σ_1'.

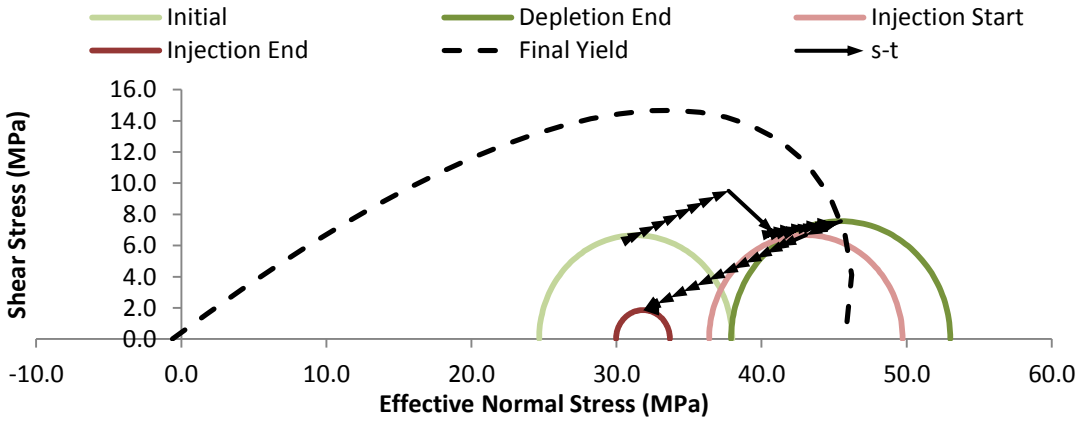

Figure 4.14 – Mohr circle diagram for the non-sealing low friction faults case with yield surface transformed into s'-t parameters and s'-t stress path plot.

As indicated by the stress path parameter, the Mohr circle plot shows that σ_1' increases in the reservoir during depletion and then decreases during injection to a lower value than observed at the initial stress. σ_3' in the reservoir also increases at a similar rate during depletion, however σ_3' does not decrease as much as σ_1' during injection and this leads to a reduction in shear stress at the end of injection. This behaviour can be observed in contour plots of the principal stresses of a section through the model shown in Figure 4.15 and Figure 4.16. The reservoir is represented by the refined section of the grid offset by a fault

and the most significant stress changes are observed within the reservoir. Only one side of the reservoir and one fault section is shown, and this represents the location of the well, the other compartment shows similar stress contours but with a less significant change in stress. The contour plots show the relative changes of effective stress in the reservoir during depletion and injection as described from the Mohr circle plot above, the plot shows that the whole reservoir follows the same general trend as the well location. The plots also show the change in principal effective stresses in the over, under and sideburden surrounding the reservoir. The contours of σ_1' show a reduction in the stress above and below the reservoir, and a slight increase at the side of the reservoir after depletion. The plot also shows that there is a minimal change in σ_1' after injection. The contours of σ_3' also show a decrease in the stress above and below the reservoir, and a slight increase at the side of the reservoir, although this is not easy to determine from the plot. The overburden is shale and is un-drained, therefore a plot of total stress is more appropriate. Figure 4.17 and Figure 4.18 shows plots of the change in total stress from the start to the end of the depletion and injection phase for σ_1 and σ_3 respectively.

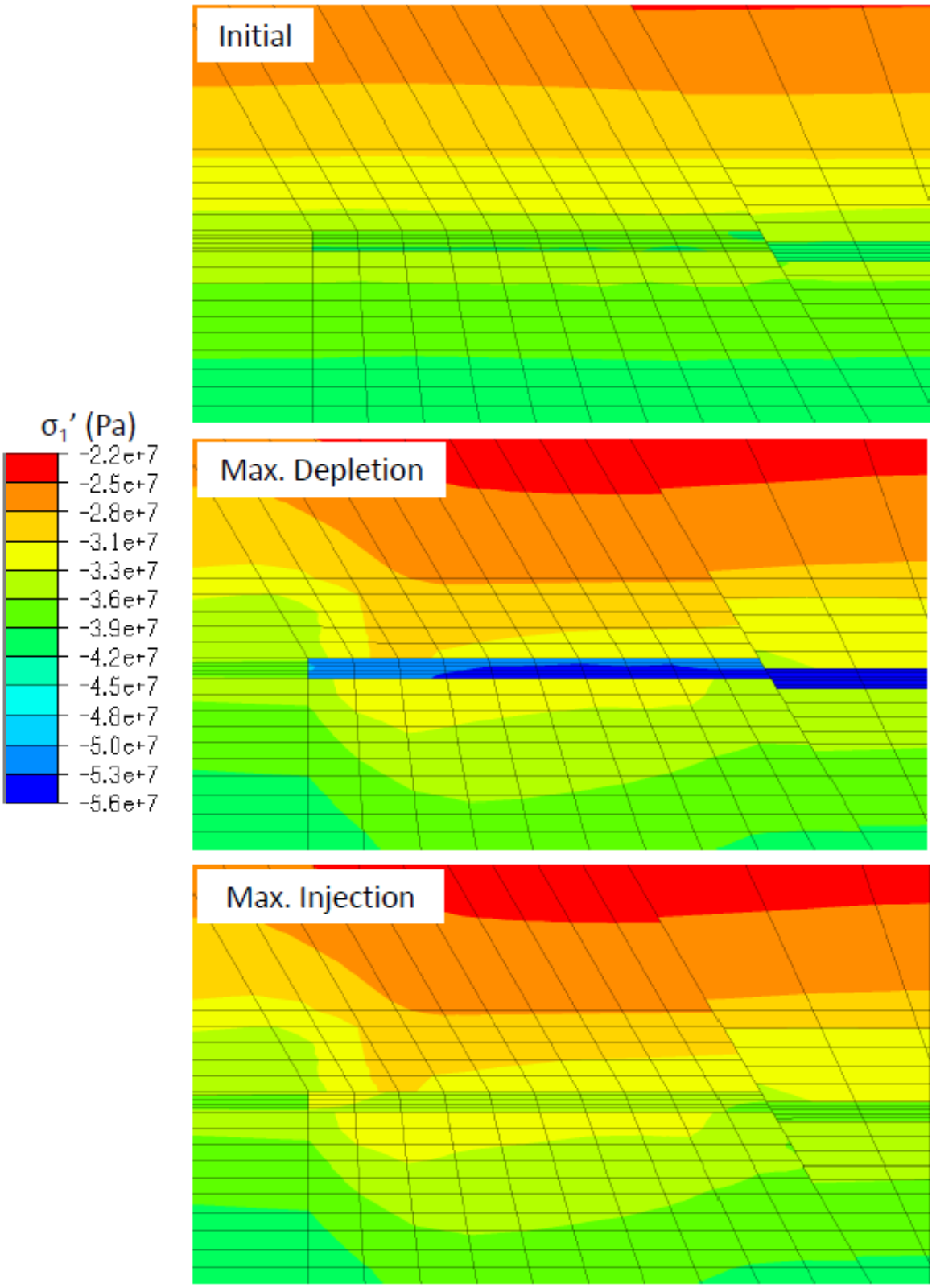

Figure 4.15 – Contour plot of σ_1' in the non-sealing low fault friction case, showing initial stage, end of depletion and end of injection. Figure shows X plane section through centre of the model at the location of the well, with well injection compartment, fault and part of the central compartment shown. Compressive stresses are negative in Elfen.

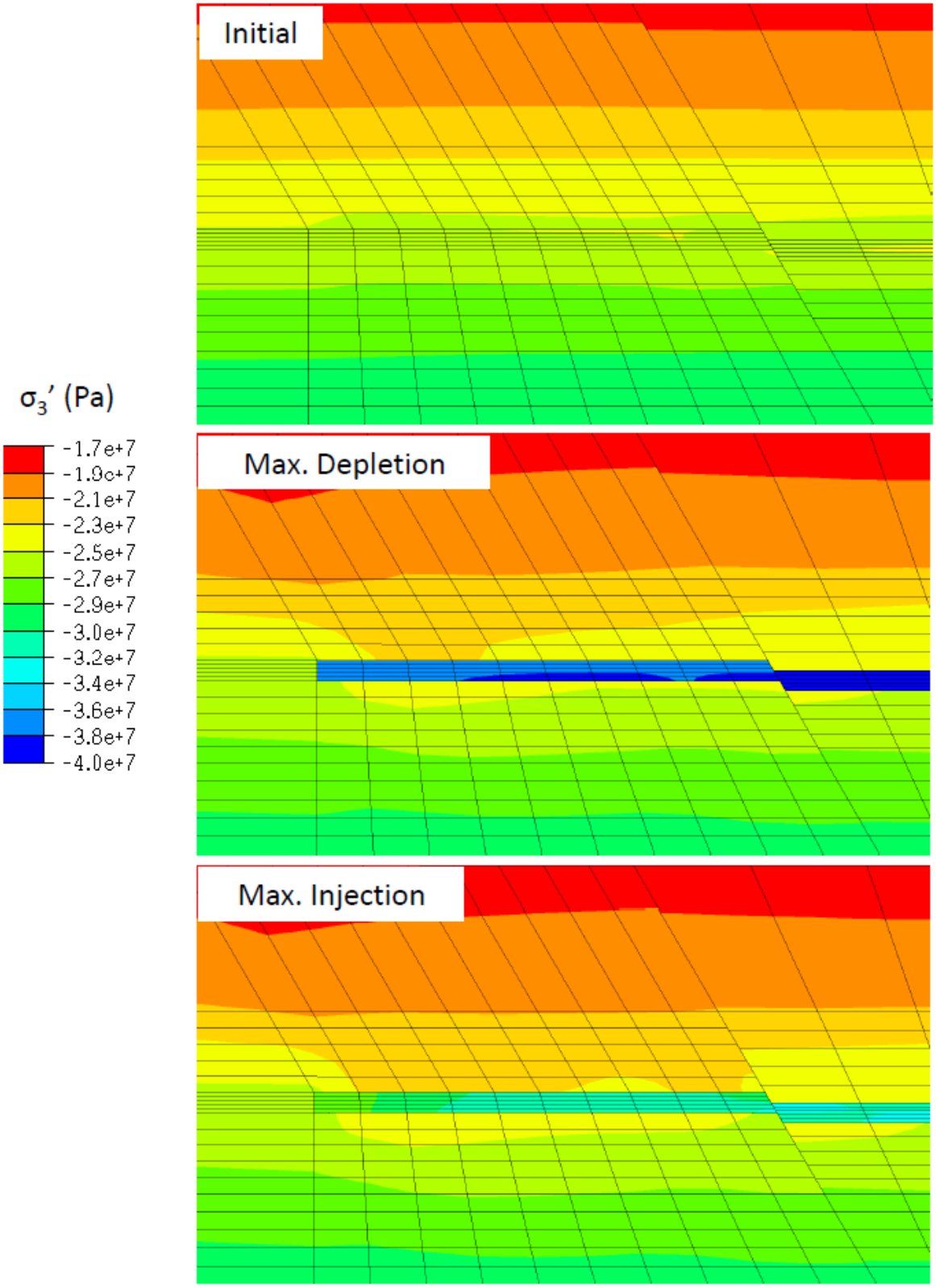

Figure 4.16 - Contour plot of σ_3' in the non-sealing low fault friction case showing initial stage, end of depletion and end of injection. Figure shows X plane section through centre of the model at the location of the well, with well injection compartment, fault and part of the central compartment shown. Compressive stresses are negative in Elfen.

The contour plot of σ_1 total stress difference in the overburden (the reservoir is omitted) clearly shows stress arching in the overburden during depletion. Stress is elevated by

around 4MPa in the sideburden adjacent to the reservoir and is reduced 3.1 – 5.5 MPa above and below the reservoir. During injection there is a slight increase in σ_1 total stress of 1 MPa or less above and below the reservoir, and the change in the sideburden is minimal. Overall, the recovery of σ_1 around the reservoir is minimal during injection compared to the reduction during depletion.

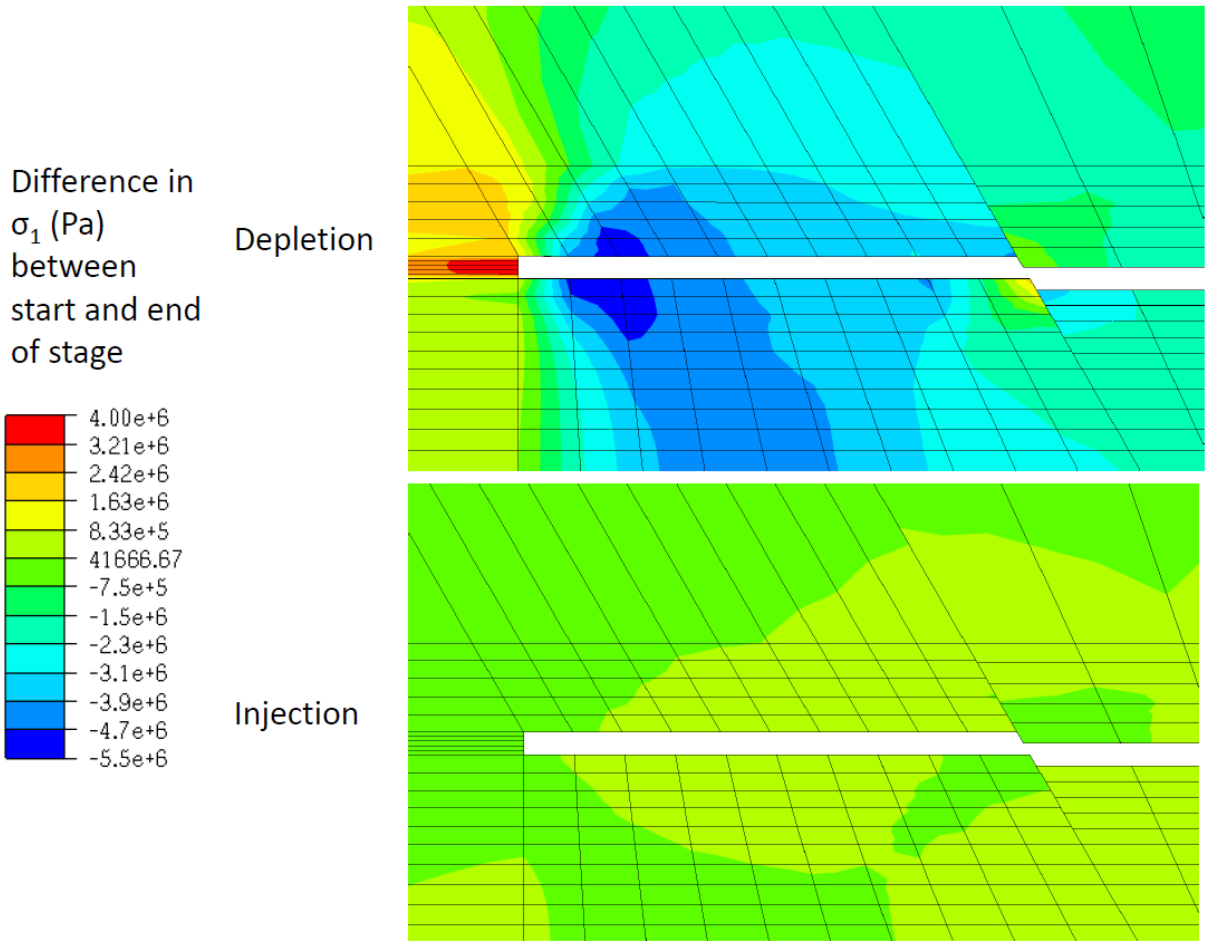

Figure 4.17 – Contour plot of the change in σ_1 during depletion and injection for the X plane section through the reservoir at the well.

The contour plot of σ_3 around the reservoir for depletion shows a similar pattern to that for σ_1, σ_3 increases by 1.5 – 2.0 MPa in the sideburden and reduces by 2.3 – 4.5 MPa in the overburden directly above and below the injected compartment. During injection there is a slight decrease in σ_3 above and below the injected compartment of 0.17 – 0.7 MPa, in the sideburden there an increase in σ_3 of 0.4 – 0.9 MPa. The σ_3 changes in the over and side burden follow the same pattern as σ_1 during depletion, but follow a different trend during injection with σ_3 continuing to increase in the sideburden and decrease in the over and underburden.

Although not shown in any of the contour plots or Mohr circles σ_2 is very similar to σ_3 and follows the same pattern of behaviour throughout the modelling.

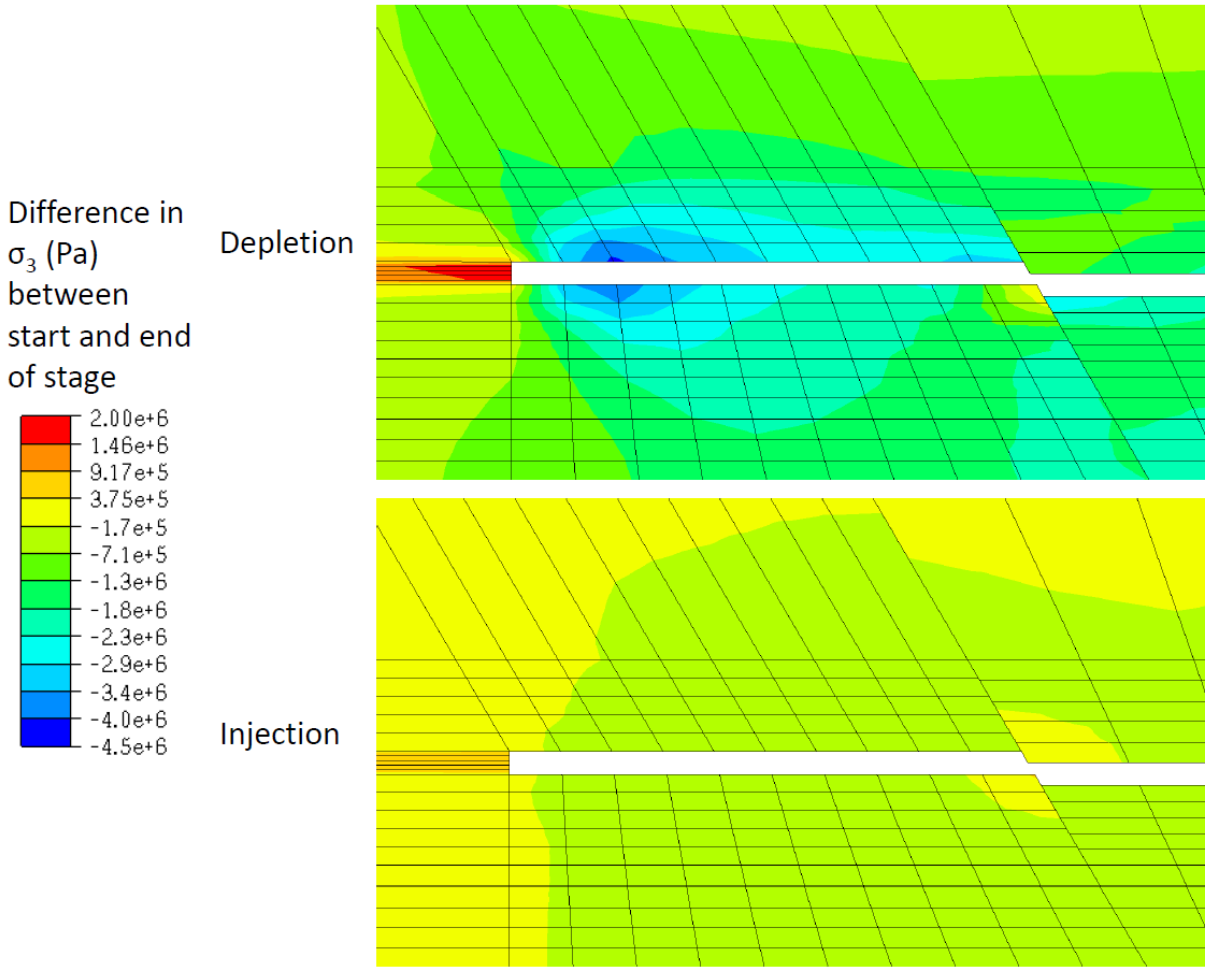

Figure 4.18 - Contour plot of the change in σ_3 during depletion and injection for the X plane section through the reservoir at the well.

The displacement in the model can also be plotted. Figure 4.19 shows the vertical displacement in the reservoir and surrounding over, under and side burden, as well as a section of the central compartment. Figure 4.20 shows the same contour plot for displacement in the horizontal plane parallel to the plane of section. In the displacement plots Z is positive for movement upwards and X is positive for movement to the right. The plots show that during depletion there is subsidence of up to 0.8 m above the reservoir and uplift of up to 0.2 m beneath the reservoir, and that the sideburden moves inwards towards the centre of the reservoir by up to 0.14 m. This movement occurs due the depletion and shrinkage of the reservoir which can also be identified on the plots. In this case during injection there is minimal vertical movement. A refined scale plot is presented in Figure 4.19 and shows that there is some uplift above the reservoir and subsidence below the reservoir in the opposite direction to that observed during depletion. However, the magnitude of this movement during injection is much less than initial movement, around 0.02 m in either case. The horizontal displacement during injection is more significant than the vertical movement and the material at the edge of the injected compartment is pushed outward by up to 0.08 m.

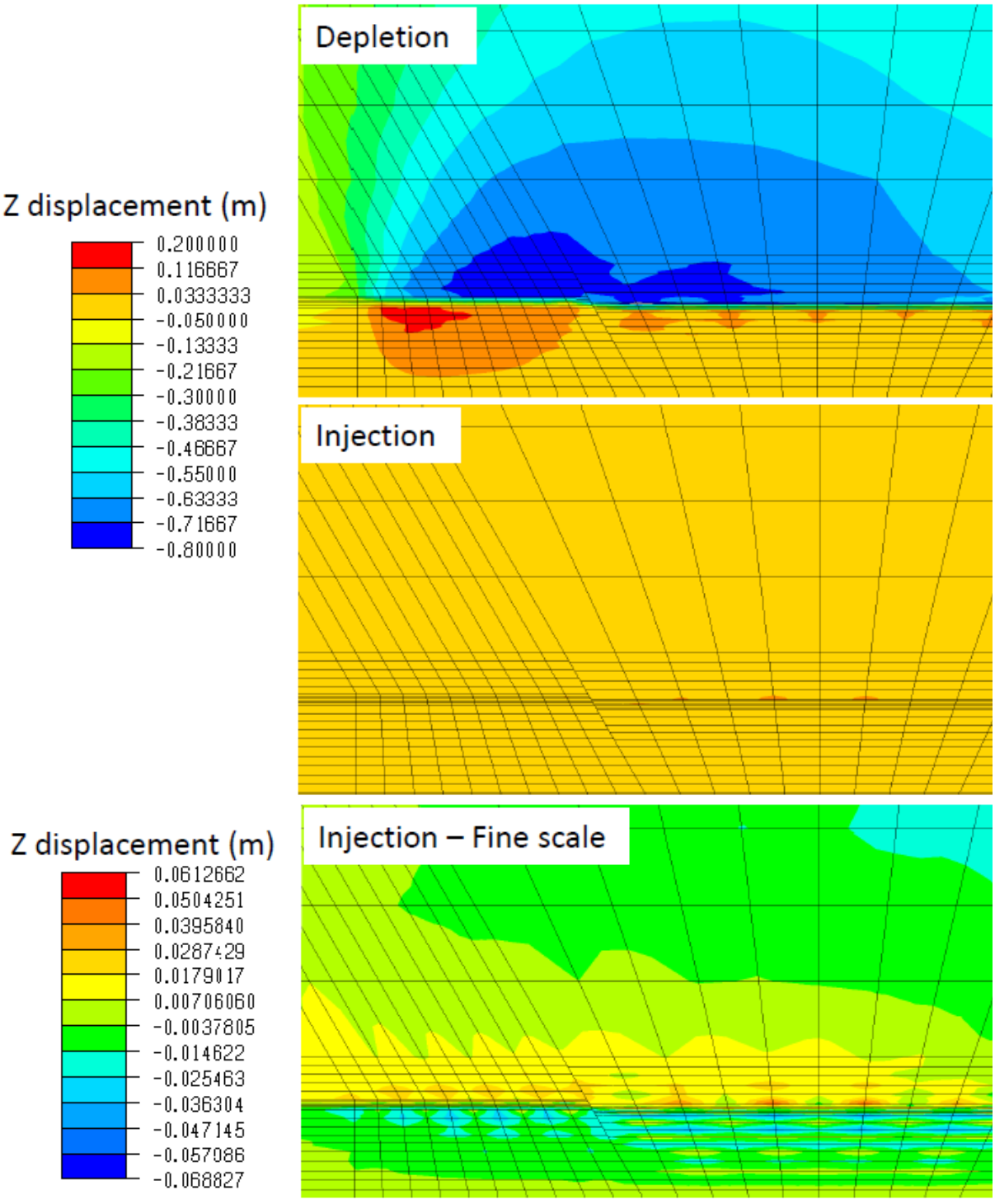

Figure 4.19 – Contour plot of displacement in the vertical direction for the central X plane section through the injection compartment and centre of model. The change in displacement during depletion and injection is shown, with a refined scale plot for the injection stage (bottom). Positive displacement represents movement upwards.

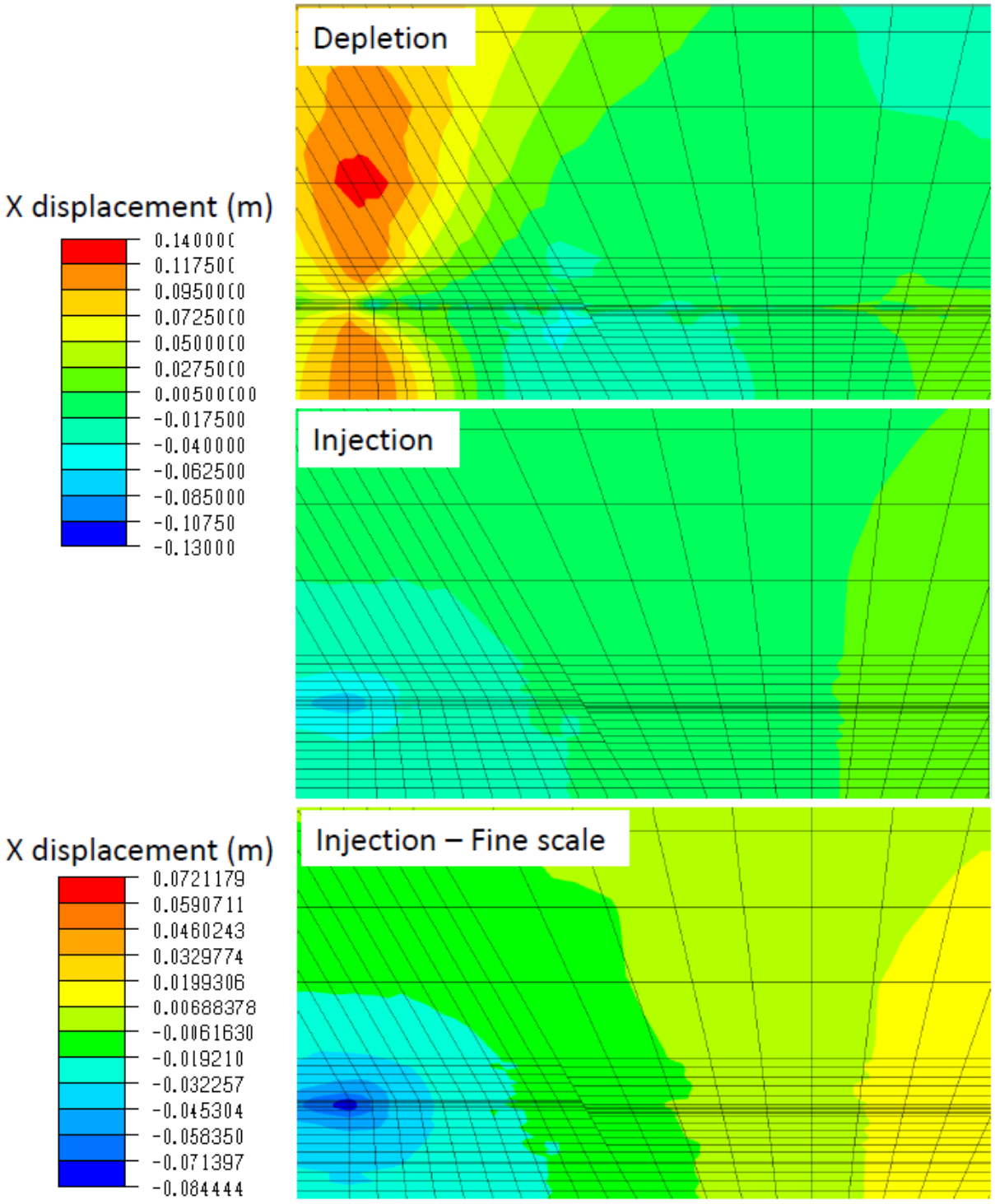

Figure 4.20 - Contour plot of displacement in the horizontal direction for central X plane section through the injection compartment and centre of model. Horizontal displacement is in the plane of the section with positive displacement left to right.

The plots of effective stress, total stress and displacement shows that when the reservoir is depleted stress arching occurs in both a vertical and horizontal sense and the increase in both σ'_3 and σ'_1 is restricted to some extent. During the depletion phase, when the deformation is elastic and plastic, most of the vertical displacement occurs. When re-pressurisation of the reservoir occurs during injection, the deformation is purely elastic as it

occurs within the yield surface, displacement is much lower in both the horizontal and vertical direction and most displacement occurs in the horizontal direction. During injection, σ'_1 behaves as if stress arching is not occurring and decreases below the initial value, this is because vertical total stress remains low above and below the reservoir. The stress changes occur mainly in the horizontal direction during injection. Total horizontal stresses above and below the reservoir are reduced further during injection but increase in the sideburden, and horizontal effective stress are higher than the initial value. This change in horizontal effective stress may represent stress transfer to the over and underburden and confinement due to the sideburden, the opposite behaviour to that observed with the vertical stress. The stresses at the end of injection in this case are tending towards the hydrostatic case and in terms of fracture formation the case is less at risk at the end of injection than at the start of depletion.

The stress and displacements in and around the reservoir can be more clearly understood by observing changes in elastic and plastic strain during depletion and injection. Figure 4.21 and Figure 4.22 show the normal strain in the horizontal (x) direction in the reservoir and overburden for the elastic and plastic depletion stage and the elastic injection stage. The plot shows that during depletion x-strain in the reservoir is compressive and the largest magnitude, up to -0.00045 is focussed at the edge of the reservoir. Strain is compressive in the overburden above and below the reservoir, and extension is observed in the sideburden above and below the reservoir. The compressive strain above and below the reservoir has a magnitude of up to -0.00025. In the overburden to the side of the reservoir the largest magnitude of strain is observed in the region directly adjacent to the side of the reservoir, up to 0.0001, and in a region above the side of the reservoir with strains of up to 0.00015. During injection the strains are elastic and the trend is reversed. In the overburden extension is observed above and below the reservoir and compression observed to the side of the reservoir. The strains in the overburden are smaller than those observed during depletion, and most of the deformation is focussed in the sideburden at the edge of the reservoir. Most of the deformation during injection in the reservoir is again focussed at the edge of the reservoir. Compression at the edge of the reservoir in the overburden has a magnitude of up to -0.0001, and extension in the reservoir adjacent to the reservoir has larger extension up to 0.0002.

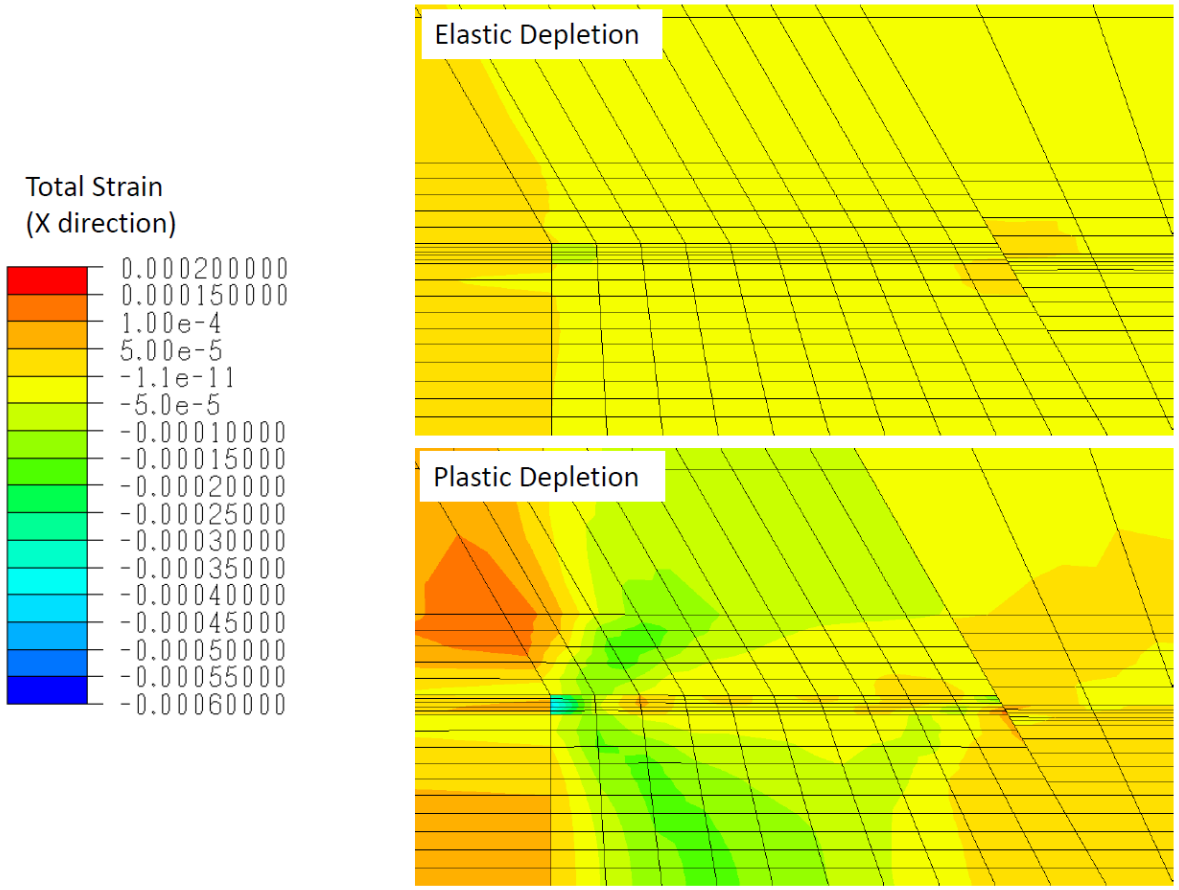

Figure 4.21 – Contour plot of strain in the X-direction (horizontal in plane of section) during the elastic and plastic depletion phase for the central X plane section through the model.

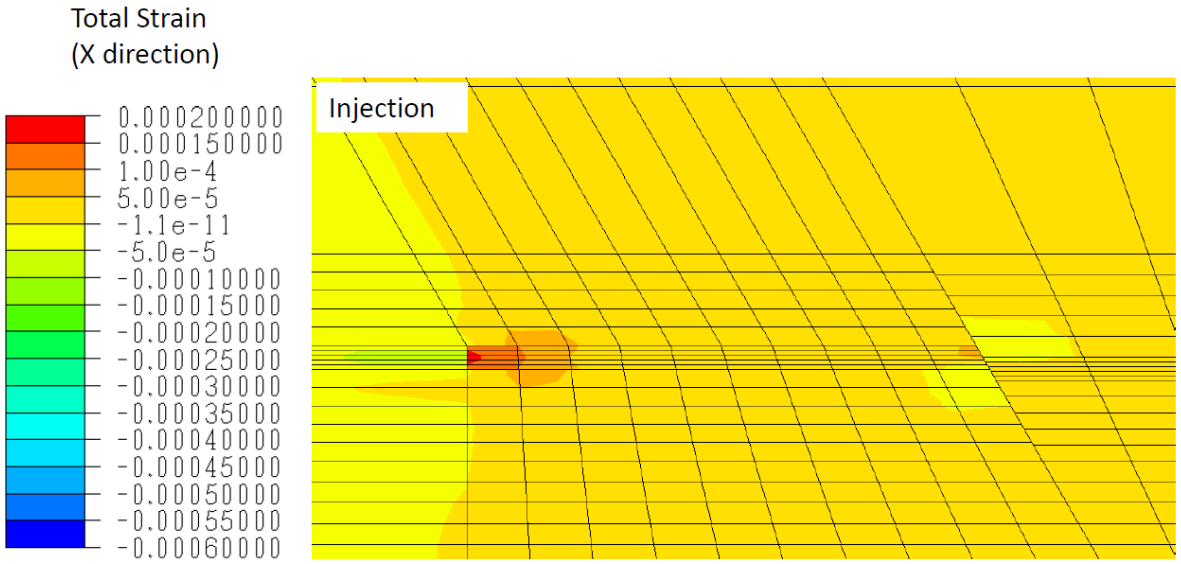

Figure 4.22 - Contour plot of strain in the X-direction (horizontal in plane of section) during the injection phase for the central X plane section through the model.

The vertical (Z) strains in the model are more variable due to the very large plastic strain in the reservoir during compaction. Figure 4.23 shows the vertical strain during elastic and plastic depletion, with the reservoir excluded for the plastic depletion plot due to the contrast in strains. Figure 4.24 shows vertical strain in the reservoir during depletion and Figure 4.25 shows elastic strain during injection in the whole model. The vertical strain shows a similar distribution to the horizontal strain during depletion and during the plastic stage of depletion is extensive above and below the reservoir and compressive in the sideburden. Extension above and below the reservoir during depletion has a magnitude of up to 0.0003 and compression at the side of the reservoir a magnitude up to -0.0002. The compressive strains observed in the reservoir during depletion are large, up to -0.014, increase towards the centre of the reservoir and result from the plastic compaction of the reservoir. Finally, strains during injection are more homogenous and represent extension in the reservoir, with strains of up to 0.0006, and unloading of the sideburden with strains of up to 0.0001.

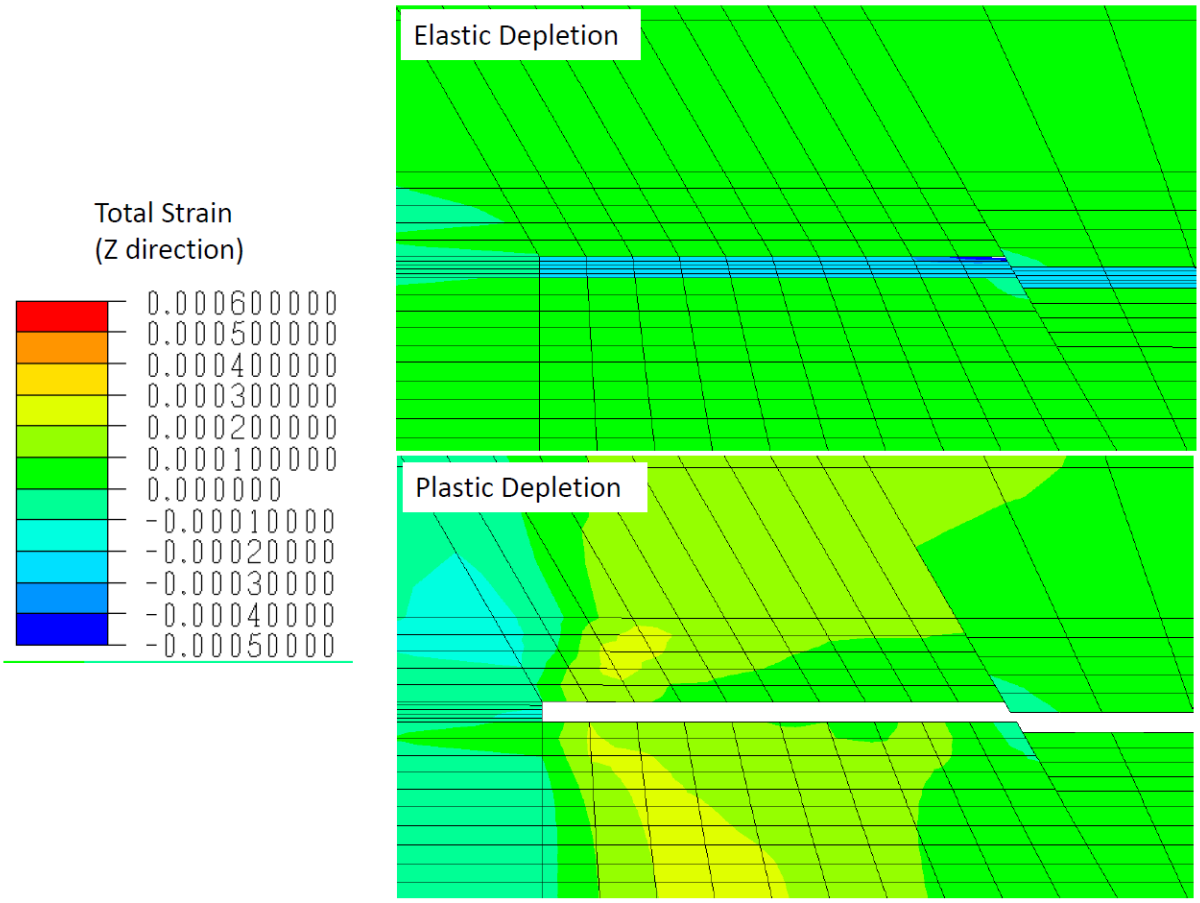

Figure 4.23 - Contour plot of strain in the Z-direction (vertical in plane of section) during the elastic and plastic depletion phase. The reservoir is excluded to emphasise strain in the overburden for the central X plane section through the model.

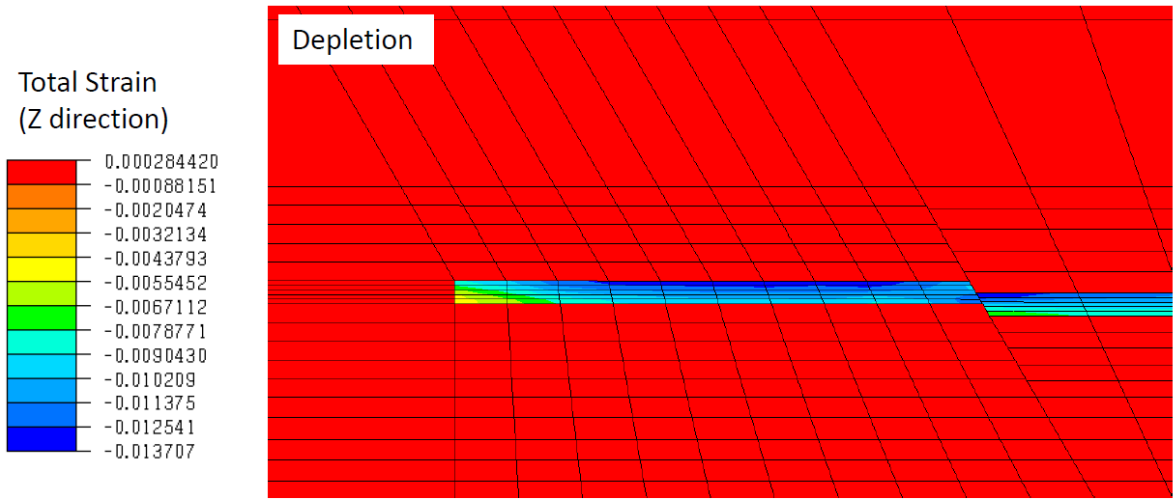

Figure 4.24 - Contour plot of strain in the Z-direction (vertical in plane of section) during the depletion phase for the central X plane section through the model. The reservoir is included to show the significant changes in the reservoir compared to the overburden.

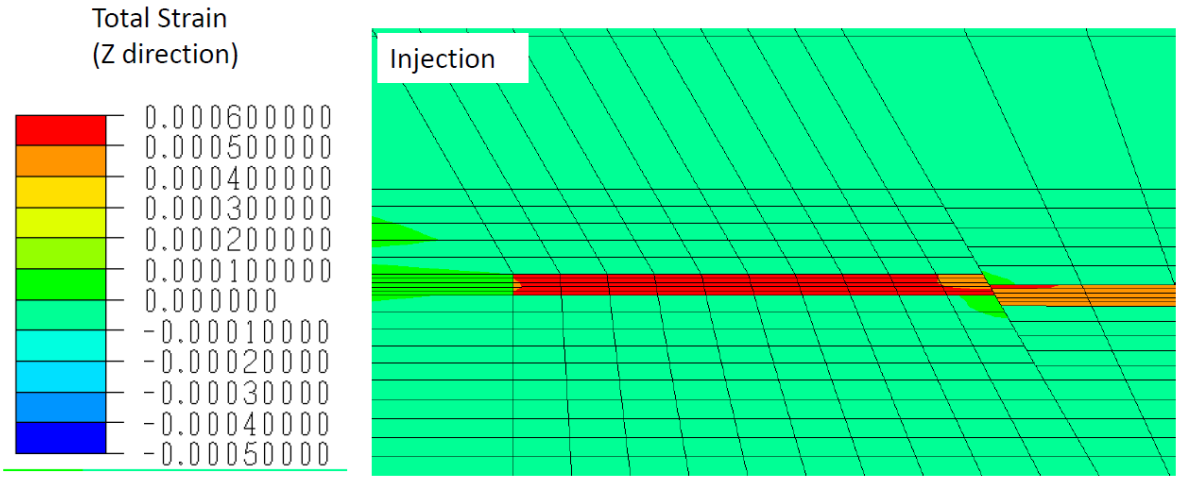

Figure 4.25 - Contour plot of strain in the Z-direction (vertical in plane of section) during the elastic injection phase for the central X plane section through the model.

The plots of strain changes in and around the reservoir show how deformation is occurring in and around the reservoir and can be linked to the displacements and stresses observed.

The vertical strain changes show compression at the side of the reservoir and extension above and below the reservoir, this is associated with the stress arching and these strains are linked to the observed vertical stress increase at the side of the reservoir and decrease above the reservoir. The vertical displacements observed are related to the significant

compaction that occurs, shown by the compressive strains in the reservoir, and the reservoir displacement is transmitted to the overburden. During injection there is vertical expansion in the reservoir and some vertical compression of the over and underburden, this is associated with a small amount of vertical stress increase in the overburden.

In terms of horizontal strain, there is expansion of the sideburden and contraction of the reservoir and overburden during depletion, this corresponds with the horizontal displacements observed. The trend is reversed for injection. The only counter-intuitive observation is the increase in horizontal stress at the edge of the reservoir in the sideburden when expansion occurs, and decrease in horizontal stress above and below the reservoir where contraction occurs. This seems to be due to a stress concentration at the interface of the reservoir and sideburden and a corresponding stress decrease above and below the reservoir. During injection, the compression in the sideburden and expansion in the edge of the reservoir is correlated to the stress increase in the sideburden and the relative stress decrease in the edge of reservoir compared to the rest of the reservoir.

4.3.1.2 *Sealing fault case*

The cases with low transmissibilities on the faults where the faults are essentially sealing can be compared with the equivalent non-sealing cases discussed above. In the sealing case the injection region acts a compartment sealed by the fault with no pressure communication to the rest of the reservoir. The p-q plot of the stress path for the sealing cases is plotted with the stress path for the non-sealing cases in Figure 4.26 for comparison.

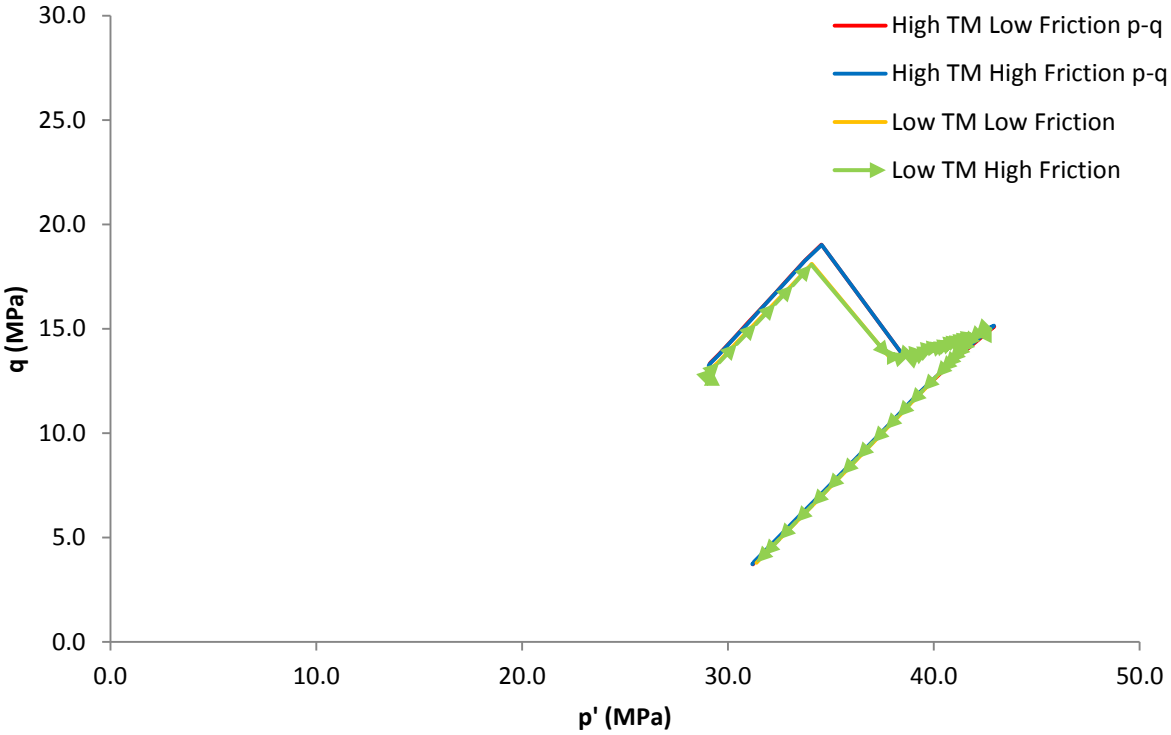

Figure 4.26 – Comparison of p'-q plots for sealing fault 'low TM' cases and non-sealing fault 'high TM' cases. The arrows on the Low TM High Friction case indicate the direction of all the stress paths from start of depletion to end of injection. The High TM and Low TM high and low friction cases follow identical stress paths to each other.

The plot shows a very similar stress path with the sealing fault case to the non-sealing fault case. The sealing case follows a slightly different elastic stress path during depletion than the non-sealing case with a slightly higher p' stress and slightly lower q stress, however the difference is minimal. The sealing case appears to yield at a slightly lower p' and q stress than the non-sealing case and the plastic phase of deformation initiates at lower p' stress, however this may be due to the resolution of the data output. The significant change in stress over a short time during the transition from elastic to plastic depletion deformation means that the transition stage is not fully captured in the data. The peak stresses reached for the sealing case during depletion are p' = 41.2 MPa and q = 14.8 MPa, which is slightly lower than the non-sealing case (p' = 42.9 MPa and q = 15.1 MPa). Elastic deformation during the injection stage occurs along the same trajectory as the non-sealing case and the final p and q stress at the end of depletion are the same. Once again it can be seen that there is minimal difference between the cases with different fault friction applied.

The calculated fracture pressure hysteresis for the sealing case is the same as the non-sealing case f_{ph} = 1.4.

The stress path parameters for the non-sealing case do vary slightly from the non-sealing case due the differences in the depletion stage. For the depletion stage γ_v = 0.24, γ_h = 0.31 and K_{sp} = 0.90 for the sealing case compared to γ_v = 0.24, γ_h = 0.33 and K = 0.88 for the previous non-sealing case. For the injection stage γ_v = 0.01, γ_h = 0.59 and K_{sp} = 0.41,

compared to γ_v = 0.02, γ_h = 0.60 and K_{sp} = 0.41 for the non-sealing case. The difference in the stress parameters is mainly due to the different end points at maximum depletion and represents increased stress arching in the compartmentalised model. The Mohr circle plot of stresses in Figure 4.27 shows the similarity between the cases. The most remarkable aspect of the Mohr circle plot is the difference in the Mohr circles for the start of injection, the circle for the sealing case shows the reduced impact of pressure increase during well shut in, with the injection start Mohr circle much close to the depletion end circle representing lower pressure increase.

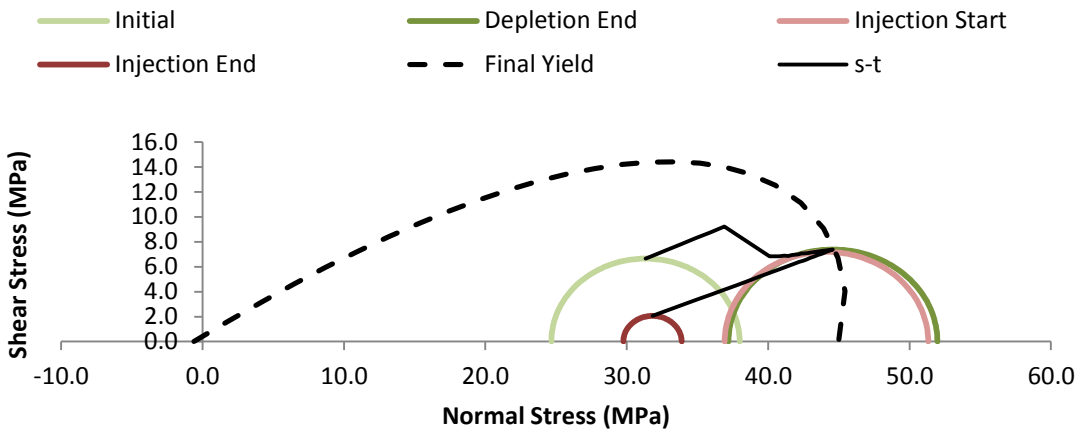

Figure 4.27 - Mohr circle diagram for the sealing low friction faults case with yield surface transformed into s'-t parameters and s'-t stress path plot.

In this case, most of the stress changes occur around the injected compartment as the faults are sealing; the general behaviour is however similar to when all compartments are open. Increased stress arching is observed and this is related to the smaller compartment, as stress arching is more likely to occur around a laterally smaller reservoir (Segura et al. 2011). Figure 4.28 to Figure 4.32 show the effective stress at the end of injection, the difference in total stress for the depletion and injection stage and displacement contours for the sealing case. The plots of effective stress show the same general trend as the non-sealing case but the stress changes are restricted to the active compartment.

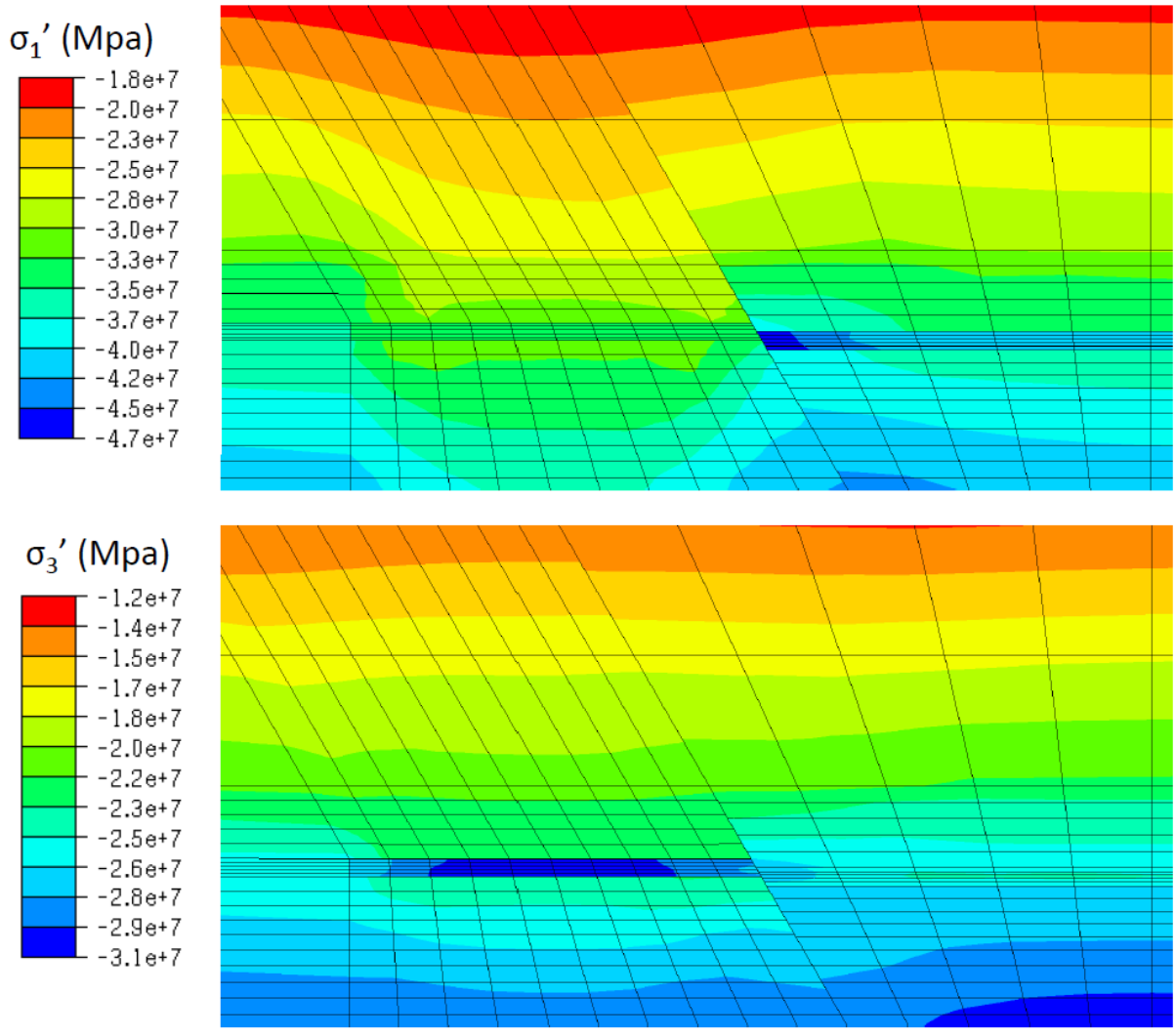

Figure 4.28 – Contour plots of effective stress in the sealing low fault friction case for the high stiffness base case at the end of the injection period for the central X plane section through the model.

The plots of change in total stress in Figure 4.29 and Figure 4.30 provide more information on the stress change around the reservoir. Figure 4.29 shows that there is increased σ_1 stress at the side of the reservoir in the sealing case, specifically in the region of the fault, compared to the non-sealing case. The contours also shows that σ_1 is lower above and below the reservoir compared to the sealing case. In the non-sealing case the maximum stress increase at the side is 4 MPa, compared to 5.11 MPa in the sealing case, and the

maximum decrease above and below the reservoir is 6 MPa, compared to 5.5 MPa. The σ_1 stress plots illustrate the increased stress arching that is observed in the sealing case. The injection stage is similar to the non-sealing case with a small increase in σ_1 above and below the reservoir, although the increase during injection is over a smaller area in the sealing case.

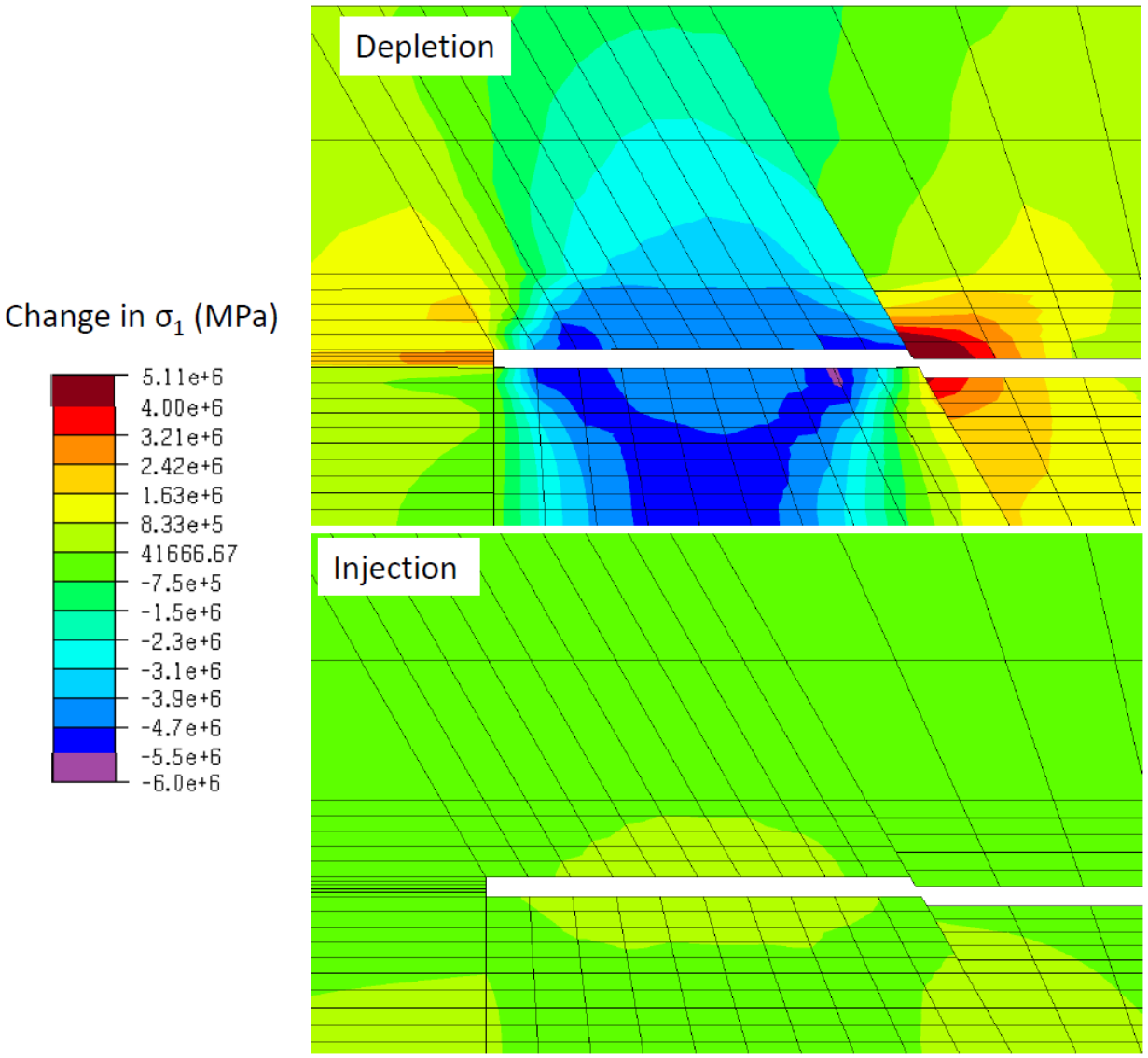

Figure 4.29 – Contour plot of the change in σ_1 in the overburden for the non-sealing case during the depletion and injection stages for the central X plane section through the model.

The σ_3 stress contours shows a similar trend to the σ_1 in the sealing model with higher stress at the side and lower stress above and below the reservoir compared to the non-sealing case during depletion. The maximum stress increase at the side of the reservoir in the sealing case is 2.5 MPa compared to 2 MPa in the non-sealing case. The maximum decrease in stress above and below the reservoir is the same magnitude of 4.5 MPa, but the stress reduction is greater across the whole region of the injection compartment in the sealing case. σ_3 stress change during injection is similar.

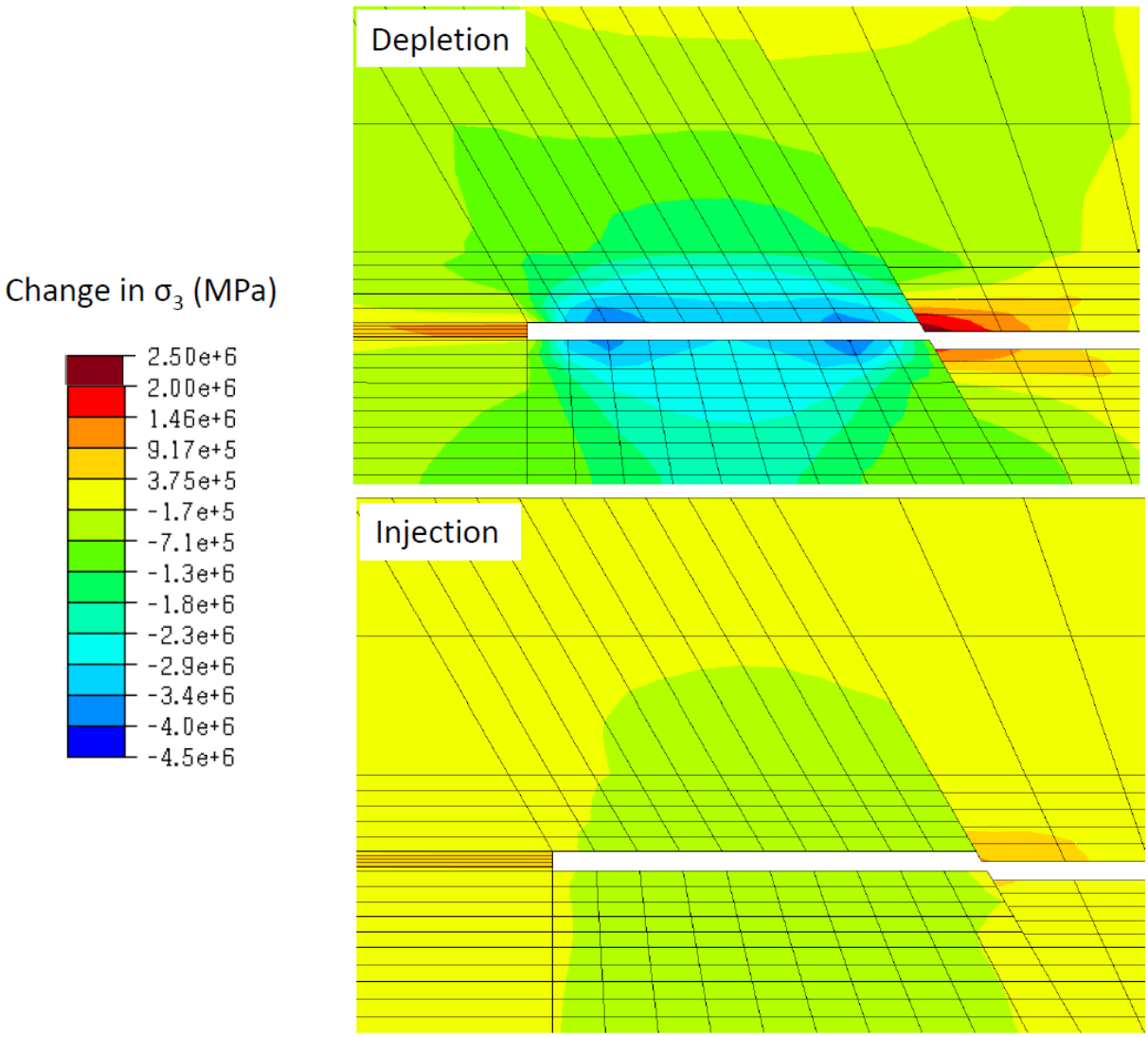

Figure 4.30 - Contour plot of the change in σ_1 in the overburden for the non-sealing case during the depletion and injection stages for the central X plane section through the model.

The displacement plots show that vertical and horizontal movement is reduced in the sealing case compared to the non-sealing case. Figure 4.31 shows that the maximum negative displacement (downwards) above the reservoir in the sealing case is 0.63 m compared to 0.8 m in the non-sealing case, uplift below the reservoir is of a similar magnitude in both cases. Horizontal movement in the overburden appears to be similar in both cases.

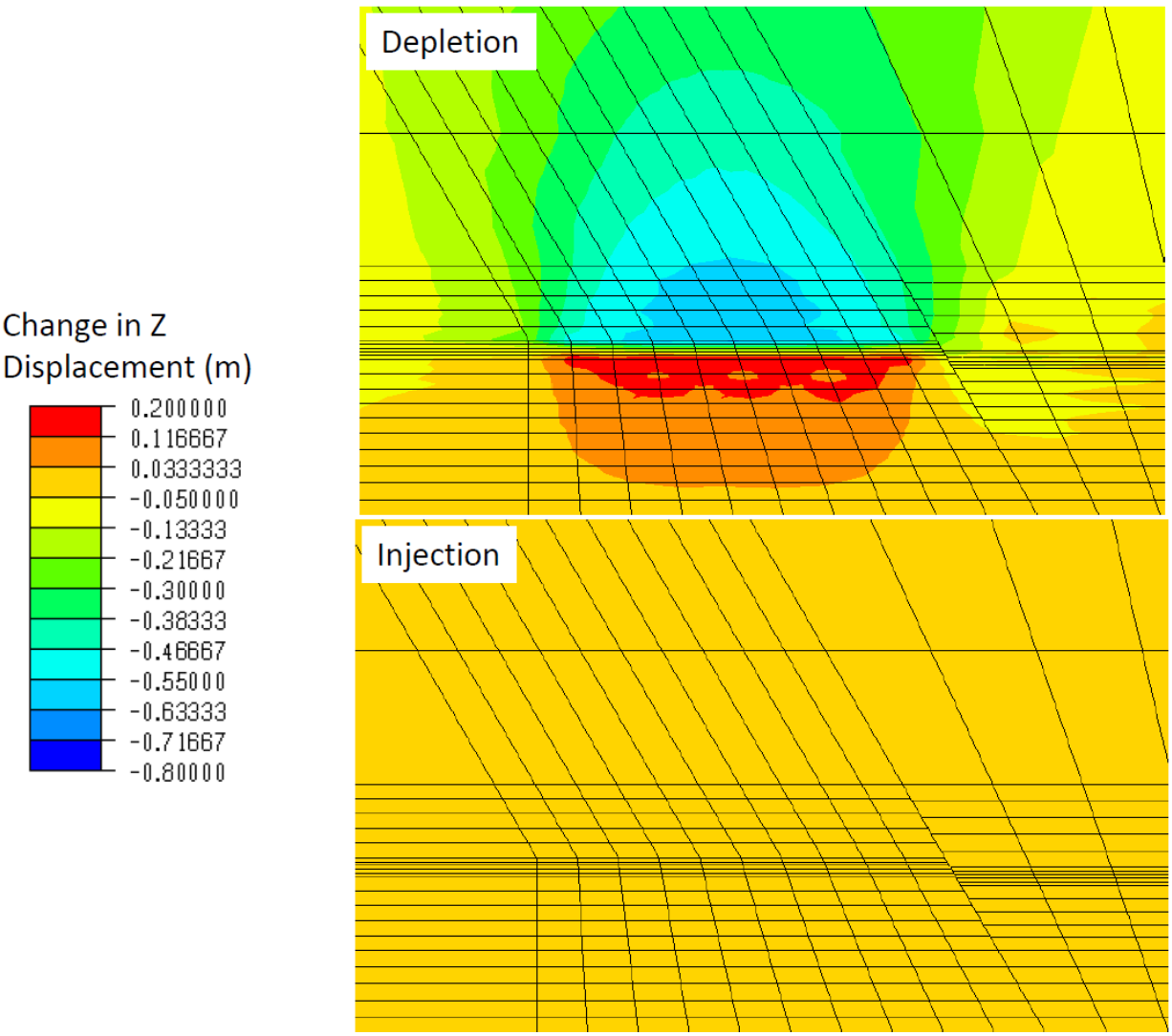

Figure 4.31 – Contour plot of Z displacement in the sealing low fault friction case for the high stiffness base case at the end of injection for the central X plane section through the model. Positive Z displacement represents upwards movement.

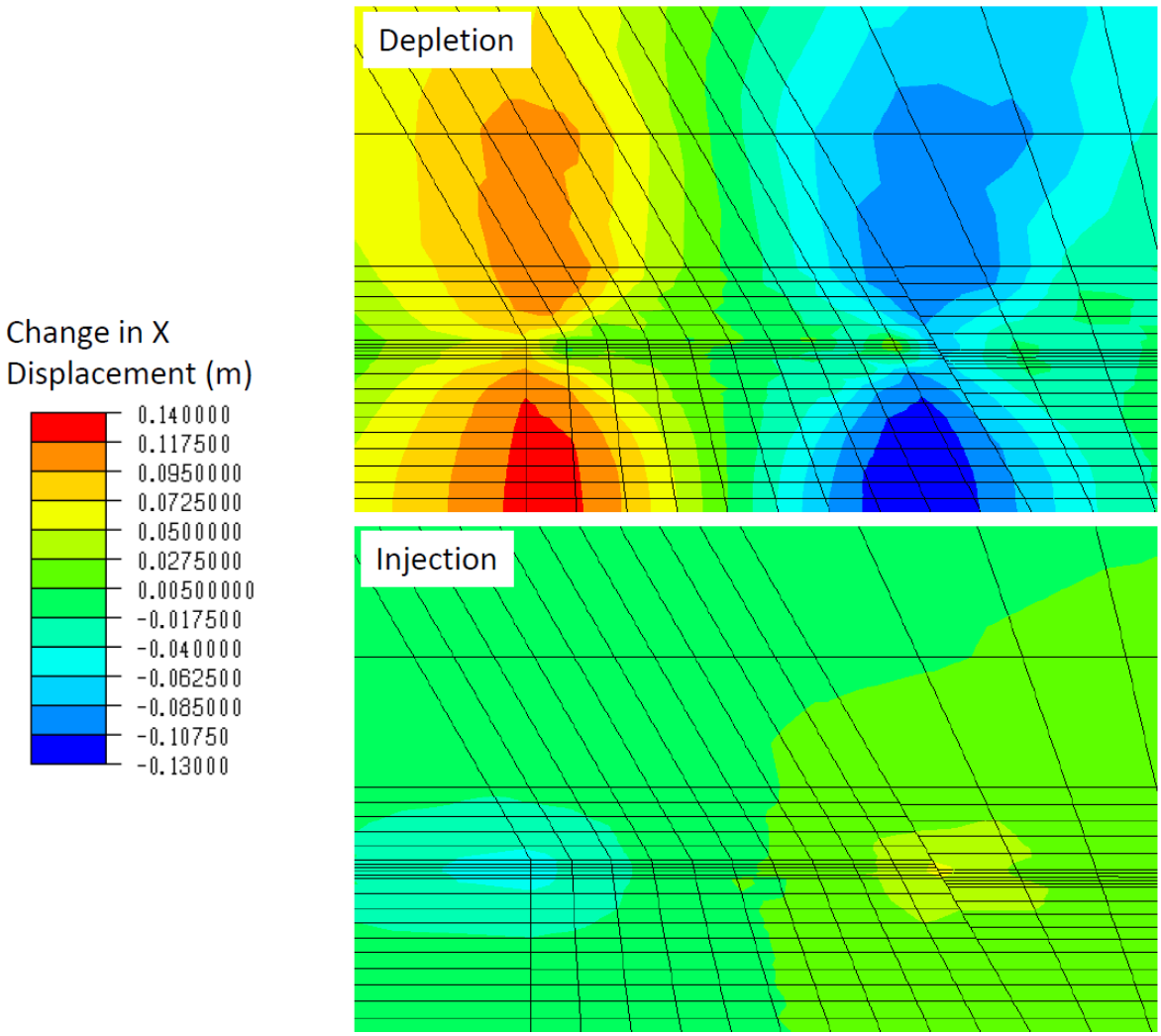

Figure 4.32 - Contour plot of X displacement in the sealing low fault friction case for the high stiffness base case at the end of injection for the central X plane section through the model. Positive X displacement represents movement left to right.

The model in the sealing case represents a compartmentalised model with a laterally restricted geometry compared to the non-sealing case. Whilst the stress path in the model does not appear to change much between the non-sealing and sealing cases, the plots of stress and displacement show that increase stress arching and reduced vertical compaction are observed in the overburden around the compartmentalised model. The reduction in compaction of the reservoir due to the increased stress arching has implications for flow modelling due to pore volume change and this aspect is discussed further in section 4.3.10.

4.3.2 **Low Stiffness Case**

The results from the lower stiffness case with a reference stiffness of 3.8 GPa can be compared against the high stiffness case. Figure 4.33 shows the stress paths for all low stiffness cases with an initial stress ratio of 0.7 compared against the non-sealing low fault friction case from the higher stiffness runs. The comparison shows that the stress paths in each of the stiffness cases are similar, with the start and end points almost identical, the main difference is the p' and q stress during depletion. In the lower stiffness case the q

stress remains higher during depletion but the p' stress is lower at the maximum depletion point. The comparison of the low stiffness cases with each other also shows that again there is little difference in stress path between the non-sealing and sealing cases and the low friction and high friction cases.

The calculated fracture pressure hysteresis for the low stiffness case is very similar to the high stiffness case and is approximately f_{ph} = 1.4.

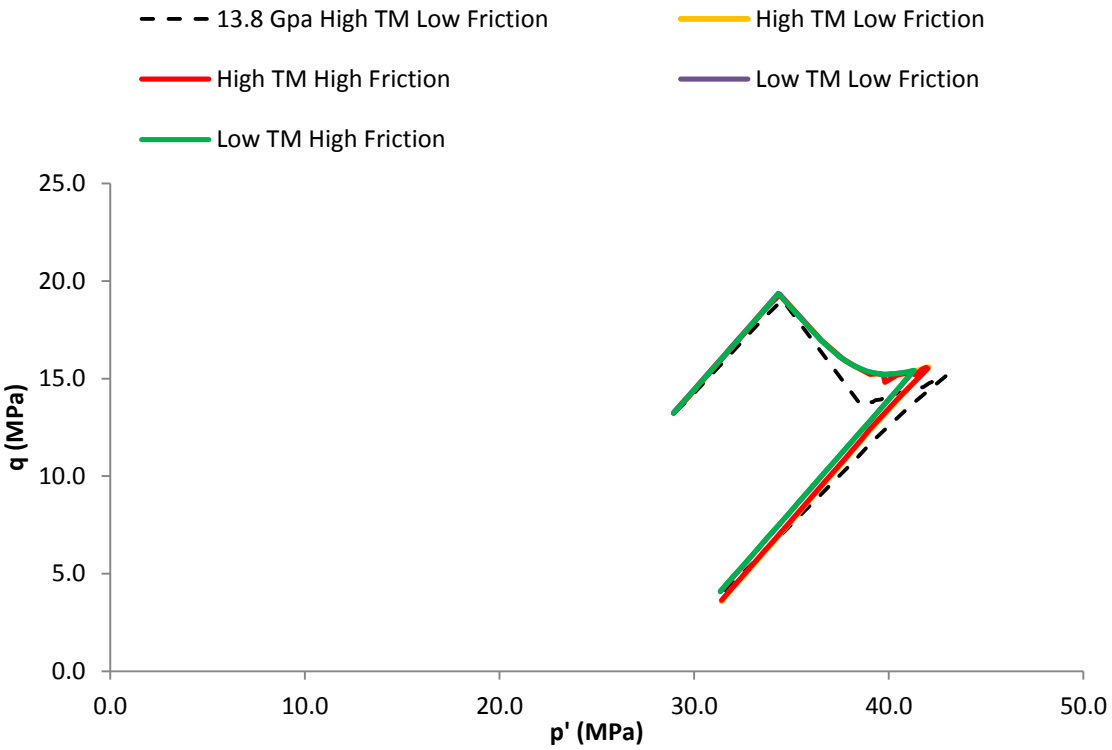

Figure 4.33 – Plot of p'-q stress paths for low stiffness cases with high stiffness non-sealing low friction case for comparison.

The Mohr circle plot for the non-sealing low friction low stiffness case is shown in Figure 4.34. The plot is similar to the same plot from the high stiffness case (Figure 4.14). The calculated stress path parameters for the non-sealing low friction low stiffness case are γ_v = 0.25, γ_h = 0.36 and K_{sp} = 0.85 for the depletion stage and γ_v = 0.04, γ_h = 0.65 and K_{sp} = 0.36 for the injection stage. For comparison the parameters from the same higher stiffness case are γ_v = 0.24, γ_h = 0.33 and K_{sp} = 0.88 for depletion and γ_v = 0.02, γ_h = 0.60 and K_{sp} = 0.41 for injection. The difference in parameters shows that during depletion the lower stiffness case Mohr circle will expand slightly more as the vertical stress arching is of a similar magnitude, but the horizontal stress arching is higher, this is reflected in the lower value of K. The opposite trend is observed in the changes in stress path parameters during injection, and this leads to a similar stress state and similar Mohr circles at the end of injection for both the high and low stiffness cases.

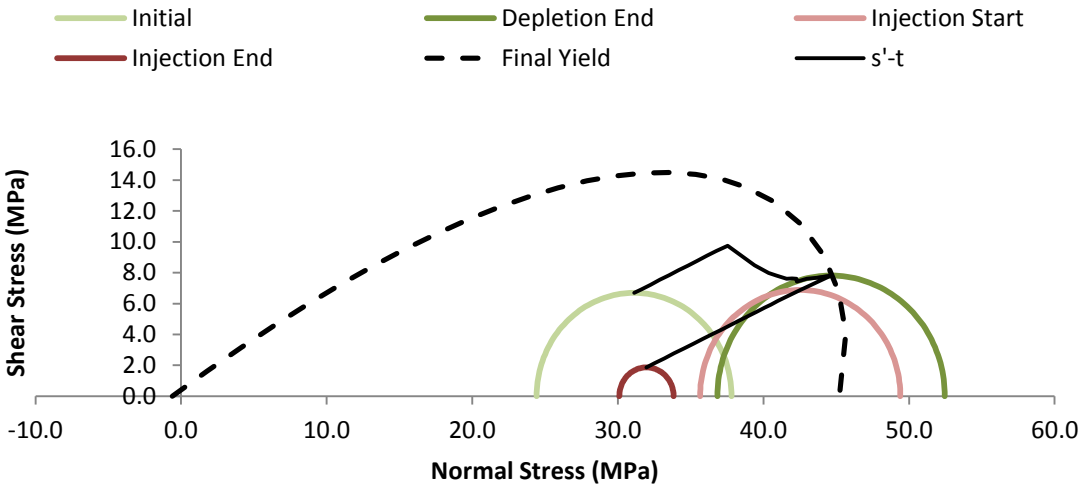

Figure 4.34 – Mohr circle and s'-t plot for non-sealing low friction fault low stiffness case.

Figure 4.35 is a plot of the effective stress in the reservoir and overburden for the low stiffness case and is comparable to Figure 4.15 and Figure 4.16 for the high stiffness case. The contour plot illustrates the similarity in the general stress changes in and around the reservoir between the high and low stiffness cases.

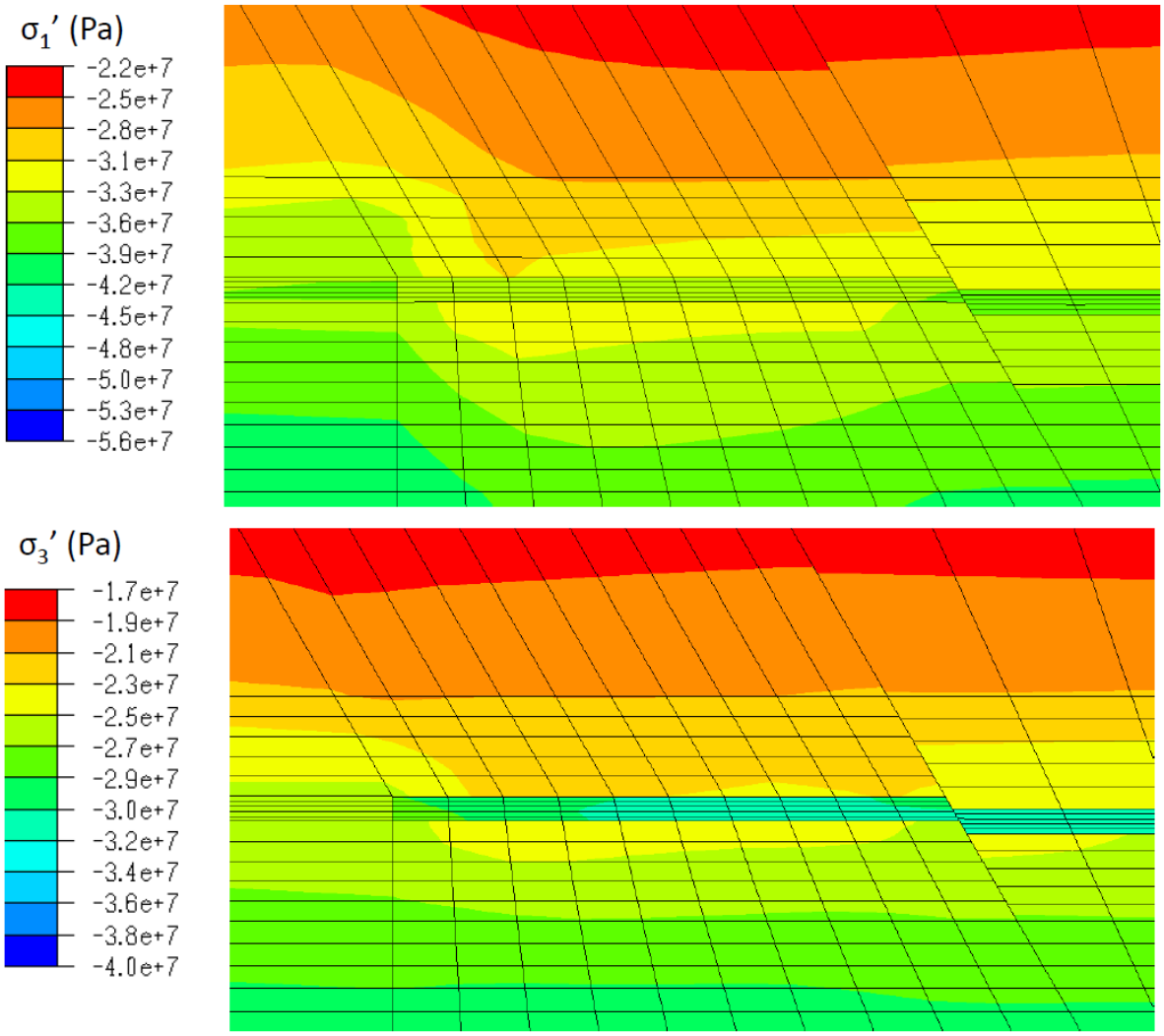

Figure 4.35 – Contour plot of effective stress in the reservoir and overburden for the low stiffness case with non-sealing low friction fault for the central X plane section through the model.

Figure 4.36 is a contour plot of the change in σ_1 in the overburden for the low stiffness case, the plot is comparable to Figure 4.17 for the high stiffness case. The σ_1 change in the low stiffness case is very similar to the high stiffness case for depletion. The main difference between the two cases is observed in the injection stage where the increase in σ_1 above and below the reservoir is much more extensive in the low stiffness case. The increase in σ_1 is of the same magnitude (maximum of 0.833 MPa) in the low stiffness case but extends vertically from the edge of the reservoir across the whole of the reservoir, compared to a vertically restricted region above and below the high stiffness reservoir.

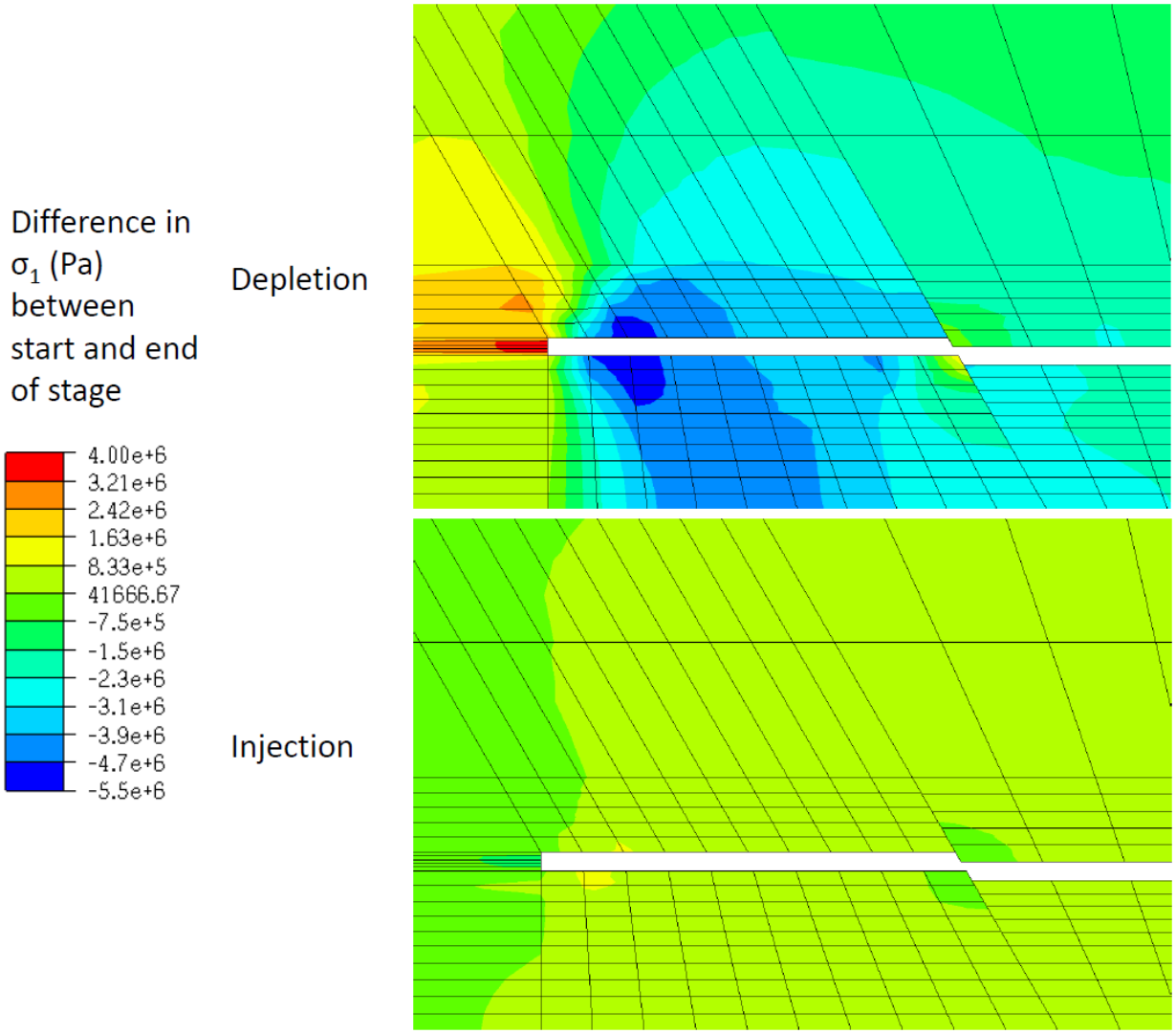

Figure 4.36 – Contour plot of a section through the reservoir at the well showing change in σ_1 during depletion and injection for the low stiffness case for the central X plane section through the model.

The contour plot of the change in σ_3 in Figure 4.37 is comparable to Figure 4.18 for the high stiffness case. Again, the plots for depletion are very similar, and the most significant difference is observed in the injection stage. In the high stiffness case σ_3 reduces by between 0.17 and 0.71 MPa above and below the reservoir during injection. In the low stiffness case the pattern is more complex, the broad contour of the plot suggests a stress change between 0.375 MPa and -0.17 MPa. A more detailed plot of the σ_3 stress in Figure 4.38 shows that the stress increase occurs above and below the outer half of the injection compartment and the small decrease of up to -0.17 MPa occurs on the inner half of the injection compartment. The stress increase above the centre and far field compartment is also very small.

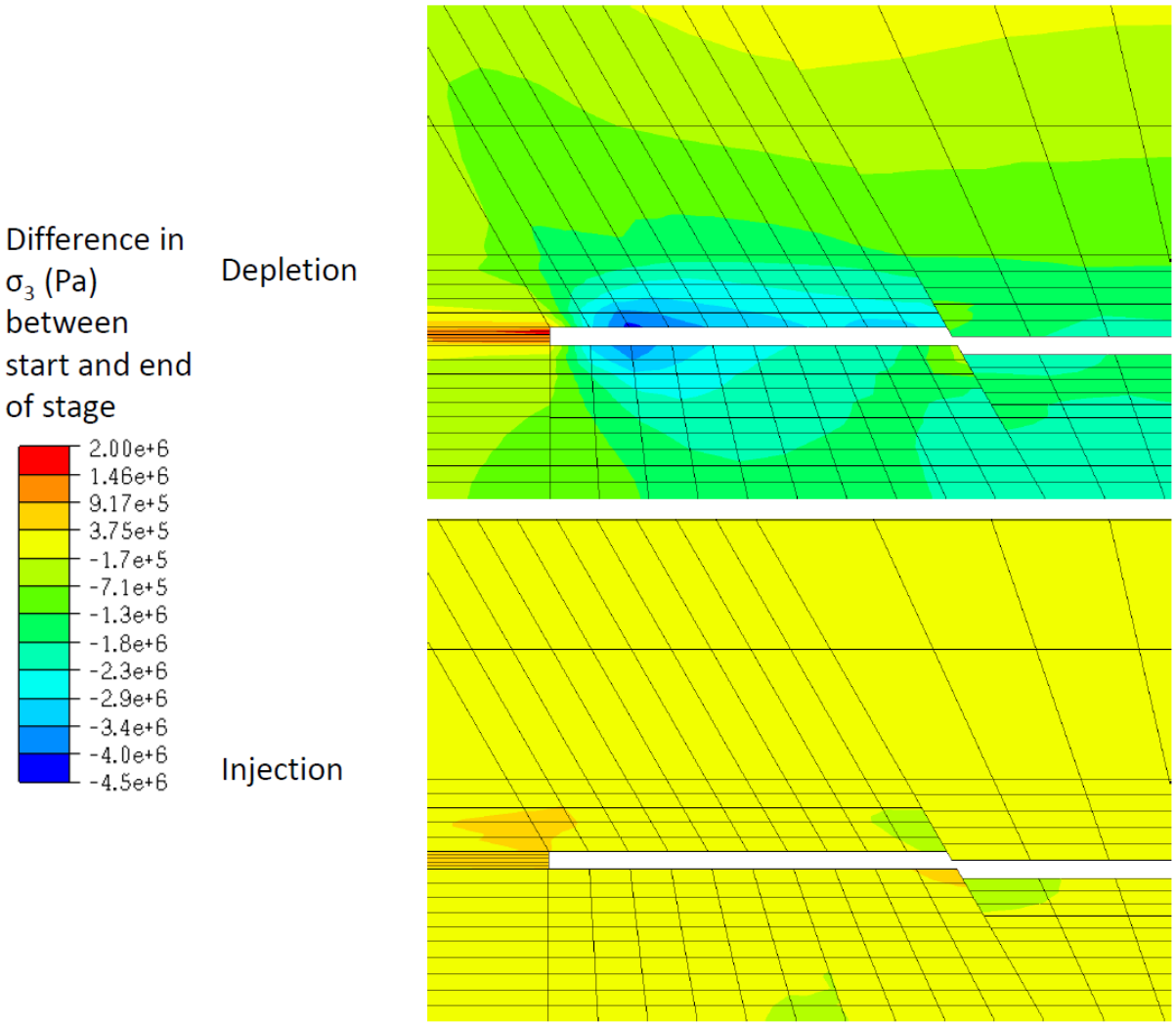

Figure 4.37 – Contour plot of a section through the reservoir at the well showing change in σ_3 during depletion and injection for the low stiffness case for the central X plane section through the model.

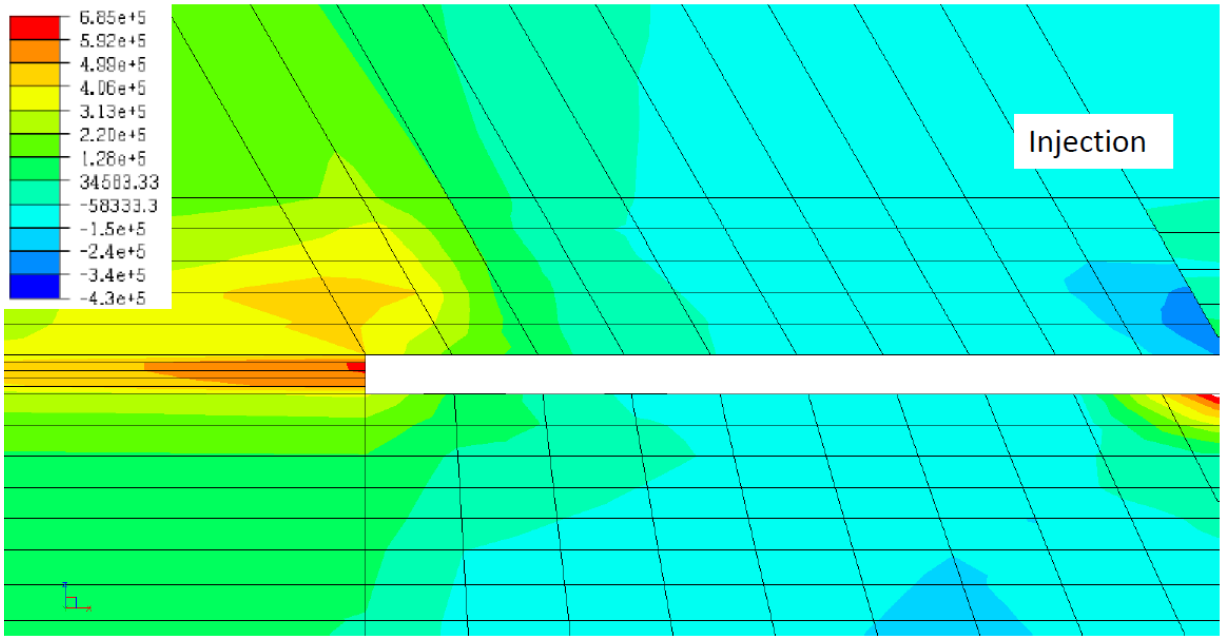

Figure 4.38 – High resolution contour plot of a section through the reservoir at the well showing change in σ_3 during injection for the low stiffness case for the central X plane section through the model.

Figure 4.39 and Figure 4.40 shows the vertical and horizontal displacement in the low stiffness case and are comparable to Figure 4.19 and Figure 4.20 for the high stiffness case. The vertical displacement in the low stiffness case is more significant with a larger maximum displacement of 0.83 m and a displacement of 0.8 m (the maximum in the high stiffness case) occurring over most of the reservoir, rather than an area restricted to the injection compartment as in the high stiffness case. There is also significant uplift in the injection stage of the low stiffness case when compared to the high stiffness case, with 0.03 to 0.11 m uplift of a large section of the overburden above and to the side of the reservoir. Uplift in the high stiffness case is smaller and varies between -0.05 and 0.03 m. Horizontal displacement in the low stiffness case is also more significant during depletion with the same maximum displacement of 0.14 m observed over a wider area above and below the side of the reservoir. Horizontal displacement at the side of the reservoir during injection in the low stiffness case is also larger between -0.09 and -0.1 m compared to between -0.06 and -0.09 m in the high stiffness case.

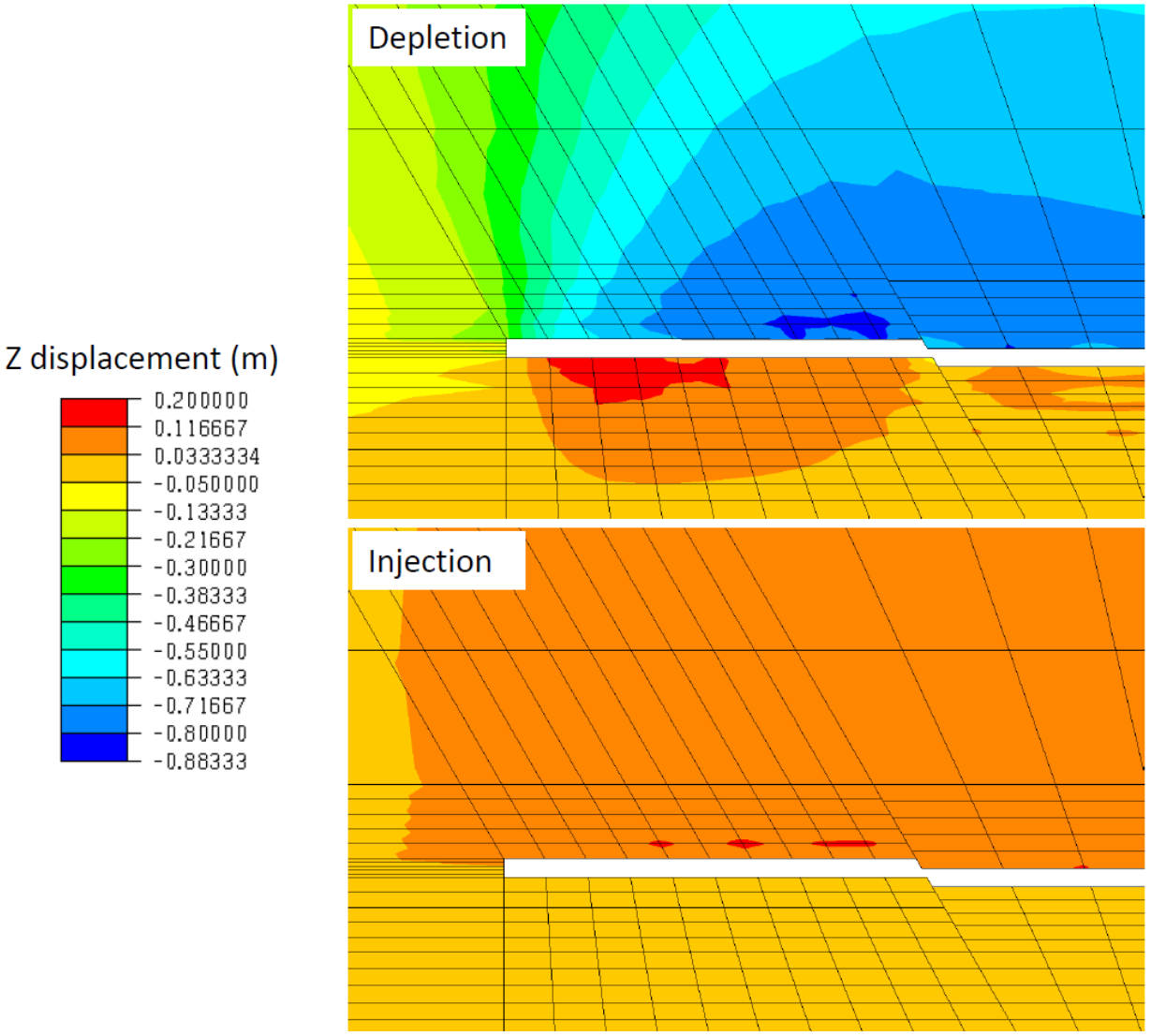

Figure 4.39 – Contour plot of displacement in the vertical direction for a section through the injection compartment for the low stiffness case for the central X plane section through the model. Positive displacement represents movement upwards.

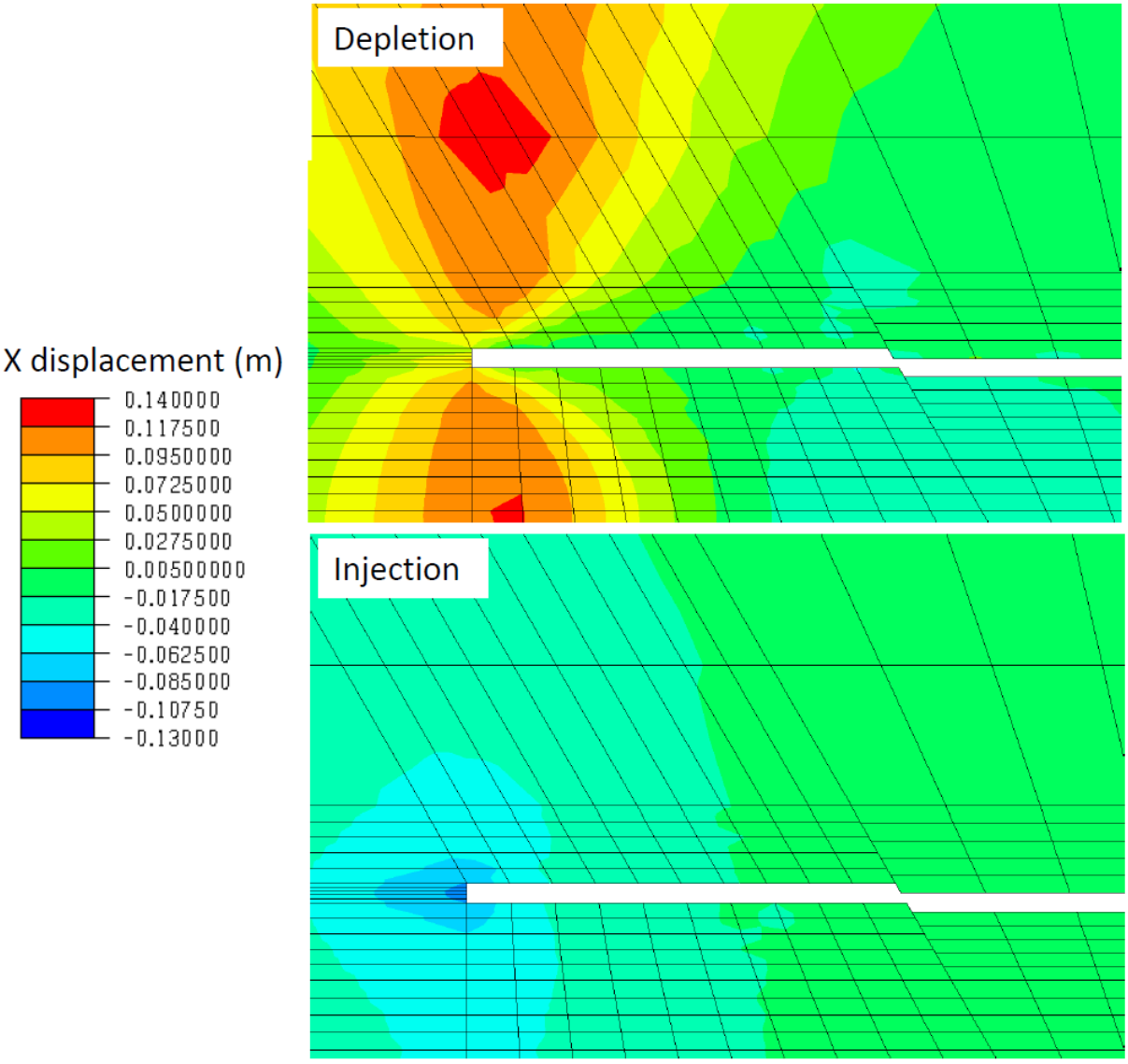

Figure 4.40 - Contour plot of displacement in the horizontal direction for a section through the injection compartment for the low stiffness case for the central X plane section through the model. Horizontal displacement is in the plane of the section with positive displacement left to right.

The strain can also be assessed during depletion and injection, Figure 4.41 and Figure 4.42 show the horizontal strain in the model during the elastic and plastic depletion phases, and the elastic injection phase. The strains are larger than the base case model. During depletion compression in the side of the reservoir is up to -0.0006, compared to -0.00045 in the base case model, although sideburden extension is similar. During injection extension in the side of the reservoir is also larger with a lower stiffness model, and is up to 0.0003 compared to 0.0002 in the base case. Vertical strains are not plotted but are also larger in magnitude in the softer reservoir. During depletion maximum strain is -0.0144 compared to 0.0137 in the base case. Vertical strains are 3 times larger during injection in the soft reservoir, at 0.0193 compared to 0.0006 in the base case.

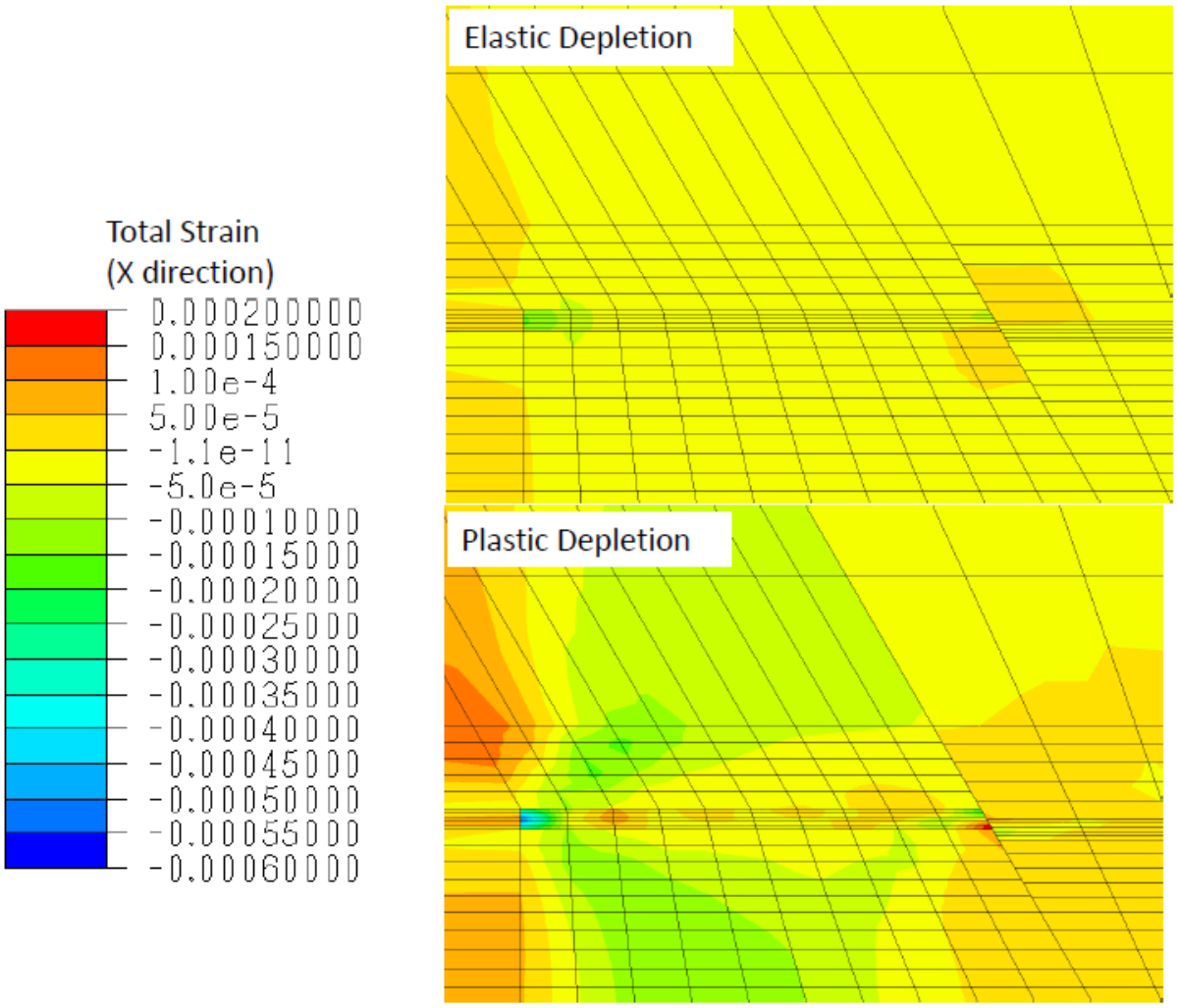

Figure 4.41 – Contour plot of strain in the X-direction (horizontal in plane of section) during the elastic and plastic depletion phase for the low stiffness reservoir for the central X plane section through the model.

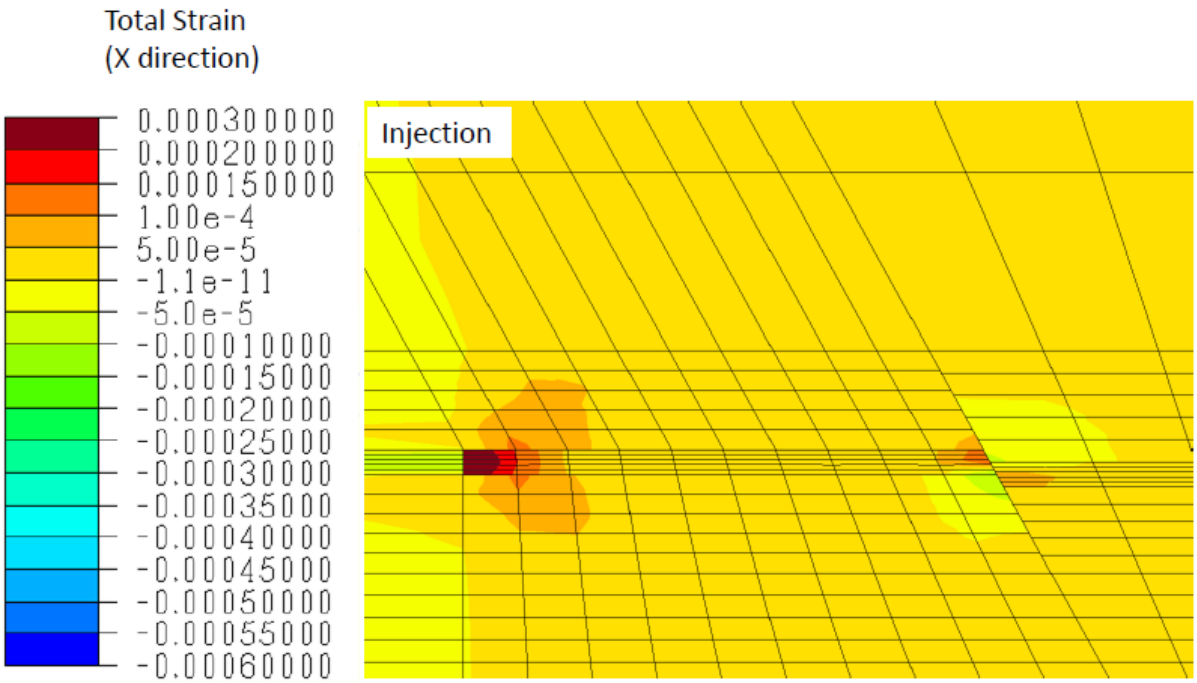

Figure 4.42 - Contour plot of strain in the X-direction (horizontal in plane of section) during the elastic injection phase for the low stiffness reservoir for the central X plane section through the model.

The stress paths in the low stiffness case do not differ significantly from the high stiffness case in terms of stress path hysteresis. The main difference in the low stiffness case is the stress changes around the reservoir in the overburden, and the increased amount of compaction that occurs in the overburden (and reservoir) during depletion and increased uplift during injection, and also increased horizontal movement during both depletion and injection. The increase movement is related to the low stiffness of the material and the larger strains that are observed.

Overall, the results show there is little difference between the stress paths for the different stiffness cases analysed for this reservoir. The cases represent situations where the overburden stiffness (with a reference stiffness of 5.35 GPa) is lower and higher than the reservoir, and shows that this also may have little impact. Further investigation of a range of stiffnesses in the overburden would provide more information on this aspect.

4.3.3 **Initial Stress Ratio Cases**

Two additional cases with an upper and lower initial stress ratio of K = 1.0 and K = 0.5 were analysed to investigate the impact on the stress path. It was found that the K = 1.0 case did not achieve the initial stress ratio set in the model, and geostatic initialisation only resulted in a K value of 0.9, therefore this model is referred to as K = 0.9 for the rest of the thesis.

Figure 4.43 shows a plot of stress paths for an initial stress ratio of K = 0.9 for all cases of fault sealing and friction compared against a case with the base case initial stress ratio of 0.7. The initial point on the stress path is now at a higher p' stress of 35.5 MPa, and

significantly lower q stress of less than 3.7 MPa. In comparison the stresses for the 0.7 stress ratio case were p' = 29.4 MPa and q = 13.3 MPa. The change in the p' and q stress is related to the fact that σ'_1 and σ'_3 are of a similar magnitude at the start of the simulation as K = 0.9, and therefore the difference between the stresses (q stress) is much smaller, and the p' stress is closer to σ'_1. During the initial stage of depletion, the stress path follows the elastic gradient parallel to the case with K = 0.7. Once the stress path reaches the yield surface there is a transition stage with a near vertical trajectory until the stress path reaches the same plastic deformation gradient observed in the previous case. The stress path then follows a very similar trajectory during the remainder of depletion and subsequent reinjection to the case with the lower initial stress ratio. The initial point in the stress path in the higher initial stress ratio case means the stress path is significantly different to the lower stress ratio case despite the plastic deformation and elastic injection stages being the same.

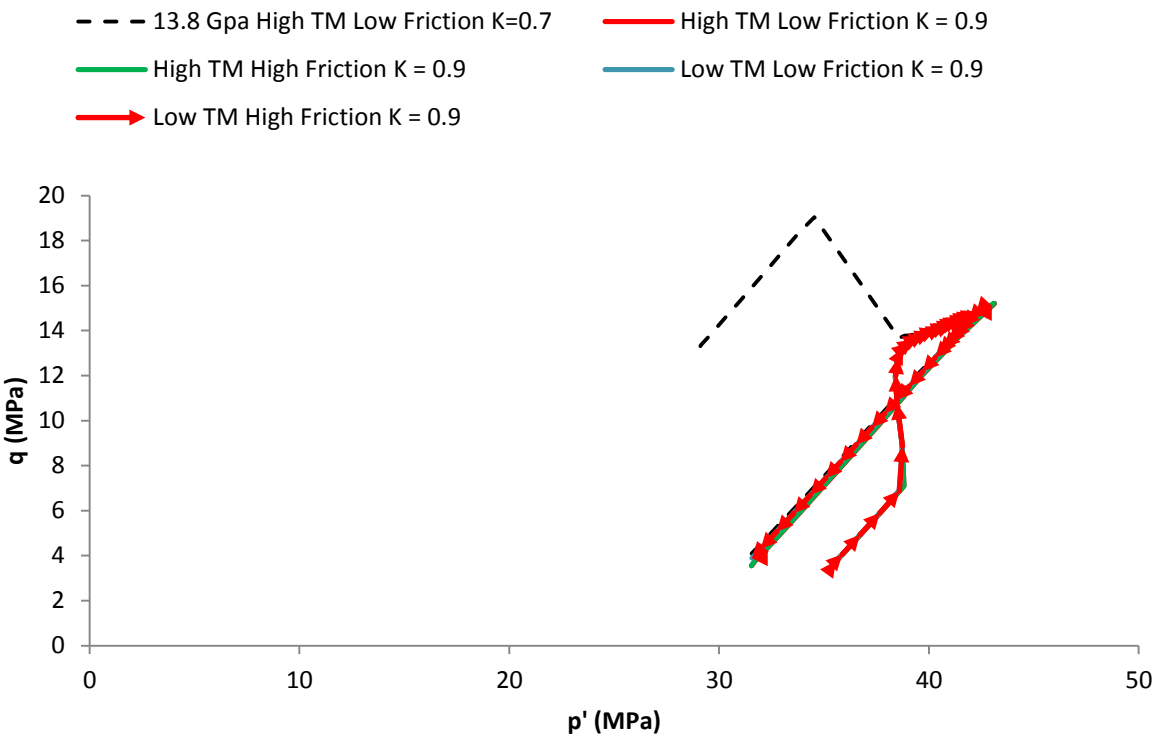

Figure 4.43 – p'-q plot for the high stiffness cases with an initial stress ratio K = 0.9, the path for the non-sealing low friction fault case with K = 0.7 is shown for comparison. Arrows demonstrate direction of stress path is reversed compared to lower initial stress ratio.

The Mohr circle plot for the non-sealing case with low friction and K = 0.9 is shown in Figure 4.44. The stress path parameters for depletion are γ_v = 0.22, γ_h = 0.80 and K_{sp} = 0.26 and γ_v = 0.02, γ_h = 0.60 and K_{sp} = 0.41 for injection. The plot of the Mohr circles shows that the main difference compared to the base case with K = 0.7 is the size and position of the initial Mohr circle, which is concurrent with the discussion of the stress path on the p-q' plot. The stress path parameters during depletion reflect the growth of the Mohr circle through a significant increase in σ'_1 with minimal stress arching, and a restriction in the increase of σ'_3 where significant horizontal stress arching is observed in the γ_h parameter. The growth of

the Mohr circle results in a low value for K_{sp} compared to the K = 0.7 case, while γ_v is the same and γ_h is much higher. The stress path parameters for injection are identical to the K = 0.7 case, as would be expected from the similar p'-q stress path.

The shape of the s'-t and p'-q stress path with the higher initial stress ratio show that f_{ph} will be much lower for the high initial stress ratio case and a value of f_{ph} = 0.89 was calculated.

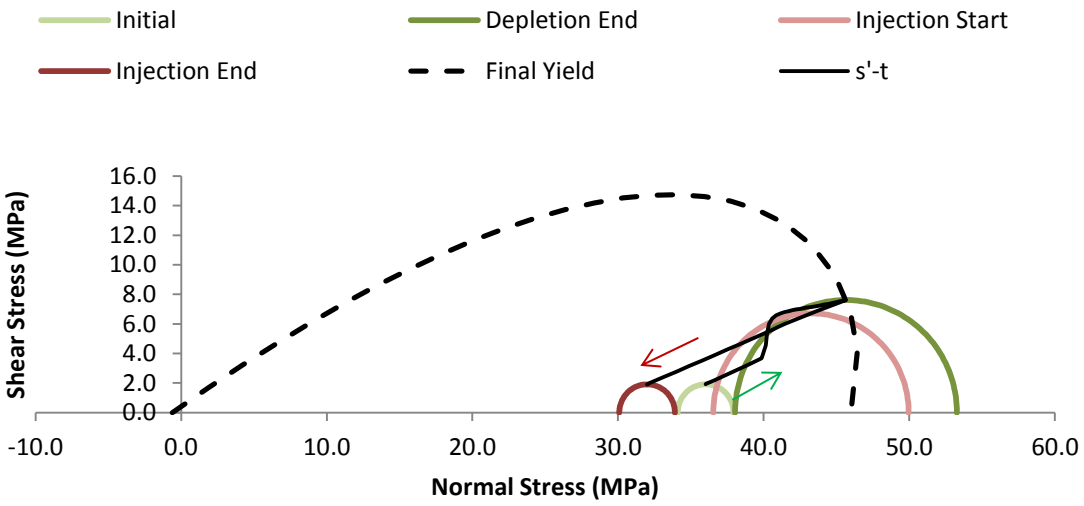

Figure 4.44 – Mohr circle plot for the high stiffness case with an initial stress ratio K = 0.9. Arrows show that the stress path is reversed compared to the lower initial stress ratio cases, green arrow shows start of depletion path direction, and red arrow shows end of injection stress path direction.

Contours of total vertical stress around the reservoir for the depletion and injection stage are plotted in Figure 4.45 and the same plot for total horizontal stress is shown in Figure 4.46. The plots of total stress show an increase in vertical total stress (σ_1) at the side of the reservoir of up to 3.13 - 3.76 MPa, and a decrease above and below the reservoir of 2.5 - 3.8 MPa. Horizontal total stress (σ_3) decreases everywhere in the model except for the area at the side of the reservoir, the decrease is between 2.1 - 5.2 MPa in the region close to the well location and the increase at the side of the reservoir is 0.23 - 0.62 MPa. Comparison to the K = 0.7 case shows σ_1 changes were more significant in the K = 0.7 case and the total stress increased at the side by approximately 4 MPa and decreased by a maximum of 5.5 MPa above and below the reservoir. For the K = 0.7 case horizontal total stress changes above and below the reservoir were less significant only reaching a maximum of 4.5 MPa, horizontal stress increase at the side of the reservoir was however more significant at 2 MPa. During injection there is minimal change in the vertical stress above and below the reservoir, however horizontal stress changes in the sideburden affect a larger area compared to the base case but are of a similar magnitude.

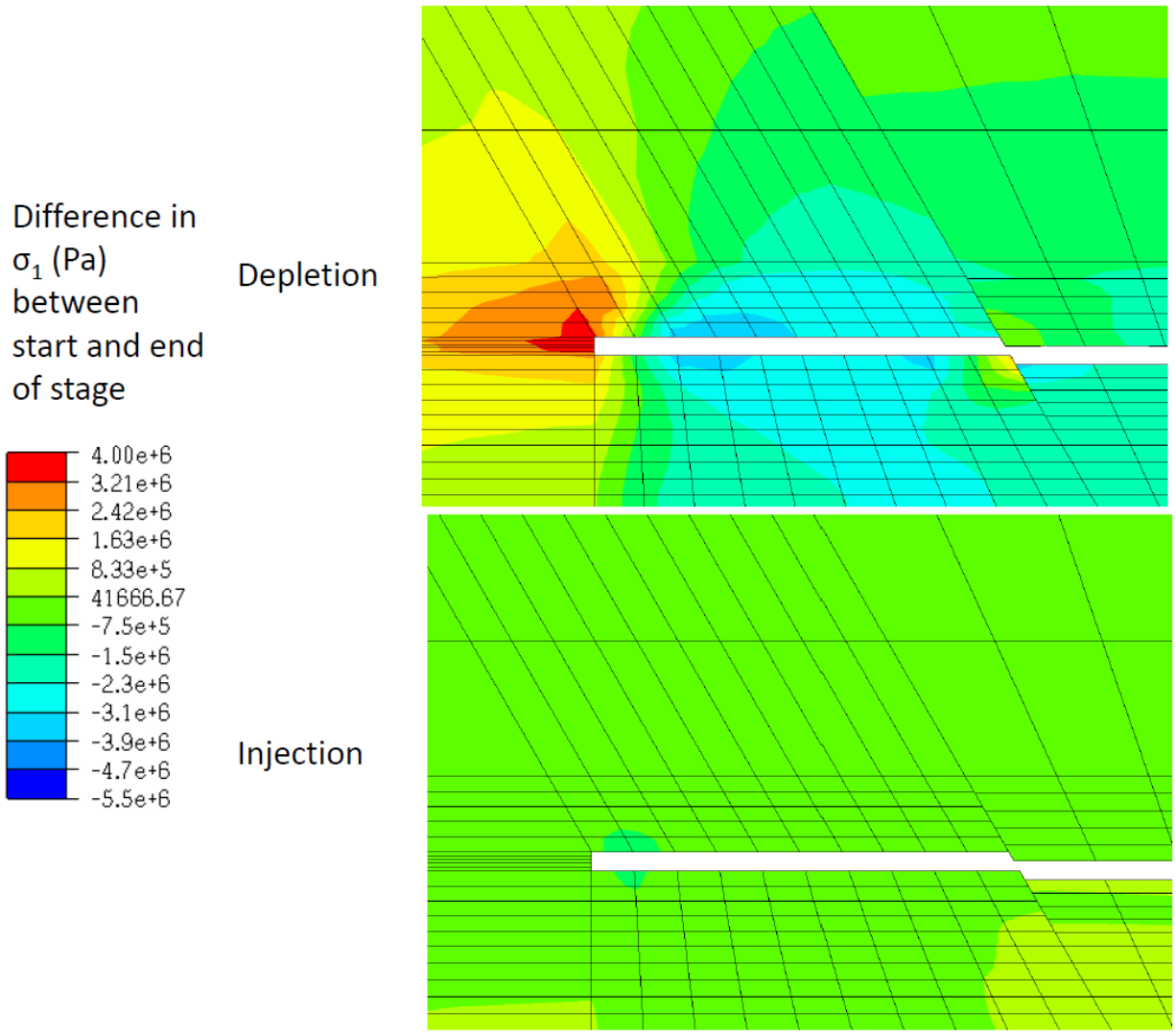

Figure 4.45 - Contour plot of the change in total vertical stress during depletion and injection for high stiffness case with non-sealing low friction faults and K = 0.9 for the central X plane section through the model.

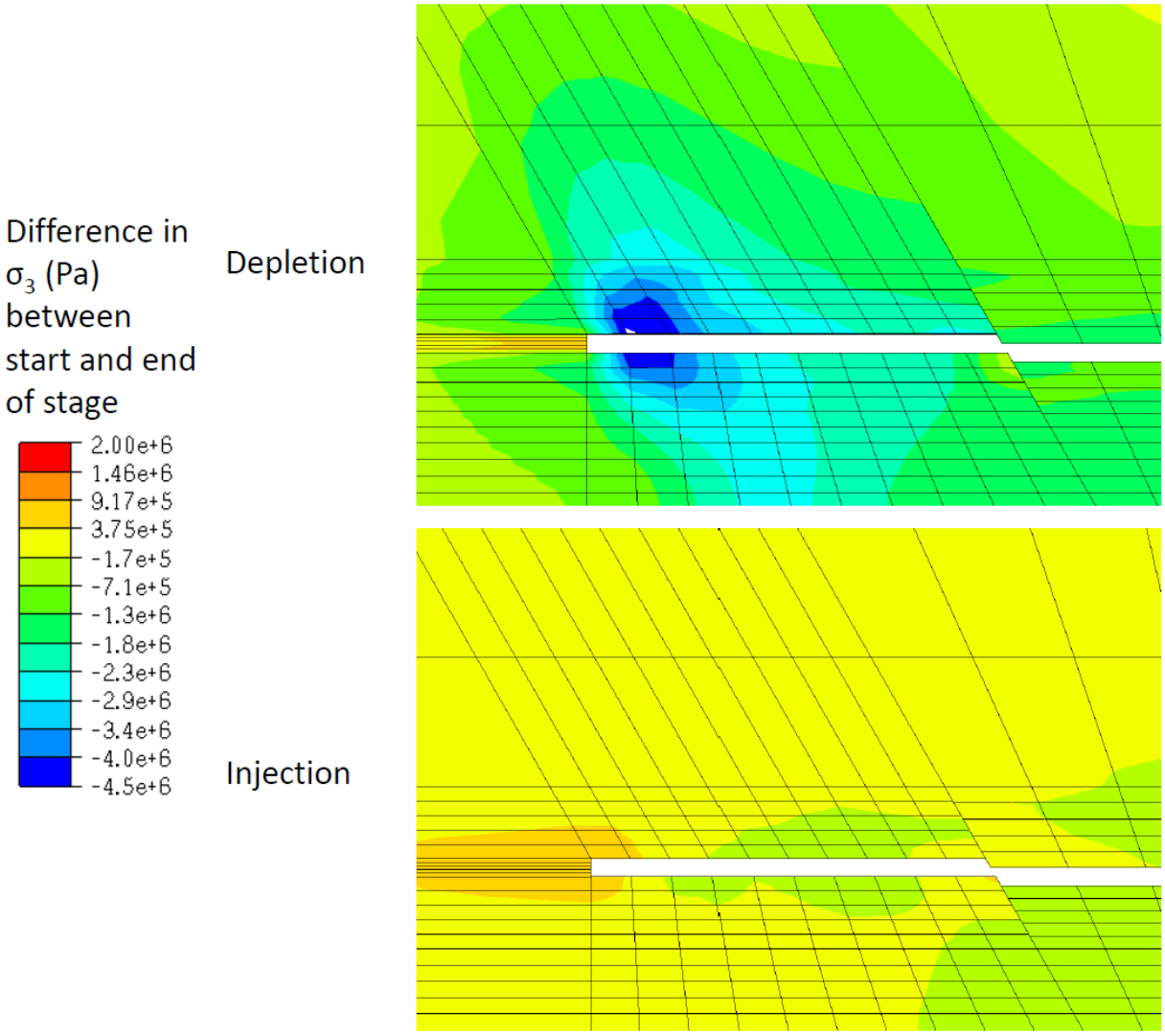

Figure 4.46 - Contour plot of the change in total horizontal stress during depletion and injection for high stiffness case with non-sealing low friction faults and K = 0.9 for the central X plane section through the model.

The displacements in and around the reservoir during depletion and injection are shown in Figure 4.47 and Figure 4.48. The displacements during injection are almost identical to the K = 0.7 case. The main difference is seen during depletion. The vertical displacement above the reservoir in the K = 0.9 case is generally of a smaller magnitude and uplift beneath the reservoir is larger particularly on the outer section of the reservoir. This is related to lower vertical compaction strains during depletion in the reservoir. Horizontal displacement is however, much more significant in the K = 0.9 case, this is related to larger plastic strains observed in the outer edge of the reservoir compared to the base case.

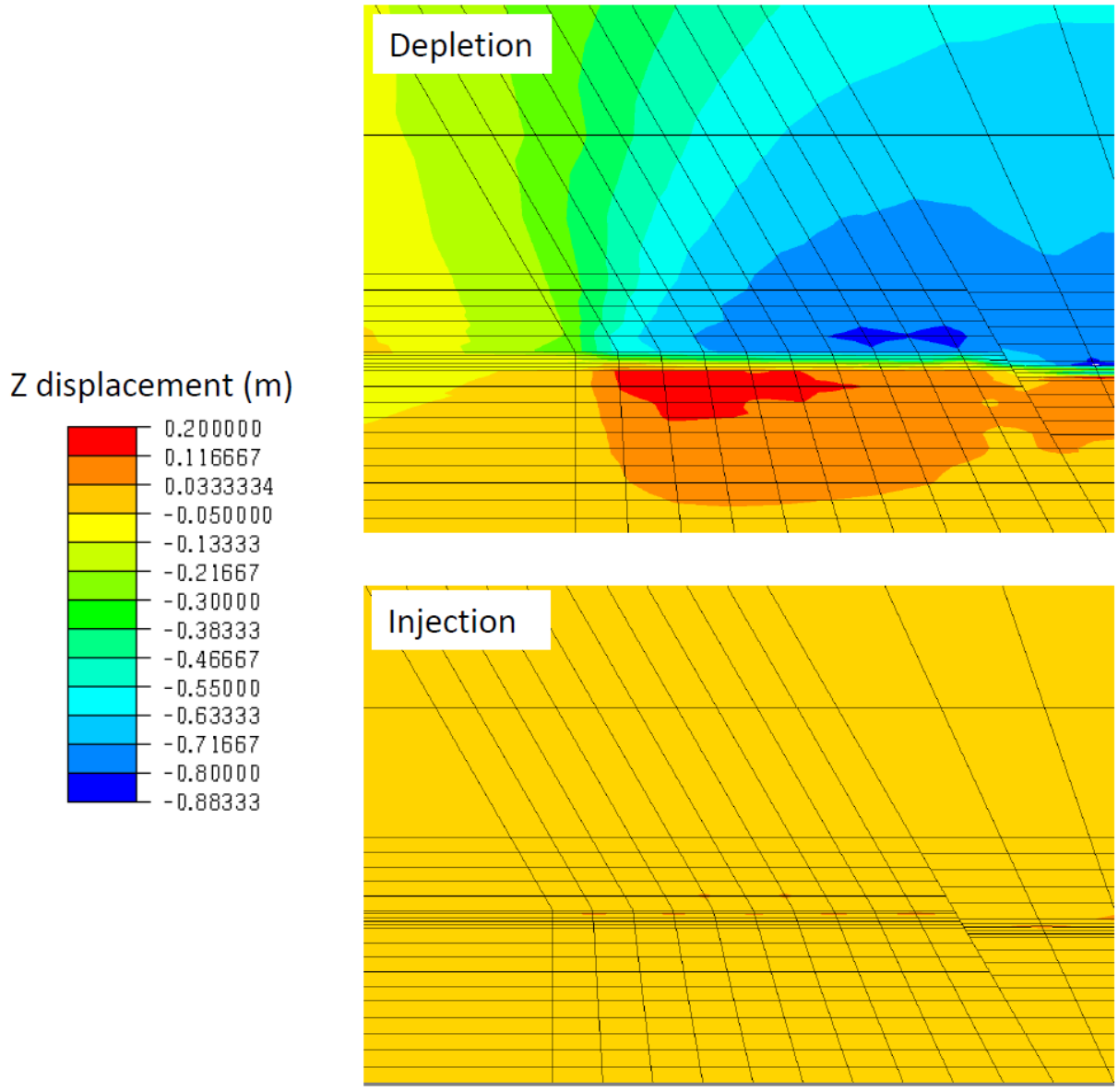

Figure 4.47 - Contour plot of displacement in the vertical direction for a section through the injection compartment for the K = 0.9 case for the central X plane section through the model. Vertical displacement is in the plane of the section with positive displacement upwards.

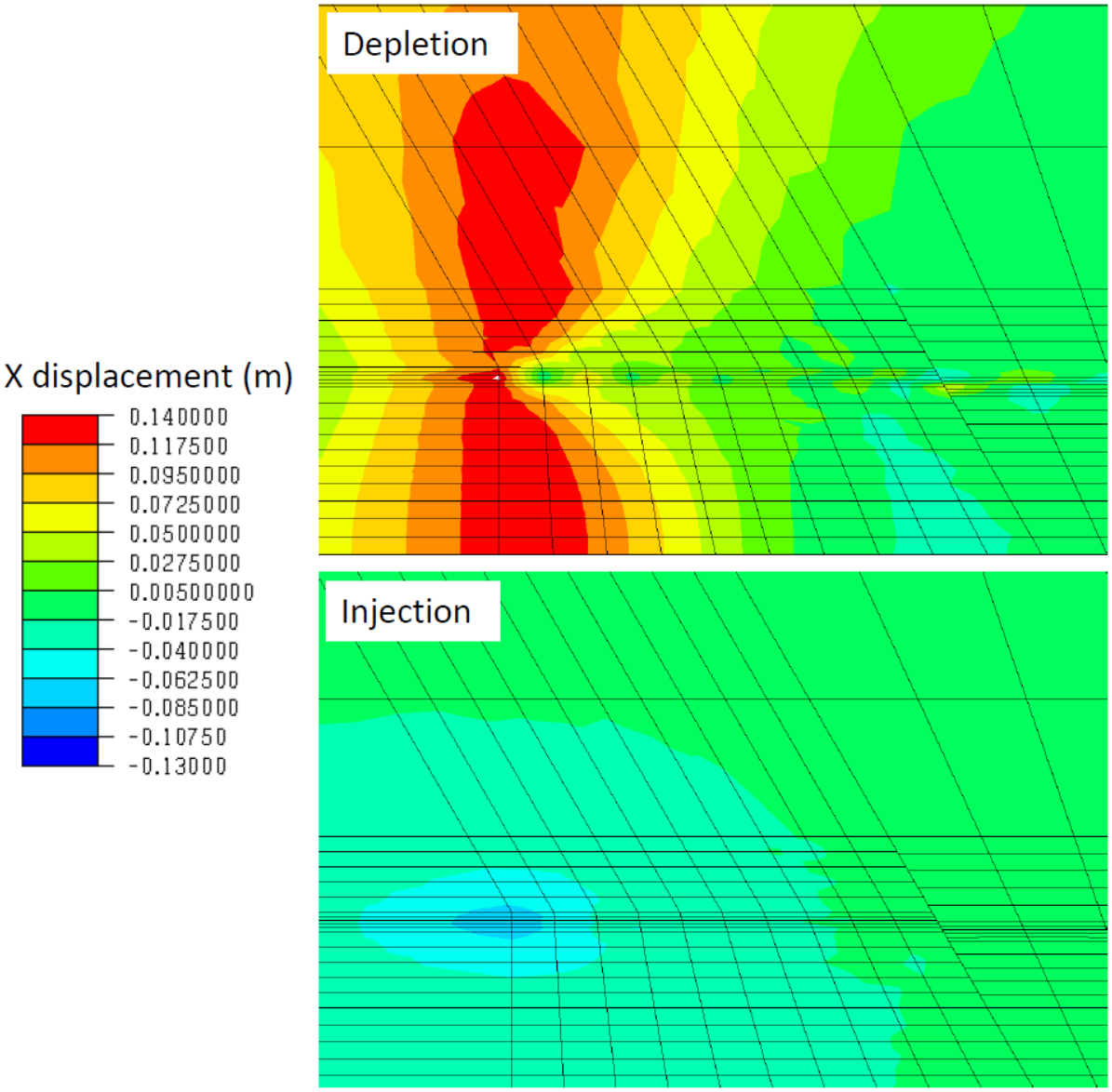

Figure 4.48 - Contour plot of displacement in the horizontal direction for a section through the injection compartment for the K = 0.9 case for the central X plane section through the model. Horizontal displacement is in the plane of the section with positive displacement left to right.

The horizontal strains are significantly different to the base during depletion in the reservoir for the K = 0.9 case, they are plotted in Figure 4.49. The most significant difference is the large contractive strain in the edge of the reservoir during plastic depletion, this is a maximum of -0.00073 compared to -0.00045 in the base case. This relates to the larger horizontal depletion deformation in the K = 0.9 case. Vertical compaction and expansion during depletion and injection, but are slightly smaller in the K = 0.9 case, with vertical negative depletion strains of -0.135 compared to -0.137 in the base case and positive expansive injection strains of 0.00053 compared to 0.0006 in the base case.

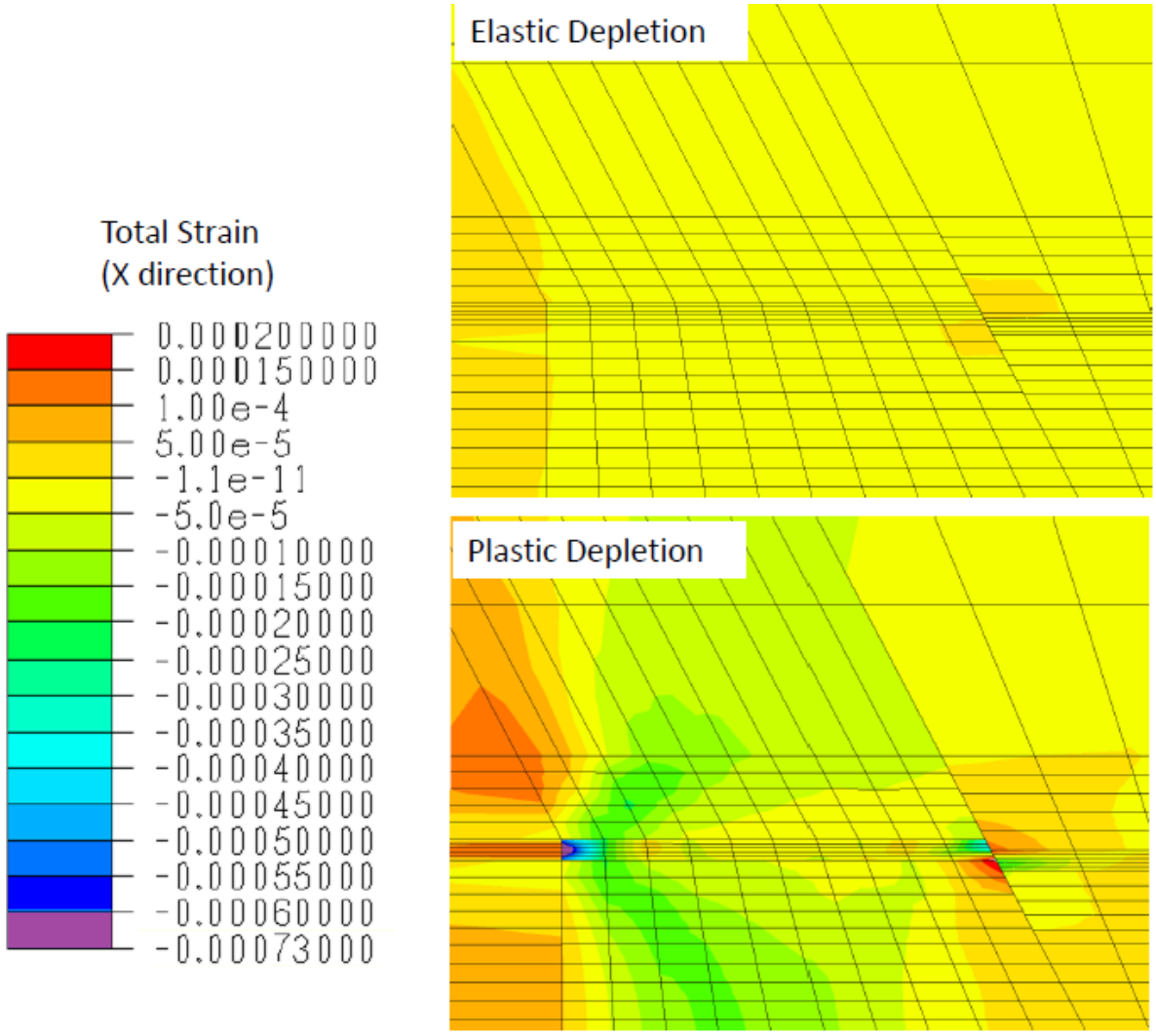

Figure 4.49 - Contour plot of strain in the X-direction (horizontal in plane of section) during the injection phase in the K=0.9 initial stress ratio case for the central X plane section through the model.

Figure 4.50 shows the p'-q plot of stress paths for an initial stress ratio of K = 0.5, again for all cases of fault friction and sealing properties. As with the plot for K = 0.9 the stress paths are very similar except for the initial stress values, which are at a higher q stress and lower p' stress due to the initial stress ratio. The calculated fracture pressure hysteresis for the K = 0.5 case is f_{ph} = 2.39.

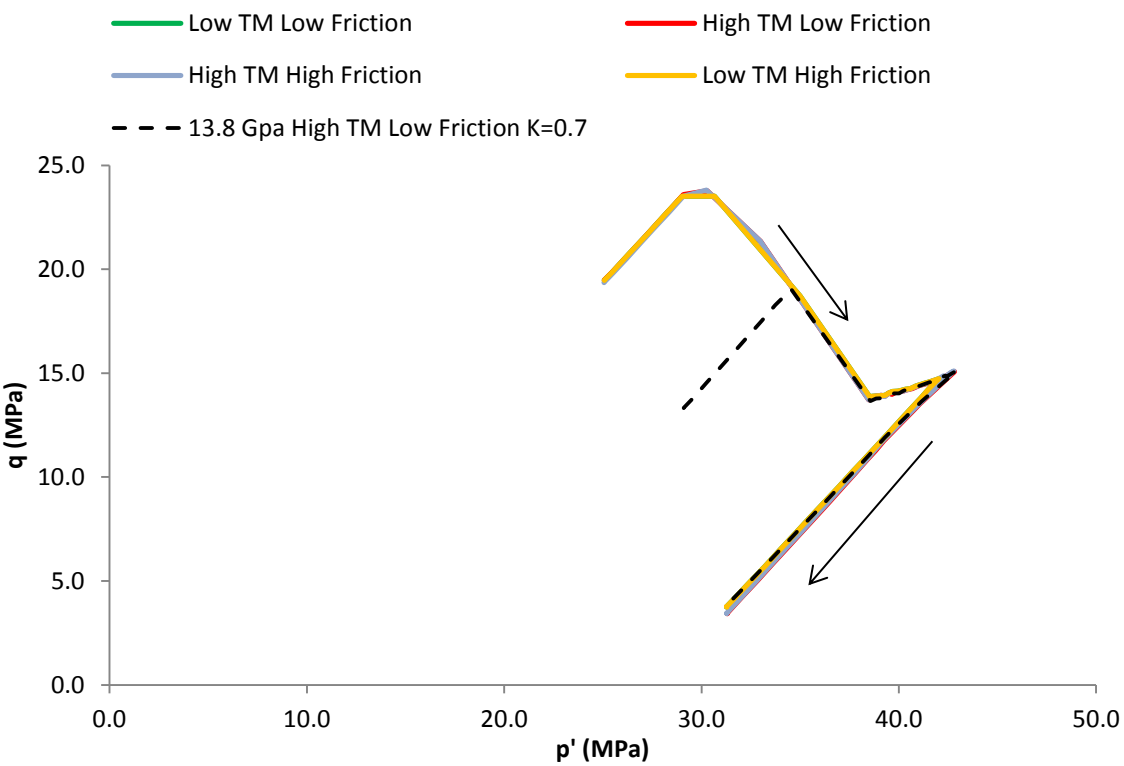

Figure 4.50 – p'-q plot for the high stiffness cases with an initial stress ratio K = 0.5, the path for the non-sealing low friction fault case with K = 0.7 is shown for comparison. Arrows show direction of stress path from initial depletion to final injection.

The Mohr circle plot for the K = 0.5 case is presented in Figure 4.51. The low initial horizontal effective stress in the reservoir means that the diameter of the initial Mohr circle is large as the vertical effective stress is the same magnitude as previous cases. During depletion the Mohr circle evolves through shrinkage to the same diameter as previous cases. The resulting stress path parameters are γ_v = 0.24, γ_h = 0.01 and K_{sp} = 1.31 and γ_v = 0.02, γ_h = 0.60 and K_{sp} = 0.41 for injection. Once again, the injection stress path parameters are the same as previous cases. During depletion K_{sp} is larger than 1 and γ_h is smaller than γ_v this is demonstrated by the shrinkage of the Mohr circle, with the horizontal effective stress intercept of the Mohr circle translating along the s' axis further than the vertical stress intercept. The parameters indicate lower horizontal stress arching in this case than the initial K = 0.7 and significantly lower than the K = 0.9 case, this is related the initial magnitude of the horizontal stress and subsequent stress path behaviour.

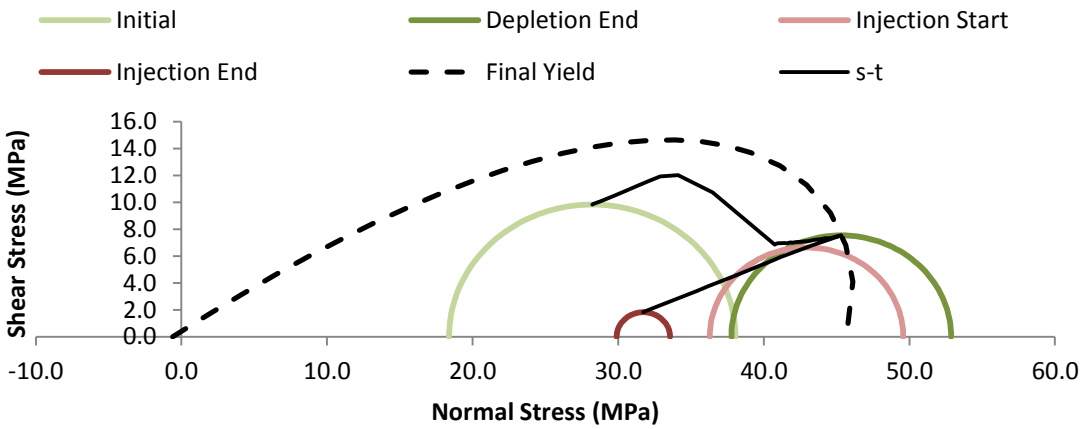

Figure 4.51 – Mohr circle plot for the high stiffness case with an initial stress ratio K = 0.5.

Contours of total stress in the overburden around the reservoir are presented in Figure 4.52. In comparison with the K = 0.7 and K = 0.9 cases the increase in vertical total stress at the side of the reservoir is lower than the K = 0.7 case, and similar to the K = 0.9 case. The decrease in total vertical stress above and below the reservoir is similar to the K = 0.7 case which is higher than the K = 0.9 case. The total horizontal stress at the side of the reservoir has the largest increase of up to 2.6 MPa in the K = 0.5 case, whilst the decrease in total horizontal stress above and below the reservoir is similar to K = 0.7 which is less than the 5.2 MPa decrease observed in the K = 0.9 model. The most significant observation from the plot of total stress in this case is the largest increase in total horizontal stress at the side of the reservoir amongst all of the cases.

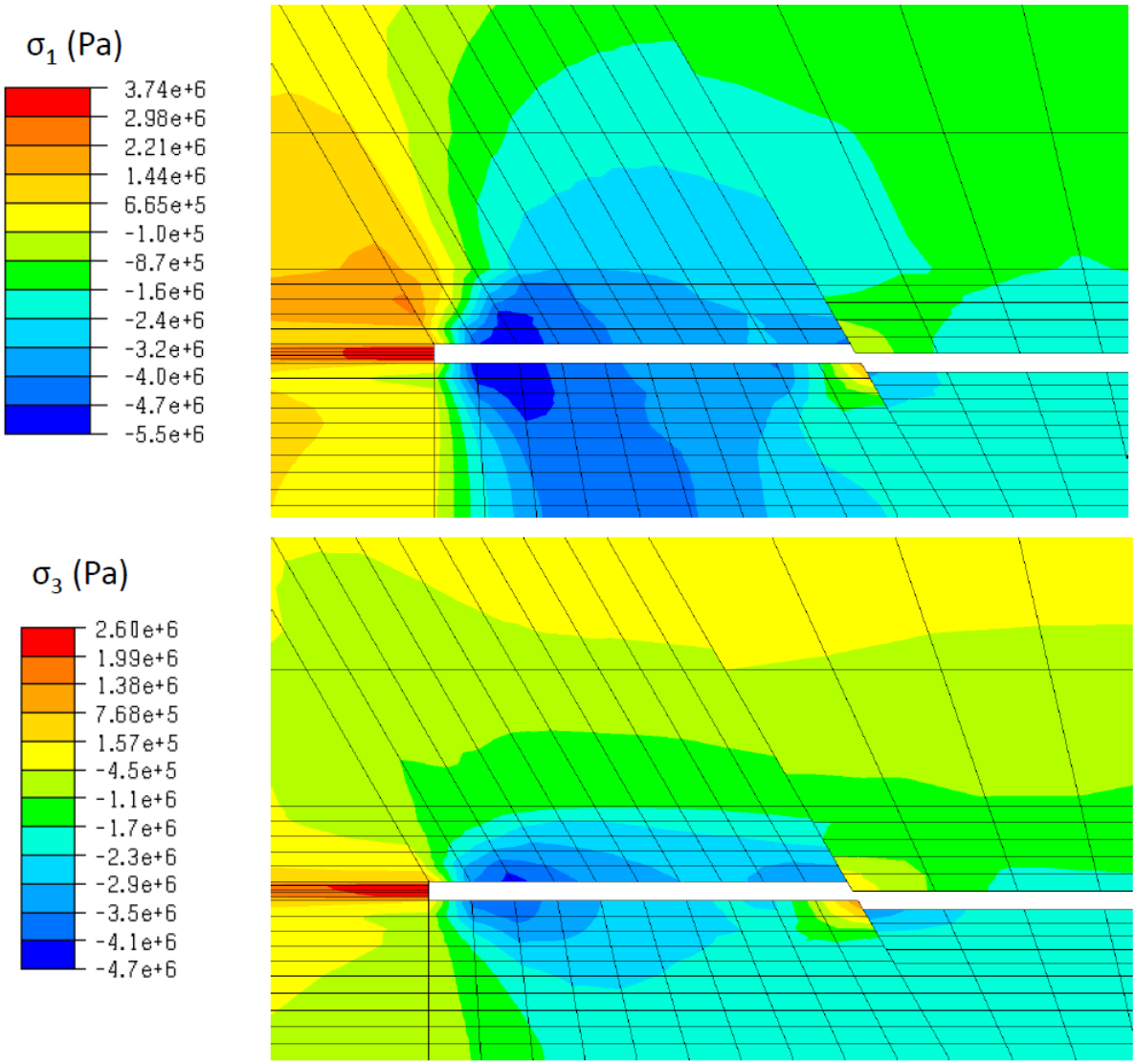

Figure 4.52 - Contour plot of the change in total stress during depletion for high stiffness case with non-sealing low friction faults and K = 0.5 for the central X plane section through the model.

The vertical and horizontal displacements in and around the reservoir are shown in Figure 4.53 and Figure 4.54 respectively. During depletion the vertical displacements are similar to the base case above the reservoir, although there is slightly less uplift below the reservoir. The main difference in the K = 0.5 case is the horizontal displacement. The horizontal displacements are smaller than both the K = 0.9 case and the base case, this is related to the fact that less plastic deformation is observed at the edge of the reservoir. The displacements during injection are again very similar to the base case.

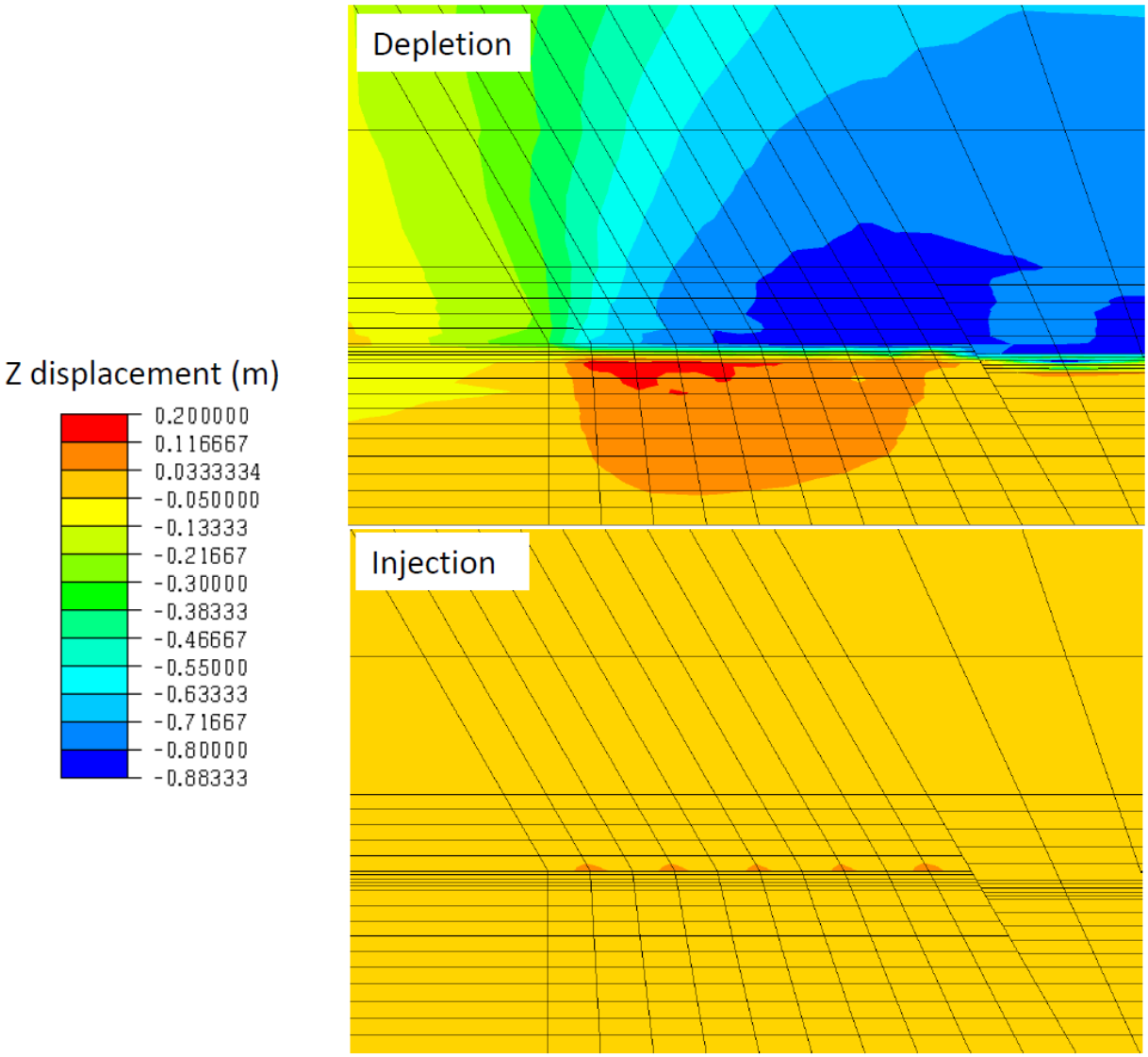

Figure 4.53 - Contour plot of displacement in the vertical direction for a section through the injection compartment for the K = 0.5 case for the central X plane section through the model. Vertical displacement is in the plane of the section with positive displacement upwards.

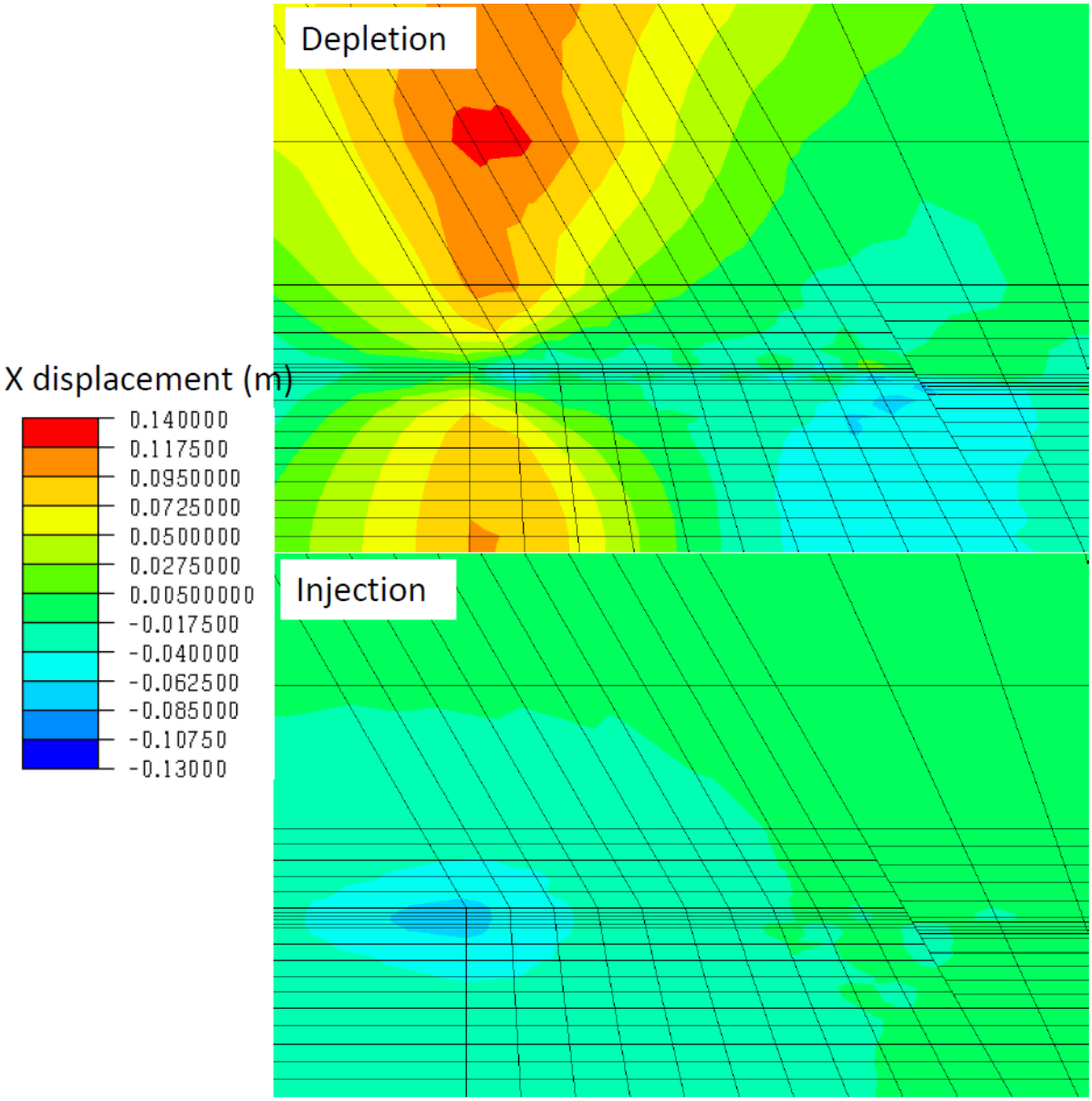

Figure 4.54 - Contour plot of displacement in the horizontal direction for a section through the injection compartment for the K = 0.5 case for the central X plane section through the model. Horizontal displacement is in the plane of the section with positive displacement left to right.

The strains in the K = 0.5 case show the opposite trend to the K = 0.9 case with lower horizontal strains during depletion corresponding to a lower level of horizontal displacement. The horizontal contractive strain in the edge of the reservoir is -0.00027 compared to -0.00045 in the base case and -0.0006 in the K = 0.9 model. Otherwise, the strains are similar to the base case, and this corresponds with a similar level of displacement to the base case model.

Figure 4.55 shows a clearer comparison of the three comparable cases with the different value of K. The graph clearly shows the convergence onto a single stress path trajectory after initial depletion and the initial points separated based upon the initial stress ratio. Based on this behaviour it is possible to plot the observed f_{ph} factors against the initial stress ratio to estimate the value of K at which the f_{ph} falls below 1 (i.e. lower fracture pressure

after injection than prior to depletion). The fracture pressure hysteresis factors are plotted against initial stress ratio in Figure 4.56.

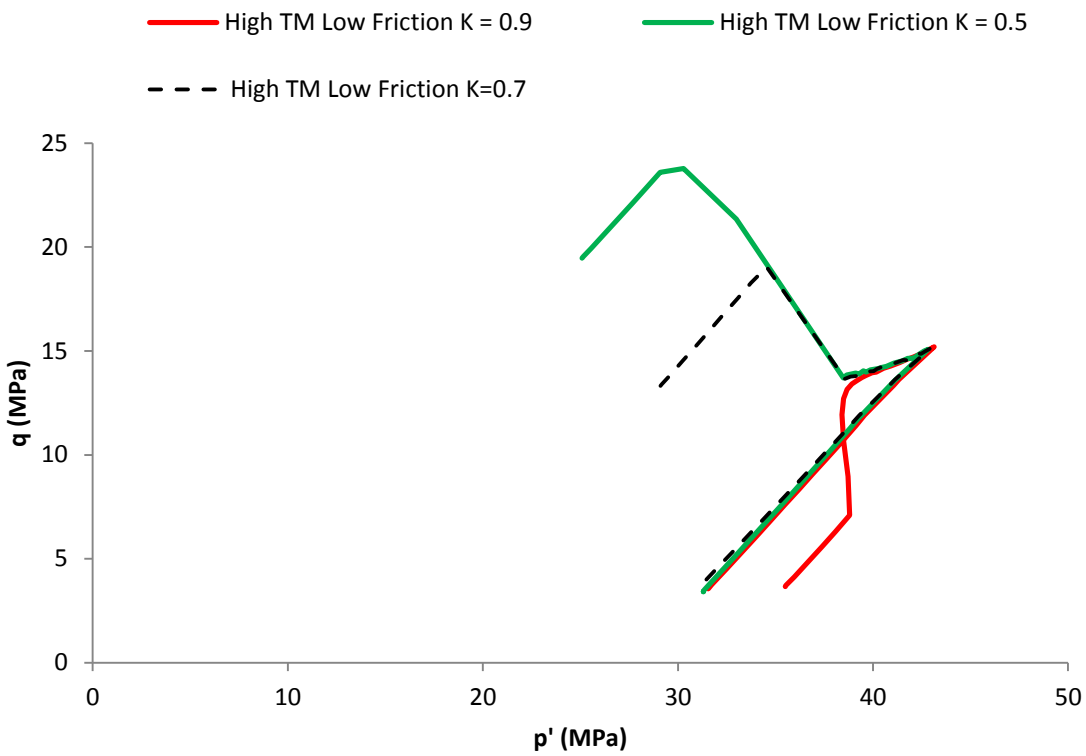

Figure 4.55 – Comparison of cases with 13.8 GPa non-sealing low friction faults for all values of K. The opposite direction of the stress path for the high initial stress ratio should be noted.

Figure 4.56 shows that at an initial stress ratio of 0.85 the fracture pressure hysteresis factor is equal to 1.0, initial stress ratios higher than 0.85 will lead to lower fracture pressures after re-pressurisation than prior to depletion in this model. The highest modelled fracture pressure hysteresis factor is at K = 0.9 and is 0.89, indicating fracture pressures at the end of depletion will be 89% of those prior to depletion. The fracture pressure hysteresis factor at K = 1.0 would be 0.82.

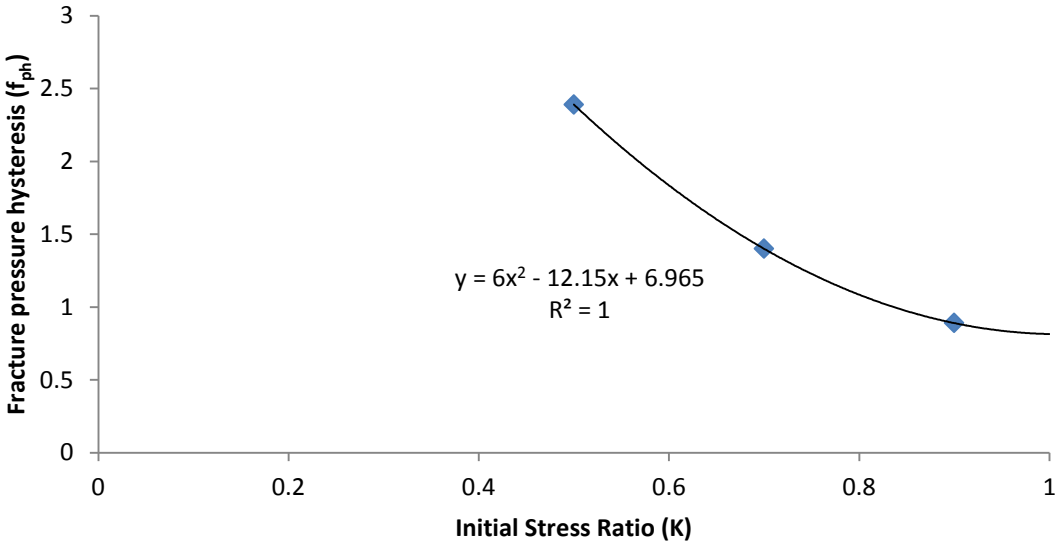

Figure 4.56 – Relationship of calculated fracture pressure hysteresis factor with initial stress ratio for the high stiffness cases.

The final plot in this section shows the results of varying the initial stress ratio in the low stiffness case, Figure 4.57 shows the p'-q plots for all faults cases compared against the higher stiffness case for comparison. The plot shows that there is minimal difference between the higher and low stiffness cases for different stress ratios, analysis of K = 0.9 for the low stiffness was not carried out due to time constraints and the similarity between other cases.

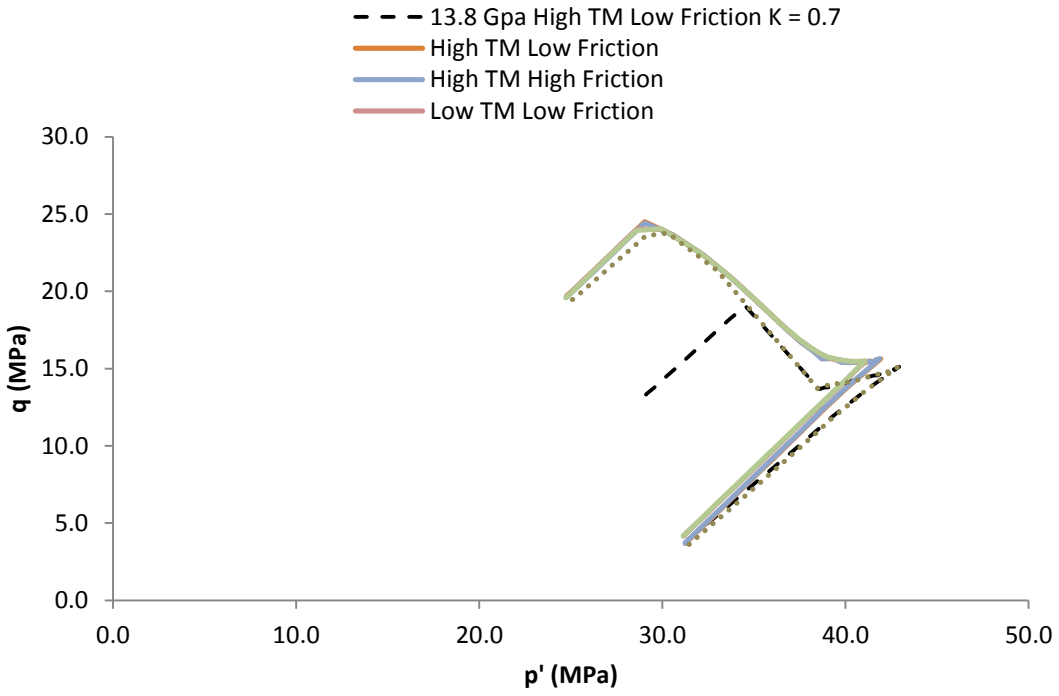

Figure 4.57 – p'-q plot for the low stiffness cases with an initial stress ratio K = 0.5, the path for the non-sealing low friction fault case for the high stiffness case with K = 0.7 is shown for comparison.

4.3.4 **Maximised Stiffness**

The variation in the stress paths with the two stiffness cases presented previously is minimal, especially when considering the initial and final states of the model, which are almost identical. Therefore, an unrealistic stiffness case was analysed with a very high stiffness, 10 times the reference value of the high stiffness case at 138 GPa. A stiffness lower than the 3.8 GPa case was not considered as the low stiffness case was already comparatively low. The unrealistically high stiffness is stiffer than pure quartz and is merely intended to highlight the impact of increasing stiffness in the model. Figure 4.58 shows p'-q plots for cases with a reference stiffness for 138 GPa and different value of initial stress ratio compared to equivalent stress paths from the 13.8 GPa stiffness runs with K = 0.5 and K = 0.7. The plot shows that increasing stiffness decreases q stress in the initial point but increase p' stress, this moves the initial point further from the shear side of the yield envelope. Increasing stiffness also changes the final point in the stress path and moves the final point closer to the shear side of the yield envelope. The overall effect of increasing the stiffness is a flattening of the stress path trajectory, which results in a final state that is closer to failure than the initial state. The calculated fracture pressure hysteresis factors for the very high stiffness case with initial stress ratio are therefore lower than other stiffness cases; f_{ph} = 1.00 at a lower value of initial stress K = 0.7, f_{ph} = 0.7 at K = 0.9 and f_{ph} = 1.51 at K = 0.5.

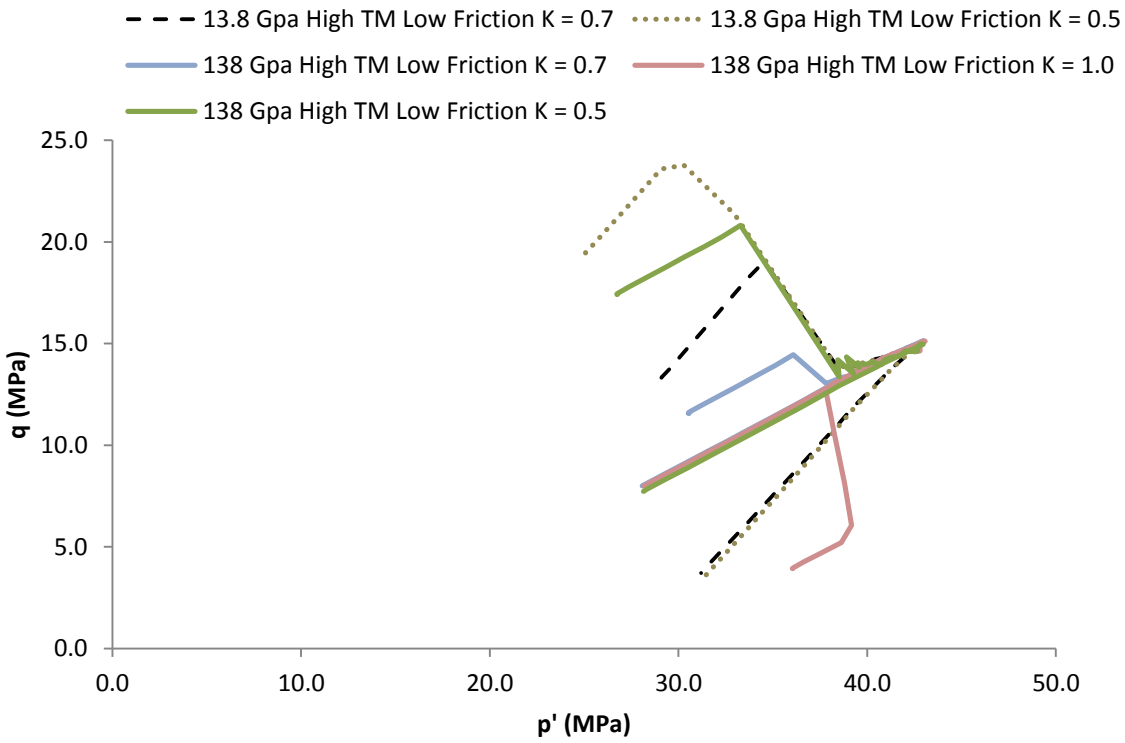

Figure 4.58 – p'-q plot for the very high stiffness cases with non-sealing low friction faults and initial stress ratios between K = 0.5 and K = 0.9. The path for the non-sealing low friction fault case for the high stiffness case with K = 0.7 and K = 0.5 is shown for comparison.

4.3.5 **Reservoir Poisson's Ratio**

The Poisson's ratio of the reservoir rock was varied to investigate the impact on the stress path. The Poisson's ratio was set to 0.35 and 0.49 in addition to the 0.25 value used in the base case. The non-sealing low friction case with a reference stiffness of 13.8 GPa was used to analyse the effect of varying the Poisson's ratio. Figure 4.59 shows the p'-q stress path for the two additional Poisson's ratio cases compared against the 0.25 base case. The figure shows that the trajectory of the stress path flattens with increasing Poisson's ratio. The initial value of q stress reduces with increasing Poisson's ratio, whilst the final value of q increases. Initial p' stress shows the opposite trend to q, and the initial p' stress increases with increasing Poisson's ratio whilst the final p' stress decreases. The behaviour of the p' and q stresses mean that the stress path overturns for the $\nu = 0.49$ case, with the initial p'-q stress point higher than the final p'-q stress point on the stress path. The overturning behaviour of the stress path with high ν is similar to behaviour seen with high initial stress ratio, and very high stiffness. Once again $\nu = 0.49$ is likely to be an unrealistic parameter for the reservoir, but is used to illustrated the trend of stress path change with increasing ν.

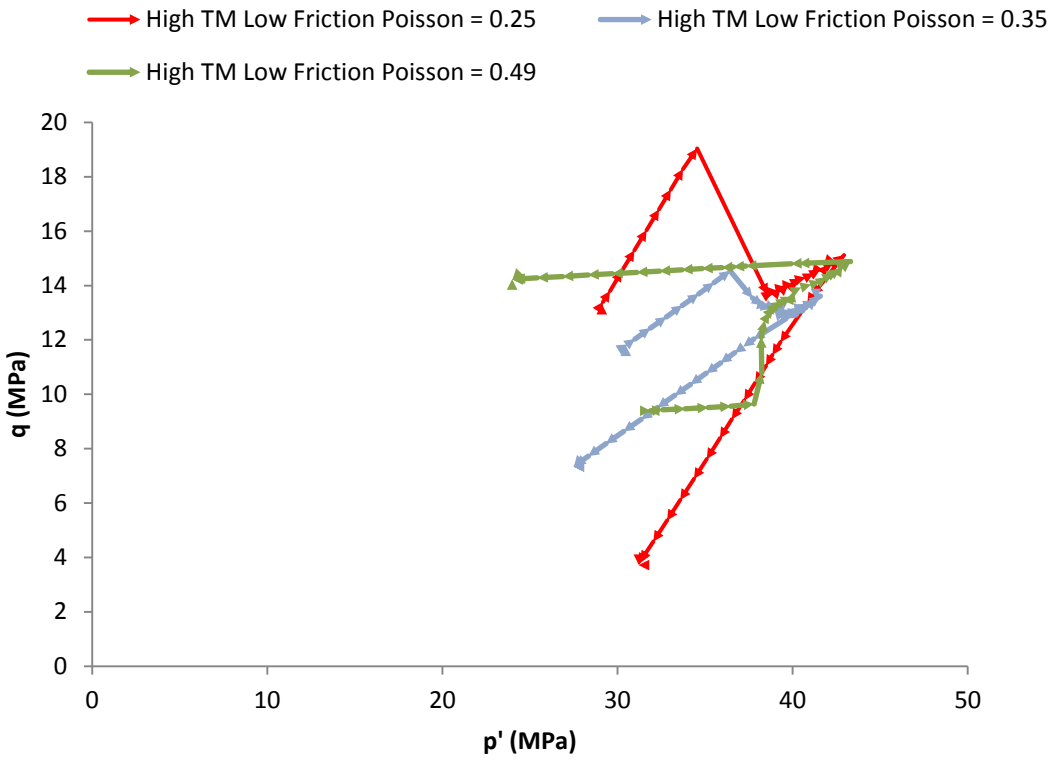

Figure 4.59 – p'-q plot for the non-sealing case with low friction faults showing stress paths for different Poisson's ratios in the reservoir.

It is evident from Figure 4.59 that the fracture pressure hysteresis factor reduces with increasing Poisson's ratio in the reservoir, as the final p' stress is much lower than the initial p' stress with high ν. Figure 4.60 shows a plot of the f_{ph} factor against Poisson's ratio for the cases analysed. The figure shows an approximately linear decrease of f_{ph} with ν, and $f_{ph} = 1.0$ at $\nu = 0.37$.

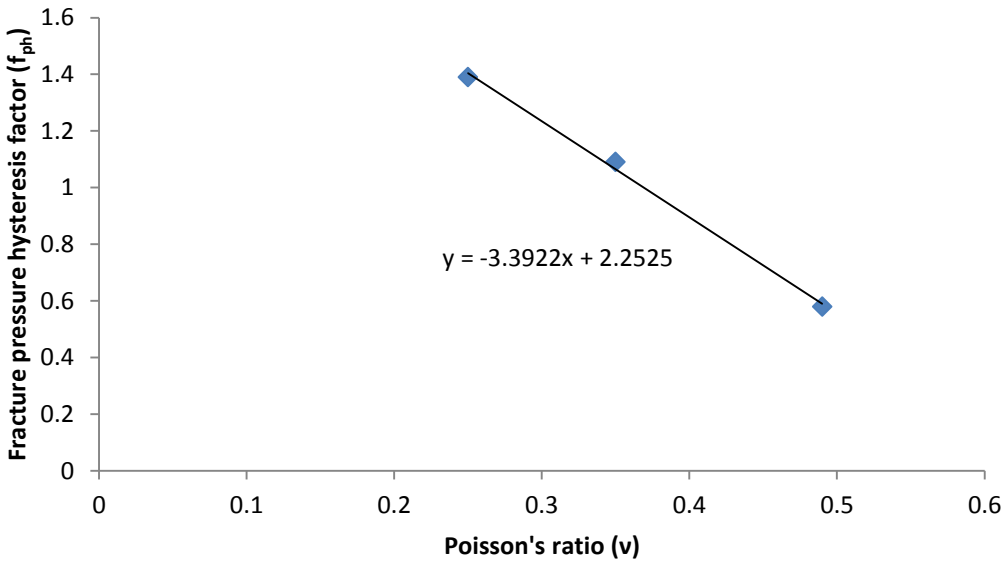

Figure 4.60 – Graph of fracture pressure hysteresis factor (f_{ph}) with Poisson's ratio (ν) for the non-sealing low friction fault case.

Figure 4.61 and Figure 4.62 show contour plots of σ_1 and σ_3 for the ν = 0.35 case for the injection compartment of the reservoir. In general the σ_1 stress distribution is similar to the same case with ν = 0.25 especially in the region to the side of the reservoir. The main difference in σ_1 with increased ν is a smaller decrease in σ_1 stress in the overburden and underburden above and below the reservoir during depletion. Close to the fault the decrease in σ_1 is only 2.3 to 3.1 MPa, compared to 3.1 to 3.9 MPa in the lower ν case. The region where a 4.7 to 5.5 MPa decrease is observed is also smaller in the higher ν case. The main difference during injection is a smaller region that experiences σ_1 increase above and below the reservoir compared to the lower ν case, overall stress change in the overburden is minimal. The difference in σ_1 is due to the behaviour of the reservoir material in relation to confining forces at the side of the reservoir, as the material has a higher ν confining forces at the side will be transmitted to the overburden more than with a lower ν, this explains the lower reduction in σ_1 above the reservoir.

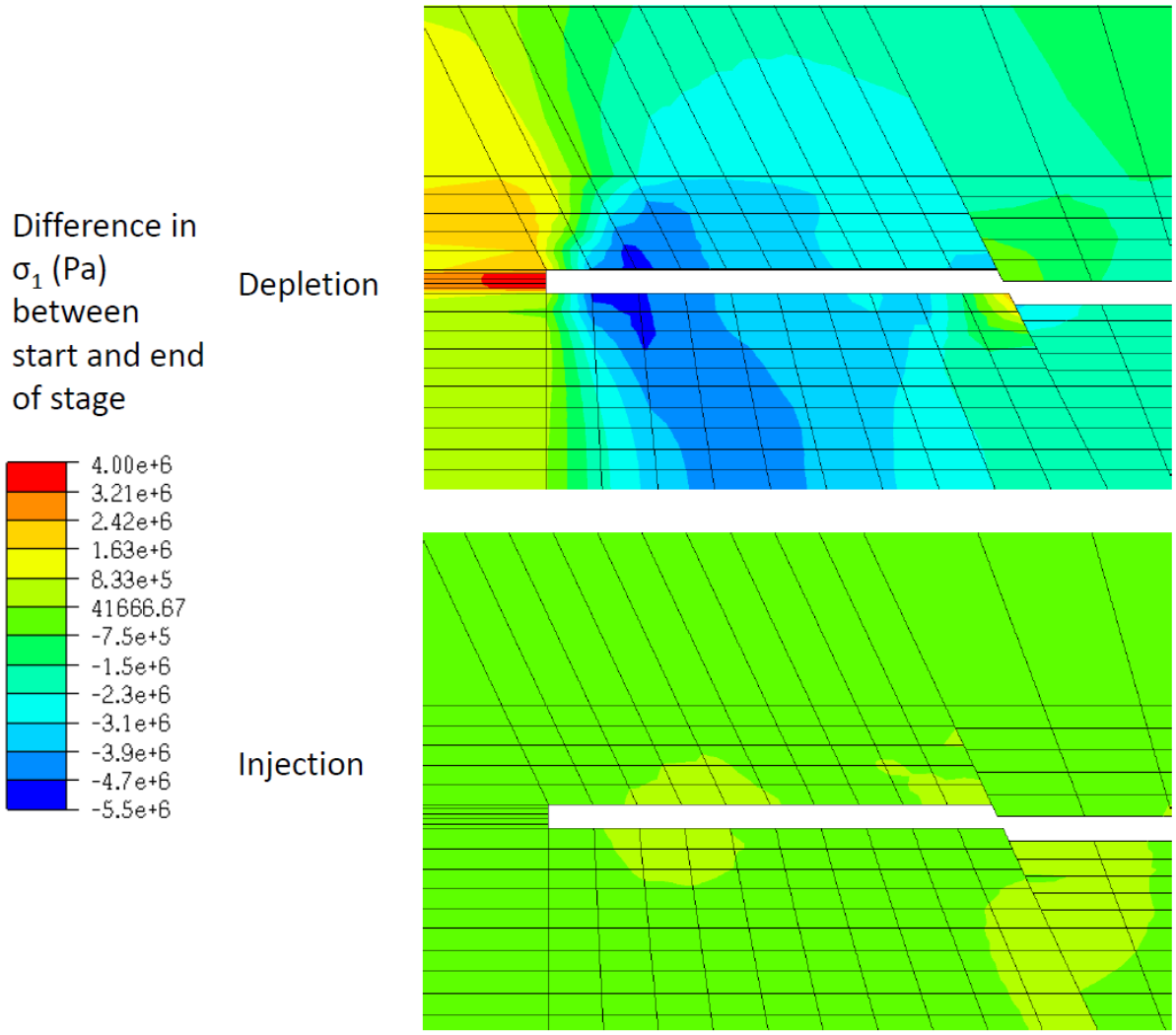

Figure 4.61 - Contour plot of the change in σ_1 during depletion for high stiffness case with non-sealing low friction faults and ν = 0.35 for the central X plane section through the model.

The contour plot of σ_3 for depletion in Figure 4.62 is very similar to the plot for the lower ν case. The main difference is observed in the injection stage where again the vertical extent of region of stress decrease above the reservoir is reduced.

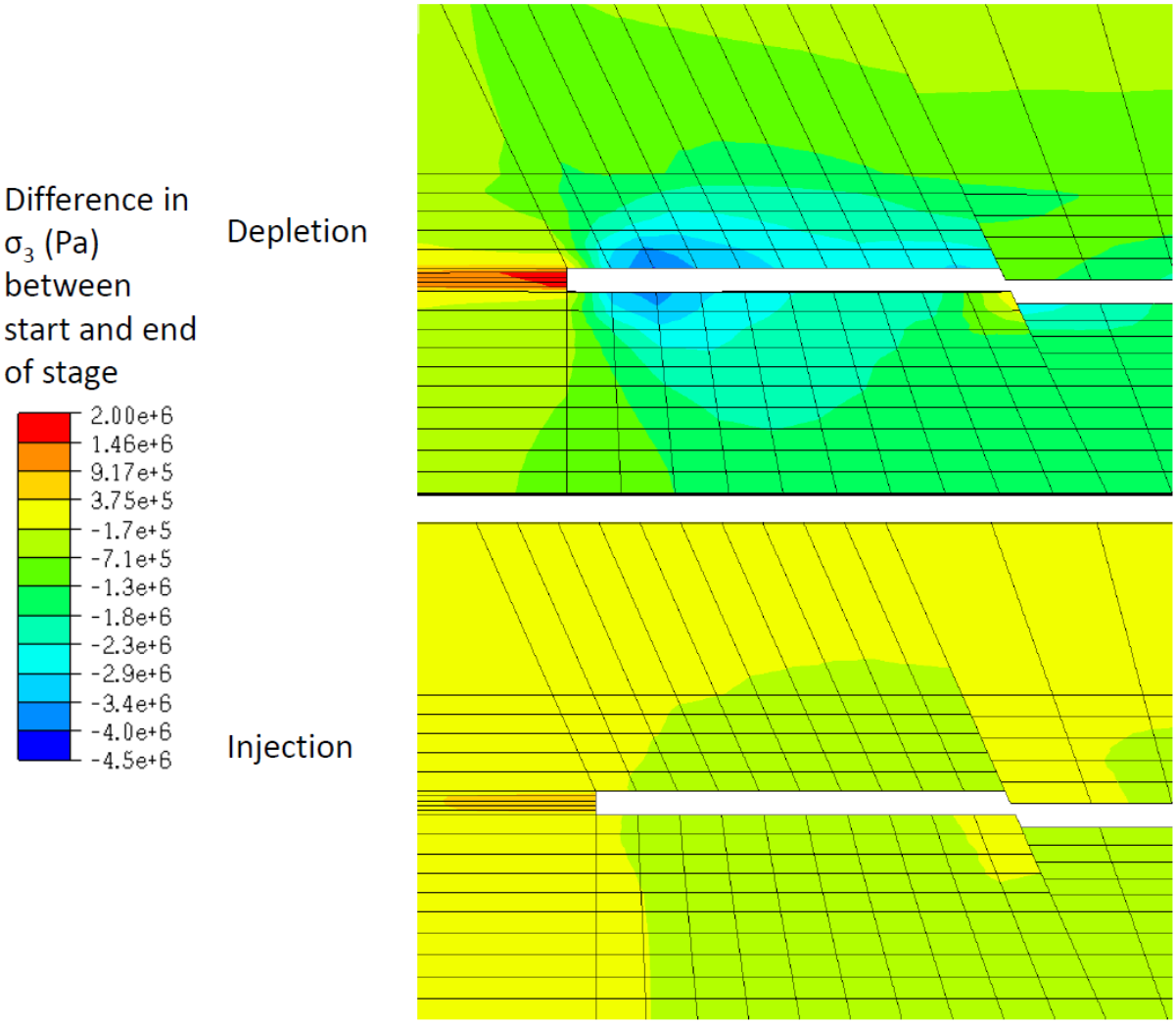

Figure 4.62 - Contour plot of the change in σ_3 during depletion for high stiffness case with non-sealing low friction faults and ν = 0.35 for the central X plane section through the model.

4.3.6 Other Material Parameters

Two other material parameters in the constitutive model were investigated, the dilation parameter, ψ, which is a material parameter that affects the shape of the plastic potential surface (and thus plastic strain) and, $\beta^{\pi}_{1,}$ which is a material parameter used in the deviatoric plane correction term. The dilation parameter was varied based on the maximum limits in the data from Rockfield Software Limited (2012) with two extreme values of 47° and 55° were chosen. The β^{π}_{1} material parameter is based on the shape of the yield surface derived from experimental data and so only one value is presented in the data from Rockfield Software Limited (2012). Therefore β^{π}_{1} was varied by one order of magnitude either side of the initial 7.25 x 10^{-7} value to determine the impact.

Figure 4.63 shows a plot of all of the results of the cases where parameters in the constitutive model were varied. The plot shows that there is minimal difference in the stress paths, even with the extreme parameters, and the stress paths follow very similar trajectories. In this type of problem, when investigating the stress path and stress path

hysteresis the variability within the constitutive model for the sand seems to be less important than other factors in the model.

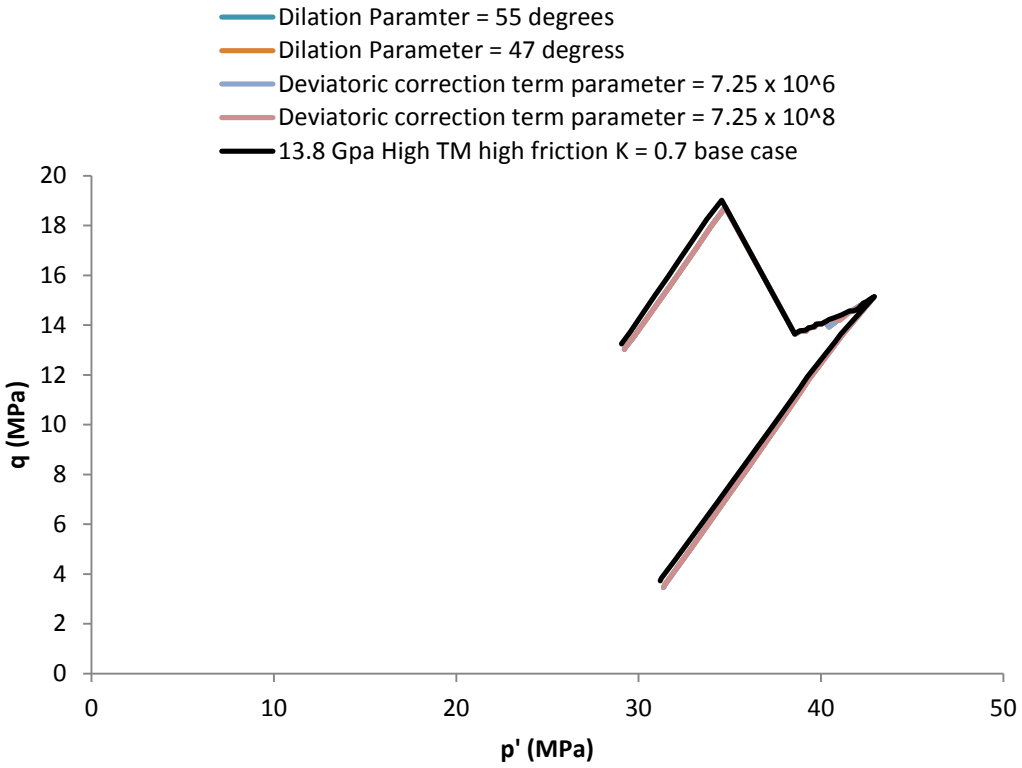

Figure 4.63 – p-q plot of simulation runs with variable constitutive model parameters compared against the base case model with high friction faults.

The choice of parameters varied within the constitutive model is not exhaustive, however the parameters that were changed are those that are routinely changed within the SR3 model, the remaining parameters that have not been assessed are not generally altered when used with Elfen.

4.3.7 **Geometric Effects**

The initial results have been presented for the cell at the well location at the top of the reservoir. A set of high resolution data points were also output for a section through the centre of the model to investigate whether the geometry of the model affects the stress path. Figure 4.64 is a section through the centre of the model intersecting the well and shows the locations of the additional cells that were analysed. The cells were located at the outer top corner of the reservoir, in the middle and bottom of the reservoir at the well location, and at the top of the reservoir either side of the fault closest to the well.

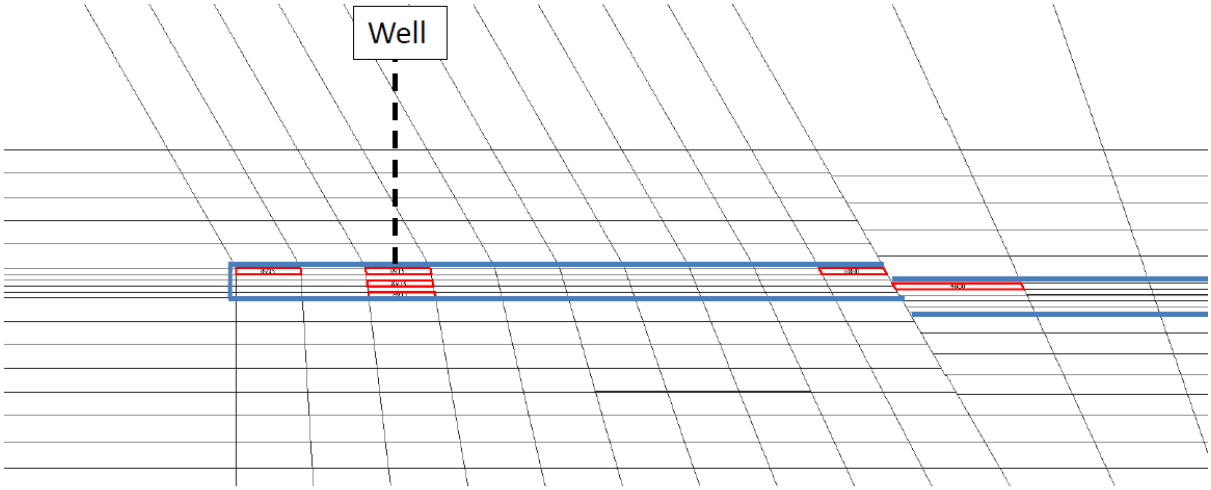

Figure 4.64 – Diagram of cell locations for analysis of the impact of model geometry on reservoir stress path.

Figure 4.65 shows p'-q stress paths for each of the different cell locations for the non-sealing low friction fault case with an initial stress ratio of K = 0.7. The stress path for the base-case cell at the top of the well discussed in previous sections is included in the figure for comparison. For the cells at the middle and bottom of the well, the plot shows that although the stress paths have higher q stress than the base-case during depletion they converge to the same final stress state and have similar initial stress states. For the cell at the fault within the middle compartment the initial stress state is similar to the base-case, depletion occurs with higher q stress and the final stress state has higher q and p' stresses than the base-case. For the cell at the fault within the injection compartment, the initial stress state is at a higher p' and q stress. However, the stress path is similar to the base-case during depletion, the injection component of the stress path has a flatter trajectory and results in a final stress state that has significantly higher q stress and a slightly higher p' stress. The stress path for the cell in the outer corner of the reservoir shows the most variation for compared to the base-case. The stress path has a similar trajectory during depletion, however the injection trajectory is much flatter, and this results in a final stress state that has a higher q stress and lower p', this will result in a lower f_{ph} factor than the base-case.

The calculated f_{ph} factor for the base-case is 1.39, for the two other cases at the well the f_{ph} is also similar. In comparison the f_{ph} for the cell in the injection compartment at the fault is f_{ph} = 1.37, on the other side of the fault in the middle compartment f_{ph} = 1.46, and in the outer corner of the model f_{ph} = 1.22. The reduction in the f_{ph} in the outer corner clearly presents most risk with a 0.17 reduction in the f_{ph} factor. The stress path parameters calculated for the outer cell are γ_v = 0.35, γ_h = 0.38 and K_{sp} = 0.95 for the depletion stage and γ_v = 0.05, γ_h = 0.50 and K_{sp} = 0.53 for the injection stage. In comparison the base-case parameters were γ_v = 0.24, γ_h = 0.33 and K_{sp} = 0.88 for depletion and γ_v = 0.02, γ_h = 0.60 and K_{sp} = 0.41 for injection. The vertical and horizontal stress path parameters are higher than the base-case and show that stress arching (both horizontal and vertical) is more significant in the outer

cell. The vertical and horizontal stress path parameters are of a similar magnitude to each other in the outer cell and this means that K_{sp} is close to 1, resulting in minimal change in the size of the Mohr circle and minimal increase in q during depletion overall. The Mohr circle translates with minimal growth during depletion and the translation is restricted to some extent by the stress arching. During injection in the outer cell the vertical stress path parameter is slightly higher, and the horizontal stress path is significantly lower than the base-case. This injection stress path parameters mean that the final horizontal effective stress is lower in the outer cell, the Mohr circle translates more, and but the size does not reduce as much resulting in higher q stress, this is demonstrated by the higher value of K_{sp} which shows less shrinkage in the circle than in the base-case. The p'-q stress path trajectory for the outer cell mainly results from a greater reduction horizontal effective stress during injection than the base case.

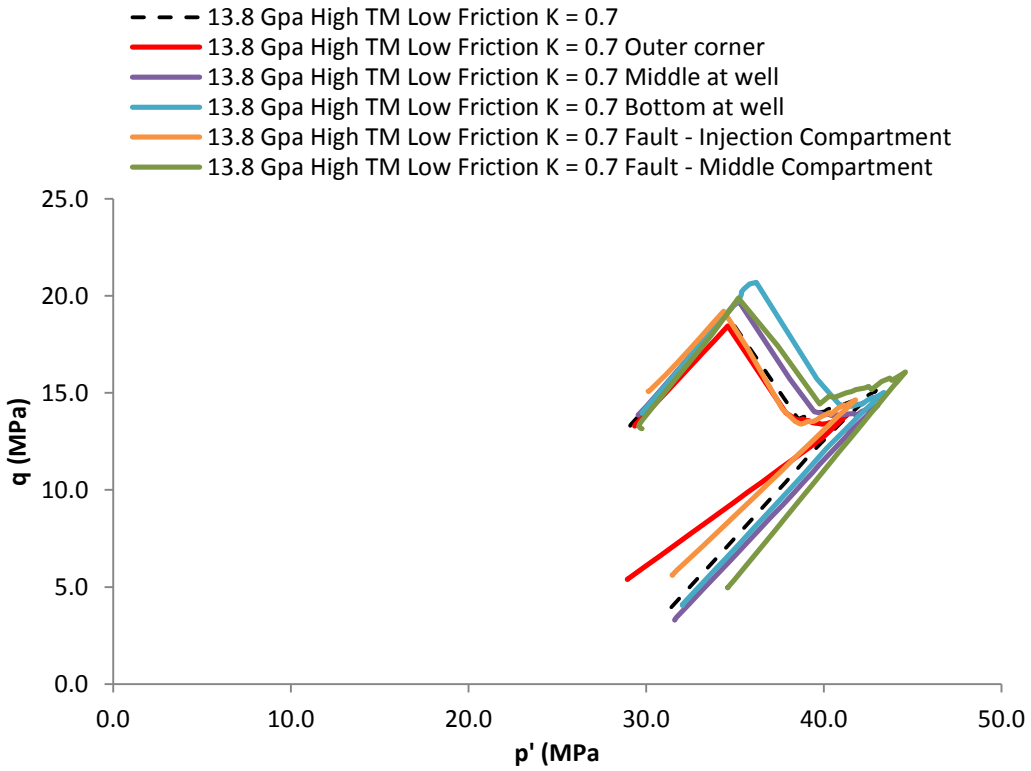

Figure 4.65 – p'-q plot of non-sealing low friction fault cases where K = 0.7 for various locations within the reservoir.

The effect of geometry in the sealed compartmentalised reservoir is also assessed, Figure 4.66 is a p'-q plot of the stress paths for the cells closest to the fault and at the outer edge of the reservoir, the cells at the well are ignored as they are similar to the base-case. The plot shows that the outer cell follows a similar stress path to the non-sealed case but the stress paths are closer to the base case and the effect of the geometry is reduced in the sealed case. The cell at the fault within the injection compartment is effectively the edge of the reservoir in the sealing case and shows greater stress arching than the non-sealed case. γ_v = 0.49 in this cell in the sealing case compared to 0.36 in the same position, and 0.35 at the outer corner of the non-sealing case, this gives a reduced vertical and horizontal stress and

lower p' and q stress for depletion stress path for the sealing case which offsets the injection stress path compared to the non-sealing case. The f_{ph} for the cell at the fault is in the sealing case is 1.33, which is lower than the equivalent non-sealing cell (1.37) where stress arching is lower, but higher than the outer edge cell in the non-sealing case (1.22) and sealing case (1.26) where stress arching is also lower. This suggests that increased stress arching reduces fracture pressure reduction for an equivalent edge cell.

A flatter injection path is also observed in the sealing case at this location as it is effectively at the edge of the reservoir, similar to the results in the corner cells. This results in lower horizontal stress in the sealed case at the end of injection. The stress path for the cell on the other side of the fault in the middle compartment is significantly different to the base case and follows a vertical trajectory during depletion, with a small reduction in q stress and increase in p' stress during injection. The f_{ph} calculated for this stress path is 0.92 and suggests that fracture pressures are lower at the end of injection than prior to depletion. In the sealed case the cell on the other side of the fault in the middle compartment is effectively outside of the reservoir and is undrained as it is not connected to the well, only pressure breakthrough across the well rather than injection would cause fracturing. Therefore, it is unclear whether this cell should be considered high risk, as it would not be involved in injection activities directly, the analysis of this cell is also complicated by the simplicity of the fault model, as it is only represented as a dimensionless sealing interface.

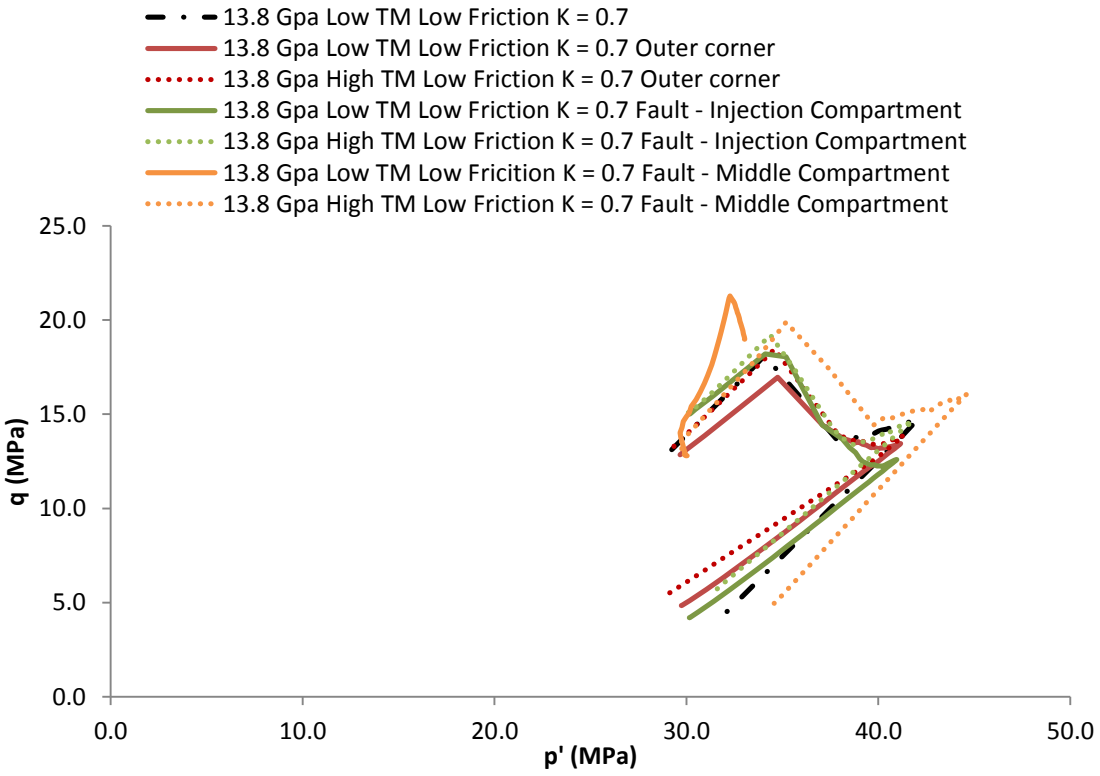

Figure 4.66 – p'-q plot of sealing low friction fault cases where K = 0.7 for various locations within the reservoir.

The most significant impact of the geometry is observed in the cell in the outer corner and so this region is focussed on to assess the combined effect of geometry and initial stress ratio. Figure 4.68 is a p'-q plot of the non-sealing low friction fault case for K = 0.5, K = 0.7 and K = 0.9 compared against the stress path of the cell at the top of the well in each case. The plot shows that in all cases the stress path for the outer corner follows a path with lower q stress than the well location during depletion. The trend reverses during injection with higher q stress for the same p' stress in all cases at the outer corner. The stress path trend at the outer corner results in a flatter injection trajectory, and the final stress state is at a lower p' stress and higher q stress than the well location. It is clear from Figure 4.68 that the stress paths at the outer corner with K = 0.5 and K = 0.9 will have lower f_{ph} factors than the well location, as observed previously for the K = 0.7 case. It is also clear that the most significant reduction in f_{ph} will be observed in the K = 0.9 case. Figure 4.67 illustrates the Mohr circle plot and s'-t path of the K = 0.9 case for the outer corner.

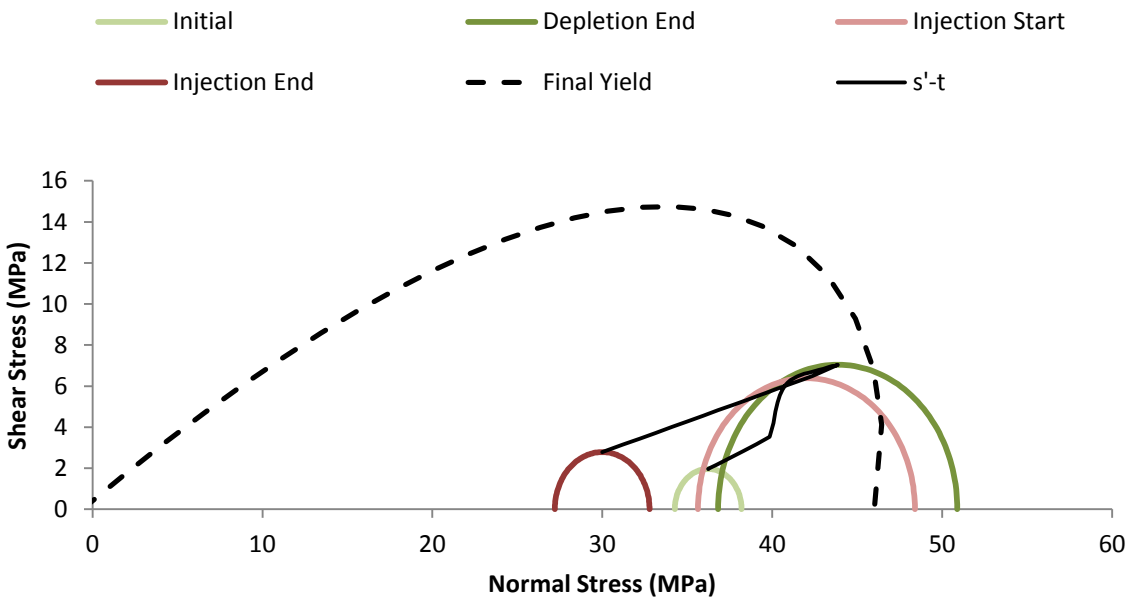

Figure 4.67 – Mohr circle diagram for the cell in the outer corner of the K = 0.9 initial stress ratio case.

The calculated f_{ph} values are f_{ph} = 2.03 for K = 0.5, f_{ph} = 1.23 for K = 0.7 (as above) and f_{ph} = 0.81 for K = 0.9. In comparison the same values at the well location are f_{ph} = 2.39 for K = 0.5, f_{ph} = 1.39 for K = 0.7 (as above) and f_{ph} = 0.89 for K = 0.9.

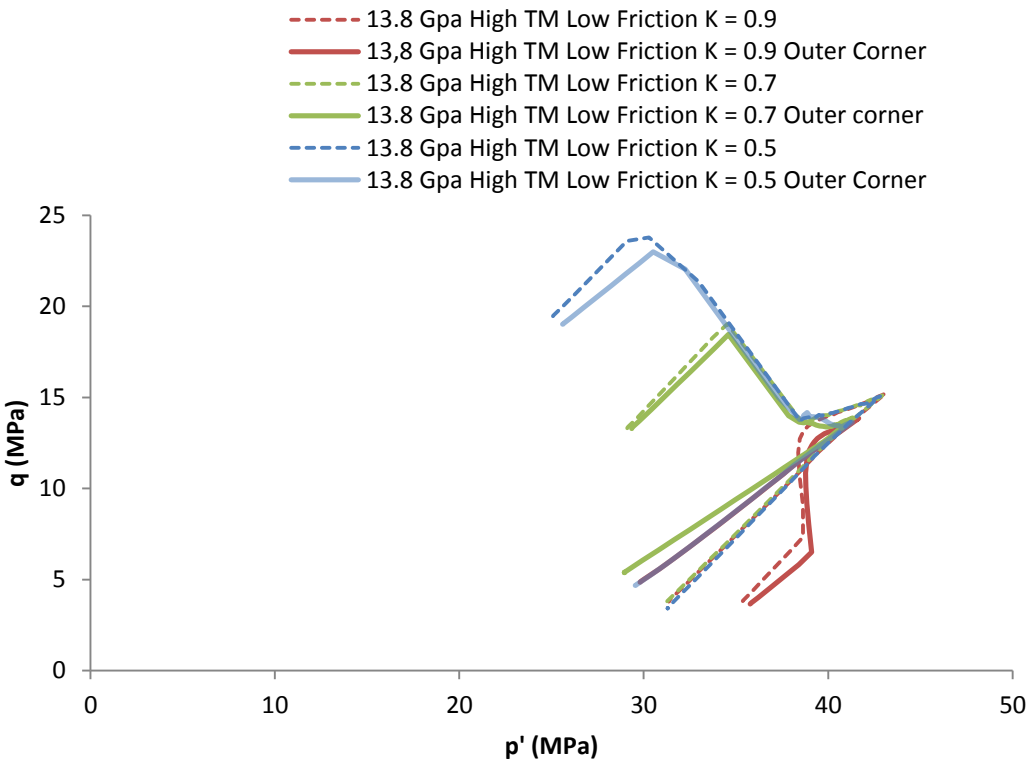

Figure 4.68 – p'-q plot of non-sealing low friction fault cases for a range of initial stress ratios comparing the cell at the well and the cell in the outer corner of the reservoir.

The f_{ph} factors are plotted against initial stress ratio in Figure 4.69 to illustrate the difference in f_{ph} between the outer cell and the cell at the well location with initial stress ratio. The f_{ph} in the outer cell is between 85 – 90% of the value at the well.

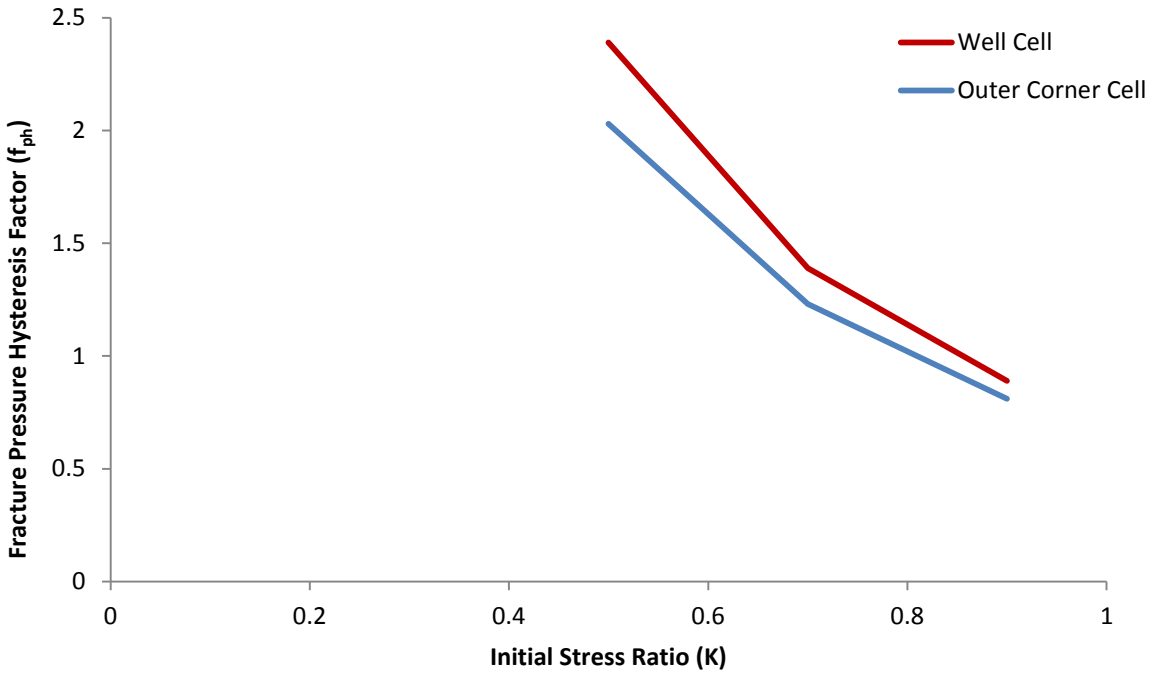

Figure 4.69 – Graph of fracture pressure hysteresis factor against initial stress ratio for the cell and the well and outer edge of the reservoir.

Finally, Figure 4.70 is included to show that the same pattern is observed with the lower stiffness case, but that the effect of the geometry is reduced. With the low stiffness case the f_{ph} factors for the outer cell are higher than the higher stiffness case with f_{ph} = 2.13 for K = 0.5 and f_{ph} = 1.32 for K = 0.7. A low stiffness case with K = 0.9 was not simulated due to time constraints.

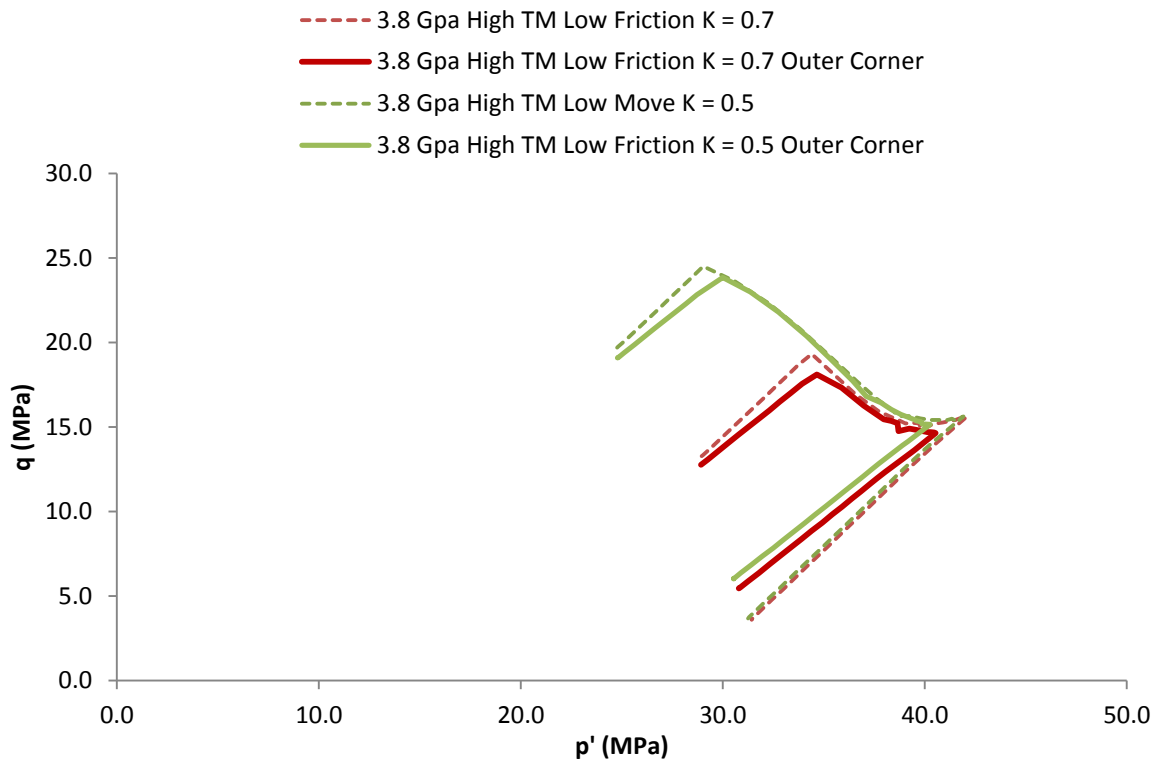

Figure 4.70 – p'-q plot of non-sealing low friction fault cases with low stiffness for a range of initial stress ratios comparing the cell at the well and the cell in the outer corner of the reservoir.

4.3.8 Overburden Parameters and Stress State

The overburden, underburden and sideburden form the confining material around the reservoir and so the properties in the overburden also have an effect on the stress path in the reservoir. The base case model was run with a reduced reference stiffness in the overburden of 2.35 GPa and a reduced Poisson's ratio of 0.3.

Figure 4.71 shows the p'-q plot comparing the effect of the lower stiffness shale against the base case stiffness shale for the cell at the well location and the cell at the outer corner of the model. The plot shows that the cases with softer shale have a flattened and rotated p'-q stress path compared to the stiffer shale. The final stress points on the stress paths are at a higher q stress and higher p' stress than the stiffer shale. The stress paths in the cases with lower stiffness overburden result in lower f_{ph} factors than the stiffer shale. For the cell at the well in the low stiffness case f_{ph} is 1.34 compared to 1.39 in the high stiffness shale, and at the outer corner f_{ph} is 1.17 compared to 1.23 in the high stiffness case.

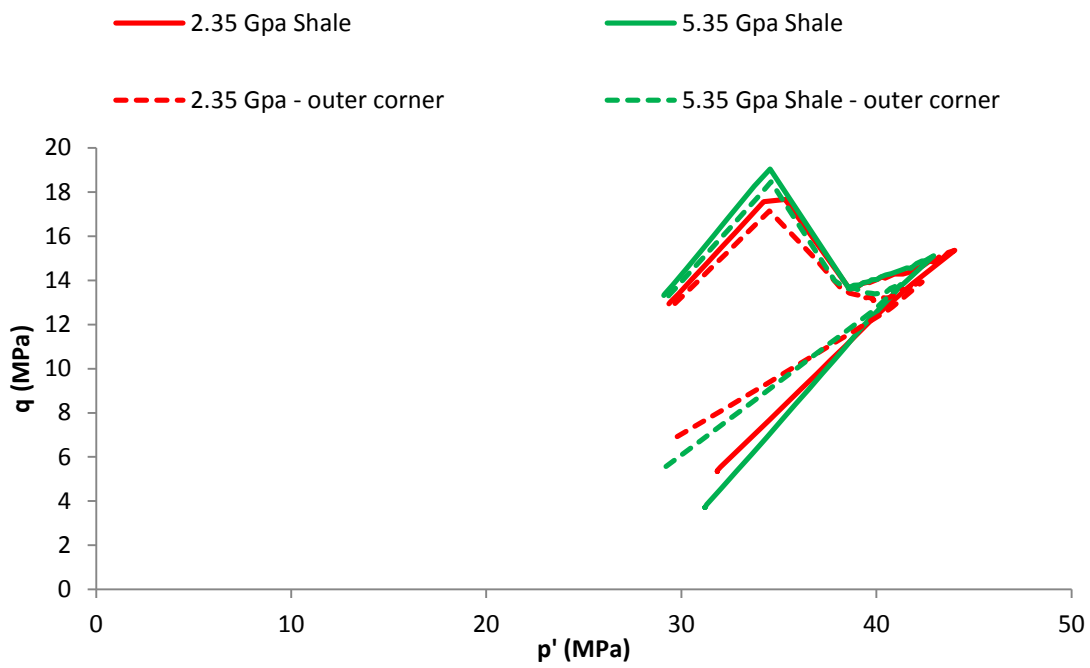

Figure 4.71 - p'-q plot of cases with low stiffness overburden compared against base case overburden stiffness, with comparison of cells at the well and the outer corner of the reservoir.

The stress path parameters for the low stiffness shale case are γ_v = 0.14, γ_h = 0.27 and K_{sp} = 0.85 for depletion and γ_v = 0.01, γ_h = 0.53 and K_{sp} = 0.47 for injection compared to, γ_v = 0.24, γ_h = 0.33 and K_{sp} = 0.88 for depletion and γ_v = 0.02, γ_h = 0.60 and K_{sp} = 0.41 for injection for the base case.

The stress changes in the overburden during depletion and injection are shown in Figure 4.72 and Figure 4.73. Analysis of the stress in the overburden during depletion in the low stiffness shale case shows a similar pattern of stress changes to the high stiffness case but with smaller magnitude. σ_1 increase at the side of the reservoir and decrease above and below the reservoir is approximately half that of the high stiffness case. σ_3 changes also follow the same pattern and are approximately half that of the high stiffness case. Interestingly in both cases stress increase is higher in the footwall of the fault beneath the reservoir in the low stiffness case, perhaps representing increase loading across the fault in the low stiffness case. During injection the small σ_1 stress increase observed in the high stiffness case is not present, interestingly however the σ_3 stress changes are identical to the high stiffness case. The stress plots and stress path parameters show that there is significantly less stress arching for the low stiffness shale case and less build-up of horizontal stress during depletion.

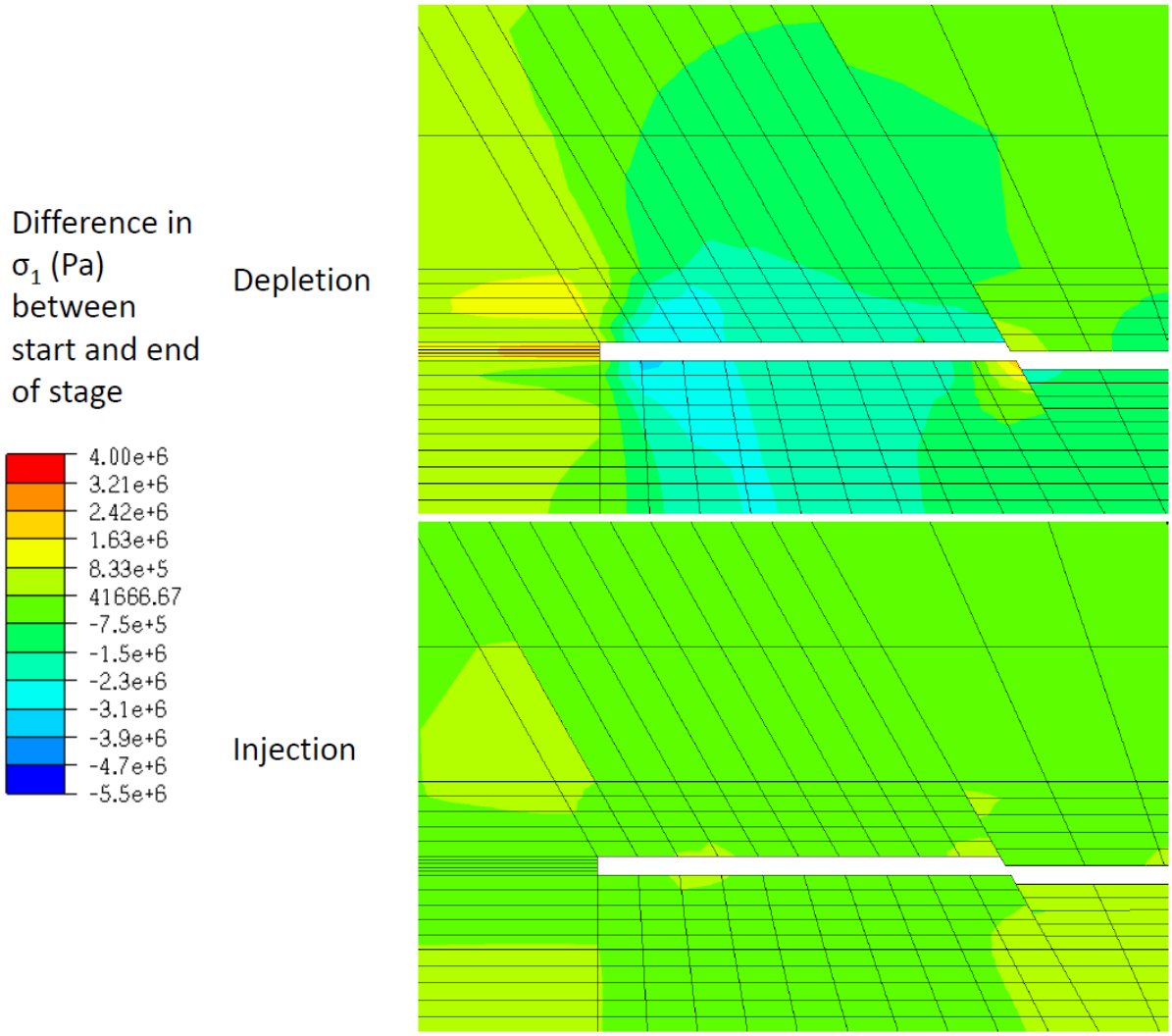

Figure 4.72 – Contour plot of the change in σ_1 for high stiffness case with non-sealing low friction faults and the overburden stiffness reduced to 2.35 GPa reference stiffness for the central X plane section through the model.

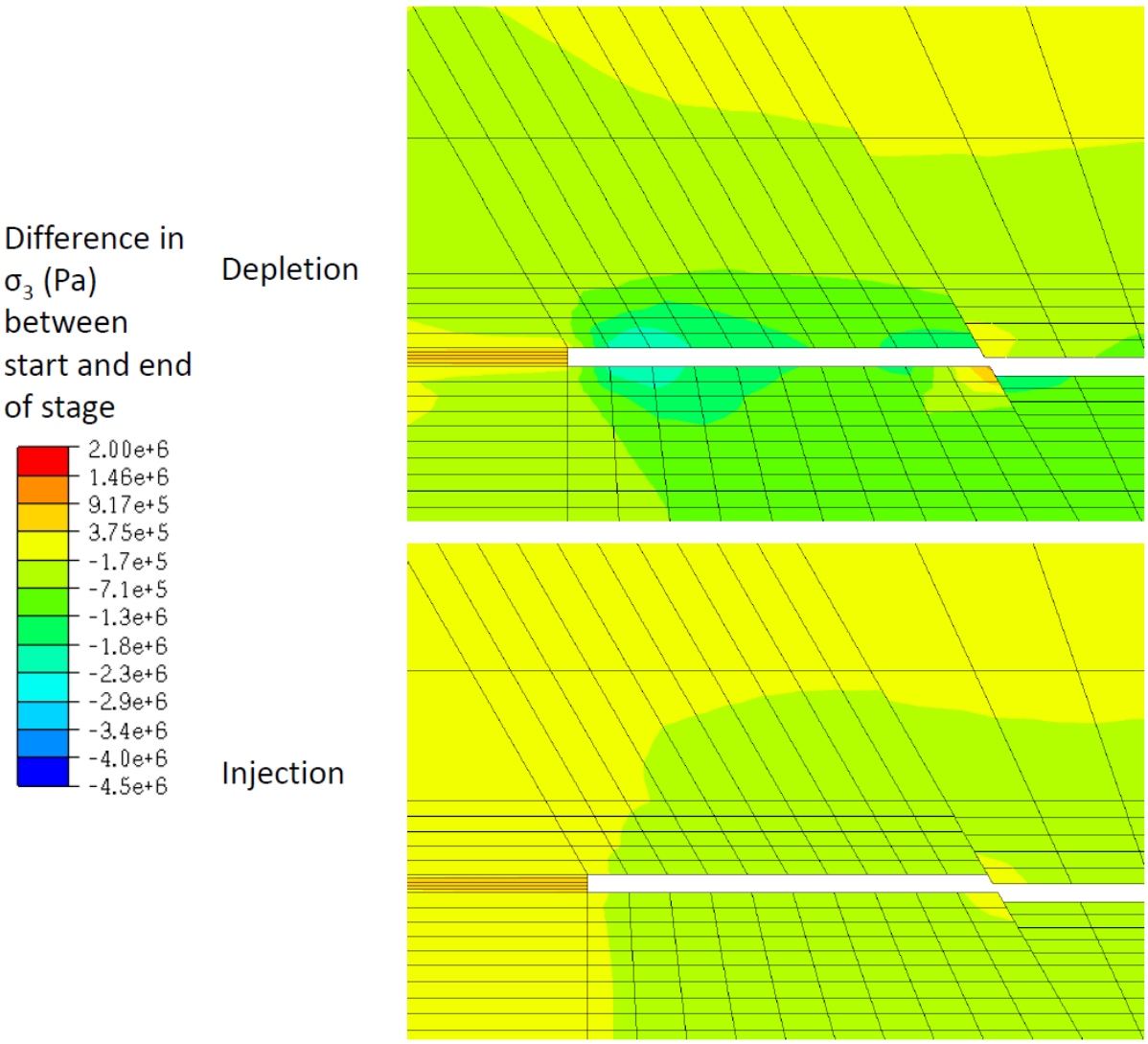

Figure 4.73 - Contour plot of the change in σ_3 for high stiffness case with non-sealing low friction faults and the overburden stiffness reduced to 2.35 GPa reference stiffness for the central X plane section through the model.

A case was also investigated where the Poisson's ratio of the overburden was reduced to ν = 0.3. The p'-q plot for the case is shown in Figure 4.74. The figure shows that the difference in Poisson's ratio in the overburden, although quite large, has an insignificant effect on the stress path in the reservoir.

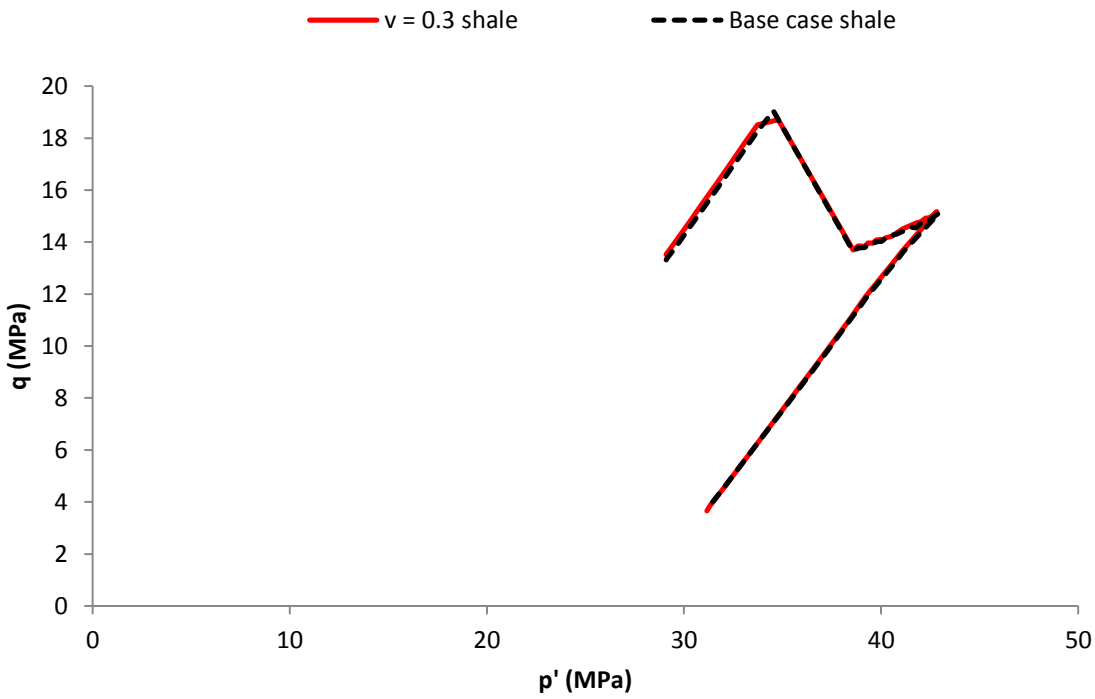

Figure 4.74 - p'-q plot base case overburden Poisson's, compared to a case with a reduced Poisson's ratio of ν = 0.3.

The main focus of this investigation is the behaviour of the material within the reservoir, however failure in the overburden would allow leakage of CO_2 in the reservoir, and so consideration of the stress state in the overburden above the reservoir is important. Figure 4.75 shows a Mohr circle plot for normal and shear stress in a cell in the overburden above the reservoir. The plot shows that the overburden above the reservoir is not close to shear failure for the scenario modelled. Similar plots are also observed for the other cases, and so failure in the overburden is not important in this case. The plot also shows that the overburden does not undergo plastic deformation, and this is also the case for locations elsewhere in the overburden. This is due to the fact that compared to the reservoir, changes in overburden stress are small, the large effective stress changes seen in the reservoir are linked to significant pore pressure changes.

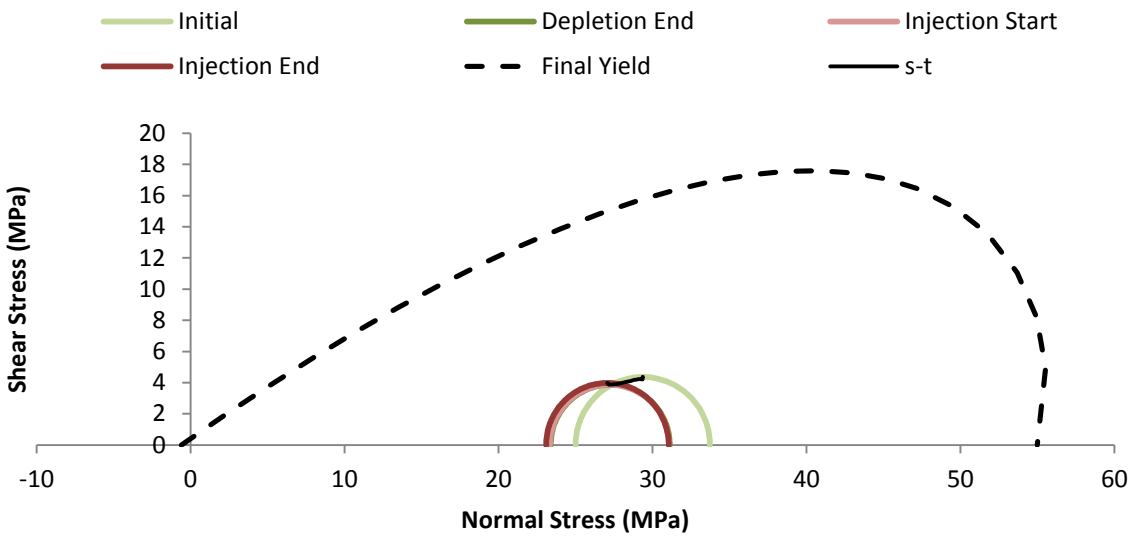

Figure 4.75 – Mohr circle plot of stress in the overburden directly above the reservoir for the non-sealing low friction case.

4.3.9 Fault Movement and Failure Potential

4.3.9.1 *Base Case Stress Ratio*

The behaviour of the faults during depletion and injection can be analysed to determine the movement along the faults and potential for failure due to stress changes around the fault. The contour plots of the total stress around the reservoir show the stress change at the faults. Figure 4.17 and Figure 4.18 show total stress for the non-sealing base case in section 4.3.1.1 and Figure 4.29 and Figure 4.30 show the same for the sealing base case in 4.3.1.2. For vertical stress in the non-sealing case the plots show a change in the stress distribution at the fault compared to the surrounded over and underburden. An increase in vertical stress in the footwall beneath the reservoir and in the hanging wall above the reservoir is observed during depletion. During injection there is a slight reduction in the vertical stress in these areas in a similar manner to that observed at the side of the reservoir. For the horizontal stress during depletion there is an increase in total stress only in the footwall of the fault beneath the reservoir. During injection there is a similar stress change to that observed in the sideburden above and below the reservoir, with a slight increase in the hanging wall above the reservoir and footwall below the reservoir. Although the resolution is too coarse to show the full change, as some areas exhibit a slight decrease in stress. The general trend is for significant stress changes during the depletion stage and smaller stress changes during injection. The plots show apparent stress transfer across the fault during depletion with the fault loaded during stress arching. The plot also shows loading of the footwall of the fault beneath the reservoir during depletion. This behaviour matches that of the side of the reservoir during depletion and injection, but to a lesser extent, with the fault acting in a similar manner to the sideburden next to the reservoir. For

the sealing case, shown in Figure 4.29 and Figure 4.30, the stress distribution is more straightforward and mirrors the response at the side of the reservoir, although the stress increases at the fault, particularly during depletion, are larger than at the side of the model. The stress increase is confined mainly to the hanging wall, and an increase is observed in vertical and horizontal stress in both the depletion and injection stage.

Figure 4.76 and Figure 4.77 show the resulting vertical and horizontal contact sliding distance along the fault next to the injection compartment for the non-sealing low friction base case during depletion. The plots represent movement of points along the edge of the contact element. The plot of vertical sliding distance shows that points above and below the reservoir in the footwall slide vertically upwards by up to 0.007 m, whilst a point below the reservoir in the hanging wall slides vertically downwards by up to 0.008 m. The same regions move horizontally from left to right (away from the well) in the footwall, and right to left (towards the well) in the hanging wall by up to 0.017 m in the footwall and up to 0.013 m in the hanging wall. The resulting sliding vector is somewhat counter-intuitive and points upwards to the right for the footwall and downwards to the left for the hanging wall, with larger displacement in the horizontal direction. This motion on the fault results from differential displacement across the fault, closer examination of the displacement contour in the region around the fault shows greater horizontal movement of the footwall to the left than the hanging wall and greater uplift beneath the reservoir in the footwall compartment. This differential motion seems to lead to motion normal to the fault plane on either side of the fault (of a small magnitude). The sliding displacement represents deformation of the fault plane within the model and represents accommodation of the deformation in and around the reservoir. The hanging wall below the reservoir drops compared to the footwall.

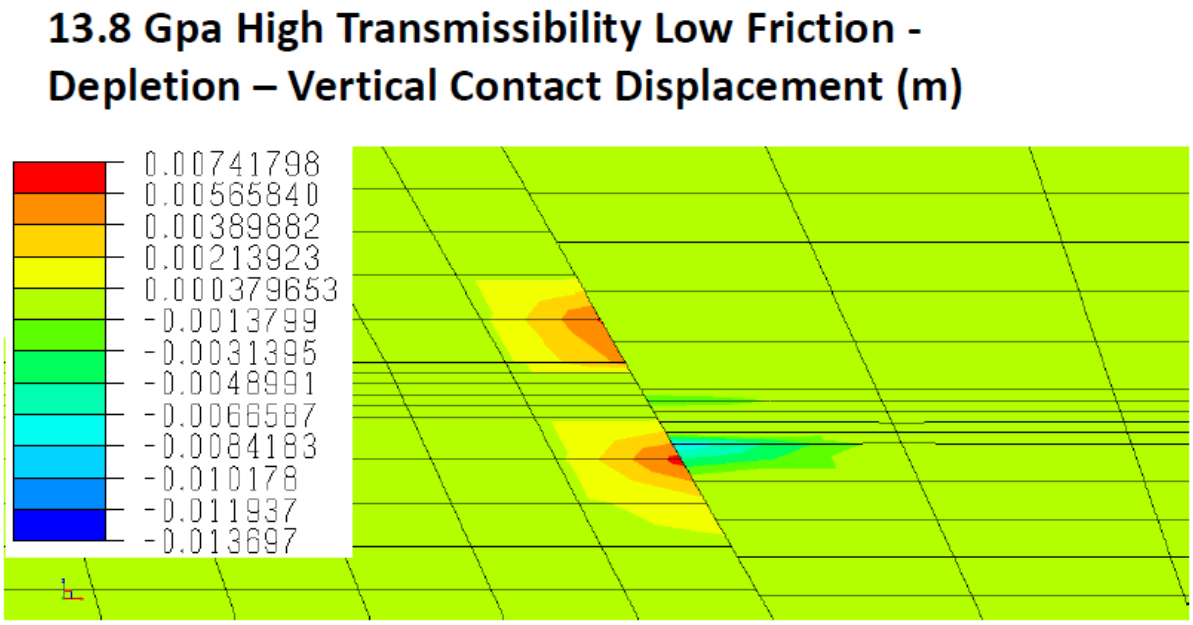

Figure 4.76 – Contour of vertical sliding along the fault contact for the non-sealing low friction base case model.

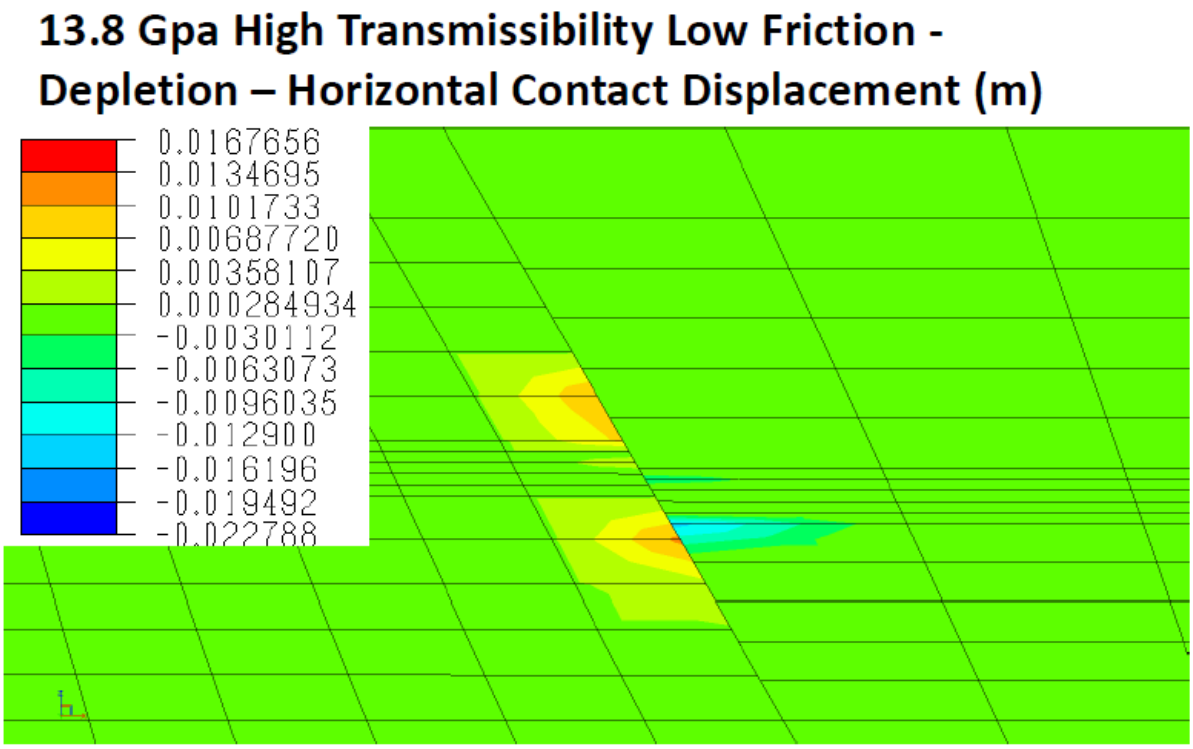

Figure 4.77 - Contour of horizontal sliding along the fault contact for the non-sealing low friction base case model.

Comparison with the fault high friction case in Figure 4.78 (vertical sliding) and Figure 4.79 (horizontal sliding) shows that sliding along the fault is restricted to a smaller area in the higher friction case, which is consistent with the higher strength of the fault. Maximum vertical sliding displacement is 0.006 m upwards. The vertical sliding displacement in the hanging wall is 0.01 m downwards, which is larger than the low friction fault however, but is restricted to a similar region. Comparison of the horizontal sliding shows the motion in the footwall is also restricted to a smaller region along the fault and is a lower magnitude of 0.010 m. Horizontal sliding on the hanging wall slide is of a larger magnitude than the low friction case (again in a similar region) at 0.019 m to the left. The high friction case seems to show smaller movement in the footwall side of the fault but larger sliding movements in the hanging wall below the reservoir.

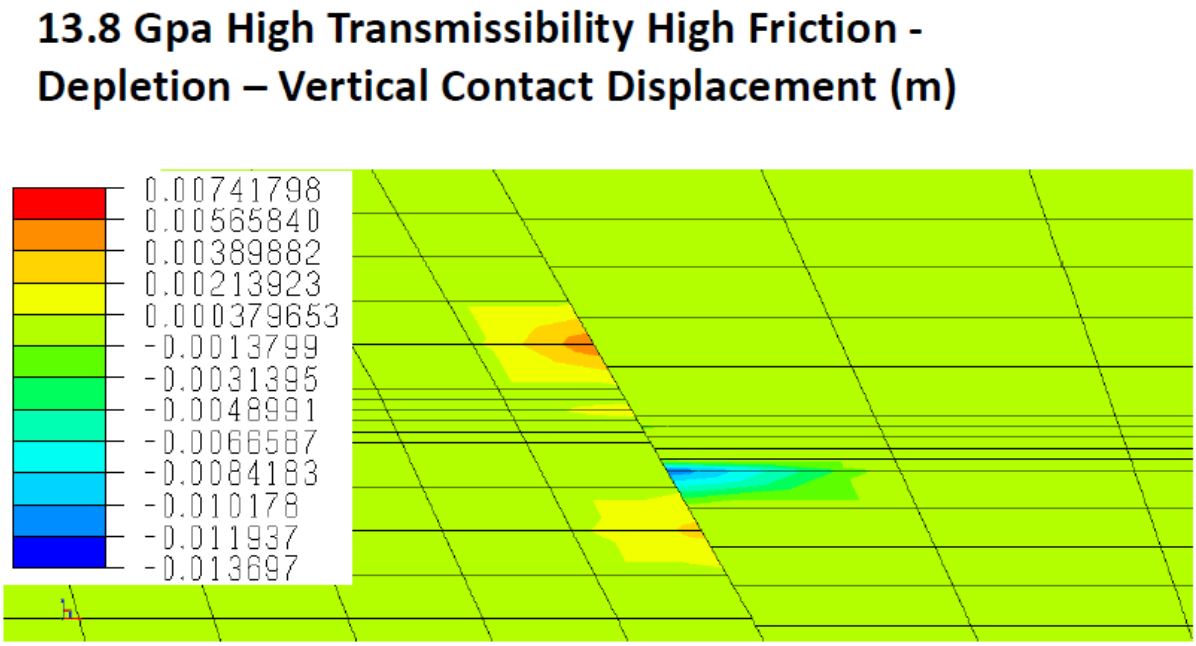

Figure 4.78 - Contour of vertical sliding along the fault contact for the non-sealing high friction base case model.

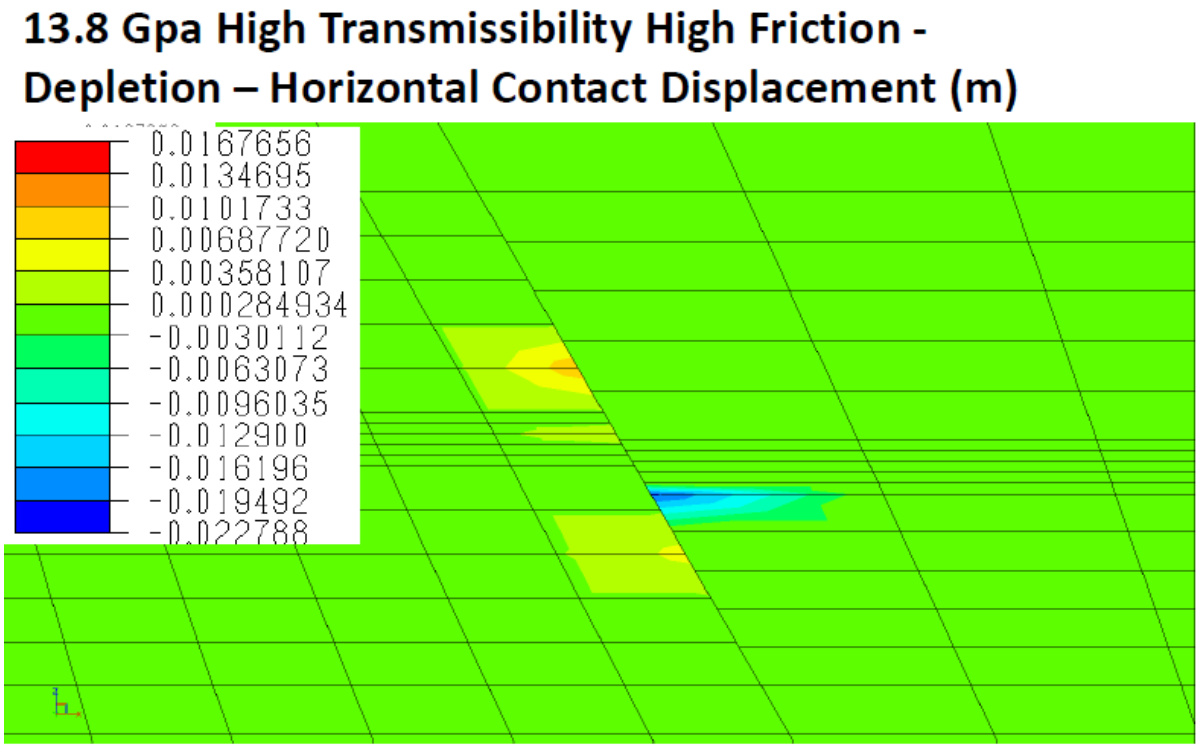

Figure 4.79 - Contour of horizontal sliding along the fault contact for the non-sealing high friction base case model.

The sealing cases are shown in Figure 4.80, Figure 4.81, Figure 4.82 and Figure 4.83. Generally for the sealing case there is more significant movement in the footwall of the model compared to the hanging wall, with the exception of the high friction case for horizontal sliding displacement. The movement on the fault is spread over a larger area in

the low friction model compared to the high friction model, and this may also be related to the strength of the fault. The sealing case has a different displacement and stress profile, as the fault essentially represents the side of a compartment, and this affects the sliding motion on the fault. The hanging wall of the fault receives larger loading due to the stress arching effect, and this may explain the relative upwards motion of the footwall side of the fault and the differences in the sliding displacement.

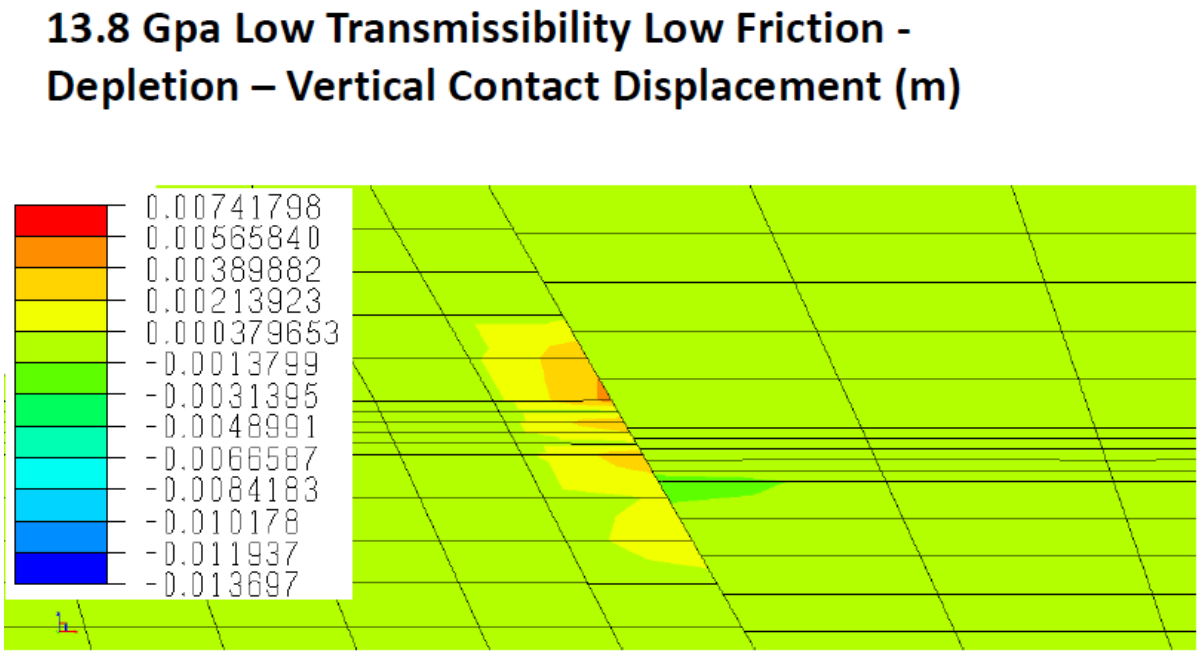

Figure 4.80 - Contour of vertical sliding along the fault contact for the sealing low friction base case model.

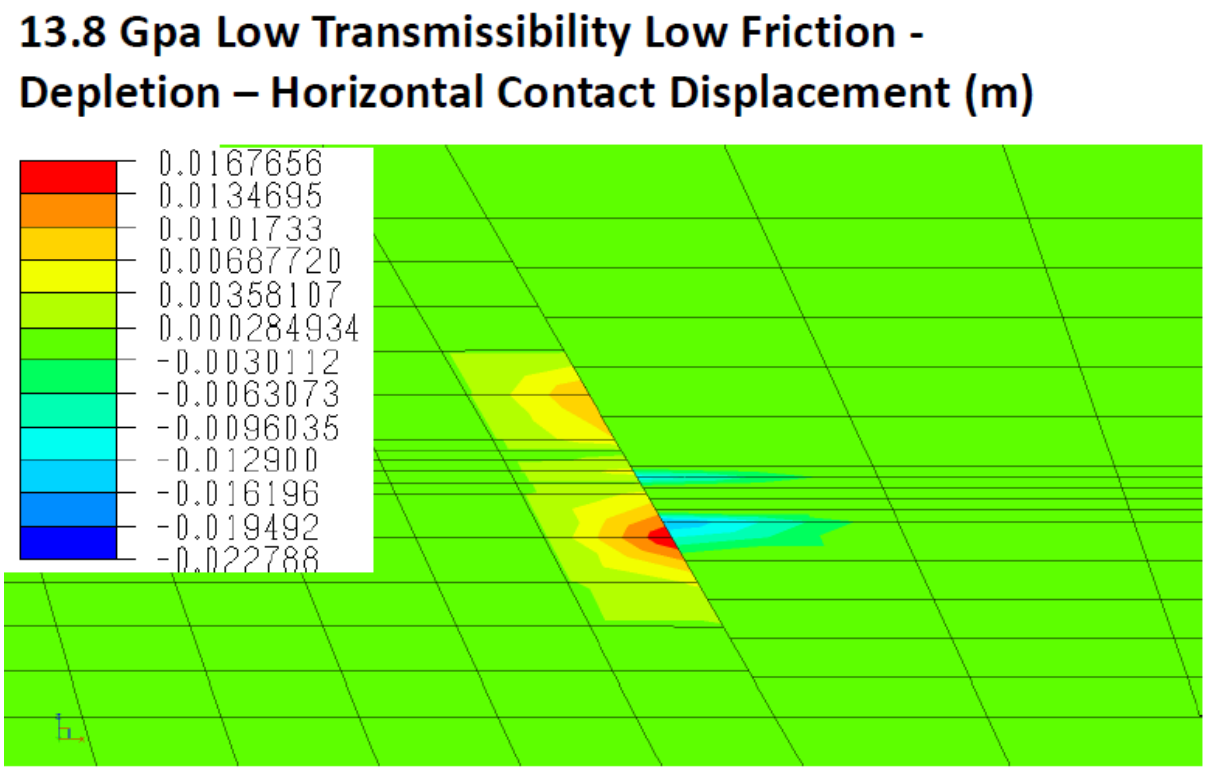

Figure 4.81 - Contour of horizontal sliding along the fault contact for the sealing low friction base case model.

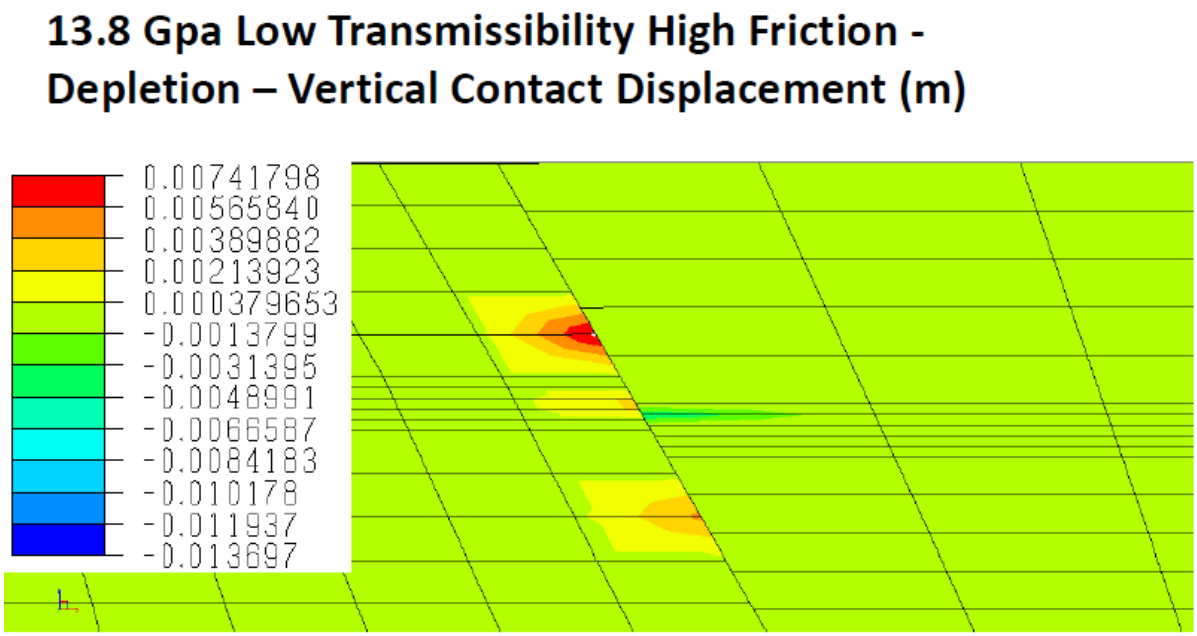

Figure 4.82 - Contour of vertical sliding along the fault contact for the sealing high friction base case model.

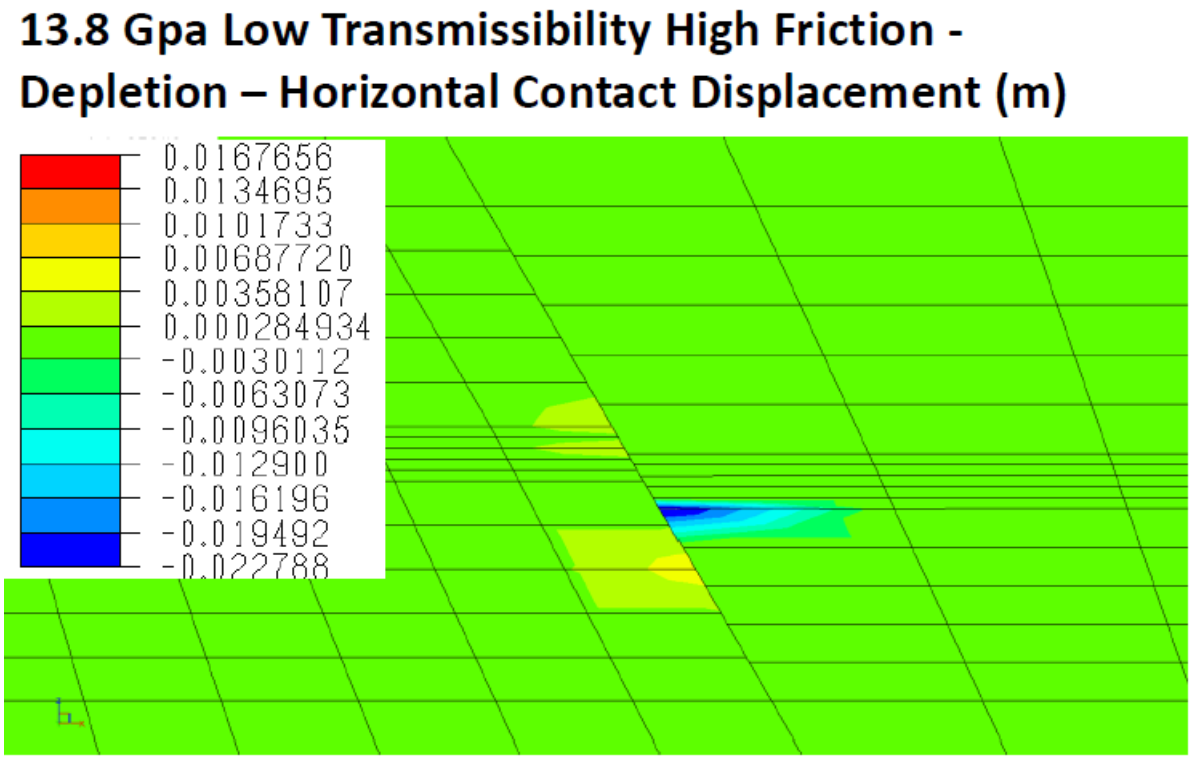

Figure 4.83 - Contour of horizontal sliding along the fault contact for the sealing high friction base case model.

The high stiffness cases showed the most significant movement along the fault, and so results are not presented for the low stiffness case. The difference is because the stiffner material resists deformation and promotes sliding along the fault. Overall, the results show that movement along the fault model seems to be related to accommodation of deformation in and around the reservoir, and does not represent significant sliding along the entire fault.

Figure 4.84 and Figure 4.85 show the worst-case stress state for the sealing low friction base case in the reservoir and overburden in terms of the frictional failure envelope on the fault. The Mohr circles plot the stress state in adjacent nodes either side of the fault closest to the well and so represent the different stresses either side of the fault. The Mohr circle that encompasses both stress states is also shown as this represents the worst case combined stress state across the fault. A zero thickness frictional sliding plane represents the fault in the model, in reality, fault rocks would be likely to exist, and the fault would have a non-zero thickness. The Mohr-Coulomb failure limit on the fault is lower than the SR3 failure limit for shear failure, and represents failure within the fault. Failure within the fault material is likely to occur before shear failure within the reservoir material. Figure 4.86 and Figure 4.87 show the stress state for cells in the reservoir of the non-sealing base case and the non-sealing low stiffness case for comparison with the previous figures for the sealing low friction case. The Mohr circle plots of stress on the fault show that the stress state in all of the cases is below that required for frictional failure along the fault, and thus also below that required for shear failure within the fault rock. The worst case observed for all of the

models is for the reservoir section of the fault in the base case with sealing faults shown in Figure 4.84, where the fault comes closest to failure.

The Mohr circle plots in conjunction with the fault sliding displacement plots show that leakage along the fault is unlikely in all of the cases. The fault does not undergo significant movement, and failure in the material around the fault does not occur, therefore CO_2 would be unlikely to be able to escape from containment within the reservoir along the fault.

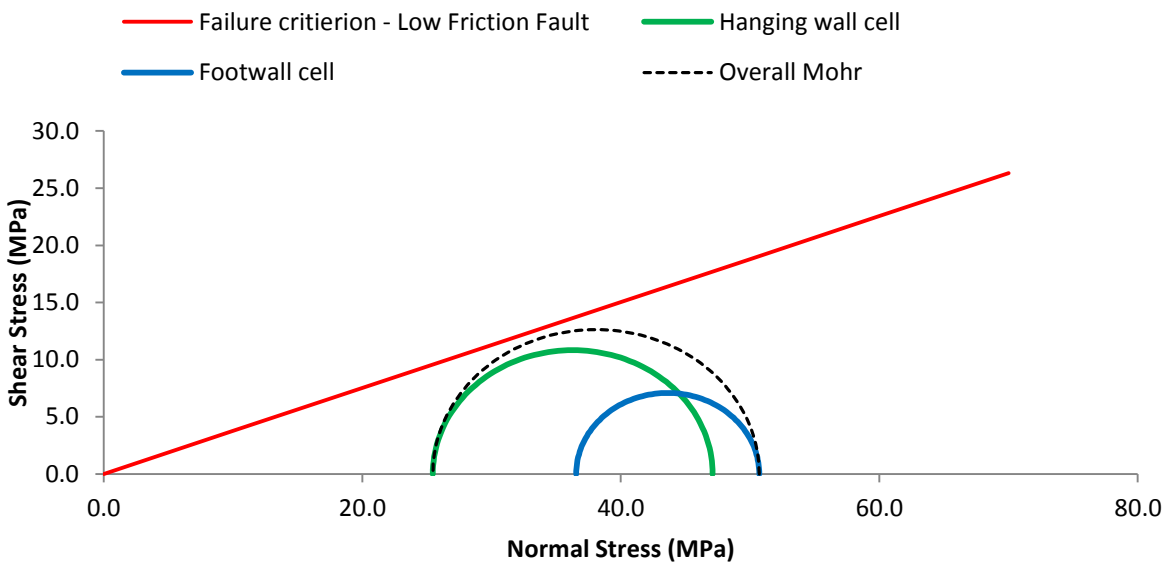

Figure 4.84 - Mohr circle plot for the stress state in the sealing low friction base case model for cells adjacent to either side of the fault within the reservoir. The failure criterion for the fault is shown for comparison with the stress state.

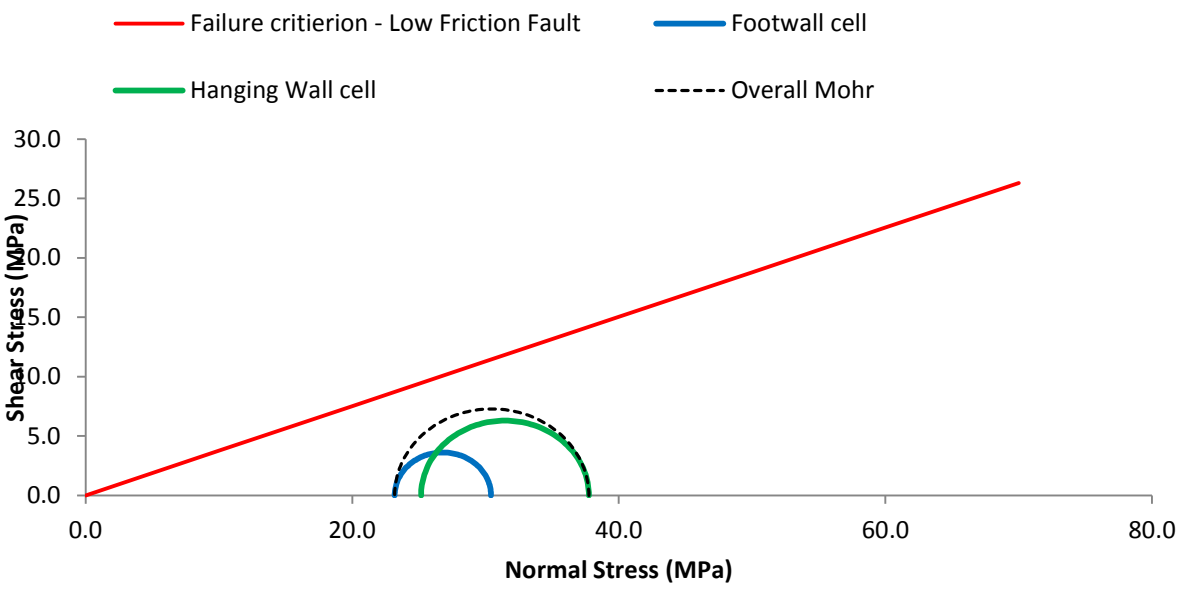

Figure 4.85 - Mohr circle plot for the stress state in the sealing low friction base case model for cells adjacent to either side of the fault within the overburden. The failure criterion for the fault is shown for comparison with the stress state.

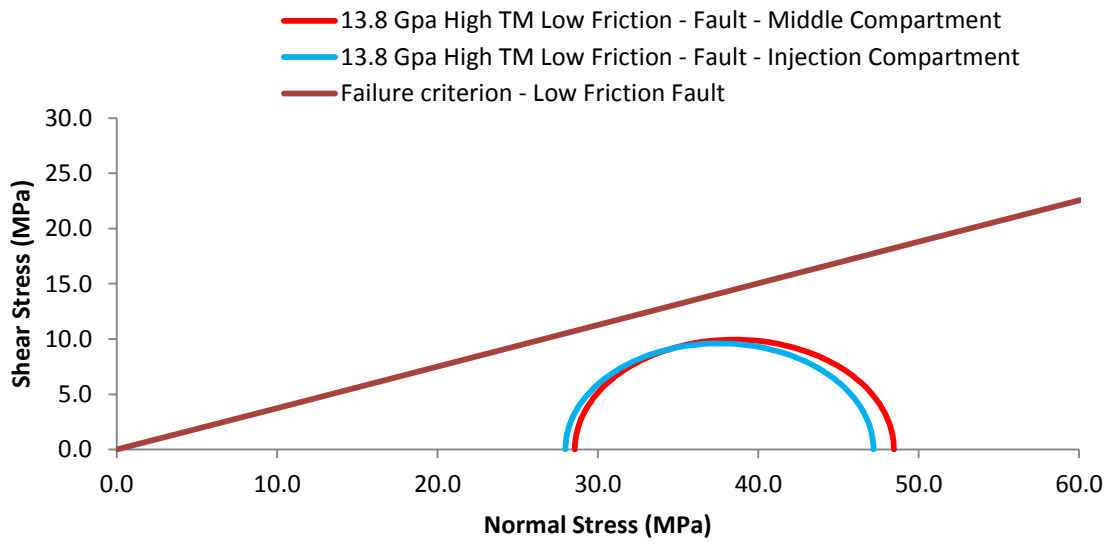

Figure 4.86 – Mohr circle plot for the stress state in the non-sealing low friction base case model for cells adjacent to either side of the fault with the failure criterion for the movement along the fault.

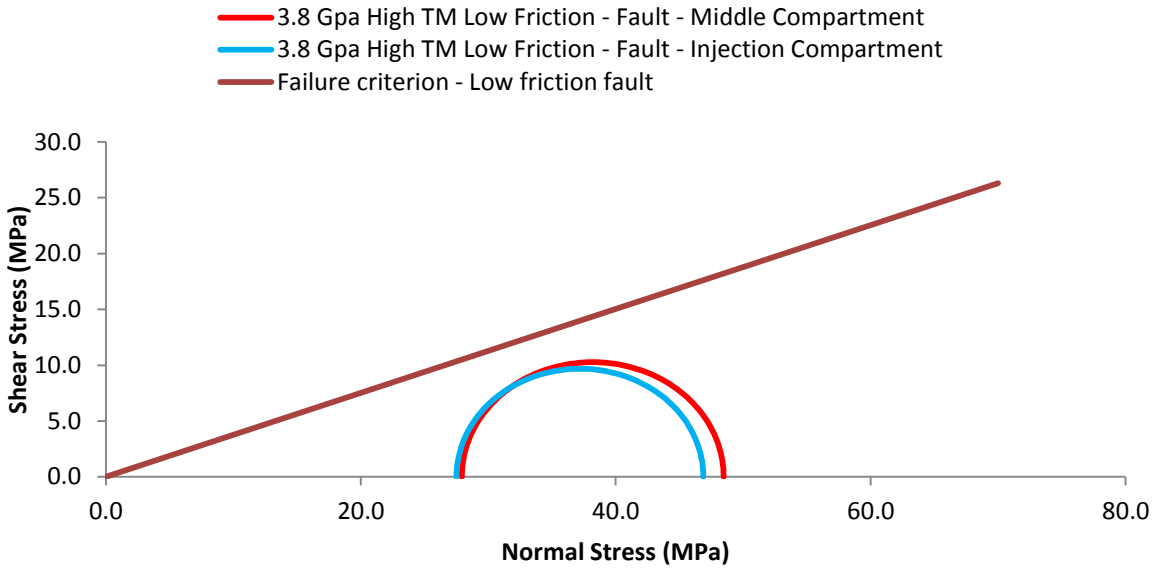

Figure 4.87 - Mohr circle plot for the stress state in the non-sealing low friction low stiffness model for cells adjacent to either side of the fault with the failure criterion for the movement along the fault.

4.3.9.2 *Initial Stress Ratio K = 0.5*

The faults in the other initial stress ratio cases all behaved in a similar manner to the K = 0.7 case however the most extreme movement was observed in the K = 0.5 case. Figure 4.88 - Figure 4.91 shows the contact displacement during depletion and injection in the horizontal and vertical axes for the sealing low friction case with K = 0.5. The figures show that displacement on the contact is significantly larger in the K = 0.5 case, up to an order of magnitude larger both horizontally and vertically for depletion. The contact displacement is focussed in the same areas as the other cases. Displacement for the injection stage is also included in the figures as movement is more significant, the movement during injection is roughly one order of magnitude less than depletion.

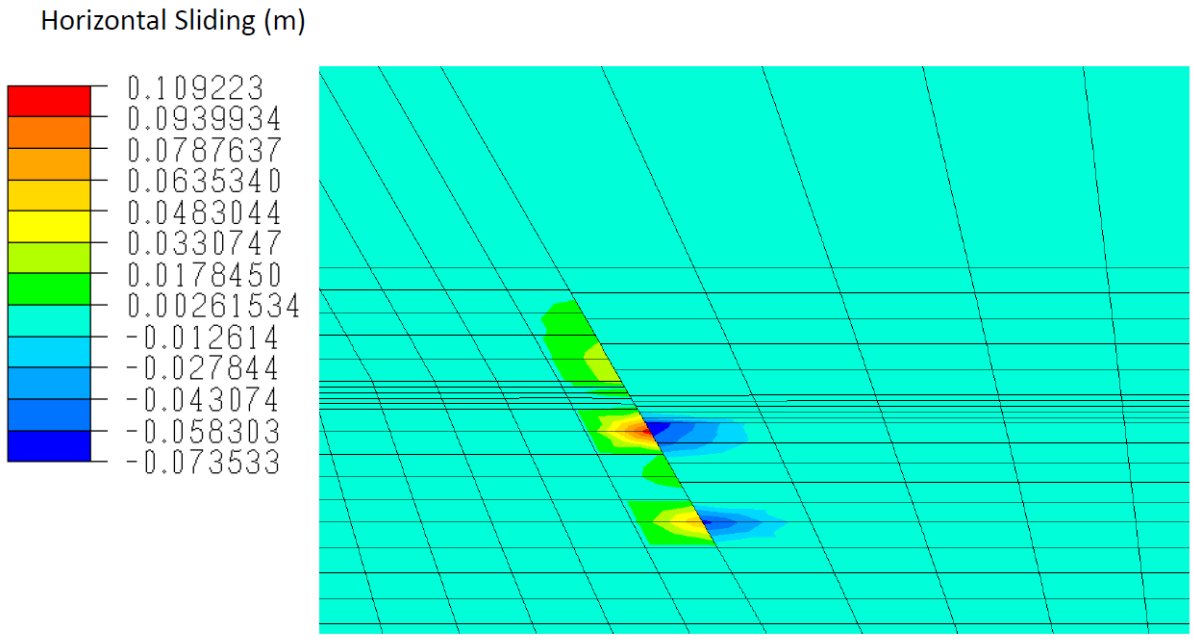

Figure 4.88 – Contour of horizontal contact displacement along the fault contact for the sealing low friction K = 0.5 model during depletion.

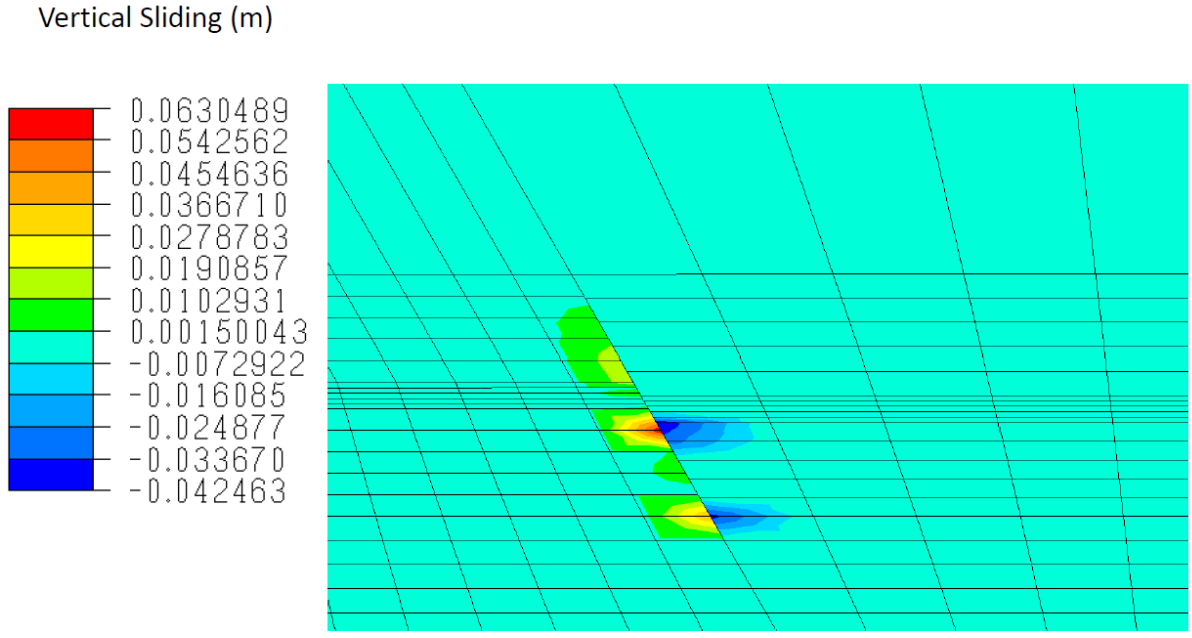

Figure 4.89 – Contour of vertical contact displacement along the fault contact for the sealing low friction K = 0.5 model during depletion.

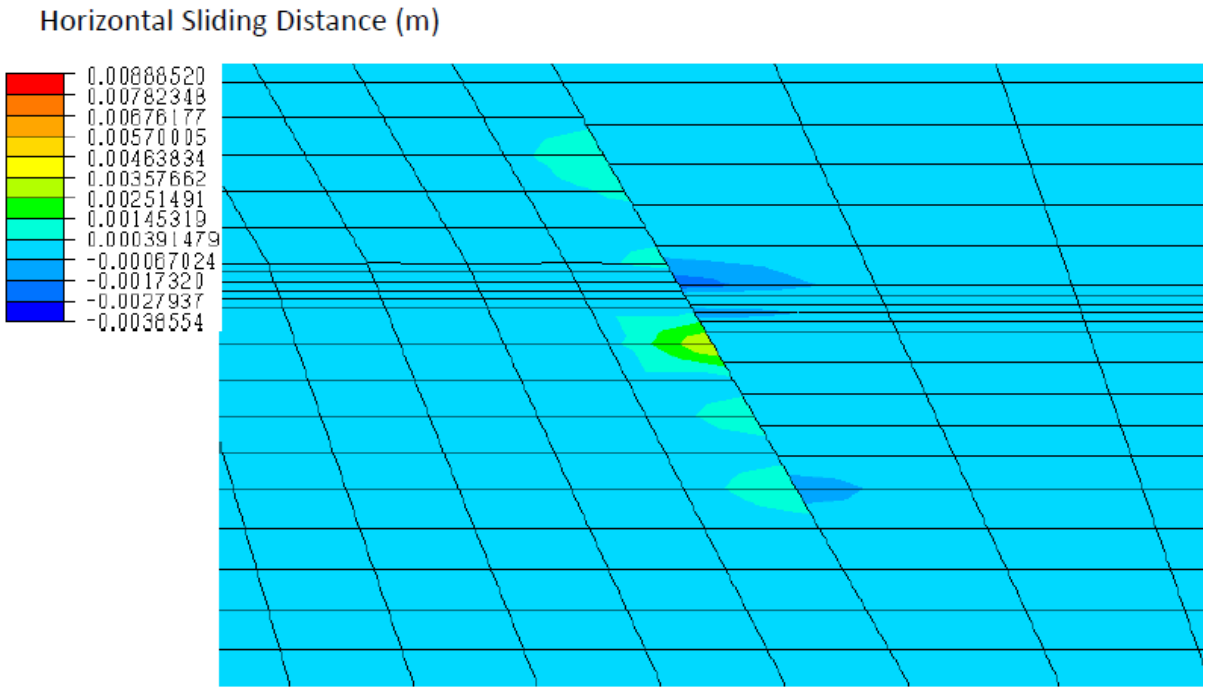

Figure 4.90 - Contour of horizontal contact displacement along the fault contact for the sealing low friction K = 0.5 model during injection.

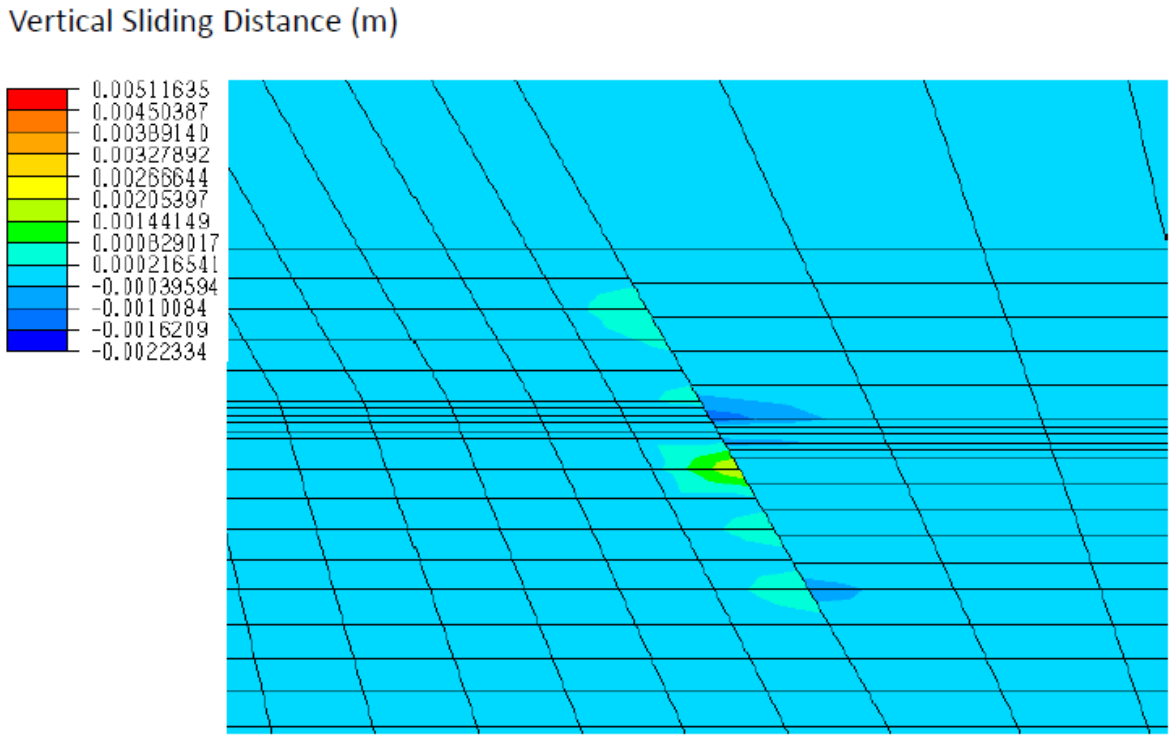

Figure 4.91 - Contour of vertical contact displacement along the fault contact for the sealing low friction K = 0.5 model during injection.

As in the K = 0.7 case the footwall moves upwards and the hanging wall downwards indicating normal movement on the fault, again the movement of the footwall is also left to right, and the hanging wall right to left, as in the previous cases. Figure 4.92 shows the

vector of movement of the nodes on the fault plane on either side of the fault, showing the upwards movement of the footwall and downwards movement of the hanging wall. The motion along the fault is difficult to visualise as it is based upon the relative movement of nodes on the contact surface, the nodes are also displaced by deformation of the grid. An exaggerated representation of the deformed grid after depletion (where most deformation occurs) is shown in Figure 4.93. The figure shows that the fault plane moves downwards to the left above and below the reservoir, and this may influence the vectors of contact displacement that are produced.

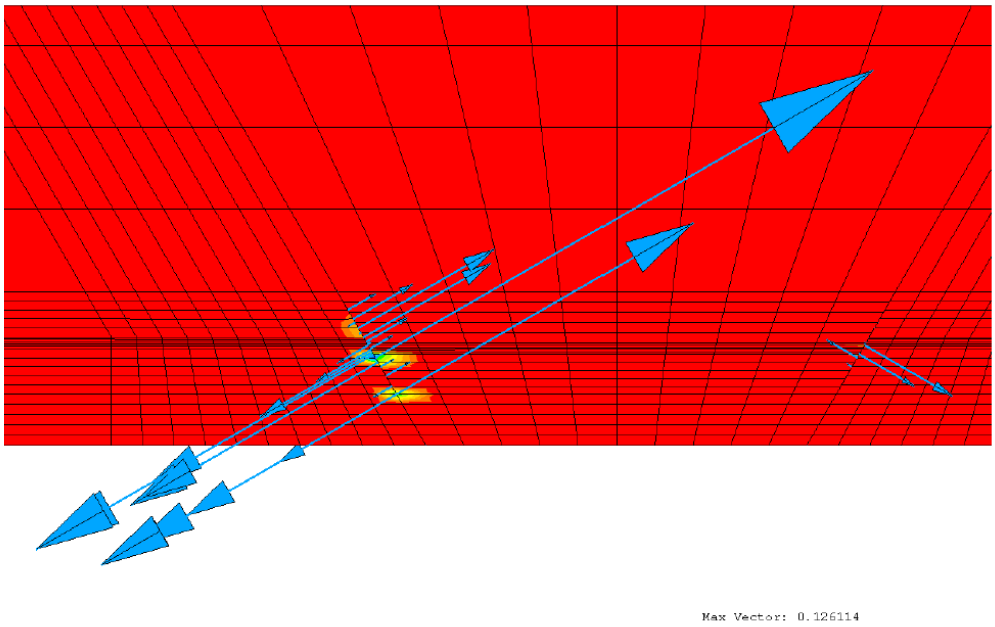

Figure 4.92 – Contact displacement vectors for nodes along the fault plane in the K = 0.5 case with sealing low friction faults.

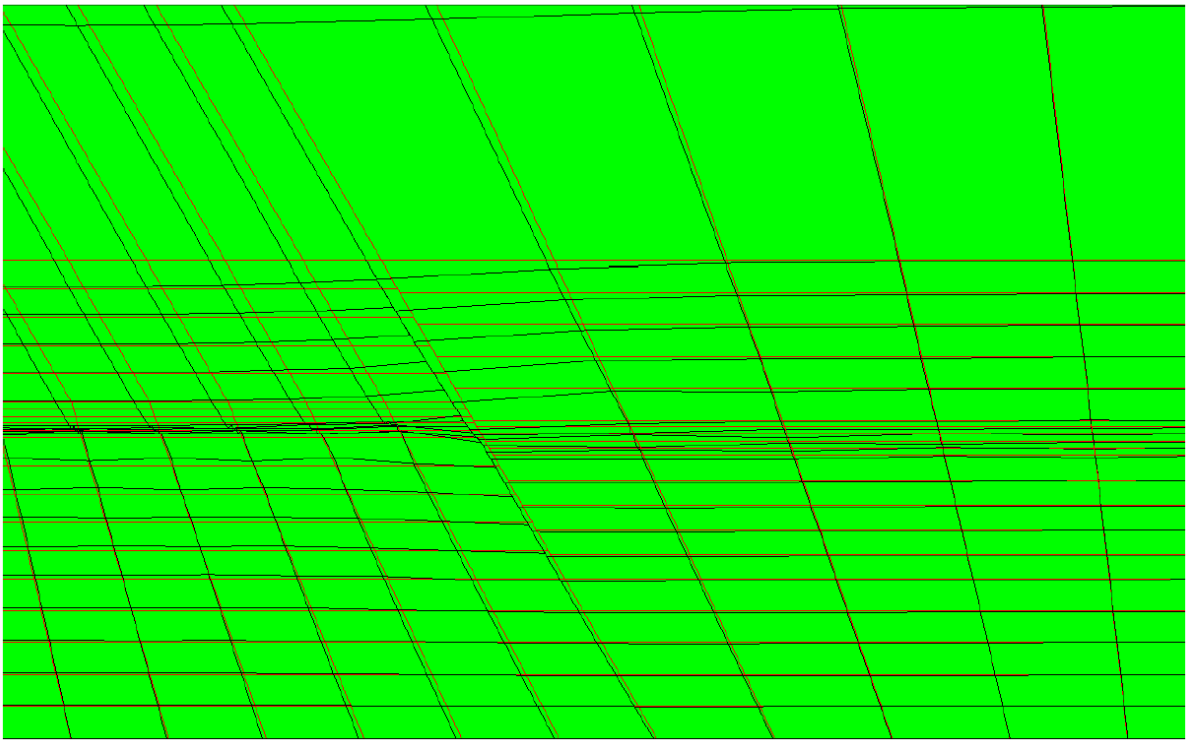

Figure 4.93 – Exaggerated representation of the deformed grid after depletion compared to the original grid for the sealing K = 0.5 case.

The stress state in the K = 0.5 case is also the most prone to failure of all the cases. Figure 4.94 - Figure 4.96 shows the stress state on the fault in the reservoir during depletion, in the reservoir at the end of injection and in the overburden above the reservoir at the start of injection for the sealing case. These stress states represent the worst case stress states observed in the model. Figure 4.94 shows that the stress in the hanging wall during depletion is significant enough to cause failure on the fault envelope, and that total stresses between the nodes would be significant enough to initiate shear failure in non-faulted material. However, Figure 4.95 shows that the worst case stress state during injection is below either of the failure criteria. Figure 4.96 shows the worst case stress state in the overburden above the reservoir at the start of injection, the figure shows that the stress state is close to or at failure for the fault failure criteria in the hanging wall, and total stresses across the fault exceed the fault failure criteria. The stress state remains close to the fault failure criteria for the remainder of injection.

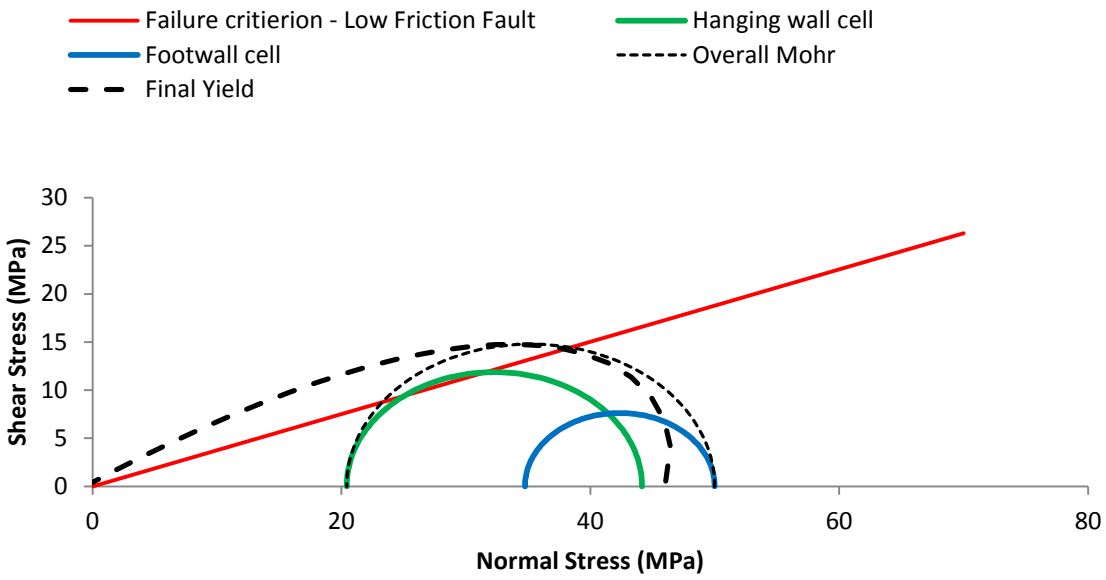

Figure 4.94 – Mohr circle plot for the stress state in the sealing low friction K = 0.5 model for cells adjacent to either side of the fault in the reservoir during depletion.

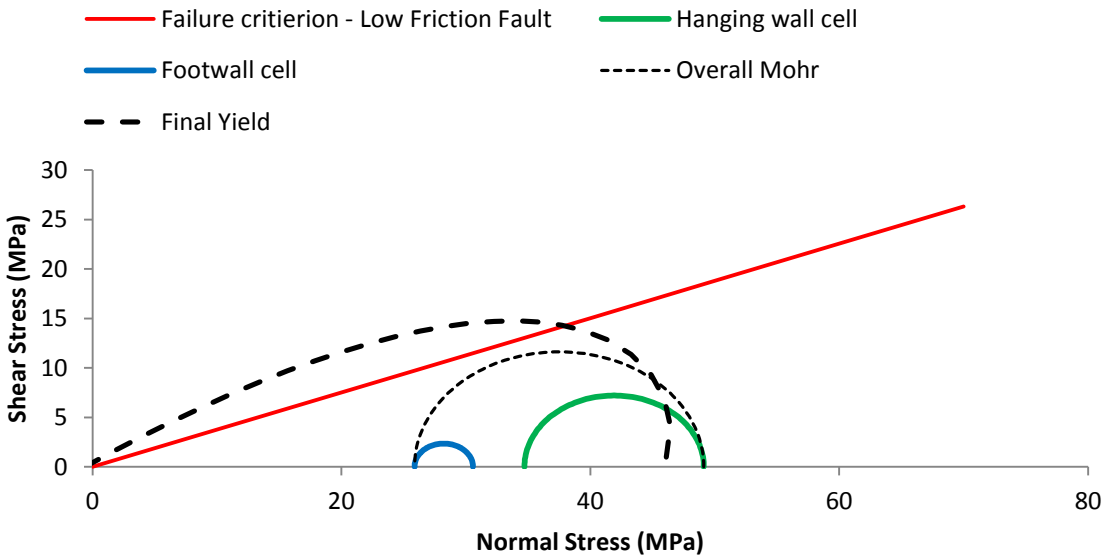

Figure 4.95 – Mohr circle plot for the stress state in the sealing low friction K = 0.5 model for cells adjacent to either side of the fault in the reservoir at the end of injection

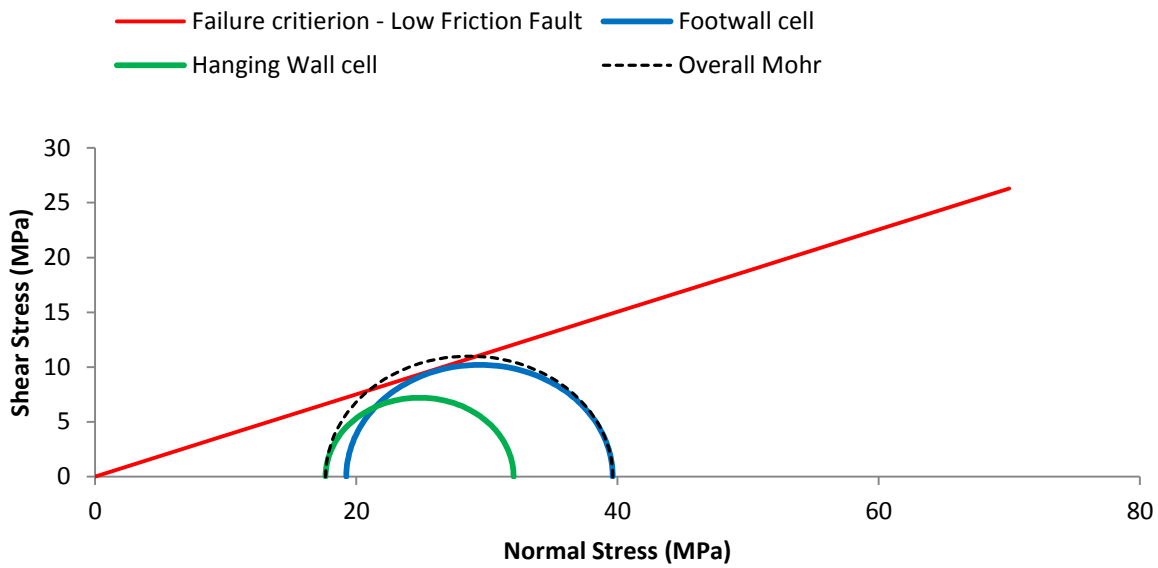

Figure 4.96 – Mohr circle plot for the stress state in the sealing low friction K = 0.5 model for cells adjacent to either side of the fault in the overburden at the start of injection.

Figure 4.97 - Figure 4.99 shows similar plots for the case with non-sealing faults. Again, stresses exceeding the strength of the fault are seen in the reservoir (hanging wall) during depletion, and total stresses across the fault that may potentially exceed the shear fracturing strength of the material yield envelope are observed at the start of the injection phase. In this case the stresses in the overburden are lower than either failure criterion throughout both depletion and injection.

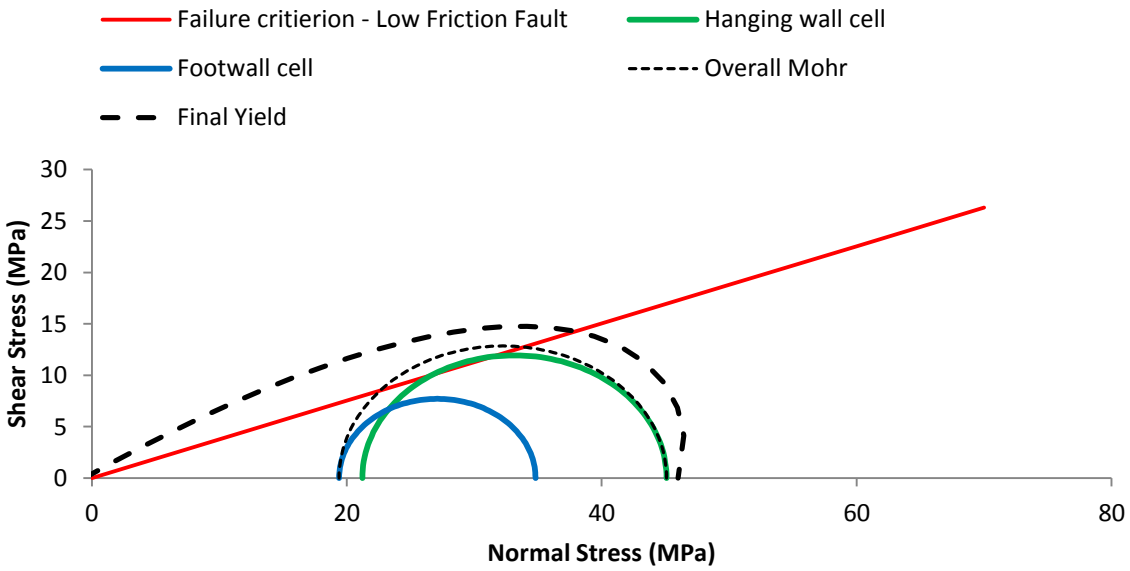

Figure 4.97 – Mohr circle plot for the stress state in the non-sealing low friction K = 0.5 model for cells adjacent to either side of the fault in the reservoir during depletion.

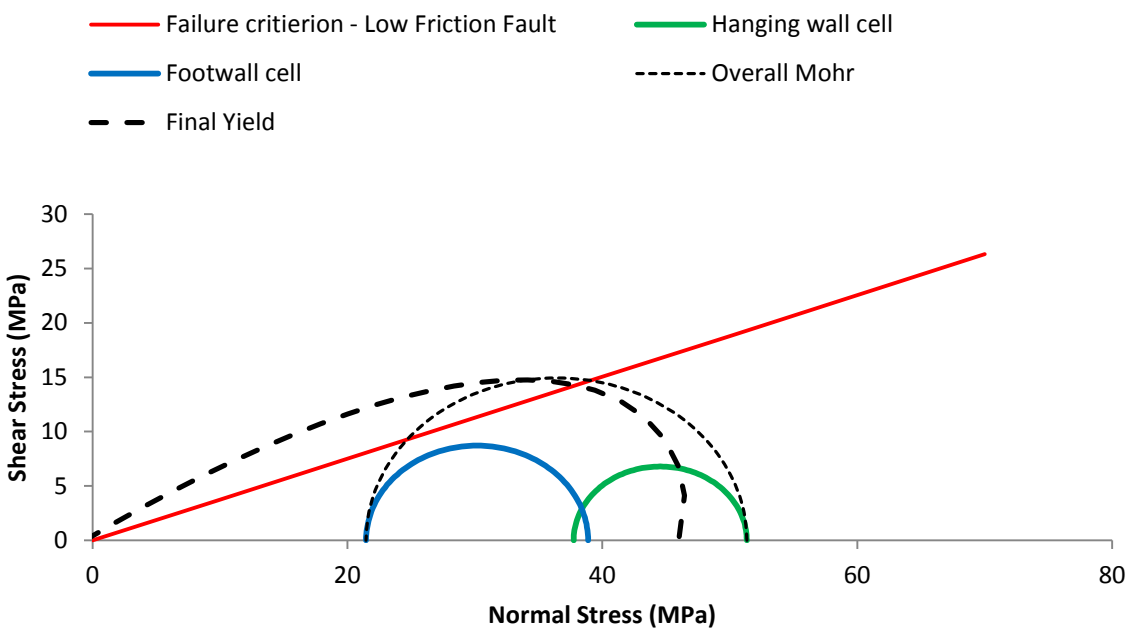

Figure 4.98 – Mohr circle plot for the stress state in the sealing low friction K = 0.5 model for cells adjacent to either side of the fault in the reservoir at the start of injection.

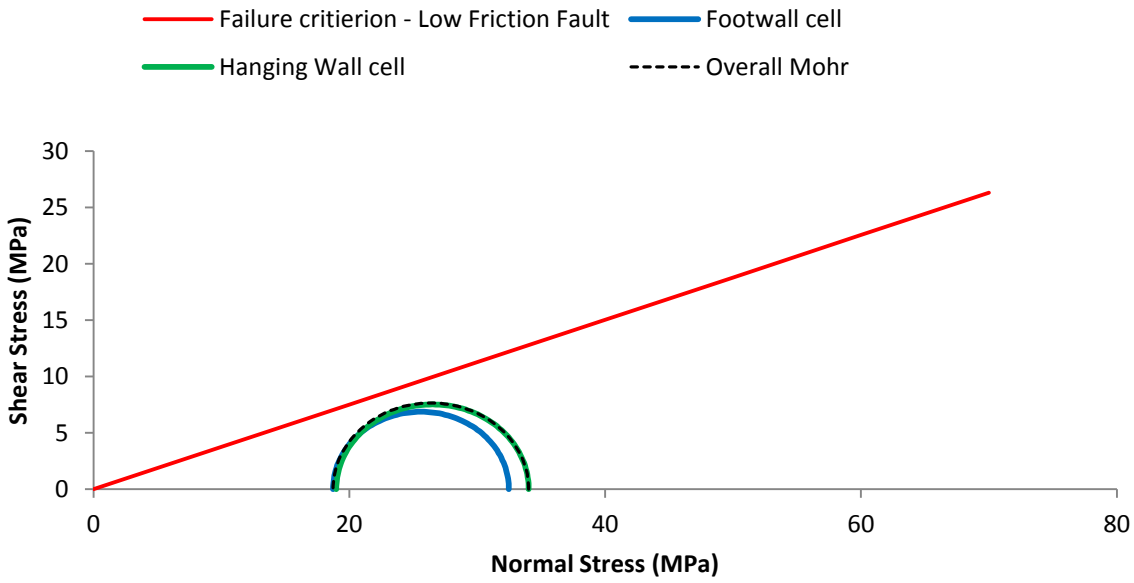

Figure 4.99 – Mohr circle plot for the stress state in the sealing low friction K = 0.5 model for cells adjacent to either side of the fault in the overburden at the end of injection.

4.3.10 Coupled and Non-Coupled Flow Simulation

The flow simulation model results can be analysed to determine the rates of production and injection, the produced and injected volumes and the pressures in the reservoir. The flow

models can be compared to assess the performance of the model when it is coupled to the geomechanical model and using the flow model alone to simulate production and injection.

Figure 4.100, Figure 4.101 and Figure 4.102 show production/injection rates, total volumes and pressures (at the well) for the high stiffness case with non-sealing low friction faults for the coupled model and a non-coupled model. All parameters are the same between the models, and only the compressibility has been adjusted in the non-coupled model to attempt to match the results of the coupled model. The compressibility was set at 1.0×10^{-4} bar^{-1} in the non-coupled model to improve the match between the models. The figures show that the production rates and total volumes can be matched well using this approach, but that the injection rates and volumes are significantly overestimated and the pressure in the model is also poorly matched during production and injection. The match between the models is poor as it does not take into account pore volume reduction, which is calculated and supplied by the geomechanical model in the coupled model. In this case, pore volume reduction during compaction is clearly significant and a more sophisticated flow model is required.

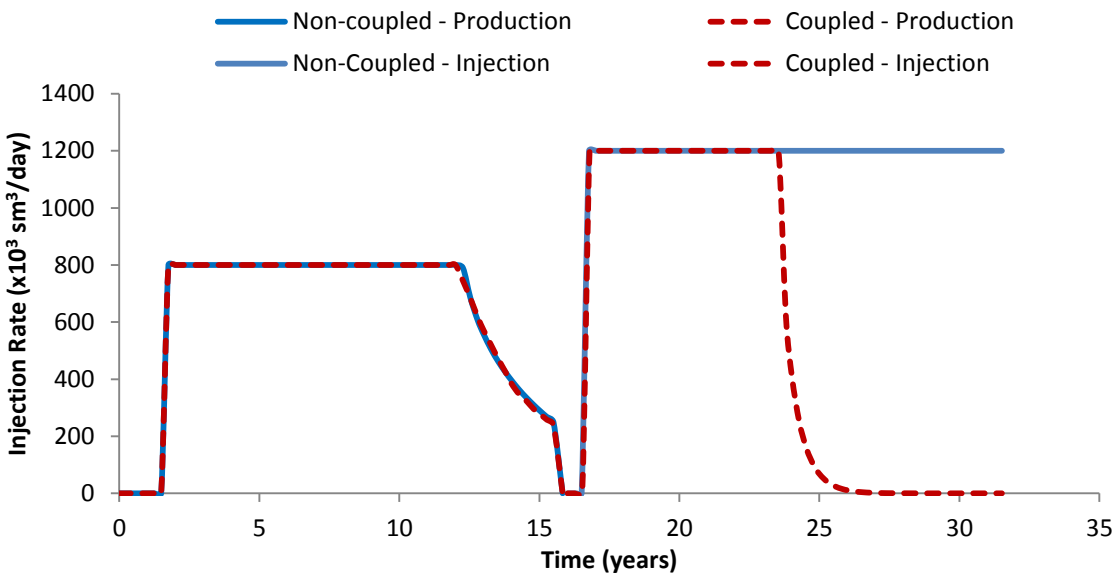

Figure 4.100 – Production and injection rate for the coupled model compared against the same model without coupling.

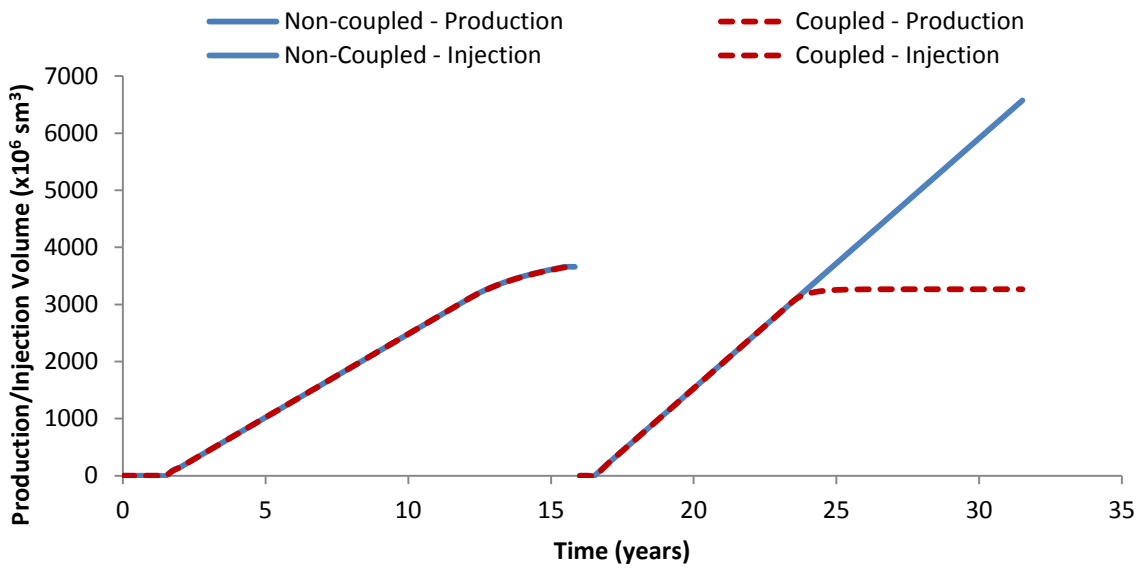

Figure 4.101 – Production and injection volumes for the coupled model compared against the same model without coupling.

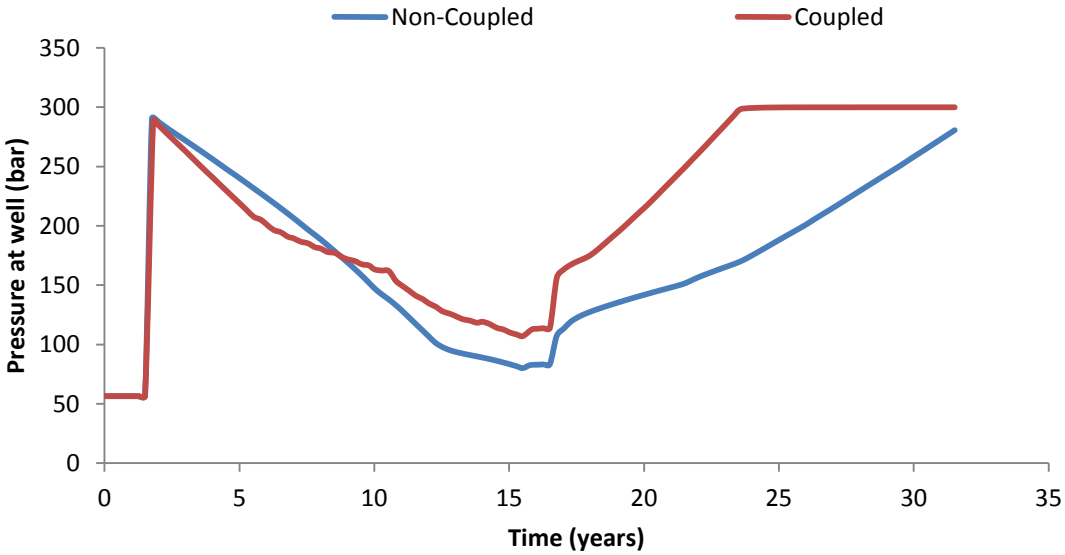

Figure 4.102 – Pressure at the well location for the coupled and non-coupled model during production and injection.

The coupled model updates the pore volume during the simulation to model compaction based on results from the geomechanical model during pressure depletion and injection. Figure 4.103 and Figure 4.104 show the porosity modification for the coupled model in each of the cells in the reservoir model. The porosity is updated by a porosity multiplier, the figures show the average initial porosity in the model multiplied by the porosity multiplier at the end of depletion, during which the majority of the porosity modification occurs. To match the non-coupled model to the coupled model it is therefore necessary to introduce the same pore volume reduction into the non-coupled model.

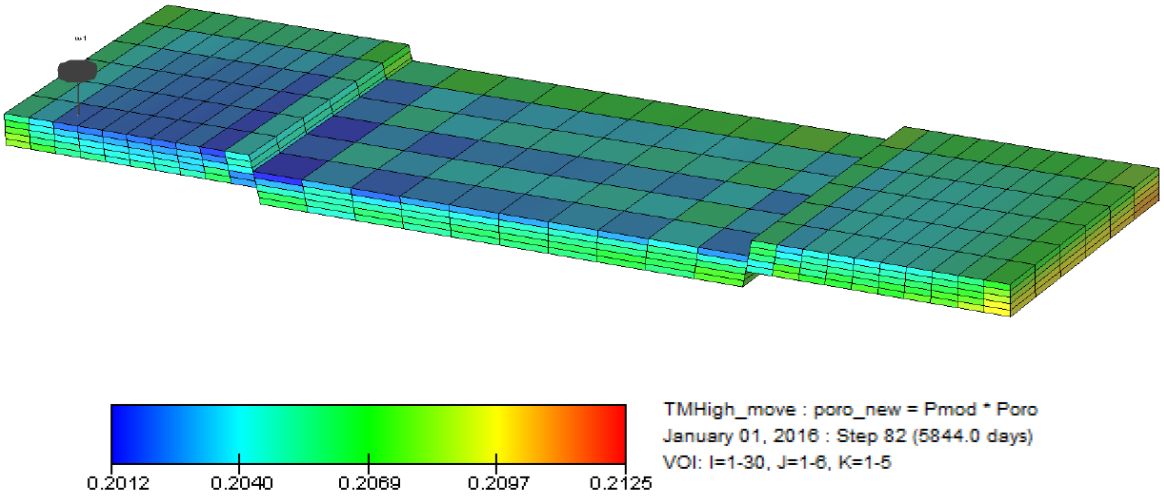

Figure 4.103 – Modified porosity in the coupled model at the end of depletion with non-sealing faults.

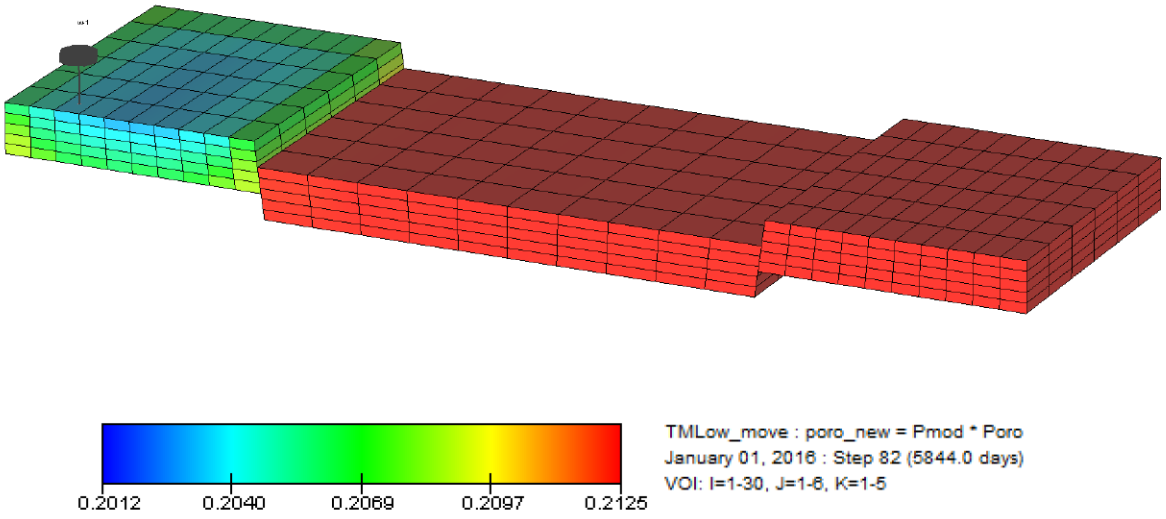

Figure 4.104 – Modified porosity in the coupled model at the end of depletion for the model with sealing faults.

To implement a pore volume change with compaction in the non-coupled model a pressure dependent pore volume modifier (KVSP) can be specified in Tempest. The modifier reduces the pore volume using a multiplier on the porosity in a cell when the pressure drops below a specified threshold. The data from the coupled simulations were used to derive the pore volume multiplier for the non-coupled model by determining the pore volume change with pressure. Figure 4.105 shows the porosity multipliers derived from the coupled model that were applied in the non-coupled model for the sealing and non-sealing case. The plot of the porosity multipliers with pressure shows the transition from elastic to plastic deformation. The elastic domain occurs above ~ 200 bar, and is characterised by a flatter gradient with minimal porosity reduction, the elastic porosity reduction follows the same trend for the non-sealing and sealing fault cases. For the plastic domain the porosity multiplier is significantly

different for the sealing and non-sealing cases, as shown by the different gradients on the graphs. The amount of porosity reduction is more significant in the plastic domain, and is more significant for the case with non-sealing faults and a larger compartment. The different compaction curves for the non-sealing and sealing cases suggests different compaction behaviour between the two models. The pressure dependent multipliers can be set to be reversible, irreversible or hysteretic with pressure, to model a range of porosity changes with pressure, for example a partial increase of pore volume with re-pressurisation. In this case, the irreversible option was applied as there was not significant porosity increase observed during injection.

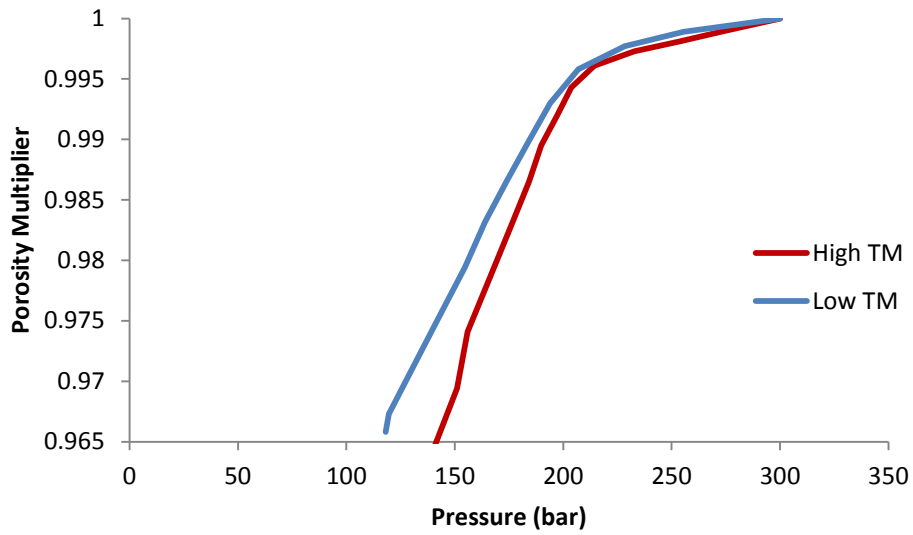

Figure 4.105 – Porosity multipliers for compaction in the non-coupled model derived from the coupled model results.

Figure 4.106 and Figure 4.107 compares rates and total volumes for depletion and injection for the non-coupled and coupled models with non-sealing faults, where compaction is included using porosity multipliers. The pressures at the well for the flow model including compaction are shown for the non-sealing and sealing case in Figure 4.108 and Figure 4.109. The figures show that a good match between the coupled and non-coupled model is achieved when compaction is considered, both injection and production rates, and volumes are matched well. The pressure in the models also matches well with only minor variations between the models. The compressibility in the non-coupled flow simulation had to be adjusted to 3.8 x 10^{-5} bar^{-1} to achieve the best match for injection volume and model pressure between the coupled and non-coupled models (compressibility is not used in the coupled model).

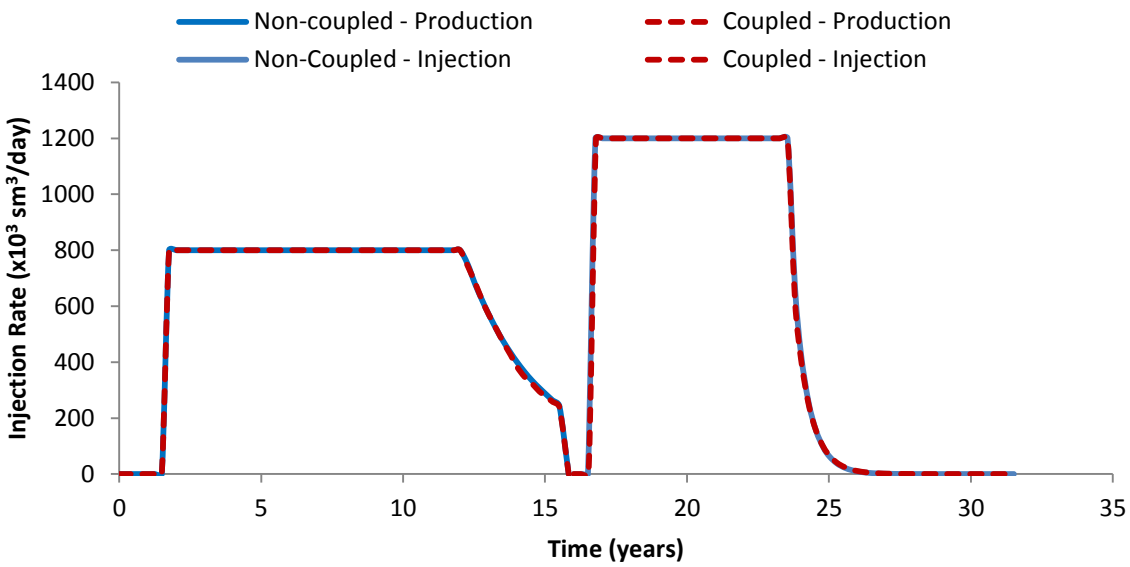

Figure 4.106 – Comparison of production and injection rates for the coupled and non-coupled model including pressure dependent pore volume multipliers to model compaction for the non-sealing low friction fault case.

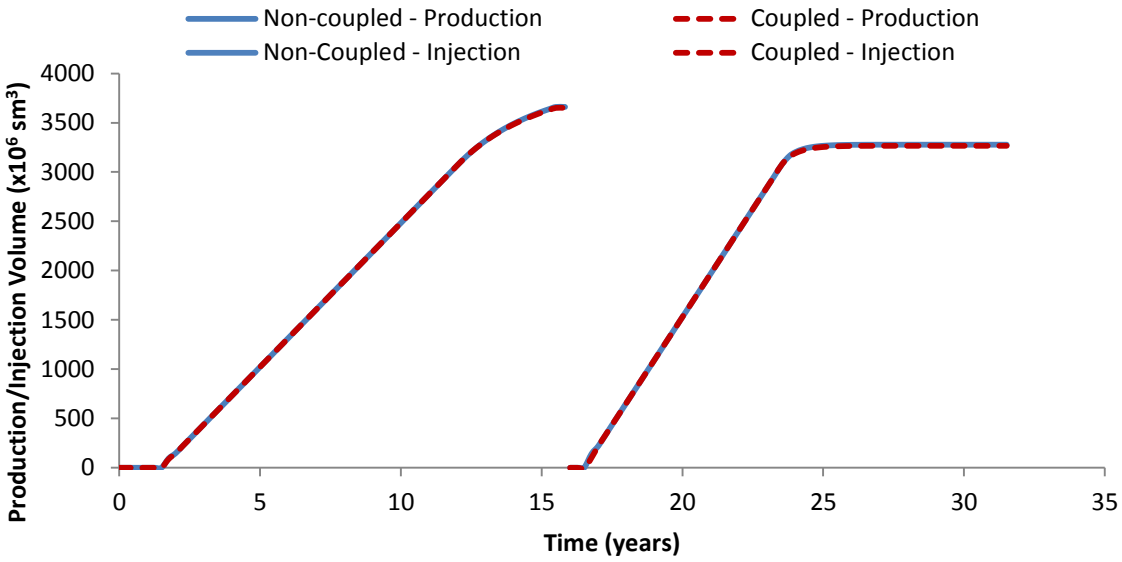

Figure 4.107 - Comparison of production and injection volumes for the coupled and non-coupled model including pressure dependent pore volume multipliers to model compaction for the non-sealing low friction fault case.

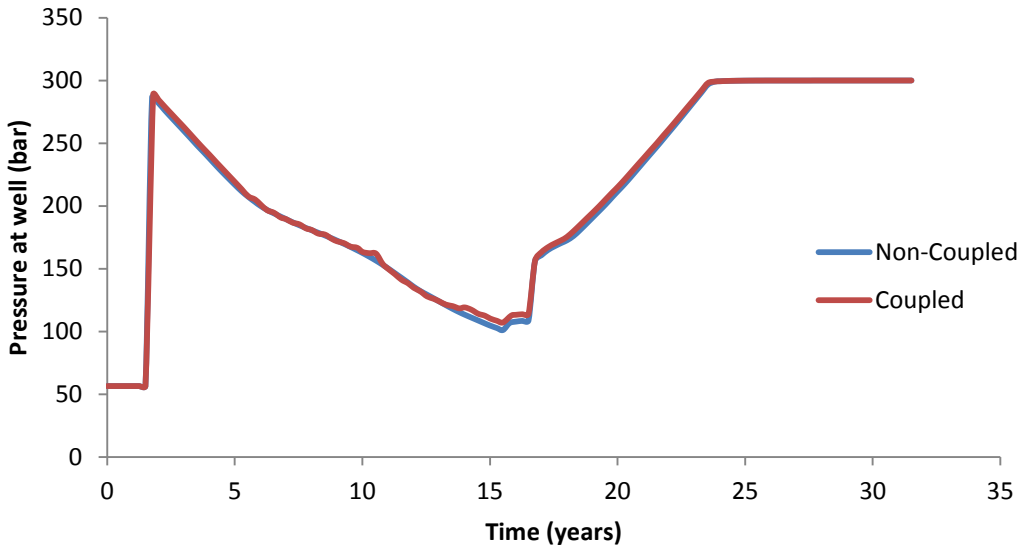

Figure 4.108 – Comparison of production and injection pressures for the coupled and non-coupled model including pressure dependent pore volume multipliers to model compaction for the non-sealing low friction fault case.

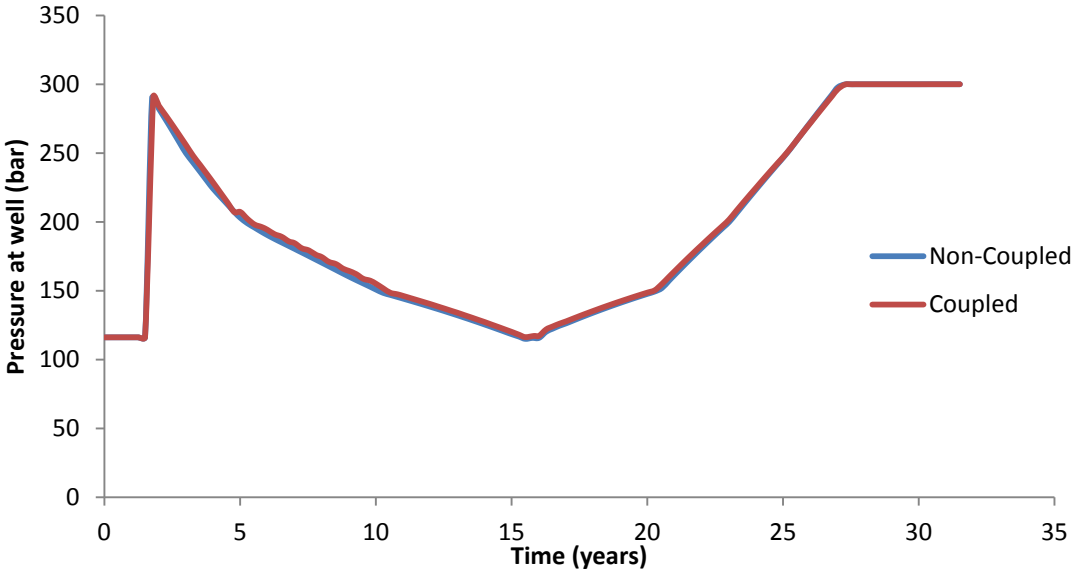

Figure 4.109 – Comparison of production and injection pressures for the coupled and non-coupled model including pressure dependent pore volume multipliers to model compaction for the sealing low friction fault case.

4.3.11 **Seismic Data**

Two different estimates of seismic properties were derived from the model, a simple Gassman's fluid substitution calculation to derive P-wave velocity from the data supplied by the flow model, and calculation of P-wave velocity for the overburden calculated using the stress sensitive seismic modelling workflow discussed in section 2.9.3.

4.3.11.1 *Gassman's Substitution – Reservoir Simulator*

The P-wave velocity was calculated from the reservoir simulator output (fluid saturations and porosity) using the Gassman's substitution relationship presented in section 2.7.1. The bulk moduli for pure quartz and CO_2, and a typical modulus for sandstone were used in the

calculation, the Voigt bound was used for patchy mixing of fluids. Figure 4.110 and Figure 4.111 show the P-wave velocity at the end of injection for a section through the middle of the model for the non-sealing and sealing case respectively. The figures compare the calculated P-wave velocity for a non-coupled model with no consideration of compaction against the coupled model. Both figures reflect the impact of the injected CO_2 plume in the left hand injection compartment of the model. The figures show that the non-coupled model underestimates the P-wave velocity throughout the parts of the model affected by changes in fluid composition, generally the upper portion of the model. Particular differences are observed in the injection compartment, at the base of the well, at the faults and the top layer of the central compartment (in the sealed case). The difference in predicted P-wave velocities are as much as 200 m/s in some areas. The changes are due to the larger volume of CO_2 injected in the non-coupled model, and the lack of consideration of the change in porosity.

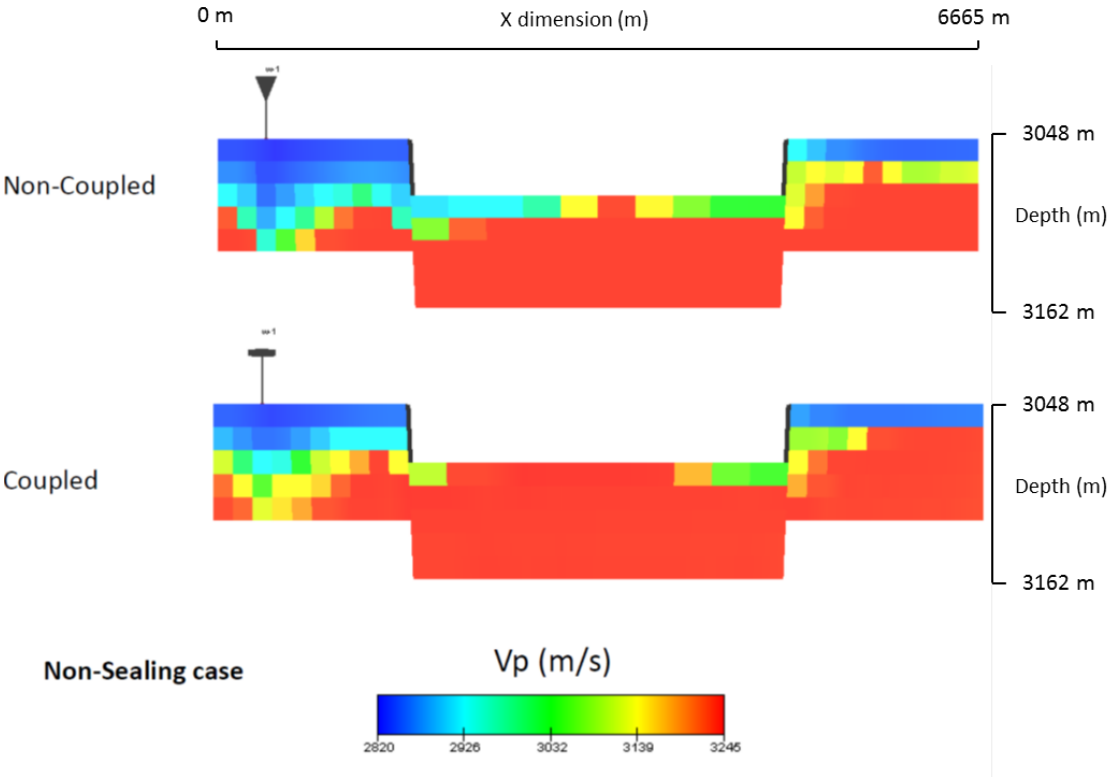

Figure 4.110 – Comparison of Gassman's P-wave velocities for the non-sealing low friction base case model at the end of injection.

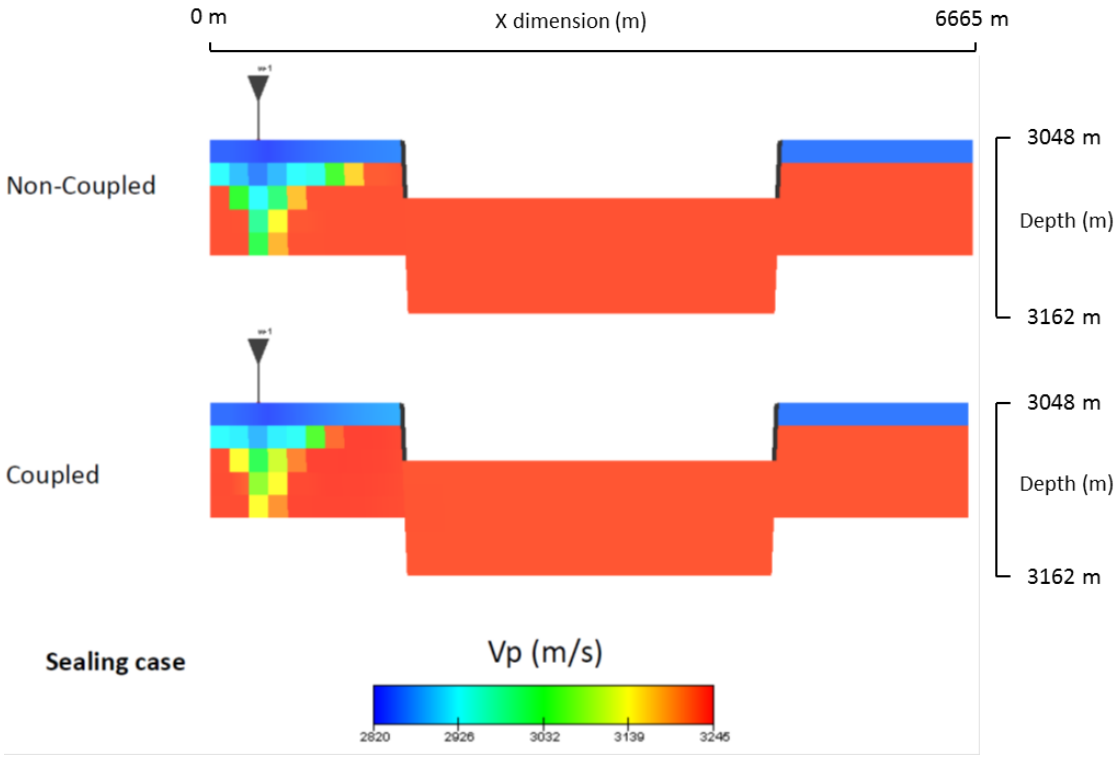

Figure 4.111 – Comparison of Gassman's P-wave velocities for the sealing low friction base case model at the end of injection.

When the pore volume multiplier is implemented to account for compaction the match between the non-coupled and coupled P-wave velocities are improved. Figure 4.112 shows the same figure as above but with the compaction pore volume multiplier implemented in the non-sealing non-coupled model. The figures show that the calculation of the P-wave velocity between the two models is almost identical particularly at the well, with the only minor differences observed in the compartment furthest from the well.

Figure 4.113 shows the difference in P-wave velocity for the coupled model with and without the porosity multiplier included in the calculation of P-wave velocity. The figure shows that the porosity term has a smaller impact, a maximum of 12.8 m/s, on the calculation of P-wave velocity than the change in fluid volume modelled when using the compaction pore volume multiplier. The change in fluid volumes in the model resulting from changing pore volume is therefore more important than the change in porosity itself when calculating the P-wave velocity in this case. The pore volume multiplier does not change in the non-coupled model during injection as there is no option for hysteresis, so the change in velocity with change in porosity multiplier would show no difference.

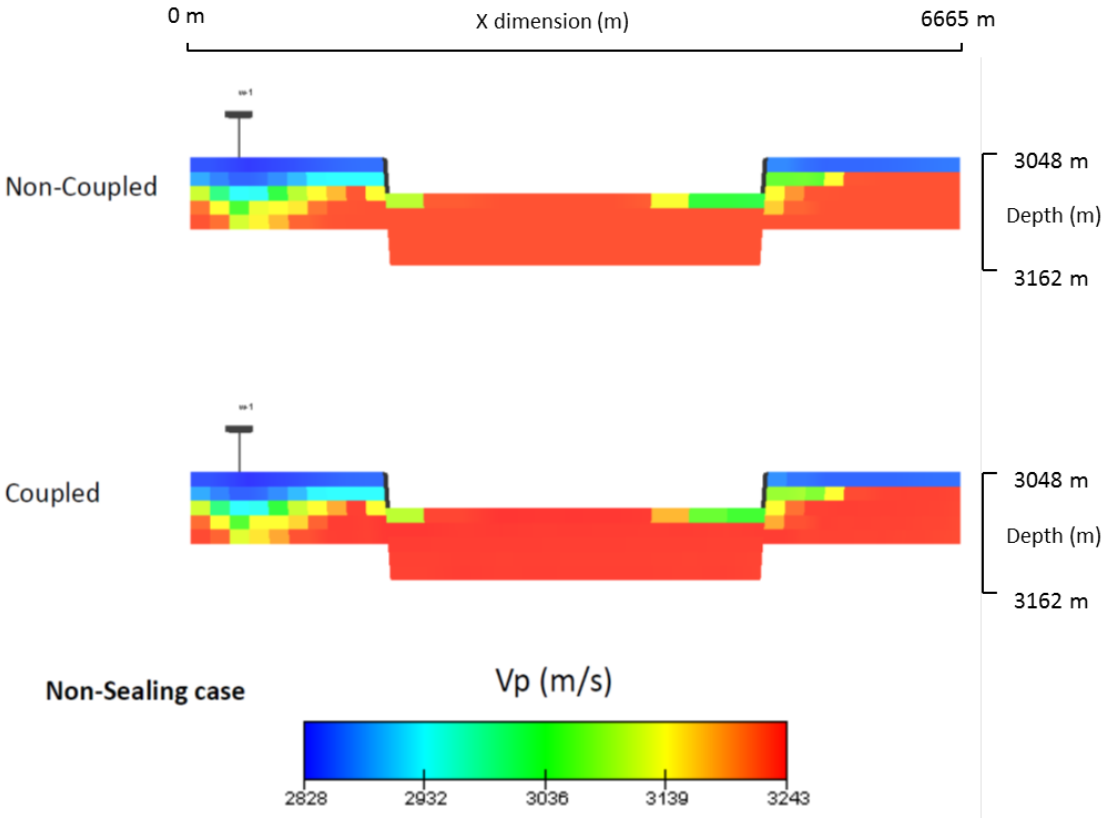

Figure 4.112 – Comparison of Gassman's P-wave velocities for the non-sealing low friction base case model at the end of injection.

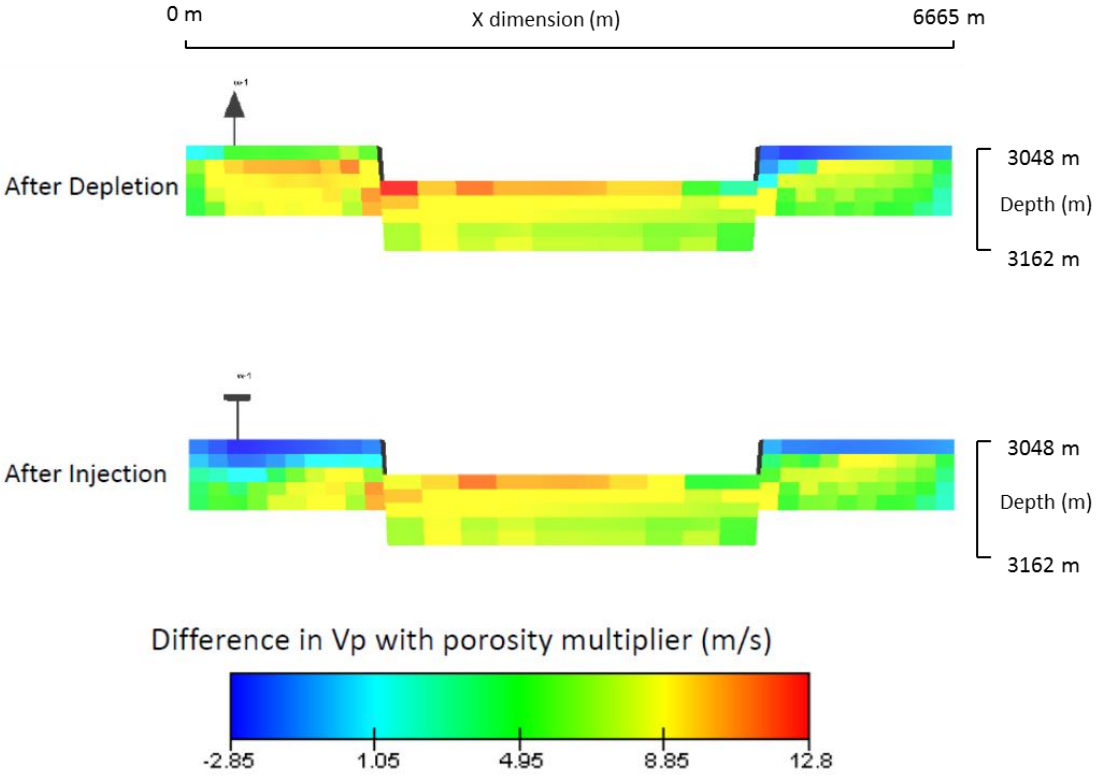

Figure 4.113 – Difference in P-wave velocity during depletion and injection in the coupled model when the porosity multiplier is included in the P-wave calculation.

4.3.11.2 *Overburden Seismic Data - High Stiffness Case*

The P-wave velocity for the overburden was calculated using the seismic output from the coupled model. Figure 4.114 shows a contour plot of the change in P-wave velocity from during the depletion stage for the high stiffness low friction non-sealing base case model. The model shows that the most significant changes occur around the reservoir. The P-wave velocity is not calculated in the reservoir as the seismic model was calibrated for modelling seismic data in plastically deforming materials. The plot shows a decrease in velocity above and below the reservoir of a maximum of 500 – 600 m/s and an increase at the sides of the reservoir of approximately 100 m/s. Velocity decrease is lower above and below the faults, and is highest at the outer corners of the reservoir. Figure 4.115 shows the plot of change in P-wave velocity for the injection stage. The plot shows a similar pattern to the depletion stage, but with a lower magnitude of change in P-wave velocity.

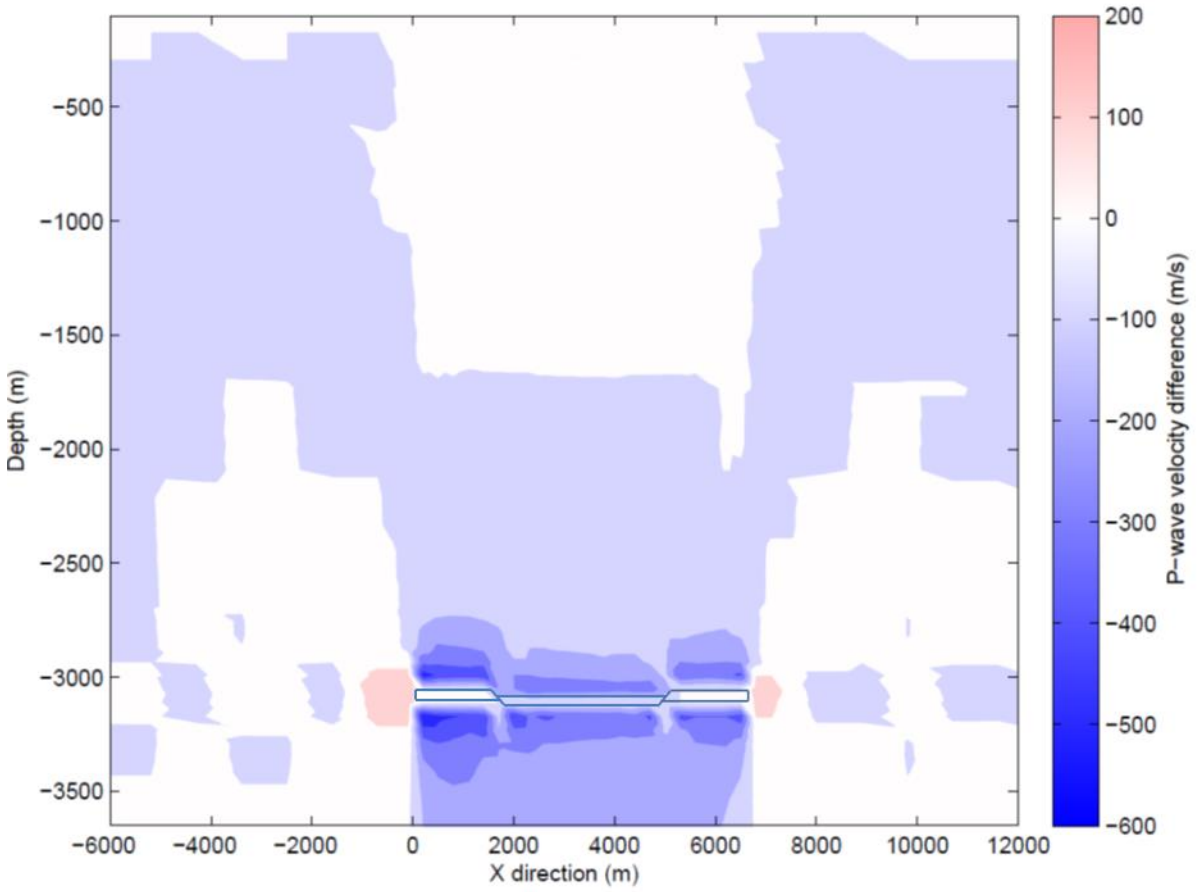

Figure 4.114 – Plot of difference in P-wave velocity in the overburden for the depletion stage in the high stiffness non-sealing low friction base case model. The approximate position of the reservoir is indicated by the blue line.

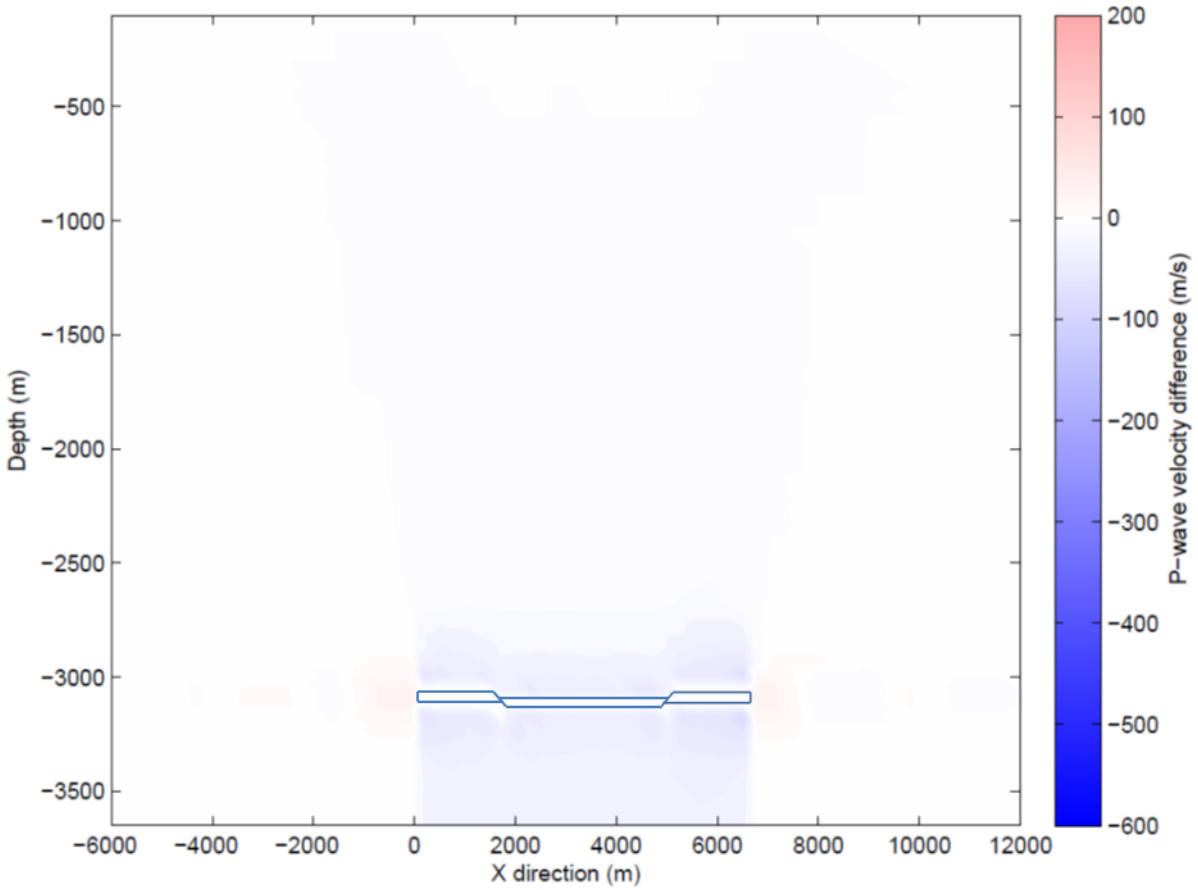

Figure 4.115 - Plot of difference in P-wave velocity in the overburden for the injection stage in the high stiffness non-sealing low friction fault base case model. The approximate position of the reservoir is indicated by the blue line.

Figure 4.116 and Figure 4.117 are plots of the difference in P-wave velocity in the overburden for the sealing high stiffness base case with low friction faults. The plots for the sealing case shows a similar pattern to the non-sealing case except that changes in velocity are restricted to the region around the injection compartment, as would be expected in the compartmentalised model. The depletion stage again shows significant reduction above and below the reservoir, with the largest decrease at the outer corners of the reservoir. There is also an increase in velocity at the sides of the injection compartment, with the largest increase on the fault side of the injection compartment. As in the non-sealing case there is a similar pattern of velocity change during injection compared to the depletion stage, again with a lower magnitude of change during injection.

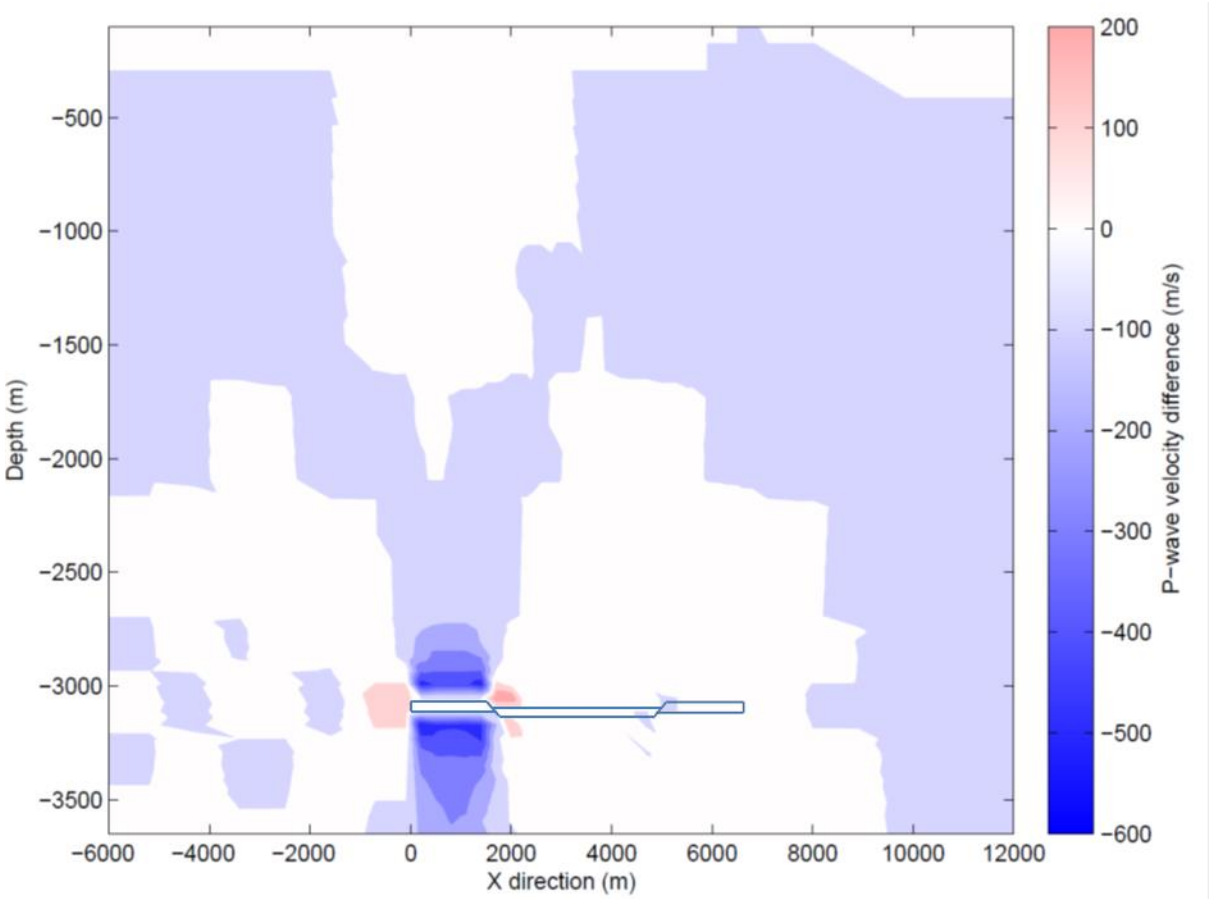

Figure 4.116 – Plot of difference in P-wave velocity in the overburden for the depletion stage in the high stiffness sealing low friction fault base case model. The approximate position of the reservoir is indicated by the blue line.

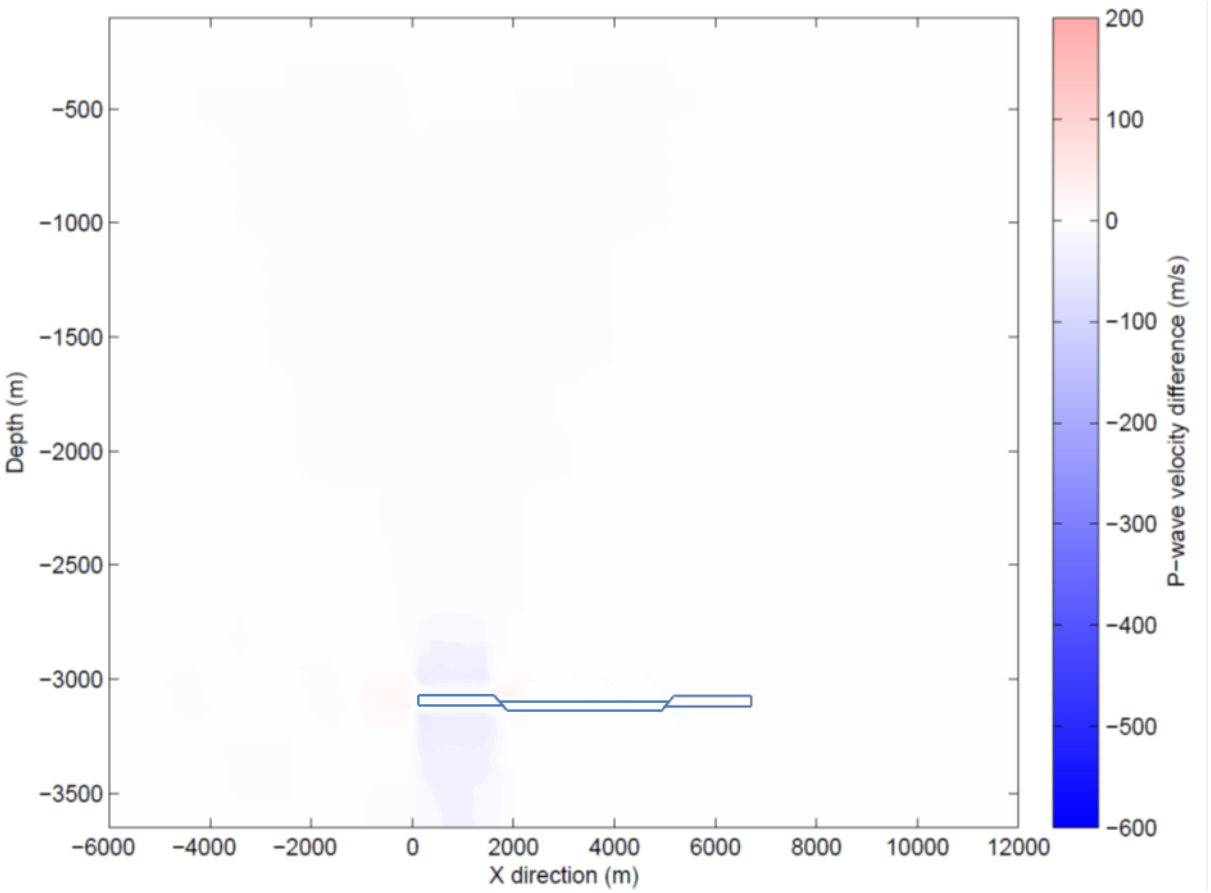

Figure 4.117 – Plot of difference in P-wave velocity in the overburden for the injection stage in the high stiffness sealing low friction fault base case model. The approximate position of the reservoir is indicated by the blue line.

4.3.11.3 *Overburden Seismic Data - Low Stiffness Case*

Figure 4.118 shows a plot of the change P-wave velocity during depletion for the low reservoir stiffness non-sealing low friction fault base case model. The plot shows a very similar reduction in P-wave velocity above and below the reservoir to the high stiffness case. The main difference in velocity reduction is a lower reduction in velocity at the corners of the compartment furthest from the well in the low stiffness case. The increase in P-wave velocity at the sides of the reservoir is also very similar to the high stiffness case. The most significant difference in the low stiffness case is the change in P-wave velocity during injection, this is illustrated in Figure 4.119 and Figure 4.120. The change in P-wave velocity during injection is of a smaller magnitude and shows an increase above and below the injection compartment rather than a decrease, there is also a small increase at the sides of the reservoir and at the faults. The change is small and so the scale is adjusted to highlight this effect in Figure 4.120. The change in P-wave velocity during injection in the low reservoir stiffness model is generally in the opposite sense to the high stiffness model and is smaller in magnitude.

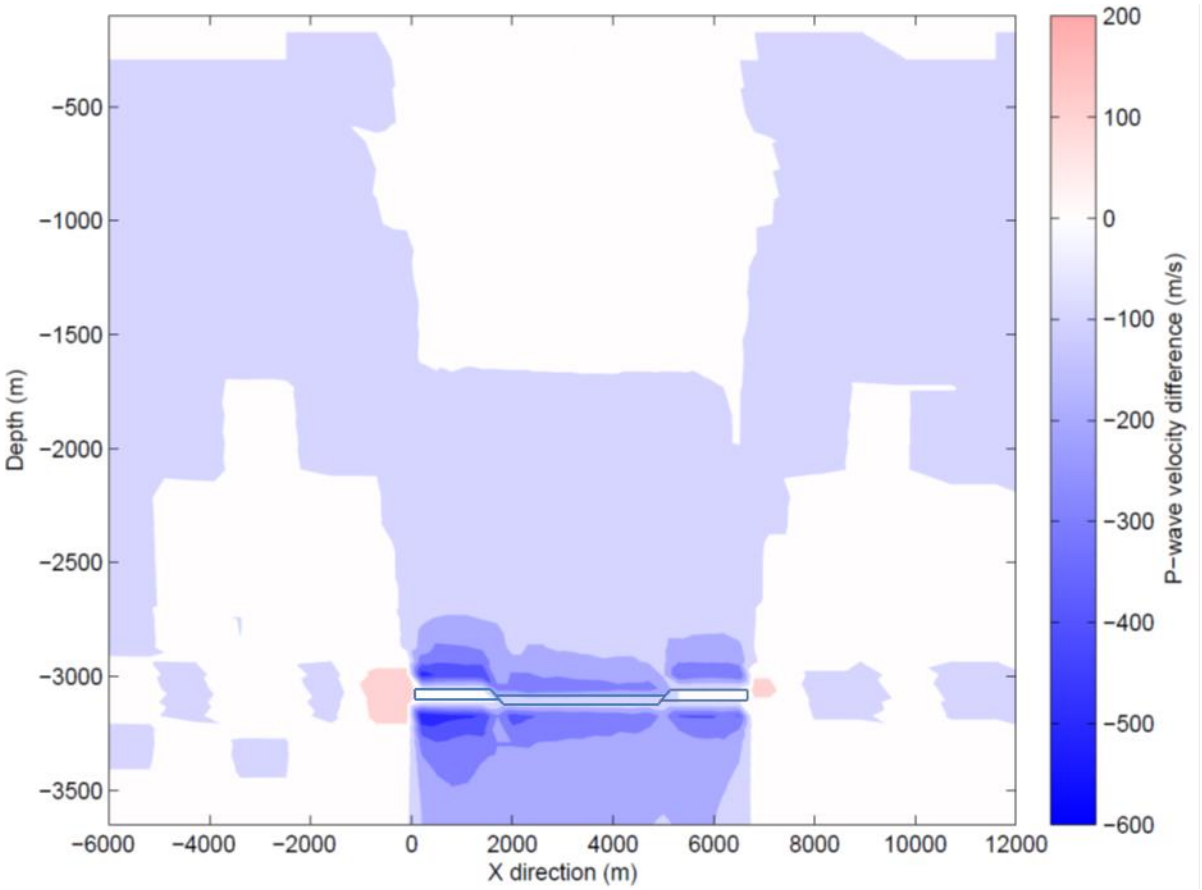

Figure 4.118 – Plot of difference in P-wave velocity in the overburden for the depletion stage in the low stiffness non-sealing low friction fault base case model. The approximate position of the reservoir is indicated by the blue line.

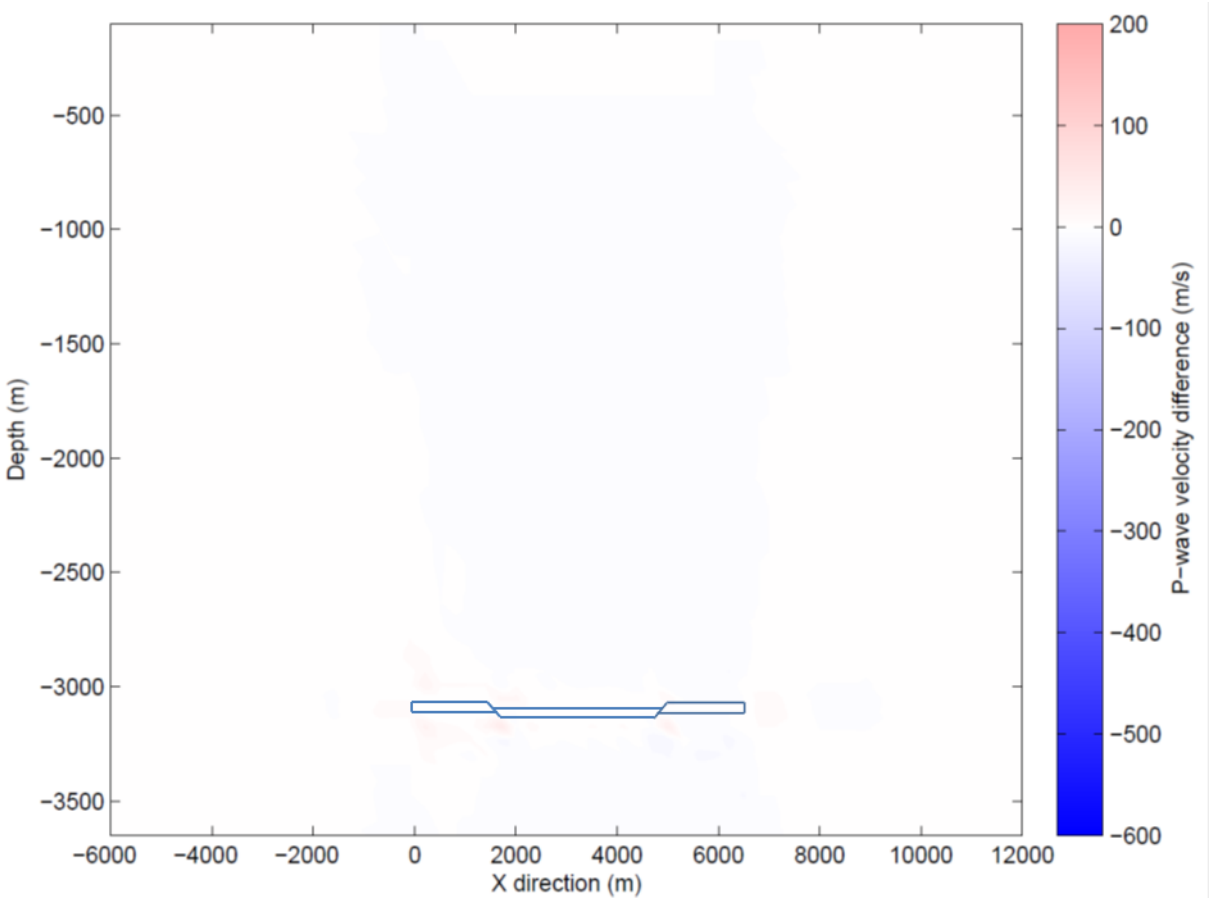

Figure 4.119 – Plot of difference in P-wave velocity in the overburden for the injection stage in the low stiffness non-sealing low friction fault base case model. The approximate position of the reservoir is indicated by the blue line.

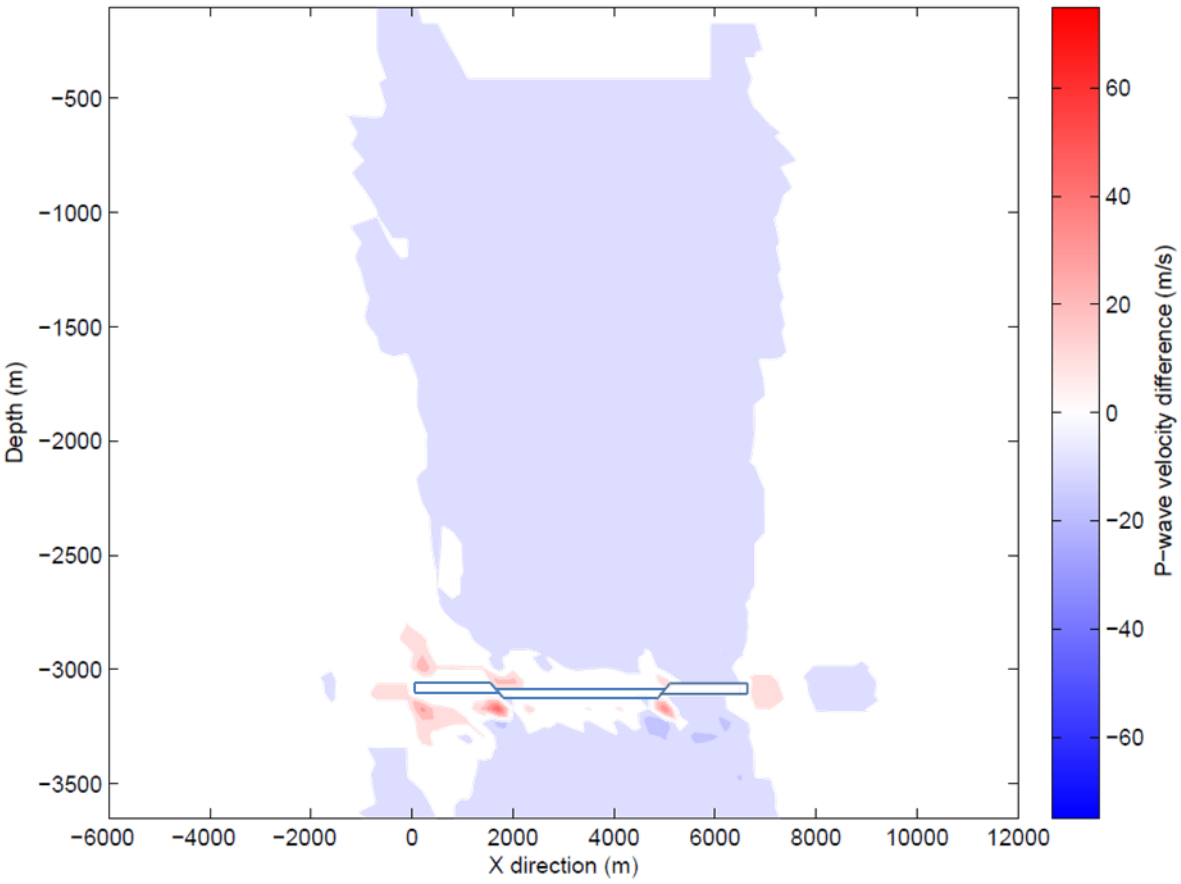

Figure 4.120 - Plot of difference in P-wave velocity in the overburden for the injection stage in the low stiffness non-sealing low friction fault base case model. The plot scale has been range is reduced to highlight the positive P-wave change around the reservoir. The approximate position of the reservoir is indicated by the blue line.

4.4 Discussion

The results from a series of coupled geomechanical fluid-flow models have been presented in Section 4.3. Material properties and constitutive model parameters have been varied in the models to examine the impact of the stress distribution in the overburden and stress path in the reservoir in order to determine the effect on CO_2 storage in depleted hydrocarbon reservoir. The results are discussed below in terms of the stress changes observed in the model, the potential for stress path hysteresis, fault behaviour in the model, the performance of the fluid flow model and seismic data derived from the fluid flow and geomechanical model.

4.4.1 Stress Arching and Stress Changes in the Model

The fluid flow scenario was the same for each of the models and involved a depletion, shut-in and depressurisation injection stage. The response of each of the models in terms of the overall pattern of stress change was generally similar. The stress changes are discussed for the overburden, and for each distinct section of the stress path for the reservoir. The changes in the overall stress path are also discussed in the final section. This discussion section aims to describe and explain the behaviour of the stress path in a depletion and CO_2

injection cycle in a hydrocarbon reservoir. This is used as a basis to discuss the implications for CO_2 storage, and particularly fracture pressure hysteresis, in the following section 4.4.2.

4.4.1.1 *Overburden*

The overburden, sideburden and underburden have a significant impact on the stress state in the reservoir. In all of the models, depletion in the reservoir causes stress arching to occur in the bounding shale. The stress arching increases the vertical stress in the shale at the edge of the reservoir and reduces vertical stress above and below the reservoir. The stress arching is similar to that observed in other elastic studies of depletion stress paths (Khan et al. 2000, Segura et al. 2011), the main difference being that plastic deformation is also occurring in this case. There is subsidence above the reservoir associated with the stress arching and uplift below the reservoir accompanying reservoir depletion compaction. The vertical movement in the overburden above and below the reservoir allows the sideburden to move inwards above and below the reservoir. At the edge of the reservoir, lateral movement of the sideburden is resisted by the reservoir and this causes stress concentration effects at the flat faces of the edge of the reservoir. The reduction in vertical stress above the reservoir means that vertical effective stress increases in the reservoir is reduced during depletion compared to a situation without stress arching. Stress arching leads to a decrease in total stress in the reservoir during depletion. The depletion stress arching parameter (γ_v) for a cell in the centre of the injection compartment is very similar for most of the cases and varies between 0.22 and 0.25. The stress arching parameter shows that stress arching is not maximised (in this case $\gamma_{v\,max} = 1.0$) in the model and is only at a moderate level. The notable exception is for the case where the stiffness is reduced in the overburden. Lower stiffness in the overburden reduces stress arching reduces and in this case $\gamma_v = 0.14$ for a cell in centre of the injection compartment. The vertical effective stress change in the reservoir during depletion is similar in all of the models regardless of the change in parameters of the reservoir material, suggesting that it is mainly controlled by the behaviour of the overburden during depletion. This finding is apparently contrary to that of Segura et al. (2011) who show that stress arching is only significant when the overburden is stiffer than the reservoir. This can be explained by the fact that Segura et al. (2011) only discuss the parameter for elastic depletion, and these results show that plastic depletion can produce a similar stress arching effect regardless of the relative stiffnesses of the reservoir and overburden. The reservoir effectively becomes less stiff with plastic depletion, and this is then analogous to the relationship found by Segura et al. (2011). The overburden did not deform plastically in any of the simulation runs, presumably plastic deformation in the overburden, particularly at the sides of the reservoir, would have further implications for stress arching behaviour.

Horizontal stresses during depletion also appear to display behaviour analogous to the stress arching observed in the vertical stresses. Total horizontal stress increases in the shale at the edge of the reservoir and decreases above and below the reservoir; there is a stress concentration at the interface of the edge of the reservoir and the sideburden, and an

associated reduction in total horizontal stress above and below the reservoir. The total horizontal stress change in the overburden is related to the total vertical stress change in the overburden. Horizontal stress increases at the side of the reservoir as vertical stress increases, due to confining stress development and the lateral movement of the sideburden against the reservoir. Similarly, the reduction of total horizontal stress with total vertical stress above and below the reservoir occurs due to the reduction in confining stress from vertical loading.

The pattern of horizontal stress change in the reservoir and the horizontal stress path parameter for a cell in the centre of the injection compartment are of a similar pattern and magnitude to the vertical stress change and stress path parameter for most cases. The horizontal stress path parameters for runs with an initial stress ratio of K = 0.7 are very similar and vary between γ_h = 0.31 and γ_h = 0.36. The horizontal stress path parameter shows that effective horizontal stress increase in the reservoir is also reduced and does not increase at the same rate as pore pressure decrease. The level of horizontal effective stress increase suggests that the full confining stress is not generated in the reservoir in line with pore pressure decrease. This behaviour is the same pore-pressure/stress coupling observed by Hillis (2001), where effective horizontal stress increase in the reservoir is inhibited during depletion. In other words total horizontal stress in the reservoir decreases during depletion. This pore-pressure/stress coupling leads to Mohr circle expansion if $\gamma_h > \gamma_v$.

The models where the horizontal stress path parameter varies from ~0.35 are the cases with different initial stress ratios (1.0 and 0.5), where γ_h = 0.80 and γ_h = 0.01, and the case with a less stiff overburden, where γ_h = 0.27. Comparison of the less stiff overburden case to the base case shows that there is a reduction in the pore-pressure/stress coupling effect during depletion with a reduction in overburden stiffness, leading to higher effective horizontal stress in the reservoir with a soft overburden. The total horizontal stress increase in the overburden at the side of reservoir is however lower with a softer overburden. This suggests that a stiffer overburden reduces the horizontal confining stress that is generated in the reservoir and increases the horizontal confining stress generated in the sideburden compared to a less stiff overburden. The mechanism that leads to this reduction in effective horizontal stress increase in the reservoir is related to the stress arching. Increased stress arching leads to increased loading and vertical stress in the sideburden at the edges of the reservoir and lower loading and vertical effective stress increase in the reservoir. This results in lower effective horizontal stress increase in the centre of the reservoir, and a total horizontal stress increase in the sideburden. Additionally, the plastic response of the material in the reservoir influences horizontal stress changes at the reservoir/sideburden interface and within the reservoir with lateral displacements of the sideburden, and this aspect is discussed further in the following subsections where relevant to the reservoir stress path.

The analysis of the horizontal stress change becomes more complex when the initial stress ratio cases are taken into account. A large change in total horizontal stress is observed in the sideburden in the low initial stress ratio (0.5) case, leading to a low γ_h, whereas minimal change in total horizontal stress is observed in the high initial stress ratio (1.0) case, leading to a high value for γ_h. The stress evolution in the overburden with changing initial stress ratio also appears to be related to the plastic deformation behaviour of the reservoir, and this aspect of horizontal effective stress change is discussed along with more detailed observations of stress changes in the reservoir in the following sections. The controls on horizontal stress increase in the reservoir are the level of stress arching, the stiffness of the overburden (which controls stress arching) and the interaction of the overburden and reservoir edges with plastic deformation.

The stress arching in the overburden is an important control on the stress path hysteresis, which in turn affects the fracture pressures in the reservoir, and so consideration of stress arching is important for assessing the change in fracture pressure in a CO_2 storage reservoir. This aspect is discussed further in the sections examining the controls on reservoir stress path.

Stress changes in the overburden during injection are much smaller than during depletion and are discussed along with the reservoir in later sections.

4.4.1.2 *Elastic Depletion*

In the reservoir, the general slope and trajectory of the p'-q stress paths observed in the depletion results are consistent with other depletion results in the literature using similar critical state based models (e.g. Yale (2002) and Pouya et al. (1998)). The elastic portion of the stress path shows an increase in q with increasing p', which represents the horizontal and vertical stress changing at a different rate. The initial elastic stress path is controlled by the Poisson's ratio of the material, the confining conditions of the over, under and side burden, the slope of the unloading-reloading line in the constitutive model, which controls the specific volume with mean stress, and the initial stress conditions (Yale 2002). The slope of the elastic depletion is similar for all cases analysed where the Poisson's ratio in the reservoir is the same, Yale (2002) shows that the slope of the elastic depletion stage can be affected by stiffness changes in the overburden. The results of the low stiffness overburden case in this thesis show that reduction in stiffness in the overburden flattens the slope of the elastic depletion stage compared to the base case. The flattening results from increased horizontal and vertical stress in the reservoir in the reservoir. This is due to a greater increase in vertical stress due to reduced stress arching, which increases the horizontal confining stress. The increased stresses lead to an increase in p stress for the same q stress. The slope of the elastic stress path can also be altered by changing the Poisson's ratio of the reservoir material. The cases analysed show a flattening of the stress path with increasing Poisson's ratio. A higher Poisson's ratio means there is greater tangential strain with axial strain in a material. The flattening is due to the increase in

horizontal stress resulting from confinement of greater horizontal strains caused by a high Poisson's ratio. Increasing Poisson's ratio also leads to a reduction in the q stress and increase in p' stress in the initial stress point on the p'-q path due to the same increase in horizontal stress during geostatic initialisation. The only parameter that increases the slope of the p'-q elastic stress path is the stiffness of the reservoir. The 3.8 GPa stiffness reservoir generates a slight increase in the p'-q elastic slope, and this is related to a lower build-up of confining stress in the softer reservoir with vertical loading.

4.4.1.3 *Transition and Plastic Depletion*

An interesting feature in all of the stress paths is the transition stage at the intersection of the stress path with the yield envelope and the onset of plastic failure in the model. Significant change in the q stress is observed (either an increase or decrease) amongst all of the cases and represents convergence to a similar plastic deformation p'-q trajectory at a constant gradient, regardless of the initial stress or material properties. This converged trajectory is shown most clearly in Figure 4.55, with comparison of cases with different initial stress ratios. The flatter plastic trajectory represents the hardening (or softening) of the material according to the plastic parameters, as observed in typical stress strain plots of elastic-plastic deformation. The only variability in this converged trajectory is the length of the plastic portion of the stress path after convergence and final p'-q stress at the end of depletion, and the level of q stress at which the trajectory occurs. For example, the plastic stress path for the less stiff shale in Figure 4.71 ends at a higher p'-q stress at the end of depletion than the stiffer shale but follows the same path, and the plastic stress paths for the edge of the reservoir have lower q stresses during plastic depletion, but the gradient remains constant. The case with the lower reservoir stiffness also has the same gradient, but the q stress is higher, this is due to lower horizontal stress build-up in the softer reservoir, which has less confinement. This convergence has been observed in other numerical analyses (e.g. Yale 2002), and combined numerical and oedometric experimental studies (e.g. Pouya et al. 1998). The same ratio of vertical to horizontal stresses is observed when the stress paths converge, and Pouya et al. (1998) term the slope of σ_h/σ_v as h, which forms a line through the origin. Based on the plastic parameters used in this model h = 0.7 - 0.72 during plastic depletion. The convergence of the p'-q stress paths during plastic deformation means that significant stress changes are observed in the horizontal stresses for different initial stress ratios. Vertical stresses are controlled by the weight of the overburden, stress arching and pressure drop, and are consistent where these factors remain constant. In the K = 0.9 initial stress ratio case the convergence causes the horizontal stress to drop once yield occurs. The onset of plastic deformation occurs the earliest out of all cases as the elastic stress path reaches the yield envelope sooner, this is due to the shape of the yield surface and starting initial stress. In the K = 0.5 case the horizontal stress increases significantly with the onset of plastic deformation, which occurs later than the other cases, again due to the shape of the yield surface and the initial starting stress. The convergence of the p' stress, horizontal stresses and vertical stresses for the two initial stress ratio cases are re-plotted with time in Figure 4.121. The graph shows that

plastic deformation starts approximately 1 year earlier in the high initial stress ratio case. The graph also shows that the q stress will also converge based on the behaviour of the stresses, as observed in the stress paths. Convergence to the plastic trajectory takes approximately 1 year in the model.

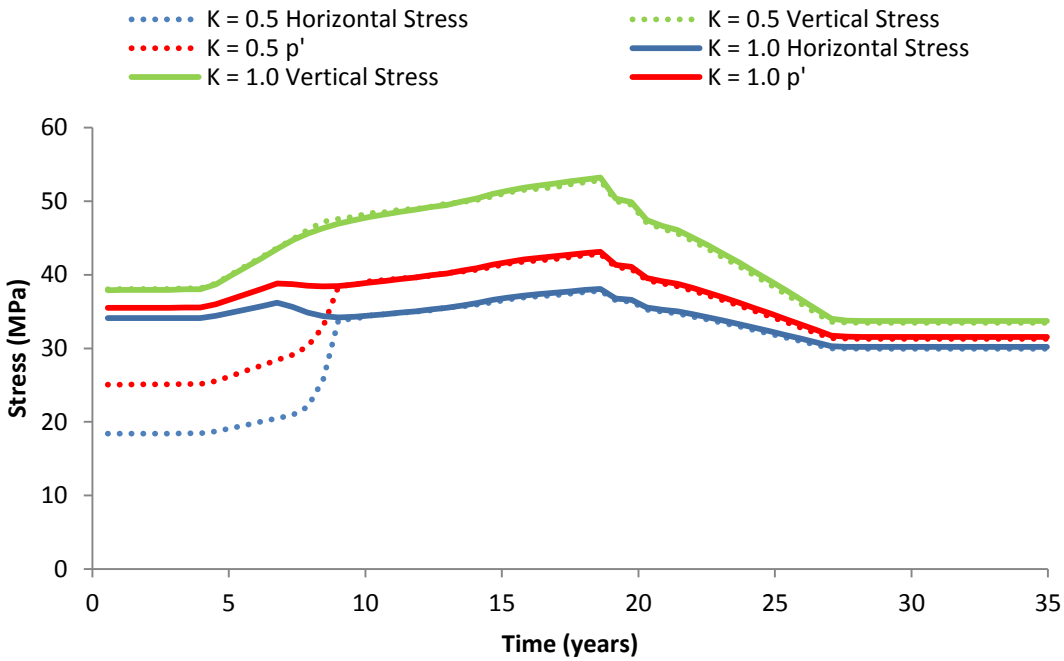

Figure 4.121 - Effective horizontal and vertical stress for the centre of the reservoir with time for each of the initial stress ratio cases.

The transition and plastic deformation behaviour with initial stress ratio is interesting as it can lead to a radically different stress path depending upon the initial stress condition. This is illustrated by comparison of the Mohr circle plots for the base case with K = 0.9 in Figure 4.44 and K = 0.5 in Figure 4.51. This plot shows much lower horizontal stress at the end of injection compared to the initial stress for K = 0.9 whereas horizontal stress is higher at the end of injection for K = 0.5. As mentioned previously, a significant difference in the horizontal stress changes is observed in the overburden in relation to different initial stress ratios, and the plastic behaviour in the reservoir is linked to the stress changes in the overburden. In the high initial stress ratio case significant plastic strain is observed in the margin of the reservoir, this is associated with a lower increase in stress in the overburden at the edge of the reservoir. In the low initial stress ratio case, less plastic deformation is observed at the edge of the reservoir and the stress increase in the overburden at the edge of the reservoir is higher. This stress change in the overburden is associated with the observed stress change in the reservoir, more plastic failure occurs in the high stress ratio case to accommodate the stress change according to the plastic stress gradient. Less plastic deformation occurs in the low stress ratio case to allow stresses to increase and converge on the plastic stress gradient. The stress change in the overburden appears to be related to the level of plastic deformation in the reservoir, with less plastic deformation leading to greater confinement and larger horizontal stress increase. The plastic

deformation in the margin of the reservoir is also linked to a significant difference in the plastic stress path compared to the centre of the reservoir. At the edge of the reservoir the plastic stress path follows a trajectory with lower p' and q stress. This is due to the fact that both the horizontal and vertical stress are lower at the edge of the reservoir during depletion, and the difference between the horizontal and vertical stress (q stress) is less. The vertical stress is reduced due to an increase in the stress arching effect at the edge of the reservoir, and the reduction in vertical stress and increased plastic strain at the margin reduces the level of horizontal stress. The stiffness in the overburden and the reservoir also affect the plastic section of the stress path. With a less stiff overburden the p'-q end point is increased. This is related to reduced stress arching in the reservoir which increases the peak p stress and corresponding q stress leading to a longer plastic stress path. The impact of the softer overburden on the p'-q stress path is less marked than the effect of the change in stress arching at the side of the reservoir, and so the soft overburden stress path is more similar to the base case stress path. With a less stiff reservoir there is less resistance to deformation in the reservoir, more deformation and larger plastic strains are observed, both horizontally and vertically. Whilst vertical stress is similar, horizontal stress is reduced due to a reduced confining effect from greater deformation, this means that q stress is higher, and the p'-q trajectory is different during depletion. Effectively, during plastic deformation the evolution of stress and strains are controlled by the amount of vertical stress arching and the plastic response of the model, and this explains the differences seen in the stress paths.

4.4.1.4 *Elastic Injection*

Once depletion stops the initial pressure rebound and subsequent injection into the reservoir results in decreasing effective stresses. The stress path is then entirely within the yield envelope, meaning that only elastic deformation is occurring. The injection stress path is the most important part of the stress path for CO_2 injection, but the implications for CO_2 storage are also dependent on the previous depletion evolution of the stress path in relation to the elastic injection stress path. The elastic deformation during injection generally occurs along a similar stress path to depletion in terms of the slope. However, as discussed, the transition to the plastic deformation stage offsets the stress path to some extent depending upon the initial stress ratio, meaning the initial and final stress states will vary. As all stress paths depleted plastically to a similar point, the resulting elastic stress paths during injection are also very similar. All of the injection stress paths show a decrease in q stress and a reduction in the size of the Mohr circle from the end of depletion to maximum injection. In all of the injection stress paths the vertical effective stress also decreases below the initial value prior to depletion.

The level of effective horizontal stress at the end of injection compared to initial stress is dependent upon the initial stress ratio, but it is higher than the initial value for K = 0.5 and K = 0.7 and lower than the initial value for K = 0.9. For the same position in the geometry, the same Poisson's ratio in the reservoir and the same overburden and reservoir stiffness the final vertical and horizontal stresses are the same between cases. This is illustrated by the

convergence of the injection stress paths for different initial stress ratio cases seen in Figure 4.55. The change in vertical stress observed in all cases represents a reduction in the total vertical stress during depletion, this reduction is not recovered during injection, and this is represented by a value of γ_v which is almost zero during injection. This change in total vertical stress is associated with significant plastic compaction of the reservoir and elastic extension in the overburden during depletion, and elastic expansion in the reservoir during injection. The total vertical stress does not increase during injection and this means that with the same increment of pore pressure the effective vertical stress is much lower, this appears to be linked to the plastic compaction in the reservoir and extension in the overburden.

The total horizontal stress change is dependent on the initial stress, but is also linked to plastic compaction. In the depletion stage the total horizontal stress decreases for the K = 0.9 and K = 0.7 cases, but shows minimal change for the K = 0.5 case, this is again due to the convergence of the plastic stress paths. During injection the total horizontal stress increases in all cases from the level at the end of depletion, this results in higher total horizontal stress in the K = 0.5 and K = 0.7 cases, but lower total horizontal stress in the K = 0.9 case compared to the start of depletion. The result is higher effective horizontal stress in the K = 0.5 and K = 0.7 cases at the end of injection compared to the initial case, and lower effective horizontal stress in the K = 0.9 case compared to the initial case as observed in the Mohr circle plots. The relative change in total vertical and horizontal stresses for the centre of the reservoir are re-plotted with time in Figure 4.122, this shows that total horizontal stresses are recovered to some extent or increase during injection, but that total vertical stresses do not. The plastic strains are much lower in the centre of the reservoir, and this is associated with greater recovery of total horizontal stresses during injection than at the edge. The most interesting point for CO_2 injection is that the total minimum horizontal stress is lower at the end of injection in the high initial stress ratio case, compared to the start of depletion. This is important as this represents a reduction in the fracture pressure in this case, as the fracture pressure is equivalent to the total minimum horizontal stress.

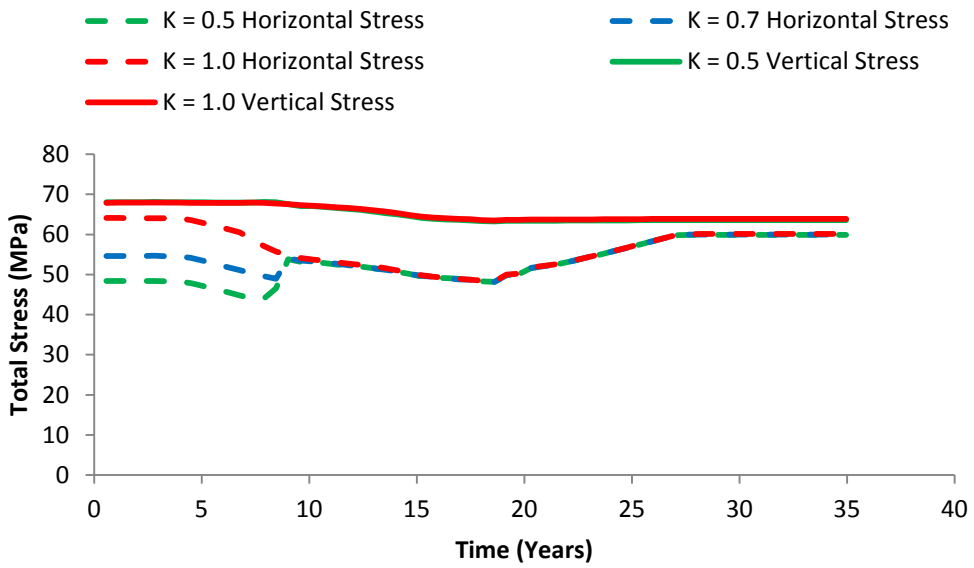

Figure 4.122 - Total horizontal and vertical stresses for the centre of the reservoir with time for each of the initial stress ratio cases.

The most significant difference observed in the injection stress path is the different slope observed in the cases where different parts of the geometry are analysed, and cases with a less stiff overburden or reservoir and higher reservoir Poisson's ratio.

The decrease in injection stress path slope with position in the geometry is related to the increased plastic strain observed at the edge of the reservoir where the most significant change in the injection stress path is observed. There is significant negative (contractive) plastic strain at the edge and corner of the reservoir, which is greater than that observed in the rest of the reservoir, there is also extension in the sideburden. The recovery of total stress is lower at the edge of the reservoir than in the centre, which leads to lower effective horizontal stresses when re-pressurisation occurs. This has obvious implications for CO_2 storage as it represents a further reduction in the fracture pressure at the edge of the reservoir. Figure 4.123 shows a comparison of total horizontal stress at the edge of the reservoir and in the centre of the reservoir for all initial stress ratio cases. The figure shows that recovery of total stress is less at the edge of the reservoir. This is a similar, albeit reduced, effect to that seen in the change in total vertical stress, where no recovery of total stress is observed during injection. A similar edge effect is seen where the fault juxtaposes the shale overburden next to the reservoir along the faults in the compartmentalised model.

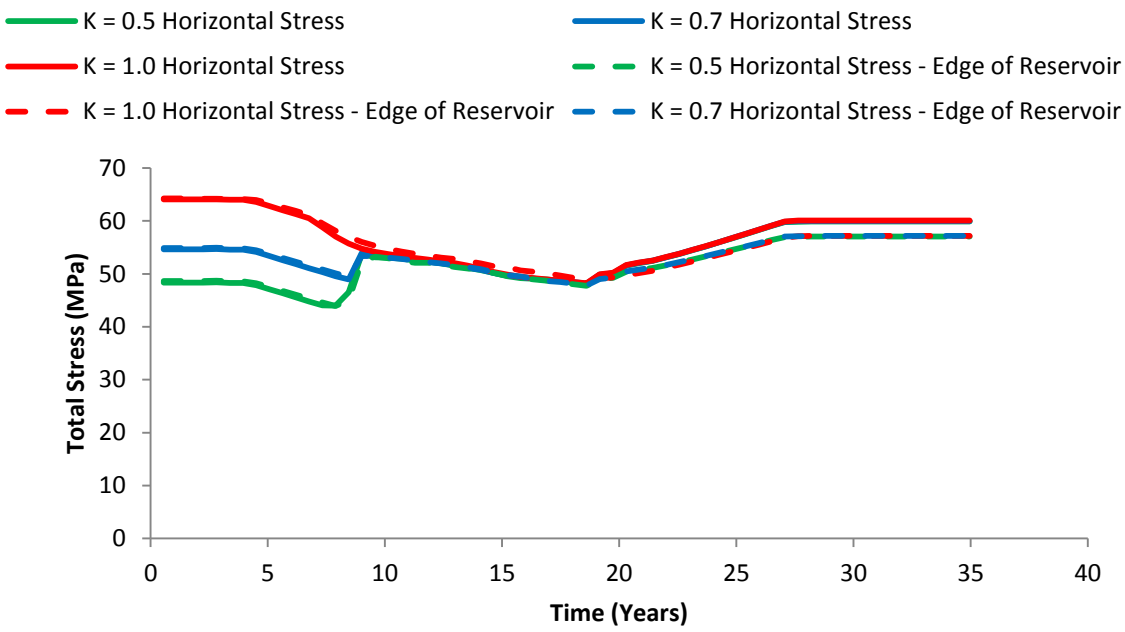

Figure 4.123 – Total horizontal stress for the centre and edge of the reservoir with time for each of the initial stress ratio cases.

The reason for the change in slope of the stress path with different Poisson's ratio has already been discussed in the elastic depletion stage.

The softer overburden reduces stress arching during depletion and so increased vertical effective stress is applied to the reservoir resulting in higher q stress for depletion. During injection the resulting increment of vertical effective stress decrease in the reservoir is the same, yielding a final higher vertical effective stress, and increased q stress during injection, which flattens the slope of the injection stress path. With a softer overburden the horizontal effective stress reaches a similar level compared to a stiffer overburden at the end of injection. This is due to the fact that although effective horizontal stress is higher at the start of injection the sides of the reservoir meet less resistance during injection and final horizontal effective stress is more, this results in a horizontal stress that is at a similar level to the stiffer overburden. The injection in the soft overburden case is effectively a reversal of the flatter depletion behaviour, where the injection trajectory follows a flatter path with higher q stress with p'stress after the offset due to plastic depletion. This shows that a reduction in stress arching decreases the fracture pressure during fracture pressure hysteresis. This effect is also seen in other situations within the model, for example increased stress arching is observed in the sealed case next to the fault, this increases the fracture pressure and reduces the fracture pressure hysteresis effect.

There is also a difference in the injection slope with a less stiff reservoir, with the horizontal stress and vertical stress higher at the end of injection, this is related to the fact that the injection starts from a higher q stress but depletes to a very similar horizontal stress, but higher vertical stress. The injection stress path follows a similar path to the stiffer reservoir

case, but the path is steeper due to a higher initial q, resulting in higher horizontal and vertical stresses at the end.

During injection, stress changes in the reservoir are of most interest, and the overburden response to the expansion of the reservoir mainly involves small stress changes to accommodate expansion of the plastically compacted reservoir. However, the pattern of stress change in the overburden, specifically the horizontal stress change is interesting. The vertical stress change is a hysteretic change with lower final vertical stress than initial vertical stress. This is due to overburden extension during plastic reservoir depletion compaction that is not fully recovered during overburden compression with reservoir expansion. This is also related to the lower vertical stress observed in the reservoir at the end of injection. Higher vertical stresses after injection are observed in the overburden with lower reservoir stiffness as the reservoir deforms more during injection. The associated horizontal stress change is interesting as in all cases a reduction in the horizontal stress is observed in the overburden above the reservoir. Whilst this is a small reduction, and the overburden is shown not to be close to failure in the results section, it does represent tendency towards shear failure during both depletion and injection. The stress reduction during injection increases with increasing stiffness, possibly due to greater vertical stress increase in the softer reservoir case, which increases horizontal stress. This counteracts the horizontal stress reduction from lateral expansion of the reservoir, and stress coupling of the expanding reservoir with the overburden. The stress changes in the overburden, and the reduction of horizontal stress are an important area for further research, as it represents a tendency towards failure of the cap rock seal. This is similar to the stress transfer and reduction in horizontal stress in the cap rock observed in the IEAGHG report on cap rocks (IEAGHG 2011b). The variable stress change in the overburden also has implications for the seismic response, which is discussed in a later section.

4.4.1.5 *Stress Path Hysteresis and Stress Path Parameters*

The most critical behaviour in the stress path in terms of the fracture pressure hysteresis and CO_2 storage is the potential for lower horizontal stress during injection compared to depletion. This will result in a potential risk for leakage if it is not recognised, and will also reduce the capacity estimate for the storage reservoirs, due to a lower injection pressure, and lower final storage pressure. For lower horizontal stresses to occur, the injection stress path, and injection end-point, must be closer to the shear failure envelope. For a lower fracture pressure at the end of re-injection, the increment of p' stress between the yield envelope and the final stress state must be smaller than at the start of depletion (virgin pressure), thus yielding f_{ph} <1. Due to the shape of the yield envelope in p'-q space and the slope of the shear/tensile failure region, a reduction in q stress at the end of re-injection requires a much lower p' stress in order for the fracture pressure to be lower than at the start of injection. Generally, in the base-case scenarios the shape of the stress path means that q stress is much lower, but p' stress is of a similar magnitude to the initial p' stress at the end of injection. This type of stress path means that the fracture pressure is actually

higher at the end of injection, and the scenario has an increased fracture pressure. For a reduction in fracture pressure the stress paths analysed show that the path, particularly for injection, must either become rotated to a flatter trajectory, for the final stress state to be closer to the yield envelope. Or, alternatively, the stress path can overturn, so that the final yield point is at a higher q stress and closer to yield for a similar p' stress. Changes in the model that lead to a flattened trajectory are an increase in Poisson's ratio in the reservoir, an increase in the stiffness of the reservoir material, a reduction in stiffness of the overburden and deformational effects observed at the margins of the model. The relative changes of stress path with these factors can be summarised with the relevant stress paths re-plotted together in Figure 4.124.

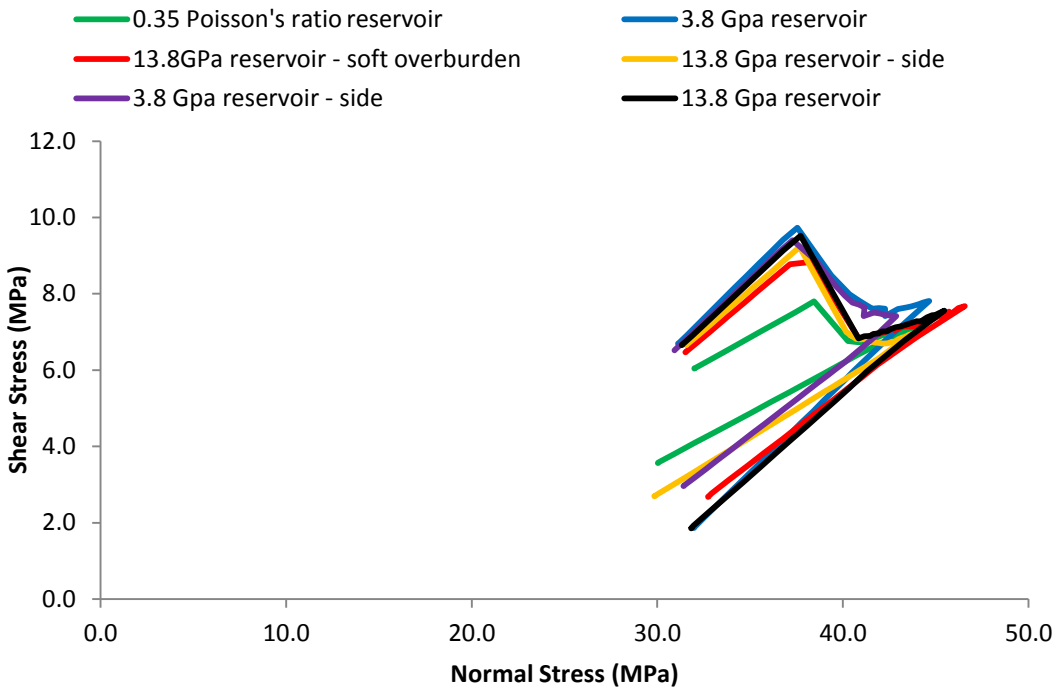

Figure 4.124 – Summary of stress path responses with change in Poisson's ratio, overburden and reservoir stiffness and position within the reservoir. Flattening of the injection stress path such as in the 0.35 Poisson's ratio case shows indicates reduce fracture pressure during injection. This is due to reduced horizontal stress, the base case 13.8 GPa stress path which has a steeper injection stress path, would have a higher horizontal stress and fracture pressure.

The figure comparing the stress paths shows that:

- Poisson's ratio increase flattens the whole trajectory;
- flattening of the injection stress path occurs at the margins of the reservoir, leading to greater fracture pressure hysteresis at the edge of the reservoir. The increase in reservoir stiffness has the most effect at the margin of the reservoir, and the paths plot together in the centre;
- flattening of the injection stress path due to a reduction in stiffness in the overburden is counteracted by an increase in p' stress during depletion, which

means the injection starts at a higher p'-q point. The final stress state has the same horizontal stress, but a higher q stress, which represents a comparatively reduced fracture pressure;

- a reduction in stress arching leads to increased injection hysteresis and a higher q stress and is associated with a softer overburden. Even with a very soft overburden stress arching is still observed due to the plastic behaviour of the reservoir. A further reduction in stress arching may only be observed in a very extensive reservoir, and this would yield the worst case in terms of stress path hysteresis upon injection. Faulting in the sealed case has been shown increase stress arching, and reduce fracture pressure hysteresis.

Changes in the model that lead to an overturned trajectory are an increase in the initial stress ratio in the model and a very high Poisson's ratio. The overturning of the trajectory results from a low q stress and high p' stress for the initial stress prior to depletion. An initial stress point with low q and high p' means that the stress path intersects the yield envelope below the converged plastic stress path (discussed in the previous section) and q must increase to reach the plastic stress path. Most of the stress paths that exhibited flattening with a change in the controlling parameters would also eventually overturn if the parameter alteration was significant enough. For example the Poisson's ratio case with $\nu = 0.5$ shows overturning of the stress path, as the high value of Poisson's ratio means that the initial p' is high and q is low, due to the relationship of vertical and horizontal stresses with Poisson's ratio. Such an extreme value of the Poisson's ratio parameter is however at the extreme end of the possible range. The initial stress ratio dictates the initial stress state and when the K value is high enough the initial stress point falls below the converged plastic stress path, leading to an overturned stress path as seen in the previous section. Combination of an overturned stress path and factors that lead to a flattening in the slope of the stress path will yield the largest hysteresis in the stress path. Stress paths at the margin of the reservoir are particularly important, in this model the margin of the model is flat and forms a sharp contrast to the model, a less abrupt geometry may alter the interaction of the overburden and reservoir, however this investigation is beyond the scope of this study. Larger injection hysteresis represents a reduction in the final total minimum horizontal stress. At a critical point the final minimum total horizontal stress becomes lower than the initial minimum horizontal stress, at this point the fracture pressure is then lower during injection than during depletion which restricts the pressure at which CO_2 can be injected, and presents a leakage risk if not properly quantified.

The impact of the different stress paths on the fracture pressure is summarised in Table 4.2 which compares the fracture pressure and hysteresis factor for cases with different parameters. It can be seen that the cases that have the flattest stress paths in Figure 4.124 also have the most reduced fracture pressures, and greatest fracture pressure hysteresis.

Table 4.2 – Table summarising modelled cases with fracture pressure change. Cases where the fracture pressure is less during injection than depletion are highlighted with red text. The parameters that have been altered from the base case are in bold.

Fault Case	Reservoir Stiffness (GPa)	Overburden Stiffness (GPa)	Reservoir Poisson's Ratio	Overburden Poisson's Ratio	Initial Stress Ratio	Reservoir Geometry Position	Fracture Pressure Change (MPa)	Fracture Pressure Hysteresis Factor
Non-sealing – Low Friction	13.8	5.35	0.25	0.45	0.7	Well	5.3	1.39
Non-sealing – High Friction	13.8	5.35	0.25	0.45	0.7	Well	5.1	1.39
Sealing – Low Friction	13.8	5.35	0.25	0.45	0.7	Well	5.1	1.38
Sealing – High Friction	13.8	5.35	0.25	0.45	0.7	Well	5.1	1.38
Non-sealing – Low Friction	**3.8**	5.35	0.25	0.45	0.7	Well	5.7	1.40
	13.8	**2.35**	0.25	0.45	0.7	Well	5.0	1.34
Non-sealing – Low Friction	13.8	5.35	**0.35**	0.45	0.7	Well	0.5	1.09
	13.8	5.35	**0.49**	0.45	0.7	Well	**-9.3**	**0.59**
	13.8	5.35	0.25	**0.30**	0.7	Well	5.3	1.39
Non-sealing – Low Friction	13.8	5.35	0.25	0.45	**0.5**	Well	11.5	2.39
	13.8	5.35	0.25	0.45	**0.9**	Well	**-4.0**	**0.89**
Non-sealing – Low Friction	13.8	5.35	0.25	0.45	0.7	**Edge**	2.3	1.23
	13.8	5.35	0.25	0.45	**0.9**	**Edge**	**-7.0**	**0.81**
	13.8	2.35	0.25	0.45	**0.9**	**Edge**	**-7.1**	**0.78**

The stress path parameters have been used to describe the change in stress path, and associated change in the Mohr circle description of stress state. The stress path parameters describe the change in vertical and horizontal total and effective stresses and the relative change between vertical and horizontal stresses. For a lower fracture pressure at the end of injection compared to the start of depletion the horizontal stress path parameters for injection must be lower than for depletion. The change in the vertical stress path parameter compared to the change in the horizontal stress path parameter will dictate the level of q stress (thus changing K_{sp}). A higher q stress means that the state of stress will be closer to the slope shear failure envelope for the same p', but in the model this does not necessarily mean the state of stress is closer to shear failure, as the p' stress may also change with a change in q stress. For example, higher vertical stress may also lead to higher horizontal confining stresses. Therefore, the fracture pressure hysteresis parameter has also been calculated for the modelling results to illustrate the relative change in fracture pressure throughout the depletion-injection. The stress path parameters and fracture pressure hysteresis factors are discussed in the following section in comparison with stress path parameter data from Santarelli et al. (1998) to compare the change in fracture modelled in this thesis with that observed in the field.

4.4.1.6 *Summary*

In summary, the results show that the stress paths are generally similar, with the largest difference being observed between stress paths with different initial stress ratios. Factors including the Poisson's ratio, stiffness of the overburden, stiffness in the reservoir, position within the reservoir and consequent level of plastic strain, all affect the trajectory of the stress path. The cases analysed show that the effective vertical stress at the end of injection was lower than the initial stress in all cases, and this is related to a reduction in total vertical stress during depletion, extensive plastic compaction and no recovery of total strain during injection. The relative level of horizontal effective stress at the end of injection compared with the start of depletion varies depending upon the initial stresses, with low initial stress the effective horizontal stress is higher at the end of injection, and with high initial stress the effective horizontal stress is lower at the end of injection. The convergence of horizontal stresses during plastic deformation for different initial stress ratio cases is responsible for the variability in initial and final horizontal stress with varying stress ratio. Effective horizontal stress at the end of injection decreases with increasing horizontal plastic strain, such as that observed at the edge of the reservoir. An increase in reservoir stiffness and Poisson's ratio reduces the final horizontal stress and a reduction in overburden stiffness reduces stress arching, increasing the q stress at the end of injection, which reduces the fracture pressure. The stress paths demonstrate that stress path hysteresis occurs in all of the cases, this is related to the plastic deformation that occurs within the reservoir. The hysteresis leads to different final states of stress, with the major difference being observed in the level of effective horizontal stress and relative level of total horizontal stress, a reduction of which leads to lower fracture pressures for the CO_2 injection phase.

The results of the modelling show the complexity of factors that control the stress path in the reservoir. The models are relatively simple and only include a single material for both the reservoir and the overburden (including sideburden and underburden), however changes in material and model parameters in either the overburden or reservoir can cause significant changes to the stress path. Faults in the model can also influence the stress path, through juxtaposition of the material types and compartmentalisation of reservoir. The stress changes are a function of many different factors that are not conveniently captured using an analytical approach. The results highlight the necessity of coupled modelling, or at least an accurate geomechanical model to understand the stress changes that will occur in a CO_2 storage reservoir that is re-pressurised after plastic depletion. The general description of the stress path in the reservoir shows that there is significant potential for stress path hysteresis, and this phenomenon is discussed in relation to the impact on reservoir fracture pressures for CO_2 injection in the following section. Plastic deformation is important in all of the stress paths, and is a significant factor in the observed stress path hysteresis. The plastic stress path is very consistent between the models and the controls on the gradient of the plastic stress path and the transition stage have not been determined from the modelling. Further investigation into the factors that affect the plastic stress path would provide more information on how hysteresis may evolve in different materials.

Whilst some studies in the literature have modelled the stress path in reservoirs, (e.g. Khan et al. 2000, Schutjens et al. 2001, Yale 2002, Vidal-Gilbert et al. 2009, Vidal-Gilbert et al. 2010, Segura et al. 2011), and some have assessed the fracture pressure in CO_2 storage reservoirs (e.g. Goodarzi et al. 2012, Goodarzi et al. 2013) most studies are either focussed on hydrocarbon related depletion problems, are only elastic and do not include plasticity, or focus on a simple analysis of the fracture pressure, without considering the underlying stress path. The modelling in this thesis is important as the full depletion-injection stress path is modelled, including consideration of material plasticity. This is particularly important for CO_2 storage, as field data has shown the potential for stress path and fracture pressure hysteresis with depletion and injection. The modelling has shown hysteresis in the fracture pressure, with both an increase and decrease in the fracture pressure observed during injection compared to depletion due to plastic deformation in the reservoir depending upon the input parameters. To the knowledge of the author, there are no other similar studies that have investigated this aspect of fracture pressure change, especially in relation to CO_2 storage, where the fracture pressure, and fracture pressure uncertainty has been shown to be critical. The assessment of the stress path has also analysis of the controls on such a depletion–injection stress path with plastic deformation. This has for example shown that stress arching appears to be independent of reservoir material stiffness where significant plastic deformation occurs, contrary to the findings of Segura et al. (2011) for elastic analyses where stress arching only becomes important when the overburden is stiffer than the reservoir. The understanding of the stress path for depletion and injection with plastic deformation is used in the following section to compare the change in fracture pressure with

the field observations by Santarelli et al. (1998) and draw conclusions for the fracture pressure in CO_2 storage.

4.4.2 **Fracture Pressure Hysteresis**

The main aim of this chapter is to investigate the potential for stress path hysteresis in a CO_2 storage reservoir, and the consequent potential for an adverse impact on fracture pressures during re-pressurisation as observed by Santarelli et al. (1998) for a field in the North Sea. Observations of the stress path in the reservoir have shown the variability of the stress path and the factors that can influence the stress path. The impact on the fracture pressure at the end of the re-pressurisation compared to the start of depletion has also been analysed and presented as a fracture pressure hysteresis factor (f_{ph}) representing the reduction (or increase) of fracture pressure at the end of re-pressurisation as a ratio of initial fracture pressure.

Analysis of the total depletion horizontal stress path parameters presented in this thesis i.e. for elastic and plastic depletion stages, show different values depending upon the initial stress ratio. The elastic depletion (prior to plastic failure) stress path parameters are however the same, approximately 0.63. The pore pressure/stress coupling observed by Hillis (2001) and Teufel et al. (1991) for the Ekofisk field has a γ_h of approximately 0.8 with an initial stress ratio of K = 0.9. Santarelli et al. (1998) also observed a similar level of horizontal stress path parameter γ_h = 0.7 in the case where they observe fracture pressure hysteresis, however they do not indicate an initial stress ratio for the field. Santarelli et al. (1998) also observed that the γ_h is much lower γ_h = 0.46 in the southern part of the field that is heavily faulted. The field studied by Santarelli et al. (1998) is likely to have a high initial stress ratio > 0.8 based on the location in the North Sea (Edwards et al. 1998). The cases analysed in this thesis for the K = 0.9 case also have a γ_h = 0.8 for depletion and appear to show that this type of strong pore pressure/horizontal stress coupling is associated with a high initial stress ratio when plastic deformation occurs. Plastic deformation (compaction) is well documented in the Ekofisk field, with severe subsidence observed above the field during depletion e.g. Guilbot and Smith (2002), Teufel et al. (1991), Boade et al. (1989) and Settari (2002). This suggests that the stress path depletion behaviour observed in the Ekofisk field and in this thesis arise through a similar mechanism. Furthermore, the stress paths modelled for the K = 0.9 case provide a likely analogue of the stress path for the Ekofisk field. The observed similarity also suggests that the modelled stress paths for the K = 0.9 case provide a reasonable representation of the depletion stage observed by Santarelli et al. (1998) if plastic deformation is occurring. The hysteretic response in the stress path observed by Santarelli et al. (1998), the likely reservoir material properties and significant depletion suggests that plastic deformation has occurred. This suggests the models presented in this thesis can also provide an analogue to the field discussed by Santarelli et al. (1998). The injection stage of the field presented by (Santarelli et al. 1998) has a γ_h of 0, this is much lower than the γ_h parameter observed for any of the cases in this

thesis. The results of this thesis are therefore discussed in terms of the extent of fracture pressure and stress path hysteresis in comparison to the data from Santarelli et al. (1998).

For the K = 0.9 case in this thesis the γ_h for depletion is 0.8, the γ_h for re-injection is 0.6, meaning the horizontal stress is lower after re-injection. However this level of γ_h is much higher than that observed by Santarelli et al. (1998). The f_{ph} factor for the K = 0.9 case is 0.89 showing that fracture pressures are 89% of depletion fracture pressures during reinjection. The data from the K= 0.9 can be re-plotted to show the stress path if the γ_h was 0, as in Santarelli et al. (1998), and the resultant reduction in fracture pressure and f_{ph}. The difference between the two cases can then be determined in terms of the difference in fracture pressures during depletion and injection and can provide an estimation of the difference between the cases modelled in this thesis and the behaviour observed by Santarelli et al. (1998). Figure 4.125 shows the K = 0.9 case with a γ_h = 0 injection stress path for comparison. The f_{ph} factor can be assessed as a percentage of the equivalent f_{ph} factor for the 0 horizontal stress path. This shows that the fracture pressure hysteresis is 19% of that reported by Santarelli et al. (1998).

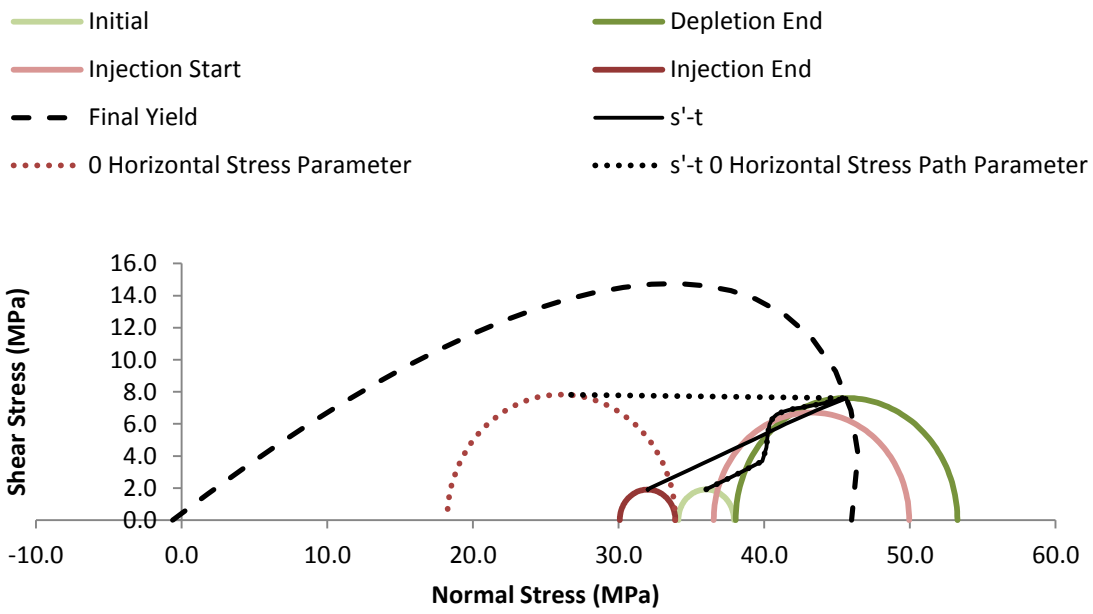

Figure 4.125 – Mohr circle and s'-t stress path plot for a cell at the well for the K = 0.9 initial stress ratio case with a projection of a case with γ_h = 0 stress path as observed by Santarelli et al. (1998).

The same change in f_{ph} factor can also be assessed for the margin of the reservoir that showed greater fracture pressure and stress path hysteresis than the centre of the reservoir. The f_{ph} factor for the reservoir margin was 0.81. Figure 4.126 shows the K = 0.9 case at the side of the reservoir with the γ_h = 0 stress path for comparison. Comparison with the γ_h = 0 stress path shows that the modelled case represents 35% of the fracture pressure hysteresis reported by in the field data.

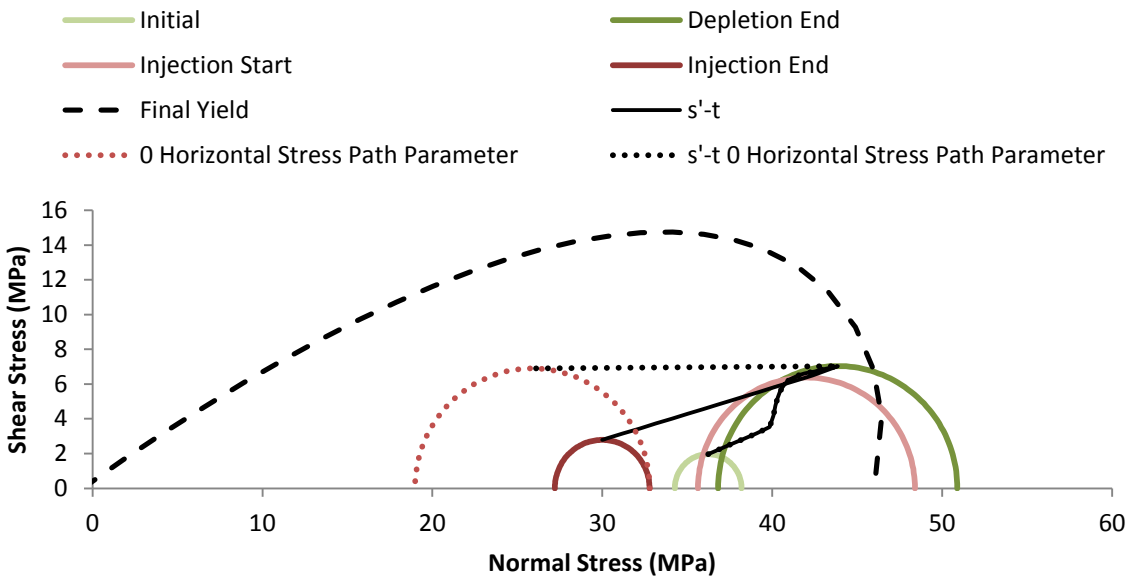

Figure 4.126 – Mohr circle and s'-t stress path plot for a cell at the well for the K = 0.9 initial stress ratio case with a projection of a case with γ_h = 0 stress path as observed by Santarelli et al. (1998).

The data from the modelling show that fracture pressure hysteresis has been modelled and that it is most likely to arise for high initial stress ratios within the range of normal material parameters for geological materials. The initial stress ratio at which the f_{ph} falls below 1 and a lower fracture pressure is observed on re-pressurisation compared to depletion in this study is K = 0.85 at the well and K = 0.80 at the margin of the reservoir. This initial stress ratio is consistent with that found below 1000 m in most areas of the North Sea, and so in materials that experience significant plastic deformation during depletion fracture pressure hysteresis could be expected with re-pressurisation (Edwards et al. 1998). The model analysed in this study is at a depth of 3 km, this is fairly deep compared to the feasible lower depth limit for CO_2 storage (1000 m) as discussed in the literature review section. The depth of the model means that there is a low risk of shear failure as the stress states do not plot close to the shear failure region of the envelope. Models at a shallower depth would have lower p' stresses in general and would plot close to the shear failure envelope, this would mean that even with a slight fracture pressure hysteresis there could be a risk of shear failure upon re-pressurisation. Therefore, the modelling shows that it would be feasible for fracture pressure hysteresis to present a risk of shear failure in fields in the North Sea, where material parameters are similar to those used in this thesis.

Whilst the modelled fracture pressure hysteresis is not insignificant, it also does not fully recreate that observed by Santarelli et al. (1998). In a later paper on the same field Santarelli et al. (2008) link the injection of colder fluids to the reduced horizontal stresses in the field. The reduction of horizontal stress occurs due to the generation of tensile thermo-elastic stresses, as defined in Equation 2.15. This temperature effect could explain the more extreme fracture pressure hysteresis observed in the field, however the modelling results

suggest that this type of field in the North Sea would already be prone to fracture pressure hysteresis. The observed fracture pressure hysteresis in the field may result from the combined effect of material plasticity, high initial stress ratio and low temperature injection fluids. A coupled model incorporating temperature induced stress generation would enable further analysis of this problem. Estimates of the reduction in horizontal stress from the injection of colder CO_2 for an idealised sandstone reservoir are presented by Luo and Bryant (2011). They suggest that reductions in the horizontal stress of the order of 10 MPa are feasible. A simple estimate of the thermo-elastic stresses in the modelled results using the approach of Luo and Bryant (2011) is shown in Figure 4.127. The thermo-elastic stress equation was applied using typical values from Luo and Bryant (2011). A temperature change between the fluid and reservoir temperature of 30°C was assumed, and the coefficient of thermo-elasticity was set at 1.5×10^{-5} $°C^{-1}$, which is a typical value for sandstone, the other parameters required are the same as those used in the constitutive model (Luo and Bryant 2011). The temperature difference is the largest difference deemed feasible for commercial scale injection accounting for equilibration of the injected CO_2 to reservoir temperature during injection. The simple analysis shows that tensile thermo-elastic stresses of up to 9.9 MPa could be feasible at the well, decreasing to 2.5 Mpa in the cells adjacent to the well, and are similar to the values from the literature. Santarelli et al. (2008) also present estimates of thermally-induced stresses, initially they use a value of 0.5×10^{-5} $°C^{-1}$ for the coefficient of thermo-elasticity, however after assessing field data from well temperatures they suggest this value should be on order of magnitude higher. The thermally induced stresses calculated by Santarelli et al. (2008) with the larger coefficient range between 6.9 and 22.2 MPa, for a less stiff rock and a temperature difference of up to 85 °C. The data from the literature shows that the thermally induced stress is quite variable, and there is uncertainty surrounding the calculation of the stresses. The stress can vary significantly with the stiffness of the material and the thermo-elasticity coefficient. Applying these significant levels of thermally induced horizontal stress reduction to the stress paths in Figure 4.125 and Figure 4.126 would produce a similar stress path to the $\gamma_h = 0$ stress path. The impact of the thermo-elastic stresses could significantly reduce horizontal stress at the well in the model, to levels similar to those of a $\gamma_h = 0$ stress path. The main issue with the simple analysis is that it doesn't take into account the evolution of stress with the temperature impact throughout the coupled simulation, so it is not possible to predict the true stress path and the level of impact the temperature difference would have. The temperature impact may also produce fracture pressure hysteresis in models with lower initial stress ratios, and different parameters. Luo and Bryant (2011) also suggest that the thermal effects can be more significant in shale, and can reduced the fracture pressure at the interface of the reservoir and cap rock, this would also be an interesting area of further research for coupled models with temperature and thermo-elastic stress capabilities, but is beyond the scope of this analysis.

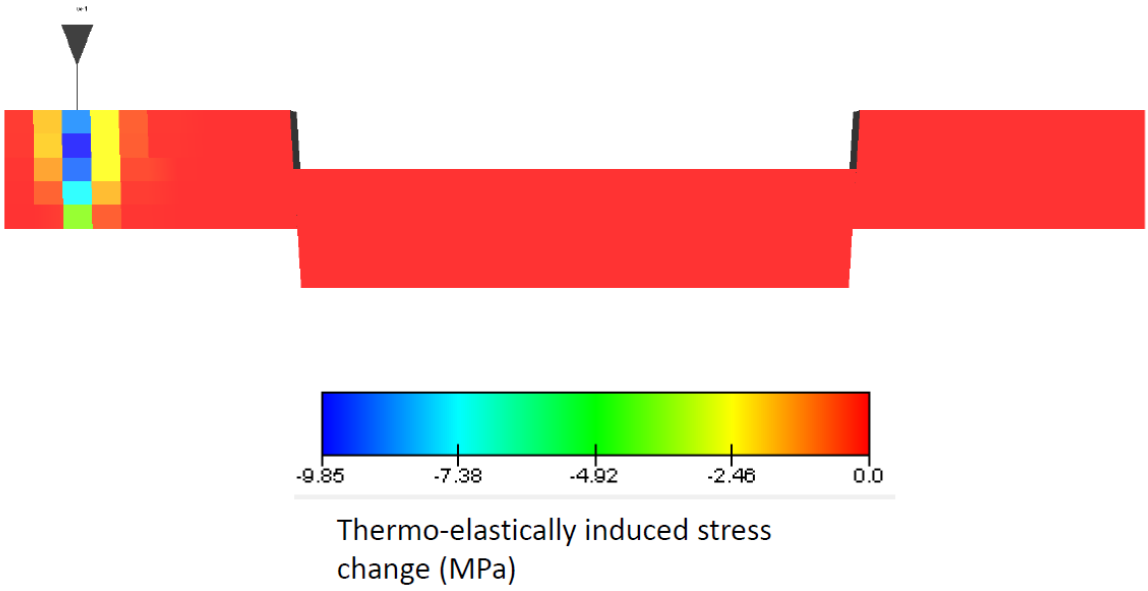

Figure 4.127 – Plot of thermally induced stress around the injection well using data from the material model and typical values from Luo and Bryant (2011).

The data from the southern part of the field from Santarelli et al. (1998), which has a γ_h = 0.46 for depletion and showed the same extreme stress path/fracture pressure hysteresis, is more comparable with the K = 0.7 case in terms of horizontal stress path parameter which is γ_h = 0.33 for depletion. The southern area is heavily faulted, and it is possible that this may alter or reduce the initial stress ratio, providing a possible explanation for the different stress path. The modelled K = 0.7 case does not show a reduction in fracture pressure at the end of injection. The fracture pressure is in fact higher at the end of injection in this case. Therefore, if the two cases are comparable the temperature effect must be entirely dominant in the field data case unless other parameters are significantly different, e.g. high very high Poisson's ratio. The relationship of γ_h with f_{ph} modelled in this thesis can be plotted, and this shows that for an $f_{ph} < 1$, γ_h must be > 0.68 for depletion. Extrapolation of a γ_h = 0 stress path for the γ_h = 0.33 K = 0.7 case shows that with the extreme temperature effects this case would still lead to fracture pressure hysteresis however as the injection γ_h of 0 would be lower than depletion. The only case where γ_h = 0 does not lead to fracture pressure hysteresis is the K = 0.5 case, which already has an initial depletion γ_h of almost 0. Temperature effects seem to be dominant in the behaviour observed by Santarelli et al. (1998) and this would be most likely mechanism for hysteresis in cases with lower γ_h in this modelling. Implicitly this would also cover the modelled cases with all but the highest initial stress ratios. The comparison seems to show that temperature may be the most important factor in fracture pressure hysteresis. However, one solution to this problem may be the heating of injection fluids (CO_2) prior to injection. The results for the modelling show that even with heating of the injected CO_2 there may also be additional hysteresis observed in the fracture pressure, particularly at the margins of the reservoir. An interesting area of further research would therefore be a more complex geometry, with a greater number of

rock types to assess the extent and controls on fracture pressure hysteresis in the absence of temperature effects, in addition to a coupled model incorporating temperature effects.

Other factors that will influence the stress path include faults, material properties and the level of stress arching. The last two factors have been discussed already, with the Poisson's ratio and stiffness of the overburden showing the largest impact on the stress path and the level of stress arching affecting the differential stress that is developed. Santarelli et al. (1998) suggest that faulting may also have an impact on the horizontal stress path parameter, they associate significant faulting with a lower $\gamma_h = 0$ in the Southern part of the field. The lower γ_h would reduce the non-temperature related fracture pressure hysteresis effect according to the results from the modelling presented in this thesis. The faults incorporated into this simulation do not seem to show any significant effect on the horizontal stress path parameter however, suggesting this may be an area for further investigation. Equally, this variability in the southern part of the field could be related to material parameters. The behaviour of the faults in this model are discussed in the following section. The modelling shows that there is a risk of a reduction in fracture pressure during CO_2 injection into plastically depleted hydrocarbon reservoirs. This would reduce overall capacity, and also present a risk of leakage if not recognised in the analysis of storage. This risk may be further compounded by the injection of cold CO_2 into the reservoir.

4.4.3 **Fault Behaviour**

Movement was observed on the faults in all of the cases modelled. Movement on the fault is represented in Elfen by the displacement of nodes on the fault plane, and this represents contact sliding between the contact surfaces of the fault. The most significant movement occurred during the depletion stage when plastic deformation was occurring in the reservoir. The movements on both of the faults were in the same sense, but the fault nearest the injection point experienced the most displacement. Fault movement vectors and contact displacement contours showed normal vertical movement, with the hanging wall moving downwards relative to the footwall. The displacement contours and vectors also showed horizontal movement however with the hanging wall and footwall faces of the fault moving towards each other horizontally. The overall vectors are normal to the fault faces with the footwall moving upwards and towards the centre of the model, and the hanging wall moving in the opposite sense. The displacement of the nodes is not distributed evenly along the fault and is focussed in the footwall and hanging wall below the reservoir and in the footwall above the reservoir, there is also movement within the reservoir. The movement on the fault does not seem to represent sliding along the whole fault, and is interpreted as representing sliding that accommodates the deformation seen in the reservoir and surrounding overburden.

In the models, the fault is represented as a zero-thickness fault plane controlled by a Mohr-Coulomb frictional interface, corresponding to a zero-thickness boundary in the flow model with a high or low transmissibility. In reality faults will have a thickness, represented by the

formation of a fault rock, and this will determine the strength and flow properties of the fault. The zero-thickness assumption also assumes a discontinuity between the reservoir and overburden rock and the fault itself, in reality there would be no sharp distinction between the fault zone and the host rock. Assessing failure in a zero-thickness fault relies on assessing the stress state across the fault, as the failure within the fault is not modelled explicitly. Two failure criteria are of interest, that of the fault contact, which is a Mohr Coulomb failure criterion in this case, and that of the host material, which is the SR3 envelope. Failure on the Mohr Coulomb envelope represents shear failure in the fault material and failure of the SR3 represents failure condition in the host rock adjacent to the fault. Different behaviour was observed on the fault depending upon on the initial stress conditions, with the most movement occurring in the K = 0.5 case, this was also the only case in which potential failure was observed. The potential failure determined using assessment of the stress state in the cells adjacent to the fault and the total stress state across the fault, i.e. the highest and lowest principal stresses in adjacent cells across the fault. The most severe potential failure was in the K = 0.5 low friction cases. During depletion in the sealing case potential failure consisted of failure of the fault failure criterion in the hanging wall, and potential failure at the SR3 shear envelope for stresses across the fault. No potential failure was observed during injection in the sealing case, but potential failure was observed in the overburden at the start of injection, with failure of the fault criterion in the footwall. Potential failure was also observed during both depletion and injection in the non-sealing case, with the stresses across the fault exceeding both failure criteria, but no potential failure was observed in the overburden. The assessment of failure and leakage along the zero-thickness fault is difficult as it does not accurately represent the geometry of the fault and failure as it would occur on the fault. For example, it appears that failure is feasible within the fault and some parts of the host rock, if this material was represented as a continuum leakage into the fault and from the reservoir is possible. A full assessment of fault leakage is beyond the scope of this thesis and this was the reason for incorporating only a simple fault representation. However, a comparison of different approaches for representing faults in coupled geomechanical models by Cappa and Rutqvist (2011) shows that the stress changes and displacement of the fault are accurately represented by a simple zero-thickness fault compared to a more complex assessment using an explicit representation of the fault thickness. Assuming the faults used in this model are accurately representing fault behaviour the modelling shows that progressively more movement (and potential leakage) is associated with decreasing initial stress ratio. This is consistent with lower compressive stress across the fault allowing more movement.

Despite the observed difference in fault movement and failure with initial stress ratio, the modelling also shows that there appears to be no impact on the stress path due to fault movement, even where different magnitudes of movement are observed between the strong and weak fault cases. Attempts to correlate faulting during depletion with stress path parameters by Addis (1997) for field data also show a weak correlation. This suggests that reservoir scale faulting is not important when considering the effect on stress paths and

stress path hysteresis, with the exception of sealing and non-sealing properties of the faults altering the geometry. The sealing case in this thesis has been shown to increase stress arching at the fault, this reduces fracture pressure hysteresis effects at the margin of the reservoir, and minimises reduction in fracture pressure during injection. Other than sealing properties, the main impact of faulting may be on the overall initial stress ratio at a larger scale, which would affect the stress path according the models presented in this thesis. This would explain differences observed by Santarelli et al. (1998) in heavily faulted regions equally this difference could result from variability in material parameters. Further investigation should focus on analysing the impact of more significant movement on faults on the stress path, and the impact of larger scale faulting on the initial stress conditions in reservoirs.

4.4.4 **Fluid Flow Simulation**

The focus of this work is the behaviour of the stress path and this means that most of the assessment focuses on the geomechanical model. However, observations can also be made about the fluid flow model, which has mainly served the function of providing pore pressure loading to the geomechanical model. Specifically, the performance of the uncoupled fluid flow model in replicating the results of the coupled model has been analysed. Coupled models are expensive and time consuming to build and run, and so there is great interest in replicating the results of the models with standard fluid flow models or combining their use to improve the accuracy of standard models (Pettersen and Kristiansen 2009, Segura et al. 2011). Coupled models are often used to provide information about subsidence and compaction drive and it is possible to represent this behaviour using only a flow simulation using pore volume multiplier tables to represent the loss in pore volume during compaction. The pore volume tables can be derived from lab and field data and analytical equations to describe simple one dimensional compaction and this can be factored into the flow simulation, however this will generally disregard the actual physical behaviour underlying the compaction (Pettersen and Kristiansen 2009). Analytical equations for calculating compressibility are usually only applicable to elastic behaviour, and are based on the stiffness, porosity and Poisson's ratio. History matching is also used during the production of a field to update the flow model to match the production history, for CO_2 injection the history matched model could be used to model CO_2 re-injection in to the field.

The results of the comparison of the non-coupled and coupled model show that production can be accurately modelled using only the compressibility in the flow model, this is essentially a history match of the data. However, whilst the production matching is good, and the compressibility variability is fairly insignificant for the results of gas withdrawal in the reservoir, the injection match is poor. This is because only a linear compressibility is used, and whilst the withdrawal of the gas is not heavily dependent on the compressibility and change in porosity, the re-pressurisation means that the pore volume during injection is

significantly overestimated. The history match essentially ignores the physical behaviour of the reservoir and applies an approximation to find the solution.

To match the coupled and non-coupled models a pore volume multiplier (PVM) table was produced from the modelled pore volume change in the coupled model, this was then applied to the non-coupled flow model, and a good match was achieved. The slope of the PVM line represents a compressibility value in bar^{-1}. The plot of the PVM table in Figure 4.105 shows that even for the simple model including two materials two different compressibilities are required for the plastic and elastic stage. Comparison of the same model with different fault properties (sealing and non-sealing) shows that this further affects the PVM table, this is due to variable stress arching in the model, the sealed model experiences more extreme stress arching than the non-sealed case. Re-plotting the PVM table with the compressibility gradients of the curves in Figure 4.128 shows the difference between the sealing and non-sealing and plastic and elastic phases and that the linear compressibility of 1×10^{-04} bar^{-1} for depletion only matching is inappropriate. The results show that stress arching affects the compressibility, and that this would be difficult to predict prior to depletion. There is an order of magnitude difference between plastic and elastic compressibility coefficients. Furthermore, the PVM tables are irreversible, and so no increase in pore volume is seen with reinjection, unlike the linear assumption. Determining the range of behaviour with stress arching and plastic behaviour in a real reservoir would be an even more complex task, but would be essential in understanding the re-pressurisation characteristics for CO_2 injection of a reservoir exhibiting stress arching and/or plastic deformation. This illustrates how coupled modelling is likely to be essential in many CO_2 injection projects, especially those in similar reservoirs in the North Sea. Pettersen and Kristiansen (2009) show a method for generating pseudo-materials that share compaction characteristics and PVM tables which can be assigned to regions of the flow model and replicated compaction behaviour. Segura et al. (2011) present a method for incorporating stress arching effects into generic PVM tables for fluid flow simulators which improve the non-coupled simulation results. However, the key point is that both of these approaches require initial tuning coupled runs in a specific reservoir to produce the improved fluid flow simulations. Additionally, without coupled modelling information on fault movement, seismic data generation and stress paths is difficult to model, and these may also be an important concern for CO_2 injection projects.

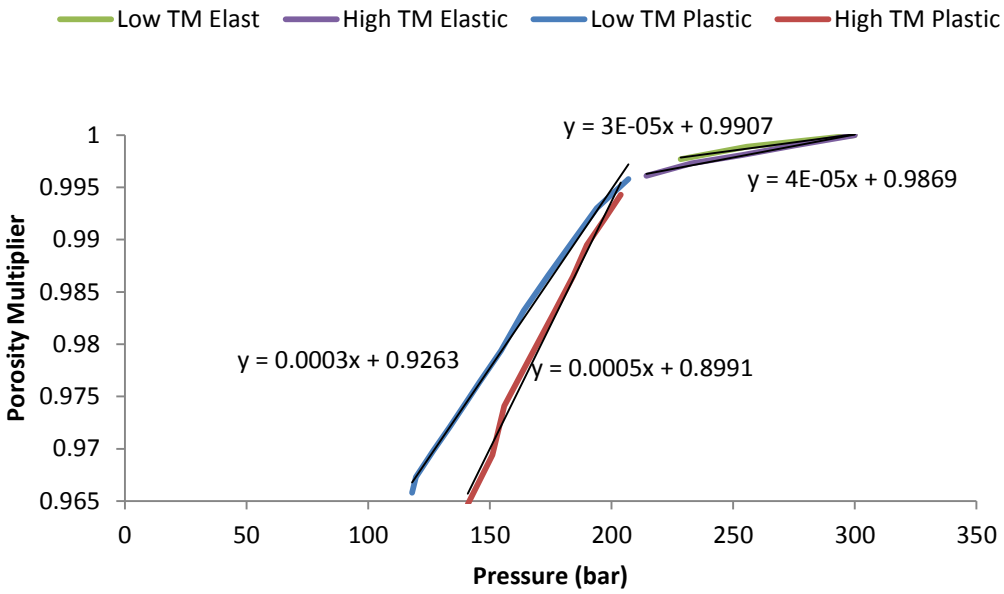

Figure 4.128 – Re-plotted PVM table comparing the compartmentalised and non-compartmentalised fluid flow simulation compressibility gradients.

4.4.5 **Seismic Data**

4.4.5.1 *Gassman's Substitution – Reservoir Model*

A simple Gassman's substitution was performed on the results of the simulation model to determine the P-wave velocity during depletion and injection. Comparison is made between the model without compaction consideration, the model tuned using the coupled model to implement compaction pore volume multipliers, and the coupled model. The comparison shows a significant difference between the non-coupled model without porosity changes and the model with porosity changes. The largest differences are seen around the well and fault, with changes on the order of 100s of m/s between the models. Calculation of the velocities for the coupled model with porosity changes affecting fluid flow, but with the porosity term neglected shows the contribution of porosity to overall changes in velocities is small on the order of <10 m/s, which is roughly 1% of the changes related to the saturation changes in the model. This is a similar result to a model from Holt et al. (2005) who show that the contribution from porosity using a stress sensitive linear elastic model is also small. The change in P-wave velocity shows the expected trend with porosity change, with an increase in velocity with decreasing porosity, which represents compaction. The coupled model also shows a decrease in velocity with increasing porosity during injection, the difference is small as porosity expansion is limited during injection. The non-coupled model is also not capable of modelling porosity dependent velocity changes during injection, as it is not capable of modelling reversible or hysteretic porosity multiplier changes. Other simulators have more advanced capabilities for modelling pore volume multipliers.

4.4.5.2 *Overburden Seismic Data*

P-wave velocities were also calculated for the overburden during depletion and injection, using synthetic seismic data generation from the geomechanical model. The results essentially a similar result to those presented by Angus et al. (2008) and Angus et al. (2011). Velocity changes are of a similar magnitude with a reduction in P-wave velocity up to 600 m/s above the reservoir, compared to a roughly 1000 m/s modelled in the literature. The velocity decrease corresponds to a reduction in both the horizontal and vertical stresses above and below the reservoir, and the velocity increase is also related to an increase in horizontal and vertical stress at the sides of the reservoir. This represents the stress arching in the model. The stress arching and seismic response is consistent between the base case model, and the model with reservoir stiffness. As with the stresses in the overburden, the seismic response during depletion is controlled by the overburden parameters and resultant level of stress arching.

The impact of stress changes and stress arching during depletion on seismic velocities are well documented in the literature. For example, Staples et al. (2007) modelled field data from the Shearwater field using geomechanical modelling and show stress arching effects, Herwanger and Horne (2009) model anisotropic stress changes in the overburden with depletion, along with the aforementioned studies. However, less attention is paid to the changes in seismic velocities during re-injection after depletion, as this is often of less interest outside of applications such as CO_2 storage. The calculations in this thesis extend the modelling to show the change in P-wave velocity in the overburden with injection into the reservoir. During injection, significant hysteresis is observed between the depletion seismic velocity changes and the injection velocity changes. Similar hysteresis has been predicted by Sayers (2007) in the reservoir and is linked with irreversible porosity changes and the stress path of the reservoir. The response in the injection profile is in general much weaker than the depletion profile, and shows a divergence in the polarity of the change. In the base case model the changes in velocity around the reservoir during injection are the same as during depletion, with a decrease above the reservoir and increase at the sides, but with the resultant change of much smaller magnitude < 20 m/s to almost 0. In the model with a reservoir with a lower stiffness the change in seismic velocity is actually positive all around the reservoir in the overburden, although again the magnitude is low. The positive velocity changes are strongest at the outer corners and edge of the reservoir and in the footwall of the fault below the reservoir and hanging wall above the reservoir. The stress changes in the overburden show how the different seismic response arises. The difference between the high and low stiffness reservoir cases is related to the change in horizontal and vertical stresses. In the higher reservoir stiffness case the velocities decrease during injection above the reservoir as horizontal stress decrease with injection (lateral expansion of the reservoir) is more dominant than the weak increase in vertical stress in the overburden. The sideburden is also loaded during injection and this increases horizontal stress in the sideburden more than the decrease in vertical stress in the sideburden due to unloading. The low stiffness reservoir experiences greater deformation during pressure

changes, both during depletion and injection, this results in greater reloading of the overburden during injection and the resultant vertical stress changes are higher than the small horizontal stress decrease. The case is similar to the high stiffness case with the outer edge of the reservoir, with a larger increase in horizontal stress observed. Generally, the lower reservoir stiffness during injection promotes greater stress changes, and reservoir properties are dominant, but in the depletion stage, the properties of the overburden control the seismic response. The results show that the seismic response in the overburden may be harder to distinguish during injection, and is also dependent on reservoir properties. The analysis is simple and does not include anisotropy in the analysis, additionally the range of scenarios investigated compared to those modelled is limited due to time constraints. The velocity change represents a bulk change in the velocity rather than anisotropic changes and does not reveal specific changes in horizontal or vertical stress, this may be important for CO_2 storage where continued reduction in horizontal stress above the reservoir could lead to fracturing. Capturing this change using time lapse seismic velocity changes would be a useful monitoring technique. Changes in overburden parameters, and the seismic profile of different initial stress ratio cases, particularly those involving a reduction in the horizontal stress in the reservoir and the end of injection could provide more insight for the specific problem of CO_2 storage.

4.5 **Conclusions**

The coupled modelling has investigated aspects of mechanical and fluid flow behaviour that are important for CO_2 injection into a re-pressurised gas reservoir. Whilst the model is not of the complexity of a full field model, the behaviour has been shown to be complex. The key findings from the modelling work are presented in the following sections.

4.5.1 **Stress Changes and Stress Arching**

4.5.1.1 *Overburden*

- The behaviour of the overburden is important in all of the models due to the effect on the reservoir stress path, this is due primarily to stress arching, which was observed in all cases.
- A stress concentration is formed at the edge of the reservoir in the sideburden due to the interface of the reservoir and laterally moving sideburden. This appears to be important for stress changes in edge of the reservoir.
- The stress arching parameter for depletion in the reservoir for almost all the cases was 0.22 – 0.25, the only significant change was observed with a less stiff overburden (0.14), indicating that the effect of reservoir parameters on the stress arching is minimal in this case.
- Comparison of controls on stress path in the literature show that in elastic problems the relative stiffness of the overburden to the reservoir is important for controlling stress arching, with a stiffer overburden compared to the reservoir promoting stress

arching. The results of the modelling in this thesis show that with significant plastic deformation the absolute stiffness of the overburden dominates, regardless of the stiffness of the reservoir. Reduction in stress arching with reservoir stiffness is important in the reservoir for fracture pressure hysteresis.

- No plastic deformation was observed in the overburden as the stress changes in the overburden were not significant enough to induce failure. A less consolidated material may deform plastically and may have further implications for the evolution of stress arching.
- The level of stress arching and plastic deformation at a stress concentration at the edge of the reservoir/sideburden interface controls the development of horizontal stress both in the reservoir and in the sideburden, which is important for fracture pressure hysteresis.

4.5.1.2 *Elastic Depletion*

- Elastic depletion in the reservoir is controlled by the elastic parameters in both the overburden and the reservoir. The elastic stress paths are important for the stress state prior to injection, and the final injection stress path which controls the fracture pressure during CO_2 injection.
- A softer overburden increases vertical stress in the reservoir, this in turn increases horizontal confining stresses, the result is flattened p'-q stress path with higher p' stress for the same level of q stress.
- Increasing Poisson's ratio in the reservoir increases the horizontal confining stress from vertical loading from the depletion. This flattens the p'-q stress path as the q stress reduced and p' stress is increased. A higher Poisson's ratio also means the material geostatically initialises at a higher p' stress and lower q stress.
- An increase in reservoir stiffness increases the horizontal confining stress in the reservoir this also flattens the p'-q stress path.

4.5.1.3 *Transition and Plastic Depletion*

- Plastic depletion in the model has two distinct phases, a transition stage and subsequent convergence to the second stage, which represents true plastic depletion at a constant p'-q gradient.
- The stress path in the transition stage depends on the point at which the elastic stress path intersects the yield envelope. To some extent this is influenced by the material parameters, as this affects the elastic depletion gradient.
- The most significant impact on the transition stage is the initial stress ratio of the model as this determines the elastic stress path, which in turn dictates the point at which the yield envelope is reached.
- All stress paths in the transition stage converge on a stress path with a similar level of q stress and the same p'-q gradient, and this represents stable plastic depletion deformation.

- The only variation in the converged plastic stress path is the length of the path (i.e. maximum p'-q stress reached) and the level of q stress at which the trajectory occurs, the p'-q gradient of the trajectory h, is consistent throughout the models at 0.70 – 0.72. Lower stiffness in the overburden extends the path, lower stiffness in the reservoir increases the q stress of the path and plastic deformation and lower vertical stress due to reduced stress arching at the edge of the reservoir lowers the q stress.
- The most significant feature of the transition and plastic phase is the convergence of stress paths with different initial stress ratios. The stress paths all converge to a single p'-q trajectory regardless of the initial stress ratio in the model, assuming they share common parameters.
- Analysis of the convergence with different stress ratios shows that vertical stress is constant and that the convergence occurs due to significant changes in the effective horizontal stress in the reservoir. Effective horizontal stress increases in low initial stress ratio cases, and decreases in the high initial stress ratio case.
- The convergence of the stress paths appears to be controlled by the onset of plastic deformation in the margins of the reservoir. Significant plastic deformation occurs in the margin of the reservoir in the high initial stress ratio case, this is associated with a decrease in effective horizontal stress in the reservoir, and lower horizontal stress increase in the sideburden. The opposite behaviour is observed in the low stress ratio case, with low levels of plastic deformation, significant increase in reservoir horizontal effective stress and a large increase in horizontal stress in the sideburden. The convergence is important for fracture pressure evolution as it promotes a significant change in the stress state from the initial stress state. This has a significant impact on the relative horizontal stress and fracture pressure during CO_2 injection.
- The edge of the reservoir is flat and forms a sharp interface with the overburden, significant plastic deformation and stress concentrations are observed at this interface. Further investigation into the geometry of the edge of the reservoir could provide information on the nature of these stress changes and deformation with different reservoir edge geometries. For example, reservoirs may often have a lens shape characteristic of a fluvial depositional body.

4.5.1.4 *Elastic Injection*

- For this investigation the most critical aspect of the stress path is the injection phase, however behaviour of the stress path during injection is also linked to the previous behaviour of the material during depletion.
- All injection stress paths start from a similar p'-q stress and consequently follow a similar injection trajectory due to the convergence during plastic deformation. The stress path generally follows the same gradient as that of the elastic depletion path, and are characterised by a decrease in q stress representing tendency towards

hydrostatic stress. The stress paths are offset form elastic depletion path through plastic deformation.

- The vertical effective stress change in the reservoir is similar for all cases and represents a stress path with a stress path parameter of almost 0. As the stress path parameter is greater than 0 in depletion due to stress arching, the vertical effective stress is actually lower after injection than prior to depletion. This appears to be linked to the significant plastic compaction that occurs in the reservoir during depletion, and subsequent elastic expansion during injection generating a hysteretic response in the vertical stress. This change represents a reduction in total vertical stress from the start of depletion to the end of injection.
- The horizontal stress change during injection is also similar between cases, but varies depending upon the position in the reservoir, reservoir Poisson's ratio, and reservoir and overburden stiffness.
- Total horizontal stresses increases during injection, and is the same between all initial stress ratio cases due to convergence. The result is higher effective horizontal stress at the end of injection compared to the start of depletion for the low and medium initial stress ratio cases, but lower horizontal effective stresses in the high initial stress ratio case.
- Recovery of total horizontal stress is lower at the edge of the reservoir where greater plastic strains are observed, and in other areas of the reservoir where similar conditions occur, for example at the reservoir fault overburden juxtaposition. The result is lower effective horizontal stresses at the edge of the reservoir at the end of injection compared to the centre.
- The change in material parameters of the model changes the slope of the p'-q stress path in a similar manner to the elastic depletion stage, with consequent differences in vertical and horizontal effective stresses. Increasing reservoir stiffness reduces the horizontal and vertical effective stresses at the end of depletion and flattens the p'-q path. Reducing the overburden stiffness results in a reduction of stress arching, higher vertical effective stress and higher q stress at the end of injection but a similar horizontal effective stress. This leads to a flatter stress path and a reduction in fracture pressure compared to the initial fracture pressure, this is important for reducing the fracture pressure for CO_2 injection. An increase in Poisson's ratio leads to lower horizontal stresses at the end of injection and a flatter stress path, as horizontal stress decreases more with decreasing vertical stress.
- Stress changes in the overburden during injection show a further reduction in horizontal stress with injection, in addition to the reduction observed during depletion. This shows that the stress state tends towards shear failure throughout depletion and injection. This behaviour appears to represent the stress transfer mechanism of horizontal stress reduction in the overburden with horizontal stress reduction in the reservoir. The magnitude of horizontal stress reduction is however not close to failure and does not present a risk in the model. Further work on the

controls on this mechanism is important for seal security as it represents a seal failure risk.

4.5.1.5 *Stress Path Hysteresis and Stress Path Parameters*

- All stress paths exhibited hysteresis due to the plastic deformation stage. This represents a change in the fracture pressure in all cases, which is a critical consideration for CO_2 storage.
- For fracture pressure hysteresis to occur in the model the stress path had to follow a trajectory which resulted in a lower horizontal effective stress in the reservoir during injection, compared to depletion. This would yield a fracture pressure hysteresis factor <1, indicating a reduction in fracture pressure, and a risk of CO_2 leakage, and constraint of CO_2 storage capacity.
- The shape of the yield envelope means that for a $f_{ph} = 1$, i.e. no change in fracture pressure, p' must decrease with decreasing q to maintain the same increment of p' stress from the yield envelope.
- To produce a lower fracture pressure during injection the stress path has to change so that the increment of p' stress from the yield envelope is smaller at the end of depletion. Changes in the stress path trajectory which promote fracture pressure hysteresis with lower fracture pressures after injection are:
  - flattening of the stress path, particularly in the injection stage and;
  - overturning of the stress path where the q stress increases during plastic deformation transition.
- Overturning of the stress path is linked to flattening, and reflects the evolution of the trajectory with extreme flattening.
- Factors that promote a flattened trajectory in the models are an increase in Poisson's ratio of the reservoir material, increase in reservoir stiffness, deformational effects at the margin of the reservoir, and a reduction in stress arching, which in this model is promoted by a reduction in stiffness in the overburden.
- A very extensive reservoir may produce even less stress arching than observed with the softer overburden, and would represent the 'worst case' stress arching for fracture pressure hysteresis, reduced fracture pressures and CO_2 injection.
- Faulting in the sealed model shows an increase in the stress arching which has shown to reduce fracture pressure hysteresis, and limit the reduction in fracture pressure at the end of injection.
- Factors that lead to an overturned trajectory in the model are an increase in the initial stress ratio in the model, and a very high Poisson's ratio and reservoir stiffness.
- The plastic stage of depletion is significant in the overall behaviour of the stress path, and controls on the plastic stress path, for example factors affecting the gradient of the stress path, are an important area for further investigation.

4.5.2 **Fracture Pressure Hysteresis**

- Comparison of the modelled stress paths to examples in the literature shows that similar γ_h values are observed for depletion in the field and the model with high initial stress ratios. The modelled stress paths with the high initial stress ratio therefore provide a likely analogue for the Ekofisk field and the field presented by Santarelli et al. (1998) for depletion. The injection stages of the models and the Santarelli et al. (1998) field can then be compared in terms of the extent of fracture pressure hysteresis observed.
- The high stress ratio case has a γ_h of 0.8 for depletion, and 0.6 for injection, and so does exhibit fracture pressure hysteresis with a lower horizontal stress at the end of depletion. However, the injection γ_h is much higher than the 0 value suggested by Santarelli et al. (1998).
- Data from the model shows that injection fracture pressures are 89% of the depletion pressures in the centre of the model, and 81% at the edge of the reservoir.
- Comparison with the 0 γ_h injection stress path from the literature shows that the modelled stress paths only reproduce 19% of the hysteresis observed in the literature in the centre of the reservoir and 35% at the margin of the reservoir.
- The modelled stress paths show that with the same parameters the initial stress ratio at which the onset of fracture pressure hysteresis will be observed is K = 0.85 in the centre of the reservoir and K = 0.8 at the margin.
- The modelling shows that fracture pressure hysteresis is feasible with consideration only of standard mechanical parameters and plastic deformation, and this therefore represents a shear failure risk for injection, and a capacity limiting factor in CO_2 storage projects.
- The modelling also shows that the behaviour observed by Santarelli et al. (1998) is not fully recreated by the modelling, and other factors must be sought to explain the additional reduction in fracture pressure observed.
- Thermo-elastic stress generation through the injection of cold fluids is suggested as a controlling factor for fracture pressure hysteresis by Santarelli et al. (2008) and the potential magnitude of temperature effects can be estimated for the modelled results.
- Estimates of the magnitude of thermo-elastic stresses in the model were produced using an approach from the literature for CO_2 injection and this suggests that thermo-elastic tensile stresses up to -9.9 MPa are feasible with the material parameters used in the models. This is comparable to estimates of between -6.9 MPa and -22.2 MPa for the field data from Santarelli et al. (2008).
- The modelled magnitudes of thermal tensile stress development would be sufficient to reduce the horizontal stress to a level consistent with a 0 γ_h stress path assuming a direct reduction in horizontal stress. However, coupled geomechanical modelling

would be required to determine the true evolution of stress in the model with temperature effects.

- Temperature effects also have the potential to induce fracture pressure hysteresis in stress paths with lower initial stress ratios, and may also have more significant impacts in the shale overburden which has a different coefficient of thermo-elasticity. Implementation of thermal effects into coupled model would therefore provide an interesting area for further research for CO_2 injection risk modelling both for capacity estimates and seal security.
- Fracture pressure hysteresis is observed by Santarelli et al. (1998) in other parts of the field which has a lower γ_h and is linked to a high level of faulting in the area. This may suggest that a lower initial stress ratio occurs if material parameters are the same and the modelled paths are comparable. This observation suggests that the temperature effect may dominate in the field, as the modelled results show that the injection path is unlikely to have such a low γ_h upon injection and will only contribute a small proportion of hysteresis at high initial stress ratios.
- Heating of CO_2 prior to injection would prevent a solution to fracture pressure hysteresis that is induced by low temperatures, but this would not be sufficient to prevent fracture pressure hysteresis occurring mechanically in reservoirs with high initial stress ratios, margins and sharp geometrical contacts in the reservoir and overburden are particularly at risk.
- Additional investigation into more complex geometries, and more natural reservoir formations could provide insights into the realistic level of marginal reservoir effects on stress path hysteresis.
- Increased stress arching in extensive reservoirs should also be investigated as this would induce stress arching above the level observed with the softer overburden. The overburden stiffness was also not reduced for the high initial stress ratio case due to time constraints, this would contribute further to fracture pressure hysteresis.
- Faulting did not appear to have a significant impact on the stress paths in the model, however this is suggested as a controlling factor on stress paths in the literature, further investigation into this aspect may also be important.

4.5.3 **Fault Behaviour**

- Faults with different frictional strength and sealing parameters were included in the models, there is little observable difference between stress paths with different fault parameters, except for the compartmentalisation observed with the sealing faults, which increases stress arching in the smaller compartments.
- Movement on the faults appears to be restricted to small sections along the fault, and does not represent ubiquitous sliding along the fault. The fault movement is interpreted as accommodative sliding developed due the deformation in the overburden and reservoir.

- Potential failure of the material in and around the fault was only observed in the lowest initial stress ratio cases, where compressive stress on the fault is lower. Potential failure was observed at certain points during both depletion and injection, in both the reservoir and the overburden in some of the models, and consisted of failure of the frictional fault criteria and the material shear failure envelope. This indicates potential for leakage from the reservoir into the overburden in the worst case.
- The main difficulty in assessing failure is the assumption of a zero-thickness fault, as failure within and surrounding the fault is not explicitly represented. Nevertheless, analyses in the literature suggest the behaviour of such fault representations is robust in terms of the overall model behaviour.
- Although the faults do not appear to be important for the stress paths in the model, significant faulting is linked to changes in the stress path in the literature and represents a similar stress path to the models with a lower initial stress ratio. Further work should focus on investigating if more significant fault movement can influence the stress path, and how larger scale faulting can influence the initial stress state in and around reservoirs.

4.5.4 **Fluid Flow Simulation**

- Comparison of coupled and non-coupled models shows that the simulation results for the coupled model can be matched for production using a simple fluid flow model and an adjusted compressibility. However, matching of both production and injection stages requires derivation of pore volume multiplier tables to accurately model the reduction in pore volume during depletion, which is critical for matching the injection of CO_2.
- Derivation of PVM tables for the models from the porosity decrease in the coupled model shows that two different PVM tables are required for the sealing and non-sealing cases. This is due to a different level of stress arching between the models, with both the elastic and plastic stages of the PVM table showing different compressibility value.
- The matched modelling also shows that an assumption of irreversible porosity decrease is a sufficient assumption for the injection stage, and significant porosity increase with injection is not observed.
- Comparison of the coupled and non-coupled models illustrates the importance of coupled modelling for CO_2 storage, particularly where plastic deformation and stress arching may have occurred during the depletion stage of the reservoir. Only two material types are used in this thesis, but much greater complexity could be expected in natural reservoir.
- Workflows to reproduce coupled results with flow simulators are presented in literature, however the key point is that these methods require coupled tuning runs to calibrate the models. Additionally, these models do not include information on

fault movement, or overburden stresses and cannot produce seismic data. This highlights the potentially important role for coupled modelling for CO_2 injection into depleted reservoirs.

4.5.5 **Seismic Data**

- Modelling of the P-wave velocity in the reservoir using Gassman's fluid substitution shows that there is a significant difference between the non-coupled model with and without a PVM table, on the order of 100 m/s in some regions of the model. However, the actual contribution to this difference from the modified porosity is small, and is mainly due to the different volumes of fluids modelled in each case.
- The modelling shows that there are also small difference between the model with a PVM table and the coupled model, as the coupled model includes a small porosity increase during injection, which decrease P-wave velocity. The flow simulator is not capable of incorporating hysteretic PVM tables, so this aspect of the seismic change with injection cannot be modelled.
- Analysis of the modelled seismic velocities in the overburden during depletion shows a consistent response between the models with different reservoir properties. This suggests the seismic response in the overburden during depletion is mainly controlled by the overburden parameters and resultant level of stress arching. The seismic velocities are similar to those modelled in the literature.
- The seismic response in the injection stage is dependent upon the reservoir material properties, and is also weaker than the injection stage, with changes of less than 20 m/s, compared to changes up to 600 m/s during depletion.
- Lower reservoir stiffness produces a positive change in P-wave velocities in the over, under and sideburden surrounding the reservoir, whereas higher stiffness produces the same, but weaker, pattern as depletion, with a decrease in velocity above the reservoir and increases at the sides. The difference is related to the different relative magnitudes of horizontal and vertical stress in the overburden cause by the deformation of the reservoir in each case. In the softer reservoir vertical and horizontal expansion is larger during deformation which produces higher vertical stress in the overburden and higher horizontal stress in the sideburden which controls the observed seismic velocity change.
- The simple analysis shows that in this case with significant plastic deformation and stress arching the injection stage seismic response is more complex than the depletion stage and also has a weaker response. This would mean changes would be harder to detect if seismic data was used for monitoring purposes. Further work should examine a greater range of parameters, including those of the overburden, and the initial stress ratios which are seen to be important for the stress path. Consideration of anisotropic parameters would provide more information on the anisotropic stress changes, which are seen to be important for the injection stage.

5 Conclusions and Further Work

The main findings from this thesis are detailed in the following section (chapter-by-chapter), followed by suggestions for areas of further research that have been identified from the work carried out.

5.1 Conclusions

5.1.1 CO_2 Storage, Risks, and Uncertainty

- Geological storage of CO_2 is complex, carries many risks and is highly uncertain. A storage project requires a secure trapping mechanism, usually a seal, good flow properties to allow large volumes of CO_2 to be injected quickly and a secure long-term ability to securely contain CO_2. It is also important to be able to verify the storage project is performing as expected. The nature of CO_2 storage in geological formations means that geological variability is important, and this aspect can affect all aspects of the project.
- Many of the risks for CO_2 storage are those common to the oil industry and relate to the determination of fluid flow properties, sealing capacities of cap rocks and leakage pathways. Depending upon the data availability and natural geological variability, these aspects can present significant risks. Storage capacity estimation is one of the primary risks, as it is often impacted by other risk factors such as leakage pathways.
- CO_2 storage also presents problems which are often less important for conventional oil and gas extraction projects due to elevated pressures and stresses from the injection of large volumes of CO_2 and stringent requirements for leakage security verification.
- The Bunter Saline Aquifer is a potentially major proportion of CO_2 storage capacity for the UK, providing up to 55% of estimated capacity. However, capacity estimates in the literature may represent a significant overestimation as they do not take extensive account of the potential variability of the parameters that will control capacity, and so further simulation modelling is carried out in this thesis.
- Brine extraction is discussed in the literature as a method to increase capacity in reservoirs where the flow properties, boundary conditions and other factors may inhibit CO_2 injection due to pressure build-up. Therefore, assessment of brine extraction in capacity estimation models is identified as a research goal in this thesis to determine the effectiveness of brine extraction in increasing capacity for the Bunter aquifer.
- The fracture pressure is an important limiting factor on the capacity of a storage reservoir, and also compromises the security of storage if breached for an extensive period. In the literature, there is evidence to suggest that the fracture pressure may be lower during injection than for an equivalent reservoir pressure during depletion.

This is known as fracture pressure hysteresis. Clearly, this is an important consideration for CO_2 storage, which may rely on injection into abandoned storage reservoirs for low risk storage capacity. Modelling is therefore carried out in this thesis to constrain the controls on fracture pressure hysteresis, and the behaviour of the reservoir stress path during CO_2 storage in abandoned hydrocarbon reservoirs.

5.1.2 UK Storage Potential – Bunter Saline Aquifer

- Using a generic pressure cell model of the Bunter Saline Aquifer (where capacity is controlled by the build-up of pressure to the fracture pressure limit), capacity estimates of between 2.4 and 11.3 Gt CO_2 were made for the aquifer. For a similar set of cases with brine extraction the capacity was estimated at between 2.4 and 19.69 Gt CO_2 . A comparable pressure model in the literature predicted a capacity 2.4 Gt CO_2 larger, due to the differing assumptions on model parameters, highlighting the change in capacity with variability in model assumptions. Without brine extraction, the modelled capacities were lower than initial static estimate in the literature.
- Brine extraction in the generic model can significantly increase capacities by almost 75%. However, this requires double the number of wells. Optimisation shows that there is also a critical limit below which it is inefficient to consider brine extraction, this corresponds to a maximum spacing of 23 – 25 kilometres. Comparison with a structurally realistic model in the literature also suggests that brine extraction may be less effective in the Bunter aquifer, as the main control on capacity is pressure build up in specific structures.
- A more realistic model of the Bunter aquifer was constructed to assess capacity with variation in the geological model, and with increasing numbers of injection wells. With few wells, the injection fracture pressure was critical and the injection rate was maximised, with increasing well numbers the fracture pressure in structural high points became critical and well injection rates were reduced. The rate of capacity increase with well numbers is a power law relationship, however this appears to break down at a threshold when well injection footprint interfere with close well spacing.
- The realistic model shows the evolution of pressure throughout the aquifer during and after injection. The time lag between the end of injection and the peak pressure point in the model is between 6 and 136 years, and the critical pressure peak is often a large distance from the injection region. This highlights the significant scale of the monitoring project involved in such an injection activity in order to avoid fracture pressure failure. Monitoring of the fracture pressure can only be achieved using down hole measurements, and the fracture pressure may also change with pore pressure. This means that monitoring will be difficult and potentially impractical, due to the large number of expensive measurements required over a large area. This highlights the necessity of producing accurate models to target the

monitoring activity to the most at risk areas, and the need for the development of a monitoring strategy. Due to the inherent uncertainty in fracture pressures and difficulty in monitoring the fracture pressure it is also likely that a remediation strategy will need to be devised in case of fracture pressure failure. The potential risk is that fracturing will occur in the aquifer and propagate into the overburden in areas where CO_2 or hydrocarbons are trapped causing leakage, and so remediation will need incorporate a strategy for mitigating this risk.

- Variation of the realistic model's permeability and comparison of a change in global and vertical permeability showed a significant decrease with both a global and vertical reduction in permeability. For cases with 12 -24 wells the estimated capacities of the model were the same with a 20 mD global permeability and a k_v/k_h ratio of 0.001 (0.1 mD vertical permeability). This suggests that a reduction in vertical permeability, which is often not apparent, can be as significant as a significant global reduction in permeability. The vertical permeability is important in the Bunter model as capacity is reliant upon vertical expulsion of brine from a seabed outcrop.
- Variation of the realistic model's compressibility produced the largest range of capacity estimates with varying numbers of wells. A 1 x 10^5 bar^{-1} change in compressibility is associated with a 150 Mt CO_2 change in the capacity of the model, which is equivalent to the CO_2 output of UK fossil fuel power stations in one year. Modelling also shows that additional wells have decreasing effectiveness with reducing compressibility. The model also only uses a single value of compressibility, in reality this varies significantly even over a single reservoir, due to material and structural differences, such as development of stress arching and plastic deformation.
- The boundary conditions of the model assume a seabed outcrop and closed marginal boundaries, however, there is little evidence to support the flow properties of the seabed outcrop or suggest that the marginal boundaries are completely sealed. Variation of the boundary conditions shows up to 36% reduction in capacity with a closed outcrop and an 18% increase by adding two open margins, a 15% decrease in capacity is observed with only the marginal boundaries open. This highlights the reliance of the model on the seabed outcrop for the storage capacity.
- With the model results extrapolated to the full area of the Bunter aquifer a capacity between 3.1 and 8.7 Gt CO_2 is predicted, this corresponds to between 19.9 and 56 years of total UK fossil fuel emissions at 2012 levels, compared to 90 years with static capacity estimates.
- Comparison between all of the methods of capacity estimation shows that comparable pressure cell estimates are 2 - 3 times higher than the estimates form the realistic model, and that the pressure cell estimates are in turn 1.4 to 1.8 times smaller than the static initial capacity estimate in the literature. The resulting capacity estimates with increasing model sophistication show that the contribution

of the Bunter Aquifer to overall estimated UK storage potential could be reduced by up to 40%.

- Evidence from the literature suggests a lower fracture pressure than that used in the structure based modelling is likely in the Bunter Aquifer, this could lower capacity estimates from the more realistic model to as low as 2.5 Gt CO_2 . Fracture pressure is likely to vary throughout the aquifer, and may vary due to fault reactivation, as modelled in the literature, and other factors such as pore pressure, this highlights the work highlights the potentially very significant variability of capacity with changes in fracture pressure.
- The significant difference in the capacity estimates between the pressure cell model and the more realistic model arises from the fundamental difference in the assessment of failure in the model, with the realistic model prone to failure in the structural highs, whereas the pressure cell model is purely fracture pressure dependent. This conforms to predictions of decreasing capacity with increasing model sophistication in the literature.

5.1.3 Modelling Stress Path and Fracture Pressure Hysteresis

- The stress path of all of the models is characterised by elastic deformation during injection and initial depletion, and significant plastic deformation during depletion, which is accompanied by significant changes in stresses during convergence to a similar plastic deformation trajectory for all the models. Stress arching is observed in all cases and all of the stress paths show a hysteretic trajectory with different final stresses compared to the initial stress state. This implies a different fracture pressure in each case, which is a critical consideration for CO_2 storage.
- The factors controlling the stress path are a complex interaction of the overburden and reservoir, the material properties, initial model stresses, model geometry and the flow and mechanical properties of the faults throughout all stages of the stress path. Understanding this interaction will be critical for accurately assessing CO_2 storage in depleted hydrocarbon reservoirs.
- The aim of the modelling was to determine the controls on producing a lower fracture pressure during injection, compared to depletion, which will represent a significant leakage risk for CO_2 storage, and perhaps more critically lower the injection capacity of the reservoir. A lower fracture pressure manifested in the stress path as a flattening, either of the whole stress path or the injection stage, or a complete ‘overturning’ of the stress path such that final p’ is lower. Factors that promoted a flattening of the stress path in these models were an increase in reservoir Poisson’s ratio, increase in reservoir stiffness, deformational effects at the flat contact at the margin of the reservoir, and a reduction in stress arching. The reduction in stress arching arises from reduced overburden stiffness, although a more extensive reservoir would also have the same effect, faulting has been shown to increase stress arching, and reduce fracture pressure hysteresis. Factors that

lead to complete overturning of the stress path in this model were an increase in the initial stress ratio of the model, and extreme value of the Poisson's ratio and reservoir stiffness. The high initial stress ratio stress path exhibited overturning when convergence to the plastic deformation stress path increased q stress in the model, typically this was for initial stress ratios above 0.8.

- The most significant reductions in fracture pressure observed in the model were produced in the model with the highest initial stress ratio with an overturned stress path. This is a similar stress state to that found in many North Sea fields. Fracture pressures during injection were 89% of those during depletion in the centre of the model, and 81% at the margins of the model.
- Stress changes in the overburden showed a reduction in horizontal stress both during depletion and to a lesser extent during injection. The magnitude of horizontal stress decrease was greater with increased reservoir stiffness. This type of stress change promotes failure in the overburden, and whilst not the direct focus of this study represents a risk for CO_2 storage through cap rock failure.
- Based on the modelling of fracture pressure hysteresis with the different stress paths in the models the extent of fracture pressure hysteresis was compared to the field example of fracture pressure hysteresis form a North Sea field in the literature. The most comparable model to the North Sea example, with an initial stress ratio of 0.9, was also the worst case in the models indicating this is a potential risk for storage of CO_2 in the UK North Sea. However, the observed fracture pressure modelling only represented between 19 – 35% of the hysteresis observed in the literature, with the higher value found at the margin of the reservoir.
- Temperature-induced stresses were identified as an important factor in stress path hysteresis in the literature example through the injection of cold fluids, and this probably explains the greater level of hysteresis observed in the field example. Calculation of potential stress impacts from injection of cold CO_2 suggests that sufficiently significant components of tensile stress could be generated to match the hysteresis observed in the field, based on the models in this thesis, this. However, the results also show that if heating was used to increase the temperature of CO_2, there could remain a fundamental level of fracture pressure hysteresis under the right conditions.
- Faults in the model had little observable impact on the stress path other than the slight increase in stress arching observed in the sealing fault case, where the compartmentalisation increased stress arching due to a less extensive reservoir. The mechanical properties of the fault seemed to have no impact in the overall stress path. Potential failure was observed along the fault in the reservoir and overburden but only in the lowest initial stress ratio case, in this case the low friction fault promoted the most failure.
- Analysis of the fluid flow simulation linked to the coupled model shows that where plastic deformation and stress arching are important, coupled modelling is likely to

be an important tool for modelling CO_2 injection, as the correct final pore volume after depletion is important in correctly calculating CO_2 injection. Non-coupled models will also be unable to provide information on stress in the overburden, seismic data and potential fault movement.

- Modelling of the P-wave velocity in the flow model shows that the change in porosity is a significant parameter in terms of the effect of fluid flow and saturation changes, but that the actual change in porosity is less important in the calculation of velocity. The non-coupled model also produces slightly different velocities during injection as it cannot model small porosity increase after depletion. The results highlight the necessity of accurately modelling the coupled change in fluid volumes with plastic porosity reduction to determine the correct seismic profile of CO_2 injection.
- Analysis of the modelled P-wave velocities in the overburden highlights the similarity in stress arching between the models during depletion, but also shows that the seismic response during injection varies with reservoir material parameters. The change in P-wave velocity during injection is small, but above and below the reservoir changes from a small increase with a low stiffness reservoir to a small decrease with a high stiffness reservoir. This is related to a more significant decrease in horizontal stress with increasing reservoir stiffness and plastic deformation in the reservoir, and is an important consideration for CO_2 storage in depleted hydrocarbon reservoirs where plastic depletion may have taken place.

5.2 Further Work

5.2.1 UK Storage Potential – Bunter Saline Aquifer

- There is little publicly available exploration data for the Bunter aquifer, and the seismic data used to make the original model is sparse, this makes further refinements to the model difficult. However, possible refinements could include analysis of the variability in flow parameters on a more detailed scale. For example, by using the probability distribution of permeability measurements from field analogues within the Bunter sandstone probabilistic models could be developed. Alternatively, a more detailed assessment of potential vertical permeability variations in the Bunter aquifer, using outcrop measurements and workflows in the literature could refine the impact of vertical permeability.
- Compressibility has also been shown to have a large impact on predicted CO_2 storage capacities, however all of the estimates in this modelling and the literature are based on typical values from the literature. Measuring real compressibilities in the laboratory will be important for constraining the true compressibility in the Bunter aquifer. Even with core measurements the compressibility is likely to vary across the aquifer, and also relies on accurate extrapolation from laboratory to field scale parameters, further work should assess both variability and upscaling of compressibility measurements.

- The fracture pressure has also been shown to be a highly uncertain parameter, simple geomechanical modelling based on the frictional properties of faults was used to produce a much lower estimate of fracture pressure in the literature. This aspect could be assessed further using finite element modelling of the potentially reactivated faults to further investigate this potential risk. More broadly the variability in the fracture pressure should also be investigated, for example the change in fracture pressure with pore pressure. This may provide a further application for coupled geomechanical-fluid flow modelling that has been applied to fracture pressure in Chapter 4.
- One of the risks identified in the modelling is the potential lag between the end of injection, peak pressures throughout the model, and the potential for the fracture pressure being exceeded after the end of injection, due to the uncertainty and difficulty in measuring the fracture pressure. Monitoring techniques for the fracture and pressure should be investigated as this will be critical in ensuring storage security. Currently modelling provides the best option through predictive modelling, however verification tools to ground truth the model, and monitor potential fracturing in the field will be required to ensure the fracture pressure will not be exceeded. The delayed and uncertain nature of the risk means that switching off injection to control fracturing is not possible and so techniques for remediation to reduce pressure in risk prone areas should also be investigated, as these will be required if failure occurs. Further work should also investigate the likely conditions for fracture closure in the overburden material, as this will be an important component of a remediation strategy, if fracturing initiates from the aquifer to the overburden, it is important to understand how this can be mitigated.
- The injection strategy in the structure-based model is quite simple, refinement of this aspect for the whole model (for example multiple wells in structures or staged injection strategies) may show improvement in the potential capacity.
- Brine extraction is only likely to be beneficial if targeted at specific failure points within the model, or within the injection structures, modelling of brine extraction scenarios in the more realistic model could provide more information on the potential for capacity increase using brine extraction.

5.2.2 **Modelling Stress Path and Fracture Pressure Hysteresis**

- Stress path hysteresis is strongly affected by convergence to a single plastic deformation trajectory – further investigation of this aspect should be considered. The plastic material parameters have been derived from a generic set of data. Investigation of specific examples from the UK North Sea would provide further understanding of the potential for hysteresis and plastic deformation.
- The effects deformation at the edge of the reservoir are seen to be important in producing fracture pressure hysteresis. Analysis of the impact of different edge

geometries on fracture pressure changes would provide a better understanding of this aspect.

- The development of a full-field geomechanical model derived from real field data with a much more complex geometry was attempted during work on this thesis. The development of a functioning model was ultimately unsuccessful, this was due to fundamental problems with developing a 'water-tight' mesh from the data. The development of a water-tight mesh is essential for construction of a finite element model, where all the nodes in a multi-layered geometrically complex mesh must be connected. The methods used to build the mesh were highly time intensive, as the work flow developed involved manual manipulation of the mesh, over 6 months of project time were used building the mesh. Development of a full-field would give further insight into the geometric effects on the fracture pressure, which has been shown to be an important aspect of the fracture pressure modelling in this thesis.
- This thesis has mainly focussed on reservoir stress paths, however important stress changes are observed in the overburden, specifically horizontal stress reduction during injection. Further analysis of a range of overburden material parameters, including the investigation of potential for plastic deformation in the overburden, should be carried out. This should include assessment of the potential onset, or re-opening of fractures in the overburden with reducing horizontal stress in the model.
- Temperature effects on the stress path appear to be important for producing lower fracture pressures with fracture pressure hysteresis. To accurately model the impact of the injection of cold CO_2 in both the reservoir and overburden thermo-elastic stress calculations should be implemented in the coupled modelling workflow.
- Seismic datasets were produced for each run analysed in the modelling, however due to time constraints only simple analyses were conducted on a limited number of results. Further investigation of this dataset would provide more information on the changes in seismic response of the depletion-injection cycle, and any changes that may be characteristic of fracture pressure reduction. The seismic estimates should also be calibrated to reflect realistic data.

5.3 **Summary of Findings**

This thesis has assessed various aspects of CO_2 storage in the UK in both saline aquifers and depleted hydrocarbon reservoirs. The main implications for CO_2 storage from the work are:

- The significant uncertainty and potential reduction that can be demonstrated in UK capacity estimates due to geological variability.
- The potentially variability shown in the fracture pressure, with conditions most favourable to fracture pressure reduction analogous to those found in some fields in the UK North Sea. This has implications for leakage, but is also intrinsically related to storage capacity, as it is a control on injection pressures.

- The identification of the risk of leakage and fracturing in the storage unit and overburden across a wide area for a significant period after the storage project has stopped operating for a saline aquifer such as the Bunter.

The work shows that further work on constraining the fracture pressure, compressibility, permeability and boundary conditions is necessary to more accurately constrain the estimates of the capacity. The capacity estimates are critical as the entire scale and scope of carbon capture projects is based on the ability to find sufficient storage volume to allow commercially viable lifetimes for CCS projects. The risk of breaching the fracture pressure due to stress path hysteresis is not only important for capacity estimation, but also for ensuring leakage does not occur if the pressure is overestimated. Although leakage through fracturing is likely to be self-sealing if pore pressures are decreased, and therefore small-scale, it does carry public perception risks, and demonstrates a poor understanding of the storage system to the regulatory authorities. With some of the aspects of the storage project assessed purely with modelling analysis, such as future pore and fracture pressure evolution, poor understanding of the storage system could invite serious regulatory penalties for a project. Post-injection leakage risks also identify the need for investigation into monitoring of fracture pressure and pore pressure changes in a large aquifer over a long period of time, and the need to develop a strategy to remediate potential fractures.

References

ACEP. (2009). "Alaska Energy Wiki." Retrieved 23/09/2013, 2013, from http://energy-alaska.wdfiles.com/local--files/natural-gas-as-a-resource/natural_gas172.jpg.

Adams, E. E. and Caldeira, K. (2008). "Ocean Storage Of CO_2." Elements **4**(5): 319-324.

Addis, M. A. (1997). "The Stress-Depletion Response of Reservoirs." SPE International **SPE 38720**.

Ahmed, T. (2010). Reservoir Engineering Handbook (4th Edition). Burlington, MA, Gulf Professional Publishing.

Al-Hinai, S., Fisher, Q. J., Al-Busafi, B., Guise, P. and Grattoni, C. A. (2008). "Laboratory measurements of the relative permeability of cataclastic fault rocks: An important consideration for production simulation modelling." Marine and Petroleum Geology **25**(6): 473-485.

Al-Zadjali, R. J. M. (2011). The Impact of Steam Injection on Fracture Permeability In Carbonate Reservoir. PhD, University of Leeds.

Allan, U. S. (1989). "Model for hydrocarbon migration and entrapment within faulted structures." AAPG Bulletin **73**: 803-811.

Angus, D. A., Kendall, J. M., Fisher, Q. J., Segura, J. M., Skachkov, S., Crook, A. J. L. and Dutko, M. (2010). "Modelling microseismicity of a producing reservoir from coupled fluid-flow and geomechanical simulation." Geophysical Prospecting **58**(5): 901-914.

Angus, D. A., Verdon, J. P., Fisher, Q. J. and Kendall, J.-M. (2009). "Exploring trends in microcrack properties of sedimentary rocks: An audit of dry-core velocity-stress measurements." Geophysics **74**(5): E193-E203.

Angus, D. A., Verdon, J. P., Fisher, Q. J., Kendall, J. M., Segura, J. M., Kristiansen, T. G., Crook, A. J. L., Skachkov, S., Yu, J. G. and Dutko, M. (2011). Integrated fluid-flow, geomechanic and seismic modelling for reservoir characterisation. CSEG Recorder. Calgary, Canadian Society of Exploration Geophysicists. **May 2011**.

Angus, D. A., Verdon, J. P., Kendall, J. M., Fisher, Q. J., Segura, J. M., Skachkov, S., Dutko, M. and Crook, A. J. L. (2008). Influence of fault transmissibility on seismic attributes based on coupled fluid-flow and geomechanical simulation. 2008 SEG Annual Meeting. Las Vegas, Nevada, SPE International. **2008-1600**.

Arts, R., Eiken, O., Chadwick, A., Zweigel, P., Van der Meer, L. and Zinszner, B. (2004). "Monitoring of CO< sub> 2</sub> injected at Sleipner using time-lapse seismic data." Energy **29**(9): 1383-1392.

Ayan, C., Colley, N., Cowan, G., Ezekwe, E., Wannell, M., Goode, P., Halford, F., Joseph, J., Mongini, A. and Pop, J. (1994). "Measuring permeability anisotropy: The latest approach." Oilfield Review **6**(4): 24-35.

Bachu, S., Bonijoly, D., Bradshaw, J., Burruss, R., Holloway, S., Christensen, N. P. and Mathiassen, O. M. (2007). "CO2 storage capacity estimation: Methodology and gaps." International Journal of Greenhouse Gas Control **1**(4): 430-443.

Bandyopadhyay, K. (2009). Seismic anisotropy: Geological causes and its implications to reservoir geophysics.

Barton, C. A., Zoback, M. D. and Moos, D. (1995). "Fluid flow along potentially active faults in crystalline rock." Geology **23**(8): 683-686.

Begg, S. H., Carter, R. R. and Dranfield, P. (1989). "Assigning Effective Values to Simulator Gridblock Parameters for Heterogeneous Reservoirs." SPE Reservoir Engineering **4**(4): 455-463.

Bennion, B. D. and Bachu, S. (2005). "Relative Permeability Characteristics for Supercritical CO_2 Displacing Water in a Variety of Potential Sequestration Zones in the Western Canada Sedimentary Basin." SPE International **SPE 95547**.

Bennion, B. D. and Bachu, S. (2008). "Drainage and Imbibition Relative Permeability Relationships for Supercritical CO_2/Brine and H_2S/Brine Systems in Intergranular Sandstone, Carbonate, Shale, and Anhydrite Rocks." SPE International **SPE 99326**.

Bentham, M. (2006). "An assessment of carbon sequestration potential in the UK–Southern North Sea case study." Tyndall Centre for Climate Change Research and British Geological Survey. Keyworth, Nottingham, UK: Kingsley Dunham Centre.

Berg, R., R. (1975). "Capillary Pressures in Stratigraphic Traps." AAPG Bulletin **59**(6): pp.939-956.

Bickle, M., Chadwick, A., Huppert, H. E., Hallworth, M. and Lyle, S. (2007). "Modelling carbon dioxide accumulation at Sleipner: Implications for underground carbon storage." Earth and Planetary Science Letters **255**(1-2): 164-176.

Bissell, R. C., Vasco, D. W., Atbi, M., Hamdani, M., Okwelegbe, M. and Goldwater, M. H. (2011). "A full field simulation of the in Salah gas production and CO2 storage project using a coupled geo-mechanical and thermal fluid flow simulator." Energy Procedia **4**: 3290-3297.

Bjørlykke, K. and Høeg, K. (1997). "Effects of burial diagenesis on stresses, compaction and fluid flow in sedimentary basins." Marine and Petroleum Geology **14**(3): 267-276.

Boade, R. R., Chin, L. Y. and Siemers, W. T. (1989). "Forecasting of Ekofisk Reservoir Compaction and Subsidence by Numerical Simulation."

Bradshaw, J., Bachu, S., Bonijoly, D., Burruss, R., Holloway, S., Christensen, N. P. and Mathiassen, O. M. (2007). "CO2 storage capacity estimation: Issues and development of standards." International Journal of Greenhouse Gas Control **1**(1): 62-68.

Brook, M., Shaw, K., Vincent, C. J. and Holloway, S. (2003). Gestco case study 2a-1: Storage Potential of the Bunter Sandstone in the UK sector of the southern North Sea and the adjacent onshore area of Eastern England. Keyworth, Nottingham, Brisith Geological Survey.

Brook, M., Shaw, K., Vincent, C. J. and Holloway, S. (2003). Storage Potential of the Bunter Sandstone in the UK sector of the southern North Sea and the adjacent onshore area of Eastern England. Keyworth, Nottingham, British Geological Survey.

Byerlee, J. D. (1968). "Brittle-ductile transition in rocks." Journal of Geophysical Research **73**(14): 4741-4750.

Cameron, T., Crosby, A., Balson, P., Jeffery, D., Lott, G., Bulat, J. and Harrison, D. (1992). "The geology of the southern North Sea. United Kingdom offshore regional report." British Geological Survey and HMSO, London.

Cappa, F. and Rutqvist, J. (2011). "Modeling of coupled deformation and permeability evolution during fault reactivation induced by deep underground injection of CO2." International Journal of Greenhouse Gas Control **5**(2): 336-346.

Cartwright, J., Huuse, M. and Aplin, A. (2007). "Seal bypass systems." AAPG Bulletin **91**(8): 1141-1166.

Cavanagh, A. J., Haszeldine, R. S. and Blunt, M. J. (2010). "Open or closed? A discussion of the mistaken assumptions in the Economides pressure analysis of carbon sequestration." Journal of Petroleum Science and Engineering **74**(1-2): 107-110.

Chadwick, A., Williams, G., Delepine, N., Clochard, V., Labat, K., Sturton, S., Buddensiek, M.-L., Dillen, M., Nickel, M., Lima, A. L., Arts, R., Neele, F. and Rossi, G. (2010). "Quantitative analysis of time-lapse seismic monitoring data at the Sleipner CO_2 storage operation." The Leading Edge **29**(2): 170-177.

Chadwick, R. A., Arts, R. and Eiken, O. (2005). "4D seismic quantification of a growing CO2 plume at Sleipner, North Sea." Geological Society, London, Petroleum Geology Conference series **6**: 1385-1399.

CO2CRC. (2010, 11/03/2010). "CO_2 long-term future after injection." Retrieved 22/04/2010.

CO2CRC. (2011). "Images &Videos - Storage images." Retrieved 08/07/2011, from http://www.co2crc.com.au/imagelibrary3/storage.php.

Company, M. (2008). Carbon Capture & Storage: Assessing the Economics, McKinsey & Company.

Cook, J., Nuccitelli, D., Green, S. A., Richardson, M., Winkler, B., Painting, R., Way, R., Jacobs, P. and Skuce, A. (2013). "Quantifying the consensus on anthropogenic global warming in the scientific literature." Environmental Research Letters **8**(2): 024024.

Cooke-Yarborough, P. and Smith, E. (2003). "The Hewett Fields: Blocks 48/28a, 48/29, 48/30, 52/4a, 52/5a, UK North Sea: Hewett, Deborah, Big Dotty, Little Dotty, Della, Dawn and Delilah Fields." Geological Society, London, Memoirs **20**(1): 731-739.

Coop, M. and Willson, S. (2003). "Behavior of Hydrocarbon Reservoir Sands and Sandstones." Journal of Geotechnical and Geoenvironmental Engineering **129**(11): 1010-1019.

Crawford, B. R., Sanz, P. F., Alramahi, B. and DeDontney, N. L. (2011). Modeling And Prediction of Formation Compressibility And Compactive Pore Collapse In Siliciclastic Reservoir Rocks, American Rock Mechanics Association.

Crook, A. J. L., Willson, S. M., Yu, J. G. and Owen, D. R. J. (2006). "Predictive modelling of structure evolution in sandbox experiments." Journal of Structural Geology **28**(5): 729-744.

Daley, T., Myer, L., Peterson, J., Majer, E. and Hoversten, G. (2008). "Time-lapse crosswell seismic and VSP monitoring of injected CO_2 in a brine aquifer." Environmental Geology **54**(8): 1657-1665.

Dean, R. H., Gai, X., Stone, C. M. and Minkoff, S. E. (2003). "A Comparison of Techniques for Coupling Porous Flow and Geomechanics." SPE International **79709-MS**.

DECC. (2013a). "Official Statistics: Provisional UK greenhouse gas emissions." Retrieved 22/11/2013, from https://www.gov.uk/government/collections/uk-greenhouse-gas-emissions.

DECC. (2013b). "UK carbon capture and storage: government funding and support." Retrieved 18/11/2013, 2013, from https://www.gov.uk/uk-carbon-capture-and-storage-government-funding-and-support#ccs-commercialisation-competition.

Dingwall, S., Furnival, S., Wright, S. and Morrison, D. (2013). Integrated Subsurface Evaluation of a Saline Aquifer Selected for CO2 Disposal. 75th EAGE Conference and Exhibition. London.

Doney, S. C., Fabry, V. J., Feely, R. A. and Kleypas, J. A. (2009). "Ocean Acidification: The Other CO2 Problem." Annual Review of Marine Science **1**(1): 169-192.

Dvorkin, J. and Nur, A. (1996). "Elasticity of high - porosity sandstones: Theory for two North Sea data sets." GEOPHYSICS **61**(5): 1363-1370.

Economides, M. J. and Ehlig-Economides, C. A. (2009). "Sequestering Carbon Dioxide in a Closed Underground Volume." SPE International **SPE 124430**.

Edwards, S., Meredith, P. and Murrell, S. (1998). "An Investigation of Leak-off Test Data for Estimating In-situ Stress Magnitudes: Application to a Basinwide Study in the North Sea." SPE/ISRM Rock Mechanics in Petroleum Engineering.

Evans, T. R. (1974). "North Sea Geothermal Gradients." Nature **247**.

Fatt, I. (1958). "Pore volume compressibilities of sandstone reservoir rocks." Journal of Petroleum Technology **10**(3): 64-66.

Felício Fuck, R., Bakulin, A. and Tsvankin, I. (2008). "Theory of traveltime shifts around compacting reservoirs: 3D solutions for heterogeneous anisotropic media." Geophysics **74**(1): D25-D36.

Fisher, Q. and Jolley, S. (2007). "Treatment of faults in production simulation models." Geological Society, London, Special Publications **292**(1): 219-233.

Fisher, Q. J., Casey, M., Clennell, M. B. and Knipe, R. J. (1999). "Mechanical compaction of deeply buried sandstones of the North Sea." Marine and Petroleum Geology **16**(7): 605-618.

Fisher, Q. J., Casey, M., Harris, S. D. and Knipe, R. J. (2003). "Fluid-flow properties of faults in sandstone: The importance of temperature history." Geology **31**(11): 965-968.

Fisher, Q. J., Harris, S. D., Casey, M. and Knipe, R. J. (2007). Influence of grain size and geothermal gradient on the ductile-to-brittle transition in arenaceous sedimentary rocks: implicaions for fault structure and fluid flow. The Relationship between Damage and Localization. Lewis, H. and Couples, G. D. London, Geological Society. **Special Publications 289:** 105-121.

Fisher, Q. J. and Knipe, R. J. (1998). "Fault sealing processes in siliciclastic sediments." Geological Society, London, Special Publications **147**(1): 117-134.

Fisher, Q. J. and Knipe, R. J. (2001). "The permeability of faults within siliciclastic petroleum reservoirs of the North Sea and Norwegian Continental Shelf." Marine and Petroleum Geology **18**(10): 1063-1081.

Fjær, E., Holt, R. M., Horsrud, P., Raaen, A. M. and Risnes, R. (2008). Petroleum Related Rock Mechanics. Amsterdam, Elsevier.

Flett, M., Gurton, R. and Taggart, I. (2004). "The Function of Gas-Water Relative Permeability Hysteresis in the Sequestration of Carbon Dioxide in Saline Formations." SPE International **SPE 88485**.

Fleury, M., Pironon, J., Le Nindre, Y. M., Bildstein, O., Berne, P., Lagneau, V., Broseta, D., Pichery, T., Fillacier, S., Lescanne, M. and Vidal, O. (2011). "Evaluating sealing efficiency of caprocks for CO2 storage: An overviewof the Geocarbone Integrity program and results." Energy Procedia **4**: 5227-5234.

Fossen, H. (2010). Structural Geology. Cambridge, Cambridge University Press.

Freeman, B., Harris, S. D. and Knipe, R. J. (2010). Cross-fault sealing, baffling and fluid flow in 3D geological models: tools for analysis, visualization and interpretation. Reservoir Compartmentalization. Jolley, S. J., Fisher, Q. J., Ainsworth, R. B., Vrolijk, P. J. and Delisle, S. London, The Geological Society of London. **347:** 257-282.

Gassmann, F. (1951). "Elasticity of porous media." Vierteljahrschrift der Naturforschenden gesellschaft in Zurich **96**: 1-21.

Geertsma, J. (1957). The Effect of Fluid Pressure Decline on Volumetric Changes of Porous Rocks, Society of Petroleum Engineers.

Gercek, H. (2007). "Poisson's ratio values for rocks." International Journal of Rock Mechanics and Mining Sciences **44**(1): 1-13.

Glennie, K. W., Ed. (1998). Petroleum Geology of the North Sea - Basic Concepts and Recent Advances. Oxford, Blackwell Science.

Goodarzi, S., Settari, A. and Keith, D. (2012). "Geomechanical modeling for CO2 storage in Nisku aquifer in Wabamun Lake area in Canada." International Journal of Greenhouse Gas Control **10**(0): 113-122.

Goodarzi, S., Settari, A., Zoback, M. and Keith, D. W. (2013). Thermal Effects on Shear Fracturing and Injectivity During CO2 Storage. Effective and Sustainable Hydraulic Fracturing. Bunger, A. P., McLennan, J. and Jeffrey, R., InTech.

Gough, C. and Shackley, S. (2005). An Integrated Assessment of Carbon Dioxide Capture and Storage in the UK, Tyndall Centre for Climate Change Research.

Griggs, D. and Handin, J. (1960). "Chapter 13: Observations on Fracture and a Hypothesis of Earthquakes." Geological Society of America Memoirs **79**: 347-364.

Guilbot, J. and Smith, B. (2002). "4-D constrained depth conversion for reservoir compaction estimation: Application to Ekofisk Field." The Leading Edge **21**(3): 302-308.

Hamilton, E. L. (1979). "Vp/Vs and Poisson's ratios in marine sediments and rocks." The Journal of the Acoustical Society of America **66**(4): 1093-1101.

Harper, M. L. (1971). "Approximate Geothermal Gradients in the North Sea Basin." Nature **230**.

Haszeldine, R. S. (2009). "Carbon Capture and Storage: How Green Can Black Be?" Science **325**(5948): 1647-1652.

Heinemann, N., Wilkinson, M., Pickup, G. and Haszeldine, R. S. (2010). CO_2 Storage Capacity in the Bunter Sandstone Limited by Local Pressure Development, UK Southern North Sea. Carbon Storage Opportunities in the North Sea. Geological Society, London.

Heinemann, N., Wilkinson, M., Pickup, G. E., Haszeldine, R. S. and Cutler, N. A. (2012). "CO_2 storage in the offshore UK Bunter Sandstone Formation." International Journal of Greenhouse Gas Control **6**: 210-219.

Henderson, C. (2006). "Ocean acidification: the *other* CO_2 problem." Retrieved 13/06/2011, from http://www.newscientist.com/article/mg19125631.200.

Herwanger, J. and Horne, S. (2009). "Linking reservoir geomechanics and time-lapse seismics: Predicting anisotropic velocity changes and seismic attributes." Geophysics **74**(4): W13-W33.

Hesse, M. A., Orr, F. M. and Tchelepi, H. A. (2008). "Gravity currents with residual trapping." Journal of Fluid Mechanics **611**: pp.35-60.

Hillis, R. R. (2001). "Coupled changed in pore pressures and stress in oil fields and sedimentary basins." Petroleum Geoscience **7**(4): 419-425.

Holloway, S. (2008). "Storage capacity and containment issues for carbon dioxide capture and geological storage on the UK continental shelf." Proc. IMechE **223**(A:1): 239-248.

Holloway, S., Vincent, C. J., Bentham, M. S. and Kirk, K. L. (2006b). "Top-down and bottom-up estimates of CO2 storage capacity in the United Kingdom sector of the southern North Sea basin." Environmental Geosciences **13**(2): 71-84.

Holloway, S., Vincent, C. J. and Kirk, K. L. (2006a). Industrial Carbon Dioxide Emissiona and Carbon Dioxide Storage Potential in the UK, British Geological Survey.

Holt, R., Nes, O. and Fjaer, E. (2005). "In-situ stress dependence of wave velocities in reservoir and overburden rocks." The Leading Edge **24**(12): 1268-1274.

Hudson, J. A. (1993). Comprehensive rock engineering: principles, practice & projects. Oxford, Pergamon.

IEA. (2009a). "World primary energy demand by fuel in the Reference Scenario." Retrieved 23/04/2010, from http://www.iea.org/country/graphs/weo_2009/fig1-1.jpg.

IEAGHG (2011b). Caprock systems for CO_2 Geological Storage, IEAGHG. **2011/01**.

IMechE. (2013, 24/09/2013). "Centrica scraps plans for new gas storage." Retrieved 06/05/2014, 2014, from http://www.imeche.org/news/engineering/centrica-scraps-plans-for-new-gas-storage.

IPCC (2005). IPCC Special Report on Carbon Dioxide Capture and Storage. Cambridge, Cambridge University Press.

Israelsson, P. H., Chow, A. C. and Adams, E. E. (2009). "An updated assessment of the acute impacts of ocean carbon sequestration by direct injection." International Journal of Greenhouse Gas Control **4**(2): 262-271.

Ji, S., Gu, Q. and Xia, B. (2006). "Porosity dependence of mechanical properties of solid materials." Journal of Materials Science **41**(6): 1757-1768.

Johnson, H., Warrington, G. and Stoker, S. J. (1994). 6. Permian and Triassic of the Southern North Sea. Lithostratigrapic Nomenclature of the UK North Sea. Knox, R. W. O. B. and Cordey.W.G., British Geological Survey Nottingham.

Johnston, J. E. and Christensen, N. I. (1995). "Seismic anisotropy of shales." Journal of Geophysical Research: Solid Earth (1978–2012) **100**(B4): 5991-6003.

Jolley, S. J., Dijk, H., Lamens, J. H., Fisher, Q. J., Manzocchi, T., Eikmans, H. and Huang, Y. (2007). "Faulting and fault sealing in production simulation models: Brent Province, northern North Sea." Petroleum Geoscience **13**(4): 321-340.

Jolley, S. J., Fisher, Q. J. and Ainsworth, R. B. (2010). Reservoir compartmentalization: an introduction. Reservoir Compartmentalization. Jolley, S. J., Fisher, Q. J., Ainsworth, R. B., Vrolijk, P. J. and Delisle, S. London, The Geological Society of London. **347:** 1-8.

Jones, R. M. and Hillis, R. R. (2003). "An integrated, quantitative approach to assessing fault-seal risk." AAPG Bulletin **87**(3): 507-524.

Juanes, R., Spiteri, E. J., Orr, F. M. and Blunt, M. J. (2006). "Impact of relative permeability hysteresis on geological CO_2 storage." Water Resources Research **42**.

Kendall, J.-M., Fisher, Q. J., Crump, S. C., Maddock, J., Carter, A., Hall, S. A., Wookey, J., Valcke, S. L. A., Casey, M., Lloyd, G. and Ismail, W. B. (2007). "Seismic anisotropy as an indicator of reservoir quality in siliciclastic rocks." Geological Society, London, Special Publications **292**(1): 123-136.

Ketter, F. J. (1991). "The Esmond, Forbes and Gordon Fields, Blocks 43/8a, 43/13a, 43/15a, 43/20a, UK North Sea." Geological Society, London, Memoirs **14**(1): 425-432.

Khan, M., Teufel, L. W. and Zheng, Z. (2000). "Determining the Effect of Geological and Geomechanical Parameters on Reservoir Stress path through Numerical Simulation." SPE International **63261**.

Kita, J., Ohsumi, T., Rubin, E. S., Keith, D. W., Gilboy, C. F., Wilson, M., Morris, T., Gale, J. and Thambimuthu, K. (2005). Biological impact assessment of direct CO2 injection into the ocean. Greenhouse Gas Control Technologies 7. Oxford, Elsevier Science Ltd**:** 783-789.

Knipe, R. J. (1997). "Juxtaposition and Seal Diagrams to Help Analyze Fault Seals in Hydrocarbon Reservoirs." AAPG Bulletin **81**(2): 187-195.

Kováčik, J. (1999). "Correlation between Young's modulus and porosity in porous materials." Journal of Materials Science Letters **18**(13): 1007-1010.

Kudryavtsev, V. A., Spooner, N. J. C., Gluyas, J., Fung, C. and Coleman, M. (2012). "Monitoring subsurface CO2 emplacement and security of storage using muon tomography." International Journal of Greenhouse Gas Control **11**(0): 21-24.

Lake, L. W. (1988). "The Origins of Anisotropy." Journal of Petroleum Technology **40**(4): 395-396.

Lee, M. Y. and Haimson, B. C. (1989). "Statistical evaluation of hydraulic fracturing stress measurement parameters." International Journal of Rock Mechanics and Mining Sciences & Geomechanics Abstracts **26**(6): 447-456.

Luo, Z. and Bryant, S. (2011). "Influence of thermo-elastic stress on fracture initiation during CO2 injection and storage." Energy Procedia **4**: 3714-3721.

Lynch, T. (2010). Carbon Capture Transport and Storage in Yorkshire and Humber, MSc Thesis. MSc Thesis, University of Leeds.

Mandl, G. (2005). Rock Joints: The Mechanical Genesis. Berlin, Springer.

Manzocchi, T., Childs, C. and Walsh, J. J. (2010). "Faults and fault properties in hydrocarbon flow models." Geofluids **10**(1-2): 94-113.

Manzocchi, T., Walsh, J. J., Nell, P. and Yielding, G. (1999). "Fault transmissibility multipliers for flow simulation models." Petroleum Geoscience **5**(1): 53-63.

Manzocchi, T., Walsh, J. J., Nell, P. and Yielding, G. (1999). "Fault transmissibility multipliers for flow simulation models." Petroleum Geoscience **5**: 53-63.

Mathieson, A., Wright, I., Roberts, D. and Ringrose, P. (2009). "Satellite imaging to monitor CO2 movement at Krechba, Algeria." Energy Procedia **1**(1): 2201-2209.

Mavko, G., Mukerji, T. and Dvorkin, J. (2009). The rock physics handbook: Tools for seismic analysis of porous media, Cambridge University Press.

McCain, W. (1990). The properties of petroleum fluids, PennWell Books.

Michael, K., Neal, P. R., Allinson, G., Ennis-King, J., Hou, W., Paterson, L., Sharma, S. and Aiken, T. (2011). "Injection strategies for large-scale CO2 storage sites." Energy Procedia **4**: 4267-4274.

Minkoff, S. E., Stone, C. M., Bryant, S. and Peszynska, M. (2004). "Coupled geomechanics and flow simulation for time-lapse seismic modeling." Geophysics **69**(1): 200-211.

Morton, K., Thomas, S., Corbett, P. and Davies, D. (2002). "Detailed analysis of probe permeameter and interval pressure transient test permeability measurements in a heterogeneous reservoir." Petroleum Geoscience **8**(3): 209-216.

Neal, P. R., Cinar, Y. and Allinson, W. G. (2011). "The economics of pressure-relief with CO2 injection." Energy Procedia **4**: 4215-4220.

Newman, G. H. (1973). "Pore-Volume Compressibility of Consolidated, Friable, and Unconsolidated Reservoir Rocks Under Hydrostatic Loading."

Noy, D. J., Holloway, S., Chadwick, R. A., Williams, J. D. O., Hannis, S. A. and Lahann, R. W. (2012). "Modelling large-scale carbon dioxide injection into the Bunter Sandstone in the UK Southern North Sea." International Journal of Greenhouse Gas Control **9**(0): 220-233.

Nygård, R., Gutierrez, M., Bratli, R. K. and Høeg, K. (2006). "Brittle–ductile transition, shear failure and leakage in shales and mudrocks." Marine and Petroleum Geology **23**(2): 201-212.

Nygård, R., Gutierrez, M., Gautam, R. and Høeg, K. (2004). "Compaction behavior of argillaceous sediments as function of diagenesis." Marine and Petroleum Geology **21**(3): 349-362.

Oñate, E. and Rojek, J. (2004). "Combination of discrete element and finite element methods for dynamic analysis of geomechanics problems." Computer Methods in Applied Mechanics and Engineering **193**(27–29): 3087-3128.

Onuma, T. and Ohkawa, S. (2009). "Detection of surface deformation related with CO2 injection by DInSAR at In Salah, Algeria." Energy Procedia **1**(1): 2177-2184.

Orr, F. M. (2004). "Storage of Carbon Dioxide in Geological Formations." Journal of Petroleum Technology **Distinguished Author Series**.

Pettersen, Ø. and Kristiansen, T. G. (2009). "Improved Compaction Modeling in Reservoir Simulation and Coupled Rock Mechanics—Flow Simulation, With Examples From the Valhall Field." Reservoir Evaluation and Engineering **SPE-113003-PA**.

Pouya, A., Djéran-Maigre, I., Lamoureux-Var, V. and Grunberger, D. (1998). "Mechanical behaviour of fine grained sediments: experimental compaction and three-dimensional constitutive model." Marine and Petroleum Geology **15**(2): 129-143.

Qi, R., LaForce, T. C. and Blunt, M. J. (2009). "Design of carbon dioxide storage in aquifers." International Journal of Greenhouse Gas Control **3**(2): 195-205.

Ramm, M. (1992). "Porosity-depth trends in reservoir sandstones: theoretical models related to Jurassic sandstones offshore Norway." Marine and Petroleum Geology **9**(5): 553-567.

Ringrose, P. S., Mathieson, A. S., Wright, I. W., Selama, F., Hansen, O., Bissell, R., Saoula, N. and Midgley, J. (2013). "The In Salah CO2 Storage Project: Lessons Learned and Knowledge Transfer." Energy Procedia **37**(0): 6226-6236.

Rockfield Software Limited (2012). ELFEN GeoDB Generic Materials. Swansea.

Roscoe, K. H., Schofield, A. N. and Wroth, C. P. (1958) "On The Yielding of Soils." Geotechnique **8**, 22-53.

Rousseau, J., Marin, P., Daudeville, L. and Potapov, S. (2010). "A discrete element/shell finite element coupling for simulating impacts on reinforced concrete structures." European Journal of Computational Mechanics/Revue Européenne de Mécanique Numérique **19**(1-3): 153-164.

RPS Energy (2009). Bacton Storage Company: Baird Gas Storage Project - Offshore Environmental Impact Assessment. **Ref: BD-017-EV-RPT-002**.

Rutqvist, J., Vasco, D. W. and Myer, L. (2010). "Coupled reservoir-geomechanical analysis of CO2 injection and ground deformations at In Salah, Algeria." International Journal of Greenhouse Gas Control **4**(2): 225-230.

Santarelli, F. J., Havmøller, O. and Naumann, M. (2008). "Geomechanical Aspects of 15 Years Water Injection on a Field Complex: An Analysis of the Past to Plan the Future." SPE International **SPE 112944**.

Santarelli, F. J., Tronvoll, J. T., Henriksen, R. and Bratli, R. K. (1998). "Reservoir Stress Path: The Depletion and the Rebound " SPE International **SPE 47350**.

Sayers, C. (2005). "Seismic anisotropy of shales." Geophysical Prospecting **53**(5): 667-676.

Sayers, C. M. (2006). "Sensitivity of time-lapse seismic to reservoir stress path." Geophysical Prospecting **54**(3): 369-380.

Sayers, C. M. (2007). "Asymmetry in the time-lapse seismic response to injection and depletion." Geophysical Prospecting **55**(5): 699-705.

Sayers, C. M. and Schutjens, P. M. (2007). "An introduction to reservoir geomechanics." The Leading Edge **26**(5): 597-601.

SCCS (2011b). Progressing Scotland's CO_2 storage opportunities, Scottish Carbon Capture and Storage.

Schlumberger. (2010b). "Waterdrive." Retrieved 22/04/2010, from http://www.glossary.oilfield.slb.com/DisplayImage.cfm?ID=532.

Schoenberg, M. and Sayers, C. M. (1995). "Seismic anisotropy of fractured rock." Geophysics **60**(1): 204-211.

Schowalter, T. T. (1979). "Mechanics of Secondary Hydrocarbon Migration and Entrapment." AAPG Bulletin **63**(5): pp.723-760.

Schutjens, P. M. T. M., Hanssen, T. H., Hettema, M. H. H., Merour, J., de Bree, J. P., Coremans, J. W. A. and Helliesen, G. (2001). Compaction-induced porosity/permeability reduction in sandstone reservoir. SPE Annual Technical Conference and Exhibition. New Orleans, Louisiana, SPE.

Scott, T. E. and Nielsen, K. (1991). "The effects of porosity on the brittle ‐ ductile transition in sandstones." Journal of Geophysical Research: Solid Earth (1978–2012) **96**(B1): 405-414.

Segura, J. M., Fisher, Q. J., Crook, A. J. L., Dutko, M., Yu, J. G., Skachkov, S., Angus, D. A., Verdon, J. P. and Kendall, J.-M. (2011). "Reservoir stress path characterization and its implications for fluid-flow production simulations." Petroleum Geoscience **17**(4): 335-344.

Senior, B. (2010). CO_2 Storage in the UK - Industry Potential. Department of Energy and Climate Change. London. **URN 10D/512**.

Settari, A. (2002). "Reservoir Compaction." Journal of Petroleum Technology **54**(08).

Settari, A. and Walters, D. (2001). "Advances in coupled geomechanical and reservoir modeling with applications to reservoir compaction." SPE Journal **6**(3): 334-342.

Smith, D. J., Noy, D. J., Holloway, S. and Chadwick, R. A. (2011). "The impact of boundary conditions on CO2 storage capacity estimation in aquifers." Energy Procedia **4**(0): 4828-4834.

Smith, R. L. and McGarrity, J. P. (2001). "Cracking the fractures—seismic anisotropy in an offshore reservoir." The Leading Edge **20**(1): 18-26.

Solberg, P., Lockner, D. and Byerlee, J. (1977). "Shear and tension hydraulic fractures in low permeability rocks." pure and applied geophysics **115**(1-2): 191-198.

Staples, R., Ita, J., Burrell, R. and Nash, R. (2007). "Monitoring pressure depletion and improving geomechanical models of the Shearwater Field using 4D seismic." The Leading Edge **26**(5): 636-642.

Stern, N. H. (2007). The Economics of Climate Change: The Stern Review. Cambridge, Cambridge University Press.

Swarbrick, R. E. and Osborne, M. J. (1998). Mechanisms that Generate Abnormal Pressures: an Overview. Abnormal pressures in hydrocarbon environments: AAPG Memoir 70. Law, B. E., Ulmishek, G. F. and Slavin, V. I. Tulsa, AAPG**:** p.13-34.

Teufel, L. W., Rhett, D. W. and Farrell, H. E. (1991). Effect of Reservoir Depletion And Pore Pressure Drawdon On In Situ Stress And Deformation In the Ekofisk Field, North Sea. 32nd U.S. Symposium on Rock Mechanics (USRMS). Norman, Oklahoma.

Thibeau, S. and Dutin, A. (2011). "Large scale CO2 storage in unstructured aquifers: Modeling study of the ultimate CO2 migration distance." Energy Procedia **4**(0): 4230-4237.

Thomas, L. K., Chin, L. Y., Pierson, R. G. and Sylte, J. E. (2003). Coupled Geomechanics and Reservoir Simulation. SPE Annual Technical Conference and Exhibition. San Antonio, Texas, Society of Petroleum Engineers. **SPE-77723-MS**.

Truss, S. W. (2004). Characterisation of sediementary structure and hydraulic behaviour within the unsaturated zone of the Triassic Sherwood Sandstone aquifer in North East England. PhD, University of Leeds.

Tueckmantel, C. (2010). Fluid flow properties and fault zone architecture of large- and small-scale normal faults. PhD, University of Leeds.

Tueckmantel, C., Fisher, Q. J., Grattoni, C. A. and Aplin, A. C. (2012). "Single- and two-phase fluid flow properties of cataclastic fault rocks in porous sandstone." Marine and Petroleum Geology **29**(1): 129-142.

Urbancic, T. I., Daugherty, J., Bowman, S. and Prince, M. (2009). "Microseismic Monitoring of a Carbon Sequestration Field Test." EAGE Passive Seismic.

Verdon, J. P., Angus, D. A., Kendall, J. M. and Hall, S. A. (2008). "The effect of microstructure and nonlinear stress on anisotropic seismic velocities." Geophysics **73**(4): 41-51.

Verdon, J. P. and Kendall, J. M. (2011). "Detection of multiple fracture sets using observations of shear-wave splitting in microseismic data." Geophysical Prospecting **59**(4): 593-608.

Verdon, J. P., Kendall, J. M., White, D. J. and Angus, D. A. (2011). "Linking microseismic event observations with geomechanical models to minimise the risks of storing CO2 in geological formations." Earth and Planetary Science Letters **305**(1-2): 143-152.

Verdon, J. P., Kendall, J. M., White, D. J., Angus, D. A., Fisher, Q. J. and Urbancic, T. (2010). "Passive seismic monitoring of carbon dioxide storage at Weyburn." The Leading Edge **29**(2): 200-206.

Vidal-Gilbert, S., Nauroy, J.-F. and Brosse, E. (2009). "3D geomechanical modelling for CO2 geologic storage in the Dogger carbonates of the Paris Basin." International Journal of Greenhouse Gas Control **3**(3): 288-299.

Vidal-Gilbert, S., Tenthorey, E., Dewhurst, D., Ennis-King, J., Van Ruth, P. and Hillis, R. (2010). "Geomechanical analysis of the Naylor Field, Otway Basin, Australia: Implications for CO2 injection and storage." International Journal of Greenhouse Gas Control **In Press, Corrected Proof**.

Walderhaug, O. (1996). "Kinetic modeling of quartz cementation and porosity loss in deeply buried sandstone reservoirs." AAPG Bulletin **80**(5): 731-745.

Washburn, E. W. (1921). "The Dynamics of Capillary Flow." Physical Review **17**(3): pp. 273-283.

White, A. J., Traugott, M. O. and Swarbrick, R. E. (2002). "The use of leak-off tests as means of predicting minimum in-situ stress." Petroleum Geoscience **8**(2): 189-193.

White, D. J. (2011). "Geophysical monitoring of the Weyburn CO2 flood: Results during 10 years of injection." Energy Procedia **4**: 3628-3635.

Wilkins, S. J. and Naruk, J. (2007). "Qunatitative analysis of slip-induced dilation with application to fault seal." AAPG Bulletin **91**(1): 97-113.

Williams, J. D. O., Holloway, S. and Williams, G. A. (2014). "Pressure constraints on the CO2 storage capacity of the saline water-bearing parts of the Bunter Sandstone Formation in the UK Southern North Sea." Petroleum Geoscience **20**(2): 155-167.

Williams, J. D. O., Jin, M., Bentham, M., Pickup, G. E., Hannis, S. D. and Mackay, E. J. (2013). "Modelling carbon dioxide storage within closed structures in the UK Bunter Sandstone Formation." International Journal of Greenhouse Gas Control **18**(0): 38-50.

Wiprut, D. and Zoback, M. D. (2000). "Fault reactivation and fluid flow along a previously dormant normal fault in the northern North Sea." Geology **28**(7): 595-598.

Wong, T.-f., David, C. and Zhu, W. (1997). "The transition from brittle faulting to cataclastic flow in porous sandstones: Mechanical deformation." Journal of Geophysical Research: Solid Earth **102**(B2): 3009-3025.

Wood, D. W. (1990). Soil behaviour and critical state soil mechanics. Cambridge, Cambridge University Press.

Yale, D. P. (2002). Coupled Geomechanics-Fluid Flow Modeling: Effects of Plasticity and Permeability Alteration. SPE/ISRM Rock Mechanics Conference. Irving, Texas, Society of Petroleum Engineers. **SPE-78202-MS**.

Yale, D. P., Nabor, G. W., Russell, J. A., Pham, H. D. and Yousef, M. (1993). Application of Variable Formation Compressibility for Improved Reservoir Analysis. SPE Annual Technical Conference and Exhibition. Houston Texas, Society of Petroleum Engineers. **SPE-26647-MS**.

Yates, P. G. J. (1992). "The material strength of sandstones of the Sherwood Sandstone Group of north Staffordshire with reference to microfabric." Quarterly Journal of Engineering Geology and Hydrogeology **25**(2): 107-113.

Yielding, G., Bretan, P. and Freeman, B. (2010). Fault seal calibration: a brief review. Reservoir Compartmentalization. Jolley, S. J., Fisher, Q. J., Ainsworth, R. B., Vrolijk, P. J. and Delisle, S. London, The Geological Society of London. **347:** 243-255.

Yielding, G., Freeman, B. and Needham, T. D. (1997). "Quantitative Fault Seal Predicition." AAPG Bulletin **81**(6): 897-917.

Zhang, J. J., Rai, C. S. and Sondergeld, C. H. (2000). "Mechanical Strength of Reservoir Materials: Key Information for Sand Prediction." SPE Reservoir Evaluation & Engineering **SPE-62499-PA**.

Zhou, Q., Birkholzer, J. T., Tsang, C. and Rutqvist, J. (2008). "A method for quick assessment of CO2 storage capacity in close and semi-closed saline formations." International Journal of Greenhouse Gas Control **2**(2008): 626-639.

Zhu, W. and Wong, T.-f. (1997). "The transition from brittle faulting to cataclastic flow: Permeability evolution." Journal of Geophysical Research: Solid Earth **102**(B2): 3027-3041.

Zienkiewicz, O. C. and Cheung, Y. K. (1964). The finite element method for analysis of elastic isotropic and orthotropic slabs. ICE Proceedings, Ice Virtual Library.
Zienkiewicz, O. C. and Taylor, R. L. (1977). The finite element method, McGraw-hill London.
Zimmerman, R. W. (1990). Compressibility of sandstones, Elsevier.
Zoback, M. D. (2007). Reservoir Geomechanics. Cambridge, Cambridge University Press.

A. Appendix

Example Tempest input script for the generic Bunter model.

```
--------------------------------------------
-- MORE General Data Input File
-- Created on November 11, 2010 at 12:42:06 PM
--------------------------------------------
--------------------------------------------
INPUT
--------------------------------------------

TITL Base Case Brine producton

--* Choose unit set - options are POFU (field) or METR (metric)
UNIT METR

--* Initial time or date
--*
IDAT    01 Jan 2000

--* Start time or date - set later than initial date for restart
run
--*
SDAT    01 Jan 2000

--* Output data required for streamlines
STREAM

--* Mobile saturation weighting for wellbore density
WDOP MSAT

--------------------------------------------
-- FLUI
--------------------------------------------
--------------------------------------------
-- MORE Fluid Data Input File
-- Created on November 2, 2010 at 8:27:40 PM
--------------------------------------------

--* Component names
CNAM    GAS   WATR

--------------------------------------------
FLUID BLACKOIL
--------------------------------------------
--Original Values
----* densSTP(kg/m3)  densRef(kg/m3)  comp(1/bar)  pRef(bar)
visc(cp)

WATR
          1082.54         1060.24  3.74673e-05    1.01353   0.55511
/

/

--

--* Basic oil and gas properties
--* Surf.Oil.Dens(kg/m3), Oil Mw, Gas gravity/Mw
BASIC
```

```
        848.9784          188.812         44.01
/

GPVT
   9.99740  107.566  0.00160   /
   25.0004  39.9651  0.00160   /
   50.0008  17.0206  0.00170   /
   75.0012  8.65724  0.00200   /
   100.002  3.42175  0.00330   /
   150.002  2.49506  0.00600   /
   200.003  2.31731  0.00720   /
   250.004  2.21726  0.00800   /
   299.998  2.14786  0.00880   /
   349.999  2.09486  0.00940   /
   399.999  2.05207  0.01000   /
   450.000  2.01625  0.01060   /
   500.001  1.98543  0.01120   /
   600.002  1.93445  0.01220   /
   700.004  1.89324  0.01310   /
   799.999  1.85865  0.01410   /
   900.000  1.82895  0.01500   /
   1000.00  1.80290  0.01590   /
/

------------------------------------------------
RELA
------------------------------------------------
------------------------------------------------
-- MORE Rel Perm Data Input File
-- Created on November 2, 2010 at 8:27:40 PM
------------------------------------------------

-- Host Rock Rel Perms from Chistian Tueckmantel Thesis
-- Converted from Eclispe - Lab data input

--Host rock

KRWO
2.100000E-01      0.000000E+00      5.850938E-01      1.661537E+03
2.200000E-01      3.906250E-07      5.703750E-01      2.937211E+02
2.300000E-01      1.977539E-06      5.558438E-01      1.065877E+02
2.400000E-01      6.250000E-06      5.415000E-01      5.192304E+01
2.500000E-01      1.525879E-05      5.273438E-01      2.972248E+01
2.600000E-01      3.164062E-05      5.133750E-01      1.884222E+01
2.700000E-01      5.861816E-05      4.995938E-01      1.281637E+01
2.800000E-01      1.000000E-04      4.860000E-01      9.178783E+00
2.900000E-01      1.601807E-04      4.725938E-01      6.837602E+00
3.000000E-01      2.441406E-04      4.593750E-01      5.254243E+00
3.100000E-01      3.574463E-04      4.463438E-01      4.140268E+00
3.200000E-01      5.062500E-04      4.335000E-01      3.330865E+00
3.300000E-01      6.972900E-04      4.208438E-01      2.726790E+00
3.400000E-01      9.378906E-04      4.083750E-01      2.265635E+00
3.500000E-01      1.235962E-03      3.960938E-01      1.906698E+00
3.600000E-01      1.600000E-03      3.840000E-01      1.622595E+00
3.700000E-01      2.039087E-03      3.720938E-01      1.394401E+00
3.800000E-01      2.562891E-03      3.603750E-01      1.208729E+00
3.900000E-01      3.181665E-03      3.488438E-01      1.055908E+00
4.000000E-01      3.906250E-03      3.375000E-01      9.288279E-01
4.100000E-01      4.748071E-03      3.263438E-01      8.221708E-01
4.200000E-01      5.719141E-03      3.153750E-01      7.319026E-01
4.300000E-01      6.832056E-03      3.045938E-01      6.549235E-01
4.400000E-01      8.100000E-03      2.940000E-01      5.888193E-01
```

```
4.500000E-01      9.536743E-03      2.835938E-01      5.316919E-01
4.600000E-01      1.115664E-02      2.733750E-01      4.820329E-01
4.700000E-01      1.297463E-02      2.633438E-01      4.386324E-01
4.800000E-01      1.500625E-02      2.535000E-01      4.005115E-01
4.900000E-01      1.726760E-02      2.438438E-01      3.668724E-01
5.000000E-01      1.977539E-02      2.343750E-01      3.370598E-01
5.100000E-01      2.254690E-02      2.250938E-01      3.105317E-01
5.200000E-01      2.560000E-02      2.160000E-01      2.868370E-01
5.300000E-01      2.895315E-02      2.070938E-01      2.655983E-01
5.400000E-01      3.262539E-02      1.983750E-01      2.464977E-01
5.500000E-01      3.663635E-02      1.898438E-01      2.292662E-01
5.600000E-01      4.100625E-02      1.815000E-01      2.136751E-01
5.700000E-01      4.575588E-02      1.733438E-01      1.995289E-01
5.800000E-01      5.090664E-02      1.653750E-01      1.866600E-01
5.900000E-01      5.648049E-02      1.575938E-01      1.749237E-01
6.000000E-01      6.250000E-02      1.500000E-01      1.641951E-01
6.100000E-01      6.898831E-02      1.425938E-01      1.543656E-01
6.200000E-01      7.596914E-02      1.353750E-01      1.453406E-01
6.300000E-01      8.346682E-02      1.283438E-01      1.370374E-01
6.400000E-01      9.150625E-02      1.215000E-01      1.293834E-01
6.500000E-01      1.001129E-01      1.148438E-01      1.223148E-01
6.600000E-01      1.093129E-01      1.083750E-01      1.157752E-01
6.700000E-01      1.191328E-01      1.020938E-01      1.097149E-01
6.800000E-01      1.296000E-01      9.600000E-02      1.040895E-01
6.900000E-01      1.407422E-01      9.009375E-02      9.885985E-02
7.000000E-01      1.525879E-01      8.437500E-02      9.399078E-02
7.100000E-01      1.651660E-01      7.884375E-02      8.945092E-02
7.200000E-01      1.785063E-01      7.350000E-02      8.521216E-02
7.300000E-01      1.926387E-01      6.834375E-02      8.124947E-02
7.400000E-01      2.075941E-01      6.337500E-02      7.753995E-02
7.500000E-01      2.234039E-01      5.859375E-02      7.406334E-02
7.600000E-01      2.401000E-01      5.400000E-02      7.080109E-02
7.700000E-01      2.577149E-01      4.959375E-02      6.773653E-02
7.800000E-01      2.762816E-01      4.537500E-02      6.485450E-02
7.900000E-01      2.958340E-01      4.134375E-02      6.214127E-02
8.000000E-01      3.164063E-01      3.750000E-02      5.958432E-02
8.100000E-01      3.380332E-01      3.384375E-02      5.717228E-02
8.200000E-01      3.607504E-01      3.037500E-02      5.489476E-02
8.300000E-01      3.845938E-01      2.709375E-02      5.274226E-02
8.400000E-01      4.096000E-01      2.400000E-02      5.070610E-02
8.500000E-01      4.358063E-01      2.109375E-02      4.877831E-02
8.600000E-01      4.632504E-01      1.837500E-02      4.695159E-02
8.700000E-01      4.919707E-01      1.584375E-02      4.521922E-02
8.800000E-01      5.220063E-01      1.350000E-02      4.357504E-02
8.900000E-01      5.533965E-01      1.134375E-02      4.201336E-02
9.000000E-01      5.861816E-01      9.375000E-03      4.052892E-02
9.100000E-01      6.204024E-01      7.593750E-03      3.911688E-02
9.200000E-01      6.561000E-01      6.000000E-03      3.777277E-02
9.300000E-01      6.933164E-01      4.593750E-03      3.649245E-02
9.400000E-01      7.320941E-01      3.375000E-03      3.527206E-02
9.500000E-01      7.724762E-01      2.343750E-03      3.410805E-02
9.600000E-01      8.145063E-01      1.500000E-03      3.299713E-02
9.700000E-01      8.582285E-01      8.437500E-04      3.193620E-02
9.800000E-01      9.036879E-01      3.750000E-04      3.092243E-02
9.900000E-01      9.509297E-01      9.375000E-05      2.995314E-02
1.000000E+00      1.000000E+00      0.000000E+00      2.902587E-02

/
-----------------------------------------------
GRID
-----------------------------------------------
```

```
--* Set datum for well bhp pressures, use top open completion
DATUM 800.000 TOPC /

--* Flow Options
HORI BLOCK
VERT BLOCK

--* Grid geometry
-----------------------------------------------
-- MORE Grid Geometry Input File
-- Created on November 21, 2013 at 11:19:10 AM
-----------------------------------------------

--* Grid dimensions
SPEC
25 25 5 /

COOR
         0.00000         0.00000         1500.00         0.00000
0.00000         1640.00
         304.800         0.00000         1500.00         304.800
0.00000         1640.00
         609.600         0.00000         1500.00         609.600
0.00000         1640.00
         914.400         0.00000         1500.00         914.400
0.00000         1640.00
         1219.20         0.00000         1500.00
GRID FILE TRUNCATED FOR BREVITY
/

--* Set Depth
ZCORn
2500*1500.00
2500*1528.00
2500*1528.00
2500*1556.00
2500*1556.00
2500*1584.00
2500*1584.00
2500*1612.00
2500*1612.00
2500*1640.00
/
--* Grid property arrays
-----------------------------------------------
-- MORE Grid Array Data Input File
-- Created on November 11, 2010 at 12:42:07 PM
-----------------------------------------------

--* Set X - Permeability
K_X VARI
3125*100.000 /

--* Set Y - Permeability
K_Y VARI
3125*100.000 /

--* Set Z - Permeability
K_Z VARI
3125*10.0000 /

--* Set Porosity
```

```
PORO VARI
3125*0.20000 /

--* Set rock compressibility
CROC UNIF
CONS
4.500000e-05 /

--* Set rock reference pressure
REFE UNIF
CONS
157.600 /

-----------------------------------------------
INIT EQUI
-----------------------------------------------
-----------------------------------------------
-- MORE Init Data Input File
-- Created on November 11, 2010 at 12:42:07 PM
-----------------------------------------------

--* Specify fluid contacts
--* Dref(m) Pref(bar) GOC(m) Pcgo(bar) GWC(m) Pcgw(bar)
EQUI
    1500  159    2* 1500 0.00000   /
/

--* Specify equilibrium conditions
-- Temp(C) PSat(bar)
CONSTANT 1
 121.111 159.092 /

-----------------------------------------------
RECU
-----------------------------------------------
-----------------------------------------------
-- MORE Dynamic Data Input File
-- Created on November 11, 2010 at 12:42:07 PM
-----------------------------------------------

--* Treat wells at edge of grid same way as other wells
WCOR OFF

--* Group targets apply to net rather than gross rates
GTAR NET

--* Report rates every step to screen and .out file, every month to
.rat file
RATE 1 MONTH
FREQ 0 0 1

--* Write array data every year
ARRAY YEAR EQUA
1 /

--* Request restart and fluid in place reports
GENE REST FLIP

--* Specify well trajectory in true xyz space
TTAB
--* x       y         z        md
WINJ
```

```
  0.000  0.000  1500.000  1500.000
  0.000  0.000  1640.000  1640.000
WPRD
  7620  7620  1500.000  1500.000
  7620  7620  1640.000  1640.000
ENDT

--* Define well completions and targets using events
EFOR 'dd/mmm/yyyy'   MDL   MDU   RAD   SKIN   MULT
ETAB
ALL
  01/Jan/2030  END      / simulation end date

WINJ
  01/Jan/2000  INJE
  01/Jan/2000  PERF    1500   1640     0.15240   0.00000   1.00000
  01/Jan/2000  BHPT    212
  01/Jan/2000  GIT     100000.0

WPRD
  01/Jan/2000  PROD
  01/Jan/2000  PERF    1500   1640     0.15240   0.00000   1.00000
  01/Jan/2000  WPT     25.000
ENDE
```

B. Appendix

The yield function $\Phi(\sigma, \varepsilon_v^p)$ represents a smooth three-invariant surface that intersects the hydrostatic axis in tension and compression (Crook et al. 2006):

$$\Phi\left(\sigma, \varepsilon_v^p\right) = g(\theta, p)q + (p - p_t)\tan\beta\left(\frac{p-p_c}{p_t-p_c}\right)^{1/n} \qquad \textbf{Equation B.1}$$

where β and n are material constants, p_c and p_t are the compressive and tensile intercepts on the hydrostatic axis, θ is the Lode angle and g (θ, p) is the deviatoric plane correction term defined in Equation B.5. The evolution of the yield function, which represents strain hardening or strain softening, is controlled by the plastic volumetric strain ε_v^p, according to the relationships:

$$p_c = p_{c0}\exp\left[\frac{v\varepsilon_v^p}{(\lambda-\kappa)}\right] \; and \; p_t = p_{t0}\exp\left[\frac{v(\varepsilon_v^p)_{max}}{(\lambda-\kappa)}\right] \qquad \textbf{Equation B.2}$$

where v is the specific volume, p_{c0} and p_{t0} are the initial p_c and p_t intercepts, $(\varepsilon_v^p)_{max}$ is the maximum dilatational volumetric plastic strain, λ is the slope of the normal compression line and κ is the slope of the unloading-reloading line (Crook et al. 2006). The flow rule in the SR3 model is non-associated and so the plastic strain rate is defined separately as:

$$\dot{\varepsilon}^p = \dot{\lambda}\frac{\partial\Psi}{\partial\sigma} \qquad \textbf{Equation B.3}$$

where the plastic potential $\Psi(\sigma, \varepsilon vp)$ is defined in Equation B.4, and $\dot{\lambda}$ is the plastic multiplier. The plastic multiplier is subject to the loading/unloading criterion $\Phi(\sigma,q) \leq 0 \;\; \dot{\lambda} \geq 0$ $\dot{\lambda}\,\Phi(\sigma,q) = 0$ and the plastic potential is:

$$\Psi\left(\sigma, \varepsilon_v^p\right) = g(\theta, p)q + (p - p_t)\tan\psi\left(\frac{p-p_c}{p_t-p_c}\right)^{1/n} \qquad \textbf{Equation B.4}$$

where ψ is a material parameter which influences the shape of the plastic potential surface, once again g (θ, p) is defined in Equation B.5. The deviatoric plane correction term controls the shape of the yield surface in the deviatoric plane, and is:

$$g(\theta, p) = \left[\frac{1}{1-\beta^\pi(p)}\left(1 + \beta^\pi(p)\frac{r^3}{q^3}\right)\right]^{N^\pi} \qquad \textbf{Equation B.5}$$

where N^π is a material constant and β^π is defined in Equation B.6, where two further material constants β^π_0 and β^π_1 are required:

$$\beta^\pi(p) = \beta_0^\pi\exp\left(\beta_1^\pi p\frac{p_c^0}{p_c}\right) \qquad \textbf{Equation B.6}$$